Understanding Solvation Dynamics and Ligand Interactions in DNA and Lipid-Bilayer Using Experiment and Simulation

A Thesis
Submitted for the Degree of

Doctor of Philosophy

Him Shweta

School of Physical Sciences
Jawaharlal Nehru University
New Delhi 110067
India

2017

जवाहरलाल नेहरू विश्वविद्यालय
JAWAHARLAL NEHRU UNIVERSITY
भौतिक विज्ञान संस्थान
SCHOOL OF PHYSICAL SCIENCES
New Delhi - 110067
नई दिल्ली - 110067

July 18, 2017

Declaration

I hereby declare that the work reported in this thesis entitled "**Understanding Solvation Dynamics and Ligand Interactions in DNA and Lipid-Bilayer Using Experiment and Simulation**" is entirely original and has been carried out by myself at the School of Physical Sciences, Jawaharlal Nehru University, New Delhi under the Supervision of Dr. Sobhan Sen. I further declare that neither this thesis nor any part of it has been submitted for any degree/diploma or any other academic award anywhere before.

Him Shweta.
Him Shweta

R. D. Shah

Sobhan Sen
Dr. Sobhan Sen
Thesis Supervisor
School of Physical Sciences
Jawaharlal Nehru University
New Delhi – 110067, India

Prof. Riddhi Shah
Dean
School of Physical Sciences
Jawaharlal Nehru University
New Delhi – 110067, India

Dedicated to
My Parents
For their unconditional support and love

Acknowledgement

First and foremost, I owe my supervisor Dr. Sobhan Sen, a great debt of gratitude for accepting me as his student and guiding me all through. His scientific temperament, ideas, motivation, encouragement and consistent support have been a driving force in my research pursuit. I consider myself extremely lucky to have a supervisor like him, whose selfless time and encouragement were sometimes all those kept me going. His passion for science has set a standard which I wish to imitate as a researcher in future as well. I am in deficit of words to write his role in this thesis compiling endeavour. My obligations to him are infinite.

I would like to thank UGC for giving financial support which helped me to carry out my research work comfortably.

It is indeed a pleasure for me to thank all the faculty members of SPS, especially Prof. R. Rajaraman for his motivation, warm encouragement and hearty wishes. I am grateful to Dr. Pritam Mukhopadhaya for upgrading my knowledge on supramolecular chemistry during Ph.D. course work and for scientific discussions.

It is an opportunity to acknowledge Prof. Riddhi Shah, Dean SPS for her kind cooperation at every step whenever needed.

I would like to express my special thanks of gratitude to my assessment committee members Dr. Neel Sarovar Bhavesh and Dr. Manoj Munde whose valuable suggestions, advice and constructive feedbacks have contributed immensely to improve the quality of the work compiled in this thesis.

I owe my sincere gratitude and very special thanks to my seniors and lab-mates: Sachin Dev Verma, Nibedita Pal, Kiran Moirangethem, Firoz Khan, Kavita, Avinash, Clovis and Deepika for their support, co-operation and encouragement and also for the healthy discussions on the course and scope of research. I am grateful to them for being a part and co-workers/co-authors in many of my research publications and projects, and also for the tremendous amount of hard work and the unending support they have provided to me in carrying out experiments and analysis. Without them, this endeavour would not have been possible. Special thanks to Sachin bhaiya and Nibedita di for being there with me whenever I needed them. They have been a pillar of support for me throughout this Ph.D. journey and for boosting my morale whenever I was low.

I extend my gratitude to Deepika and Clovis for their selfless continuous support and for all the pain they have taken to stay till late hours for making necessary corrections and proof reading of countless pages.

A special thanks to Kiran bhaiya and Firoz bhaiya for sharing their knowledge and for teaching me new techniques and science, as well as to Kavita and Neha for enriching my memories of JNU.

I express my thanks to entire non-teaching staff of the SPS for ensuring wonderful working conditions in the School and in the labs. I also wish to acknowledge the technical staff of AIRF for proving instrumental help in the research work.

I wish to convey sincere thanks to my colleagues and friends: Jyoti, Shravan, Kalyan, Sudhir, Manoj, Girish, Premlata, Varsha, Pragya, Priyanka, Bhavana, Neha, Neetu, Indrajeet, Amodini, Renu, Jyoti Shakya, Lachit, Alok and Puneet with whom I have enjoyed discussing many useful and entertaining events and for their support over last few years and making my life more happening in JNU.

I am lucky enough to have been given the supportive gift of amazing people in my life especially Deepali, Pooja, Anwesha, Vikas, Kshitij, Puspal, Deepika and Nirmal Deep Singh for sharing my worries and happiness and bringing more joy to my life.

It is a proud moment for me to thank Sharmista ma'am for treating me with her unconditional love, and care as a family member. The thought of thanking Gogol gives me immense pleasure whose pure hearted affection has always given me a feeling of being loved.

I convey special thanks to Santosh Bhaiya and chotu for the warmth they showed and for filling my hungry stomach with their yummy snacks and comforting tea.

I owe a big thanks to Tushar for his unrelenting support throughout this process and for instilling confidence in me and my work.

I am forever indebted to my parents for providing me with the best education possible and for their unconditional support, affection and tremendous amount of love that have helped me to complete this thesis. They stood by me all through with tremendous amount of patience and tolerance. They have not only supported me, but also believed in me. My word of thanks cannot repay what they have given me, yet I take this opportunity to thank them for making me what I am. I owe my sincere gratitude to my family members Abhishek, Naveen, Archana for their support, encouragement and for being with me through all thick and thin of my Ph.D. process. I am so proud to thank the youngest member of my family; Shreyansh (Golu) for his pure innocent love and affection and for adding more colours to my life with his lovely talks and stories.

At last I would like to thank almighty god for blessing me with best of what I could have had.

Him Shweta

Contents

Chapter 3: Experimental and Simulation Methods: Application in DNA and Lipid Bilayer

Chapter 4: New Insight of Solvation Dynamics in DNA: Hoechst in A_nT_n-Rich Minor Groove of DNA

Chapter 5: Effect of T·T-Mismatch on Solvation Dynamics in Minor Groove of DNA

Chapter 6: Differential Effects of Mismatched Base-Pairs on Solvation Dynamics in Minor Groove of DNA

Chapter 7: Solvation Dynamics in G-quadruplex DNA

Chapter 8: Solvation Dynamics in G-quadruplex DNA: Dependence of Quadruplex and Ligand Structures

Chapter 9: Static and Dynamic Properties of Lipid Membrane: An Overview

Chapter 10: Precise Quantification of Probe-Location Dependent Polarity and Hydration at Lipid/Water Interfaces

List of Publications

1. “Understanding Ligand Interaction with Different Structures of G-Quadruplex DNA: Evidence of Kinetically Controlled Ligand Binding and Binding-Mode Assisted Quadruplex Structure Alteration”
Verma, S. D.; Pal, N.; Singh, M. K.; Shweta, H.; Khan, M. F.; Sen, S.
Anal. Chem. **2012**, *84,* 7218 – 7226.

*2. “Power-Law Solvation Dynamics in G-Quadruplex DNA: Role of Hydration Dynamics on Ligand Solvation inside DNA”
Pal, N.;[†] Shweta, H.;[†] Singh, M. K.; Verma, S. D.; Sen, S.
J. Phys. Chem. Lett. **2015**, *6,* 1754 – 1760.
([†]Authors contributed equally)

*3. “New Insight into Probe-Location Dependent Polarity and Hydration at Lipid/Water Interfaces: Comparison Between Gel- and Fluid-Phases of Lipid Bilayers”
Singh, M. K.;[†] Shweta, H.;[†] Khan, M. F.; Sen, S.
Phys. Chem. Chem. Phys. **2016**, *35,* 24137 – 24758.
([†]Authors contributed equally) (Inside Front Cover Article)

*4. “Dispersed Dynamics of Solvation in G-quadruplex DNA: Comparison of Dynamic Stokes Shifts of Probes in Parallel and Antiparallel Quadruplex Structures”
Singh, M. K.; Shweta, H.; Sen, S.
Methods Appl. Fluoresc. **2016**, *4,* 034009. (Invited article for Optics Within Life Sciences -2016 special issue) (Author Spotlight)

5. “Probe-Location Dependent Resonance Energy Transfer at Lipid/ Water Interfaces: Comparison Between the Gel- and Fluid-Phase of Lipid Bilayer”
Singh, M. K.; Khan, M. F.; Shweta, H.; Sen, S.
Phys. Chem. Chem. Phys. **2017** (Published online on 10th July, 2017; DOI: 10.1039/C7CP03108D)

6. “Dynamics of Water and Ions near DNA: Perspective from Time-Resolved Fluorescence Stokes Shift Experiments and Molecular Dynamics Simulation”
Shweta, H.; Pal, N.; Singh, M. K.; Verma, S. D.; Sen, S.
Book Chapter - *Reviews in Fluorescence* 2017, Springer (Submitted)

*7. “Effect of T·T-Mismatch on DNA Dynamics Probed by Minor Groove Binders: Comparison of Dynamic Stokes Shifts of Hoechst and DAPI”
Shweta, H.; Singh, M. K.; Yadav, K.; Verma, S. D.; Pal, N.; Sen, S.
2017 (Submitted)

*8. “Differential Effects of Mismatched Base-Pairs on Solvation Dynamics in Minor Groove of DNA”
Shweta, H.; Yadav, K.; Kumar, A.; Sen, S.
(Under Preparation)

*9. “New Insight of Solvation Dynamics in DNA: Hoechst in A_nT_n- Rich Minor Grooves of DNA”
Shweta, H.; Sen, S.
(Under preparation)

---

*Included in this thesis

Chapter 1

Introduction

1.1. Motivation

Water not only acts as elementary solvent, but also directly and/or indirectly participates to facilitate chemical and physical changes in various biomolecules and their complexes, initiating vital biological processes for sustaining life on earth (and may be elsewhere).[1-3] For such reasons, water is rightly called the "matrix of life".[4] Involvement of water molecules in various cellular functions are assisted by their unique properties.[3] Understanding these unique properties of water in-and-around biomolecules is rather a complex task than exploring the biomolecule itself. These (bound) water molecules (and also ions) provide biomolecules the desired flexibility to perform their physiological functions.[3] Interestingly, the water molecules that comprise the outer hydration layer of biomolecules and those inside grooves of DNA, pockets of proteins, and near polar head-groups of lipid bilayers show retarded dynamics, compared to bulk water, owing to partial or full loss of extended hydrogen bond network of (bulk) water near the biomolecules.[2,5-9] Such water molecules exhibit remarkable properties (both static and dynamic) primarily due to multitude of external influence of additional interactions (mainly Coulombic and hydrogen bond) that modify the properties of water molecules – thus, making the complex features of water fascinating, yet highly puzzling, unusual and elusive.[5-9] Molecular re-arrangements of water molecules around biomolecules are highly dynamic that facilitate breaking and formation of fluctuating hydrogen bond networks with the biomolecules as well as among themselves, leading to dynamically heterogeneous hydration/solvation shells around biomolecules. Dynamics of water (and ions), perturbed by these biomolecules, are strongly impacted due to intimate correlation between the structures and dynamics of these biomolecules and the hydration water (and ions). Therefore, the local hydration/solvation properties may vary distinctly from one biomolecular structure to other and even from one site to another within the same biomolecule. However, recent literature argued that hydration water *per se* in-and-around biomolecules is only moderately retarded by factor of 2-3 compared to the bulk water – suggesting that there may not be any strict requirement of a dynamical hydration shell for biomolecular function.[9] On contrary, recent simulation study suggested that the average retardation of protein hydration water is 2-3 times larger than bulk water, but this represents the behaviour of hydration water poorly because there are unusually broad distributions of retarded water molecules which define the hydration layer of proteins.[10] More so, it has been also shown that coupled solvation dynamics of water and protein-segments can vary depending on positions within the proteins.[11-14] Thus, understanding and explanations of the static and dynamic properties of water (and ions) in-and-around biomolecules, which define the local environments within biomolecules, remain highly debated and controversial.[15,16]

Proteins, DNA and lipid-bilayers are different in many ways, but their underlying static and dynamic features are expected to be similar, at least in the outer hydration layers of these biomolecules.[9,10,17,18] However, several recent time-resolved experiments and molecular dynamics (MD) simulation studies showed that the dynamics in DNA, especially in the grooves of DNA, are rather dispersed owing to the fact that there lies strong electrostatic coupling among the negatively charged DNA, positively charged counterions and dipolar water molecules.[9-25] It has been actually shown that dynamics of electrostatic interaction energy (solvation) in DNA is highly non-exponential and dispersed which extend over several decades in time following mostly power-law type relaxations.[9-25] The explanation of such dispersed (solvation) dynamics in DNA remains elusive, and thus, the interpretations are debated strongly. However, it seemed that such differences in the interpretations of DNA solvation arise primarily because of studies (both experiments and simulations) that only focused on either the ultrafast or the ultraslow part of the dynamics, and also only few DNA sequences and structures are explored. This could not help better understand the solvation dynamics in DNA.[26-30] This situation prompted to revisit several previous studies on DNA solvation which only focused on one part of dynamics, and also perform new studies on different DNA sequences and structures. The Part I of this thesis present such extensive experimental and simulation results in various DNA structures, which help to comprehend the nature and origin of disperse solvation dynamics in DNA to a large extent. Chapter 4, particularly, includes extensive time-resolved experimental and simulation studies that allow for a better understanding of the solvation dynamics in the minor grooves of duplex-DNA.

Similar in line, the question arises that how far such collective solvation dynamics in DNA minor grooves control the recognition of DNA-damage (base-pair mismatch) by the mismatch-repair enzymes (MutS in *E. coli* and homologous MutSα in humans), because such enzymes are shown to interact with the mismatch-sites within DNA from the minor groove side of duplex-DNA.[31] In fact, recent proposal has been made based on simulation studies that mismatched bases induce significant alteration in the surrounding ion environment, and (possibly) hydration structure – such that the signal transfer from DNA-mismatch site to the repair enzymes possibly occurs through-space involving the surrounding water and ions.[32] The hypothesis that different mismatched base-pairs affect the local solvation dynamics in the minor grooves of DNA differently is tested in chapters 5 and 6 for the first time. It is also hypothesized that such dynamical changes may be acting as important cues for the differential mismatch recognition efficiencies of repair enzymes as reported earlier.

Although the dynamics of solvation and other processes are well explored in Watson-Crick duplex-DNA, it is fully unknown whether the feature of such dynamics remains same or changes in non-canonical higher order DNA structures such quadruplex DNA. These higher order G-quadruplex structures are shown to play important roles in the *telomere* maintenance and cancer, transcription and translation regulation, and as potent ligand (drug) targets.[33,34] Most importantly, G-quadruplex DNA are found to possess high structural diversity with various topologies in solution based on ion environment and/or induced by small molecules,[33,34] and that the structural polymorphism is drastically induced by local hydration/solvation state.[35,36] However, no information is available regarding the dynamics of water and ions as well as their role on solvating ligands bound inside such G-quadruplex DNA structures. The last two chapters (7 and 8) in Part I describe elaborative solvation dynamics studies on different structures of G-quadruplex DNA performed using both time-resolved experiments and MD simulations.

On the other hand, it is well documented in the literature that hydration and dielectric properties in-and-around lipid membranes play significant role in the electrostatics of lipid/water interfaces, which govern various essential biological processes across and within the lipid-rich cell-membrane.[37] Due to differential partitioning of water and ions near the hydrophobic and hydrophilic parts of lipid membranes, the dielectric properties across the lipid/water interface vary drastically.[38,39] Such drastic variations in the local dielectric properties within regions separated by few Angstroms across the lipid/water interfaces are expected to control the ligand partitioning at the interface as well as other trans-membrane processes.[40] However, quantifying such variations in local dielectric environment (polarity) across the lipid/water interfaces remains challenging mainly because of scarcity of suitable probe molecules. The Part II of this thesis compiles such study based on a series of newly synthesised fluorescent probe-molecules and extensive MD simulations which provide unprecedented details about the static dielectric properties (polarity) and hydration across the lipid/water interfaces created by different lipid phases.

1.2. Objective

The primary objective of this thesis is to understand the solvation dynamics and molecular interactions in different structures of DNA and lipid-bilayer by directly comparing the experimental and simulation results, whenever possible, rather than only reporting some new results/phenomenon in these bio-macromolecular systems. Thus, a large part of this thesis discusses and directly compares previously reported results with the new ones and also reports further studies in these systems – so as to explain the complex static and dynamic solvation properties in DNA and lipid-bilayer. The results presented here will allow a thoughtful but fair discussion on earlier proposals and the on-going debates about the dynamical characteristics in these biomolecules, particularly in DNA. In fact, the objective of this thesis is to discuss several specific but critical questions and their possible answers regarding the static and dynamic solvation in DNA and lipid-bilayer. Some such questions are:

(1) What is the nature of solvation dynamics in the grooves of DNA? Is it highly dispersed that follow power-law relaxation over broad time-range or is it exponential type?

(2) Is power-law solvation relaxation an intrinsic general property associated with DNA molecule?

(3) How such dispersed solvation dynamics change depending on DNA base-sequence, especially in the minor groove of DNA?

(4) Can equilibrium MD simulations capture the features of non-equilibrium experimental solvation dynamics in DNA?

(5) What is the origin of such dispersed (solvation) dynamics in DNA?

(6) Is it *slow* water solvation that helps solvating ligands bound to DNA minor grooves?

(7) What is the effect of ions on minor groove solvation probed by groove-binders?

(8) How far the dispersed dynamics seen in Watson-Crick duplex-DNA resemble to the dynamics in higher order non-canonical DNA structures such as G-quadruplex DNA?

(9) How far can the highly dispersed (power-law) dynamics be modulated by the introduction of mismatched base-pairs near the probe site?

(10) Is there any possible role of such collective solvation dynamics around the mismatch-sites in the mismatch recognition process of repair enzymes?

(11) How local dielectric environment (polarity) profiles vary at the lipid/water interfaces created by fluid- and gel-phase lipid bilayer?

(12) How the interactions of solutes of varying lipophilicities differ at these interfaces?

(13) What is the role of lipid hydration on defining the local dielectric properties at different depths across these interfaces?

To address above questions, this thesis compiles extensive steady-state and time-resolved fluorescence studies on various structures of DNA and lipid-bilayer using fluorescent ligands/probes (Hoechst, DAPI and 4AP-C*n*) that specifically bind to minor grooves of

DNA or partition across the lipid/water interfaces depending on the overall lipophilicity of the probe-solutes.

In Part I of this thesis, time-resolved data from femtosecond-resolved fluorescence up-conversion (UPC) and picosecond-resolved time-correlated single photon counting (TCSPC) techniques are combined to follow dynamic Stokes shifts of ligands (Hoechst and DAPI) in duplex-DNA of different base-sequences and in different structures of G-quadruplex DNA over very broad time-window of five decades from 100 fs to 10 ns. Extensive all-atom MD simulations are also performed here on same ligand/DNA systems (longest simulation on DNA solvation performed till date), which allow for a direct comparison of simulated dynamics with the experimental Stokes shifts dynamics and explain the origin of the dispersed (power-law) solvation dynamics in various structures of DNA. The results presented in this part of the thesis will show two most important properties, along with others, about DNA solvation dynamics: (1) Power-law solvation dynamics is inherent in DNA molecule. (2) There is very *slow* solvating water near DNA that stabilizes minor groove-bound ligands inside DNA of particular sequence.

On the other hand, in Part II of this thesis, a new homologous series of (non-covalent) 4-aminophthalimide-based fluorescent molecules (4AP-C*n*; *n* = 2-10, 12) having different lipophilicity (i.e., octanol/water partition coefficient – log*P*) are synthesized that are used to study the static solvation properties at different depths across the lipid/water interfaces created by gel- and fluid-phase bilayers at room temperature. Also, very extensive MD simulations are performed on same probe-lipid systems that allow deciphering the intricate details of probe interactions with lipid-bilayer and their hydration structures at the lipid/water interfaces. The 4AP-C*n* probes are thus shown to be extremely useful for studying the (solvation) properties at lipid/water interfaces of gel- and fluid-phase of lipid bilayer simultaneously.

1.3. Summary of Work

1.3.1. New Insight of Solvation Dynamics in DNA: Hoechst in A_nT_n-Rich Minor Groove of DNA

Water is essential for maintaining structure and function of biomolecules. However, studying the dynamic characteristics of water in the vicinity of biomolecules remain challenging, especially in-and-around the negatively charged DNA molecule. It is still hard to explain how water and ion motions in/near grooves of DNA solvate the DNA as well as its complexes with proteins and ligands (drugs). This chapter highlights the importance of water solvation in solvating minor groove binders inside DNA by measuring the time resolved fluorescence Stokes shifts (TRFSS) of Hoechst 33258 in A_nT_n - rich minor grooves over broad time-range from 100 fs to 10 ns. TRFSS results show that Stokes shift dynamics of Hoechst in the minor grooves created by central sequence of –AATTC– is faster than that in the minor groove created by –AAATTTG–. Very long equilibrium simulations (total 1.2 μs) performed on both Hoechst/DNA systems capture the essential features of the solvation response as observed in TRFSS experiments, particularly the power-law type dispersed dynamics and faster relaxation in minor groove of –AATTC– compared to –AAATTTG–. Decomposition of the total simulated solvation response into individual component reveals that *DNA* motion governs the slow dynamics in the minor groove formed by to –AAATTTG– sequence, whereas *water* controls the slow (power-law) dynamics in the minor groove formed by –AATTC– sequence. Analysis of minor groove-widths suggests that the differences in the local groove-width fluctuations in the two DNA systems possibly control the relative contributions of water and DNA relaxations to dictate the overall slow solvation dynamics in the DNA minor grooves.

1.3.2. Effect of T·T-Mismatch on Solvation Dynamics in Minor Groove of DNA

Base mismatch in DNA is a type of DNA damage (or defect) in which two non-complementary bases are paired within the stacks of normal Watson-Crick base-pairs of duplex DNA. These DNA mismatches are unwanted for genomic stability, which get repaired by mismatch repair enzymes post replication. MutS in *E. coli* (and homologous MutSα proteins in humans) plays an important role in the first step of such DNA mismatch recognition. Several earlier studies showed that these mismatches induce local structural changes in DNA double helix which are different for different types of mismatches. Such local structural changes at/near mismatch sites may provide the cue to repair enzymes for mismatch recognition. However, it is expected that such structural changes would certainly affect the local ion and water structure and dynamics. Thus, one hypothesis is that repair enzymes sense the changes of local collective dynamics of water, ion and DNA parts, rather than only the structural changes specifically. The hypothesis that mismatched base-pair affects the local collective solvation dynamics in DNA minor groove is tested in the study by monitoring TRFSS of two popular minor groove binders, Hoechst 33258 and DAPI near a T·T mismatch base-pair in the AT-rich minor groove of DNA, and compared the same with the dynamics measured in the minor groove of normal DNA over five decades of time from 100 fs to 10 ns. Results show that the Hoechst and DAPI depict somewhat different dynamic Stokes shift in the minor groove of normal-DNA; however, introduction of T·T mismatch in the minor groove gives rise to very similar Stokes shift dynamics, which follow a single power-law relaxation (with exponent ~0.23-0.24) over five decades of time from ~100 fs to 10 ns. These results suggest that incorporation of single base-mismatch induces unique coupled dynamics, for a given flanking canonical base-sequence, in the minor groove of DNA, which may have important role in the mismatch recognition of repair enzymes and subsequent repair mechanism, because repair enzymes bind to the mismatched-site from the minor groove side.

1.3.3. Differential Effects of Mismatched Base-Pairs on Solvation Dynamics in Minor Groove of DNA

It is believed that because different mismatches have their inherent static and dynamic properties, they will perturb their local environment at different levels, which will possibly lead to the differential local collective solvation dynamics. This is the focus of this chapter, where collective solvation dynamics is measured by monitoring the time-resolved fluorescence Stokes shifts (TRFSS) of the minor groove binder, DAPI, near *eight* possible base-pair mismatches and a normal matched base-pairs in the AT-rich minor groove of DNA The results are compared over five decades of time from 100 fs to 10 ns, which show that in all cases, the underlying Stokes shift dynamics follow similar power-law relaxation, but multiplied with single or double exponential relaxations in most of these DNA systems, except T·T-DNA which follow only a single power-law over entire five decades of time. Importantly, it is observed that the relative variations in the average values of extra exponential relaxations are found to nicely correlate to the differential mismatch recognition and repair by enzymes as reported earlier. This suggests that not only local structural changes, but also the modulation in local solvation dynamics due to incorporation of mismatches may provide important cues to the repair enzymes for their differential mismatch recognition and repair mechanism.

1.3.4. Solvation dynamics in G-quadruplex DNA

This study will show that dynamics of water is crucial for solvating ligand bound inside G-quadruplex DNA. Quadruplex are highly diverse DNA structures formed by the self-assembly of guanine rich sequences in presence of cations and/or small molecules, which have attracted huge attention due to its utility as a target for anticancer drugs. Despite the availability of large number of structural data, it is yet not known how the dynamics of water, DNA and ions solvate ligand inside these DNA. This work tackles these issues by measuring Stokes shift dynamics of DAPI inside antiparallel G-quadruplex DNA, and directly comparing the time-resolved experimental results to the all atom MD simulation from ~100 fs to 10 ns. Dynamic Stokes shifts of DAPI bound to G-quadruplex DNA prepared in H_2O buffer and D_2O are compared to illuminate the impact of water dynamics on ligand solvation. Results show that solvation dynamics in antiparallel G-quadruplex DNA follows power-law relaxation (summed with fast exponential relaxation) from ~100 fs to 10 ns. Comparison of experimental results with the dynamics computed from 65 ns simulation reveals that the water motion governs the relaxation below ~5 ps, whereas, dynamics of both water and DNA contribute comparably to dictate long-time power-law dynamics. Ion shows negligible contribution. Simulation results also suggest that this complex behavior may arise from the subdiffusive motion of water molecules, perturbed by the G-quadruplex DNA, which show broad distribution of residence times.

1.3.5. Solvation Dynamics in G-quadruplex DNA: Dependence of Quadruplex and Ligand Structures

After discussing solvation dynamics in anti-parallel G-quadruplex DNA in the previous work, this study will shed light on how such dynamics depend on the G-quadruplex and ligand structures as well as ligand binding modes and positions inside different quadruplex structures. These issues are addressed by measuring the solvation dynamics in parallel G-quadruplex DNA probed by Hoechst from 100 fs to 10 ns. Results show that the dynamic Stokes shift of Hoechst in parallel G-quadruplex DNA follows power-law relaxation, summed with an exponential relaxation of 2 ps. Comparing the dynamics probed by Hoechst in parallel and by DAPI in antiparallel G-quadruplex DNA, it is found that the two ligand/DNA complexes show solvation dynamics that follow a power-law relaxation with only small difference in the exponents (0.16 for DAPI/antiparallel GqDNA and 0.06 for Hoechst/parallel GqDNA*)*. This reveals that dynamics in quadruplex DNA remains similar that follow power-law relaxation, irrespective of probes position and mode of binding in different G-quadruplex DNA structures. Simulation result shows that Hoechst binds to the outer G-tetrads through end-stacking to the parallel and DAPI binds in the groove of antiparallel G-quadruplex DNA. Based on the previous experimental and simulation results, the fast exponential relaxation of 2 ps has been assigned to the motion of water molecules that are weakly perturbed by parallel G-quadruplex DNA, whereas, the coupled dynamics of DNA-parts and water molecules in the proximity of Hoechst inside parallel G-quadruplex DNA control the power-law relaxation.

1.3.6. Precise Quantification of Probe-Location Dependent Polarity and Hydration at Lipid/Water Interfaces

The precise understanding of hydration, polarity and interaction of solute at the lipid/water interfaces of lipid-bilayer is vital to explore their importance in membrane biology. A large number of studies have investigated the static solvation and polarity at lipid/water interfaces of fluid-phase lipid bilayer, but such properties at lipid/water interfaces created by lipid gel-phase are less explored primarily due to unavailability of suitable fluorescent probes which can be incorporated within the rigid gel-phase of lipid bilayer. This study uses a new homologous series of fluorescent 4-aminopthalimide based probes (4AP-C*n; n* = 2-10, 12) with varying lipophilicities which can scan different region of ($L_{\beta'}$) DPPC bilayer in its gel-phase and (L_{α}) DOPC bilayer in its fluid-phase at room temperature. Results show a unique stepwise polarity-profile at lipid/water interface of DPPC bilayer in gel-phase, whereas, only subtle but continuous change in the local polarity at lipid/water interface of DOPC bilayer in fluid-phase. Very long MD simulation on probes-lipid systems in both the phases of bilayer reveals intricate details indicating that apart from the relative probe's position, their orientations also play critical role in defining the local solvation by changing their access toward water molecules at the two lipid/water interfaces, thus defining varying hydration of the probes across the interfaces.

1.4. Plan of Thesis

The organization of the thesis is as follows:

Chapter 1: This chapter includes introduction of the field of research, motivation and objective of the thesis, along with the summaries of work presented in other chapters.

Chapter 2: This chapter provides brief overview on the structural aspects of DNA such as duplex, triplex and quadruplex DNA. It also describes the structure and properties of minor groove binders, DNA intercalators, end-stacking ligands and their interactions with various structures of DNA. Theory of solvation dynamics and different types of solvation probes used for solvation dynamics studies in DNA are also discussed. Brief discussion on molecular dynamics simulation methods to interpret TRFSS experimental results are presented as well. Finally, a detailed overview of considerable efforts which gone into understanding the solvation dynamics in water, protein, DNA, DNA-ligand and DNA-protein complexes are provided in this chapter.

Chapter 3: It describes the basics and working principles of experimental techniques, molecular docking and molecular dynamics simulation methods used to carry out the experimental and computational studies.

Chapter 4: This chapter highlights the time resolved Stokes shift dynamics of Hoechst in A_nT_n-rich minor grooves formed by two different sequences –AAATTTG– and –AATTC– from 100 fs to 10 ns. Time resolved experimental results were directly compared with MD simulation results to provide intricate details about the origin of slow dispersed dynamics in minor grooves of DNA.

Chapter 5: This chapter comprises of time resolved fluorescence Stokes shift studies of minor groove binders, DAPI and Hoechst 33258 near a T·T–mismatch site in the AT-rich minor groove of DNA, and its comparison with the dynamics measured in normal DNA over five decades of time from 100 fs to 10 ns.

Chapter 6: This chapter focuses on the collective dynamic response of the surrounding environment near *eight* different mismatched base-pairs in minor groove of DNA by monitoring time-resolved fluorescence Stokes shift of DAPI, showing that changes in local solvation may act as important cues for differential recognition and repair of mismatched base-pairs by repair enzymes.

Chapter 7: This Chapter describes the significance of water dynamics in solvating a ligand inside the groove of antiparallel G-quadruplex DNA structure by measuring dynamic Stokes shift of DAPI from 100 fs to 10 ns. Comparison of experimental findings with MD simulations interprets the origin of power-law solvation dynamics in G-quadruplex DNA.

Chapter 8: This chapter shows the effect of ligand structures and binding modes in different G-quadruplex DNA by measuring TRFSS dynamics in parallel and anti-parallel G-quadruplex structures, probed by Hoechst and DAPI from 100 fs to 10 ns.

Chapter 9: This chapter introduces the general properties of lipid bilayers and biological membranes, phases of lipid membrane, and lipid/water interfaces. A concise overview on the previous studies of static and dynamic properties in lipid bilayer using molecular probes is provided. It also includes an overview on how molecular dynamics simulation is implemented to study lipid/water interfaces and describe the intricate biochemical implications of solvation properties at various lipid/water interfaces.

Chapter 10: This chapter deals with the study of depth dependent environment polarity and hydration across gel-phase DPPC and fluid-phase DOPC lipid/water interfaces using series of newly synthesized 4-aminophthalimide-based fluorescent molecules (4AP-C*n*; *n* = 2–10, 12) having different hydrophobicity, employing steady state fluorescence experiments and all atom molecular dynamics simulations.

References

1. Rothschild, L. J.; Mancinelli, R. L. Life in Extreme Environments. *Nature* **2001,** 409, 1092-1101.
2. Bagchi, B. *Water in biological and chemical processes: from structure and dynamics to function*. Cambridge, UK, **2013**.
3. Ball, P. Water as an Active Constituent in Cell Biology. *Chem. Rev.* **2008**, 108, 74-108.
4. Drost-Hansen, W.; Clegg, J. S. *Cell-Associated Water*. Boston, Massachusetts, New York, **1979**.
5. Pal, S. K.; Zewail, A. H. Dynamics of Water in Biological Recognition.*Chem. Rev.* **2004**, *104*, 2099–2124.

6. Bhattacharyya, K. Solvation Dynamics and Proton Transfer in Supramolecular Assemblies. *Acc. Chem. Res.* **2003**, *36*, 95–101
7. Bhattacharyya, K.; Bagchi, B. Slow Dynamics of Constrained Water in Complex Geometries**.** *J. Phys. Chem. A* **2000**, *104*, 10603–10613.
8. Berg, M. A.; Coleman, R. S.; Murphy, C. J. Nanoscale Structure and Dynamics of DNA. *Phys. Chem. Chem. Phys.* **2008**,*10*, 1229–1242.
9. Laage, D.; Elsaesser, T.; Hynes, J. T. Water Dynamics in the Hydration Shells of Biomolecules. *Chem. Rev.* **2017**, (DOI: 10.1021/acs.chemrev.6b00765)
10. Mukherjee, S.; Mondal, S.; Bagchi, B. Distinguishing Dynamical Features of Water Inside Protein Hydration Layer: Distribution Reveals What is Hidden Behind the Average. *J. Chem. Phys.* **2017**, *147*, 024901 (1-12).
11. Mondal, S.; Mukherjee, S.; Bagchi, B. Decomposition of total Solvation Energy into Core, Side-chains and Water Contributions: Role of Cross Correlations and Protein Conformational Fluctuations in Dynamics of Hydration Layer. *Chem. Phys. Lett.* **2017**, *683*, 29-37.
12. Li, T.; Hassanali, A. A.; Kao, Y. -T.; Zhong, D.; Singer, S. J. Hydation Dynamics and Time Scales of Coupled Water-Protein Fluctuations *J. Am. Chem. Soc.* **2007**, *129*, 3376–3382.
13. Golosov, A. A.; Karplus, M. Probing Polar Solvation Dynamics in Proteins: A Molecular Dynamics Simulation Analysis *J. Phys. Chem. B* **2007**, *111*, 1482-1490.
14. Abbyad , P.; Shi , X.; Childs , W.; McAnaney, T. B.; Cohen, B. E.; Boxer, S. G. Measurment of Solvation Responses at Multiple Sites in a Globular Protein *J. Phys. Chem. B* **2007**, *111*, 8269-8276.
15. Jungwirth, P. Biological Water or Rather Water in Biology? *J. Phys. Chem. Lett.* **2015**, *6*, 2449–2451
16. Halle, B.; Nilsson, L. Does the Dynamic Stokes Shift Report on Slow Protein Hydration Dynamics? *J. Phys. Chem. B* **2009**, *113*, 8210-8213.
17. Duboué-Dijon, E.; Fogarty, A. C.; Hynes, J. T.; Laage, D. Dynamical Disorder in the DNA Hydration Shell. *J. Am. Chem. Soc.* **2016**, *138*, 7610–7620
18. Saha, D.; Supekar, S.; Mukherjee, A. Distribution of Residence Time of Water around DNA Base Pairs: Governing Factors and Origin of Heterogeneity. *J. Phys. Chem. B* **2015**, *119*, 11371-11381.
19. Andreatta, D.; Sen, S.; Pérez Lustres, J. L.; Kovalenko, S. A.; Ernsting, N. P.; Murphy, C. J.; Coleman, R. S.; Berg, M. A. Ultrafast Dynamics in DNA: “Fraying” at the End of the Helix. *J. Am. Chem. Soc.* **2006**, *128*, 6885-6892.
20. Andreatta, D.; Pérez Lustres, J. L.; Kovalenko, S. A.; Ernsting, N. P.; Murphy, C. J.; Coleman, R. S.; Berg, M. A. Power-Law Solvation Dynamics in DNA over Six Decades in Time. *J. Am. Chem. Soc.* **2005**, *127*, 7270-7271.
21. Pal, N.; Verma, S. D.; Sen, S. Probe Position Dependence of DNA Dynamics: Comparison of the Time-Resolved Stokes Shift of Groove-Bound to Base-Stacked Probes. *J. Am. Chem. Soc.* **2010**, *132*, 9277-9279.
22. Pal, N.; Shweta, H.; Singh, M. K.; Verma, S. D.; Sen, S. Power-Law Solvation Dynamics in G-Quadruplex DNA: Role of Hydration Dynamics on Ligand Solvation inside DNA. *J. Phys. Chem. Lett.* **2015,** *6*, 1754-1760.
23. Verma, S. D.; Pal, N.; Singh, M. K.; Sen, S. Sequence-Dependent Solvation Dynamics of Minor-Groove Bound Ligand Inside Duplex-DNA. *J. Phys. Chem. B* **2015**, *119*, 11019-11029.
24. Sen, S.; Andreatta, D.; Ponomarev, S. Y.; Beveridge, D. L.; Berg, M. A. Dynamics of Water and Ions Near DNA: Comparison of Simulation to Time-Resolved Stokes-Shift Experiments. *J. Am. Chem. Soc.* **2009**, *131*, 1724-1735.
25. Furse, K. E.; Corcelli, S. A. Dynamical Signature of Abasic Damage in DNA. *J. Am. Chem. Soc.* **2011**, *133*, 720-723.
26. Pal, S. K.; Zhao, L.; Zewail, A. H. Water at DNA Surfaces: Ultrafast Dynamics in Minor Groove Recognition. *Proc. Natl. Acad. Sci. U.S.A.* **2003**, *100*, 8113-8118.
27. Pal, S. K.; Zhao, L.; Xia, T.; Zewail, A. H. Site and Sequence-Selective Ultrafast Hydration of DNA. *Proc. Natl. Acad. Sci. U.S.A.* **2003**, 100, 13746-13751.
28. Banerjee, D.; Pal, S. K. Dynamics in the DNA Recognition by DAPI: Exploration of the Various Binding Modes. *J. Phys. Chem. B* **2008**, *112*, 1016-1021.

29. Pal, S.; Maiti, P. K.; Bagchi, B.; Hynes, J. T. Multiple Time Scales in Solvation Dynamics of DNA in Aqueous Solution: The Role of Water, Counterions, and Cross-Correlations. *J. Phys. Chem. B* **2006**, *110*, 26396-26402.
30. Furse, K. E.; Corcelli, S. A. The Dynamics of Water at DNA Interfaces: Computational Studies of Hoechst 33258 Bound to DNA. *J. Am. Chem. Soc.* **2008**, *130*, 13103-13109.
31. Lamers, M. H.; Perrakis, A.; Enzlin, J. H.; Winterwerp, H. H. K.; Wind, N. D.; Sixma, T. K. The Crystal Structure of DNA Mismatch Repair Protein MutS Binding to a G·T Mismatch. *Nature* **2000**, *407,* 711-717.
32. Rossetti, G.; Dans, P. D.; Gomez, P. I.; Ivani, I.; Gonzalez, C.; Orozco, M. The Structural Impact of DNA Mismatches. *Nucleic Acids Res.* **2015**, *43*, 4309-4321.
33. Neidle, S. The Structures of Quadruplex Nucleic Acids and Their Drug Complexes. *Curr. Opin. Struct. Biol*. **2009**, *19*, 239-250.
34. Balasubramanian, S.; Hurley, L. H.; Neidle, S. Targeting G-quadruplexs in Gene Promoters: A Novel Anticancer Strategy. *Nat. Rev. Drug Discov.* **2011**, *10*, 261-275.
35. Miller, M. C.; Buscaglia, R.; Chaires, J. B.; Lane, A. N.; Trent, J. O. Hydration is a Major Determinant of the G-Quadruplex Stability and Conformation of the Human Telomere 3′ Sequence of d(AG3(TTAG3)$_3$). *J. Am. Chem. Soc.* **2010**, *132*, 17105-17107.
36. Heddi, B.; Phan, A. T. Structure of Human Telomeric DNA in Crowded Solution. *J. Am. Chem. Soc.* **2011**, *133*, 9824-9833.
37. Stillwell, W. *An Introduction to Biological Membranes*; Elsevier: San Diego, CA, USA, **2013**.
38. Marsh, D. Polarity and Permeation Profiles in Lipid Membranes. *Proc. Natl. Acad. Sci. U.S.A.* **2001**, *98*, 7777-7782.
39. Marsh, D. Membrane Water-Penetration Profiles from Spin Labels. *Eur. Biophys. J.* **2002**, *31*, 559-562.
40. Haldar, S.; Chaudhuri, A.; Chattopadhyay, A. Organization and Dynamics of Membrane Probes and Proteins Utilizing the Red Edge Excitation Shift. *J. Phys. Chem. B* **2011**, *115*, 5693-5706.

<u>Part I</u>

Study of Solvation Dynamics in Duplex and G-Quadruplex DNA

Chapter 2

Solvation Dynamics and Ligand Interaction in DNA: An Overview

2.1. Introduction

Importance of deoxyribonucleic acids (DNA) to life is known since its very discovery in 1868, a landmark year in genetic research, by Swiss physiological chemist, Friedrich Miesher.[1] Laying the spadework of Miesher, a physician turned chemist, Phoebus Levene led to the discovery of three major components of nucleotide: phosphate, sugar and base. Strengthening the foundation, Erwin Chargaff, an Austrian biochemist expanded the work of Levene and gave Chargaff's rule for complementary binding of bases in DNA. These evidences put together with important X-ray crystallography work by Rosalind Franklin and Maurice Wilkins encouraged James D. Watson and Francis Crick for more detailed exploration of the DNA structure. One of the famous statement in science is: *"This structure has novel features which are of considerable biological interest"* by Watson and Crick, published in a scientific paper in 1953 wherein they presented the discovery of double helical model for DNA structure.[2] To what Miesher called "nuclein" in 1869 was later changed to "nucleic acid" by Richard Altmann in 1889 and eventually to "deoxyribonucleic acid" (DNA).

DNA structure is depicted as a perfect B-form with an anti-parallel arrangement of two complementary strands which are stabilized by Watson-Crick base pairing.[2,3] Helical B-form DNA is resilient and flexible enough to store genetic information. However, local changes in structure, base sequences, ionic strength, pH and level of hydration can result in variety of structural form such as A-, B- and Z-form, stem-loop, hairpins, bulges, pseudoknots, tetraloops, triplex and quadruplex DNA.[3-7] Such structural polymorphism of DNA leads to its functional diversity, making it ideal for its involvement in several other biological processes apart from just storing and translating genetic information. Regardless of several structural forms of DNA, its functional diversity cannot be understood completely without considering its dynamical aspects. Indeed, *dynamics* of biomolecules are considered as a connecting link between their *structures* and *functions*.

Presence of negatively charged phosphate groups makes DNA, a highly charged species. Therefore, at physiological conditions DNA gets stabilized by positively charged counterions and dipolar water molecules for its biological functioning.[8,9] Without water, double helical structure of DNA would become unstable due to repulsion between the phosphate groups of complementary or even same strands. High dielectric constant of water and counterions screen the electrostatic repulsion between these phosphate groups. Interaction of DNA with surrounding water and ions makes it highly dynamic in nature and facilitates its interactions with proteins, lipids and drugs.[10-14] These interactions are very crucial for the survival of life on earth. Active participation, rearrangement and release/uptake of water molecules and ions near DNA-binding sites mediate the process of molecular recognition by DNA.[14-18] Interestingly, repulsion of water and ions is observed in the case of protein-DNA complex formation. In fact, dynamics of water and ions can drive protein folding and catalytic activity of an enzyme.[19] It is also indicated by recent large-scale MD simulation study that changes in ion and water environment and their dynamics in the vicinity of mismatched base pairs of DNA may have vital role to play in the mismatch recognition by repair enzymes (MutS in E. Coli. And MutSα proteins in human) compared to only the structural changes of the mismatched base pair.[20,21]

Hydration dynamics around DNA is also critical for effective binding of ligands to nucleic acids. Double helical structure of DNA has distinct major and minor grooves which are fully hydrated.[22] Interaction of small molecules (ligands) to DNA is either mediated by water molecules or facilitated by the displacement of water and ions from DNA minor grooves. In addition, hydration dynamics plays a vital role in either entropic or enthalpic stabilization of ligands inside DNA structure.[15-18] Apart from water and ion dynamics, sequence dependent dynamics and groove widths of DNA are also significant for varied proteins to recognize the DNA sequences. Similarly, binding of ligand to DNA also depends on base sequences and groove widths near ligand binding sites.[23] Minor groove binders recognize and bind with high affinity to narrow grooves formed by AT–rich sequences than GC–rich sequences in DNA. The GC-step is found to be more hydrated compared to AT-step; thus hydration of DNA is not only decided by its conformation but also by its base sequences.[24-28] In fact, ions and water molecules are active components of biomolecular system as they participate in both, dynamic and structural functions. Therefore, correlating water and ion dynamics around DNA and protein with its structure will help in recognising many underlying concepts that can serve as a connecting link between *Structure-Function-Dynamics* of biomolecules.

Behaviour of water and ions in and around complex biomolecular systems can be explored in terms of its structure and functions utilizing experimental, theoretical and molecular dynamics simulation studies. Experimental techniques such as Dielectric relaxation, X-ray diffraction, Nuclear magnetic resonance, Neutron scattering, and ultrafast laser spectroscopy are used to monitor dynamics around biomolecules.[29-35] However, study of solvation dynamics through time-resolved fluorescence Stokes shifts (TRFSS) experiments is one of the fascinating methods that measure the response of surrounding environment to the optical perturbation of the fluorescent probe in ultrafast time scales that are in similar range as the time-scales of motions of constituent molecules. Such solvation dynamics experiment has been employed to understand dynamics from simple liquids to dispersed dynamics of complex biomolecules in restricted environment.[36-46] Apart from experimental studies, molecular dynamics (MD) simulation is a vital computational tool that has evolved exponentially in recent times and aided in understanding the behaviour, structure, dynamics and functions of biological macromolecules with atomic details. Simulations can be used to capture particle motion as a function of time and to address effects of different conditions on the dynamics of biomolecules *in silico*. Results of TRFSS experiments are corroborated with MD simulation to extract microscopic details about the origin of the complex dynamics of water and ions around biomolecules as well as for interpretation of time-resolved experimental results.[47-55]

The results in the first part of this thesis include studies on ligand interactions to duplex and quadruplex DNA as well as their dynamics which unfold some of the unknown but tremendously important information about the dynamics in various structures of DNA. The studies presented in this thesis unfold the important information on effects of base sequences, variation in groove widths, effects of mismatch base pairs, and quadruplex structures on the mode of interactions and local collective dynamics of ligands inside duplex and G-quadruplex DNA. The experimental and simulation results presented here will tremendously help to upgrade the existing understanding of complex dynamics in DNA of different structures with several new findings which were not anticipated in earlier studies. Few highlights of such results presented in this thesis are:

(1) Direct comparison of TREFSS experiments to MD simulations shows that the nature of solvation dynamics in ligand (Hoechst)/DNA systems depend on base-sequence of the minor groove which can drastically influence to allow very slow water relaxation near the ligand binding site in one sequence compared to other.

(2) Introduction of single base-mismatch in the minor groove of DNA drastically affects ligands' binding and the collective solvation dynamics probed by those ligands in the minor groove, compared to those in normal DNA. Dynamics probed by minor groove binders show significant dependence on the mismatch type, which correlate well to the relative mismatch recognition by repair enzymes – indicating importance of collective dynamics of water, ions and DNA in mismatch recognition mechanism.

(3) Probe positions merely affect solvation dynamics in different structures of G-quadruplex DNA, although the probe-ligands show different binding sites and affinity to the different quadruplex DNA structures. Results show dynamics of solvation in G-quadruplex DNA structures are also dispersed in nature which mainly follows power-law relaxation over long times, similar as found in duplex-DNA.

However, before discussing these new results in following chapters, we will first review the previous studies on dynamics of solvation in bulk water, protein, DNA, DNA-ligand and DNA-protein complexes to highlight the existing understanding of dynamics of water and ions around these biomolecules/biomolecular complexes. We will briefly discuss the previous results in all these systems, including DNA, because the dynamical features in all these systems are similar and have strong connections among themselves. Also, note that we will mainly focus the discussion on the TRFSS and related experimental results on solvation dynamics as well as related MD simulation studies in these systems.

This chapter is arranged as follows: first, a brief introduction of DNA structure, forms and topology is given in Section 2.2. Section 2.3 will then discuss the process of solvation dynamics, followed by the description of the methodologies that is used to study solvation dynamics and the probe molecules used for studying solvation dynamics in DNA. Section 2.4 describes standard methods of all atom molecular dynamics simulation which are used to compliment time-resolved fluorescence experiments. Section 2.5 compiles earlier results on water solvation; Section 2.6 discusses solvation studies in proteins, followed by discussion of existing results of DNA dynamics and hydration in Section 2.7 and those of protein-DNA complexes in Section 2.8.

2.2. Structure of DNA

Deoxyribonucleic acid (DNA) can adopt vast array of conformations depending on base sequences, hydration level, direction of supercoiling and ion concentration. In fact, presence of ligand can also induce structural modification in DNA. Although, B-form of DNA is most abundant in cellular environment, other possible forms and morphologies of DNA such as A-form, Z-form, triplex, quadruplex, hairpins, bulges, pseudoknots, tetraloops can also exist.[3-7] A brief description of double helical DNA, triplex DNA and quadruplex DNA is provided in the section below, out of which the ligand interactions and dynamics in duplex and quadruplex DNA are explored in this thesis.

2.2.1. Duplex DNA

James Watson and Francis Crick in 1953, revealed the iconic double helical model of DNA which is indeed a remarkable molecule that carries genetic information from one generation to other.[2] Duplex DNA consists of strands that are coiled in helical fashion around the same axis which runs in opposite direction to each other. The DNA strands are composed of monomer units called nucleotides, where each nucleotide comprises of three main components: a 5-carbon sugar (pentose sugar), phosphate group and nitrogenous base.[56,57] These pentose sugar and phosphate groups are connected to each other in an alternate fashion through phosphodiester linkages. It should be noted that strands of DNA are not only stabilized by the hydrogen bonds between complementary bases, but also by stacking interaction between aromatic faces of the base. These stacking interactions also strengthen the helix against the repulsive forces between negatively charged phosphate groups. The bases on the antiparallel strands are bound in a precise manner according to

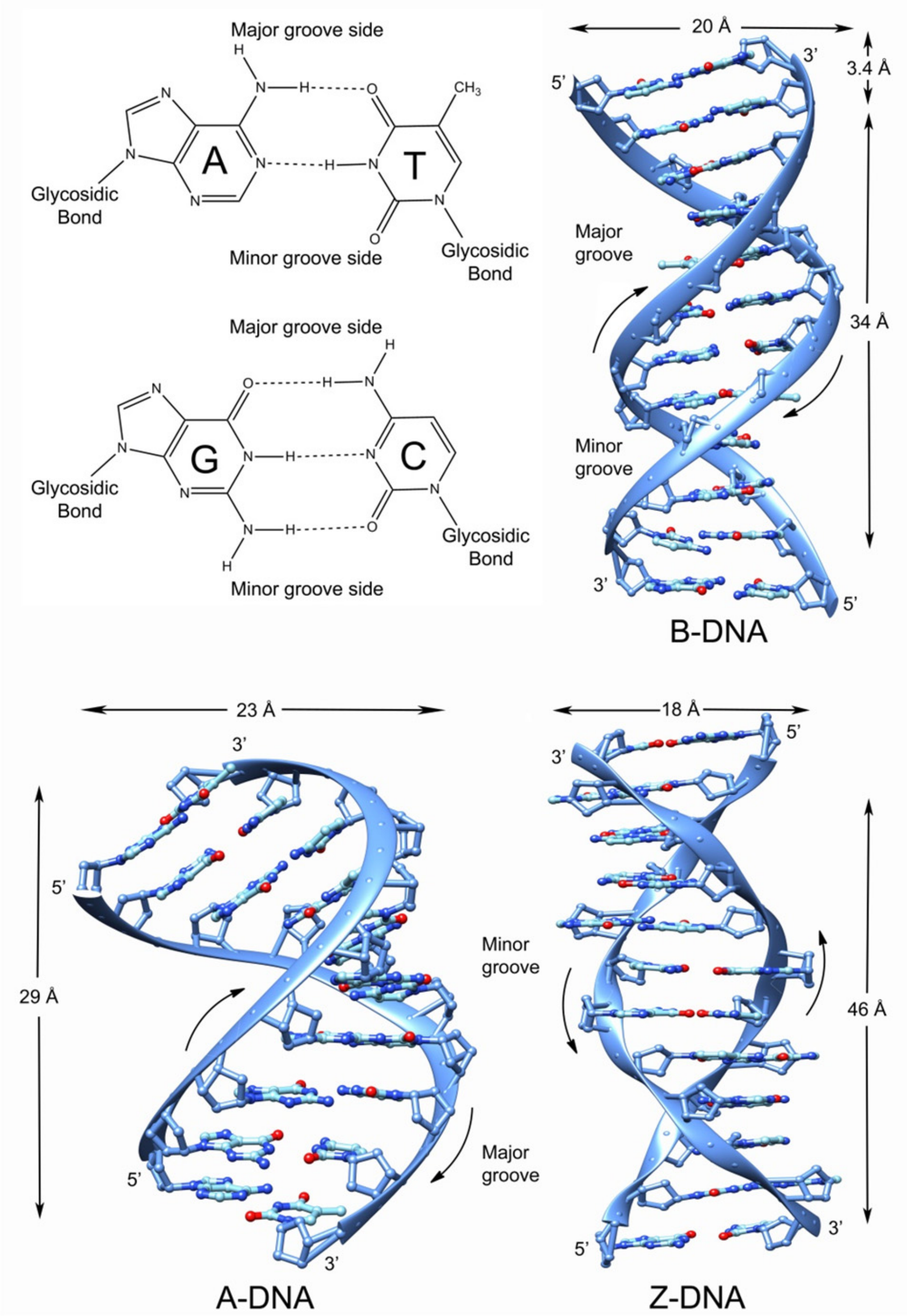

Figure 2.1: Watson-Crick hydrogen bonds and different forms of duplex DNA.

Chargaff's rule, where A is paired with T by two hydrogen bonds and G is paired with C by three hydrogen bonds (Figure 2.1).[58]

Though B-form of duplex DNA is the most stable right-handed structure, it can adopt other forms depending on the level of hydration[59,60] and under certain conditions which involve major changes in helix geometry. As discussed, it can acquire three different conformations or forms: A-, B- and Z-form. Although A- and Z-form of duplex-DNA possesses helical structure, their geometry and dimensions differ significantly from most abundant B-DNA (Figure 2.1).[61] In general, the helices in B- and A-DNA are twisted in right handed manner, whereas, it coils in left handed fashion resulting in pronounced zig-zag pattern for Z-form of DNA. Even though the right and left handed helices fall in the category of allowed conformations, right handed structures stand out to be energetically more favourable due to minimal steric hindrance between the backbone and side chains. The helical structure of DNA can be characterized by the coordinates of slide, tilt, shift, roll, rise and twist which differ for different forms of DNA. It has been observed that the helical pitch for B-, A- and Z-forms are 34 Å, 28 Å and 46 Å, respectively, which highly depend on the stacking forces exerted by the bases on its neighbours in the helical strand. On the other hand, double helix of B-DNA completes one turn about its axis in every 10.5 base-pairs, while for A- and Z-form complete one turn every 11 and 12 base pairs, respectively.[62-64]

Though B-form is abundant,[61] A-DNA is generally found in dehydrated states.[62] It has wider minor groove while major groove is deep and narrow. A-DNA is relatively wider than B-DNA which can be easily distinguished by proteins interacting with them. Z-form of DNA is named because of the zig-zag course of backbone twisted in an anti-clockwise manner as compared to B-form of DNA that makes these two helical form mirror images of each other.[62-64] Unlike A- and B-form, Z-DNA is more elongated with a narrow minor groove and wide major groove extending to the axis of helix.[62-64]

2.2.2. Triplex DNA

Felsenfeld and Rich in 1957 described triple stranded DNA for the first time.[65] Triplex DNA is formed when purine or pyrimidine bases bind to the major groove of duplex DNA. Owing to high potential of purine to form hydrogen bonds, the incoming third strand follows the path towards purine rich strands of duplex DNA.[66-72] Hoogsteen and reverse Hoogsteen type hydrogen bonds hold the stability and specificity of these triple stranded DNA. Triplex DNA is classified into intermolecular and intramolecular triplexes (Figure 2.2). In particular, intermolecular triplexes are formed when a polypyrimidine strand binds to polypurine duplex DNA through Hoogsteen hydrogen bond resulting in parallel structure or when a polypurine third strand binds to polypurine duplex DNA via reverse Hoogsteen bond forming antiparallel structure.[67] Intramolecular triplexes or H-DNA structures are formed when third strand is provided by one of the strand of same duplex DNA. It has indeed been observed that triplex DNA act as promising *gene-drugs* and it can be used in an anti-gene strategy.[73,74] On the other hand, it can also be used to modulate

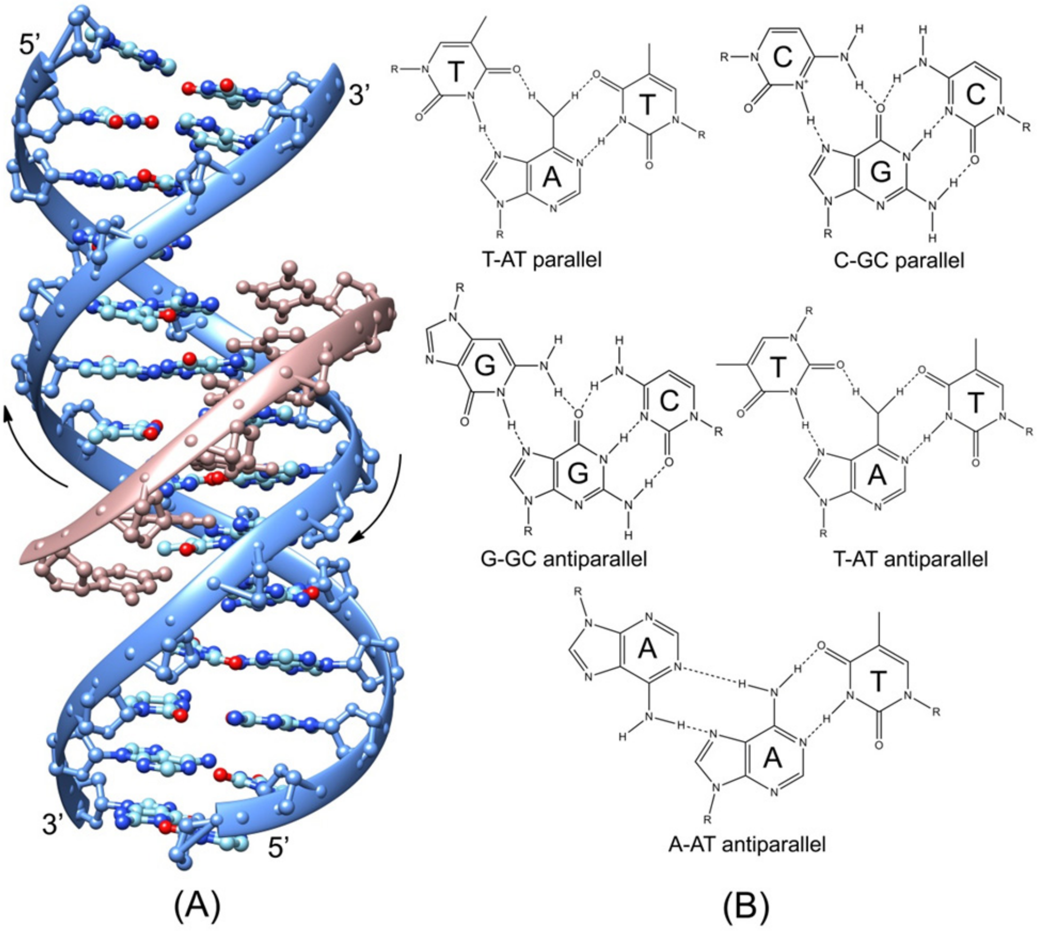

Figure 2.2: (A) Structure of triplex DNA. (B) Hydrogen bonding in triplex DNA.

gene activity in vivo, thus, opens up the possibility of selectively controlling the expression of specific genes that could be of considerable importance in treating genetic disorders.[73,74]

2.2.3. Quadruplex DNA

Apart from double and triple helical forms of DNA, there exist four stranded higher order structures called G-quadruplex DNA. Davies and co-workers in 1962 reported these unusual structures whose core is built of guanine rich sequences.[75] Moreover, it consists of G-quartets made up of four guanine bases arranged on a plane and stabilized by Hoogsteen hydrogen-bonds. These G-quartets stack on top of each other through π-π non-bonded interactions to give rise to G-quadruplex structures. These structures are thermodynamically very unstable unless it gets stabilized by ions such as K^+ and Na^+ placed within two G-quartets (Figure 2.3).[76-78] Presence of alkali metal ions adds stability to quadruplex structures by interacting with the lone pairs present on the O6 atoms of guanine. Quadruplex structures are shown to exhibit topological variations and such

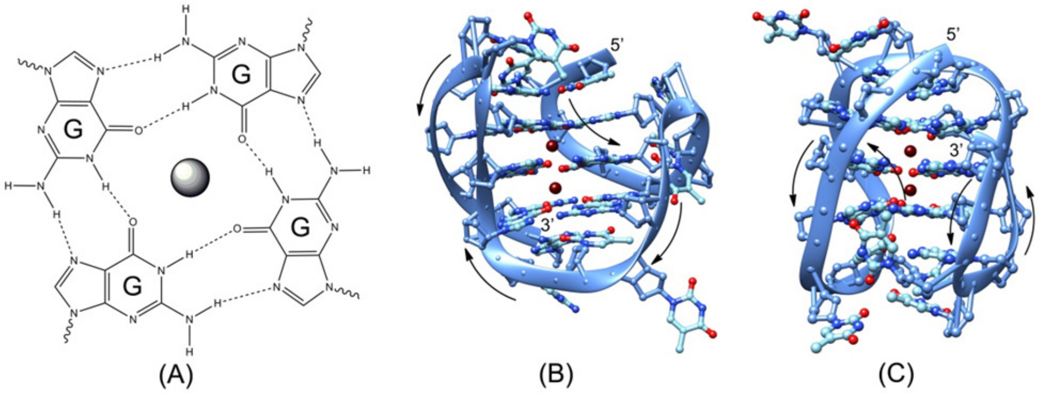

Figure 2.3: (A) Hoogsteen hydrogen bonds formed in a G-tetrad in quadruplex DNA. Structures of (B) (3+1) hybrid parallel and (C) antiparallel G-quadruplex DNA structures.

structural polymorphism arises from presence of ions, ligands, crowding agents and strand stoichiometry, arrangement of strand polarity, glycosidic torsion angle and location of loop linking the guanine strands. Depending on the direction of strands, quadruplex structures can adopt a range of different folding patterns such as parallel, antiparallel and (3+1) hybrid parallel structures.[77-81]

G-quadruplex forming sequences have been identified at telomeric ends, mutational hot spots, immunoglobulin switch regions and gene promoters of oncogenes such as c-MYC, c-KIT and KRAS.[82-84] In fact, presence of G-quadruplex structures has indeed been observed in human cells.[85] Quadruplex structures at telomeric end are found to inhibit telomerase activity, thus supressing telomere elongation and multiplication of tumour cells.[86] The structural variations of quadruplex DNA provide selective recognition sites for small molecules that can possibly be utilized as therapeutic targets for binding of anticancer drugs and for treating numerous disorders. Another interesting aspect of quadruplex structure is the presence of large π surface and high negative charge. Thus, a majority of ligands with π surfaces interact with these DNA structures through π-π interactions in different manner.[87,88]

2.3. Solvation Dynamics

All biological functions take place in an aqueous environment. A complete understanding of any biochemical reaction performed by biomolecules demands elucidation of dynamical features of surrounding solvent molecules, both water and ions. The fact that solvation process influences various chemical/biochemical reactions (e.g., electron and proton transfer) triggered continued attention to study solvent relaxation in simple liquids as well as in complex biological systems. However, obtaining a clear picture of the extremely complex solvation dynamics of water and ions around biomolecules, especially around negatively charged DNA, remains a hard task to both experimentalists and theoreticians.

Solvent relaxation dynamics are studied through various experimental means of varying degree of spatial and temporal resolutions. For example, three-pulse photon echo peak shift (3PEPS) is a nonlinear optical gating technique with extremely high time-resolution which is utilized to study fast solvent relaxations.[89,90] Four-wave-mixing (FWM) is another variant of nonlinear optical technique with femtosecond (fs) time-resolution that is applied to study both vibrational and diffusive solvation dynamics in femtosecond and picosecond time range.[91] Time-resolved infrared spectroscopy is also utilized to measure solvation dynamics with picosecond time-resolution.[92,93] NMR is used to study water residence time, which has spatial resolution of few Angstroms but limited time-resolution.[94,95]

On the other hand, dielectric-relaxation experiment is a method that can measure fast molecular dynamics in solution.[96] In this experiment, charge is quickly injected onto two plates of a capacitor, which creates a uniform electric field within the sample between the plates. The rotation and translation of solvent and other dipolar molecules and/or diffusion of ions create a polarization which opposes the applied electric field. The development of this opposing polarization field with time changes the voltage on the plates, which is measured to follow the time-dependent voltage change. However, standard dielectric-relaxation experiments do not have spatial resolution; they average over the entire sample. Thus, the majority of the response in such experiment comes from bulk water, while effects from biomolecule-specific parts and ion motion remain suppressed.

2.3.1. Time-Resolved Fluorescence Stokes Shifts Experiments

Measurement of solvation dynamics through time-resolved fluorescence Stokes shift (TRFSS) experiment provides a way to study properties and solvation response of a probe's surrounding environment in real time. TRFSS experiments utilize an ultrashort laser pulse to excite fluorescent probe from its electronic ground (S_0) state to excited (S_1) state. In ground state, the solute probe remains in equilibrium with its surrounding solvent molecules which are weakly and randomly oriented around the probe. This equilibrium state of solute-probe with the surrounding solvent molecules undergoes an optical Franck-Condon transition upon light excitation, thus altering the charge distribution of the probe. The surrounding solvent molecules at this time $t = 0$, still remain in the same previous spatial and orientational configuration, thus making a highly non-equilibrium situation for the system. The dipoles of the solvent molecules begin to reorient and rearrange themselves around the solute-probe to accommodate the new charge distribution in order to minimize the overall free energy in probes' excited state. During this process, the time dependent rearrangement of solvent molecules around the probe, i.e., reduction in the free energy separation of ground and excited state is reflected in frequency down-shift of the

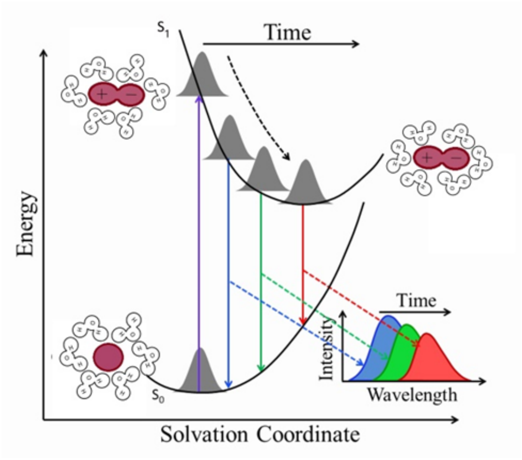

Figure 2.4: Schematic representing the solvent relaxation around a (fluorescent) dipolar probe.

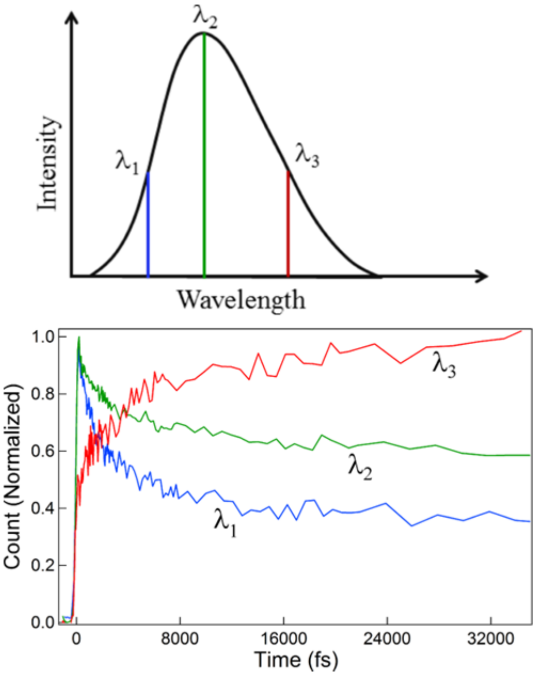

Figure 2.5: Wavelength dependent fluorescence decays.

emission spectrum. The solute-excited-solvent system then relaxes and attains an equilibrium state following the time-dependent fluorescence Stokes shift (TDFSS) of the probe which shifts towards the longer wavelength side with time (Figure 2.4). This time dependent shift in the emission spectrum is called Time-resolved emission spectra (TRES). Hence, the temporal characteristics of solvation can be monitored by spectral response of the solute (Figure 2.4).

The quantitative estimation of solvation dynamics can be made experimentally by collecting the fluorescence decay at different wavelength scanning the entire steady-state emission spectrum of the fluorescent probe (Figure 2.5). The fluorescence decays rapidly at shorter wavelength (λ_1) showing fast lifetime which corresponds to un-solvated state of probe molecule, whereas, the decay at the longer wavelength (λ_2 around peak position of the steady-state emission spectra) decays slowly with a small rise component in the initial time scale owing to moderately solvated probe. The contribution of the rise component increases for the decays collected at higher wavelength (λ_3) that corresponds to fully solvated state of the probe which decays with slower lifetime (Figure 2.5). This sharp decay at the shorter wavelength followed by rise and slow decay at longer wavelength is the typical signature of probe experiencing progressive solvation. Fluorescence decays collected at different wavelengths are fitted with multi-exponential functions. The contributions and time constant of each exponential functions for a particular wavelength is renormalized with respect to the corresponding steady-state emission spectrum to obtain time resolved emission spectra (TRES). Finally, TRFSS is expressed in terms of peak or mean frequency shift with time. The dynamics of the system are described wither by spectral frequency shifts with time or by the solvation time correlation function, $C(t)$, as,

$$C_E(t) = \frac{\bar{\nu}(t) - \bar{\nu}(\infty)}{\bar{\nu}(0) - \bar{\nu}(\infty)} \qquad (2.1)$$

where, $\bar{\nu}(0)$, $\bar{\nu}(t)$, and $\bar{\nu}(\infty)$ are the (average) fluorescence frequencies at time t = 0, t and ∞, respectively.

2.3.2. Molecular Probes for Studying Solvation Dynamics in duplex DNA

Characteristics of dynamics in DNA are difficult to obtain from bare DNA due to low fluorescence quantum yield of DNA bases (A, G, T and C,) and backbone, which decays in few picoseconds.[97,98] Therefore, study of DNA dynamics requires incorporation of a long lived solvatochromic fluorescent probe to extract site-specific dynamics. Binding of drugs (ligand) to DNA is broadly classified into two main groups: Through covalent interactions and non-covalent interactions. DNA-ligand systems formed through covalent interactions between the ligand and DNA are generally irreversible. Such interactions are used by several anticancer drugs. On the other hand, intercalators and non-intercalators (groove binders) form the major class of ligands that bind via non-covalent interactions with DNA bases and/or grooves. Both, covalently and non-covalently attached (fluorescent) ligands are utilized in studying dynamics in DNA experimentally.

2.3.2.1. Covalent Interactions: Base-Stacked Probes

Ligands that are covalently attached to DNA sugar or other parts are irreversible and invariably lead to inhibition of DNA processes; for example, Cis-platin (cis-diamminedichloroplatinum), an anticancer drug, binds to DNA via covalent interactions making an intra/interstrand crossing through chloro groups with the nitrogen of DNA bases. Other examples of covalently attached probes are carboplatin, nitrogen mustard and cyclosporamide. However, measuring TRFSS in DNA requires well-chosen external fluorescent-probe molecules that are incorporated as a part of DNA structure, mainly in place of a base or a base-pair. Such *base-stacked* probes are attached to DNA through covalent interaction replacing a natural base or a base-pair. 2-Aminopurine (2AP), an adenine analogue, is one such base-stacked fluorescent probe that can pair to thymine through normal Watson-Crick hydrogen bonds with limited perturbation to DNA structure (Figure 2.6).[99] 2-AP has high fluorescence quantum yield in solution, but that yield drops considerably when incorporated into nucleic acids due to electro transfer from DNA bases to 2-AP.[100] Thus, using 2-AP several facets of site-specific dynamical properties of DNA can be explored.[101-103] Coumarin-102 is another excellent polarity sensitive fluorescent probe that is synthetically incorporated into DNA by replacing a native base-pair opposite an abasic-site, which was used to monitor site-specific ultrafast dynamics in DNA (Figure

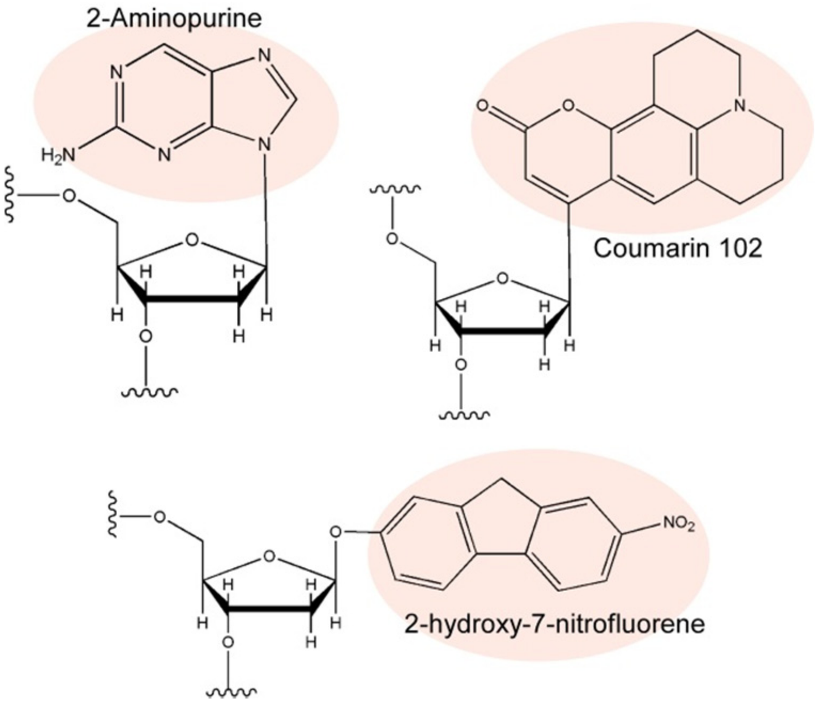

Figure 2.6: Molecular structures of fluorescent DNA-base analogues. Probe molecules are highlighted.

2.6).[104,105] Other base-stacked fluorescent probes such as Nitrofluorene,[106] 3-methyl-isoxanthopterin (3-MI), 6-methyl-isoxanthopterin (6-MI)[107] and 4-aminophthalimide/2,4-diaminopyrimidine[108] are also used to enhance the underlying dynamical process in DNA.

2.3.2.2. Non-covalent Interactions: Intercalators and Groove-Bound Probes

Ligands that are non-covalently bound to DNA fall into two classes: Intercalators and Groove binders. Intercalating molecules such as ethidium bromide, quinacrine and

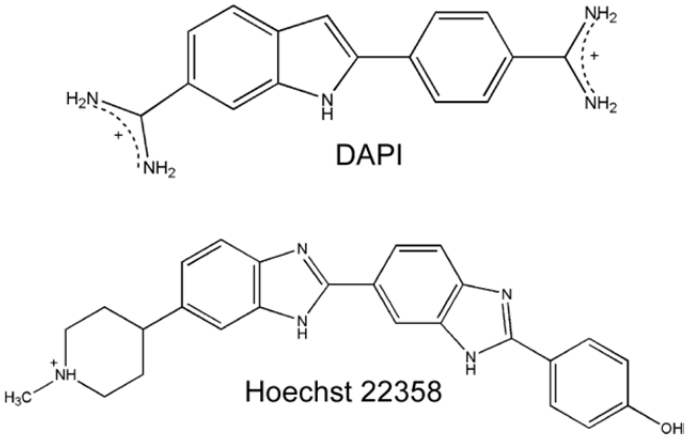

Figure 2.7: Molecular structures of DNA minor-groove binders.

daunomysine that are attached to DNA through intercalative mode have been significantly used as drugs.[109] Intercalators contain planar heterocyclic groups that stack non-covalently between DNA base pairs and gets stabilized via π-π interactions, often in combination with hydrogen bonds. Intercalation of these molecules induces strong structural perturbations which even unwinds helix of DNA and unstack the base pairs causing significant distortion to native DNA conformation. Because GC-rich sequences get unstacked easily, intercalation of ligands occurs preferentially at these sites. Ethidum bromide, proflavin and quinacrine are the most studied intercalators that bind to DNA through stacking interaction of their respective heteroaromatic rings with DNA bases.[110,111] A number of intercalators, including anthracyclines and actinomycins are used as anticancer agents.[110]

Groove binders (Figure 2.7) are another major class of non-covalentaly attached molecules to DNA that play a very important role in drug development. Major and minor grooves of DNA exhibit different dimensions, steric properties, electrostatic potential, hydration, environment polarity and hydrogen bonding properties.[112] Hence, targeting these two grooves require molecules of different shapes, sizes and properties. In general, most of the protein recognizes and binds major grooves of DNA by reading the sequence information in the groove.[113] Minor groove binders are usually crescent shaped that compliments the shape of minor groove of DNA and promotes its binding via electrostatic, van der Waals, hydrophobic and hydrogen bonding. These ligands show greater binding affinity and higher sequence specificity. Most of the minor groove binders are positively

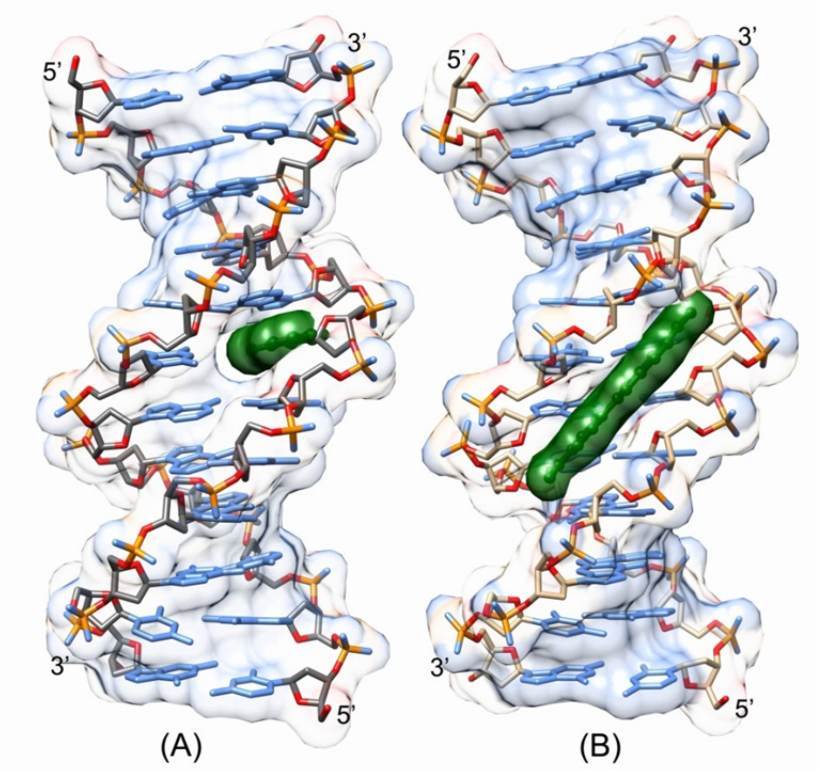

Figure 2.8: (A) Fluorescent base-stacked probe and (B) minor groove binder incorporated inside DNA.

charged which facilitates strong interaction with the electronegative pockets of -A_nT_n-region.[15] Minor groove formed by AT-rich sequences is narrow and deeper as compared to GC-rich sequences which allows the minor groove binders to bind near AT-region with greater selectivity and van der Waals contacts. In addition to wider groove, the amino group of guanine in GC rich sequences protrudes into the groove prohibiting van der Waals contacts. Netropsin, distamycin, DAPI and Hoechst 33258 are well known cationic molecules that have high binding affinity towards minor groove of AT rich sequences (Figure 2.7).[15,18,114-119] Cartoons showing the base-stacked and groove-bound fluorescent probe-molecules inside DNA are included in Figure 2.8. Such base-stacked and groove-bound probe/DNA systems are widely used for solvation dynamics studies in DNA.

2.3.3. Molecular Probes for Studying Solvation Dynamics in G-Quadruplex DNA

Since higher order G-quadruplex structures interfere with telomerase replication and inhibit cell multiplication as well as play vital role in transcription and translation, a large volume of research has been dedicated toward their structural exploration and designing molecules (ligands) that can recognize and bind specifically to these structures in order to stabilize them – leading to inhibition of telomerase and several other proteins' activity. Ligands with high inclination and specific recognition towards G-quadruplex DNA, even in presence of duplex DNA, have been found to affect telomere lengthening.[120-122] Morphological variations of G-quadruplex DNA with diverse loops and G-tract orientations allow recognition of different sites by ligands. Planar aromatic rings of ligands help them to interact with quadruplex structures through stacking at the ends of the G-tetrad core.[123-127] Aromatic ligands, besides end stacking, bind to the loop of quadruplex structures either by stacking with the bases of the loop or by forming intermolecular hydrogen bonds.[123-127] Most of the ligands recognize the backbone (core and loops) of quadruplex DNA and bind through electrostatic and hydrophobic interactions.[128-132] BARCO 19, TMPyP4, Telomestatin, Quarfloxin, Thioflavin T, Acriflavin, Distamycin A, Actinomycin D, Porphyrin derivatives, Perylene derivatives, Hoechst 33258, DAPI and Cresyl violet have been shown to form stable complexes with G-quadruplex DNA through different modes of interactions such as π-π interactions, end stacking, loop recognition, groove binding or by base stacking (Figure 2.9).[133-141]

Solvation dynamics in duplex and G-quadruplex DNA have been studied by utilizing base-stacked, groove-bound and end-stacked ligands which show large fluorescence Stokes shifts, making these molecules ideal for the dynamics study. Fluorescence quantum yield of DAPI[18] and Hoechst 33258,[88] increases significantly upon binding to DNA as compared to that in water. Thus, DAPI and Hoechst 33258 act as excellent fluorescent probes to study solvation dynamics in duplex and G-quadruplex DNA of different sequences using TRFSS

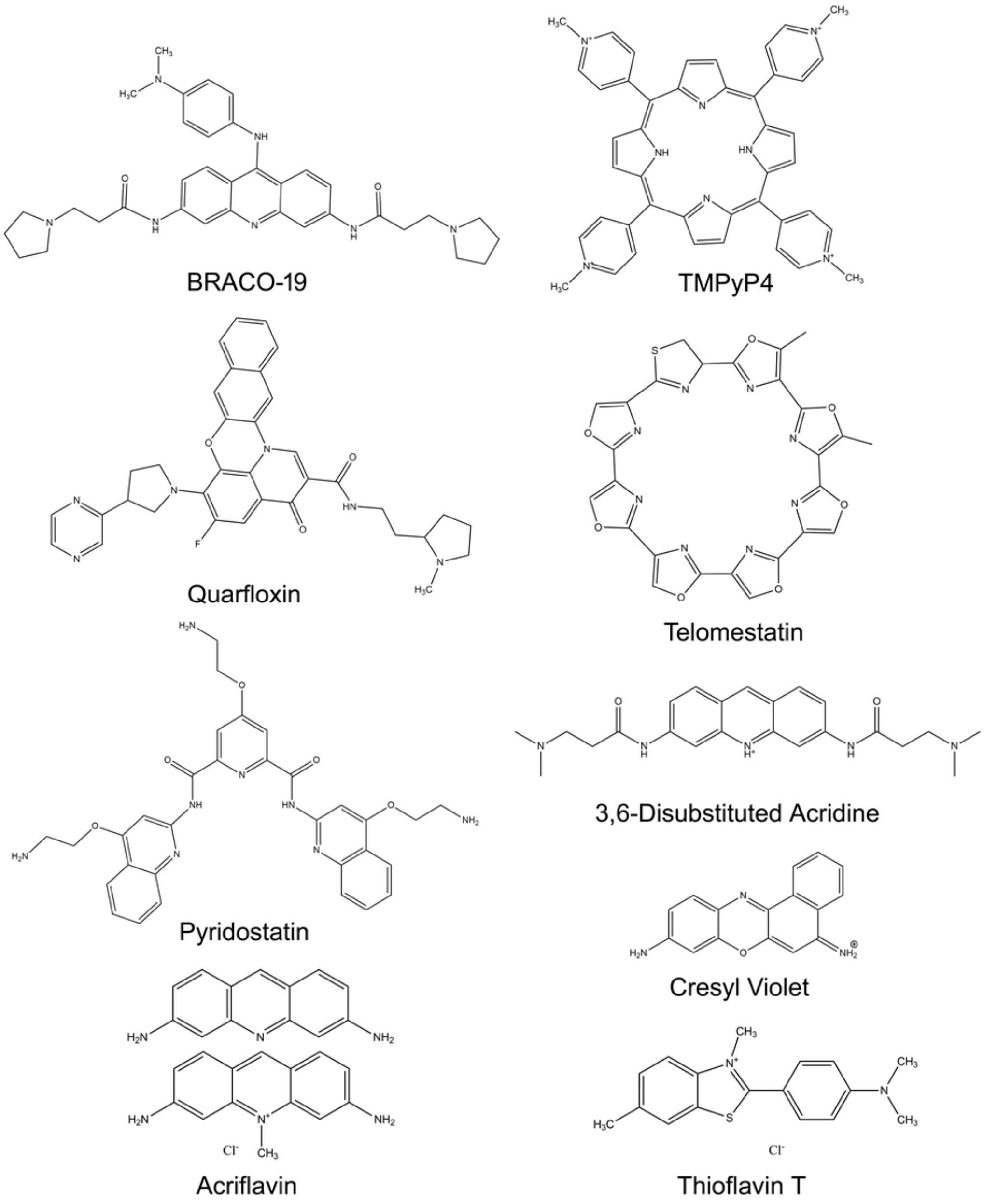

Figure 2.9: Molecular structure of probes that bind to G-quadruplex DNA.

experiments. In fact a major part of this thesis will discuss the solvation dynamics in duplex and G-quadruplex DNA probed by DAPI and Hoechst 33258.

2.4. Molecular Dynamics Simulation

Molecular dynamics (MD) simulation is an excellent tool that complements experimental results and can be used to study dynamics of biomolecular systems *in silico*. MD simulation has the ability to explain the complexity so as to solve the dynamics of complex biomolecular systems. MD simulation is a subset of theoretical research which has the ability to provide details concerning the motion of a system-of-particles with time by applying classical laws of physics and chemistry.[142] MD simulation can be used to address specific static and dynamic properties of the systems in order to obtain insightful information about the system at atomic length-scale. Many such dynamical properties are difficult to obtain from only experiments.

MD simulations are useful to investigate the behaviour, structure, functions and dynamics of simple liquids as well as complex biological macromolecules at atomic length-scale[142] MD simulation of biomolecules is carried out by obtaining the coordinates of model-structure of the system-of-interest in space from NMR or X-ray crystallographic or molecular docking studies. MD simulation describes the atomic motions of molecular system with time in a small time step of typically 2 fs by applying Newton's law of motion in order to understand the physical basis of structure, function and dynamics of biomolecules under the influence of a well-defined (classical) force-field.

MD simulations have been evolved as a powerful tool for complete interpretation of experimental data, although direct comparison of simulation data to experiments may also invoke properties of systems that may be actually different than the real ones. One such example is discussed in Chapter 7. Another interesting aspect of simulation is its capability to decompose the total response of the system into the contribution from individual constituent components – so as to predict the nature and origin of the dynamics of complex biomolecular systems. Several simulation packages are available for simulating DNA, protein and lipids such as AMBER, CHARMM, GROMACS, NAMD, etc., out of which AMBER simulation package is widely used for DNA simulation to obtain intricate structural and dynamical properties.

Interpreting experimental results from view point of structure and dynamics of the simulated molecules employ calculation of either the electric filed interactions or the electrostatic interaction energy of a probe of interest with its surrounding charged/dipolar molecules. Several methodologies have been developed for calculating these interaction energies: In one procedure, electric field components ($\boldsymbol{E}$) from the surrounding molecules along the direction of change in dipole moment ($\boldsymbol{\delta\mu}$) of the probe from its ground to excited state is calculated,[52]

$$E(t) = \boldsymbol{E} \bullet \boldsymbol{\delta\mu} \qquad (2.2)$$

Under this assumption, the fluorescence frequency shift $\omega(t)$ with time in TRFSS experiment can be expressed as,

$$\omega(t) = \omega_0 - \boldsymbol{E} \bullet \boldsymbol{\delta\mu} / \hbar \qquad (2.3)$$

In other procedure, pairwise Coulomb interactions between point charges is performed to calculate the electrostatic interaction energy as,[50,51]

$$E(t) = \left(\sum_{i=1}^{N_{probe}} q_i^{g/e} \sum_{j=1}^{N_{solvent}} q_j\right)/r \qquad (2.4)$$

or
$$E(t) = \left(\sum_{i=1}^{N_{probe}} \Delta q_i \sum_{j=1}^{N_{solvent}} q_j\right)/r \qquad (2.5)$$

In equation 2.4, interactions of either ground (*g*) or excited (*e*) state atomic charges of the probe with surrounding solvent atomic charges is considered; however, it is also proposed that the interactions of partial charge difference, Δq (i.e., $q_{excited} - q_{ground}$) of the probe with surrounding solvent charges can be calculated (equation 2.5). More so, to eliminate the artefacts that arise from the truncation of long-range electrostatic interaction in simple pairwise Coulomb sum, a cutoff neutralized damped shift force (DSF) method is also proposed.[143] In this DSF formalism the electrostatic interaction energy is calculated as,[51,143]

$$E(t) = \sum_{i=1}^{N_{probe}} q_i^{g/e} \sum_{j=1}^{N_{solvent}} q_j \left[\frac{erfc(\alpha r)}{r} - \frac{erfc(\alpha R_c)}{R_c} + \left(\frac{erfc(\alpha R_c)}{R_c^2} + \frac{2\alpha}{\sqrt{\pi}}\frac{exp(-\alpha^2 R_c^2)}{R_c}\right)(r - R_c)\right] \qquad (2.6)$$

or

$$E(t) = \sum_{i=1}^{N_{probe}} \Delta q_i \sum_{j=1}^{N_{solvent}} q_j \left[\frac{erfc(\alpha r)}{r} - \frac{erfc(\alpha R_c)}{R_c} + \left(\frac{erfc(\alpha R_c)}{R_c^2} + \frac{2\alpha}{\sqrt{\pi}}\frac{exp(-\alpha^2 R_c^2)}{R_c}\right)(r - R_c)\right] \qquad (2.7)$$

where interactions of either ground (*g*) or excited (*e*) state atomic charges of the probe with surrounding solvent charges (equation 2.6), or the interactions of partial charge difference, Δq (i.e., $q_{excited} - q_{ground}$) of probe with surrounding solvent charges (equation 2.7) are calculated. Finally, time-correlation functions of either electric field-field fluctuations or electrostatic energy-energy fluctuations are generated as,[50-52]

$$C_S(t) = \frac{\langle \delta E(0)\delta E(t)\rangle_{g/e}}{\langle \delta E(0)^2\rangle_{g/e}} \qquad (2.8)$$

where $\delta E = E(t) - \langle E \rangle$ is the fluctuation of the electrostatic energy (or field) of the probe. Subscripts, *g* and *e* represent the time-correlation functions in ground and excited states, respectively.

Mathematically, all the above procedures are correct. Thus, the real test of simulation methods to predict the actual experimental results boils down to the fact that the simulated correlation, $C_S(t)$, should match well to the experimental solvent response function, $C_E(t)$. Experimentally, the normalized solvent response function can be calculated using equation 2.1. Now, in experiment, as long as the molecular system stays within linear response regime to an external perturbation, the experimental solvent response function, $C_E(t)$, becomes equivalent to the simulated *equilibrium* (or non-equilibrium) energy-energy (or electric field-field) time-correlation function, $C_S(t)$, within the approximation of fluctuation-dissipation theorem.[52,144] However, direct comparison of simulation to experimental results have been performed mainly in bulk water and DNA systems, and few in proteins, showing the validity of linear response theory.

2.5. Dynamics of Water

Leonardo da Vinci recognized long ago the diverse roles of water and termed it as "vehicle of natural changes". Water, directly or indirectly participates and controls chemical and physical changes facilitating important biological processes for sustaining life on earth. Small size, large dipole moment and the ability to form stable structure enables water molecules to actively participate in many biological functions. Water stabilizes biomolecules either by directly making hydrogen bonds or through hydrophobic interactions. Thus, involvement of water paves the way to many cellular processes such as enzyme kinetics, molecular recognition, ease conformational fluctuations, protein folding/aggregation, protein-ligand recognition, DNA-protein and DNA-ligand interactions.[14-19] Water molecules, thus affect the dynamics of biomolecules, and accordingly, fluctuations of biomolecules affect water dynamics. However, obtaining simplified picture of the complex solvent dynamics around biomolecules still remains a challenge.

Significance of water in life's process and as a unique universal solvent for biological and chemical processes continues to encourage experimental, theoretical and computational endeavours to understand its structural and dynamical aspects. Uncorrelated motion of water molecules by random step is the primary mode of displacement of water in liquids forming strong network of three-dimensional hydrogen bonds. Water molecules interact strongly with its neighbours through extensive hydrogen bond network forming four hydrogen bonds, two via hydrogen-donating OH groups and two via hydrogen-accepting oxygen atom.[145] This molecular arrangement being very dynamic, participates in breaking and reforming of hydrogen bonds in picosecond time scales. Water molecules are characterised by intra and inter-molecular vibrational modes which occur on a time scale between several tens to several hundreds of femtoseconds. These vibrational and librational motions of water molecules are expected to be modified significantly when it is in a close proximity with heterogeneous surface. However, rates of breaking and reforming of hydrogen bonds affect the rotational and translational motion of water molecules. Therefore, complete understanding of the water dynamics requires knowledge of its detailed molecular motions (rotational, translational and vibrational).

Dynamical aspect of solvation in polar solvent is investigated by simulating liquids such as water,[36,38] methanol[146,147] and acetonitrile.[48,148] Computer simulations have revealed that the response of solvent to the altered charge of solute in its excited state is bimodal in nature.[149,150] It is interesting to note that one part of relaxation time consists of initial ultrafast response owing to inertial vibrational motion of solvent molecules and accounts for ~80% of total relaxation. This initial response occurs on a time scale of 10-20 fs and is well fitted by a Gaussian function. Such ultrafast response from inertial motion of solvent molecules indicates that solvent dynamics plays an important role in many aqueous charge transfer processes.[151,152] The second dynamical component which accounts for remaining relaxation is much slower owing to diffusive motions and occurs on a time scale of ~1 ps.[38]

Experimental examination of molecular relaxation of liquids is made possible by the development of time domain and frequency domain techniques with high spatial and temporal resolution. However, the ability to experimentally resolve intra and intermolecular motion and dynamics occurring in ultrafast timescale is limited by instrument response. Jimenez *et al.*, through TRFSS experiment measured water relaxation around excited state of dye, coumarin 343 (C343).[38] The decay of solvation time correlation function obtained in their experiment is fitted well with a Gaussian component summed with two exponential relaxations. The fit extracts initial part of water solvation as extremely fast Gaussian component of 28 fs which accounts to 48% of the total amplitude and is attributed to liberational motion of solvent. A slow exponential component of 126 and 880 fs respectively, corresponding to 20% and 35 % of the total relaxation is also extracted.[38] In another study by Huppert and co-workers, it has been reported that the solvation dynamics of rhodamine 800 in water shows a bimodal behaviour with an ultrafast component of less than 100 fs.[153] More recently, Fleming and co-workers have carried out 3-pulse photon echo peak shift measurement for dye (eosin) in water. Their experimental result was modelled with three exponential fit (upto 100 ps) which resolved ultrafast time component of ~17 fs contributing to 73% of the total response, along with two slow exponential component of 330 fs (15%) and 3 ps (12%).[154]

Though the experimental results show that the inertial component of solvation dynamics of dye molecules occurs at very fast timescales of few tens of femtoseconds, theoretically, water solvation is predicted to be even faster. Using MD simulation Maroncelli and Fleming,[155] and Bader and Chandler[156] have predicted faster dynamics of ~25 fs with even larger amplitude decay of 70%–90%. Song and Chandler,[157] reconstructed the theoretical solvation time correlation function using dynamic dielectric continuum theory to compare the fluorescence up-conversion experimental results of Jimenez *et al.*.[38] However, the time scale of solvation dynamics predicted theoretically is again much faster than that observed in previous experiments. In an elaborate work by Corcelli and co-workers on equilibrium and nonequilibrium simulation of a well-known minor groove binder (Hoechst 33258), they found that the solvation dynamics of Hoechst 33258 in water decays with three exponential component of ~9 fs (~50%), ~170 fs (~30%) and 1.4 ps (~18%).[158]

From all the above studies it is found that dynamics in neat water are found to proceed in three distinct time-scales of specific dynamical origin. The ultrafast inertial component with a time constant of ~10-50 fs followed by intermediate component of time constant ~250 fs and the slowest component of ~1 ps. The ultrafast component of ~10-50 fs is attributed to the collective polarization which is gradually reducing towards equilibrium, accelerated in speed by large dielectric constant of water. Intermediate component of ~250 ps originates from the rotational and translational motions of water molecules, whereas, decelerated damped polarization relaxation due to intermolecular correlation is assigned for the slow ~1 ps component. Combining experimental and computational methods, the quantitative measurement of the time scale of the solvent response has helped to understand the essential relevance of water dynamics in ionic conductivity,[151] chemical reactions,[15,159] and reaction rate for processes involving charge motion.[151,152] Extensive work has been done in order to explore structural and dynamical aspects of bulk water. However, the knowledge acquired on the behaviour of solvent in constrained environments, especially in-and-around biomolecules[41-45,160] in terms of its structure and dynamics is difficult to comprehend which triggered tremendous activities over last few decades with new insights coming out from such studies now and then changing our perspectives time-to-time. This thesis compiles such studies in DNA and lipid bilayer which upgrade the current perspective, providing new insights on the structure and dynamics of these systems.

From the view point of dynamics, solvent behaviour in bulk water differs significantly from that of water near biological and chemical macromolecules. Thus, attempts to study water solvation and dynamics of hydrated complex systems like micelles,[43,161] reverse micelles,[43,160,255] ionic liquid,[162-164] cryoprotectant mixture,[256] binary mixture,[257] deep eutectic (DU) melts,[258] protein,[43,36,195,196] DNA,[43,45,107,165,166] DNA-protein complex,[167-169] etc., using combination of theoretical, computational and experimental techniques with spatial resolution of few angstrom and time resolution of few femtoseconds allow us to comprehend intricate structural and dynamical aspects of these systems. Despite, continuous research activities to understand the dynamics of solvation in DNA, proteins, DNA-ligand and protein-DNA complexes, many conflicting concepts and crucial interconnected questions reappear time-and-again that needs thorough investigations. Hence, exploring the relationship between biomolecules structure, its intrinsic dynamics and the dynamics of its hydration water requires considerable further studies. A brief discussion on the existing understanding of dynamics of solvation in biologically important biomolecules is compiled in the following sections – in order to provide an overall picture of existing progress in understanding of water and ion dynamics around biomolecules, viz. protein, DNA and DNA-protein complex.

2.6. Dynamics of Solvation in Protein

Proteins are fascinating macromolecules made up of amino acid residues, which perform broad range of functions in living species. Biological functions of proteins substantially depend on its structure and dynamical properties. Water molecules residing near protein surface are fundamental to its structural stability, flexibility and dynamical fluctuations. Interactions of water molecules with proteins govern many biological activities such as protein folding, acceleration of enzymatic catalysis, molecular recognition, electron and proton transfer in protein, protein-protein, protein-DNA and antibody-antigen interactions.[14-19] Therefore, in order to understand vast array of functions performed by proteins, it is vital to characterize the dynamical profile of water in-and-around proteins.

Earlier studies have confirmed the presence of water molecules around protein.[170-172] Kauzmann introduced the concept of hydrophobicity and iceberg model and came up with an important finding of waters' involvement in protein folding process.[173,174] Motion of hydration water and their interactions with proteins have been studied tremendously by series of experimental techniques which primarily include NMR, X-ray diffraction, neutron scattering, THz and 2D-IR spectroscopy and by MD simulation. Dielectric relaxation measurement[175] and neutron scattering experiments[176] have given a clue for different behaviour of bulk and protein-bound water. With improved temporal and spatial resolutions, several studies have shown slow solvation dynamics near protein surface as compared to bulk water and even different solvation response for water molecules present at different regions of same protein. In a study, Wüthrich and co-workers have reported the residence time of water molecules at protein surfaces to be 300-500 ps.[177] Another study by Halle and co-workers has shown relaxation time of surface water ~10-50 ps,[178] whereas Bryant and co-workers have talked about translation motion of water around protein with a time constant of 30-40 ps.[179]

Use of extrinsic probe to study solvation dynamics in protein can add many complicacies as the probe can affect the biological activities of proteins. Therefore, fluorescent amino acid, tryptophan, is used as an intrinsic probe to explore hydration dynamics around protein. Tryptophan being natural probe does not disturb the conformation of protein and can help in exploring the solvation dynamics of its inherent state. Solvation dynamics of tryptophan in bulk water completes within ~1 ps, but shows 10-20 times slower decay in protein.[95,180] In an attempt to study solvation dynamics of melettin in coiled primary structure using intrinsic tryptophan shows that the total energy of the system relaxes with two time components of 620 fs which is assigned to bulk water and 14.7 ps that is attributed to bound water at protein surface.[180] Further, Flemming and co-workers studied the dynamics of non-covalently bound eosin to lysozyme using 3PEPS and found a slow component of 530 ps owing to water molecules bound to protein.[181] Another solvation dynamics study of non-covalently attached DCM dye to human serum albumin shows two distinct time constants of 600 ps and 10 ns, where the slow time component of 600 ps is assigned to bound water and 10 ns to the overall tumbling of protein.[182] More so, Bhattacharya and co-workers showed hydration dynamics at different active sites of enzyme, glutaminly-tRNA synthetase (GlnRs), using covalently attached fluorescent probe, acrylodan. They found that dynamics of GlnRs relaxes with two time constants of 400 ps and 2 ns, which changes significantly showing different time constants for solvent relaxation upon binding of tRNA and glutamine to GlnRs, respectively.[183]

Soon after, femtosecond solvation dynamics study of monellin using tryptophan as an intrinsic probe exhibited biphasic relaxation with time constants of 1.3 ps owing to free and quasi-free water molecules and 16 ps owing to surface-bound water layers. However, denatured monellin relaxes with slower time constants of 3.5 ps and 56 ps. Time constant of 3.5 ps is attributed to bulk water and 56 ps reflects bound water along with the motion of protein backbone.[184] Several other hydration dynamics studies on staphylococcus nuclease[185] and human thioredoxin[186] using tryptophan as a local molecular probe show distinct relaxation times of 5.1 ps and 153 ps, and 670 fs and 13.2 ps, respectively. The observed fast time constants are assigned to bulk like water, whereas slow time constant to the bound water relaxation. In another solvation dynamics study of bovine pancreatic phospholipase A_2 (PLA2) using tryptophan shows relaxation with time constants of 900 fs and 14.2 ps,[187] whereas, in human serum albumin the system shows initial solvation in picoseconds followed by dynamics in tens to hundreds of picoseconds.[188] The above elucidation of solvation dynamics in protein provides a clear illustration that protein dynamics is biphasic in nature which further shows relaxation in distinct time constant of few picoseconds owing to bulk like water and tens to hundreds of picoseconds due to bound structured water at protein surface and/or from exchange between bound and free water.

Very recent studies by Zhong and co-workers on DNA polymerase IV and Staphylococcal nuclease (SNase) with buried single tryptophan have shown that relaxation of hydration water and fluctuation of protein are coupled together. They have also discovered that the dynamic interactions between water molecules and protein, as well as protein side chain fluctuations on picosecond time scale are governed by the motion of hydration water.[189-191] However, water relaxation is always faster than the side chain relaxation. These studies have thus clarified that there exist a relationship between protein fluctuations and motion of hydration water. In another study, they have characterized the hydration dynamics around β-barrel protein at 17 different sites using tryptophan as molecular probe and found three distinct time scales for hydration water relaxation from hundreds of femtosecond to hundred picoseconds. The outer layer of hydration shell relaxes in femtosecond time scale and behaves like bulk water, whereas, reorientational motions of inner water layer occur in few picoseconds and restructuring of water networks takes place in tens to hundred picoseconds.[192] These studies indicate that motion of water molecules on varied protein surfaces makes water dynamics highly heterogeneous which is not only correlated with its local structure, but also to the overall protein architecture.[192]

As experiments collect collective response of the surrounding environment including water and protein, it is very difficult to resolve the contributions from individual component in order to explore the origin of slow dynamics. Although water dynamics around protein differs from protein to protein and from sites to sites, but several questions about the origin of slow dynamics still remain and need to be investigated more thoroughly using MD simulations. MD simulation is used to investigate protein dynamics as it has the ability to disentangle the total response of complex macromolecules into its individual components and can reveal details concerning dynamics of individual components in the system. The first MD simulation of protein was carried out in vacuum on bovine pancreatic trypsin inhibitor with four strongly bound water molecules in its interior showed various motional phenomenon and fluid-like behaviour of folded protein.[193] With steady progress to simulate biomolecules in presence of water, Sharon and Levitt performed 210 ps of simulation on solvated bovine pancreatic trypsin inhibitor and revealed that the water molecules near protein surface show decelerated rotational motion with higher water density.[194] Karplus and Brooks explored the dynamical effect of solvation on the active site of lysozyme and observed that water molecules play crucial role in stabilizing the charged networks in active sites of enzyme and the interaction of solvent-protein regulates the magnitude of solvent effect on the dynamical behaviour.[195] Among several solvation models, the one given by Nandi and Bagchi,[196] which is based on two state model depicting free and bound state of water molecules around protein, and the other by Zewail and Bagchi,[197] where they considered the exchange between layer of free and bound water, were reconsidered by Zewail and Wang to account for the exchange between free and bound water including the coupling of bulk water with the surface layer.[198] It has been found that the residence time of these water molecules in shell shows a bimodal distribution with two time scales, the fast component arises from the free bulk-like water and the slow time component is inversely proportional to the amplitude of contribution of slow component to overall dynamics. Observations of this model are found to be in agreement with the experimental solvation dynamics results of monellin.[184] Pettit and co-workers simulated myoglobin to obtain the lifetime of water molecules on the surface of protein. They found that the residence times of water molecules are widely distributed from extremely short to extremely long time components and shows biphasic behaviour. They observe that the residence times of water molecules close to proteins are found to exhibit longer time components in tens of picosecond, whereas the residence times of interfacial mobile water depend on the extent of access of hydration sites to bulk water and decays in hundreds of femtosecond to few picoseconds.[199] This finding is consistent with the experimental results of Boxer and co-workers.[200] In another simulation on myoglobin at different temperature from Karplus's group shows mobility of water molecules to be governing factor for protein fluctuations above 180 K.[201] In order to determine the origin of dynamics observed by Zewail and co-workers in Stokes shift experiment,[184] Nilson and Halle simulated monellin in water. After decomposing the total response of the system into its contributions from water and protein based on linear response theory, they found that water decays with a time constant of 1.5 ps and the long correlation time of 74 ps is attributed to protein motion, thus ruling out the possibility of interconversion between free and bound water near surface of protein.[53] Further, Zhong, Singer and co-workers, based on equilibrium and non-equilibrium simulation of myoglobin assigned the long-time constant to coupled motion of water and protein in contrary to Nilsson-and-Halle's assertion.[54] In another study, Bagchi and co-workers have performed simulation on globular protein H-36 to observe the sensitivity of polar solvation dynamics on the extent of exposure of a probe (tryptophan) and found that there exists an interesting correlation between solvation dynamics and surface exposure of the probe, i.e., more the probe is exposed towards surface water, faster the dynamics of solvation.[202] In another study, Golosov and Karplus simulated immunoglobulin binding domain (B1) of protein-G (GB1) and calculated the correlation functions at 11 different sites of the protein using linear response approximation.[202] They reported that dynamics is highly heterogeneous and occurs in time scales from 20 to 200 ps for different sites and suggested coupled water-protein motion for the slow response similar to the observations of Zhong, Singer and co-workers.[54] More recently, Toptygin and co-workers on decomposing the total response of non-equilibrium simulation on GB1 using tryptophan as fluorescent probe found that water relaxes with a time constants of 5 - 113 ps and the long 2.6 ns of slow dynamics is assigned to the protein motion.[203] Very recently, Laage and co-workers by combining extensive MD simulation on lysozyme and analytical jump reorientation model for water found that ~80% of hydration water slowed down by a factor of ~2-3 which does not arise from only slow bound water, but results from the coupled motion of protein and water molecules.[204] In order to find the origin of dynamical perturbation of water molecules of hydration shell compared to bulk, Laage and Fogarty simulated a series of globular protein. They found that the within the hydration shell, the distribution of reorientation dynamics of individual water is independent of protein size and its secondary structure showing similar distribution of reorientation times.[205] Very recently, Bagchi and co-workers have investigated the role of coupled dynamics of water molecules and side-chain residues of proteins in the dynamics of hydration layer by selecting naturally occurring probes located at various positions on protein surface. They observed that relaxation timescales exhibited by differently located probes are different because of the restricted orientation of quasi-free water molecules of that region which are strongly hydrogen bonded with longer life-time. They have gathered considerable amount of insight on self and cross correlations, obtained from the decomposed total solvation energy, which reveals that water and protein segment motions are anti-correlated. They also observed significant aspect of conformational fluctuations which profoundly influences solvation dynamics, showing that the dynamics gets accelerated or decelerated depending on probe's position upon freezing the motion of protein side-chain.[206]

2.7. Dynamics of Solvation in DNA

2.7.1. Experimental Studies

Bases and backbone of DNA are abundant in highly polar/charged groups such as oxygen, nitrogen, carboxylic, amide group, and phosphates; therefore water plays a critical role in stabilizing the DNA bases and the whole structure. Thus, water is of fundamental importance for their cellular functions. Water molecules present in the proximity of DNA reside in grooves and in the hydration shell next to these grooves. Constrained water molecules bound to minor and major grooves, which form spine-of-hydration,[207] as well as the spanning water network in the hydration shell of DNA provide stability to DNA structure, facilitate charge transfer within, allow conformational mobility, and govern many crucial chemical processes involving DNA-protein and DNA-ligand interactions.

DNA shows a number of divergences in its hydration because of their polyanionic nature and uneven twisted ladder shape. In order to stabilize the net negative charge under physiological conditions, DNA interacts with the surrounding cations and dipolar water,[165] thus making the functional hydration shell of DNA to extend to several water layers from its surface – as a whole known as condensation layer.[8,208,209] Interaction of DNA with the surrounding solvent molecules makes it very dynamic in nature. Therefore, depending on hydration number, i.e., number of water molecules per nucleotide, DNA adopt different conformational forms and undergo transitions from B-form to A-form or to Z-form.[59,60] Motions of counterions and water molecules near DNA show diverse dynamical properties with spatial disorder and dispersed relaxation. Though the atomic level investigation has revealed the importance of water in maintaining structures of DNA, its role on hydration and counterion dynamics is very versatile which did not allow to answer many relevant questions clearly till now. The first part of this thesis is dedicated to discussion of such questions and their probable answers.

Earlier experimental studies on fluorescence anisotropy decay of ethidium bromide bound to duplex DNA provided evidence for internal motion in nucleic acid on nanosecond time scale in contrary to known rigid DNA helix,[210] and also interpreted about the torsional dynamics of DNA.[211] Fluorescence anisotropy decay of intercalated dyes such as quinacrine and its derivative 9-amino-6-chloro-2-methoxyacridine (ACMA) also emphasized on internal flexibility of double stranded DNA.[212] These initial studies suggested that DNA holds significant internal flexibility.[213-216] In late nineties, Berg and co-workers studied temperature dependent Stokes shifts of acridine orange intercalated in DNA which illustrates that the internal motion of DNA is diffusive in nature rather than being vibrational – a typical dynamics as seen in crystals.[217] Experimental techniques including EPR[218] and fluorescence anisotropy[219] anticipated the evidence of DNA deformation in terms of bending and twisting of DNA helix and existence of internal DNA motion. These results, however, suggested that the long length fluctuations in DNA relax in picoseconds timescale for shortest motion and in microseconds for the longest mode. However, quantitative estimation of DNA dynamics at the level of individual bases in time scale of picoseconds and sub-picoseconds remained hard using these techniques.

Around this time, dynamics of pure liquid probed by fluorescent molecules in solution and protein dynamics using tryptophan as an intrinsic probe were measured extensively by TRFSS technique.[95,188,220] However, unlike tryptophan, fluorescence quantum yields of natural DNA bases are very low. Thus, study of DNA dynamics through TRFSS experiment requires incorporation of external fluorescent probes into DNA that can be used as an intrinsic probe in order to monitor the dynamics in DNA. Toward this end, E. T. Kool presented innovative molecular strategies of replacing natural bases of DNA with designed molecules having enhanced fluorescent properties.[148] Based on this concept, R. S Colman incorporated covalently attached coumarin-102 opposite abasic-site in place of a natural base-pair, which stacked between flanking natural base-pairs and acted as an excellent probe for dynamic studies in duplex-DNA.[104] Using such fluorescently labelled DNA, Berg and co-workers measured solvation dynamics in DNA following TRFSS of this covalently attached *base-stacked* coumarin 102 for the first time using TCSPC technique.[105] Large change in dipole moment upon optical excitation makes coumarin 102 an ideal probe for TRFSS experiments. They found that the solvation response function for DNA shows bi-exponential decays from 100 ps to 30 ns and extracted two distinct time-components of 300 ps (47%) and 13 ns (53%).[105] This result showed that DNA relaxes much slower than pure water, but the origin of such distinct dynamics remained unclear at that time. They also speculated that the slow dynamics could result due to the relaxation of DNA proper or motion of the counterions along the DNA helix and/or the constrained motion of spine-of-hydration and/or exchange of slow groove water with ions. Shortly after this finding, Berg and co-workers again measured TRFSS of base-stacked coumarin 102 over three decades of time from 40 ps to 40 ns with improved resolution of TCSPC technique.[221] They came up with an exciting result that solvent response function for DNA follows logarithmic relaxation from 40 ps to 40 ns instead of bi-exponential as seen in their previous work.[105] This logarithmic decay of DNA relaxation does not show convergence even at 40 ns. They further demonstrated that the energy relaxation process stretched over three decades in time which shows complicated underlying solvent response which could arise from motion of charged moieties of DNA structure. Berg and co-workers even predicted the possibility of faster process in DNA dynamics that could be explored with techniques of ultrafast time resolution.

Around similar time, Zewail and co-workers reported site- and sequence specific solvation dynamics in DNA using covalently attached base adenine analog, 2-aminopurine (2-AP) from 100 fs to 50 ps using fluorescence up-conversion technique.[101] They modelled solvation correlation function of 2-AP modified DNA using bi-exponential decay that revealed two time-constants of 1.5 ps and 11.6 ps. In same fashion, they also investigated DNA hydration dynamics using minor grooves binder, Hoechst 33258.[119] Following TRFSS of Hoechst bound to DNA from femtoseconds to tens of picoseconds, they found that DNA hydration again shows "bimodal" behaviour. The solvation correlation function was again modelled with bi-exponential function with two distinct time constants of 1.4 ps (64%) and 19 ps (36%), although Hoechst in bulk water decays with the time constants of 195 fs (33%) and 1.2 ps (67%). At that time these results indicated that solvation dynamics in minor groove of DNA differ significantly from that of bulk water and these two well separated time constants for DNA dynamics originate from labile bulk water (1.4 ps) and weakly bound ordered water (19 ps).

Apart from Hoechst, there are known ligands that have a high propensity of binding to minor groove of DNA. Out of these, DAPI, another popular minor groove binder is widely used to probe dynamics in DNA. Complimentary to Zewails's work, Pal and co-workers reported the dynamics of duplex DNA probed by groove bound DAPI and Hoechst 33258 using picosecond resolved TCSPC technique.[222] They found bi-exponential solvation correlation function with a time constants of 130 ps (75%) and 2.35 ns (25%) for DAPI-DNA system and 110 ps (68%) and 2.58 ns (32%) for Hoechst-DNA complex. Similar time constants associated with the response of the surrounding environment show that both the ligands occupy minor groove of the DNA. They have attributed the fast time constant (~130 ps) to intramolecular proton transfer and electron transfer processes from bases of DNA to DAPI, whereas the slow time constant to the DNA motion.

Ernsting and co-workers measured time-resolved emission Stokes shift of a molecular probe 2-hydroxy-7-nitrofliorene (HNF) incorporated inside 13-mer DNA duplex opposite to an abasic site in femtosecond time scale using pump-probe transient absorption technique.[106] The dynamic Stokes shift obtained in their experiment is modelled using sum-of-three exponentials of time constants 221 fs, 2.35 ps and 18.7 ps, concluding that water molecules bound to DNA is the major contributor to the observed dynamics.[106] Further, Vauthey *et al.* studied the dynamics of fluorescent probe, oxazole yellow, intercalated into DNA using ultrafast fluorescence spectroscopy and found that the measured dynamic Stokes shift shows two decay time components of 1 ps and 20 ps.[223]

For long, all the above results remained fragmented and reported in segments of 100 ps to 30 ns,[221] 100 fs to 50 ps,[101] 100 fs to 100 ps,[119] 100 ps to 10 ns[222] and 40 ps to 40 ns[105] using different ligands either base-stacked or groove-bound which mostly reported bi-exponential (or logarithmic) decay of solvation correlation functions in DNA. However, none of these studies provided complete picture of DNA dynamics ranging from femtosecond to nanosecond timescale. Thus, to comprehend the entire DNA dynamics from femtoseconds to nanoseconds, Berg-Murphy-Ernsting-Coleman and co-workers combined the measured TRFSS of base-stacked coumarin 102 in DNA of generic sequence using three different techniques; pump-probe transient absorption (40 fs to 120 ps), fluorescence up-conversion (1 ps to 150 ps) and time correlated single photon counting (40 ps to 40 ns) to map six decades of time from 40 fs to 40 ns.[224] Their study revealed very exciting finding, showing that the solvation response of coumarin 102 follows a single power law, quantified with an exponent of 0.15 covering the entire time range from 40 fs to 40 ns.[224] However, these techniques are reported to measure only 70% of the total Stokes shift (from 85 to 15%), indicating that the reorganization of DNA proceeds even beyond the longest time measured (40 ns). This kind of power-law behaviour is observed in glassy materials[225,226] and such kinetics is very surprising in DNA. Moreover, non-existence of any distinct time-component in the overall dynamics, as predicted earlier, indicates that the surrounding solvent (water and ions) and motion of DNA proper (bases and backbone) are coupled together through complex electrostatic interactions, thus following dispersed power-law over entire six decades of time range. As this result did not show any separate time scales which can be assigned to any specific motion of constituent molecules, it raised several questions concerning the origin of power-law dynamics in DNA.

Interestingly, in addition to the power law dynamics seen in the above study, an additional fast motion at the end of the helix was observed when coumarin 102 was stacked near the helix-end. TRFSS results show an additional exponential relaxation of 5 ps. This time constant was attributed to the unique “fraying” motions present at the helix end.[227] This suggests that the power-law relaxation is considered as baseline dynamics of unmodified DNA with an extra rapid fraying relaxation at the end of helix which is highly localized and weakly coupled to the dynamics of the rest of the system. All these data are well convincing that the DNA dynamics is much more complicated than the dynamics in proteins as discussed in previous section.

In spite of the fact that DNA is structurally less diverse than protein, yet the position of the probe inside DNA remarkably changes the observed dynamics. An interesting study from our research group showed that the TRFSS of a minor groove binder, DAPI bound to duplex DNA follows same power-law relaxation, as found in case of base-stacked coumarin by Berg and co-workers, multiplied with sum of two exponentials from 100 fs to 10 ns. It is very compelling to note that the measured dynamics in DNA either with base stacked or groove bound probe experiences a very similar dynamics in the time span of 100 fs to ~100 ps, but differs remarkably from ~100 ps to 10 ns. This qualitative change in dynamics was speculated to originate from the displacement of groove bound water molecules (and possibly ions) which are otherwise believed to be intact in the base-stacked system, thus suppressing the slow contribution to the overall dynamics.[117]

In order to understand the influence of counterions on DNA dynamics probed by base-stacked and groove-bound ligands, TDFSS of coumarin 102 stacked into duplex DNA in presence of various counterions (Li^+, Na^+, K^+, Rb^+, Cs^+, NH_4^+, $N(CH_3)_4^+$, $N(C_2H_5)_4^+$, and $N(C_4H_9)_4^+$) of different hydrodynamic radius were measured from 40 ps to 40 ns.[267] It was observed that the counterions with smaller hydrodynamic radii show almost identical power-law type dynamics, whereas, larger ions (Li^+ and the tetraalkylammonium ions) show an extra exponential component in addition to power-law decay which is directly correlated with hydrodynamic radii of the ions.[228] However, TDFSS of DAPI groove bound to duplex DNA in presence of three different counterions (Na^+, Rb^+ and TBA^+) are found to be nearly identical from ~100 fs to 10 ns.[18] Thus, revealing the fact that unlike the base-stacked probe in which the counterions have tendency to visit the probe's site, groove-bound DAPI cannot sense the motion of these counterions as it displaces them away from its binding site.

Regardless of large number of studies describing the DNA dynamics probed by groove-bound and base-stacked fluorophores, none of the studies have talked about how the ligand gets solvated inside the minor groove of DNA formed by varying AT-/TA-rich sequences. In an attempt to explore the sequence dependent solvation dynamics of a groove binder DAPI in the minor groove formed by four different sequences, Sen and co-workers investigated the TRFSS of DAPI over broad range of time from 100 fs to 10 ns.[229] These sequences differ near the binding site (−AATTG−, −TTAAG−, −TTAAC− and −AATTC−) of DAPI. Sen *et al.* found that the Stokes shift dynamics of groove-bound DAPI in three sequences (−AATTG−, −TTAAG− and −AATTC−) follow a power-law multiplied with sum-of-two exponentials, whereas, changing the sequence from −TTAAG− to −TTAAC− influences the dynamics significantly such that it follows a single power-law over five decades of time from ~100 fs to 10 ns. They concluded that dynamics of the water molecules near the ligand-binding sites, coupled to the local DNA motion, can be a possible reason for the divergence seen in the dynamics.[229]

2.7.1. Simulation Results: Comparison of TRFSS Results to Simulation

There have been several experimental observations of DNA dynamics that show the effects of DNA motion (bases and backbone), DNA sequences, displacement of water molecules, ion atmosphere, binding mode of probe, and probe positions on the DNA dynamics over broad time-ranges. However, exact explanation of such dynamics in DNA was not clear till the time MD simulation studies started dissecting the overall dynamics into the dynamics of individual components of the system, i.e., water, DNA and counterions. Over the years, MD simulation became quite a complimenting method to TRFSS experiment which has the capability to disentangle the complex interactions of multicomponent systems like DNA. With revolutionary progress in computational technology, power, and algorithmic advancement, MD simulation has become one of the most potential methodologies that can explore the complexity of molecular systems and bring out the new insights about the structure and dynamics of the systems.

It's been four decades since the first MD simulation on bovine pancreatic trypsin inhibitor protein in vacuum was published.[193] After that, it took several years to perform simulation on nucleic acid. The first atomic level MD simulation of duplex DNA solvated with explicit water and in presence of counterions for charge neutrality was reported by Kollman and co-workers for 106 ps in 1985.[230] With algorithmic development and accurate parameterization, MD simulations of nucleic acids have become abundant of late. A study by Young *et al.* interpreted the water molecules residing in the minor groove of DNA as "spine-of-hydration" from 1.5 ns long MD simulation.[231] Soon after, Beveridge and co-workers simulated B-DNA extending for 5 ns with explicit water molecules and Na^+ ions and compared the results with NMR and crystallographic studies of corresponding DNA sequence.[232] This study provided details concerning groove widths and dynamics of axis bending in B-DNA. They have also found that the counterions intrude inside minor groove of DNA and may reside along with the constrained groove water molecules, thus affecting the environmental structure and thermodynamics.

NMR, X-ray crystallography and theoretical studies have shown that structural framework and diffusion of water molecules in the immediate proximity of biological macromolecules are different from those of bulk water.[233-235] Therefore, in order to explore the translational mobility of ions and water molecules around biological macromolecule, Makarov and co-workers performed MD simulation on sperm whale myoglobin and A-DNA for 1.1 ns and 10 ns, respectively. They found that the effect of macromolecules on the mobility of water and ions is similar for both proteins and DNA which extends upto 15 Å from the solute. It is also reported that the diffusion of water molecules around DNA is slower than that of bulk water.[236] Differences in the network of hydrogen bonding to the water molecules were also seen in MD simulations of the DNA duplex $d(CGCGCG)_2$ at varying range of temperatures from 20 K to 340 K.[237] Another study has reported longer residence time of water molecules in minor groove of DNA as compared to major groove.[238] In an earlier study, Bagchi and co-workers showed that the dynamics of water molecules residing in minor groove and major groove differ substantially in terms of hydrogen bond lifetime, translational and rotational motion. They found that translational motion of minor groove water molecules is sub-diffusive, whereas, the rotational time constant of water molecules at the interface shows non-exponential decay with a slow time constant of ~200 ps. More so, the hydrogen bonds formed between the water molecules in minor groove are found to have an average lifetime of ~50 ps and maximum lifetime of ~115 ps, whereas the average lifetime of hydrogen bond of major groove water molecules is ~20 ps with maximum lifetime of 35 ps.[239] These time constants suggest slow dynamics of water molecules near DNA as compared to bulk water by an order of magnitude. Though order parameters, properties of DNA, residence time of water molecules, mobility of ions, hydrogen bond lifetime and effective correlation times were determined, but none of the above studies has explored the details of DNA solvation dynamics. On the other hand, Mukherjee *et al.* showed that the dynamics of water uptake and release facilitate drug binding to duplex-DNA – a process that occurs on a complex free energy surface.[240]

In order to capture the effect of counterions on DNA dynamics and convergence of ion motion in the vicinity of DNA, Beveridge and co-workers performed first longest MD simulation of d(CGCGAATTGCGC)$_2$ duplex for 60 ns.[209] They found that the only 94% of ion motion converges till ~60 ns of simulation even though the relaxation time for internal structural motions of DNA converges within ~5 ns.[209] However, a recent simulation of 150 ns from the group of Corcelli have shown that a reasonable degree of convergence for ion motion in-and-around DNA is achieved within 100 ns and to near completion at 150 ns. All these results indicated that motion of ions in the proximity of native DNA is sensitive to long-time dynamics and can contribute to the solvation inside DNA.[241]

To add understanding on the origin and nature of the slow dynamics as seen by Berg and co-workers[105,221,224] and Zewail and co-workers[101,119] in TRFSS studies, Hynes-Bagchi and co-workers carried out 15 ns long MD simulation on 38 base-pair duplex DNA in presence of Na$^+$ counterions and water molecules.[50] Using each of the DNA-bases (A, T, G, C) as an intrinsic probe, instead of base-stacked or groove-bound probes as used in experimental studies, they calculated the energy-energy time correlation functions for each base to characterise solvation dynamics. They found that the average solvation time correlation function shows non-exponential decay with inertial fast component of ~60-80 fs, followed by two time components of ~1 ps and 20-30 ps.[50] These time constants are in close agreement with the time constants observed in experimental results by Zewail and co-workers.[101,119] To get insights of the origin of observed timescales, they decomposed the total response into auto- and cross-correlations of constituent molecules, i.e., water, ions and DNA. They found that ultrafast time component of ~100 fs is dominated entirely by water molecules near the nucleotide, which was attributed to bulk water in experimental results.[101,119] However, presence of large negative cross-correlation between ion and water rules out the possibility of attributing the dynamics to a specific component. Thus, the slow dynamics of 20-30 ps was interpreted to be due to coupled motion of water molecules and ions. Moreover, they suggested the discrepancies in the slow time constant obtained in experiment ~12 ps[101] and simulation ~20-30 ps could be because of the different probe and length of the DNA base pairs used in experimental studies. However, this study did not observe the dispersed power-law dynamics in DNA as found in the experiments of Berg and co-workers. To find the origin of the slow power-law dynamics observed by Berg and co-workers,[224] they have calculated average time correlation functions for four bases which resulted into slow component of ~250 ps, but this finding fails to solve the origin of slow power-law dynamics due to the limited simulation length (15 ns).[50]

More recently, Furse and Corcelli used MD simulation to associate simulated result with TRFSS experimental results of Zewail and co-workers[119] to further explore the dynamics of water molecules around DNA.[51] They have performed equilibrium and non-equilibrium simulation of Hoechst 33258 bound to the minor groove of dickerson DNA, same as used in experiment by Zewail and co-workers, and measured the response of solvent to the change in charge distribution in the Hoechst-probe. Non-equilibrium solvation response and equilibrium correlation functions for ground and excited state were fitted with tri-exponential function within the time range of 10 fs to 100 ps. Their analysis extracted similar relaxation time for both equilibrium and non-equilibrium correlation functions.[51] It was observed that the relaxation time for Hoechst in solution (0.17 and 1.4 ps) and bound to duplex DNA (1.5 and 20 ps) are in excellent agreement with the experimental findings (0.2 and 1.2 ps and 1.4 and 19 ps).[119] Further, they calculated the solvation response of individual components by decomposing the total correlation function into its individual component following linear response decomposition method,[51] proposed by Nilson and Halle.[53] Decomposition of the total response shows that water component decays quickly with maximum contribution from first solvation shell. The DNA component decays slowly and is accountable for the long time component of 20 ps, which mainly originates from the central A-T region near the probe binding site. This result is not in accordance with the interpretation of Zewail and co-workers, where they attributed the slow dynamics to weakly bound water molecules near DNA.[119] Findings of Corcelli and co-workers also agree with results of solvation dynamics in protein given by Nilsson and Halle,[53] but diverge from the findings of Hynes and Bagchi.[50] This study could not observe slow power-law dynamics either as seen by Berg and co-workers in TRFSS experiments.[224]

The power-law dynamics was not anticipated in any of the above mentioned simulation studies, as the emphasis was on simulating experimental results till ~100 ps. Therefore, to provide a clear interpretation about the nature and origin of power-law dynamics in DNA, Berg and co-workers analysed 46 ns of equilibrium MD simulation trajectories of Dickerson DNA, performed by Beveridge and co-workers.[52] They have used central adenine as a test probe to calculate electric field dynamics where the observed dynamics of thermal fluctuations are characterized by electric field correlation function. This simulated solvation correlation function was then compared to non-equilibrium TRFSS experiment based on linear response theory. Comparison of simulation data shows striking similarity of power-law dynamics as observed in TRFSS experiment with base-stacked C102.[224] Further, to find the complicated aspect of the DNA dynamics, total response was decomposed into individual component using a *"polarisation model"*. This model was used to eliminate the signal contribution that originates from strong coupling among the components (cross-correlations) of the system to the total response, so that the contribution from individual components (auto-correlations of intrinsic components) can be predicted independently. They found that under polarisation decomposition method, water contribution to TRFSS response of probe is found to be maximum of ~90% of total dynamics that governs the power-law dynamics at all times. The contribution from counterions was small (~6% of total) and relaxes with an exponential time constant of ~200 ps, whereas contribution of DNA to the total signal is minor (~4%) with a stretched exponential relaxation of 30 ps. Hynes and Bagchi[50] have shown that the slow dynamics originates from the coupled motion of water and counterions, but the decomposition by Sen *et al.* using polarisation model, which eliminates the cross-correlations, showed that contribution of water is much more dominated than that of counterions. Even after applying linear response decomposition method, the results were significantly different from that of simulation data of Hoechst/DNA system reported by Furse and Corcelli[51] which showed DNA motion is responsible for the slow TRFSS response. This inconsistency suggests that there are noteworthy differences between the base-stacked and groove-bound probe/DNA systems which are directly reflected in the components' dynamics as calculated.

Recently, Furse and Corcelli have analysed a set of long simulations on DNA with and without Hoechst 33258 and with Coumarin-102 charges on DNA bases.[242] They showed that when the probes are incorporated into DNA, Coumarin102/DNA system decays slowly compared to native DNA and Hoechst 33258/DNA system, showing nearly power-law type behaviour of the dynamics which is in line with the experiment of Berg and co-workers. They emphasised on the fact that Hoechst replaces significant number of water molecules when it binds to the minor groove of DNA, whereas, minor groove gets widen when a base pair is replaced by Coumarin-102 (opposite an abasic site). In contrary to Berg and co-workers, this study does not support the idea of water being responsible for slow dynamics in DNA. Further, decomposition of the total response into individual component showed that water contributes maximum to the total response in initial times, but after ~100 ps DNA becomes the major contributor and ion contribution being almost negligible. Most of above studies, mainly the recent ones, by both TRFSS experiments and MD simulations which extend into broad time-range (typically 10 ns or more) saw the collective solvation dynamics in DNA is rather dispersed which mainly follow power-law type relaxation features.

2.8. Dynamics of Solvation in DNA-Protein Complex

Even though a considerable amount of experimental and simulation studies have been performed to explore and interpret the structural and dynamical aspects of protein, DNA, yet another system that needs more exploration is the DNA-protein complex. Despite its importance in various cellular processes, the dynamics of water and ions near such complexes are least understood. Dynamic assemblies of protein and DNA initiate cellular signals for various biological activities and facilitate several biological functions in living cells such as transcription, replication, recombination and DNA repair. A considerable number of X-ray and NMR studies have helped to gain insights into static picture of DNA-protein complexes,[243-246] yet deeper understanding of dynamical recognition, possible influence of water and ions on protein-DNA interactions is still incomplete. It has been seen that the change in dynamics around DNA/protein complexes can influence the affinity and specificity of protein-DNA interactions.[10,11,247-250] Elucidation of one such complex interaction includes recognition of mismatched base pair of DNA by DNA mismatch recognition protein (MutS and MutSα). Further, it has been indicated that local effect of mismatched base pairs in DNA such as bending/unbending at mismatch sites, kinking in DNA helix and motional dynamics of mismatch sites act as clue for recognition by MutS and MutSα.[20,21,251,252] In fact a substantial part of this thesis will discuss how insertion of mismatched bases alter the collective solvation of groove bound probe-ligands, which may also act as cue for its recognition and repair by MutS and other proteins.

Rearrangement and release/uptake of water molecules and ions are involved in the formation of stable protein-DNA complexes. Zewail and co-workers explored the dynamics of Histone 1/DNA complex through TRFSS experiment using TNS and DC as fluorescent probes which bind through noncovalent electrostatic interactions and by covalent adduction, respectively.[167] They found that TRFSS data show a strong recognition mechanism between protein and DNA via electrostatic interaction which leads to dynamically rigid complex formation and involvement of hydration water and interface polarity in specificity and stability of the complex.[167] Another time resolved Stokes shift study by Pal and Sarkar has explored the interaction of DNA with nucleic protein histone 1 (H1) and the effect of complexation on ligand binding to the DNA. Solvation studies revealed insignificant change in local environment of DNA-H1 complex upon binding of Hoechst 33258, while base stacking of ethidium bromide in DNA is severely perturbed upon complexation with protein.[253] Other time resolved experiment of base-stacked coumarin 102 in DNA/APE1 complex showed that the slow dynamics as seen in bare DNA persist in DNA/APE1 complex which can influence the rate of reaction and stability of the transition state.[168]

MD simulation study has been employed to understand the heterogeneity in water motion in-and-around DNA/protein complexes. Bandhopadhyay and Sinha have carried out MD simulation to explore the heterogeneity in dynamics of water molecules that resides in different sites of the complex formed by human TRF1 protein and telomeric DNA.[254] They attributed such heterogeneous behaviour of water motion around the protein-DNA complex to the relaxation times of hydrogen bonds formed with the complex. They also showed that formation of such complexes affects the motion of water molecules in a non-uniform manner.[254] All these above studies reveal that the presence of ions and water molecules in the proximity of protein-DNA complexes show dynamical properties which differ from bulk and influences the stability and specificity of the complex.

2.9. Conclusion

The fact that understanding nature of water and ion dynamics near DNA and other biomolecules is vital, but critical, is emerged from all these previous studies. Nevertheless, it has been well-established that TRFSS experiments and MD simulation have tremendous power to unfold the intricate details of DNA dynamics because they can measure dynamics of biomolecular solution in the similar timescales of constituent molecular motions. The current understanding of DNA solvation dynamics clearly indicates that one needs combined experimental and simulation explorations to fully comprehend the intricate coupling of perturbed water and counterion motions near negatively charged DNA. Although, strongly debated discussions have been made in literature regarding the explanations of origin of slow dynamics in DNA, one thing is evident from many of these experimental and simulation studies which extended the measurement time-window over broad range that overall dynamics in DNA follow dispersed power-law type relaxation over broad time-range. Such dispersed dynamics in DNA is found to be rather different from that in proteins. However, it is also found that if this (local) dispersed dynamics in DNA is influenced by counterion motions and/or base-sequence dependent ligand binding to minor grooves then the power-law dynamics can be modulated to exponential type relaxations. It is also evident that there is serious constraint to explain the DNA dynamics accurately if measurement time-window of TRFSS experiments and simulation becomes small, which actually leads to debated conclusions in many occasions. Nevertheless, the recent success of interpreting TRFSS experiments through (direct) comparison of simulated dynamics is very promising, which has surely started upgrading our knowledge of perturbed water and ion dynamics near DNA (and other biomolecules). However, the endeavour to arrive at a unified picture of the biomolecular dynamics is still in its nascent state; although, it is believed that hydration layer water on the outer surface of DNA, proteins and lipids are retarded only moderately by a factor of 2-5 compared to bulk water. The dynamics of water molecules (and ions) in/near grooves of DNA or in clefts of protein surfaces or in hydrophobic pockets of proteins or buried inside lower head-group region of phospholipid bilayer are, however, much retarded, which show dispersed dynamics over very long time extending over decades.

Most of studies discussed in this chapter, mainly the recent ones, on both TRFSS experiments and MD simulations which extend into broad time-range (typically 10 ns or more) show that the collective solvation dynamics in DNA is rather dispersed that mainly follow power-law type relaxations. However, there has been substantial debate on the origin of such dispersed power-law dynamics in DNA. In this regard, some studies indicated water to be dominant and ions with substantial contributor, while some others indicated DNA-motion to be dominated that control the slow dispersed dynamics. The following chapters in this thesis will however show, comparing TRFSS to MD simulation results, that it is actually much harder to explain the dispersed solvation dynamics in DNA, and one may need to study each DNA or DNA/ligand systems separately to explain the origin of dispersed (power-law) dynamics. In fact, this thesis includes results that clearly show that '*there are perturbed slow water molecules near grooves of DNA which control the dispersed power-law solvation dynamics in duplex and G-quadruplex DNA*'. In fact, results presented here will actually disprove some existing understanding about the DNA solvation. Furthermore, through TRFSS experiments this thesis will show that the dispersed power-law dynamics can get significantly modulated by the presence of a single mismatched base-pair inside the minor groove. Through such measurements it has been hypothesised that the changes in collective solvation dynamics in minor groove of DNA, induced by the mismatched base-pairs, may have important role in the mismatch recognition and repair mechanism by the repair enzymes.

Reference

1. Dahm, R. Discovering DNA: Friedrich Miescher and The Early Years of Nucleic Acid Research. *Human Genetics* **2008**, *122*, 565-581.
2. Watson, J. D.; Crick, F. H. C. Molecular Structure of Nucleic Acids: A Structure for Deoxyribose Nucleic Acid. *Nature* **1953**, *171*, 737-738.
3. Drew, H. R.; Wing, R. M.; Takano, T.; Broka, C.; Tanaka, S.; Itakura, K.; Dickerson, R. E. Structure of a B DNA Dodecamer: Conformation and Dynamics. *Proc. Natl. Acad. Sci. USA* **1981**, *78*, 2179-2183.
4. Wutrich, K. *NMR of Proteins and Nucleic Acids*; John Wiley & Sons, 1986.
5. Parkinson, G. N.; Lee, M. P. H.; Neidle, S. Crystal Structure of Parallel Quadruplexes from Human Telomeric DNA. *Nature* **2002**, *417*, 876-880.
6. Wang, Y.; Patel, D. J. Solution Structure of The Human Telomeric Repeat d[AG3(T2AG3)3] G-Tetraplex. *Structure* **1993**, *1*, 263-282.
7. Dai, J.; Punchihewa, C.; Ambrus, A.; Chen, D.; Jones, R. A.; Yang, D. Structure of the Intramolecular Human Telomeric G-Quadruplex in Potassium Solution: A Novel Adenine Triple Formation. *Nucleic Acids Res.* **2007**, *35*, 2440-2450.
8. Manning, G. S.; Ray, J. Counterion Condensation Revisited. *J. Biomol. Struct. Dyn*. **1998**, *16*, 461-476.
9. Anderson, C. F.; Record, M. T. Salt Nucleic Acid Interactions. *Annu. Rev. Phys. Chem.* **1995**, *46*, 657-700.
10. Chiu, T. K.; Sohn, C.; Dickerson, R. E.; Johnson, R. C. Testing Water-Mediated DNA Recognition by The Hin Recombinase. *EMBO J.* **2002**, *21*, 801-814.
11. Royer,W. E. Jr.; Pardanani, A.; Gibson, Q. H.; Peterson, E. S.; Friedman, J. M. Ordered Water Molecules as Key Allosteric Mediators in a Cooperative Dimeric Haemoglobin. *Proc. Natl. Acad. Sci. USA* **1996**, *93*, 14526-14531.
12. Haran, T. E.; Joachimiak, A.; Sigler, P. B. The DNA Target of the Trp Repressor. *EMBO J.* **1992**, *11*, 3021-3030.

13. Woda, J.; Schneider, B.; Patel, K.; Mistry, K.; Berman, H. M. An Analysis of the Relationship between Hydration and Protein-DNA Interactions. *Biophys. J.* **1998**, *75,* 2170-2177.
14. Jayaram, B.; Jain, T. The Role of Water in Protein-DNA Recognition. *Annu. Rev. Biophys. Biomol. Struct.* **2004**, *33*, 343-361.
15. Larsen, T. A.; Goodsell, D. S.; Cascio, D.; Grzeskowiak, K.; Dickerson, R. E. The Structure of DAPI Bound to DNA. *J. Biomol. Struct. Dyn.* **1989**, 7, 477-491.
16. Mikheikin, A. L.; Zhuze, A. L.; Zasedatelev, A. S. Molecular Modelling of Ligand-DNA Minor Groove Binding: Role of Ligand-Water Interactions. *J. Biol. Struct. Dyn*. **2001**, *19*, 175-178.
17. Han, F.; Taulier, N.; Chalikian, T. V. Association of the Minor Groove Binding Drug Hoechst 33258 with d(CGCGAATTCGCG)(2): Volumetric, Calorimetric, and Spectroscopic Characterizations. *Biochemistry* **2005**, *44*, 9785-9794.
18. Verma, S. D.; Pal, N.; Singh, M. K.; Sen, S. Probe Position-Dependent Counterion Dynamics in DNA: Comparison of Time-Resolved Stokes Shift of Groove-Bound to Base- Stacked Probes in the Presence of Different Monovalent Counterions. *J. Phys. Chem. Lett.* **2012**, *3*, 2621-2626.
19. Robinson, C. R.; Sligar, S. G. Molecular Recognition Mediated by Bound Water. A Mechanism for Star Activity of the Restriction Endonuclease EcoRI. *J. Mol. Biol*. **1993**, *234*, 302-306.
20. Rossetti, G.; Dans, P. D.; Gomez-Pinto, I.; Ivani, I.; Gonzalez, C.; Orozco, M. The Structural Impact of DNA Mismatches. *Nucleic Acids Res*. **2015**, 43**,** 4309-4321.
21. Nag, N.; Rao, B. J.; Krishnamoorthy, G. Altered Dynamics of DNA Bases Adjacent to a Mismatch: A Cue for Mismatch Recognition by MutS. *J. Mol. Biol.* **2007**, *374*, 39-53.
22. Kopka, M. L.; Fratini, A. V.; Drew, H. R.; Dickerson, R. E. Ordered Water Structure Around B-DNA Docamer: A Quantitative Study. *J. Mol. Biol*. **1983**, *163*, 129-146.
23. Verma, S. D.; Pal, N.; Singh, M. K.; Sen, S. Sequence-Dependent Solvation Dynamics of Minor-Groove Bound Ligand Inside Duplex-DNA. *J. Phys. Chem. Lett*. **2012**, *3*, 2621-2626.
24. Eisenstein, M.; Shakked, Z. Hydration Patterns and Intermolecular Interactions in A-DNA Crystal Structures. Implications for DNA Recognition. *J. Mol. Biol*. **1995**, 248, 662-678.
25. Elcock, A. H.; McCammon, J. A. Sequence Dependent Hydration of DNA—Theoretical Results. *J. Am. Chem. Soc.* **1996,** *117*, 10161-10162.
26. Breusegem, S. Y.; Clegg, R. M.; Loontiens, F. G. Base-Sequence Specificity of Hoechst 33258 and DAPI Binding to Five (A/T)4 DNA Sites With Kinetic Evidence for more than One High-Affinity Hoechst 33258-AATT Complex. *J. Mol. Biol.* **2002**, *315*, 1049-1061.
27. Vlieghe, D.; Sponer, J.; Meervelt, L. V. Crystal Structure of d(GGCCAATTGG) Complexed with DAPI Reveals Novel Binding Mode. *Biochemistry* **1999**, *38*, 16443-1645.
28. Spackova, N.; Cheatham, T. E., III; Ryjacek, F.; Lankas, F.; Meervelt, L. V.; Hobza, P.; Sponer, J. Molecular Dynamics Simulations and Thermodynamics Analysis of DNA-Drug Complexes. Minor Groove Binding Between 4′,6-diamidino-2-phenylindole and DNA Duplexes in Solution. *J. Am. Chem. Soc*. **2003**, *125*, 1759-1769.
29. Gregory, R. B. *Protein Solvent Interactions,* Marcel Dekker, New York, USA, **1995**.
30. Burling, F. T.; Weis, K. M.; Flaherty, K. M.; Brunger, A. T. Direct Observation of Protein Solvation and Discrete Disorder with Experimental Crystallographic Phases. *Science* **1996,** *271*, 72-77.
31. Settles, M.; Doster, W. Anomalous Diffusion of Adsorbed Water: A Neutron Scattering Study of Hydrated Myoglobin. *Faraday Discuss* **1996**, *103*, 269-279.
32. Ottig, G.; Liepinsh, E.; Wüthrich, K. Protein Hydration in Aqueous Solution. *Science* **1991**, *254*, 974-980.
33. Denisov, V. P.; Halle, B. Protein Hydration Dynamics in Aqueous Solution. *Faraday Discuss* **1996**, *103*, 227-244.
34. Modig, K.; Liepinsh, E.; Otting, G.; Halle, B. Dynamics of Protein and Peptide Hydration. *J. Am. Chem. Soc.* **2004**, *126*, 102-114.
35. Grebenkov, D. S.; Goddard, Y. A.; Diakova, G.; Korb, J. P.; Bryant, R. G. Dimensionality of Diffusive Exploration at the Protein Interface in Solution. *J. Phys. Chem. B* **2009**, *113*, 13347-13356.
36. Jarzeba, W.; Walker, G. C.; Johnson, A. E.; Kahlow, M. A.; Barbara, P. F. Femtosecond Microscopic Solvation Dynamics of Aqueous Solutions. *J. Phys. Chem.* **1988**, *92*, 7039-7041.
37. Maroncelli, M.; Macinnis, J.; Fleming, G. R. Polar Solvent Dynamics and Electron-Transfer Reactions. *Science* **1989**, *243*, 1674-1681.

38. Jimenez, R.; Fleming, G. R.; Kumar, P. V.; Maroncelli, M. Femtosecond Solvation Dynamics of Water. *Nature* **1994**, *369*, 471-473.
39. Hynes, J. T. Wet Chemistry. *Nature* **1994**, *369*, 439-440.
40. Rossky, P. J.; Simon, J. D. Dynamics of Chemical Processes in Polar Solvents. *Nature* **1994**, *370*, 263-269.
41. Bhattacharyya, K. Solvation Dynamics and Proton Transfer in Supramolecular Assemblies. *Acc. Chem. Res.* **2003**, *36*, 95-101.
42. Bhattacharyya, K.; Bagchi, B. Slow Dynamics of Constrained Water in Complex Geometries. *J. Phys. Chem. A* **2000**, *104*, 10603-10613.
43. Bhattacharyya, K. Nature of Biological Water: A Femtosecond Study. *Chem. Commun.* **2008**, 2848-2857.
44. Nandi, N.; Bhattacharyya, K.; Bagchi, B. Dielectric Relaxation and Solvation Dynamics of Water in Complex Chemical and Biological Systems. *Chem. Rev.* **2000**, *100*, 2013-2046.
45. Pal, S. K.; Zewail, A. H. Dynamics of Water in Biological Recognition. *Chem. Rev.* **2004**, *104*, 2099-2124.
46. Benderskii, A. V.; Eisenthal, K. B. Effect of Organic Surfactant on Femtosecond Solvation Dynamics at the Air-Water Interface. *J. Phys. Chem. B* **2000**, *104*, 11723-11728.
47. Rahman, A.; Stillinger, F. H. Molecular Dynamics Study of Liquid Water. *J. Chem. Phys.* **1971**, *55*, 3336-3359.
48. Maroncelli, M. Computer Simulations of Solvation Dynamics in Acetonitrile *J. Chem. Phys.* **1991**, *94*, 2084.
49. Balasubramanian, S.; Bagchi, B. Slow Solvation Dynamics near an Aqueous Micellar Surface. *J. Phys. Chem. B* **2001**, *105*, 12529-12533.
50. Pal, S.; Maiti, P. K.; Bagchi, B.; Hynes, J. T. Multiple Time Scales in Solvation Dynamics of DNA in Aqueous Solution: The Role of Water, Counterions, and Cross-Correlations. *J. Phys. Chem. B* **2006**, *110*, 26396-26402.
51. Furse, K. E.; Corcelli, S. A. The Dynamics of Water at DNA Interfaces: Computational Studies of Hoechst 33258 Bound to DNA. *J. Am. Chem. Soc.* **2008**, *130*, 13103-13109.
52. Sen, S.; Andreatta, D.; Ponomarev, S. Y.; Beveridge, D. L.; Berg, M. A. Dynamics of Water and Ions near DNA: Comparison of Simulation to Time-Resolved Stokes-Shift Experiments. *J. Am. Chem. Soc.* **2009**, *131*, 1724-1735.
53. Nilsson, L.; Halle, B. Molecular Origin of Time-Dependent Fluorescence Shifts in Proteins. *Proc. Natl. Acad. Sci. USA* **2005**, *102*, 13867-13872.
54. Li, T.; Hassanali, A. A.; Kao, Y.-T.; Zhong, D.; Singer, S. J. Hydration Dynamics and Time Scales of Coupled Water-Protein Fluctuations. *J. Am. Chem. Soc.* **2007**, *129*, 3376-3382.
55. Bandyopadhyay, S.; Chakraborty, S.; Balasubramanian, S.; Pal, S.; Bagchi, B. Atomistic Simulation Study of the Coupled Motion of Amino Acid Residues and Water Molecules Around Protein HP-36: Fluctuations at and around the Active Sites. *J. Phys. Chem. B* **2004**, *108*, 12608-12616.
56. Wolf, G. Friedrich Miescher: The Man Who Discovered DNA. *Chemical Heritage* **2003**, *21*, 10-11, 37-41.
57. Levene, P. A. The Structure of Yeast Nucleic Acid: IV. Ammonia Hydrolysis. *J. Biol. Chem.* **1919**, *40*, 415-424.
58. Chargaff, E. Chemical Specificity of Nucleic Acids and Mechanism of Their Enzymatic Degradation. *Experientia* **1950**, *6*, 201-209.
59. Gu, B.; Zhang, F. S.; Wang, Z. P.; Zhou, H. Y. Solvent-Induced DNA Conformational Transition. *Phys. Rev. Lett.* **2008**, *100*, 088104.
60. Saenger, W. *Principle of Nucleic Acids Structure*; Springer-Verlag: Berlin, **1984**.
61. Richmond, T. J.; Davey, C. A. The Structure of DNA in the Nucleosome Core. *Nature* **2003**, *423*, 145-150.
62. Shakked, Z.; Guerstein-Guzikevich. G.; Eisenstein, M.; Frolow, F.; Rabinovich, D. The Conformation of the DNA Double Helix in the Crystal is Dependent on its Environment. *Nature* **1989**, *342*, 456-460.
63. Rich, A.; Zhang, S. Z-DNA: The Long Road to Biological Function. *Nature Reviews Genetics* **2003**, *4*, 566-572.
64. Dickerson, R. E.; Drew, H. R.; Conner, B. N.; Wing, R. M.; Fratini, A. V.; Kopka, M. L. The Anatomy of A-, B-, and Z-DNA. *Science* **1982**, *216*, 475-485.

65. Felsenfeld, G.; Rich, A. Studies of the Formation of Two-and Three-Stranded Polyribonucleotides. *Biochem Biophys Acta* **1957**, *26*, 457-468.
66. Beal, P. A.; Dervan, P. B. Second Structural Motif for Recognition of DNA by Oligonucleotide-Directed Triple-Helix Formation. *Science* **1991**, *251*, 1360-1363.
67. Gowers, D. M.; Fox, K. R. Towards Mixed Sequence Recognition by Triple Helix Formation. *Nucleic Acids Res.* **1999**, 27, 1569-1577.
68. Beal, P. A.; Dervan, P. B. Second Structural Motif for Recognition of DNA by Oligonucleotide-Directed Triple-Helix Formation. *Science* 1991, 251, 1360-1363.
69. Letai, G. A.; Palladino, M. A.; Fromm, E.; Rizzo, V.; Fresco, J. R. Specificity in Formation of Triple-Stranded Nucleic Acid Helical Complexes: Studies With Agarose-Linked Polyribonucleotide Affinity Columns. *Biochemistry* **1988**, *27*, 9108-9112.
70. Durland, R. H.; Kessler, D. J.; Gunnell, S.; Duvic, M.; Pettitt, B. M.; Hogan, M. E. Binding of Triplex Forming Oligonucleotides to Sites in Gene Promotors. *Biochemistry* **1991**, *30*, 9246-9255.
71. Frank-Kamenetskii, M. D.; Mirkin, S. M. Triplex DNA structures. *Annu. Rev. Biochem*. **1995**, *64*, 65-95.
72. Radhakrishnan, I.; Patel, D. J. DNA Triplexes: Solution Structures, Hydration Sites, Energetics, Interactions, and Function. *Biochemistry* **1994** *33*, 11405-11416.
73. Grigoriev, M.; Praseuth, D.; Guieysse, A. L.; Robin, P.; Thuong, N. T.; Hélène, C.; Harel-Bellan, A. Inhibition of Gene Expression by Triple Helix-Directed DNA Cross-Linking at Specific Sites. *Proc. Natl. Acad. Sci. USA* **1993**, *90*, 3501-3505.
74. Strobel, S. A.; Dervan, P. B. Triple Helix Mediated Single-Site Enzymatic Cleavage of Megabase Genomic DNA. *Methods Enzymol.* **1992**, *216*, 309-321.
75. Gellert, M.; Lipsett, M. N.; Davies, D. R. Helix Formation by Guanylic Acid. *Proc. Natl. Acad. Sci. USA* ***1962**, 48, 2013-2018.*
76. Spackova, N.; Berger, I.; Sponer, J. Structural Dynamics and Cation Interactions of DNA Quadruplex Molecules Containing Mixed Guanine/Cytosine Quartets Revealed by Large-Scale MD Simulations. *J. Am. Chem. Soc.* **2001**, *123*, 3295-3307.
77. Wang, Y.; Patel, D. J. Solution Structure of the Human Telomeric Repeat d[AG3(T2AG3)3] G-Tetraplex. *Structure* **1993**, *1*, 263-282.
78. Luu, K. N.; Phan, A. T.; Kuryavyi, V.; Lacroix, L.; Patel, D. J. Structure of the Human Telomere in K^+ Solution: An Intramolecular (3 + 1) G-Quadruplex Scaffold. *J. Am. Chem. Soc.* **2006**, *128*, 9963-9970.
79. Parkinson, G. N.; Lee, M. P.; Neidle, S. Crystal Structure of Parallel Quadruplexes from Human Telomeric DNA. *Nature* **2002**, *417*, 876-880.
80. Lim, K. W.; Amrane, S.; Bouaziz, S.; Xu, W.; Mu, Y.; Patel, D. J.; Luu, K. N.; Phan, A. T. Structure of the Human Telomere in K^+ Solution: A Stable Basket-Type G-Quadruplex With Only Two G-Tetrad Layers. *J. Am. Chem. Soc.* **2009**, *131*, 4301-4309.
81. Phan, A. T.; Kuryavyi, V.; Luu, K. N.; Patel, D. J. Structure of Two Intramolecular G-Quadruplexes Formed by Natural Human Telomere Sequences in K^+ Solution. *Nucleic Acids Res.* **2007**, *35*, 6517-6525.
82. Phan, A. T.; Kuryavyi, V.; Burge, S.; Neidle, S.; Patel, D. J. Structure of an Unprecedented G-Quadruplex Scaffold in the Human c-kit promoter. *J. Am. Chem. Soc.* **2007**, *129*, 4386-4392.
83. Siddiqui-Jain, A.; Grand, C. L.; Bearss, D. J.; Hurley, L. H. Direct Evidence for a G-Quadruplex in a Promoter Region and its Targeting With a Small Molecule to Repress C-MYC Transcription. *Proc. Natl. Acad. Sci. USA* **2002**, *99*, 11593-11598.
84. Cogoi, S.; Xodo, L. E. G-Quadruplex Formation Within the Promoter of the KRAS Proto-Oncogene and its Effect on Transcription. *Nucleic Acids Res.* **2006**, *34*, 2536-2549.
85. Biffi, G.; Tannahill, D.; McCafferty, J.; Balasubramanian, S. Quantitative Visualization of DNA G-Quadruplex Structures in Human Cells. *Nat. Chem.* **2013**, *5*, 182-186.
86. Zahler, A. M.; Williamson, J. R.; Cech, T. R.; Prescott, D. M. Inhibition of Telomerase by G-Quartet DNA Structures. *Nature* **1991**, *350*, 718-720.
87. Verma, S. D.; Pal, N.; Singh, M. K.; Shweta, H.; Khan, M. F.; Sen, S. Understanding Ligand Interaction With Different Structures of G-Quadruplex DNA: Evidence of Kinetically Controlled Ligand Binding and Binding-Mode Assisted Quadruplex Structure Alteration. *Anal. Chem*. **2012**, *84*, 7218-7226.

88. Singh, M. K.; Shweta, H.; Sen, S. Dispersed Dynamics of Solvation in G-Quadruplex DNA: Comparison of Dynamic Stokes Shifts of Probes in Parallel and Antiparallel Quadruplex Structures. *Methods Appl. Fluoresc*. **2016**, *4*, 034009.
89. Oh, M. H. J.; Salvador, M. R.; Wong, C. Y.; Scholes, G. D. Three Pulse Photon-Echo Peak Shift Spectroscopy and Its Application For the Study of Solvation and Nanoscale Excitons. *ChemPhys Chem.* **2011**, *12*, 88-100.
90. Park, S.; Joo, T. Diffractive Optics Based Three-Pulse Photon Echo Peak Shift Studies of Spectral Diffusion in Polar Liquids: Evidence for Long Lived Frequency Correlations. *J. Chem. Phys.* **2009**, *131*, 164508.
91. Myllyperkiö, P.; Herranen, O.; Rintala, J.; Jiang, H.; Mudimela, P. R.; Zhu, Z.; Nasibulin, A. G.; Johansson, A.; Kauppinen, E. I.; Ahlskog, M.; Pettersson, M. Femtosecond Four-Wave-Mixing Spectroscopy of Suspended Individual Semiconducting Single-Walled Carbon Nanotubes. *ACS Nano* **2010**, *4*, 6780-6786.
92. Moilanen, D. E.; Fenn, E. E.; Wong, D.; Fayer, M. D. Water Dynamics in Large and Small Reverse Micelles: From Two Ensembles to Collective Behavior. *J. Chem. Phys.* **2009**, *131,* 014704.
93. Nibbering, E. T. J.; Fidder, H.; Pines, E. Ultrafast Chemistry: Using Time-Resolved Vibrational Spectroscopy for Interrogation of Structural Dynamics. *Annu. Rev. Phys. Chem. B* **2005**, *56*, 337-367.
94. Denisov, V. P.; Halle, B. Protein Hydration Dynamics in Aqueous Solution. *Faraday Discuss*. **1996**, *103*, 227-244.
95. Pal, S. K.; Peon, J.; Bagchi, B.; Zewail, A. H. Biological Water: Femtosecond Dynamics of Macromolecular Hydration. *J. Chem. Phys. B* **2002**, *106,* 12376-12395.
96. Saif, B.; Mohr, R. K.; Montrose, C. J.; Litovitz, T. A. On the Mechanism of Dielectric Relaxation in Aqueous DNA Solutions. *Biopolymers* **1991**, *31*, 1171-1180.
97. Pecourt, J. M. L.; Peon, P.; Kohler, B. Ultrafast Internal Conversion of Electronically Excited RNA and DNA Nucleosides in Water. *J. Am. Chem. Soc*. **2001**, 122, 9348-9349.
98. Peon, J.; Zewail, A. H. DNA/RNA Nucleotides and Nucleosides: Direct Measurement of Excited-State Lifetimes by Femtosecond Fluorescence Up-Conversion. *Chem Phys. Lett.* **2001**, *348*, 255-262.
99. Law, S. M.; Eritja, R.; Goodman, M. F.; Breslauer, K. J. Spectroscopic and Calorimetric Characterizations of DNA Duplexes Containing 2-Aminopurine. *Biochemistry* **1996**, *35*, 12329-12337.
100. Ward, D. C.; Reich, E.; Stryler, L. Fluorescence Studies of Nucleotides and Polynucleotides. I. Formycin, 2-Aminopurine Riboside, 2,6-Diaminopurine Riboside, and Their Derivatives. *J Biol. Chem.* **1969**, *244*, 1228-1237.
101. Pal, S. K.; Zhao, L.; Xia, T.; Zewail, A. H. Site- and Sequence-Selective Ultrafast Hydration of DNA. *Proc. Natl. Acad. Sci. USA* **2003**, *100*, 13746-13751.
102. Ramreddy, T.; Kombrabail, M.; Krishnamoorthy, G.; Rao, B. J. Site-Specific Dynamics in TAT Triplex DNA as Revealed by Time-Domain Fluorescence of 2-Aminopurine. *J. Phys. Chem. B* **2009**, *113*, 6840-6846.
103. Rachofsky, E. L.; Osman, R.; Ross, J. B. Probing Structure and Dynamics of DNA with 2-Aminopurine: Effects of Local Environment on Fluorescence. *Biochemistry* **2001**, *40*, 946-956.
104. Coleman, R. S.; Madaras, M. L. Synthesis of a Novel Coumarin C-Riboside as a Photophysical Probe of Oligonucleotide Dynamics. *J. Org. Chem.* **1998**, *63*, 5700-5703.
105. Brauns, E. B.; Madaras, M. L.; Coleman, R. S.; Murphy, C. J.; Berg, M. A. Measurement of Local DNA Reorganization on the Picosecond and Nanosecond Time Scales. *J. Am. Chem. Soc.* **1999**, *121*, 11644-11649.
106. Dallmann, A.; Pfaffe, M.; Mügge, C.; Mahrwald, R.; Kovalenko, S. A.; Ernsting, N. P. Local Thz Time Domain Spectroscopy of Duplex DNA via Fluorescence of an Embedded Probe *J. Phys. Chem. B* **2009**, *113*, 15619-15628.
107. Hawkins, M. E. Fluorescent Pteridine Nucleoside Analogs: A Window on DNA Interactions. *Cell Biochem. Biophys.* **2001**, *34*, 257-281.
108. Weinberger, M.; Berndt, F.; Mahrwald, R.; Ernsting, N. P.; Wagenknecht, H. A. Synthesis of 4-Aminophthalimide and 2,4-Diaminopyrimidine C-Nucleosides as Isosteric Fluorescent DNA Base Substitutes. *J. Org. Chem.* **2013**, *78*, 2589-2599.

109. Graves, D. E.; Velea, L. M. Intercalative Binding of Small Molecules to Nucleic Acids. *Curr. Org. Chem*. **2000**, *4*, 915-929.
110. Hurley, L. H. DNA and its Associated Processes as Targets for cancer Therapy DNA and its Associated Processes as Targets for Cancer Therapy. *Nat. Rev. Cancer* **2002**, *2*, 188-200.
111. Lerman, L. S. Structural Considerations in the Interaction of DNA and Acridines. *J. Mol. Biol*. **1961**, *3*, 18-30.
112. Blackburn, G. M. *DNA and RNA structure*. *Nucleic acids in Chemistry and biology*, 2nd ed. Eds. Blackburn, G. M.; Gait, M. J. Oxford University Press, New York, USA, **1996**.
113. Praveen Reddy, B. S.; Sondhi, S. M.; Lown, J. W. Synthetic DNA Minor Groove-Binding Drugs. *Pharmacol. Ther*. **1999**, *84*, 1-111.
114. Denham, D. A.; Suswillo, R. R.; Rogers, R.; Mcgreevy, P. B.; Andrew, B. J. Studies on *Brugia Pahangi*. 13. The Anthelmintic Effect of Compounds F151 (Friedheim), HOE 33258 (Hoechst) and Their Reaction Product. *J. Helminthol*. **1976**, *50*, 243-250.
115. Haq, I.; Ladbury, J. E.; Chowdhry, B. Z. ; Jenkins, T. C.; Chaires, J. B. Specific Binding of Hoechst 33258 to The d(CGCAAATTTGCG)2 Duplex: Calorimetric and Spectroscopic Studies. *J. Mol. Biol*. **1997**, *271*, 244-257.
116. Kapuscinsky, J.; Szer, W. Interactions of 4', 6-Diamidine-2-phenylindole with Synthetic Polynucleotides. *Nucleic Acids Res*. **1979**, *6*, 3519-3534.
117. Pal, N.; Verma, S. D.; Sen, S. Probe Position Dependence of DNA Dynamics: Comparison of the Time-Resolved Shift of Groove-Bound to Base-Stacked Probes. *J. Am. Chem. Soc*. **2010**, *132*, 9277-9279.
118. Verma, S. D.; Pal, N.; Singh, M. K.; Sen, S. Probe Position Dependent Counterion Dynamics in DNA: Comparison of Time-Resolved Stokes Shift of Groove-Bound to Base-Stacked Probes in the Presence of Different Monovalent Counterions. *J. Phys. Chem. Lett*. **2012**, *3*, 2621-2626.
119. Pal, S. K.; Zhao, L.; Zewail, A. H. Water at DNA Surfaces: Ultrafast Dynamics in Minor Groove Recognition. *Proc. Natl. Acad. Sci. USA* **2003**, *100*, 8113-8118.
120. Neidle, S.; Parkinson, G. Telomere Maintenance as a Target for Anticancer Drug Discovery. *Nature Rev. Drug Discov*. **2002**, *1*, 383-393.
121. Rezler, E. M.; Bearss, D. J.; Hurley, L. H. Telomere Inhibition and Telomere Disruption as Processes for Drug Targeting. *Annu. Rev. Pharmacol. Toxicol*. **2003**, *43*, 359-379.
122. Cuesta, J.; Read, M. A.; Neidle, S. The Design of G-Quadruplex Ligands as Telomerase Inhibitors. *Mini Rev. Med. Chem*., **2003**, *3*, 11-21.
123. Singh, M. K.; Shweta, H.; Sen, S. Dispersed Dynamics of Solvation in G-Quadruplex DNA: Comparison of Dynamic Stokes Shifts of Probes in Parallel and Antiparallel Quadruplex Structures. *Methods Appl. Fluoresc*. **2016**, *4*, 034009.
124. Haider, S. M.; Parkinson, G. N.; Neidle, S. Structure of a G-Quadruplex–Ligand Complex. *J. Mol. Biol*. **2003**, *326*, 117-125.
125. Parkinson, G. N.; Ghosh, R.; Neidle, S. Structural Basis for Binding of Porphyrin to Human Telomeres. *Biochemistry*, **2007**, *46*, 2390–2397.
126. Campbell, N. H.; Parkinson, G. N.; Reszka, A. P.; Neidle, S. Structural Basis of DNA Quadruplex Recognition by an Acridine Drug. *J. Am. Chem. Soc*. **2008**, 130, 6722–6724.
127. Parkinson, G. N.; Cuenca, F.; Neidle, S. Topology Conservation and Loop Flexibility in Quadruplex–Drug Recognition: Crystal Structures of Inter- and Intramolecular Telomeric DNA Quadruplex– Drug Complexes. *J. Mol. Biol*. **2008**, *381*, 1145–1156.
128. Campbell, N. H.; Patel, M.; Tofa, A. B.; Ghosh, R.; Parkinson, G. N.; Neidle, S. Selectivity in Ligand Recognition of G-Quadruplex Loops. *Biochemistry*, **2009**, *48*, 1675-1680
129. Phan, A. T.; Kuryavyi, V.; Gaw, H. Y.; Patel, D. J. Small Molecule Interaction With a Five-Guanine-Tract G-Quadruplex Structure From the Human MYC Promoter. *Nature Chem. Biol*. **2005**, *1*, 167–173.
130. Dixon, I. M.; Lopez, F.; Tejera, A. M.; Estève, J. P.; Blasco, M. A.; Pratviel, G.; Meunier, B. A. G-Quadruplex Ligand with 10000-Fold Selectivity over Duplex DNA. *J. Am. Chem. Soc*. **2007**, *129*, 1502–1503.
131. Jain, A. K. Reddy, V. V.; Paul, A.; Muniyappa, K.; Bhattacharya, S.; Synthesis and Evaluation of a Novel Class of G-Quadruplex-Stabilizing Small Molecules Based on the 1,3-phenylene-bis(piperazinyl benzimidazole) System. *Biochemistry* **2009**, *48*, 10693-10704.

132. Kettani, A.; Gorin, A.; Majumdar, A.; Hermann, T.; Skripkin, E.; Zhao, H.; Jones, R.; Patel, D. J. A Dimeric DNA Interface Stabilized by Stacked A(GGGG)A Hexads and Coordinated Monovalent Cations. *J. Mol.Biol*. **2000**, *297*, 627–644.
133. Burger, A. M.; Dai, F.; Schultes, C. M.; Reszka, A. P.; Moore, M. J.; Double, J. A.; Neidle, S. The G-Quadruplex-Interactive Molecule BRACO-19 Inhibits Tumor Growth, Consistent with Telomere Targeting and Interference with Telomerase Function. *Cancer Res*. **2005**, *65*, 1489-1496.
134. Drygin, D.; Siddiqui-Jain, A.; O'Brien, S.; Schwaebe, M.; Lin, A.; Bliesath, J.; Ho, C. B.; Proffitt, C.; Trent, K.; Whitten, J. P.; Lim, J. K.; Hoff, D. V.; Anderes, K.; Rice, W. G. Anticancer Activity of CX-3543: A Direct Inhibitor of rRNA Biogenesis. *Cancer Res*. **2009**, *69*, 7653-7661.
135. Shin-ya, K.; Wierzba, K.; Matsuo, K.; Ohtani, T.; Yamada, Y.; Furihata, K.; Hayakawa, Y.; Seto, H. Telomestatin, A Novel Telomerase Inhibitor from Streptomyces Anulatus. *J. Am. Chem. Soc.* **2001**, *123*, 1262-1263.
136. Martino, L.; Virno, A.; Pagano, B.; Virgilio, A.; Di Micco, S.; Galeone, A.; Giancola, C.; Bifule, G.; Mayol, L.; Randazzo, A. Structural and Thermodynamic Studies of the Interaction of Distamycin A with the Parallel Quadruplex Structure [d(TGGGGT)]4. *J. Am. Chem. Soc.* **2007**, *129*, 16048-16056.
137. Hudson, J. S.; Brooks, S. C.; Graves, D. E. Interactions of Actinomycin D with Human Telomeric G-Quadruplex DNA. *Biochemistry* **2009**, *48*, 4440-4447.
138. Anantha, N. V.; Azam, M.; Sheardy, R. D. Porphyrin Binding to Quadrupled T4G4. *Biochemistry* **1998**, *37,* 2709-2714.
139. Fedoroff, O. Y.; Salazar, M.; Han, H. Y.; Chemeris, V. V.; Kerwin, S. M.; Hurley, L. H. NMR-Based Model of a Telomerase-Inhibiting Compound Bound to G-quadruplex DNA. *Biochemistry* **1998**, *37*, 12367-12374.
140. Maiti, S.; Chaudhury, N. K.; Chowdhury, S. Hoechst 33258 Binds to G-Quadruplex in the Promoter Region of Human C-Myc. *Biochem. Biophys. Res. Comm.* **2003**, *310*, 505-512.
141. Pal, N.; Shweta, H.; Singh, M. K.; Verma, S. D.; Sen, S. Power-Law Solvation Dynamics in G-quadruplex DNA: Role of Hydration Dynamics on Ligand Solvation Inside DNA. *J. Phys. Chem. Lett.* **2015**, *6*, 1754-1760.
142. Karplus, M.; McCammon, J. A. Molecular Dynamics Simulations of Biomolecules. *Nature Struct. Biol.* **2002**, *9,* 646-652.
143. Fennell, C. J.; Gezelter, J. D. Is the Ewald Summation Still Necessary? Pairwise Alternatives to the Accepted Standard for Long-Range Electrostatics. *J. Chem. Phys.* **2006** *124*, 234104.
144. Bagchi, B. *Molecular Relaxation in Liquids*. Oxford, New York, USA, **2012**.
145. Luzar, A.; Chandler, D. Hydrogen-Bond Kinetics in Liquid Water. *Nature*, **379**, 1996, 55-57.
146. Castner, E. W.; Maroncelli, M.; Fleming, G. R. Subpicosecond Resolution Studies of Solvation Dynamics in Polar Aprotic and Alcohol Solvents. *J. Chem. Phys.* **1987**, *86*, 1090-1097.
147. Bingemann, D.; Ernsting, N. P. Femtosecond Solvation Dynamics Determining the Band Shape of Stimulated Emission from a Polar Styryl Dye. *J. Chem. Phys.* **1995**, *102*, 2691-2700.
148. Kool, E. T. Replacing the Nucleobases in DNA with Designer Molecules. *Acc. Chem. Res.* **2002**, *35*, 936-943.
149. Maroncelli, M.; Fleming, G. R. Computer Simulations of the Dynamics of Aqueous Solvation. *J. Chem. Phys.* **1988**, *89*, 5044-5069.
150. Fonseca, T.; Ladanyi, B. M. Breakdown of Linear Response for Solvation Dynamics in Methanol. *J. Phys. Chem.* **1991**, *95*, 2116-2119.
151. Bagchi, B.; Jana, B. Solvation Dynamics in Dipolar Liquids. *Chem. Soc. Rev.* **2010**, *39*, 1936-1954.
152. Fiebig, T.; Wan, C.; Kelley, S. O.; Barton, J. K.; Zewail, A. H. Femtosecond Dynamics of the DNA Intercalator Ethidium and Electron Transfer with Mononucleotides in Water. *Proc. Natl. Acad. Sci. USA* **1999**, *96*, 1187-1192.
153. Zolotov, B.; Gan, A.; Fainberg, B. D.; Huppert, F. D. Resonance Heterodyne Optical Kerr Spectroscopy of Solvation Dynamics in Water and D_2O. *Chem. Phys. Lett*. **1997**, *265*, 418-426.
154. Lang, M. J.; Jordanides, X. J.; Song, X.; Fleming, G. R. Aqueous Solvation Dynamics Studied by Photon Echo Spectroscopy. *J. Chem. Phys.* **1999**, *110*, 5884-5892.
155. Maroncelli, M.; Fleming, G. R. Computer Simulation of the Dynamics of Aqueous Solvation. *J. Chem. Phys*. **1988,** *89*, 5044.
156. Bader, J. S.; Chandler, D. Computer Simulation of Photochemically Induced Electron Transfer. *Chem. Phys. Lett*. **1989**, *157*, 501-504.

157. Song, X.; Chandler, D. Dielectric Solvation of Molecules of Arbitrary Shape and Charge Distribution. *J. Chem. Phys*. 1998, *108*, 2594-2600.
158. Furse, K. E.; Lindquist, B. A.; Corcelli, S. A. Solvation Dynamics of Hoechst 33258 in Water: An Equilibrium and Nonequilibrium Molecular Dynamics Study. *J. Phys. Chem. B* **2008**, *112*, 3231–3239.
159. Kropman, M. F.; Bakker, H. J. Dynamics of Water Molecules in Aqueous Solvation Shells. *Science* **2001**, *291*, 2118-2120.
160. Fayer, M. D.; Levinger, N. E. Analysis of Water in Confined Geometries and at Interfaces. *Annu. Rev. Anal. Chem.* **2010**, *3*, 89-107.
161. Bagchi, B. Water Dynamics in the Hydration Layer Around Proteins and Micelles. *Chem. Rev.* **2005**, *105*, 3197-3219.
162. Samanta, A. Solvation Dynamics in Ionic Liquids: What we have Learned from the Dynamic Fluorescence Stokes Shift Studies. *J. Phys. Chem. Lett.* **2010**, *1*, 1557-1562.
163. Samanta, A. Dynamic Stokes Shift and Excitation Wavelength Dependent Fluorescence of Dipolar Molecules in Room Temperature Ionic Liquids. *J. Phys. Chem. B* **2006**, *110*, 13704-13716.
164. Saha, S.; Mandal, P. K.; Samanta, A. Solvation Dynamics of Nile Red in a Room Temperature Ionic Liquid using Streak Camera. *Phys. Chem. Chem. Phys.* **2004**, *6*, 3106-3110.
165. Makarov, V.; Pettitt, B. M. Solvation and Hydration of Proteins and Nucleic Acids: A Theoretical View of Simulation and Experiment. *Acc. Chem. Res.* **2002**, *35*, 376-384.
166. Ramreddy, T.; Rao, B. J.; Krishnamoorthy, G. Site-Specific Dynamics of Strands in ss- and dsDNA As Revealed by Time-Domain Fluorescence of 2-Aminopurine. *J. Phys. Chem. B* **2007**, *111*, 5757-5766.
167. Zhong, D.; Pal, S. K.; Zewail, A. H. Femtosecond Studies of Protein ± DNA Binding and Dynamics : Histone I. *ChemPhysChem*. **2001**, *2,* 219–227.
168. Sen, S.; Paraggio, N. A.; Gearheart, L. A.; Connor, E. E.; Issa, A.; Coleman, R. S.; Wilson, D. M. 3rd; Wyatt, M. D.; Berg, M. A. Effect of Protein Binding on Ultrafast DNA Dynamics: Characterization and Measurement of a Complex with APE1. *Biophys. J.* **2005**, *89*, 4129-4138.
169. Goel. T.; Mukherjee, T.; Rao, B. J.; Krishnamoorthy, G. Fluorescence Dynamics of Double- and Single-Stranded DNA Bound to Histone and Micellar Surfaces. *J. Phys. Chem. B* **2010**, *114*, 8986-8993.
170. Perutz, M. F.; Rossmann, M. G.; Cullis, A. F.; Muirhead, H.; Will, G.; North, A. C. Structure of Hæmoglobin: A Three-Dimensional Fourier Synthesis at 5.5-Å. Resolution, Obtained by X-Ray Analysis. *Nature* **1960,** *185*, 416-422.
171. Kendrew, J. C.; Dickerson, R. E.; Strandberg, B. E.; Hart, R. G.; Davies, D. R.; Phillips, D. C.; Shore, V. C. Structure of Myoglobin: A Three-Dimensional Fourier Synthesis at 2 Å. Resolution. *Nature* **1960,** *185*, 422-427.
172. Bernal, J. D.; Crowfoot, D. X-Ray Photographs of Crystalline Pepsin. *Nature* **1934***, 133,* 794-795.
173. Kauzmann, W. Some Factors in the Interpretation of Protein Denaturation. *Adv. Protein Chem.* **1959,** *14,* 1-63.
174. Frank, H. S.; Evans M. W. Free Volume and Entropy in Condensed Systems III. Entropy in Binary Liquid Mixtures; Partial Molal Entropy in Dilute Solutions; Structure and Thermodynamics in Aqueous Electrolytes. *J. Chem. Phys.* **1945,** *13,* 507.
175. Gregory, R. B. Protein–Solvent Interactions, Marcel Dekker, New York, **1995**.
176. Burling, F. T.; Weis, W. I.; Flaherty, K. M.; Brunger, A. T. Direct Observation of Protein Solvation and Discrete Disorder with Experimental Crystallographic Phases. *Science* **1996,** 271, 72-77.
177. Otting, G.; Liepinsh, E.; Wüthrich, K. Protein Hydration in Aqueous Solution. *Science* **1991,** *254,* 974-980.
178. Denisov,V. P.; Halle, B. Protein Hydration Dynamics in Aqueous Solution. *Faraday Discuss* **1996,** *103,* 227-244.
179. Grebenkov, D. S.; Goddard, Y. A.; Diakova, G.; Korb, J. P.; Bryant, R. G. Dimensionality of Diffusive Exploration at the Protein Interface in Solution *J. Phys. Chem. B* **2009,** *113,* 13347-13356.

180. Qiu, W. H.; Zhang, L. Y.; Okobiah, O.; Yang, Y.; Wang, L. J.; Zhong, D.; Zewail, A. H. Ultrafast Solvation Dynamics of Human Serum Albumin: Correlations and Conformational Transitions and Site-Selected Recognition. *J. Phys. Chem. B* **2006**, *110*, 10540-10549.
181. Jordanides, X. J.; Lang, M. J.; Song, X.; Fleming, G. R. Solvation Dynamics in Protein Environments Studied by Photon Echo Spectroscopy. *J. Phys. Chem. B* **1999**, *103*, 7995-8005.
182. Pal, S. K.; Mandal, D.; Sukul, D.; Sen, S.; Bhattacharyya, K. Solvation Dynamics of DCM in Human Serum Albumin. *J. Phys. Chem. B* **2001**, *105*, 1438-1441.
183. Guha, S.; Sahu, K.; Roy, D.; Mondal, S. K.; Roy, S.; Bhattacharyya, K. Slow Solvation Dynamics at the Active Site of an Enzyme: Implications for Catalysis. *Biochemistry*, **2005**, *44*, 8940-8947.
184. Peon, J.; Pal, S. K.; Zewail, A. H. Hydration at the Surface of the Protein Monellin: Dynamics with Femtosecond Resolution. *Proc. Natl. Acad. Sci. USA* **2002**, 99, 10964-10969.
185. Qui, W.; Kao, Y. T.; Zhang, L.; Yang Y.; Wang, L.; Stites W. E.; Zhong D.; Zewail, A. H. Protein Surface Hydration Mapped by Site-Specific Mutations. *Proc. Natl. Acad. Sci. USA* **2006**, *103*, 13979-13984.
186. Satputea, A. B.; Wagerb, T. D.; Cohen-Adadc, J.; Bianciardid, M.; Choid, J. K.; Buhlee, J. T.; Wald, L. L.; Barrett, L. F. Identification of Discrete Functional Sub Regions of the Human Periaqueductal Gray. *Proc. Natl. Acad. Sci. USA* **2010**, *107*, 17101-17106.
187. Zhao, L.; Pal, S. K.; Xia, T.; Zewail, A. H. Dynamics of Ordered Water in Interfacial Enzyme Recognition: Bovine Pancreatic Phospholipase A_2. *Angew. Chem. Int. Ed.* **2004**, 43, 59.
188. Qiu, W.; Zhang, L.; Okobiah, O.; Yang, Y.; Wang, L.; Zhong, D. Ultrafast Solvation Dynamics of Human Serum Albumin: Correlations with Conformational Transitions and Site-Selected Recognition. *J. Phys. Chem. B* **2006,** *110*, 10540-10549.
189. Qin, Y.; Wang, L.; Zhong, D. Dynamics and Mechanism of Ultrafast Water–Protein Interactions. *Proc. Natl. Acad. Sci. USA* **2016**, *113*, 8424-8429.
190. Qin, Y.; Jia, M.; Yang, J.; Wang, D.; Wang, L.; Xu, J.; Zhong, D. Molecular Origin of Ultrafast Water–Protein Coupled Interaction. *J. Phys. Chem. Lett.* **2016**, *7*, 4171-4177.
191. Jia, M.; Yang, J.; Qin, Y.;Dihao, W.; Pan, H.; Wang, L.; Xu, J.; Zhong, D. Determination of Protein Surface Hydration by Systematic Charge Mutations. *J. Phys. Chem. Lett.* **2015**, 6, 5100–5105.
192. Yang, J.; Wang, Y.; Wang, L.; Zhong, D. Mapping Hydration Dynamics around a β-Barrel Protein. *J. Am. Chem. Soc.* **2017**, *139*, 4399-4408.
193. McCammon, A.; Gelin, B. R.; Karplus, M. Dynamics of Folded Proteins. *Nature* **1977,** *267*, 585-590.
194. Levitt, M.; Sharon, R. Accurate Simulation of Protein Dynamics in Solution. *Proc. Natl. Acad. Sci. USA* **1988**, *85*, 7557-7561.
195. Brooks, C. L.; Karplus, M. Solvent Effects on Protein Motion and Protein Effects on Solvent Motion: Dynamics of the Active Site Region of Lysozyme. *J. Mol. Biol.* **1989**, *208*, 159-181.
196. Nandi, N.; Bagchi, B. Dielectric Relaxation of Biological Water. *J. Phys. Chem. B* **1997**, *101*, 10954-10961.
197. Pal, S.; Peon, J.; Bagchi, B.; Zewail, A. H. Biological Water: Femtosecond Dynamics of Macromolecular Hydration. *J. Phys. Chem. B* **2002**, 106, 12376-12395.
198. Bhattacharyya, S. M.; Wang, Z. G.; Zewail, A. H. Dynamics of Water near a Protein Surface. *J. Phys. Chem. B* **2003**, *107*, 13218–13228.
199. Makarov, V. A.; Andrews, B. K.; Smith, P.E.; Pettitt, B. M. Residence Times of Water Molecules in the Hydration Sites of Myoglobin. *Biophys. J.* **2000**, *79*, 2966-2974.
200. Abbyad, P.; Shi, X.; Childs, W.; McAnaney, T. B.; Cohen, B. E.; Boxer, S. G. Measurement of Solvation Responses at Multiple Sites in a Globular Protein. *J. Phys. Chem. B*. **2007**, 111, 8269-8276.
201. Vitkup, D.; Ringe, D.; Petsko, G. A.; Karplus, M. Solvent Mobility and the Protein 'glass' Transition. *Nat. Struct. Biol* **2000**, 7, 34-38.
202. Bandyopadhyay, S.; Chakraborty, S.; Chakraborty, S.; Balasubramanian, S.; Bagchi, B. Sensitivity of Polar Solvation Dynamics to the Secondary Structures of Aqueous Proteins and the Role of Surface Exposure of the Probe. *J. Am. Chem. Soc.* **2005**, 127, 4071–4075.
203. Toptygin, D; Woolf, T. B.; Brand, L. Picosecond Protein Dynamics: The Origin of the Time-Dependent Spectral Shift in the Fluorescence of the Single Trp in the Protein GB1. *J. Phys. Chem. B*, **2010**, *114*, 11323–11337.

204. Sterpone, F.; Stirnemann, G.; Laage, D. Magnitude and Molecular Origin of Water Slowdown Next to a Protein. *J. Am. Chem. Soc.* **2012**, *134*, 4116-4119

205. Fogarty, A. C.; Laage, D. Water Dynamics in Protein Hydration Shells: The Molecular Origins of the Dynamical Perturbation. *J. Phys. Chem. B* **2014**, *118*, 7715-7729.

206. Mondal, S.; Mukherjee, S.; Bagchi, B. Decomposition of Total Solvation Energy into Core, Side-Chains and Water Contributions: Role of Cross Correlations and Protein Conformational Fluctuations in Dynamics of Hydration Layer. *Chem. Phys. Lett*. **2017**, *683,* 29–37.

207. McDermott, M. L.; Vanselous, H.; Corcelli, S. A.; Petersen, P. B. DNA's Chiral Spine of Hydration. *ACS Cent Sci* **2017 (**DOI: 10.1021/acscentsci.7b00100).

208. Young, M. A.; Jayaram, B.; Beveridge, D. L. Intrusion of Counterions into the Spine of Hydration in the Minor Groove of B-DNA: Fractional Occupancy of Electronegative Pockets. *J. Am. Chem. Soc.* **1997**, *119*, 59-69.

209. Ponomarev, S. Y.; Thayer, K. M.; Beveridge, D. L. Ion Motions in Molecular Dynamics Simulations on DNA. *Proc. Natl. Acad. Sci. USA* **2004**, *101*, 14771–14775.

210. Wahl, Ph.; Paoletti, J.; Le Pecq, J. B. Decay of Fluorescence Emission Anisotropy of the Ethidium Bromide-DNA Complex Evidence for an Internal Motion in DNA. *Proc. Natl. Acad. Sci. USA*, **1970**, *65*, 417-421.

211. Genest, D.; Wahl, P. Fluorescence Anisotropy Decay due to Rotational Brownian Motion of Ethidium Intercalated in Double Strand DNA. *Biochim. Biophys. Acta* **1978**, *52*, 502-509.

212. Hard, T.; Fan, P.; Magde, D.; Kearns, D. R. On the Flexibility of DNA: Time-Resolved Fluorescence Polarization of Intercalated Quinacrine and 9-Amino-6-chloro-2-methoxyacridine. *J. Phys. Chem.* **1989**, *93*, 4338-4345.

213. Thomas, J. C.; Schurr, J. M. Fluorescence Depolarisation and Temperature Dependence of the Torsion Elastic Constant of Linear Φ29 Deoxyribonucleic Acid. *Biochemistry* **1983**, *22*, 6194-6198.

214. Millar, D. P.; Robbins, R. J.; Zewail, A. H. Direct Observation of the Torsional Dynamics of DNA and RNA by Picosecond Spectroscopy. *Proc. Natl. Acad. Sci. USA*. **1980**, *77*, 5593-5597.

215. Millar, D. P.; Robbins, R. J.; Zewail, A. H. Picosecond Dynamics of Electronic Energy Transfer in Condensed Phases. *J. Chem. Phys*, **1981**, *75*, 3649-3659.

216. Millar, D. P.; Robbins, R. J.; Zewail, A. H. Torsion and Bending of Nucleic Acids Studied by Subnanosecond Time-Resolved Fluorescence Depolarisation of Intercalated Dyes. *J. Chem. Phys.* **1982**, *76*, 2080-2094.

217. Brauns, E. B.; Murphy, C. J.; Berg, M. A. Local Dynamics in DNA by Temperature-Dependent Stokes Shifts of an Intercalated Dye. *J. Am. Chem. Soc.* **1998,** *120*, 2449-2456.

218. Robinson, B. H.; Mailer, C.; Drobny, G. Site-Specific Dynamics in DNA: Experiments. *Annu. Rev. Biophys. Biomol. Struct.* **1997,** *26*, 629-658.

219. Schurr, J. et al. *Fluorescence Spectroscopy*, edited by J. R. Lakowicz ,Plenum Press, New York, **1992**, *3,* 137.

220. Cohen, B. E.; McAnaney, T. B.; Park, E. S.; Jan, Y. N.; Boxer, S. G.; Jan, L. Y. Probing Protein Electrostatics with a Synthetic Fluorescent Amino Acid. *Science* **2002**, *296*, 1700-1703.

221. Brauns, E. B.; Madaras, M. L.; Coleman, R. S.; Murphy, C. J.; Berg, M. A. Complex Dynamics in DNA on the Picosecond and Nanosecond Time Scales. *Phys. Rev. Lett.* **2002**, *88*, 158101-158104.

222. Banerjee, D.; Pal, S. K. Dynamics in the DNA Recognition by DAPI: Exploration of the Various Binding Modes. *J. Phys. Chem. B* **2008**, *112*, 1016–1021.

223. Fürstenberg, A.; Vauthey, E. Ultrafast Excited-State Dynamics of Oxazole Yellow DNA Intercalators. *J. Phys. Chem. B* **2007**, *111*, 12610-12620.

224. Andreatta, D.; Lustres, J. L. P.; Kovalenko, S. A.; Ernsting, N. P.; Murphy, C. J.; Coleman, R. S.; Berg, M. A. Power-Law Solvation Dynamics in DNA over Six Decades in Time. *J. Am. Chem. Soc.* **2005**, *127*, 7270–7271.

225. Sollich, P.; Lequeux, F.; Hébraud, P.; Cates, M. E. Rheology of Soft Glassy Materials. *Phys. Rev. Lett.* **1997**, *78*, 2020-2023.

226. Coussot, P.; Raynaud, J. S.; Bertrand, F.; Moucheront, P.; Guilbaud, J. P.; Huynh, H. T.; Jarny, S.; Lesueur, D. Coexistence of Liquid and Solid Phases in Flowing Soft-Glassy Materials. *Phys. Rev. Lett.* **2002**, *88*, 218301.

227. Andreatta, D.; Sen, S.; Lustres, J. L. P.; Kovalenko, S. A.; Ernsting, N. P.; Murphy, C. J.; Coleman, R. S.; Berg, M. A. Ultrafast Dynamics in DNA: "Fraying" at the End of the Helix. *J. Am. Chem. Soc.* 2006, 128, 6885-6892.
228. Sen, S.; Gearheart, L. A.; Rivers, E.; Liu, H.; Coleman, R. S.; Murphy, C. J.; Berg, M. A. Role of Monovalent Counterions in the Ultrafast Solvation Dynamics of DNA. *J. Phys. Chem. B* **2006**, *110,* 13248-13255.
229. Verma, S. D.; Pal, N.; Singh, M. K.; Sen, S. Sequence-Dependent Solvation Dynamics of Minor-Groove Bound Ligand Inside Duplex-DNA. *J. Phys. Chem. B* **2015**, *119*, 11019-11029.
230. Seibel, G. L.; Singh, U. C.; Kollman, P. A. A Molecular Dynamics Simulation of Double-Helical B-DNA Including Counterions and Water. *Proc. Natl. Acad. Sci. USA* **2004**, *101*, 14771–14775.
231. Duan, Y.; Wilkosz, P.; Crowley, M.; Rosenberg, J. M. Molecular Dynamics Simulation Study of DNA Dodecamer d(CGCGAATTCGCG) in Solution: Conformation and Hydration. *J. Mol. Biol.* **1997**, *272*, 553-572.
232. Young, M. A.; Ravishankar, G.; Beveridge, D. L. A 5-Nanosecond Molecular Dynamics Trajectory for B-DNA: Analysis of Structure, Motions, and Solvation. *Biophys. J.* **1997**, *73*, 2313-2336.
233. Teeter, M. M. Water-Protein Interactions: Theory and Experiment. *Annu. Rev. Biophys. Biophys. Chem.* **1991,** *20*, 577-600.
234. Brunne, R. M.; Liepinsh, E.; Otting, G.; Wüthrich, K. Van Gunsteren, W. F. Hydration of Proteins. A Comparison of Experimental Residence Times of Water Molecules Solvating the Bovine Pancreatic Trypsin Inhibitor with Theoretical Model Calculations. *J. Mol. Biol.* **1993,** *231,* 1040-1048.
235. Jiang, J. S.; Brünger, A. T. Protein Hydration observed by X-Ray Diffraction: Solvation Properties of Penicillopepsin and Neuraminidase Crystal Structures. *J. Mol. Biol.* **1994,** *243* 100–115.
236. Makarov, V.; Feig, M.; Andrews, B. K.; Pettitt, B. M. Diffusion of Solvent Around Biomolecular Solutes: A Molecular Dynamics Simulation Study. *Biophys. J.* **1998**, *75*, 150–158.
237. Norberg, J.; Nillson, L. Glass Transition in DNA From Molecular Dynamics Simulations. *Proc. Natl. Acad. Sci. USA* **1996**, *93*, 10173-10176.
238. Castrignanò, T.; Chellemi, G.; Desideri, A. Structure and Hydration of BamHI DNA Recognition Site: A Molecular Dynamics Investigation. *Biophys. J.* **2000**, *79*, 1263-1272.
239. Pal, S.; Maiti, P. K.; Bagchi, B. Exploring DNA Groove Water Dynamics through Hydrogen Bond Lifetime and Orientational Relaxation. *J. Chem. Phys.* **2006**, 125, 234903.
240. Mukherjee, A.; Lavery, R.; Bagchi, B.; Hynes, J. T. On the Molecular Mechanism of Drug Intercalation into DNA: A Simulation Study of the Intercalation Pathway, Free Energy, and DNA Structural Changes. *J. Am. Chem. Soc.* **2008**, 130, 9747.
241. Furse, K. E.; Corcelli, S. A. Effects of an Unnatural Base Pair Replacement on the Structure and Dynamics of DNA and Neighboring Water and Ions. *J. Phys. Chem. B.* **2010**, 114, 9934-9945.
242. Furse, K. E.; Corcelli, S. A. Dynamical Signature of Abasic Damage in DNA. *J. Am. Chem. Soc* **2011**, *133*, 720-723.
243. Iwahara, J.; Wojciak, J. M.; Clubb, R. T. Improved NMR Spectra of a Protein–DNA Complex through Rational Mutagenesis and the Application of a Sensitivity Optimized Isotope-Filtered NOESY Experiment. *J Biomol NMR* **2001**, *19*, 231–241.
244. Rambo, R. P.; Tainer, J. A. Bridging the Solution Divide: Comprehensive Structural Analyses of Dynamic RNA, DNA, and Protein Assemblies by Small Angle X-Ray Scattering. *Current Opin. Struct. Biol.* **2010**, *20*, 128-137.
245. Pretto, D. I.; Tsutakawa, S.; Brosey, C. A.; Castillo, A.; Chagot, M. E.; Smith, J. A.; Tainer, J. A.; Chazin, W. J. Structural Dynamics and Single-Stranded DNA Binding Activity of the Three N-Terminal Domains of the Large Subunit of Replication Protein A from Small Angle X-Ray Scattering. *Biochemistry* **2010**, *49*, 2880–2889.
246. Campagne, S.; Gervais, V.; Milon, A. Nuclear Magnetic Resonance Analysis of Protein–DNA Interactions. *J. R. Soc. Interface* **2011**, *8*, 1065-1078.
247. Higo, J.; Kono, H.; Nakamura, H.; Sarai, A. Solvent Density and Long-Range Dipole Field around a DNA-Binding Protein Studied by Molecular Dynamics. *Proteins* **2000**, *40,* 193–206.
248. Reddy, Ch. K.; Das, A.; Jayaram, B. Do Water Molecules Mediate Protein-DNA Recognition? *J. Mol. Biol.* **2001**, *314,* 619–632.

249. Pelmenschikov, A.; Yin, X.; Leszczynski, J. Revealing the Role of Water in the Acid-Base Interaction Between the Phosphate Groups of DNA and the Amino Acid Side Chains of Proteins: A Density Functional Theory Study of Molecular Models. *J. Phys. Chem. B* **2000**, *104,* 2148–2153.
250. Giudice, E.; Lavery, R. Simulations of Nucleic Acids and Their Complexes. *Acc. Chem. Res.* **2002**, *35*, 350–357.
251. Yuan, C., Rhoades, E., Heuer, D. M. and Archer, L. A. Mismatch-Induced DNA Unbending upon Duplex Opening**.** *Biophys. J.* **2005**, *89*, 2564.
252. Wang, H., Yang, Y., Schofied, M. J., Du, C., Fridman, Y., Lee, S. D. DNA Bending and Unbending by MutS Govern Mismatch Recognition and Specificity**.** *Proc. Natl Acad. Sci. USA* **2003**, *100*, 14822-14827.
253. Sarkar, R.; Pal, S. K. Interaction of Hoechst 33258 and Ethidium with Histone1−DNA Condensates. *Biomacromolecules* **2007**, *8*, 3332–3339.
254. Sinha. S. K.; Bandyopadhyay, S. Dynamic Properties of Water around a Protein-DNA Complex From Molecular Dynamics Simulations. *J. Chem. Phys* **2011**, *135*, 135101.
255. Guchhait, B. and Biswas, R. Solute and Solvent Dynamics in Confined Equal-Sized Aqueous Environmetns of Charged and Neutral Reverse Micelles: A Combined Dynamic Fluorescence and All-Atom Molecular Dynamics Simulation Study. *J. Phys. Chem. B* **2013**, *117*, 3345-3361.
256. Indra, S. and Biswas, R. How Heterogeneous are Trehalose/Glycerol Cryoprotectant Mixtures? A Combined Time-Resolved Fluorescence and Computer Simulation Investigation. *J. Phys. Chem. B* **2016**, *120*, 11214-11228.
257. Indra, S.; Guchhait, B. and Biswas, R. Structural anomaly and dynamic heterogeneity in cycloether/water binary mixtures: Signatures from composition dependent dynamic fluorescence measurements and computer simulations. J. Chem. Phys. **2016**, *144*, 124506 (1-14).
258. Das, A.; Das, S. and Biswas, R. Fast fluctuations in deep eutectic melts: Multi-probe fluorescence measurements and all-atom molecular dynamics simulation study. *Chem. Phys. Lett.* **2013**, *581*, 47-51.

Chapter 3

Experimental and Simulation Methods: Application in DNA and Lipid Bilayer

Experimental and computational methods are employed to gain knowledge about various natural phenomena. This knowledge is further used to predict other similar phenomena. The superiority of any method depends on the scientific knowledge of the method itself, and as the knowledge grows, methods also evolve with time, therefore upgrading both knowledge and methods. This chapter discusses the experimental and simulation methods used to carry out the research work on static and dynamic properties of biomolecules, particularly DNA and lipid bilayer/vesicles in the present thesis. The experimental techniques used are: steady-state absorption and fluorescence spectroscopy, Time Correlated Single Photon Counting (TCSPC), fluorescence Up-Conversion (UPC) and Circular Dichroism (CD) spectroscopy. This chapter describes, in detail, experimental principles, instrumentation and data analysis used in the present works. It also contains detailed methodologies used to perform molecular docking and molecular dynamics (MD) simulations as well as the analysis of simulation trajectories for direct comparison of simulation results to experiments.

3.1. Experimental Methods

3.1.1. Steady-State Absorption and Fluorescence Spectroscopy

Measurement of steady-state absorption spectra of molecules using spectrophotometer is the first step to obtain electronic properties and concentration of molecules. Spectrophotometer works based on the Beer-Lambert's law as,

$$A = log\left[\frac{I_0(\lambda)}{I(\lambda)}\right] = \varepsilon(\lambda)Cl \qquad (3.1)$$

where A is the absorbance. $I_0(\lambda)$ and $I(\lambda)$ are the intensities of incident and transmitted light at wavelength λ, respectively. $\varepsilon(\lambda)$ is molar extinction coefficient at that wavelength, C is concentration of absorbing molecules and l is the path length of sample. For all steady-state absorption measurements, a dual-beam *Shimadzu UV-2450* spectrophotometer was used. *Jasco UV-Vis-NIR spectrophotometer* (*V-670*), equipped with temperature controlled bath, was also used to measure the concentration of single-stranded DNA at 90°C by monitoring the absorption at 260 nm. Finally, the concentrations of DNA samples were calculated using the extinction coefficient of DNA from nearest-neighbor model in several cases.[1,2]

To acquire steady-state fluorescence spectra, the fluorophore is irradiated with a continuous light source. Hence, the excited state population is continuously created and de-excited to ground state, thus reaching a steady-state. *Agilent Cary Eclipse* fluorescence spectrometer was used to measure the steady-state fluorescence spectra of the samples with excitation and emission band-pass set at 5 nm and 5 nm, respectively, for DNA samples and 5 nm and 1.5 nm, respectively, for lipid-vesicle samples. All fluorescence spectra were corrected for instrumental error and band-pass using standard spectrum of Quinine Sulphate solution.[3,4] Finally the spectra were converted into either *photon/nm* vs. *nm* or *photon/*cm^{-1} vs. cm^{-1} for further analysis.

3.1.2. Time-Resolved Fluorescence Spectroscopy

Time-resolved spectroscopy measures the dynamic processes in molecules. The theory of time-resolved spectroscopy is not new, but with the development of pulsed lasers, pulse shaping techniques and fast detectors, the stability and time-resolution of these techniques has improved to unprecedented levels. Unlike steady-state fluorescence spectroscopy, time-resolved fluorescence spectroscopy works based on the excitation of a fluorophore with a pulsed light source and subsequently measuring the fluorescence transients without the light excitation. Many established time-resolved techniques are available. Among them, fluorescence-based Time Correlated Single Photon Counting (TCSPC) and Up-conversion (UPC) techniques are unique and are widely used to study dynamical processes in molecules from tens of femtoseconds to microseconds. These time-resolved techniques, together with steady-state absorption and fluorescence, were used for the research works presented in chapters 4–8. Brief descriptions of the principles of TCSPC and UPC techniques are given below.

3.1.2.1. Time Correlated Single Photon Counting

Time Correlated Single Photon Counting (TCSPC) has the highest sensitivity of single photon detection, large dynamic range, excellent signal-to-noise ratio and high time-resolution. TCSPC is widely used to measure fluorescence lifetimes of molecules from tens of picoseconds to microseconds.

3.1.2.1.1. Instrumentation: TCSPC

TCSPC works on the principle of detection of a single photon with reference to an excitation pulse.[5,6] The schematic diagram of TCSPC instrument is shown in Figure 3.1. In TCSPC, sample is excited by an ultrashort laser pulse and the emitted fluorescence photon is detected by a fast detector in perpendicular direction. Laser light is focussed

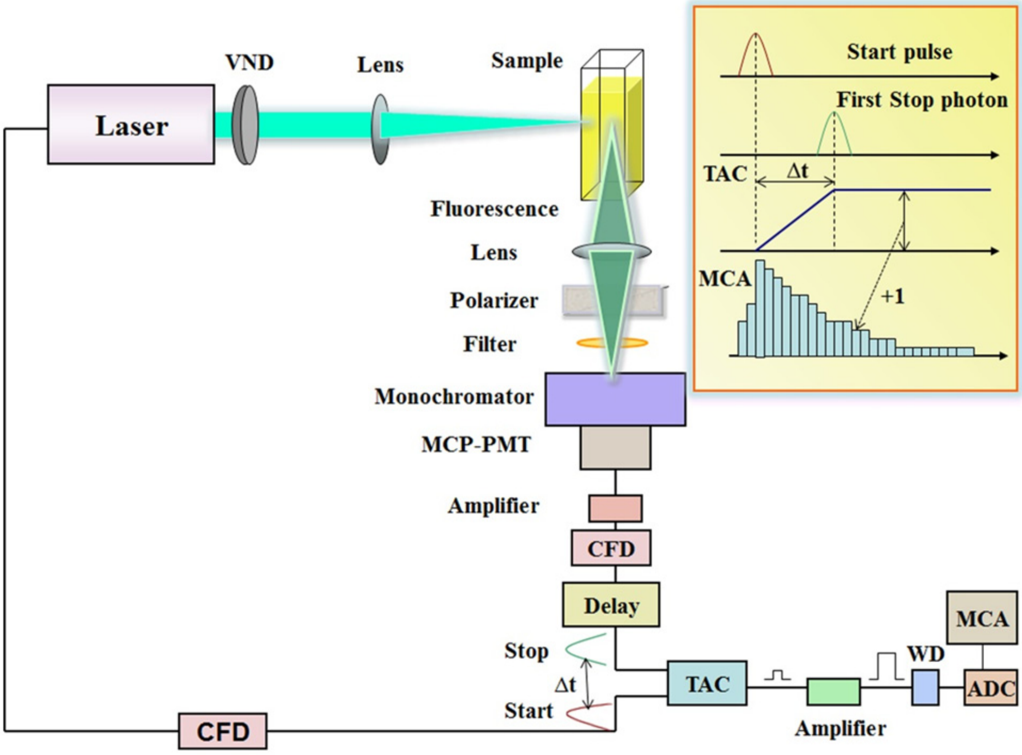

Figure 3.1: Schematic Diagram of TCSPC Setup.

inside sample by a lens. Power of laser falling on sample is controlled by a variable neutral density (VND) filter. Fluorescence photons from the sample are then detected with a fast micro channel plate-photomultiplier tube (MCP-PMT) after passing through a filter and monochromator. The output signal of MCP-PMT is used as *Start* pulse for the time-to-amplitude converter (TAC) after amplifying and reducing noise through a constant fraction discriminator (CFD), which triggers the charging of a capacitor inside the TAC. A *sync-out* signal from the laser is also fed to another CFD to reduce the noise after delaying the pulse through an electronic-delay or signal-cable before it is finally inserted into the TAC, which acts as *Stop* pulse. Arrival of *Stop* pulse to TAC discharges the capacitor inside TAC. The time difference between *Start* and *Stop* provide the arrival time of detected fluorescence photon relative to the excitation pulse. The time-difference is then converted to voltage TTL-pulse which is actually the output signal of TAC. This output TTL-voltage is then amplified and fed into a window discriminator (WD) which put a threshold voltage as to discard the false signal counting. The output voltage is then converted to digital signal by an analog-to-digital converter (ADC) and stored as single photon event in a multi-channel analyzer (MCA) by adding a number into the memory with an address proportional to the time difference between *Start* and *Stop*. Many such photon events are registered in MCA with multiple laser excitations which finally generate a histogram of detected photons that follow Poisson distribution. This distribution corresponds to fluorescence decay profile of molecules under investigation. To discard rotational motions of fluorophores in the detected photons, emission polarization is set at 54.7° (magic angle), relative to vertical polarization of excitation. The time-resolution of TCSPC setup depends on both pulse duration of laser and electron transit time of detector. Using a MCP-PMT and a femtosecond laser source the minimum time-resolution of TCSPC can be brought down to ~30 ps.

TCSPC works based on the principle that: on an average, less than one photon is detected for each excitation pulse. There are many events of excitations when no photon is detected. Typically, the photon detection rate is maintained at <1% of the laser repetition rate to minimize the pulse-pileup in measured decay. The instrument response function (IRF) is measured by the instantaneous scattering profile of a scattering solution in place of sample. Width of the laser pulse, transit-time of electrons inside PMT and electronics used in TCSPC contribute to the IRF of the system. Thus, laser pulse-width and detector are chosen in such a way that the IRF is much shorter than the lifetime of molecule to be measured. Laser pulse repetition rate is also set in such a manner that the longest decay reaches nearly to zero before the next laser-pulse arrives at the sample.

We have used a TCSPC set-up (*FL920, Edinburgh Instruments, UK*) equipped with picosecond pulsed diode laser (emission @375nm) of pulse-width ~60 ps and selectable pulse-repetition rates. The *FL920* TCSPC setup uses a compact PCI-interfaced TCC900 card that contains all the electronics including CFDs, amplifiers, TAC, ADC, WD, delay and MCA. Generally, *sync-out* signal from the MCP-PMT output (*Start* pulse) and the laser (*Stop* pulse) are directly fed into Start and Stop connectors of TCC900 card, and the final fluorescence decay is registered in the MCA of the TCC900 card. For measuring the fluorescence decays, laser repetition rates were fixed at either 5 MHz or 10 MHz such that the TAC time-range becomes 200 ns or 100 ns, respectively. All decays were measured at magic angle using 4096 channels of MCA. The typical time-resolution (FWHM of IRF) of our TCSPC setup was ~100 ps.

3.1.2.1.2. Data Analysis

The excited-state population of fluorophores follows the decay law:[7]

$$\frac{dn^*(t)}{dt} = -kn^*(t) \qquad (3.2)$$

where $n^*(t)$ is the excited state population at time t and k is the rate constant of de-excitation process. Equation 3.2 can also be rewritten as,

$$\frac{n^*(t)}{n^*(0)} = e^{-kt} \qquad (3.3)$$

Lifetime (τ) is the inverse of rate constant k. Hence, equation 3.3 can be expressed as,

$$\frac{n^*(t)}{n^*(0)} = e^{-t/\tau} \qquad (3.4)$$

In practice, the fluorescent molecules are excited by an ultrashort laser pulse at time t=0 and the fluorescence intensity is measured at later time t. Thus, time-dependent fluorescence intensity can be written as $I(t) = k_f\, n^*(t)$, where k_f is the deactivation rate constant through fluorescence. Fluorescence intensity decay can then be expressed as,

$$I(t) = I(0)e^{-t/\tau} \tag{3.5}$$

For multi-exponential decays, $I(t)$ can be written as,

$$I(t) = \sum_{i=1}^{n} a_i\, e^{-t/\tau_i} \tag{3.6}$$

where a_i is the amplitude of the i^{th} component of lifetime τ_i.

In general, the measured decay is obtained as a convolution of IRF with the actual fluorescence decay.[8] Hence, measured decay is written as,

$$F(t) = \int_0^t R(t')\, I(t - t')dt' \tag{3.7}$$

where $F(t)$ is the measured fluorescence decay, $R(t')$ is the IRF and $I(t - t')$ is the actual decay function of the sample.

To extract *actual* fluorescence lifetime(s) from the *measured* fluorescence decays, it is necessary to deconvolute IRF from the measured data. Considering the *actual* fluorescence decay as single exponential, $I(t - t')$ can be written as: $I(t - t') = exp(-(t - t')/\tau)$. Equation 3.7 then takes the form

$$F(t) = exp(-t/\tau) \int_0^t R(t')\, exp(t'/\tau)dt' \tag{3.8}$$

The *measured* decay $F(t)$, and IRF $R(t)$ are obtained by collecting fluorescence decays of sample and Rayleigh scattering from LUDOX solution in water, respectively.

Deconvolution of IRF from the measured decay uses the iterative least-square re-generative convolution method.[8,9] Deconvolution procedure starts with evaluating the integral in eq. 3.8 using measured IRF $R(t')$ and projected decay $I(t - t')$ to form a new re-convoluted function $F(t)$. This $F(t)$ function is then compared with the *measured* fluorescence decay through iterative least-square method. The difference between the calculated and measured decays is summed over all time points to generate the χ^2 (goodness-of-fit) for the fit. Thus, χ^2 is defined as,

$$\chi^2 = \sum_{i=1}^{n} \left[\frac{Y^{theo}(t_i) - Y^{expt}(t_i)}{\sigma_i}\right]^2 \tag{3.9}$$

where $Y^{theo}(t_i)$ is the calculated decay and $Y^{expt}(t_i)$ is the (experimentally) *measured* decay. σ_i is the standard deviation of the i^{th} data point and n is the total number of data points (4096 channels in the present case). As TCSPC data follow the Poisson distribution, σ_i can be expressed as square root of the photon count of the i^{th} point, i.e., $\sigma_i = [N(t_i)]^{1/2}$. The reduced χ^2 or χ_r^2 is defined as,

$$\chi_r^2 = \frac{1}{n-q}\sum_{i=1}^{n}\left[\frac{Y^{theo}(t_i)-Y^{expt}(t_i)}{\sigma_i}\right]^2 \tag{3.10}$$

or,

$$\chi_r^2 = \frac{\chi^2}{n-q} = \frac{\chi^2}{\nu} = \frac{s^2}{\overline{\sigma_i^2}} \tag{3.11}$$

where q is the number of free parameters used in the fit. ν is called the degrees of freedom. If the fit function exactly predicts the original function, then the estimated variance of the fit, s^2 , will be equal to weighted average of σ_i^2, i.e.; $\overline{\sigma_i^2}$. Hence the ratio, i.e., χ_r^2 will be equal to 1.[9] For inferior fit this should lead to $\chi_r^2 > 1$. In the iterative least-square regenerative convolution method, χ_r^2 is calculated for each projected $Y^{theo}(t_i)$ to achieve χ_r^2 as close to 1. The interpretation of goodness-of-fit in terms of χ_r^2 is more reliable than χ^2 only because the value of the later depends on the number of data points, but not for the former.

In complex systems, such as in DNA, the actual decay, $I(t - t')$ can have multi-exponential time-constants. Dealing with multi-exponential decays is not straightforward. In general, increasing the number of exponentials makes fit better than the smaller number of exponentials. Although, increasing the number more than what required for modeling the decay should always provide more than one time-component which are similar. Many times it is also difficult to have meaningful decay times, especially those time-components which are faster than the IRF. Theoretically, decay time-constant which is 1/10th of the IRF is accessible from the measured decay through deconvolution method. Although in practice, the limit depends on the complexity of the system under investigation. Another problem with multi-exponential decay fitting in complex systems is that there is always a trade-off between the time-constants (τ_i) and the amplitudes (a_i) of the fit. Hence, ample care was taken to obtain the reliable a_i and τ_i while fitting the time resolved data.

In TCSPC data analysis, a least-square fitting program developed by Prof. Mark Maroncelli (Penn State University) was used to deconvolute the IRFs from the measured decays to obtain lifetimes and their contributions. Typically, sum of 3 – 4 exponentials (decay) times were used to fit the data of DNA/ligand systems. The fitted parameters were then used, together with the steady-state fluorescence spectra, to construct the time-resolved emission spectra (see below).

3.1.2.2. Fluorescence Up-conversion

Fluorescence up-conversion (UPC) technique works on the principle of generation of sum-frequency by mixing fluorescence signal from a sample with an intense ultrashort laser pulse inside a nonlinear optical (NLO) crystal. UPC is a pump-probe based technique where non-coherent fluorescence (pump) is mixed with the coherent femtosecond laser pulse (probe/gate) inside the NLO crystal, typically a β-barium borate (BBO) crystal, satisfying the phase-matching condition of the two pulses inside the crystal.[10] Time evolution of fluorescence is then achieved by delaying the probe/gate–pulse with respect to pump-pulse (fluorescence) using a mechanical decay stage.[11,12] Unlike TCSPC, the UPC technique is developed based on the idea of replacing slow electronic components of TCSPC with optical components and obtaining the fluorescence decay in a pump-probe scheme. Fluorescence up-conversion was first introduced by Mahr and Hirsch.[13] However, with the development of stable femtosecond-pulsed laser sources and design of UPC spectrometer, the capability of this technique has improved several folds. Moreover in recent times the development of femtosecond broadband UPC technique has made it possible to measure the time-dependence of entire fluorescence spectra of samples without performing any spectral reconstruction.[14,15] Because of the high time-resolution (typically ~50 – 300 fs), fluorescence UPC technique is now routinely used to measure fluorescence decays from tens of femtoseconds to nanoseconds.

3.1.2.2.1. Principle of UPC

In UPC technique, the mixing of gate-pulse with fluorescence inside the NLO crystal gives rise to the up-converted or sum-frequency signal only during the spatial and temporal overlap of the gate-pulse and fluorescence inside the crystal. Thus, theoretically it is possible to gate the time-dependent fluorescence with the temporal resolution same as the pulse-width of the gate-pulse. However, dispersing elements present inside UPC spectrometer introduce group velocity dispersion (GVD) which makes the IRF of UPC setup higher than the pulse-width of gate-pulse. In fluorescence UPC, the detected sum-frequency signal can be obtained as,

$$\lambda_s^{-1} = \lambda_f^{-1} + \lambda_g^{-1} \qquad (3.12a)$$

or

$$\omega_s = \omega_f + \omega_g \qquad (3.12b)$$

where λ_s (or ω_s) is the detected wavelength (or sum-frequency). λ_f (or ω_f), and λ_g (or ω_g) are fluorescence and gate wavelengths (or frequencies), respectively. The sum-frequency signal is obtained only when the phase-matching condition for the two pulses are achieved inside the NLO crystal. The phase matching conditions are given by,

$$\hbar\omega_s = \hbar\omega_f + \hbar\omega_g \qquad (3.13a)$$

$$\hbar k_s = \hbar k_f + \hbar k_g \qquad (3.13b)$$

where k_s, k_f and k_g are the wave-vectors of the three photons and $\hbar$ is the Plank's constant divided by 2π. For any non-dispersive NLO medium, eq. 3.13 is directly satisfied. However, in practice all materials are dispersive in nature and the photons with different frequencies travel with different velocities inside the medium. In that case, phase-matching condition takes the form

$$n_s\omega_s = n_f\omega_f + n_g\omega_g \qquad (3.14)$$

where n_s, n_f and n_g are the refractive indices related to the three photons. In fluorescence UPC setup, the above condition is achieved by utilizing the birefringence property of the (uniaxial) NLO crystal where different photons can have different polarizations. The process can be either *o-o-e* or *o-e-e*, that is, two input waves are ordinary and output wave is extra-ordinary (type-I phase matching) or one input wave is ordinary and other is extra-ordinary and the output wave is extra-ordinary (type-II phase matching).[16] In practice, adjusting the angle of the optic-axis of NLO (BBO) crystal with respect to the input beam directions (k – directions), eq. 3.14 can be satisfied through the birefringence property of the crystal. In the present UPC setup, we used a 0.5 mm thick BBO crystal (θ = 38° and Φ = 90°) for generating the up-converted signal which works on *o-o-e* configuration (type-I phase matching).

3.1.2.2.2. UPC Instrumentation

The schematic of UPC set-up is shown Figure 3.2. The fundamental laser beam (ω_g) is first focussed on to a 0.5 mm thick BBO crystal by lens (L1), after being guided by mirrors M1 and M2, to generate the second harmonic pulse ($2\omega_g$) that is used for sample excitation. The generated $2\omega_g$ and residual ω_g are then collected by lens (L2) and directed towards the dichroic beam-splitter BS1 which reflects the $2\omega_g$ and passes the fundamental ω_g. After BS1, a red filter (F1) is used in the fundamental beam-path to cut the small residual $2\omega_g$ and have pure ω_g pulse which is then used as the gate-pulse. In the other arm, a blue filter (F2) and a set of neutral density (ND) filter (F3) are used to cut any residual fundamental ω_g and to control the power of $2\omega_g$, respectively. In our setup we kept the excitation power of $2\omega_g$ below 20 mW to minimize sample photobleaching and scattering. The reflected $2\omega_g$ pulse passes through a Berek compensator which sets the polarization of $2\omega_g$ to magic angle with respect to fundamental ω_g (i.e., 35.3° from horizontal polarization of gate-pulse in present case). $2\omega_g$ is then focussed into the sample by lens L3, after getting reflected from BS2. The sample is kept in a rotation cell chamber to avoid photobleaching. Fluorescence (ω_f) is collected and collimated by lens L4. Residual excitation light is removed by the filter F4. Pure fluorescence is then focussed by lens L5 on to another 0.5 mm thick BBO crystal (θ = 38° and Φ = 90°). In the other arm, the gate-beam is guided by mirrors M3 and M4 into the retro-reflector (RR) which is connected to a computer controlled delay stage. Retro-reflector is a combination of gold coated mirrors which reflects back the light in the direction of the source with minimum scattering. After reflection, the electric field vector remains parallel but travels opposite to the source. The purpose of using the gold coated mirrors is to gain

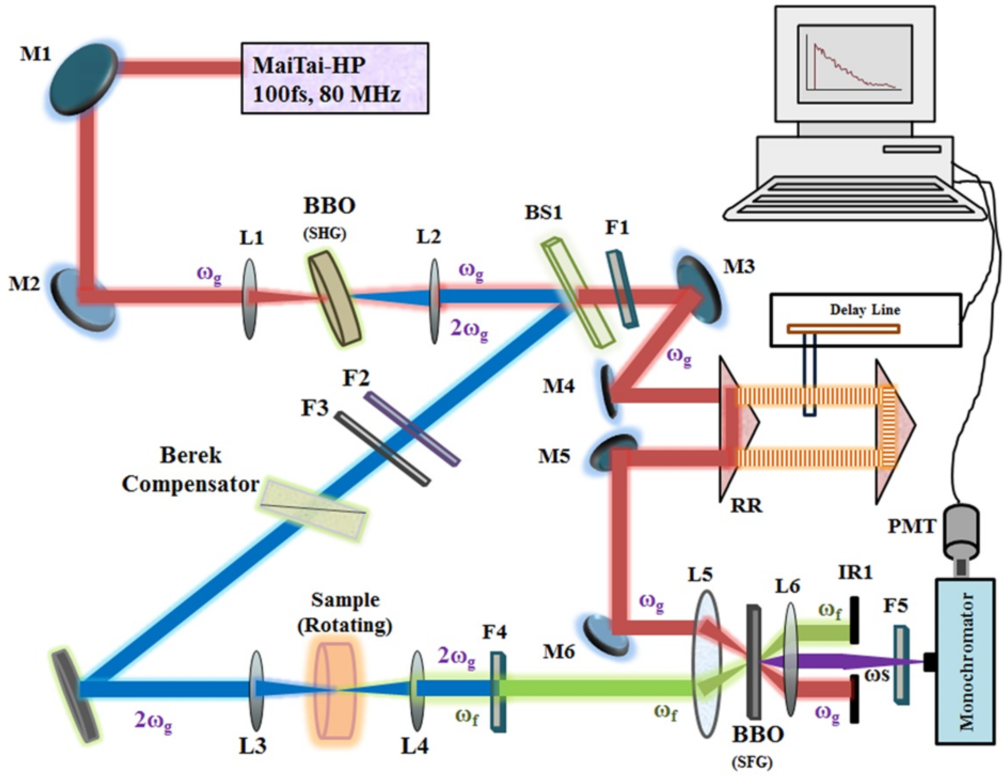

Figure 3.2: Schematic Diagram of UPC Setup.

high reflectivity over a broad wavelength range. After reflected by RR, the gate-pulse is guided through mirrors M5 and M6, and focussed onto the same crystal by the lens L5 to spatially overlap the gate-pulse with fluorescence. Up-converted or sum-frequency signal ω_s (= $\omega_f + \omega_g$) is generated inside BBO crystal by rotating the crystal optic-axis to a certain angle which satisfies the phase-matching condition for a particular set of input and output frequencies (ω_f, ω_g and ω_s). The sum-frequency signal (ω_s) is then collected through a lens system (L6) and again focused on the entrance slit of a double-monochromator. An iris (IR1) is used to cut residual fluorescence and gate signal. A PMT is connected at the exit slit of the double-monochromator which finally converts the optical signal to electrical signal. A computer controls the delay stage and monochromator, and the data is collected in (Lumex) software. In our UPC experiments, the wavelength dependent decays were collected by setting the (phase-matching) angle of BBO crystal and monochromator for desired wavelengths. For example, if the gate-pulse was set at 750 nm and decay was to be collected at 460 nm then the monochromator was set at 285.12 nm. The BBO crystal was then rotated to achieve the phase-matching condition where maximum up-converted signal was obtained. The stepper-motor controlled delay stage was moved in desired time-steps to collect the fluorescence decays. Figure 3.3 shows how the fluorescence is gated by the fundamental laser pulse inside BBO crystal to obtain the final fluorescence decay.

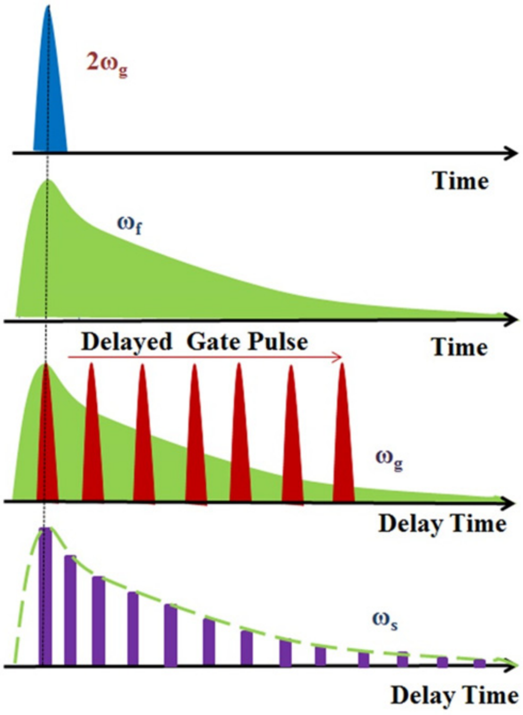

Figure 3.3: Generation of Fluorescence Decay.

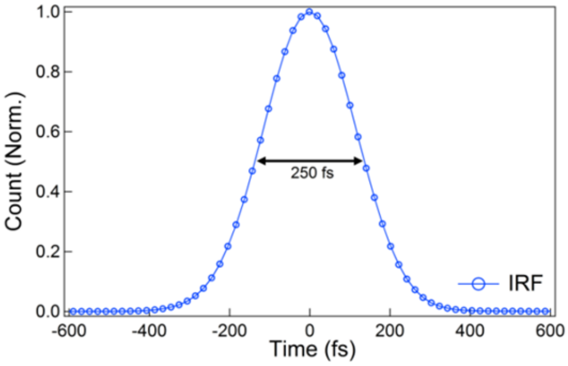

Figure 3.4: Instrument response function measured from the cross-correlation of water Raman signal.

The UPC spectrometer (*FOG-100*, CDP Corp., Moscow, Russia) is pumped with a mode-locked Ti:Sapphire oscillator laser (*Maitai-HP*, Spectra Physics, USA). *MaiTai-HP* provides pulses of ~100 fs pulse-width at 80 MHz pulse-repetition rate with average power ~2.5 W at 800 nm. Wavelength tuneability of this laser is from 690 nm to 1040 nm. For all UPC data reported in this thesis, the fundamental laser wavelength was tuned at 750 nm which produced excitation wavelength (SHG) at 375 nm that excites the DAPI-DNA samples. The decays were collected at magic angle polarization within the time-window of 10 fs to 1.5 ns. The IRF was measured by replacing the sample with water and collecting the cross-correlation of the water Raman signal with the gate-pulse. Typical time-resolution (IRF) of UPC setup was ~250 fs (FWHM) (Figure 3.4).

3.1.2.2.3. UPC Data Analysis

Analysis of UPC data to extract fluorescence lifetimes also uses procedure of deconvolution of IRF from the measured decay using least-square regenerative convolution method, similar as in TCSPC data analysis. However, unlike IRF in TCSPC, the measured IRF in UPC setup shows symmetric Gaussian shape. Hence, rather than directly deconvoluting the measured IRF from the decay, UPC data analysis uses indirect method of deconvolution of a Gaussian function (similar as the measured IRF) from the decay through an error function analysis that uses the regenerative convolution.

The fluorescence decays were fitted using equation 3.15[17] by nonlinear least square fitting method in IGOR-Pro software.

$$I(t) = \frac{1}{2}\sum_i a_i \, exp\left(\frac{\tau_g^2}{2\tau_i} - \frac{(t-t_0)}{\tau_i}\right) erf\left(\frac{\tau_g^2 - \tau_i(t-t_0)}{\sqrt{2}\tau_i\tau_g}\right) \qquad (3.15)$$

where, τ_g is the width of Gaussian-shaped IRF, t_0 is the time offset between the IRF and the decay and τ_i's are the exponential decay time-constants. A macro based on the above equation was written in IGOR-Pro software which was used for final UPC decay analysis. For DNA/ligand samples 3-4 exponential time-constants were used to model the UPC decays. Finally, the fitted parameters were used to obtain the time-dependent fluorescence Stokes shifts (TDFSS) and solvation correlation functions through TRES analysis (see below).

3.1.3. Construction of Time Resolved Emission Spectra

The dynamic information of any molecular assembly can be obtained by following the evolution of fluorescence spectra with time through constructing of time-resolved emission spectra (TRES) from lifetime decays. TRES provide many insights about the dynamics of solute-solvent interactions, which is otherwise not easy to retrieve from only the time-constants obtained from decay fits. TRES are generally reconstructed from the wavelength dependent decay parameters and steady-state emission spectrum.[18] To construct TRES, first the wavelength dependent intensity decays are fitted with multi-exponential function by deconvoluting IRF, and then the fitted parameters are used together with steady-state fluorescence spectrum. Steady-state spectrum is generally the time average of the intensity decay, which can be written as

$$I_{ss}(\lambda) = \int_0^\infty I(\lambda, t)dt = F(\lambda)\int_0^\infty I(t)\, dt \qquad (3.16)$$

where, $I(t) = \sum_{i=1}^{n} a_i \, e^{-t/\tau_i}$

Thus, $\int_0^\infty I(t)dt = \sum_{i=1}^{n} a_i\tau_i \qquad (3.17)$

Therefore, from above equations,

$$F(\lambda) = \frac{I_{ss}(\lambda)}{\int_0^\infty I(t)dt} = \frac{I_{ss}(\lambda)}{\sum_{i=1}^{n} a_i\tau_i} \qquad (3.18)$$

Hence, wavelength- and time-dependent fluorescence intensity can be written as

$$I(\lambda, t) = \frac{I_{ss}(\lambda)}{\sum_{i=1}^{n} a_i\tau_i}\sum_{i=1}^{n} a_i \, e^{-t/\tau_i} \qquad (3.19)$$

If the steady-state spectrum is represented in frequency (ν) then eq. 3.19 can be rewritten as

$$I(\nu, t) = \frac{I_{ss}(\nu)}{\sum_{i=1}^{n} a_i\tau_i}\sum_{i=1}^{n} a_i \, e^{-t/\tau_i} \qquad (3.20)$$

In actual measurements, the interval between the wavelengths at which the intensity decays are collected across steady-state emission spectrum is kept as small as possible. However, in practice it is kept typically in 10 to 20 nm gap. The constructed scattered TRES is then fitted with a Log-normal function (eq. 3.21) which models the accurate line-shape of the spectra, i.e. the typical asymmetric profile of spectra.[18]

$$I(\nu) = I_0 exp\left[-ln(2)\left(\frac{ln\left(1+\frac{2b(\nu-\nu_p)}{\gamma}\right)}{b}\right)^2\right] \qquad (3.21)$$

when $(2b(\nu\text{-}\nu_p)/\gamma) > - 1$,

but $I(\nu) = 0$ when $(2b(\nu\text{-}\nu_p)/\gamma) \leq - 1$

Here, I_0 is the peak intensity of TRES, ν_p is the corresponding peak frequency, γ is related to the width of the spectra and b is the asymmetric factor.

Generally, time-dependent fluorescence Stokes shift (TDFSS) and solvation correlation function are represented in terms of time-dependent peak frequency shift of spectra. However, the spectral shift in terms of average frequency (or first moment) rather than the peak frequency has several advantages: It not only takes into account the contribution from entire fluorescence spectrum, but also the asymmetric feature of the spectrum. Moreover, the shift in average frequency is directly proportional to the shift in the total (average) energy of the system with time.[19] Thus, the 1st moment frequency (or average frequency) was calculated from the log-normal fits to TRES using equation 3.22 and plotted with time to obtain the final TRFSS and solvation correlation functions of DNA/ligand systems, which directly represents the dynamic nature of energy relaxation (dynamics of solvation) in DNA.

$$\bar{\nu} = \frac{\int_0^\infty \nu I(\nu)d\nu}{\int_0^\infty I(\nu)d\nu} \qquad (3.22)$$

3.1.4. Merging of Stokes Shifts from UPC and TCSPC Techniques

DNA dynamics can spread over wide range of time scales. Hence, one single experimental technique is not sufficient to cover the entire time range of the dynamics. TRES were combined that were obtained from UPC and TCSPC data, and matched them in a self-consistent manner to get the entire Stokes shift dynamics of ligand/DNA systems over five decades in time from 100 fs to 10 ns. Ideally, the independently constructed TRES from different techniques should automatically match at common time-points of the two techniques. However, in actual practice it does not match automatically. The TCSPC setup had a time resolution of ~100 ps. Further, the TCSPC data generally have very high S/N

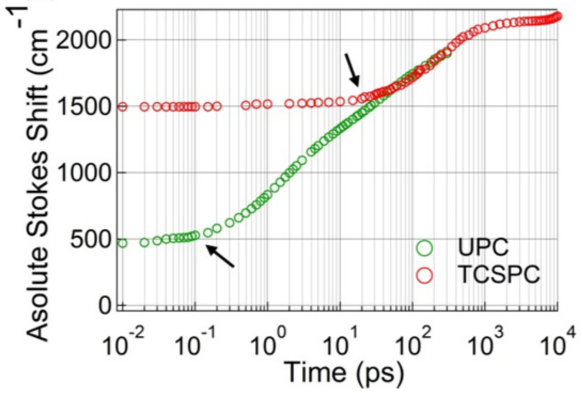

Figure 3.5: Example of matching of absolute Stokes shifts obtained from TRES constructed using UPC (green) and TCSPC (red) data. Arrows show time below which Stokes shifts could not be extracted due to limited time-resolutions of the UPC and TCSPC setups.

ratio. Thus, one can take TRES data obtained from TCSPC as reference at a time (100 ps in this case), after deconvoluting IRF from decays. However, in the UPC data the S/N ratio and longest time measurable (1 ns in the present cases) were limited. Thus, free fit to UPC data sometimes construct TRES in which several frequency points may deviate from the actual spectrum. Such deviations can lead to the estimation of 1st moment frequencies from TRES which may not match at common time points of the two techniques. Therefore, TRES data at 100 ps from TCSPC was taken as the reference time-point to match the UPC-TRES at that time point. To perform this matching, the UPC fitting analysis was done by manually adjusting the τ_3 and τ_4 (within the error limit of raw-data) at different wavelengths, and subsequently checking the matching of TRES for UPC and TCSPC data at 100 ps. During fitting analysis, τ_3 and τ_4 were kept fixed and other parameters were set free. Performing this fitting analysis iteratively, finally the self-consistent amplitudes and time-constants were obtained for all decays at different wavelengths in the UPC data-set. Subsequently, the constructed TRES from UPC decays were matched nicely with TRES obtained from TCSPC at 100 ps (see results in chapters 4-8). During the fitting analysis of UPC decays, goodness of fit was monitored by checking the residuals. Performing TRES matching at 100 ps for UPC and TCSPC data led to TRES matching at other common time points automatically, which ultimately led to the matching in 1st moment frequency shifts of probe of two techniques (for example, see Figure 3.5).

3.1.5. Time-Zero Spectrum and Absolute Stokes Shift

If a fluorescent molecule is electronically excited to higher energy state, its fluorescence emission spectrum shifts with time because of its energy stabilization in the excited state. Initially, the emission spectrum (from locally excited (LE) state) is close to the absorption spectrum, and as time proceeds, the fluorescence spectrum shifts to longer wavelength side. The time-dependent Stokes shifts due to solvent relaxation was first observed by Ware et al.[22] In the measurements of dynamic Stokes shift in any system, the energy position from where the Stokes shift starts is important. Theoretical understanding predicts that it should start from the same wavelength as that of absorption. This is true in gas-phase, but in condensed phase the spectral broadening makes it difficult to identify the 0-0 transition. Thus, estimating the time-zero position by extrapolating the Stokes shift back in time to zero-position is often practised. However, the zero-position estimated this way is exclusively depended on the time-resolution of the instrument. Fee and Maroncelli developed a method to estimate the time-zero emission spectrum using steady-state emission spectra.[23] Using theoretical calculation they showed,

$$\nu(t=0)=\nu_p(abs)-\left[\nu_{np}(abs)-\nu_{np}(em)\right] \qquad (3.23)$$

where $\nu_p(abs)$ is the absorption peak-maximum in polar solvent and $\nu_{np}(abs)$ and $\nu_{np}(em)$ are the absorption and emission peak-maxima in a non-polar solvent, respectively.[23] However the equation does not consider the line-shape of the spectrum. Moreover, this method loses its applicability when the probe is polar or charged. Most of the fluorescent probes (like DAPI and Hoechst used in the present thesis) are charged. Hence, it is not possible to dissolve them in non-polar liquid like hexane.

The best alternative method is to measure the time-zero emission spectrum experimentally by freezing the sample where all diffusive relaxations are stopped. In frozen glass, all large amplitude diffusive relaxations are frozen, but very fast intramolecular librational and phonon motions can be alive.[19]

In actual practice of measuring time-zero spectra a clear transparent glass was prepared by mixing aqueous solution of fluorophores (DAPI and Hoechst in this case) and macromolecule (DNA) with glycerol at ratio of 1:2 (water/glycerol). The sample was kept inside a quartz tube that was placed inside a glass dewar flask. The flask was filled with mixture of dry-ice and acetone which produced temperature of -78°C (195 K).[19] At this temperature the sample makes a transparent glass (see Figure 3.5). The entire set-up was then inserted inside the fluorescence spectrometer and the fluorescence spectrum was measured. For example, time-zero spectrum measured this way is shown in Figure 3.6. As evident from the Figure 3.6, the time-zero spectrum is blue shifted compared to the room temperature spectrum. Once the glass spectrum is measured, the calculation of absolute Stokes shift becomes straightforward. The absolute Stokes shift is calculated by taking the difference of 1st moment frequencies of the room temperature and the time-zero spectra. This difference (absolute Stokes shift) directly measures the (only) diffusion controlled energy relaxation processes in the system under investigation. Hence, the absolute Stokes shift is calculated as,

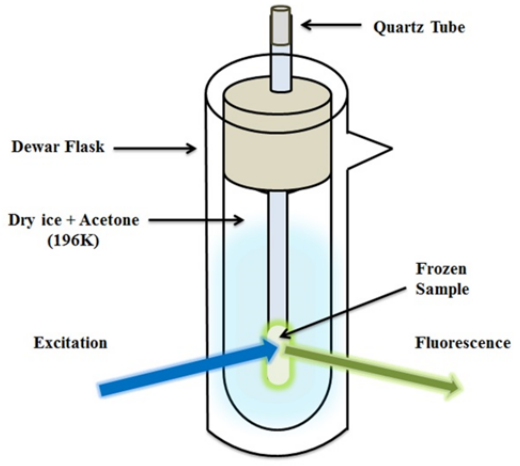

Figure 3.5: Schematic diagram of Dewar containing frozen sample in dry-ice/acetone mixture for time-zero spectrum measurement.

$$S(t) = \bar{\upsilon}_{glass} - \bar{\upsilon}(t) \qquad (3.24)$$

where $\bar{\upsilon}_{glass}$ and $\bar{\upsilon}(t)$ are the average frequencies of time-zero spectrum and time-resolved emission spectra at time t, respectively. The solvation correlation function, $C(t)$, is then calculated as,

$$C(t) = \frac{S(\infty) - S(t)}{S(\infty)} \qquad (3.25)$$

or, $$C(t) = \frac{S(10\,ns) - S(t)}{S(10\,ns)} \qquad (3.26)$$

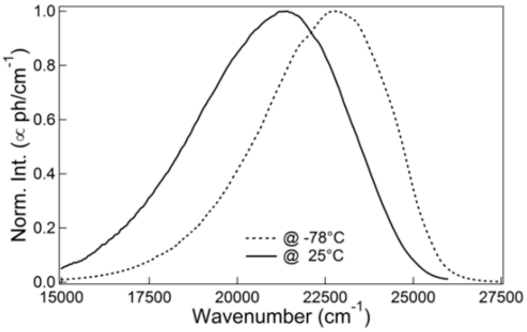

Figure 3.6: Time-zero emission spectrum measured in frozen glass (dotted line) and room temperature (solid line).

where $S(\infty)$ (or S(10 ns)) is the Stokes shift at infinite time (or at 10 ns). Sometimes it is not easy to find $S(\infty)$, without which it is difficult to calculate the $C(t)$. Many times the relaxation of the system may not complete within the lifetime of the fluorescent dye or may be even complete. The choice of exact $S(\infty)$ is thus subject to system to system. Both equations 3.25 and 3.26 are used in this thesis with proper justification for the choice in respective chapters.

3.1.6. Fluorescence Anisotropy Decay

Fluorescence anisotropy decay measurement provides a wealth of information about the inherent properties of a molecule as well as the surrounding environment.[24-26] Anisotropy decay measurements are performed to measure equilibrium binding constant as well.[3,27] The idea of anisotropy is based on the concept that the transition moment of absorption and emission lie in particular directions within the fluorophore. In a group of randomly oriented molecules, if a polarized light is applied then the molecules will have maximum probability of absorption whose absorption (transition) dipole moment is oriented within a particular range of angle with respect to the excitation polarization. If the molecules are not mobile then the emitted fluorescence will also have the polarization within the same range of angle as to the excitation. This is the intrinsic anisotropy of the system. The degree of polarization will decrease if the molecules are allowed to orient themselves. How quickly the degree of polarization decreases depends on the rotational lifetime of the molecules, and thus gives rise to fluorescence anisotropy decay. The depolarization can occur due to tumbling motion of entire fluorophore as well as rotation of segments (internal motion).

Time dependent anisotropy is generally measured by exciting the fluorophores with vertically polarised light. Fluorescence intensity decays are detected with the emission polarizer once parallel ($I_{\parallel}(t)$) to the excitation and next oriented perpendicular ($I_{\perp}(t)$) to the vertical excitation. Thus, the time-resolved anisotropy can be written as,

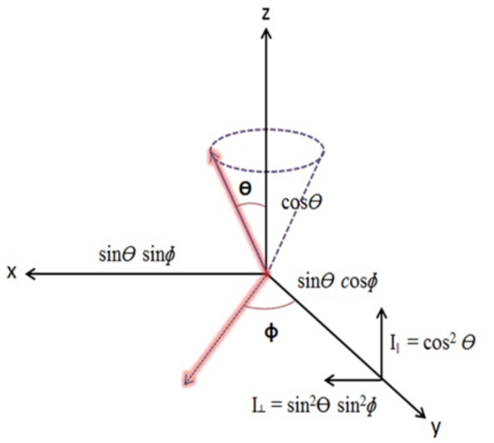

Figure 3.7: Intensity components along co-ordinate axes.

$$r(t) = \frac{I_{\parallel}(t) - G I_{\perp}(t)}{I_{\parallel}(t) + 2G I_{\perp}(t)} \qquad (3.27)$$

G is the correction factor arising from the polarization dependent sensitivity of the instrument and other instrumental errors. The complete polarization of fluorescence is never possible duo to the angular dependence of photo-selection.

Let us assume that the transition moment of the fluorophore is oriented in such a direction that it makes angle θ with the Z-axis and the projection of the transition moment makes an angle Φ with the Y-axis (Figure 3.7). The excitation pulse is linearly polarized along the vertical Z-axis. The components of the electric field vector along the X-, Y- and Z-axis will be proportional to $\cos\theta$, $\sin\theta\cos\phi$ and $\sin\theta\sin\phi$, respectively. As the intensity is proportional to the square of the magnitude of electric field, hence,

$$I_{\parallel}(\theta,\phi) = \cos^2\theta \qquad (3.28)$$

and

$$I_{\perp}(\theta,\phi) = \sin^2\theta\ \sin^2\phi \qquad (3.29)$$

For randomly oriented molecules, all molecules whose transition dipole moment makes an angle Φ with the Y-axis will be excited with equal probability where Φ ranges from 0 to 2π. Anisotropy is calculated considering the average over all the possible values of θ and Φ. Hence,

$$\langle \sin^2\phi \rangle = \frac{\int_0^{2\pi} \sin^2\phi\, d\phi}{\int_0^{2\pi} d\phi} = {}^{1}\!/_{2} \qquad (3.30)$$

thus,

$$I_{\parallel}(\theta,\phi) = \cos^2\theta \quad \text{and} \quad I_{\perp}(\theta,\phi) = \frac{1}{2}\sin^2\theta \qquad (3.31)$$

The anisotropy can be rewritten as (neglecting G factor),

$$r = \frac{3\langle\cos^2\theta\rangle - 1}{2} \qquad (3.32)$$

when $\theta = 0$, $r = 1$. But, in reality r is always less than 1. To be excited by the light polarised along Z-direction, the molecules need not to be precisely oriented along the Z-direction. The molecules making an angle of θ has the probability proportional to $\cos^2\theta$ for excitation, i. e. partially oriented molecules can also have certain probability as a result of photo-selection. Hence considering all possible values of θ between 0 to $\pi/2$ one can write,

$$\langle \cos^2 \theta \rangle = {}^{3}/_{5} \tag{3.33}$$

Thus, the maximum value r can have is 0.4, provided the absorption and emission dipole moments are collinear. Scattering is perfectly polarized as it is an instantaneous process. Thus for scattering value of r can be 1, where $I_{\perp}(t) = 0$. When $\langle \cos^2 \theta \rangle = 1/3$, i.e., θ = 54.7°, r = 0 for vertically polarized excitation. This angle is called the *Magic Angle* where the fluorescence decays become devoid of any anisotropic contribution. Hence, it is preferred to acquire the life time decays at *Magic Angle* so that the decays contain information only from life time not anisotropy. For horizontally polarized excitation at *Magic Angle* is θ = 35.3°. In TCSPC, the decays were measured at magic angle of 54.7° relative to vertical excitation polarization, and in UPC the decays were gated at magic angle of 35.3° with horizontally polarized fundamental laser beam.

3.1.7. Circular Dichroism

Circular Dichroism (CD) spectroscopy is a popular technique which is routinely used to obtain insight about the topological structure of biomolecules.[28,29] CD spectroscopy has several advantages over other techniques for structural analysis, for example, it has high sensitivity to work with low concentration of samples and has capability of fast data acquisition.[29] The phenomenon of circular dichroism was first discovered in early 19th century and is based on the differential absorption of left and right circularly polarized light.[30] Linearly polarized light consists of left (L) and right (R) circularly polarized light of equal magnitude. For an incident polarized light, after passing through the sample, if the left and right circularly polarised lights are absorbed to different extent by the sample then the resultant light will be elliptically polarised (Figure 3.8).

A molecule can absorb different amounts of L and R circularly polarized light, showing CD signal, if the molecule is chiral. The chirality originates from the asymmetric nature of the molecules.[31] The reason for chirality in biomolecule is the presence of asymmetric carbon atoms. Refractive index and extinction coefficient for left and right circularly polarised light are also different for chiral molecules.

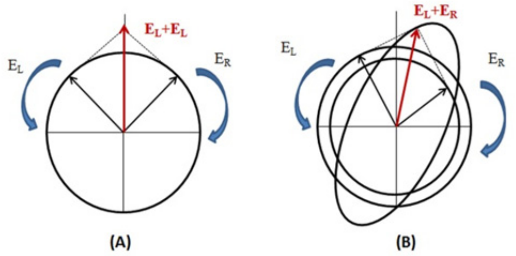

Figure 3.8: (a) Linear polarized light as a superposition of left and right circular polarized light of equal amplitude and phase. (b) Difference in absorption of the left and right circularly polarized light leads to ellipticity.

The schematic diagram of a CD spectrometer is shown in Figure 3.9.

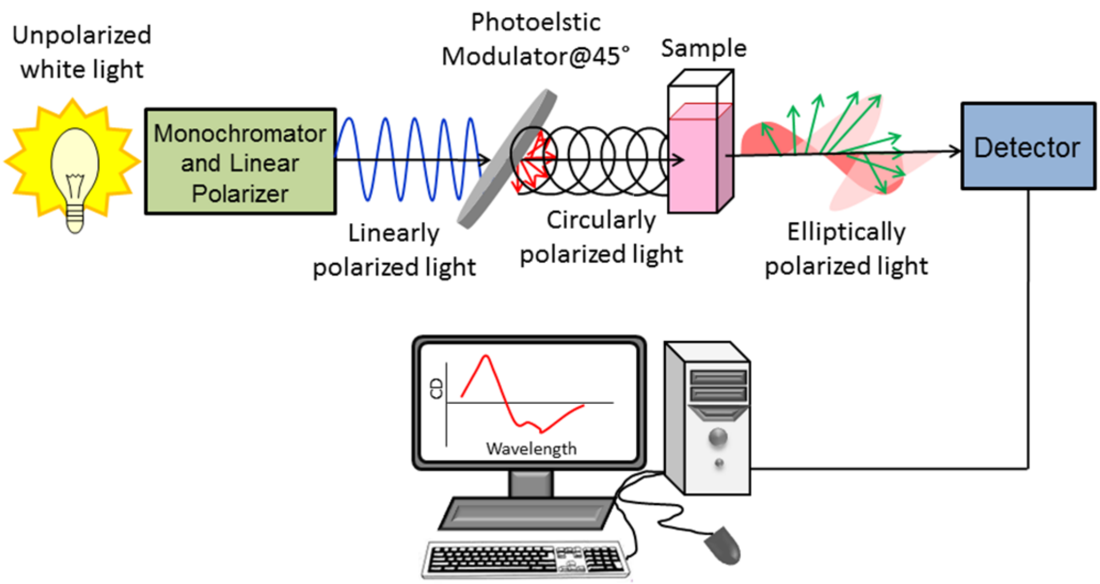

Figure 3.9: Schematic diagram of circular dichroism (CD) spectrometer.

Un-polarized white-light is used as source. Linearly polarised light is then generated from the white-light using a polarizer. The light is also passed through a monochromator to select particular wavelength. A photo-elastic modulator, made up of a piezoelectric transducer and a half wave resonant bar of fused silica, is used to convert the linearly polarised light into a circular one. The transducer is adjusted to the resonance frequency of the silica bar. The resonance sets birefringence in the transparent silica bar. Most commercial instruments operate at ~50 kHz and the modulator periodically generates phase retardation between the components parallel and perpendicular to its stress axis. It is to be noted that photo-elastic modulator only changes the polarization, but not the total photon flux. The circularly polarised light is transmitted through the sample, and depending on the chirality the molecule absorbs or transmits light as a function of polarization.

In the above process the molar circular dichroism is given by

$$\Delta\varepsilon = \varepsilon_L - \varepsilon_R \quad , \qquad (3.34)$$

where ε_L is the molar extinction co-efficient for left circularly polarized light and ε_R is that for right circularly polarized light. Thus, if the concentration of the sample is *C* and the path length is *l* then the difference in absorbance is

$$\Delta A = \Delta\varepsilon\, C\, l \qquad (3.35)$$

Circular dichroism generally expressed is terms of molar ellipticity which is expressed in terms of degree. After correcting for the concentration, molar ellipticity can be expressed as

$$[\theta] = 3298.2\ \Delta\varepsilon \qquad (3.36)$$

CD signal can be positive or negative depending on whether the left circularly polarized light is absorbed more than the right circularly polarized light or the opposite. CD spectra were measured using a *Chirascan* (Applied Photophysics) spectro-polarimeter, equipped with temperature controlled sample-bath.

3.2. Simulation Methods

3.2.1. Molecular Modelling

Molecular modelling is a method of building and mimicking molecules/molecular complexes *in silico.* In classical molecular modelling, atoms are treated as smallest unit. However, quantum chemistry approach considers the electrons and nucleus as building blocks. For the studies included in chapters 7 and 8, DAPI and Hoechst were docked into quadruplex DNA using molecular docking, followed by subsequent molecular dynamics (MD) simulations to find the dynamical behaviour of water, ions and DNA. This was done because there are no X-ray crystals or NMR structures available for these complexes. Finally, the simulation results were compared to the experimental TRFSS results to show how simulation and experiments can aid each other to unravel the intricate dynamical information in DNA. Brief descriptions of the docking and simulation methods are given below. The exact protocols of the simulation methods used for different systems are included in respective chapters.

3.2.1.1. Molecular Docking

Molecular docking is a procedure which predicts the binding modes and energetics of a ligand binding to a macromolecule.[32] The use of molecular docking is becoming immensely popular in the field of drug discovery because it can predict the binding mode and affinity of any ligand to a macromolecule in no time and at very low cost. In molecular docking methods, one searches for energetically favourable ligand-binding sites inside a macromolecule through non-bonded interactions.[33] It uses classical molecular mechanics force fields to find the stable ligand-macromolecule complexes. Among several docking programmes, AutoDock is popular one.[34-37]

AutoDock is a package of C programs employed to determine the interactions between macromolecules and small ligands (flexible).[34] Lamarckian genetic algorithm are used to search for conformational space in order to execute docking for energy computation utilizing method based on AMBER force field. Combining these two functions give rise to atomic coordinates framing the most probable docked conformation of ligand, which can be further used as starting point for molecular dynamics (MD) simulations.

AutoDock has two programs: (1) AutoDock that docks the ligand within a specified grid and (2) AutoGrid, which is used to calculate those grids for the ligand to dock on the macromolecule. AutoDock uses a variation on the AMBER-95 force field (Cornell *et al.*, 1995) with terms empirically determined by linear regression analysis from a set of protein-ligand complexes with known binding constants.[34] Free energy (Gibbs, ΔG) is represented by six pair-wise evaluations to model dispersion/repulsion, hydrogen bonding, electrostatic interactions, deviation from covalent geometry, internal ligand torsional constraints, and desolvation effects.[34,37]

$$\Delta G = \Delta G_{vdw} + \Delta G_{hbond} + \Delta G_{elec} + \Delta G_{conform} + \Delta G_{tor} + \Delta G_{sol} \qquad (3.37)$$

Initially, a three dimensional grid is generated around the target molecules upon which the ligand is to be docked. A probe atom is placed at each grid point and interaction energy is calculated. The interaction energy includes 12-6 Lennard Jones dispersion or repulsion term, 12-10 hydrogen bonding term, screened Coulomb electrostatic potential energy, and a term measuring the unfavourable entropy change due to restriction on the conformational degrees of freedom and lastly desolvation terms.[34,37] The interaction energy for ligand is calculated using values from the grid and partial charge on each atom. This interaction energy is adaptive to AMBER force field.

In AutoDock, the actual simulation is run where the ligand is placed according to the map of interaction calculated from the AutoGrid. During simulation in AutoDock, ligand is allowed to six degrees of freedom; rotational, translational and arbitrary number of torsional degrees of freedom.[34,35] Random perturbation is applied to each of the degrees of freedom and interaction energy is calculated for each new configuration. The new configuration is accepted or rejected depending on the annealing temperature of the system. Initially, the temperature of the entire system is high. The ligand explores almost entire area and almost all the conformations are accepted. As the temperature is decreased, unfavourable moves are increasingly discarded. Finally, the ligand finds the energetically most favourable position within the molecule. Through multiple simulations, reliable favourable binding conformation can be found.

The work presented in chapters 7 and 8 use AutoDock 4.2 software to dock ligand (DAPI or Hoechst) inside G-quadruplex DNA. Finally, the most stable and favourable docked conformation was used as starting structure of the ligand/DNA complex for running the MD simulations. Finally, MD simulation results are directly compared to the experimental TRFSS data.

3.2.1.2. Molecular Dynamics Simulation

Even though TRFSS experiments can provide direct information on the dynamics of complex systems in ultrafast time-scales, many times it becomes difficult to predict which component of the complex system is responsible for the overall dynamics of the system. MD simulation has been shown to complement the TRFSS results by providing deeper understanding of the complex systems in terms of their dynamics.[38-41] With the advent of super-computers, high performance parallel computing and smart programmes, MD simulation has now become a powerful tool for studying bio-macromolecules *in silico*. MD simulation not only predicts the structural behaviour of a complex system at atomic resolution, but also provides the temporal behaviour of the molecular system at femtosecond time-resolution.

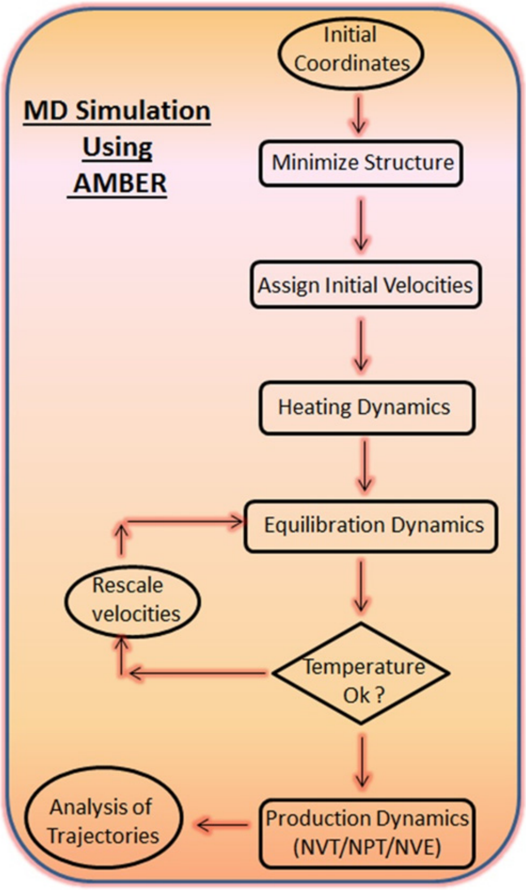

Figure 3.10: Flowchart of MD Simulation.

In order to perform MD simulation on macromolecules, one generally starts with X-ray crystal structure or solution NMR structure as initial co-ordinates whose time-dependent dynamics is studied under the influence of a classical force-field. However, in many cases the X-ray or NMR structures of ligand-macromolecule complexes may not be available. In such a scenario, the molecular docking method helps to construct the initial co-ordinates of the complex to run MD simulation on it. If the structure is not available from experiments, the ligand is first docked on a macromolecule considering all non-bonded interactions among the ligand and macromolecule. Finally, the most stable structure of the complex is taken as the initial structure for MD simulation run. Several simulation packages such as AMBER, CHARMM, GROMACS, NAMD, etc., are available to simulate biomolecules, out of which AMBER simulation package is widely used for DNA simulation, whereas GROMACS is used for simulating lipid bilayers – so as to obtain intricate structural and dynamical properties of these systems. The studies included in the Part-I of the thesis employ AMBER-12 or AMBER-14 for simulating DNA/ligand complex. GROMACS is explored in the study of depth-dependent hydration and polarity at lipid bilayer interfaces in Part-II of the thesis. A typical flowchart used for running MD simulation in AMBER and GROMACS simulation packages are presented in Figure 3.10 and Figure 3.11.

With advancement of new algorithms, improved parameterization and development of new hardware platforms, MD simulations have been demanded for more complexity,

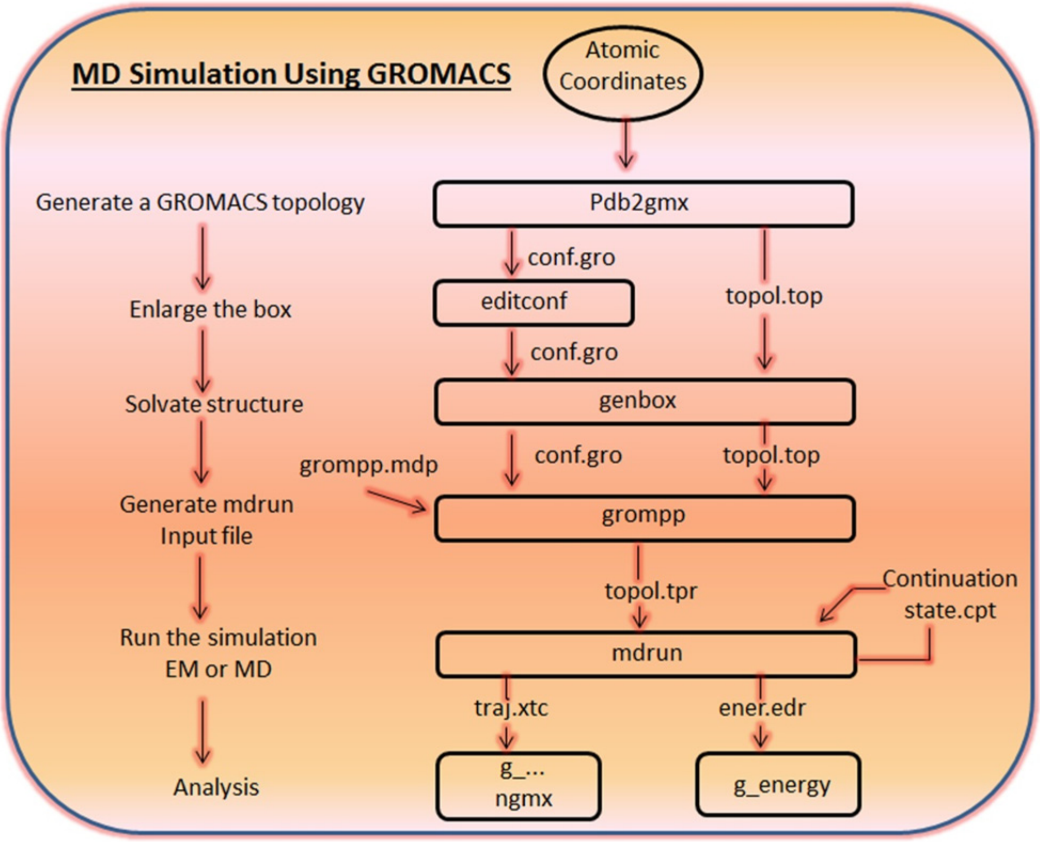

Figure 3.11: Flowchart of MD Simulation using GROMACS simulation packages.

size and length of simulating systems, which are often difficult to produce in old-style CPU based computation. Graphics processing units (GPUs), in particular, have originated as efficient, cost-effective and compelling alternatives to traditional CPUs for scientific computation of large atomic systems with much extended time of simulations (Figure 3.12).[42-45] Supercomputers of latest generation are now GPU enabled in such a way that if programmed accurately, software processing on GPUs can incomparably outperform jobs that are running on CPUs. NVIDIA in 2007 turn up with the first GPUs that have features especially designed for scientific computation. A numbers of MD simulation packages that are designed for simulating biological system in their condensed phase, such as NAMD,[46-47] AMBER,[48-49] GROMACS,[50-51] CHARM[52] and OpenMM,[53] have now been efficiently ported with new codes to run on GPUs. Performance of GPU accelerated simulation packages using graphics card exceeds the performance of all CPU-based supercomputers and clusters. GPU cards are targeted at algorithms that offer extensive single and double precision floating points calculations, which have eventually been tuned very efficiently to fixed precision calculations for improved performance of different hardware designs without compromising the integrity of underlying mathematics.[54] Three most extensively used statistical mechanical ensembles (NVE, NVT and NPT) as well as particle mesh Ewald for treating long-range electrostatic interactions accurately are supported by GPU

Figure 3.12: GPU accelerators for workstations.

accelerated MD simulations in said packages using graphics cards, which provide results that are statistically identical to the results generated by software ported to run on CPUs.[54,55] In chapter 10, GROMACS simulation package is used on GPU card (Tesla K-20) to simulate the ligand/lipid bilayer systems.

3.2.1.3. Analysis of MD Trajectories: Electrostatic Interaction Energy and Solvation Correlation Function

Analysis of MD trajectories can provide several structural and dynamical information, e.g. root mean square deviation (RMSD), kinetic and potential energy, electrostatic interaction energy, etc. The work presented in the Part-I of this thesis deals with the correlation function calculation of electrostatic interaction energy of ligand with DNA and surrounding water and ions. In the present scenario, different models have been developed to calculate the long range electrostatic interaction potential energy. In MD trajectories, either the electric field interactions or the electrostatic interaction energy of a probe with its surrounding charged/dipolar molecules is calculated. Several methodologies are proposed towards this end, especially for DNA simulation. In one procedure, the components of electric field ($\boldsymbol{E}$) from the surrounding molecules along the direction of change in dipole moment ($\boldsymbol{\delta\mu}$) of the probe from its ground to excited state is calculated as,[41]

$$E(t) = \boldsymbol{E} \bullet \boldsymbol{\delta\mu} \qquad (3.38)$$

Under this assumption, the fluorescence frequency shift $\omega(t)$ with time in TRFSS experiment can be expressed as,[41]

$$\omega(t) = \omega_0 - \boldsymbol{E} \bullet \boldsymbol{\delta\mu} / \hbar \qquad (3.39)$$

In other procedure, the simple calculation of electrostatic interaction energy is performed as pairwise Coulomb interactions between point charges as,[38,40]

$$E(t) = \left(\sum_{i=1}^{N_{probe}} q_i^{g/e} \sum_{j=1}^{N_{solvent}} q_j\right)/r \qquad (3.40a)$$

or

$$E(t) = \left(\sum_{i=1}^{N_{probe}} \Delta q_i \sum_{j=1}^{N_{solvent}} q_j\right)/r \qquad (3.40b)$$

In equation 3.40a, one considers interactions of either ground (*g*) or excited (*e*) state atomic charges of the probe with surrounding solvent atomic charges; however, it is also proposed that the interactions of partial charge difference, Δq (i.e., $q_{excited} - q_{ground}$) of the probe with surrounding solvent charges can also be calculated (equation 3.40b).

The treatment of electrostatic energy, however, may influence the time dependent response calculated from MD simulation. Accurate calculation of the electrostatic potential energy of a periodic system concerns the sum of Coulomb energy of every atom along with energy of the periodic image, and this costs huge computational memory. This limitation can be overcome by introducing a spherical cut-off which prunes the system. This strategy is not straight forward and brings some additional complicacies. Firstly, the cut-off incorporates discontinuity in electrostatic force and potential. Both the potential energy, and hence the force drop to zero immediately after the cut-off. More importantly, the cut-off rules out the possibility of convergence of the electrostatic energy function. To overcome this problem, several methods have been developed but particle mesh Ewald (PME) sum method is more accepted and accurate one.[56] Ewald sum divides the electrostatic sum into two convergent parts; one is the sum within the cut-off in real space and another is the long-range sum in reciprocal space. The setback with PME is that it is impossible to decompose the total response into individual components, which is needful in order to clarify the existing controversy in the field of ultrafast DNA solvation dynamics. Fennell and Gezelter came up with an alternate method, called damped shift force (DSF) method.[57-59] DSF method is a variation of simple pair-wise Coulomb method and originates from the method proposed by Wolf *et al.* where the Coulombic sum is damped over distance and cutoff-neutralized.[57] DSF method makes both the Coulomb force and potential energy smoothly to zero at the cut-off boundary, thereby eliminating the discontinuities. Another advantage of DSF is that there is absolutely no need to calculate the energies of the periodic images, thus decreases the computational cost. The straightforward pair-wise calculation eliminates the limitation of decomposition of individual contributions. Using DSF, time dependent electrostatic energy, *E*, can be calculated as,[59]

$$E(t) = \sum_{i=1}^{N_{probe}} q_i^{g/e} \sum_{j=1}^{N_{solvent}} q_j \left[\frac{erfc(\alpha r)}{r} - \frac{erfc(\alpha R_c)}{R_c} + \left(\frac{erfc(\alpha R_c)}{R_c^2} + \frac{2\alpha}{\sqrt{\pi}}\frac{exp(-\alpha^2 R_c^2)}{R_c}\right)(r - R_c)\right] \qquad (3.41a)$$

or

$$E(t) = \sum_{i=1}^{N_{probe}} \Delta q_i \sum_{j=1}^{N_{solvent}} q_j \left[\frac{erfc(\alpha r)}{r} - \frac{erfc(\alpha R_c)}{R_c} + \left(\frac{erfc(\alpha R_c)}{R_c^2} + \frac{2\alpha}{\sqrt{\pi}}\frac{exp(-\alpha^2 R_c^2)}{R_c}\right)(r - R_c)\right] \qquad (3.41b)$$

where interactions of either ground (*g*) or excited (*e*) state atomic charges of the probe with surrounding charged/dipolar species (equation 3.38a), or the interactions of partial charge difference, Δq (i.e., $q_{excited} - q_{ground}$) of probe with surrounding species (equation 3.38b) are calculated. Finally, time-correlation functions of electrostatic energy-energy fluctuations are generated as,[61]

$$C_S(t) = \frac{\langle \delta E(0)\delta E(t)\rangle_{g/e}}{\langle \delta E(0)^2\rangle_{g/e}} \tag{3.42}$$

where $\delta E = E(t) - <E>$ is the fluctuation of the electrostatic energy of the probe. Subscripts, *g* and *e* represent the time-correlation functions in ground and excited states, respectively.

Furse and Corcelli, through proper checking, suggested that DSF not only shows good agreement with the reference PME method, but also it is computationally advantageous.[40,60] Thus, in analysis of MD trajectories in Part-I, electrostatic interactions energies were calculated using DSF method (equation 3.38).

Under linear response theory, non-equilibrium experimental solvation correlation function, $C_E(t)$, becomes equivalent to the simulated solvation correlation function, $C_S(t)$ as,

$$C_E(t) = \frac{E(t)-E(\infty)}{E(0)-E(\infty)} \equiv C_s(t) \tag{3.43}$$

where $E(0)$ and $E(t)$ are the solute-solvent interaction energy at time $t = 0$ and t, respectively and $E(\infty)$ is that at $t = \infty$, i.e., when the relaxation dynamics has completed.

The elucidation of the long-time dynamics in biomolecules like DNA and protein remain the central concern in experiment as well as simulation. MD simulation is exercised as a powerful tool to disentangle the cross-correlation between individual components with the aim to construct a clear molecular picture. The method of decomposition is based on the fact that the total response is the sum of the response coming from all the individual components in the system. Hence, if there is *n* number of components in the system then one can write,

$$E = \sum_n E_n(t) \tag{3.44}$$

The first strategy of decomposition was used by Bagchi and co-workers, where the equilibrium correlation function is decomposed in terms of auto-correlations and the cross-correlations of the response of individual components (water, ion and biomolecule).[38] Hence, if there are three components present in the system then there will be three auto-correlations and three cross-correlations.

$$C_S(t) = \sum_m \sum_n \frac{\langle \delta E_m(0)\delta E_n(t)\rangle}{C(0)} \tag{3.45}$$

or

$$C_S(t) = \sum_m \sum_n C_{mn}(t) \qquad (3.46)$$

The second method of decomposition is based on generalised fluctuation-dissipation theorem. On the basis of this theorem, Nilsson and Halle applied linear response approximation to decompose the total response according to equation 3.44.[39]

$$C_S(t) = \sum_n \frac{\langle \delta E_n(t) \delta E(0) \rangle}{C(0)} \qquad (3.47)$$

The decomposition method was applied to investigate the solvation dynamics of tryptophan in protein monellin observed experimentally.[63] The decomposition of the total response into protein and water revealed that protein is responsible for the slow relaxation. This same decomposition method (Linear Response Decomposition or LRD) was applied by Corcelli *et al.* in Hoechst/DNA system.[40]

The third method of decomposition was developed by Sen *et al.* Unique polarization model was proposed based on the concept that one component in the system induces linear polarization on others thus creating the cross-correlation.[41] Sen *et al.* calculated electric field on central Adenine of Dickerson dodecamer. The total field from individual component was written as sum of the intrinsic component (E_W, E_D,E_I) and the polarization due to other component (E_w, E_d,E_i) (eq. 3.43).[41]

$$\begin{aligned} E_W &= E_w + x_{wd}E_d + x_{wi}E_i \\ E_D &= (1 - x_{wd})(E_d + x_{di}E_i) \qquad (3.48) \\ E_I &= (1 - x_{wi} - x_{di} + x_{wd}x_{di})E_i \end{aligned}$$

where, χ_{pq} is the susceptibility representing the fraction of the electric field E_p induced by E_q. By carefully choosing the values of susceptibilities, the cross-correlations are made zero for the entire time range, from 40 fs to 40 ns.[41] The total correlation successfully reproduced the power-law dynamics seen in experiment with Coumarin102-DNA system.[64] After the cross-correlations are made zero, it was unravelled that water is responsible for the long power-law dynamics seen both in experiment and simulation.[41,64]

Despite being mathematically correct, LRD and polarization model have intrinsic differences on explaining the component's dynamics in DNA/ligand systems. Both, LRD and polarization model have been employed to decompose the total correlation function and validate experimental finding. In this thesis, both direct decomposition and LRD methods are used (in Part-I of the thesis) to calculate the auto- and cross-correlations of individual component as well as to decompose the component's contributions to the total dynamics in DNA/ligand systems, respectively. The details of application of these methods are included in respective chapters.

Reference

1. Tataurov, A. V.; You, Y.; Owczarzy, R. Predicting Ultraviolet Spectrum of Single Stranded and Double Stranded Deoxyribonucleic Acids. *Biophys. Chem*. **2008**, *133*, 66-70.
2. http://biophysics.idtdna.com.
3. Lakowicz, J. R. *Principles of Fluorescence Spectroscopy*, 3rd Edition, Springer, USA, **2000**.
4. Velapoldi, R. A.; Mielenz, K. D. *Standard Reference Materials: A Fluorescence Standard Reference Material: Quinine Sulfate Dihydrate*; U.S. Government Printing Office, Wasington, D.C., 1980; Nat. Bur. Stand. (U.S.), Spec. Publ. 260 – 264.
5. O' Connnor, D. V. O.; Phillips, D. *Time Correlated Single Photon Counting*, Academic Press: New York, USA, **1984**.
6. Becker, W. *Advanced Time-Correlated Single Photon Counting Techniques*, Springer, USA, **2005**.
7. Turro, N. J. *Modern Molecular Photochemistry,* University Science Books, CA, USA, **1991**.
8. O'Connor, D. V.; Ware, W. R.; Andre, J. C. Deconvolution of Fluorescence Decay Curves. A Critical Comparison of Techniques *J. Phys. Chem.* **1979**, *83*, 1333–1343.
9. Bevington, P. R. *Data Reduction and error Analysis for the Physical Sciences*, McGraw-Hill, New York, USA, **1969**.
10. Boyd, R. W. *Nonlinear Optics*, Third Edition, Academic Press, Elsevier, USA, **2008**.
11. Kahlow, M. A.; Jarzba, W.; DuBruil, T. P.; Barbara, P. F. Ultrafast Emission Spectroscopy in the Ultraviolet by Time-Gated Upconversion *Rev. Sci. Instrum.* **1988**, *59*, 1098.
12. Shah, J. Ultrafast Luminescence Spectroscopy Using Sum Frequency Generation. *IEEE J. Quant. Electron.* **1988**, *24*, 276-288.
13. Mahr, H.; Hirsch, M. D. An Optical Up-conversion Light Gate with Picosecond Resolution. *Opt. Comm*. **1975**, *13*, 96–99.
14. Schanz, R.; Kovalenko, S. A.; Kharlanov, V.; Ernsting, N. P. Broad-Band Fluorescence Upconversion for Femtosecond Spectroscopy. *Appl. Phys. Lett*. **2001**, *79*, 566–568.
15. Zhang, X. X.; Würth, C.; Zhao, L.; Resch-Genger, U.; Ernsting, N. P. Femtosecond Broadband Fluorescence Upconversion Spectroscopy: Improved Setup and Photometric Correction. *Rev. Sci. Instrum.* **2011**, *82*, 063108.
16. Midwinter, J. E.; Warner, J. The Effects of Phase Matching Method and of Uniaxial Crystal Symmetry on the Polar Distribution of Second-Order Non-Linear Optical Polarization. *Brit. J. Appl. Phys.* **1995**, *16*, 1135-1142.
17. Yasuda, R.; Harvey, C. D.; Zhong, H.; Sobczyk, A.; Aelst, L. Van; Svoboda, K. Supersensitive Ras Activation in Dendrites and Spines Revealed by Two-Photon Fluorescence Lifetime Imaging. *Nature Neuroscience* **2006**, *9*, 283-291.
18. Maroncelli, M.; Fleming, G. R. Picosecond Solvation dynamics of Coumarin 153: The Importance of Molecular Aspects of Solvation. *J. Chem. Phys.* **1987**, *86*, 622–6239.
19. Somoza, M. M.; Andreatta, D.; Murphy, C. J.; Coleman, R. S.; Berg, M. A. Effect of Lesions on the Dynamics of DNA on the Picosecond and Nanosecond Timescales using a Polarity Sensitive Probe. *Nucleic Acids Res*. **2004**, *32*, 2494–2507.
20. Koti, A. S. R.; Krishna, M. M. G.; Periasamy, N. Time-Resolved Area-Normalized Emission Spectroscopy (TRANES): A Novel Method for Confirming Emission from Two Excited States. *J. Phys. Chem. A* **2001**, *105*, 1767–1771.
21. Koti, A. S. R.; Periasamy, N. Application of Time Resolved Area Normalized Emission Spectroscopy to Multicomponent Systems. *J. Chem. Phys*. **2001**, *115*, 7094–7099.
22. Ware, W. R.; Chow, P.; Lee, S. K. Time-Resolved Nanosecond Emission Spectroscopy: Spectral Shift Due to Solvent-Solute Relaxation. *Chem. Phys. Lett.* **1968**, *2*, 356–358.
23. Fee, R. S.; Maroncelli, M. Estimating the Time-Zero Spectrum in Time-Resolved Emmsion Measurements of Solvation Dynamics. *J. Chem. Phys*. **1994**, *183*, 235–247.
24. Jha, A.; Ishii, K.; Udgaonkar, J. B.; Tahara, T.; Krishnamoorthy, G. Exploration of the Correlation Between Solvation Dynamics and Internal Dynamics of a Protein. *Biochemistry* **2011**, *50*, 397–408.
25. Singh, T. S.; Rao, B. J.; Krishnamoorthy, G. GTP Binding Leads to Narrowing of the Conformer Population While Preserving the Structure of the RNA Aptamer: A Site-Specific Time-Resolved Fluorescence Dynamics Study. *Biochemistry* **2012**, *51*, 9260–9269.
26. Jha, A.; Narayan, S.; Udgaonkar, J. B; Krishnamoorthy, G. Solvent-Induced Tuning of Internal Structure in a Protein Amyloid Protofibril. *Biophys. J.* **2012**, *103*, 797–806.

27. Verma, S. D.; Pal, N.; Singh, M. K.; Shweta, H. Khan, M. F.; Sen, S. Understanding Ligand Interaction with Different Structures of G-Quadruplex DNA: Evidence of Kinetically Controlled Ligand Binding and Binding-Mode Assisted Quadruplex Structure Alteration. *Anal. Chem.* **2012**, *84*, 7218–7226.
28. Kelly, S. M.; Jess, T. J.; Price, N. C. How to Study Proteins by Circular Dichroism. *Biochimica et Biophysica Acta* **2005**, *1751*, 119–139.
29. Kypr, J.; Kejnovská, I.; Renčiuk, D.; Vorlíčková, M. Circular Dichroism and Conformational Polymorphism of DNA. *Nucleic Acids Res*. **2009**, *37,* 1713–1725.
30. Fasman, G. D. *Circular Dichroism and the Conformational Analysis of Biomolecules*, Springer, USA, **1996**.
31. Eliel, E. L.; Wilen, S. H. *Stereochemistry of Organic Compounds,* Wiley-India Edition, **2008**.
32. Bikadi, Z.; Hazai, E. Application of the PM6 Semi-Empirical Method to Modeling Proteins Enhances Docking Accuracy of AutoDock. *J. Cheminformatics* **2009**, *1*, 15.
33. Halperin, I.; Ma, B.; Wolfson, H.; Nussinov, R. Principles of Docking: An Overviewof Search Algorithms and A Guide to Scoring Functions. *Protein: Struct. Funct. Genet.* **2002**, *47*, 409–443.
34. Morris, G. M.; Goodsell, D. S.; Halliday, R. S.; Huey, R.; Hart, W. E.; Belew, R. K.; Olson, A. J. Automated Docking Using a Lamarckian Genetic Algorithm and an Empirical Binding Free Energy Function *J. Comput. Chem.* **1998**, *19*, 1639–1662.
35. Goodsell, D. S.; Morris, G. M.; Olson, A. J. Automated Docking of Flexible Ligands: Applications of AutoDock. *J. Mol. Recognit*. **1996**, *9*, 1-5.
36. Sousa, S. F.; Fernandes, P. A.; Ramos, M. J. Protein-Ligand Docking: Current Status and Future Challenges. *Protein: Struct. Funct. and Genet.* **2006**, *65*, 15–26.
37. Dhamodharan, V.; Harikrishna, S.; Jagadeeswaran, C.; Halder, K.; Pradeepkumar, P. I. Selective G-Quadruplex DNA Stabilizing Agents Based on Bisquinolinium and Bispyridinium Derivatives of 1,8-Naphthyridine. *J. Org. Chem*. **2012**, *77*, 229–242.
38. Pal, S.; Maiti, P. K.; Bagchi, B.; Hynes, J. T. Multiple Time Scales in Solvation Dynamics of DNA in Aqueous Solution: The Role of Water, Counterions, and Cross-Correlations. *J. Phys. Chem. B* **2006**, *110*, 26396–26402.
39. Nilsson, L.; Halle, B. Molecular Origin of Time-Dependent Fluorescence Shifts in Proteins. *Proc. Nat. Acad. Sci. USA* **2005**, *102*, 13867–13872.
40. Furse, K. E.; Corcelli, S. A. The Dynamics of Water at DNA Interfaces: Computational Studies of Hoechst 33258 Bound to DNA. *J. Am. Chem. Soc.* **2008**, *130*, 13103–13109.
41. Sen, S.; Andreatta, D.; Ponomarev, S. Y.; Beveridge, D. L.; Berg, M. A. Dynamics of Water and Ions Near DNA: Comparison of Simulation to Time-Resolved Stokes-Shift Experiments. *J. Am. Chem. Soc.* **2009**, *131*, 1724–1735.
42. Harvey, M. J.; De Fabritiis, G. A. Survey of Computational Molecular Science Using Graphics Processing Units. *WIREs Comput. Mol. Sci*. 2012, 2, 734-742
43. Garland, M.; Le Grand, S.; Nickolls, J.; Anderson, J.; Hardwick, J.; Morton, S.; Phillips, E.; Zhang, Y.; Volkov, V. Parallel Computing Experiences With CUDA. *IEEE Micro*. **2008**, *28*, 13-27.
44. Preis, T. GPU-Computing in Econophysics and Statistical Physics. *Eur. Phys. J. Spec. Top.* **2011**, *194*, 87-119.
45. Pratx, G.; Lei, X. GPU Computing in Medical Physics: A Review. *Med. Phys*. **2011**, *38*, 2685-2697.
46. Phillips, J. C.; Braun, R.; Wang, W.; Gumbart, J.; Tajkhorshid, E.; Villa, E.; Chipot, C.; Skeel, R. D.; Kale, L.; Schulten, K. Scalable Molecular Dynamics with NAMD. *J. Comput. Chem.* **2005**, *26*, 1781-1802.
47. Stone, J. E.; Phillips, J. C.; Freddolino, P. L.; Hardy, D. J.; Trabuco, L. G.; Schulten, K. Accelerating Molecular Modeling Applications with Graphics Processors. *J. Comput. Chem.* **2007**, *28*, 2618-2640.
48. Case, D.; et al. *AMBER 12*, University of California, San Francisco, **2012**.
49. Salomon-Ferrer, R.; Case, D. A.; Walker, R. C. An Overview of the Amber Biomolecular Simulation Package. *WIREs Comput. Mol. Sci*. **2013**, *3*, 198-210.
50. Van Der Spoel, D.; Lindahl, E.; Hess, B.; Groenhof, G.; Mark, A. E.; Berendsen, H. J. C. GROMACS: Fast, Flexible, and Free. *J. Comput. Chem*. **2005**, *26*, 1701-1718.
51. Hess, B.; Kutzner, C.; van der Spoel, D.; Lindahl, E. GROMACS 4: Algorithms for Highly Efficient, Load-Balanced, and Scalable Molecular Simulation. *J. Chem.Theory Comput*. **2008**, *4*, 435-447.

52. Brooks, B. R.; et al. CHARMM: The Biomolecular Simulation Program. *J. Comput. Chem.* **2009**, *30*, 1545-1615.
53. Eastman, P.; et al. OpenMM 4: A Reusable, Extensible, Hardware Independent Library for High Performance Molecular Simulation. *J. Chem. Theory Comput.* **2013**, *9*, 461-469.
54. Ferrer, R. S.; Götz, A. W.; Poole, D.; Le Grand, S.; Walker, R. Routine Microsecond Molecular Dynamics Simulations with AMBER on GPUs. 2. Explicit Solvent Particle Mesh Ewald. *J. Chem. Theory Comput*. **2013**, *9*, 3878-3888.
55. Götz, A. W.; et. al. Routine Microsecond Molecular Dynamics Simulations with AMBER on GPUs. 1. Generalized Born. *J. Chem.Theory Comput.* **2012**, *8*, 1542-1555.
56. Darden, T.; York, D.; Pedersen, L. Particle Mesh Ewald: An N·log(N) Method for Ewald Sums in Large Systems. *J. Chem. Phys.* **1993**, *98*, 10089–10092.
57. Wolf, D.; Keblinski, P.; Phillpot, S. R.; Eggebrecht, J. Exact Method for the Simulation of Coulombic Systems by Spherically Truncated, Pairwise r^{-1} Summation. *J. Chem. Phys.* **1999**, *110*, 8254–8282.
58. Zahn, D.; Schilling, B.; Kast, S. M. Enhancement of the Wolf Damped Coulomb Potential: Static, Dynamic, and Dielectric Properties of Liquid Water from Molecular Simulation. *J. Chem. Phys. B* **2002**, *106*, 10725–10732.
59. Fennell, C. J.; Gezelter, J. D. Is the Ewald summation still necessary? Pairwise Alternatives to the Accepted Standard for Long-Range Electrostatics. *J. Chem. Phys.* **2006**, *124*, 234104.
60. Furse, K. E.; Corcelli, S. A. Effects of Long-Range Electrostatics on Time-Dependent Stokes Shift Calculations. *J. Chem. Theory Comput.* **2009**, *5*, 1959–1967.
61. Carter, E. A.; Hynes, J. T. Solvation Dynamics for an Ion Pair in a Polar Solvent: Time-Dependent Fluorescence and Photochemical Charge Transfer. *J. Chem. Phys.* **1991**, *94*, 5961–5979.
62. Pal, S. K.; Zhao, L.; Xia, T.; Zewail, A. H. Site- and Sequence-Selective Ultrafast Hydration of DNA. *Proc. Natl. Acad. Sci. USA* **2003**, *100*, 13746–13751.
63. Peon, J.; Pal, S. K.; Zewail, A. H. Hydration at the Surface of the Protein Monellin: Dynamics with Femtosecond Resolution. *Proc. Natl. Acad. Sci. USA* **2002**, *99*, 10964–10969.
64. Andreatta, D.; Pérez Lustres, J. L.; Kovalenko, S. A.; Ernsting, N. P.; Murphy, C. J.; Coleman, R. S.; Berg, M. A. Power-Law Solvation Dynamics in DNA over Six Decades in Time. *J. Am. Chem. Soc.* **2005**, *127*, 7270–7271.

Chapter 4

New Insight of Solvation Dynamics in DNA: Hoechst in A_nT_n-Rich Minor Groove of DNA

This chapter will highlight the current understanding of DNA solvation/hydration and the controversies associated with it. The results presented in this chapter will shed new light on the understanding of solvation dynamics in minor groove of DNA, probed by a popular minor grove binder, Hoechst 33258. The results will try to explain most of the existing (debated) views on DNA solvation dynamics. The direct comparison of results of several new and old time-resolved fluorescence Stokes shifts experiments with the results of extended MD simulations, performed here, will convince that solvation dynamics in minor groove of DNA is much more complex than that thought earlier. Results will show that there are very slow water molecules in the vicinity of groove-binder, which play vital role in the dispersed (power-law) solvation dynamics in DNA minor groove; although, such slow water dynamics is dependent on the length of A_nT_n sequence that create the minor groove of DNA.

4.1. Introduction

The fact that water molecules (and ions) do not act as mere spectators for biomolecules – but maintain the structure and function of biomolecules – is now well established.[1-3] The dynamics of water and ions in-and-around biomolecules such as proteins and nucleic acids actually facilitate several important biochemical processes ranging from enzyme catalysis,[4] protein folding[5,6] and protein activity,[7,8] to the interactions of DNA with proteins[9,10] and drugs (ligands).[11,12] Hence, understanding structure and function of biomolecules remains incomplete if the effects of water and ion dynamics on the biomolecular dynamics are neglected. In fact, this chapter highlights that dynamics of water is crucial for solvation of minor groove binders inside DNA. Thus, understanding the dynamics of water and ions near Watson-Crick duplex-DNA remains a major research field for last two decades or so.

Proteins and DNA are different in many ways, but their underlying dynamical features remain similar; although, it has been shown in several recent time-resolved fluorescence experiments and simulation studies that the dynamics in DNA is rather dispersed owing to the fact that there lies strong electrostatic coupling among the negatively charged DNA, positively charged counterions and dipolar water molecules.[22-28,34,36] Considerable efforts have gone into understanding the dynamics in proteins and DNA through experiments,[13-30] theory[31,32] and computer simulations.[27,33-51] The overall dynamics in these biomolecules is found to extend in times >10 ps,[52-55] while dynamics in simple water complete within few picoseconds.[56] More importantly, it has been shown that dynamics of electrostatic interaction energy in DNA is highly non-exponential and dispersed which extend over several decades in time following mostly power-law type relaxations.[22-28,34,36] The explanation of such dispersed (solvation) dynamics in DNA remains elusive, thus, the interpretations are debated strongly, primarily because of its very origin from intricate coupling between the motions of charged/dipolar components in DNA solution (i.e., water, ions and DNA).[22-28,34,36] In fact, question remains whether it is the independent dynamics of water or ions or DNA or it is the inextricable coupled motions of these components which control the solvation dynamics in DNA. These perturbed hydration-shells and counterions participate in the interactions of DNA with proteins and drugs (ligands).[11,57-59] Hence, understanding and quantifying the dynamics of water and ion solvation near DNA is of primary importance to elucidate the complex molecular recognitions involving DNA.

As discussed in chapter 2, time-resolved fluorescence Stokes shift (TRFSS) and related experiments have the capability to measure dynamics of complex molecular systems in sub-picoseconds to nanoseconds time-scales, hence TRFSS experiments have been widely used to study solvation dynamics in DNA.[17-30] Although such TRFSS experiments capture the overall solvation response in DNA near a probe-site, the full interpretation of TRFSS results is not possible from only experiments.[33-42] Molecular dynamics (MD) simulations provide a direct route to interpret TRFSS data and quantify the dynamics of water and ions near biomolecules.[27,33-38,41] Several such simulation studies have been performed to unveil the complex dynamics in DNA.[27,33-42] However, comparisons of MD simulations to TRFSS results of DNA solvation dynamics have so far been reported only in few studies.[27,33-38] Nevertheless, these studies showed the routes to explore such comparisons of simulations to experiments, and provided important information about the nature of solvation in DNA grooves, but with debated views.[27,33-38]

TRFSS studies with probes placed inside duplex-DNA either by covalent attachment to sugar as *base-stacked* (replacing a base/base-pair) or by minor *groove-binding* fluorophores have provided important information about DNA solvation dynamics from sub-picoseconds to nanosecond time-scales.[17-30] Berg and co-workers were the first to measure the TRFSS of a covalently attached *base-stacked* coumarin-102 (placed opposite an abasic-site) in DNA double helix of generic sequence, and showed that DNA dynamics extend into nanosecond time-scales.[17] Subsequently, Zewail and co-workers reported TRFSS of a base-stacked probe (2-aminopurine) and a (minor) groove-bound probe (Hoechst 22358) to show that both probes sense similar dynamics inside duplex-DNA till 100 ps.[18,19] Ernsting and co-workers reported high-accuracy time-resolved stimulated emission shifts of base-stacked probe (HNF) till 25 ps and showed that water plays important role in controlling the local dynamics inside duplex-DNA.[20] On the other hand, Pal and co-workers reported nanosecond dynamics in duplex-DNA using groove-bound probes, Hoechst and DAPI.[21] However, combining Stokes shift data from different techniques over broad time-range, Berg and co-workers showed that solvation dynamics in duplex-DNA actually follow a power-law decay (with exponent 0.15) from 40 fs to 40 ns.[22,23] Recently, Sen and co-workers also showed that TRFSS of groove-bound DAPI inside duplex-DNA follow similar power-law till ~100 ps, but beyond this time the dynamics converge rapidly to equilibrium near 10 ns.[24]

Much of the current understanding of complex solvation response in DNA came from MD simulation studies.[27,33-41] Simulations have been used to study water and ion distributions in-and-around DNA.[27,33-41] Dynamics of water and counterions around duplex-DNA have also been characterized in terms of diffusion coefficients,[39] hydrogen-bond dynamics,[40] orientational relaxation,[40] H-bond jump,[60] and ion-distribution convergence.[41] However, simulation studies on dynamics of solvation in DNA are limited.[27,33-41] In fact, the comparisons of simulations to TRFSS experiments in duplex-DNA have so far been reported only by Hynes-Bagchi and co-workers,[33] Furse and Corcelli,[35-37] Berg and co-workers,[34] and Sen and co-workers.[27] Hynes-Bagchi and co-workers simulated native duplex-DNA[33] and compared their simulation results to experiments of Zewail and co-workers on base-stacked 2-AP and groove-bound Hoechst.[18,19] They, for the first time, found that slow dynamics in DNA (till 250 ps) is mainly controlled by water and ion motions (strong cross-correlation among them); but their simulation was not long enough to capture the nanosecond dynamics.[33] Analysing 46 ns simulation trajectory, Sen *et al.* found excellent agreement between TRFSS results of base-stacked coumarin-102 and correlation of simulated electric-field fluctuations inside native duplex-DNA.[34] Through decomposition of contributions from individual components using a 'polarization model', this study also showed that water controls the power-law dynamics in duplex-DNA.[34] On the other hand, Furse and Corcelli simulated duplex-DNA with groove-bound Hoechst,[35] similar to experiment of Zewail and co-workers,[18] and saw that the slow dynamics (till 100 ps) is dominated by DNA motion, but not the water or ion motions – suggesting that most of slow water and ions are displaced by the groove-bound Hoechst.[35] When they extended their simulation upto 150 ns and compared the results to the simulated dynamics of duplex-DNA with coumarin/abasic pair,[36] similar as in experiments of Berg and co-workers,[22,23] they saw significant contribution from abasic-site flipping motions between intra- and extra-helical to the slow (power-law type) relaxation which is significantly different from the dynamics probed by groove-bound Hoechst.[36] Based on these simulation results, they proposed that DNA motions control the slow dispersed solvation dynamics in DNA, and not the water and ions.[36]

All these above observations raised several debated, but important, questions:

1. Is power-law solvation dynamics really a general feature in DNA?
2. How far dynamics probed by base-stacked (Coumarin) and groove-bound (Hoechst) really differ in experiment?

3. Can TRFSS experiments really capture the effect of abasic-site flipping motions on slow solvation dynamics in DNA as suggested by simulation?
4. Is there any base-sequence dependency of the solvation dynamics probed by minor groove-binder (mainly Hoechst)?
5. Can MD simulation capture such dispersed power-law relaxation in DNA, as seen in some experiments?
6. What is the origin of dispersed (power-law) dynamics in DNA?
7. Is there slow water present near a ligand bound inside the minor groove of DNA?

The present chapter (and also chapters 5 – 8) will shed new light on these issues and try to address the above questions. This chapter (and also chapter 7) will also show that there are slow water molecules in the vicinity of groove-binders in DNA which control dispersed power-law dynamics in DNA in nanosecond time scales; although, contributions of such (slow) water relaxations to the slow dynamics can vary depending on the length of A_nT_n sequence creating the minor groove of DNA. These studies will convincingly show that power-law dynamics is a general feature of DNA solvation dynamics.

In order to address above issues, TRFSS of minor groove-bound Hoechst in DNA of two different sequences (5'–CGC<u>AAATTTG</u>CG–3' and 5'–CGCG<u>AATTC</u>GCG–3') are measured using UPC and TCSPC setups covering a broad time-range of five decades from 100 fs to 10 ns. These TRFSS data are then compared to other existing experimental data on base-stacked coumarin[22,23] and those reported by Zewail *et al.*[18] and Pal *et al.*[21] on same DNA/Hoechst systems. TRFSS dynamics of Hoechst in minor groove containing central sequence of —AATTC— is found to be faster than that in the minor groove containing —AAATTTG—. Very long (equilibrium) MD simulations (total 1.2 μs) on these two DNA/Hoechst systems are performed here in the excited state of Hoechst – so as to calculate the simulated solvation correlation functions and compare them directly to the new TRFSS results of the same systems. For this, 3 different MD trajectories of 200 ns each are computed for each DNA/Hoechst system (total: 3 × 200 ns + 3 × 200 ns = 1.2 μs). Finally, these 3 trajectories (200 ns each) for every DNA/Hoechst system are averaged to obtain the final dynamics of electrostatic interaction energy fluctuations of excited-state Hoechst with all the surrounding entities, viz. DNA, water, Na^+ and Cl^-. Equilibrium MD simulation captures the essential features of the solvation dynamics (e.g., power-law type dispersed dynamics, faster relaxation in minor groove of —AATTC— compared to —AAATTTG—), similar as obtained in experimental TRFSS results. Direct comparison of TRFSS and simulated dynamics shows good agreement with similarity of (power-law) dynamics in the DNA/Hoechst systems. Linear response decomposition of total simulated response into individual components as well as auto- and cross-correlations of individual components reveals that (power-law) solvation response of Hoechst in the minor groove of —AAATTTG— is dominated by DNA motions, similar as found earlier by Furse and Corcelli;[35] however, the same Hoechst response in the minor groove created by —

AATTC— is dominated by slow (power-law type) water relaxation, leading to overall faster solvation response in the minor groove of —AATTC— compared to that of —AAATTTG—. Analysis of minor groove-widths suggests that the differences in the local groove-width fluctuations in the two DNA systems possibly control the relative contributions of water and DNA to dictate the overall slow solvation response of groove-bound Hoechst in DNA. Contributions from ion motions are found to be negligible in both DNA/Hoechst systems. These results indeed show for the first time that local DNA dynamics is dependent on the minor groove A_nT_n rich sequence which dictates the slow water or slow DNA motions to define the overall solvation dynamics in the minor grooves of duplex-DNA depending on the lengths of A_nT_n sequence.

4.2. Methods

4.2.1. Experimental Methods

DNA minor groove binder, Hoechst 33258 (2′-(4-hydroxyphenyl)-5-(4-methyl-1-piperazinyl)-2,5′-bi(1H-benzimidazole) trihydrochloride hydrate) was purchased from Sigma-Aldrich, and was used without further purification (see Figure 2.7 in chapter 2). Self-complimentary (12-mer) DNA oligonucleotides of sequences, 5'–CGCAAATTTGCG–3' and 5'–CGCGAATTCGCG–3', respectively, were from Integrated DNA Technologies. B-form DNA duplexes were prepared by re-suspending single-stranded oligonucleotides in buffer of 100 mM sodium phosphate with 50 mM NaCl of pH 7, and annealing them from 95°C to room temperature (25°C) over ~5 hours. Formation of double-stranded B-DNA was confirmed by circular dichroism (CD) spectra (Figure 4.1). Spectra show characteristic negative peak ~255 nm confirming formation of right handed B-DNA. All samples were prepared in HPLC grade water (Merck). All experiments were performed with concentration ratios of [Hoechst]/[DNA] of 1:5 where Hoechst fluorescence reach saturation such that nearly all Hoechst molecules remain bound to the DNA. Fluorescence decays were measured at magic angle using TCSPC and UPC (see chapter 3 for details). UPC measurements were carried out at concentrations; [Hoechst] = 40 µM and [DNA] = 200 µM. TCSPC measurements were carried out with samples of concentrations, [Hoechst] = 5 µM and [DNA] = 25 µM. Time-zero fluorescence spectra of the samples were

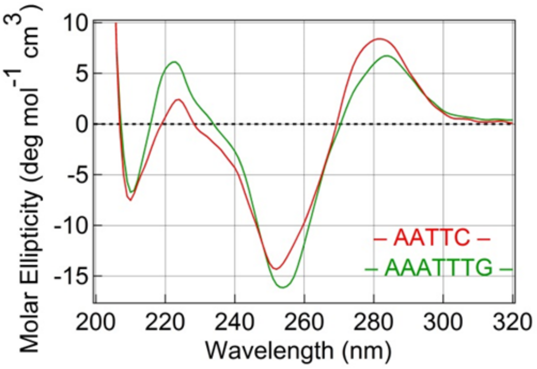

Figure 4.1: Circular dichroism (CD) spectra of 12-mer DNA (15 mM) of sequences: 5'–CGCAAATTTGCG–3' and 5'–CGCGAATTCGCG–3'. Spectra show characteristic negative peak ~255 nm confirming right handed B-form DNA.

measured by making glass in 1:2 buffer/glycerol mixture, followed by measuring the spectra at -78 °C in dry-ice/acetone mixture (see chapter 3 for details.

4.2.2. Simulation Methods

The initial coordinates for simulating 5'–CGC<u>AAATTTG</u>CG–3' and 5'–CGCG<u>AATTC</u>GCG–3' with groove-bound Hoechst was obtained from protein data bank (PDB id. 264D for —AAATTTG— and PDB id. 8bna for —AATTC—).[61,62] Crystal water molecules of 18 in numbers in the case of —AAATTTG— and 174 in numbers in the case of —AATTC— were included in the simulations.[61,62] MD simulations for both the sequence (—AAATTTG— and —AATTC—) were carried out by solvating the Hoechst/DNA complexes with 8750 and 8668 SPCE water molecules,[63] respectively, which extend upto 10 Å from DNA molecules in each side, resulting into a periodic cubic box of 70 × 70 × 70 Å. Both, Hoechst/DNA complexes were charge neutralized by adding 21 Na^+ ions (Note here that Hoechst itself contains one positive charge, thus a total of only 21 Na^+ ions were required for total charge neutrality for both DNA systems). In addition to 21 Na^+ ions, another 25 Na^+ and 25 Cl^- ions were added to have ionic concentrations of 150 mM Na^+ and Cl^- in the solutions, similar as in experimental samples. Na^+ and Cl^- were modelled with Aquist parameters.[64,65] Excited state partial charges of Hoechst atoms were obtained from previous study.[35] Hoechst/DNA systems contained a total of 26,979 atoms for —AAATTTG— DNA and 27,196 atoms for —AATTC— DNA.

Both Hoechst/DNA systems were relaxed prior to MD through energy minimization using steepest decent and conjugate gradient algorithms. During initial 1000 steps of energy minimization, DNA, Hoechst and ions were restrained with a force constant of 25 kcal mol^{-1} $Å^{-2}$ and water molecules were kept free without any restraint. This was followed by two cycles of 1000 steps minimization of entire system with restraint of 25 kcal mol^{-1} $Å^{-2}$ on water molecules, keeping the other components free in the first step; and a force constant of 25 kcal mol^{-1} $Å^{-2}$ on DNA and Hoechst, keeping the other components free in the second step. Restraint of 25 kcal mol^{-1} $Å^{-2}$ on DNA and Hoechst was then reduced to 5 kcal mol^{-1} $Å^{-2}$ over four cycles of minimization of 1000 steps each. Finally, 1000 steps of minimization were carried out without any restraint on the entire system. After energy minimization, the entire system was subjected to several steps of equilibration process. First step of equilibration was performed in NVT ensemble for 20 ps by restraining the Hoechst/DNA complex with a force constant of 25 kcal mol^{-1} $Å^{-2}$, while water and ions were kept free. In the same step, the system was heated over the course of 20 ps and temperature of the system was raised from 0 to 300 K using Langevin temperature control.[66] To achieve proper density, Hoechst/DNA complex was equilibrated over next five cycles of simulation in NPT ensemble of 20 ps each during which the restraint on Hoechst/DNA complex was reduced down to 5 kcal mol^{-1} $Å^{-2}$. Further, 50 ps equilibration of the entire system was performed without any restraint in NPT ensemble. The dimensions of the periodic cubic box were reset at this stage to reflect the average volume of the cubic box after 50 ps of NPT simulation. This equilibration process was extended by 150 ps of NVT simulation without any restraint, after which the velocities from the final trajectories were scaled to reflect production temperature of 300 K. This was followed by final equilibration of the system by running 600 ps of simulation in NVE ensemble. At this point, 3 independent additional trajectories were generated by randomly assigning new velocities for each atom from Boltzmann distributions at 300 K. The 3 independently generated trajectories were further equilibrated for 50 ps of NVT and 50 ps of NVE simulations. Before proceeding for final production simulation, all these three independent trajectories were further equilibrated for 5 ns using SANDER module, followed by another 5 ns of NVE simulation in PMEMD implementation of SANDER module of AMBER-14.[67] All atom 200 ns of production simulations for the three trajectories of both Hoechst/DNA systems (total six independent trajectories) were performed in NVE ensemble in PMEMD module of AMBER-14 using *parmbsc0* modification of *parm99* force-field for DNA in CPU.[76] The simulations were performed on fully free Hoechst/DNA/water/ions systems. SHAKE algorithm[68] was used to treat covalent bonds containing hydrogen atoms and particle-mesh Ewald (PME) sum for treating long range electrostatic interactions.[69] The simulation step size was 2 fs. Co-ordinates were saved in every 100 fs steps over the entire 200 ns trajectory (total 12 million snap-shots). Analysis of the MD trajectories was performed using codes written in FORTRAN-90 and IGOR Pro software. VMD[70] and Chimera[71] were used for trajectory visualization and graphics rendering.

4.3. Results and Discussion

4.3.1. Steady State Fluorescence Spectra: Effect of A_nT_n - Length

Hoechst shows very low fluorescence quantum yield in bulk water, but its quantum yield is enhanced by several folds upon binding to A_nT_n-rich DNA minor groove.[18,21] The ligand sits iso-helically in the floor of the minor groove through strong (bifurcated) hydrogen bonds as well as electrostatic and van der Walls interactions with DNA parts.[61,62] In water, the fluorescence quantum yields of Hoechst is very low (~0.015) which arise from non-radiative processes, possibly involving excited-sate proton transfer and/or rotation of flexible bonds between aromatic rings.[72] On binding to A_nT_n-rich minor groove of DNA, the fluorescence signal increases several folds. It has been shown earlier that the binding affinity, fluorescence quantum yields of such ligands depend on base-sequence near their binding site.[26,73,74] However, it is not known how the fluorescence characteristics of Hoechst change upon binding to minor grooves created by different lengths of A_nT_n-sequence.

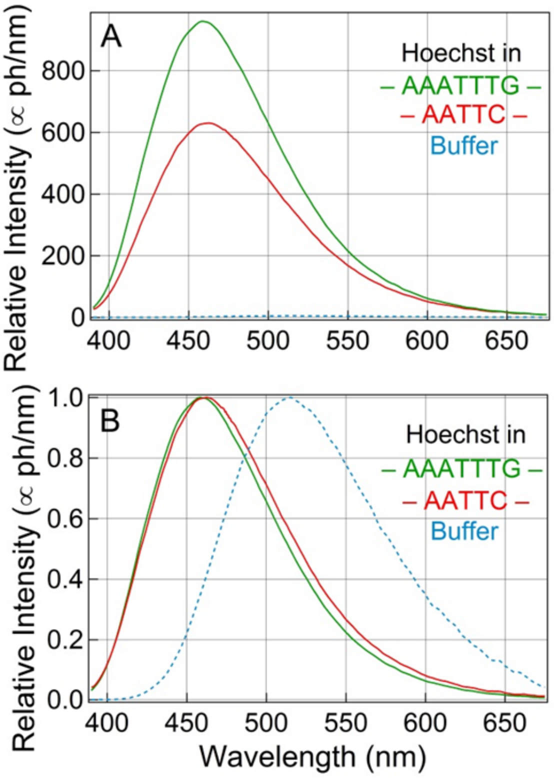

Figure 4.2: (A) Corrected (relative) fluorescence spectra of Hoechst in buffer and bound to minor grooves created by –AAATTTG– and –AATTC–. (B) Same spectra intensity normalized to one, showing the relative peak shifts. Relative changes in fluorescence spectra (peak shifts and spectral broadening) indicate that Hoechst sense a bit more polar environment in the minor groove of –AATTC– compared to that of –AAATTTG–.

Figure 4.2A compares the corrected fluorescence spectra of Hoechst in the minor groove of DNA of central sequences, —AAATTTG— and —AATTC—, and also in buffer. Upon binding to minor grooves of —AAATTTG— and —AATTC— Hoechst shows significant fluorescence signal enhancement of ~192 and ~126 times, respectively, compared to that in buffer. The spectral peaks of Hoechst in buffer, —AAATTTG— and —AATTC— are found to be at ~515 nm, ~459 nm and ~463 nm, respectively (Figure 4.2B). The Hoechst spectra are blue shifted by ~56 nm and ~52 nm when bound to —AAATTTG— and —AATTC—, respectively, compared to that in buffer. Furthermore, it is seen that Hoechst spectrum is a bit broadened in minor groove of —AATTC— compared to that in —AAATTTG—. These results indicate that interior of minor groove of —AAATTTG—, sensed by Hoechst, is a bit less polar compared that in —AATTC—. These results give the first indication that possibly Hoechst in —AATTC— senses more polar environment where local water molecules may play a role, because the solvent polarity dependent spectral shifts are found to be large for Hoechst (see Figure 5.3 in chapter 5).

4.3.2. Comparison of Fluorescence Decays

The time-resolved fluorescence data of Hoechst in the minor groove of —AAATTTG— and —AATTC— are compared to see the effect of A_nT_n length on fluorescence decays. In fact, to monitor the effect of A_nT_n-length on collective (solvation) dynamics over broad time range, we measured wavelength dependent fluorescence decays of Hoechst in the minor grooves of both DNA using UPC and TCSPC techniques. Total 20–22 fluorescence decays were measured in UPC and TCSPC for each Hoechst/DNA sample. The raw decays follow characteristic features of solvation dynamics, showing fast-decay at shorter wavelengths, fast-rise (or decay) followed by slow decay near peak wavelengths, and slow-rise followed

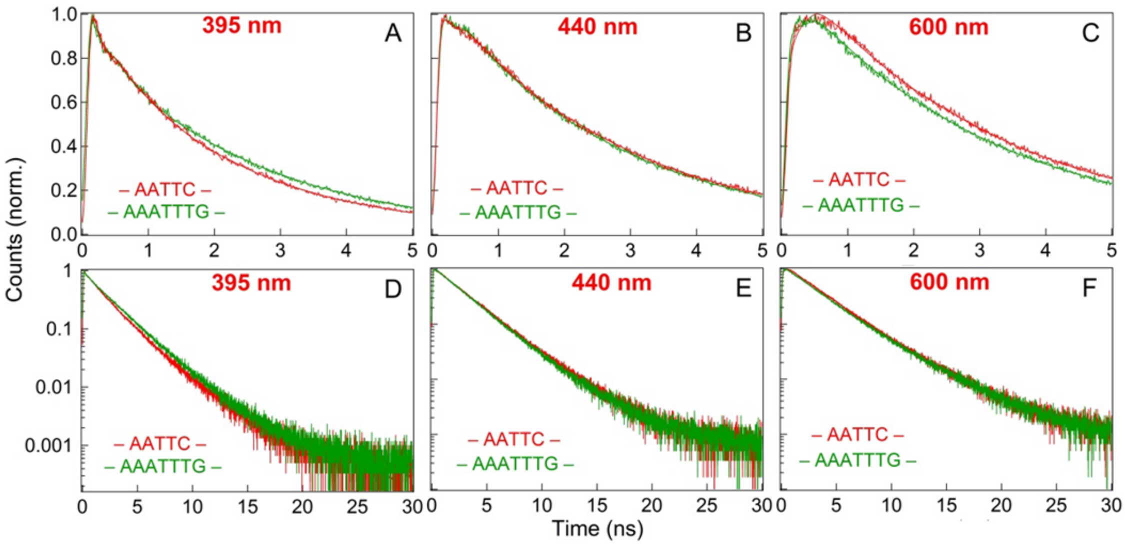

Figure 4.3: Fluorescence decays of Hoechst bound to minor grooves of –AAATTTG– and –AATTC–, measured in TCSPC at blue-side (395 nm), near peak (440 nm) and red-side (600 nm) of the fluorescence spectra. (A) – (C) Decays in short time-range upto 5 ns, and (D) – (F) decays in the full time-range plotted in semi-log scale. Lines through raw decays are fits using sum of 3-4 exponentials.

by slow-decay at longer wavelengths. These decays were fitted using sum of 3-4 exponentials, and the fitted parameters were used in the re-construction of TRES following procedures reported in chapter 3.

Figure 4.3 compares the decays of Hoechst at shorter, peak and longer wavelengths measured in TCSPC (see Figure 4.5 for other decays). Comparison shows some small effect of the A_nT_n sequence length on the decay patterns. These raw fluorescence decays suggest that there could be difference in nanosecond solvation dynamics of Hoechst in the minor

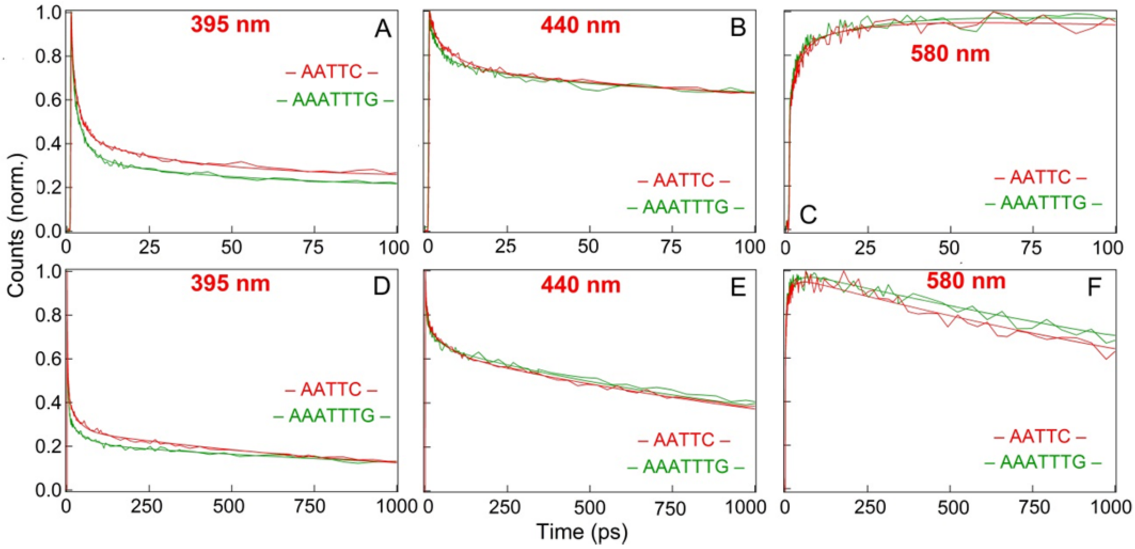

Figure 4.4: Fluorescence decays of Hoechst bound to minor grooves of –AAATTTG– and –AATTC–, measured in UPC at blue-side (395 nm), near peak (440 nm) and red-side (580 nm) of the fluorescence spectra. (A) – (C) Decays in short time-range upto 100 ps, and (D) – (F) decays in the longer time-range upto 1000 ps. Lines through raw decays are fits using sum of 3-4 exponentials.

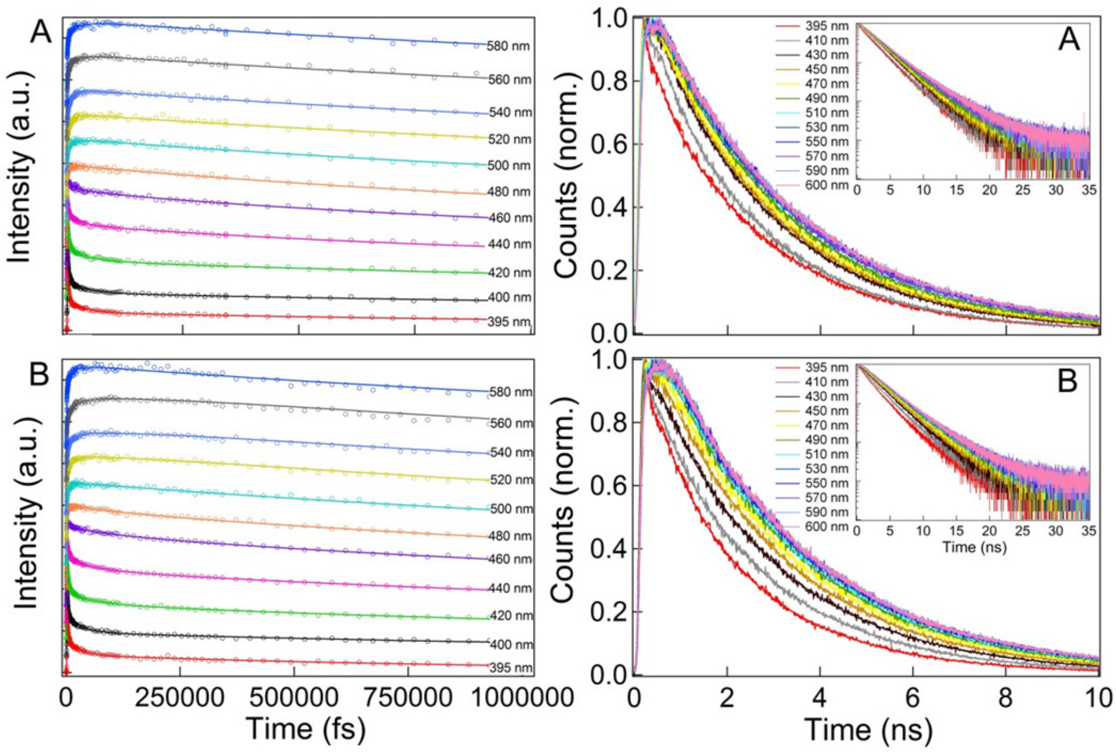

Figure 4.5: Wavelength dependent fluorescence decays (with fits) of Hoechst bound to minor grooves created by (A) –AAATTTG– and (B) –AATTC–, collected using UPC (left panels) and TCSPC (right panels). The decays show characteristic trend of solvation dynamics, that is, fast decay in blue-side, fast rise/decay followed by slow decay in peak region and slow rise followed by slow decay in red region of fluorescence spectra. Total 11 decays, out of 20-22 decays, covering entire fluorescence spectra of Hoechst in respective DNA are plotted here to minimize clumsiness. Fits to the raw data using sum of 3-4 exponential decays are also included in the figures (solid lines through raw data).

grooves of the two DNA sequences. Figure 4.4 compares the raw fluorescence decays in faster time-scales, measured in UPC setup (see Figure 4.5 for other decays). A similar effect of A_nT_n-length on the femtosecond decay patterns is also observed on the Hoechst decays in femtoseconds to picoseconds time-scales. Nevertheless, the quantitative effect of minor groove sequence on the solvation dynamics is captured in the dynamic Stokes shifts (i.e., average frequency shifts) of Hoechst as discussed below.

4.3.3. Comparison of Dynamic Stokes Shifts: Effect of A_nT_n - Length

It was not known whether the solvation dynamics from femtoseconds to nanoseconds in the minor grooves of DNA of varying A_nT_n-length, probed by groove-bound Hoechst, are similar or not. At first impression, it may seem that minor groove created by any A_nT_n sequence would provide similar environment to a groove-binding ligand. However, it is not the case, because above steady-state and time-resolved fluorescence properties of Hoechst showed that there are some subtle differences in the properties inside minor grooves of two DNA sequences. This test is important because dynamics probed by the other minor groove binder, DAPI, was shown earlier to depend on the base-sequence near its binding site.[26] Previously, Stokes shift dynamics of Hoechst in minor groove of DNA having same —AAATTTG— sequence was reported by Zewail and co-workers, measured using only UPC, showing bi-exponential relaxation till 100 ps;[18] however, no long time dynamics was reported for this Hoechst/—AAATTTG— system. Here the full dynamics in this Hoechst/DNA system is measured from 100 fs to 10 ns. To validate the present results on same system, Figure 4.6A plots the solvation correlation function, $C(t)$, calculated from present data the same way as that of Zewail and co-workers,[18] and fitted with same time-constants (and amplitudes) as reported by them.[18] Current data show nearly identical features as reported earlier by Zewail *et al.*[18] However, here the measurement of Stokes shifts in this system is also extended in longer times using TCSPC setup. On the other hand, Pal and co-workers reported the nanosecond solvation dynamics of Hoechst in the minor groove created by —AATTC—, measured using TCSPC, showing bi-exponential decay till ~5 ns.[21] Figure 4.6B plots the $C(t)$ calculated from present TCSPC data, fitted with the same time-constants (and amplitudes) reported by Pal *et al.*[21] These plots in Figure 4.6 validate the current as well as previously reported solvation dynamics data. However, no ultrafast solvation dynamics was measured for this Hoechst/—AATTC— sample either. This chapter extends the measurements in femtosecond time scales using UPC setup in this sample as well to capture the full dynamics from 100 fs to 10 ns.

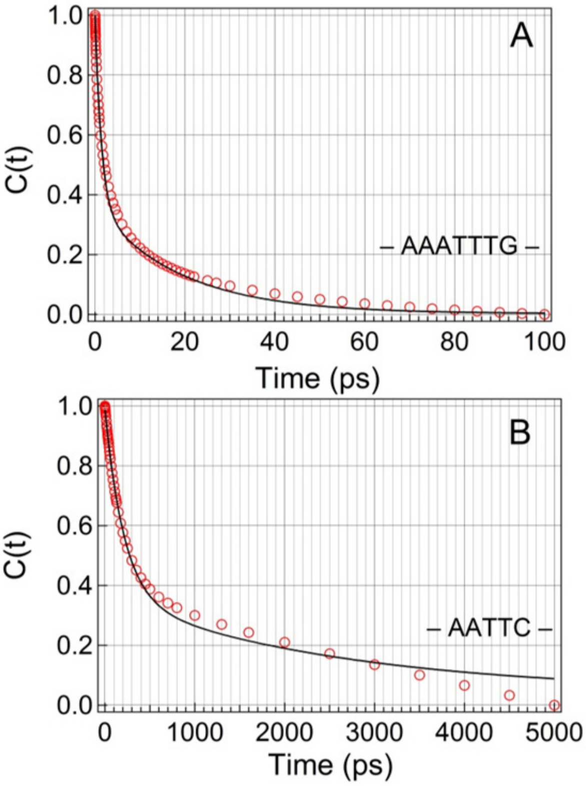

Figure 4.6: (A) Solvation correlation function of Hoechst in –AAATTTG– calculated from UPC data as, $C(t) = [\nu(t)-\nu(100\ \text{ps})]/[\nu(0)-\nu(100\ \text{ps})]$ and fitted with bi-exponential decay parameters reported earlier by Zewail *et al.*[18] (B) Solvation correlation function of Hoechst in –AATTC– calculated from TCSPC data as, $C(t) = [\nu(t)-\nu(5\ \text{ns})]/[\nu(0)-\nu(5\ \text{ns})]$ and fitted with bi-exponential decay parameters reported by Pal *et al.*[21]

Figure 4.7 plots the TRES (along with time-zero glass spectra) of Hoechst in the minor grooves of —AAATTTG— and —AATTC— over five decades of time from 100 fs to 10 ns, constructed using methods described in chapter 3. Figure 4.8 plots the absolute Stokes shifts (relative to time-zero frequency) of Hoechst in the minor grooves of the two DNA samples from 100 fs to 10 ns, constructed from the TRES data by merging the Stokes shifts at common time-points of the two techniques (see chapter 3 for details). It is seen that the

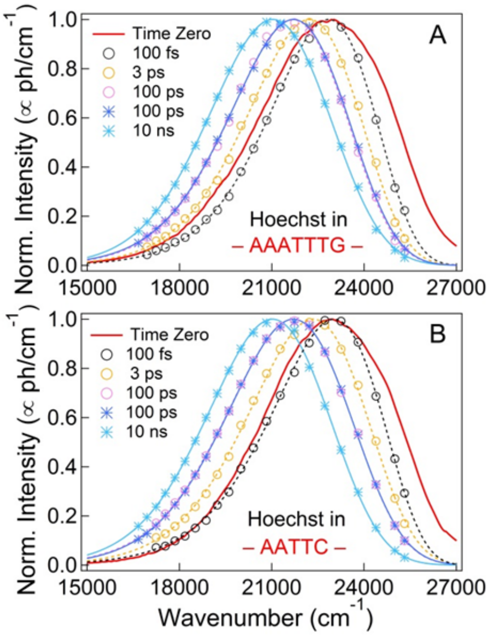

Figure 4.7: Time-resolved emission spectra (TRES) of Hoechst bound to the minor grooves created by the (A) –AAATTTG– and (B) –AATTC–, constructed from fluorescence decays measured in UPC (circles) and TCSPC (stars). Dashed and solid lines denote log-normal fits to the TRES data. Red solid-line spectra are time-zero glass-spectra of the respective samples.

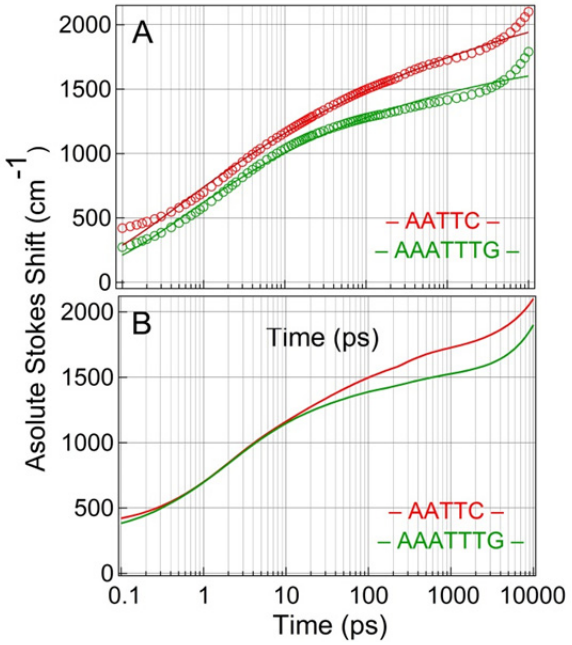

Figure 4.8: (A) Comparison of 'absolute' Stokes shifts of Hoechst bound in the minor grooves of DNA with sequences –AAATTTG– and –AATTC–, with fits (solid lines) using single power-law relaxation (equation 6.1). (B) Raw absolute Stokes shift data compared after shifted vertically to match the initial time-decades and show the difference in long-time dynamics.

Stokes shift dynamics is very smooth over the entire time-range, although apparent faster dynamics are observed in both data after ~6 ns. The origin of this faster relaxation near the end of time-window is not known, but seems to originate from excited state processes possibly other than solvation relaxation. Also, the plateau region in faster time-scales (< ~200 fs) originate from the limited time-resolution of the UPC setup used here that has time-resolution of ~250 fs, which is unable to extract the compete relaxation in the faster time-scales. Nevertheless, one can see that the dynamics are very smooth from ~200 fs to ~6 ns. These data could be well fitted with single power-law relaxations (equation 4.1) of exponents ~0.16 and ~0.11 for Hoechst dynamics in –AAATTTG– and –AATTC–, respectively.

$$S(t) = S_\infty\left[1-\left(1+\frac{t}{t_0}\right)^{-n}\right] \qquad (4.1)$$

where S_∞ is the Stokes shift at $t = \infty$, t_0 is the time where power-law start converging toward zero near $t = 0$, n is the power exponent. The overall faster rate of Stokes shift change in –AATTC– suggests that the overall solvation dynamics is faster in –AATTC– compared to that in –AAATTTG–, although the dynamics is more dispersed/stretched in –AATTC– (power exponent ~0.11) than in –AAATTTG– (power exponent ~0.16). This is in line with the observation of steady-state fluorescence properties where Hoechst spectrum in —AATTC— shows a bit broadened and red-shifted compared to that in —AAATTTG—, indicating more polar environment in —AATTC— than in —AAATTTG—. These experimental TRFSS results clearly show that solvation dynamics in minor groove of duplex-DNA is dispersed which mainly follow power-law relaxation, and not bi-exponential type relaxations as perceived earlier in same Hoechst/DNA systems.

4.3.4. Comparison of Dynamic Stokes Shifts of *Groove-Bound* Hoechst and *Base-Stacked* Coumarin in Duplex-DNA

Another very important observation is made here, that is, the solvation dynamics probed by *groove-bound* Hoechst in —AAATTTG— (measured here) show a power-law relaxation of exponent ~0.16 which is very similar to the value (exponent 0.15) obtained earlier for covalently attached *base-stacked* Coumarin-102 (opposite an abasic-site) in DNA of generic sequence, previously reported by Berg and co-workers.[22,23] A direct comparison of experimental absolute Stokes shifts of groove-bound Hoechst (in the minor groove of —AAATTTG—) and base-stacked Coumarin-102 (opposite an abasic-site in DNA of generic sequence)[22,23] is shown in Figure 4.9. This plot clearly shows that both probes sense very similar Stokes shift dynamics over nearly the entire five decades of time. This observation suggests that solvation dynamics in duplex-DNA follow single power-law relaxation (of exponent ~0.15-0.16) over broad time-range, when probed by either *base-stacked* Coumarin or *groove-bound* Hoechst.

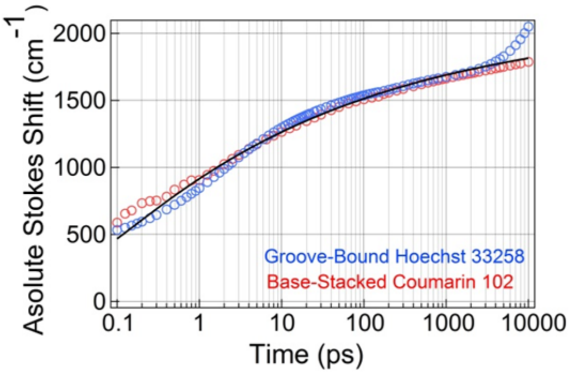

Figure 4.9: Comparison of 'absolute' Stokes shifts from 100 fs to 10 ns of minor *groove-bound* Hoechst in 12-mer DNA with central sequence –AAATTTG– (measured here) and the *base-stacked* Coumarin-102 opposite an abasic-site in a 17-mer DNA of generic sequence (measured earlier by Berg *et al.*[22,23]) Data show very similar (single) power-law solvation dynamics of power-law exponent ~0.15 (solid black line) over broad time-range, suggesting that inherent differences in the DNA systems do not affect the solvation dynamics in duplex-DNA.

The fact that minor groove-bound Hoechst and base-stacked Coumarin (opposite an abasic site) sense very similar (power-law) dynamics in duplex-DNA, however, differs from the observation of simulated dynamics in similar systems reported by Furse and Corcelli.[36] They saw substantial difference between the simulated solvation correlation functions of groove-bound Hoechst and base-stacked (model) Coumarin (opposite an abasic-site).[36] Based on their simulation data, they suggested that the slower (power-law type) relaxation observed by base-stacked Coumarin-102 (opposite an abasic-site) arises from the intra- and extra-helical conformational changes of abasic-sugar, which were found to be kinetically stable on nanosecond time-scale.[36] The comparison of experimental dynamics of groove-bound Hoechst and base-stacked Coumarin made in Figure 4.9, however, suggests that such conformational changes of abasic-sugar may have minimal or no effect on the solvation process around Coumarin, because such changes may get averaged out in ensemble-level experiments. This issue has been a point of discussion in literature – which suggested that base-stacked Coumarin does not report the true solvation dynamics of DNA, rather it reports on dynamics of damaged site inside DNA.[36] However, the present direct comparison of experimental TRFSS data of same systems clearly does not approve the previous claims. In fact, following the results of several dynamic Stokes shift experiments on various (normal) DNA systems (many of them presented also in chapters 5-8), spanning over broad time-ranges, it can be suggested that solvation dynamics in DNA mainly follow power-law relaxation with exponent of ~0.15 – 0.16,[22,23,26-28,34,36] but with few exceptions including the dynamics in —AATTC— presented here.[24-26,28]

4.3.5. Molecular Dynamics Simulation Results

4.3.5.1. Electrostatic Interaction Energy Fluctuations and Solvation Correlation Functions

Although the above TRFSS experiments showed that Hoechst sense faster relaxation in the minor groove of —AATTC— compared to that of —AAATTTG—, it is still very difficult to explain fully the TRFSS results only from experiments. MD simulations have been shown to provide a clear route to explain the TRFSS results. However, such explanations of TRFSS results through MD simulations are valid only if those simulations are directly compared with the experimental results to see if simulation captures the essential features of experimental results or not. Under linear response theory, it has been shown that non-equilibrium TRFSS experimental results can be directly compared with the equilibrium simulation results, provided in experiment the properties of system under study do not deviate much from equilibrium conditions. This has been tasted in various occasions and found that linear response theory generally holds for most physical systems.[27,29-45] Nonetheless, not many similar studies on DNA systems are found in literature, except few reported by Bagchi-Hynes and co-workers,[33] Furse and Corcelli,[30,35-37] Berg and co-workers,[34] and Sen and co-workers.[27]

In this chapter equilibrium simulations on both Hoechst/DNA systems are performed over very long time (200 ns) for 3 independent trajectories that are used to get better averaging of dynamics in each Hoechst/DNA system (total simulation run is 1.2 μs). The co-ordinates were saved in every 100 fs step (2 million × 3 × 2 systems = 12 million snap-shots). In fact, these simulations are the longest till date which are used to calculate the solvation correlation functions in DNA (see below).

For direct comparison of TRFS results with simulation, electrostatic interaction energies of excited state charges of Hoechst with surrounding water, ions (both Na^+ and Cl^-) and DNA were calculated in each snap-shot of the MD trajectories. Damped Shift Force (DSF)[75] sum method was used to calculate the electrostatic interaction energy of Hoechst with the surrounding molecules, similar as used in earlier simulation studies of duplex-DNA by Furse and Corcelli.[30,35-37] Effects of long range electrostatic interactions among atoms of the system are efficiently included by DSF sum method.[75] The electrostatic interaction energy using DSF method is calculated as,[75]

$$E(t) = \sum_{m=1}^{N_{solute}} q_m \sum_{n=1}^{N_{solvent}} q_n \left[\frac{erfc(\alpha r)}{r} - \frac{erfc(\alpha R_c)}{R_c} + \left(\frac{erfc(\alpha R_c)}{R_c^2} + \frac{2\alpha}{\sqrt{\pi}} \frac{exp(-\alpha^2 R_c^2)}{R_c} \right) (r - R_c) \right] \qquad (4.2)$$

where, q_m is the charge of m^{th} atom of the solute (here, excited-state charges of Hoechst), q_n

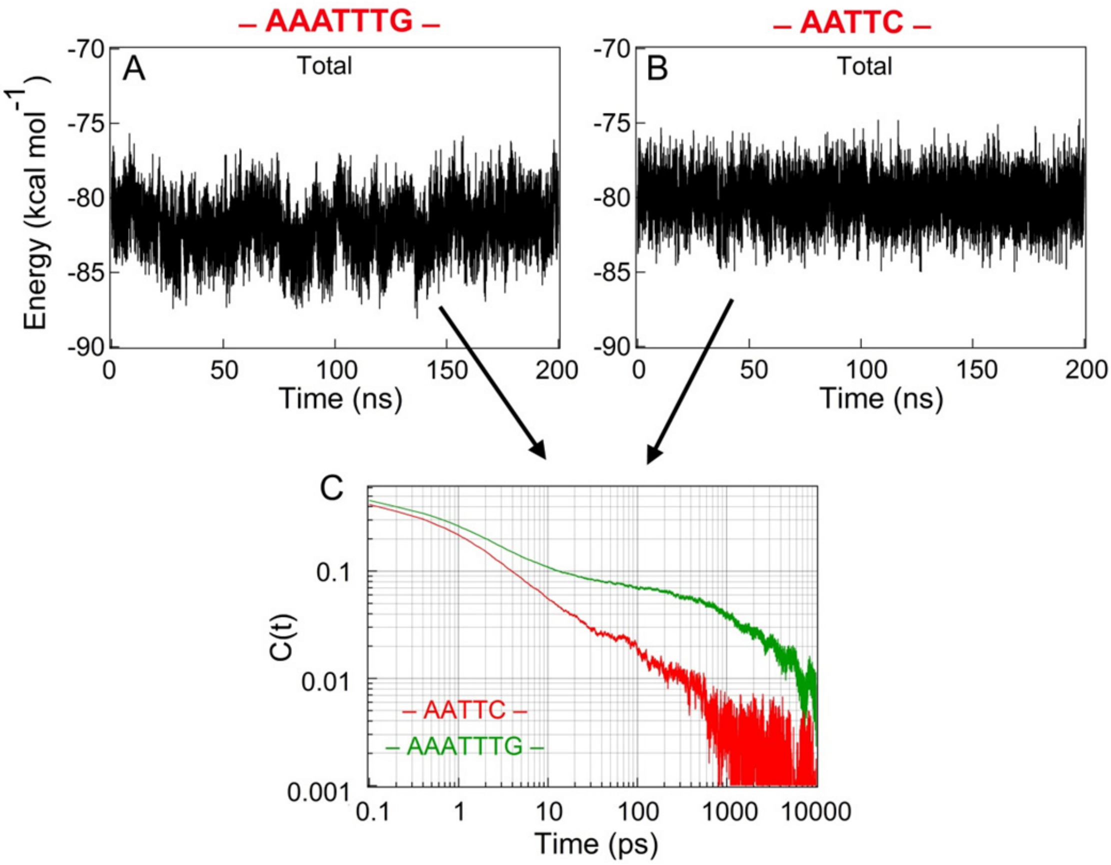

Figure 4.10: Total electrostatic interaction energy fluctuations of excited-state Hoechst with surrounding water, ions and DNA in the minor groove created by —AAATTTG— (A) and —AATTC— (B) over 200 ns simulation (average of 3 independent trajectories of 200 ns each), calculated using DSF sum method (equation 4.2). Energies are calculated at 100 fs step and the fluctuations are smoothed with 200 ps running average for clearly showing the inherent fluctuation features of the DNA systems. (C) Comparison of (simulated) solvation correlation functions calculated as auto-correlations of total energy fluctuations (equation 4.3) of excited Hoechst in the two Hoechst/DNA systems. See figure for legends.

is the charge of the n^{th} solvent atom (here water, ions and DNA atoms), r is the interatomic distance between q_m and q_n, R_c is the cut-off radius ($r \leq R_c$) and α is the damping factor that controls the convergence of the Coulomb sum over distance. In this work, R_c is defined as 32 Å (half of the final box size) and α is chosen as 0.2 Å^{-1} (similar as used in simulation of duplex DNA earlier).[30,35-37] The electrostatic interaction energy fluctuations of Hoechst with water, DNA, ions and total system has been calculated over entire 200 ns of simulation, averaged over 3 independent 200 ns trajectories, and plotted in Figure 4.10. The plot shows large DNA and water energies which are strongly anti-correlated in both Hoechst/DNA samples. However the features of fluctuations are somewhat different in two systems with larger DNA fluctuations in case of —AAATTTG— (Figure 4.10A) than that in case of —AATTC— (Figure 4.10B). Contributions of Na^+ and Cl^- are found to be small.

The total interaction energy fluctuations were used to calculate the total equilibrium solvation correlation function, $C_{simu}(t)$, in the excited state of Hoechst as,[33,34]

$$C_{simu}(t) = \frac{\langle \Delta E(0) \Delta E(t) \rangle_e}{\langle \Delta E(0)^2 \rangle_e} \qquad (4.3)$$

where $\Delta E(t) = (E(t) - \langle E(t) \rangle)_e$, is fluctuation in interaction energy of (excited-state) Hoechst charges and partial charges of DNA, ions and water molecules, relative to average energy. Figure 4.10C compares the simulated solvation correlation functions, $C_{simu}(t)$, of Hoechst in the two Hoechst/DNA systems. These simulated correlation functions capture the essential features of experimental TRFSS dynamics, i.e., power-law type dispersed solvation relaxation over broad time-range and faster solvation dynamics in —AATTC— compared to that in —AAATTTG—, similar as observed in experiments; although, the relative changes in rate of relaxations are somewhat different in simulated dynamics as compared to the experimental dynamics (see Figures 4.8B and 4.10C). Nevertheless, simulations capture the main features of the experimental dynamics in the two DNA systems.

4.3.5.2. Comparison of Simulated and Experimental Stokes Shifts Dynamics

Within linear response approach, the simulated equilibrium solvation correlation function, $C_{simu}(t)$, can be equated to the (non-equilibrium) experimental solvation correlation function, $C_{expt}(t)$, of a probe as; $C_{simu}(t) \cong C_{expt}(t)$.[33-35] However, comparison of $C_{simu}(t)$ to $C_{expt}(t)$ is not straightforward because $C_{simu}(t)$ includes large amount (~70–90%) of fast inertial component which is absent in the measured experimental 'absolute' Stokes shift dynamics.[33-35] Sen *et al.* suggested a unique way to directly compare simulated and experimental dynamics by calculating simulated absolute Stokes shifts from simulated solvation correlation function as,[34]

$$S(t) = \delta S_0 + b[1 - C_{simu}(t)] \qquad (4.4)$$

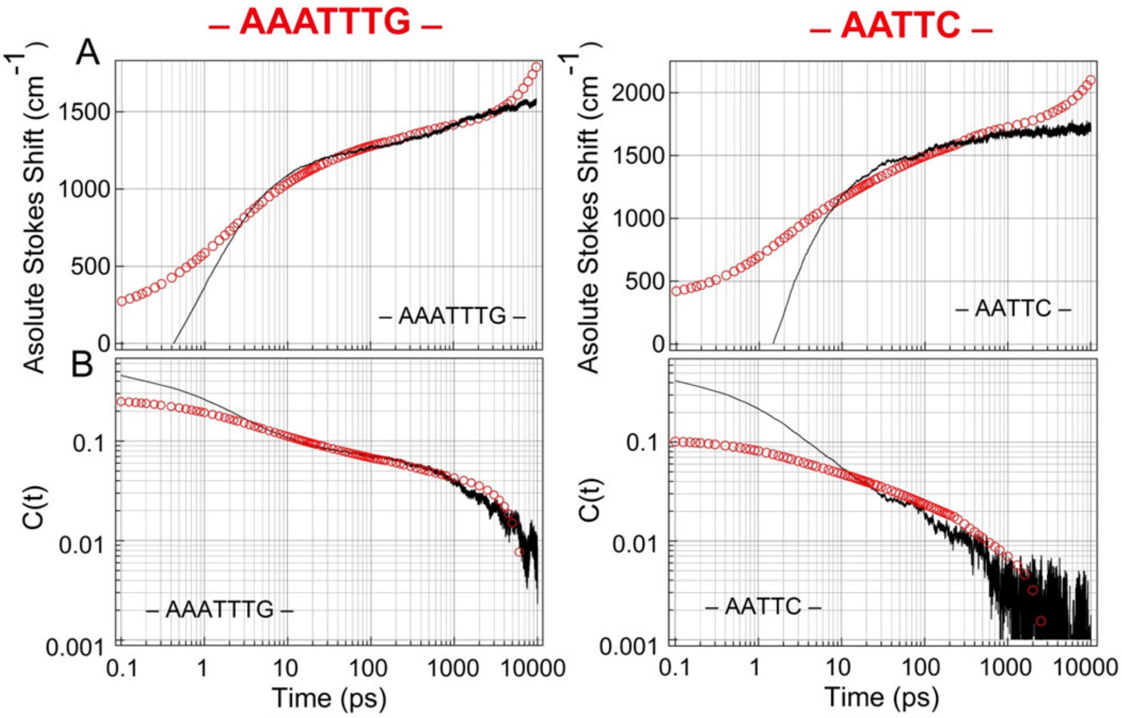

Figure 4.11: (A) Comparison of 'absolute' Stokes shifts of Hoechst obtained from experiment (red circles) and simulation (black lines) in the minor grooves of —AAATTTG— (left panel) and —AATTC— (right panel). Simulated absolute Stokes shifts were calculated from simulated solvation correlation functions using equation 4.4 (see text for details). Limited time-resolution of UPC setup (~250 fs) could not allow extraction of full dynamics by ~450 – 500 cm^{-1} at 100 fs, which leads to the deviation between experimental and simulation data below ~2 – 5 ps. (B) Comparison of simulated solvation correlation functions to experimental solvation correlation functions of Hoechst after scaling the experimental data to discard initial inertial component in simulation in case of —AAATTTG— (left panel) and —AATTC— (right panel). The matching of simulation and experimental data is very good in case of —AAATTTG—, but inferior in case of —AATTC—.

In equation 4.4, δS_0 is the fast inertial contribution and b is the total (simulated) Stokes shifts. Using this method, Figure 4.11A compares the experimental and simulated absolute Stokes shifts and Figure 4.11B compares the (multiplicatively scaled) experimental $C_{expt}(t)$ and simulated $C_{simu}(t)$ of Hoechst in the minor grooves of —AAATTTG— and —AATTC— . The matching is found to be good over broad time-range for —AAATTTG—, while the matching of data is reasonably good for —AATTC—. To do the matching of simulated Stokes shift to experimental TRFSS, values of δS_0 and b (and multiplication factor for direct $C(t)$ matching in Figure 4.11B) were adjusted such that ~75% of inertial contribution was needed to be subtracted from the total simulated Stokes shift in case of —AAATTTG—, while those values were adjusted to subtract ~85% of inertial component in case of —AATTC—. These numbers are consistent with the fact that a large amount of inertial dynamics (~75-85%) contributes to the simulated dynamics, which is eliminated in the experimental "absolute" Stokes shift which subtracts the TRES frequencies from the frequency of time-zero glass-spectrum where diffusive motions are frozen but inertial motions persist. It should be noted here that the time-resolution of the UPC setup (~250 fs) limits the full extraction of dynamics by ~450-500 cm^{-1} at 100 fs. This leads to the deviations between simulated and experimental dynamics within 100 fs to ~2 ps (see Figure 4.11A). Nevertheless, the matching between simulated and experimental Stokes shifts over broad time-range validates the linear response approach, although the matching of simulated and TRFSS data for —AATTC— is rather inferior. Nonetheless, it is found that simulations capture the essential features of the experimental solvation dynamics.

4.3.5.3. Decomposition of Total Simulated Correlation into Individual Components: Origin of Dispersed Power-law Dynamics in DNA

In order to find the origin of dispersed (power-law) solvation dynamics in the minor grooves of DNA of two different central sequences, the total simulated correlations were decomposed into partial correlations of water, DNA-proper, Na$^+$ and Cl$^-$ using linear response decomposition (LRD) method.[45-48] LRD had been proposed by Nilson and Halle,[44] and used by Golosov and Karplus,[45] Furse and Corcelli[35-37] and Sen *et al.*[27,34] in the decomposition analysis of total solvation correlations in proteins and duplex-DNA. In this method, the total correlation is decomposed into its components by calculating the cross-correlations between individual component's energy fluctuation and total energy fluctuation of system. In LRD, the total solvation correlation function, $C_{simu}(t)$, can be expressed as the sum of partial correlations of individual components as,[44]

$$C_{simu}(t) = \sum_i \frac{\langle \Delta E_i(t) \Delta E(0) \rangle}{C(0)} \qquad (4.5)$$

where i is individual component (i.e., water, Na$^+$, Cl$^-$ and DNA-proper) and $C(0)$ is total correlation at zero-time.

Figure 4.12A and 4.12B plots the partial correlations of water, DNA, Na$^+$ and Cl$^-$, along with the total correlation. Plot shows that in case of —AAATTTG—, below ~3 ps water contributes the most to control the fast dynamics, although water relaxation levels off to zero within ~20 ps. DNA motions, however, contribute fully to dictate the dispersed slow relaxation in longer times (>20 ps). It can be seen that DNA correlation follows nearly a power-law type relaxation over broad time window. The motional contributions from Na$^+$ and Cl$^-$ however are found to be negligible over the entire time-range. These main results agree very well with the previous simulation results of Furse and Corcelli on the same Hoechst/DNA system, which also saw that DNA is the main contributor to the slow dynamics (> 10ps) in the minor groove of —AAATTTG— when probed by groove-bound Hoechst.[35] Furse and Corcelli indirectly compared their simulation results[35] to the exponential time-components from TRFSS results of Zewail and co-workers till 100 ps.[18] However, this chapter showed for the first time the direct comparison of TRFSS experiment and simulation results over very broad time-range of ~100 fs to 10 ns, which show excellent similarity of dispersed power-law relaxation in the minor groove of DNA, probed by the

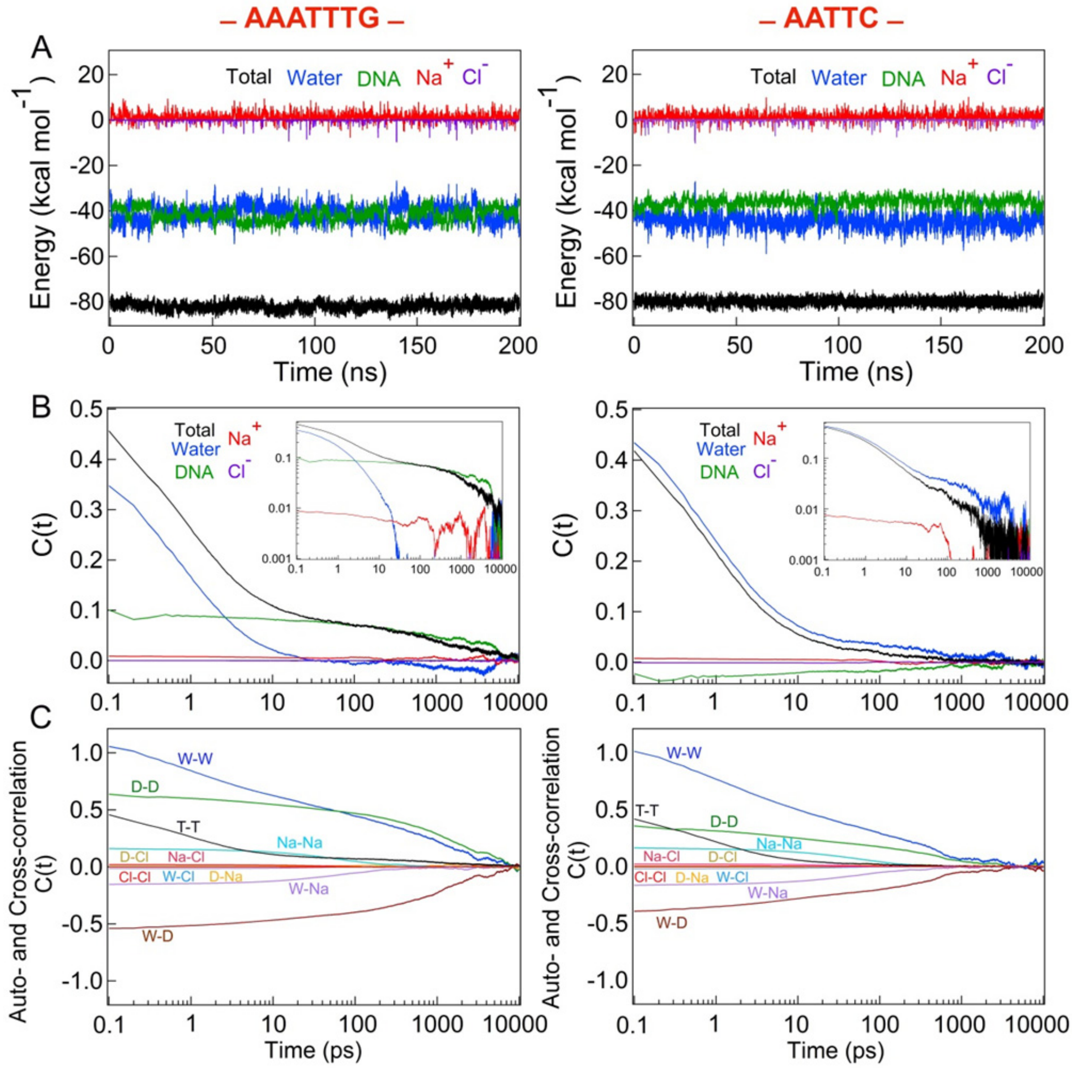

Figure 4.12: (A) Electrostatic interaction energy fluctuations of excited-state Hoechst with surrounding water (blue), DNA (green), Na$^+$ (red) and Cl$^-$ (purple) in the minor grooves created by —AAATTTG— (left panel) and —AATTC— (right panel) over 200 ns simulation (average of 3 independent trajectories of 200 ns each), calculated using DSF sum method (equation 4.2). Energies are calculated at 100 fs step and the fluctuations are smoothed with 200 ps running average for clearly showing the inherent fluctuation features of the DNA systems. (B) Linear response decomposition (LRD: equation 4.5) of total simulated correlation (black) into individual correlations of components of water (blue), DNA (green), Na$^+$ (red) and Cl$^-$ (purple) in the case of —AAATTTG— (left panel) and —AATTC— (right panel). DNA correlation contributes the most to the total correlation in longer time (> 3 ps) in case of —AAATTTG—, while water controls the total correlation almost entirely in case of —AATTC—. (C) Decomposition of total correlation (black) into all possible auto- and cross-correlations of individual components (equation 4.6) in case of —AAATTTG— (left panel) and —AATTC— (right panel). See figures for legends. Again DNA-DNA auto-correlation contributes most in total response in case of —AAATTTG— and water-water auto-correlation contributes the most to the total response in —AATTC—. Also amplitude of water-DNA cross-correlation is higher in —AAATTTG— compared to that in —AATTC—.

Hoechst. However, in case of –AATTC–, the situation is opposite, despite the fact that same Hoechst probes the dynamics in this minor groove. Figures 4.12A and 4.12B (right panel) shows the LRD of total correlation into the individual components. It is readily seen that water relaxation mainly controls the full dynamics over entire time-range. DNA motion is rather anti-correlated to the water motions, which shows negative relaxations with very small amplitude. The sum of these partial water and DNA correlations mainly define the total correlation of the system that shows nearly a power-law relaxation (see Figure 4.12B – right panel), because contributions from Na^+ and Cl^- are negligible over entire time range.

Figure 4.12C plots all 4 auto-correlations of individual components and 6 cross-correlations among the components; the summation of which define the total correlation of the system as,[33]

$$\begin{aligned} C_{simu}(t) = C_{WW}(t) + C_{DD}(t) + C_{NaNa}(t) + C_{ClCl}(t) + C_{WNa}(t) + C_{WCl}(t) + C_{WD}(t) \\ +C_{NaCl}(t) + C_{DNa}(t) + C_{DCl}(t) \qquad (4.6) \end{aligned}$$

where subscripts, *W*, *D*, *Na*, *Cl*, define the water, DNA, sodium ion, and chloride ion, respectively. Comparison of auto- and cross-correlations of individual components in the two Hoechst/DNA systems in Figure 4.12C clearly show that amplitude of C_{DD} is much higher in minor groove of —AAATTTG— than that in —AATTC—, which supersedes the water-water auto-correlation (C_{WW}) beyond ~50 ps. Furthermore, the amplitude of cross-correlation between water and DNA (C_{WD}) is larger in —AAATTTG— than that in —AATTC—. On the other hand, the water-water auto-correlation (C_{WW}) always supersedes the DNA-DNA auto-correlation (C_{DD}) in case of —AATTC—, together with lesser amplitude of cross-correlation between water and DNA, suggesting that water mainly control the overall dynamics in the minor groove created by —AATTC—. The contributions of ion-ion auto-correlation and water-ion cross-correlations are found to be small compared to the above auto- and cross-correlations. Thus, Figure 4.12C indicates that water is the main contributor in —AATTC— and DNA is main contributor in —AAATTTG—, which control the dispersed solvation dynamics in A_nT_n — length dependent minor grooves of DNA.

4.3.5.4. Minor-Groove Width Fluctuation and Water Distribution around Hoechst

The question arises at this point – why local DNA motion controls the solvation dynamics in one minor groove while water controls the dynamics in other minor groove created by similar A_nT_n-rich sequence? This immediately prompted to check the differences of local structural fluctuations and dynamics of DNA minor groove widths as well as the differences in water distributions around Hoechst bound to —AAATTTG— and —AATTC—. The simulations show Hoechst remains bound to both minor grooves at similar place near A_nT_n sequence spanning from 6th adenine to 9th thymine in —AAATTTG— and from 6th adenine to 9th cytosine in —AATTC— over the entire 200 ns simulation run (Figure

4.13). This suggests that the differences in static and dynamic solvation properties do not arise from the differences of binding positions of Hoechst in the two DNA systems as the sites are similar (the A_nT_n region). Thus, the possibility of such difference may arise from the local DNA structural dynamics that in turn can perturb the nearby water molecules so as to dictate the relative contributions of motions of water and DNA to the total dynamics. The fluctuations of minor groove widths near the Hoechst binding were calculated in terms of the distance fluctuations of three phosphorus atoms in the backbones of opposite strands near the Hoechst binding site. The distance fluctuations of P7-P18, P8-P17 and P7-P16 were calculated over the entire 200 ns for all 3 trajectories in both Hoechst/DNA systems and averaged over all three trajectories (see Figure 4.13 for positions of the phosphorus atoms chosen). Figure 4.14A shows the relative distributions of the distance fluctuations between P7-P18, P8-P17 and P7-P16 in DNA with –AAATTG– and –AATTC–. It can be seen that the distance fluctuations for all three pairs of phosphorus are broader in case of –AAATTTG– compared to those of –AATTC–. This suggests that internal structural fluctuations of the minor groove widths created by –AAATTTG– are larger which can possibly perturb the local hydration dynamics in this minor groove larger than that in –AATTC–. More so, these

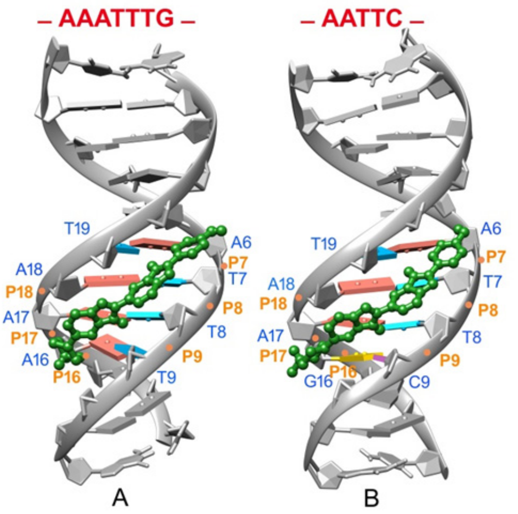

Figure 4.13: Cartoon showing binding sites of Hoechst in the two minor grooves created by –AAATTTG– (A) and –AATTC– (B) Hoechst binds to A_nT_n region of minor groove spanning from 6th adenine to 9th thymine (in –AAATTTG–) and 6th adenine to 9th cytosine (in –AATTC–). Minor groove width fluctuations over 200 ns simulation were calculated in terms of distance fluctuations between phosphorus atoms of P7-P18, P8-P17 and P9-P16 as shown in the cartoons.

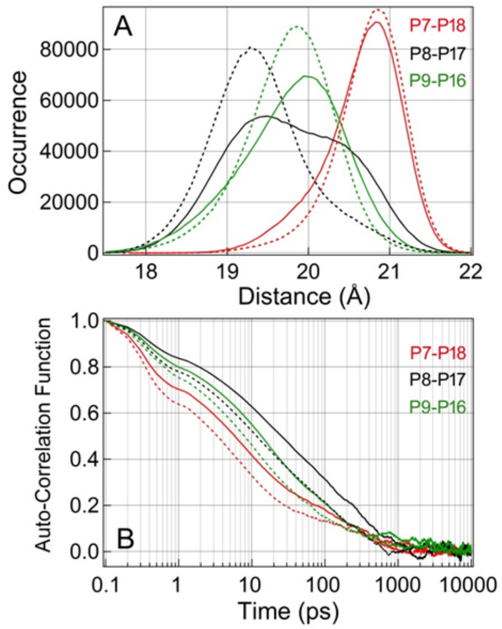

Figure 4.14: (A) Distributions of distance fluctuations of P7-P18, P8-P17 and P9-P16 over 200 ns in case of —AAATTTG— (solid lines) and —AATTC— (dashed lines). See also Figure 4.13 for chosen phosphorus atom positions near the minor groove. (B) Auto-correlation functions of the P-P distance fluctuations in —AAATTTG— (solid lines) and —ATTC— (dashed lines). The distributions are comparatively broader and auto-correlation functions are slower in case of —AAATTTG— relative to that in —AATTC—.

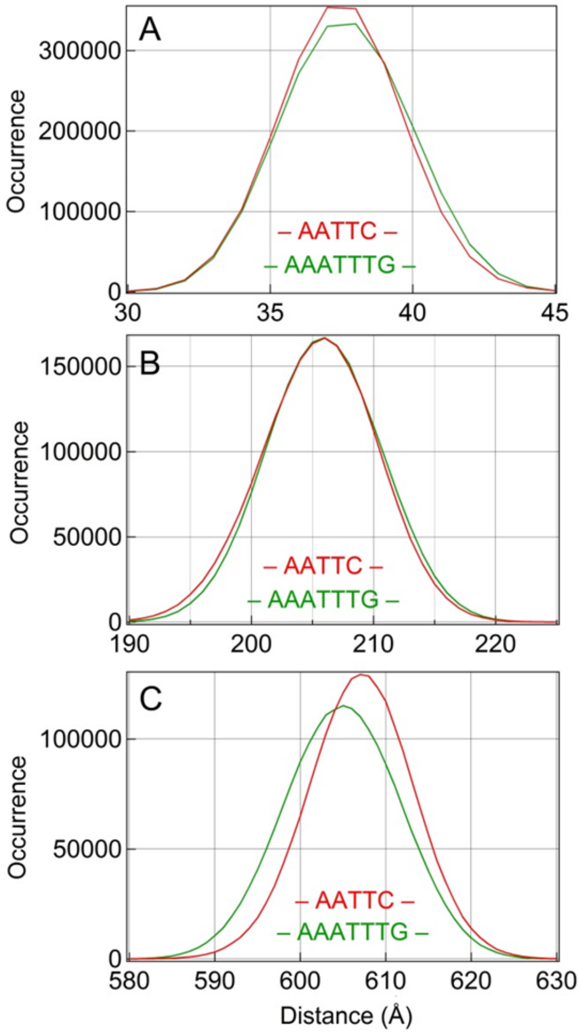

Figure 4.15: Distributions of number of water molecules, calculated over entire 200 ns, those come within the 1st solvation shell (A), 2nd solvation shell (B) and 3rd solvation shell (C) around the probe-Hoechst bound inside the minor grooves created by –AAATTTG– (green) and –AATTC– (red). Distributions are similar in both minor grooves, except somewhat larger number is observed in 3rd shell near –AATTC–.

larger groove width fluctuations can indeed produce larger fluctuations in the electrostatic interaction energy of DNA-parts with probe-ligand, leading to dominance of DNA local motion in the overall solvation response of Hoechst in case of –AAATTTG– compared to that in –AATTC–. This relative difference in the groove-width fluctuations between the two DNA systems may be sufficient enough to induce the local hydration dynamics in the two minor grooves. In fact, it is observed that the correlations of these groove-width fluctuations over 200 ns are slower in case of –AAATTTG– compared to those of –AATTC– (see Figure 4.14B). Thus, it seems that the relative changes in solvation dynamics as well as relative contributions of water and DNA to the total dynamics observed in the two Hoechst/DNA systems can be directly linked to the local structural dynamics of the minor grooves of DNA created by different lengths of A_nT_n repeats.

The above observation may immediately lead to a conclusion that there may be different distributions of water molecules around the probe-Hoechst in the two minor grooves created by –AAATTTG– and –AATTC–. Surprisingly, it is observed that the distributions of number of water molecules in the 1st solvation shell (within 4 Å from any Hoechst-atom), 2nd shell (within 4 -8 Å from any Hoechst-atom) and 3rd shell (within 8-12 Å from any Hoechst-atom) remain very similar over the entire 200 ns simulation in the minor grooves of both DNA systems, except a little higher number in the 3rd shell in case of –AATTC– (Figure 4.15). However, it is well known that the 1st and 2nd shell water molecules contribute the most to the electrostatic interaction energy at the probe-site. All these above observations point to the possibility that it is not the number of water molecules near minor groove, but their dispersed motions - perturbed by local DNA fluctuations – define the static and dynamic solvation properties in the minor grooves of

DNA. This immediately leads to more questions that whether the motional characteristics of these water molecules such as distributions of water residence time, diffusion, etc. in the minor grooves of two DNA systems are different or not. Such calculations can surely be performed on these trajectories; however, due to time limitations, these calculations could not be performed. Further studies toward this end are undergoing which may be able to unfold more information on the structure and dynamics of water and DNA in these ligand/DNA systems. Nevertheless, this chapter clearly showed that nature of hydration dynamics as well as overall solvation response in the minor grooves of DNA can be significantly modulated by the minor groove A_nT_n sequence and widths.

4.4. Conclusion

This chapter presented very extensive TRFSS and MD simulation results on two different Hoechst/DNA systems to clearly understand the minor groove solvation in DNA. The Hoechst/DNA systems chosen here are same as those explored earlier partly by Zewail *et al.*[18] and Pal *et al.*[21] using TRFSS experiments and by Furse and Corcelli[35,36] using MD simulation. However, those studies were rather scattered and they, together with other studies, raised several debated questions regarding the explanation of DNA solvation dynamics. Thus, choice of the present Hoechst/DNA systems was rather intentional, because it was required to study, observe and explain the DNA solvation in a more comprehensive manner, which this chapter did. The main conclusions that originate from the above results are:

I. Solvation dynamics in DNA mainly follow power-law relaxation (of exponent ~0.15-0.16) over broad time-range that extends over decades. In fact, results presented in following chapters 5-8 will also show that this dynamical feature is inherent in DNA.

II. The TRFSS dynamics in DNA probed by base-stacked Coumarin (opposite an abasic-site) in DNA of generic sequence and that probed by minor groove-bound Hoechst in DNA of central sequence –AAATTTG– show very similar dynamics over broad time-range. This suggests that the earlier proposal of the effects intra- and extra-helical conformational changes of abasic-sugar on local solvation dynamics, based on simulation data, may not be valid – possibly because in actual ensemble-level TRFSS experiments the effect of these structural changes may get averaged out to have minimal or no effect on the overall solvation dynamics, or at least TRFSS experiments are not sensitive enough to capture such specific dynamics of abastic-site inside DNA.

III. DNA minor groove solvation is a complex process that heavily depends on the local A_nT_n stretch and groove-fluctuations, which ultimately define the slow dispersed hydration dynamics around a probe-ligand.

IV. Long MD simulations can certainly capture the essential features of TRFSS experimental results to a large extent, particularly the dispersed power-law type solvation dynamics in DNA and minor groove sequence dependence on dynamics; although, it has been seen that the direct matching of simulated solvation correlation function to the experimental one was rather inferior in case of DNA with central ─AATTC─ sequence.

V. MD simulation results showed that dispersed (power-law) relaxations in DNA may have different origins, but it is either the slow water or DNA motions that control the dispersed solvation dynamics in the minor grooves of DNA when probed by groove-bound Hoechst.

VI. Results showed there are very slow and dispersed (perturbed) water molecules in/near the minor grooves of DNA which can also contribute nearly independently to the total solvation dynamics in DNA, but only when the local DNA fluctuations/motions are less turbulent in the vicinity of the probe-site.

Reference

(1) Bagchi, B. *Water in Biological and Chemical Processes: From Structure and Dynamics to Function*. Oxford Press, Cambridge, UK, **2013**.

(2) Fogarty, A. C.; Duboue-Dijon, E.; Sterpone, F.; Hynes, J. T.; Laage, D. Bimolecular Hydration Dynamics: A Jump model Perspective. *Chem. Soc. Rev.* **2013**, *42*, 5672-5683.

(3) Ball, P. Water as An Active Constituent in Cell Biology. *Chem. Rev.* **2008**, *108*, 74-108.

(4) Grossman, M.; Born, B.; Heyden, M.; Tworowski, D.; Fields, G. B.; Sagi, I.; Havenith, M. Correlated Structural Kinetics and Retarded Solvent Dynamics at the Metalloprotease Active Site. *Nat. Struct. Mol. Biol.* **2011**, *18*, 1102-1108.

(5) Kim, S. J.; Born, B.; Havenith, M.; Gruebele, M. Real-Time Detection of Protein–Water Dynamics upon Protein Folding by Terahertz Absorption Spectroscopy. *Angew. Chem. Int. Ed.* **2008**, *47*, 6486-6489.

(6) Silva, J. L.; Vieira, T. C. R. G.; Gomes, M. P. B.; Bom, A. P. A.; Lima, L. M. T. R.; Freitas, M. S.; Ishimaru, D.; Corderio, Y.; Foguel. D. Ligand Binding and Hydration in Protein Misfolding: Insights from Studies of Prion and p53 Tumor Suppressor Proteins. *Acc. Chem. Res.* **2010**, *43*, 271-279.

(7) Meister, K.; Ebbinghaus, S.; Xu, Y.; Duman, J. G.; DeVries, A.; Gruebele, M.; Leitner, D. M.; Havenith, M. Long-Range Protein–Water Dynamics in Hyperactive Insect Antifreeze Proteins. *Proc. Natl. Acad. Sci. U.S.A.* **2013**, *110*, 1617-1622.

(8) Ebbinghaus, S.; Meister, K.; Born, B.; DeVries, A. L.; Gruebele, M.; Havenith, M. Antifreeze Glycoprotein Activity Correlates with Long-Range Protein-Water Dynamics. *J. Am. Chem. Soc.* **2010**, *132*, 12210-12211.

(9) Gruschus, J. M.; Ferretti, J. A. Quantitative Measurement of Water Diffusion Lifetimes at a Protein/DNA Interface by NMR. *J. Biomol. NMR* **2001**, *20*, 111-126.

(10) Gorfe, A. A.; Caflisch, A.; Jelesarov, I. The Role of Flexibility and Hydration on the Sequence-Specific DNA Recognition by the Tn916 Integrase Protein: A Molecular Dynamics Analysis. *J. Mol. Recognit.* **2004**, *17*, 120-31.

(11) Mukherjee, A.; Lavery, R.; Bagchi, B.; Hynes, J. T. On the Molecular Mechanism of Drug Intercalation into DNA: A Simulation Study of the Intercalation Pathway, Free Energy, and DNA Structural Changes. *J. Am. Chem. Soc.* **2008**, *130*, 9747-9755.

(12) Williams, H. E. L.; Searle, M. S. Structure Dynamics and Hydration of the Nogalamycin-d(ATGCAT)(2) Complex Determined by NMR and Molecular Dynamics Simulation in Solution. *J. Mol. Biol.* **1999**, *290*, 699-716.

(13) Li, T.; Hassanali, A. A.; Kao, Y.T.; Zhong, D.; Singer, S. J. Hydration Dynamics and Time Scales of Coupled Water−Protein Fluctuations. *J. Am. Chem. Soc.* **2007**, *129*, 3376-3382.

(14) Abbyad, P.; Shi, X.; Childs,W.; McAnaney, T. B.; Cohen, B. E.; Boxer, S. G. Measurement of Solvation Responses at Multiple Sites in a Globular Protein. *J. Phys. Chem. B* **2007**, *111*, 8269-8276.

(15) Chang, C. W.; He, T. F.; Guo, L.; Stevens, J. A.; Li, T.; Wang, L.; Zhong, D. Mapping Solvation Dynamics at the Function Site of Flavodoxin in Three Redox States. *J. Am. Chem. Soc.* **2010**, *132*, 12741-12747.

(16) Volk, M.; Kholodenko, Y.; Lu, H. S. M.; Gooding, E. A.; DeGrado, W. F.; Hochstrasser, R. M. Peptide Conformational Dynamics and Vibrational Stark Effects Following Photoinitiated Disulfide Cleavage. *J. Phys. Chem. B* **1997**, *101*, 8607-8616.

(17) Brauns, E. B.; Madaras, M. L.; Coleman, R. S.; Murphy, C. J.; Berg, M. A. Measurement of Local DNA Reorganization on the Picosecond and Nanosecond Time Scales. *J. Am. Chem. Soc.* **1999**, *121*, 11644-11649.

(18) Pal, S. K.; Zhao, L.; Zewail, A. H. Water at DNA Surfaces: Ultrafast Dynamics in Minor Groove Recognition. *Proc. Natl. Acad. Sci. U.S.A.* **2003**, *100*, 8113-8118.

(19) Pal, S. K.; Zhao, L.; Xia, T.; Zewail, A. H. Site and Sequence-Selective Ultrafast Hydration of DNA. *Proc. Natl. Acad. Sci. U.S.A.* **2003**, 100, 13746-13751.

(20) Dallmann, A.; Pfaffe, M.; Mügge, C.; Mahrwald, R.; Kovalenko, S. A.; Ernsting, N. P. Local THz Time Domain Spectroscopy of Duplex DNA via Fluorescence of an Embedded Probe. *J. Phys. Chem. B* **2009**, *113*, 15619-15628.

(21) Banerjee, D.; Pal, S. K. Dynamics in the DNA Recognition by DAPI: Exploration of the Various Binding Modes. *J. Phys, Chem. B* **2008**, *112*, 1016-1021.

(22) Andreatta, D.; Sen, S.; Pérez Lustres, J. L.; Kovalenko, S. A.; Ernsting, N. P.; Murphy, C. J.; Coleman, R. S.; Berg, M. A. Ultrafast Dynamics in DNA: "Fraying" at the End of the Helix. *J. Am. Chem. Soc.* **2006**, *128*, 6885-6892.

(23) Andreatta, D.; Pérez Lustres, J. L.; Kovalenko, S. A.; Ernsting, N. P.; Murphy, C. J.; Coleman, R. S.; Berg, M. A. Power-Law Solvation Dynamics in DNA over Six Decades in Time. *J. Am. Chem. Soc.* **2005**, *127*, 7270-7271.

(24) Pal, N.; Verma, S. D.; Sen, S. Probe Position Dependence of DNA Dynamics: Comparison of the Time-Resolved Stokes Shift of Groove-Bound to Base-Stacked Probes. *J. Am. Chem. Soc.* **2010**, *132*, 9277-9279.

(25) Verma, S. D.; Pal, N.; Singh, M. K.; Sen, S. Probe Position-Dependent Counterion Dynamics in DNA: Comparison of Time-Resolved Stokes Shift of Groove-Bound to Base-Stacked Probes in the Presence of Different Monovalent Counterions. *J. Phys. Chem. Lett.*, **2012**, *3*, 2621-2626.

(26) Verma, S. D.; Pal, N.; Singh, M. K.; Sen, S. Sequence-Dependent Solvation Dynamics of Minor-Groove Bound Ligand Inside Duplex-DNA. *J. Phys. Chem. B* **2015**, *119*, 11019-11029.

(27) Pal, N.; Shweta, H.; Singh, M. K.; Verma, S. D.; Sen, S. Power-Law Solvation Dynamics in G-Quadruplex DNA: Role of Hydration Dynamics on Ligand Solvation inside DNA. *J. Phys. Chem. Lett.* **2015,** *6*, 1754-1760.

(28) Singh, M. K.; Shweta, H.; Sen, S. Dispersed Dynamics of Solvation in G-quadruplex DNA: Comparison of Dynamic Stokes Shifts of Probes in Parallel and Antiparallel Quadruplex Structures. *Methods Appl. Fluoresc.* **2016**, *4*, 034009.

(29) Sen, S.; Gearheart, L. A.; Rivers, E.; Liu, H.; Coleman, R. S.; Murphy, C. J.; Berg, M. A. Role of Monovalent Counterions in the Ultrafast Dynamics of DNA. *J. Phys. Chem. B* **2006**, *110*, 13248-13255.

(30) Sajadi, M.; Furse, K. E.; Zhang, X. X.; Dehmel, L.; Kovalenko, S. A.; Corcelli, S. A.; Ernsting, N. P. Detection of DNA–Ligand Binding Oscillations by Stokes-Shift Measurements. *Angew. Chem. Int. Ed.* **2011**, *50*, 9501-9505.

(31) Bagchi, B. Anomalous Power Law Decay in Solvation Dynamics of DNA: A Mode Coupling Theory Analysis of Ion Contribution. *Mol. Phys.* **2014**, *112*, 1418-1426.

(32) Granek, R.; Klafter, J. Fractons in Proteins: Can They Lead to Anomalously Decaying Time Autocorrelations? *Phys. Rev. Lett.* **2005**, *95*, 098106.

(33) Pal, S.; Maiti, P. K.; Bagchi, B.; Hynes, J. T. Multiple Time Scales in Solvation Dynamics of DNA in Aqueous Solution: The Role of Water, Counterions, and Cross-Correlations. *J. Phys. Chem. B* **2006**, *110*, 26396-26402.

(34) Sen, S.; Andreatta, D.; Ponomarev, S. Y.; Beveridge, D. L.; Berg, M. A. Dynamics of Water and Ions Near DNA: Comparison of Simulation to Time-Resolved Stokes-Shift Experiments. *J. Am. Chem. Soc.* **2009**, *131*, 1724-1735.

(35) Furse, K. E.; Corcelli, S. A. The Dynamics of Water at DNA Interfaces: Computational Studies of Hoechst 33258 Bound to DNA. *J. Am. Chem. Soc.* **2008**, *130*, 13103-13109.

(36) Furse, K. E.; Corcelli, S. A. Dynamical Signature of Abasic Damage in DNA. *J. Am. Chem. Soc.* **2011**, *133*, 720-723.

(37) Furse, K. E.; Corcelli, S. A. Molecular Dynamics Simulations of DNA Solvation Dynamics. *J. Phys. Chem. Lett.* **2010**, *1*, 1813-1820.

(38) Furse, K. E.; Corcelli, S. A. Effects of an Unnatural Base Pair Replacement on the Structure and Dynamics of DNA and Neighboring Water and Ions. *J. Phys. Chem. B* **2010**, *114*, 9934-9945.

(39) Jana, B.; Pal, S.; Bagchi, B. Enhanced Tetrahedral Ordering of Water Molecules in Minor Grooves of DNA: Relative Role of DNA Rigidity, Nanoconfinement, and Surface Specific Interactions. *J. Phys. Chem. B* **2010**, *114*, 3633-3638.

(40) Pal, S.; Maiti, P. K.; Bagchi, B. Exploring DNA Groove Water Dynamics through Hydrogen Bond Lifetime and Orientational Relaxation. *J. Chem. Phys.* **2006**, *125*, 234903.

(41) Ponomarev, S. Y.; Thayer, K. M.; Beveridge, D. L. Ion Motions in Molecular Dynamics Simulations on DNA. *Proc. Natl. Acad. Sci. U.S.A.* **2004**, *101*, 14771-14775.

(42) Pal, S.; Maiti, P. K.; Bagchi, B. Anisotropic and Sub-Diffusive Water Motion at the Surface of DNA and of an Anionic Micelle. *J. Phys. Condens. Matter* **2005**, *17*, S4317.

(43) Halle, B.; Nilsson, L. Does the Dynamic Stokes Shift Report on Slow Protein Hydration Dynamics? *J. Phys. Chem. B* **2009**, *113*, 8210-8213.

(44) Nilsson, L.; Halle, B. Molecular Origin of Time-Dependent Fluorescence Shifts in Proteins. *Proc. Natl. Acad. Sci. U.S.A.* **2005**, *102*, 13867-13872.

(45) Golosov, A. A.; Karplus, M. Probing Polar Solvation Dynamics in Proteins: A Molecular Dynamics Simulation Analysis. *J. Phys. Chem. B* **2007**, *111*, 1482-1490.

(46) Sterpone, F.; Stirnemann, G.; Laage, D. Magnitude and Molecular Origin of Water Slowdown Next to a Protein. *J. Am. Chem. Soc.* **2012**, *134*, 4116-4119.

(47) Pizziutti, F.; Marchi, M.; Sterpone, F.; Rossky, P. J. How Protein Surfaces Induce Anomalous Dynamics of Hydration Water. *J. Phys. Chem. B* **2007**, *111*, 7584-7590.

(48) Bizzarri, A. R.; Cannistraro, S. Molecular Dynamics of Water at the Protein−Solvent Interface. *J. Phys. Chem. B* **2002**, *106*, 6617-6633.

(49) Lagi, M.; Baglioni, P.; Chen, S. H. Logarithmic Decay in Single-Particle Relaxation of Hydrated Lysozyme Powder. *Phys. Rev. Lett.* **2009**, *103*, 108102.

(50) Kämpf, K; Klameth, F.; Vogel, M. Power-Law and Logarithmic Relaxations of Hydrated Proteins: A Molecular Dynamics Simulations Study. *J. Chem. Phys.* **2012**, *137*, 205105.

(51) Li, T. Validity of Linear Response Theory for Time-Dependent Fluorescence in Staphylococcus Nuclease. *J. Phys. Chem. B* **2014**, *118*, 12952-12959.

(52) Bagchi, B. Water Dynamics in the Hydration Layer around Proteins and Micelles. *Chem. Rev.* **2005**, *105*, 3197-3219.

(53) Pal, S. K.; Zewail, A. H. Dynamics of Water in Biological Recognition. *Chem. Rev.* **2004**, 104, 2099-2124.

(54) Berg, M. A.; Coleman, R. S.; Murphy, C. Nanoscale Structure and Dynamics of DNA. *Phys. Chem. Chem. Phys.* **2008**, *10*, 1229-1242.

(55) Bhattacharyya, K. Nature of Biological Water: A Femtosecond Study. *Chem. Commun.* **2008**, *0*, 2848-2857.

(56) Jimenez, R.; Fleming, G. R.; Kumar, P. V.; Maroncelli, M. Femtosecond Solvation Dynamics of Water. *Nature* **1994**, *369*, 471-473.

(57) Yang, Y.; Qin, Y.; Ding, Q.; Bakhtina, M.; Wang, L.; Tsai, M. D.; Zhong, D. Ultrafast Water Dynamics at the Interface of the Polymerase−DNA Binding Complex. *Biochemistry* **2014**, *53*, 5405-5413.

(58) Sen, S.; Paraggio, N. A.; Gearheart, L. A.; Connor, E. E.; Issa, A.; Coleman, R. S.; Wilson, D. M. III; Wyatt, M. D.; Berg, M. A. Effect of Protein Binding on Ultrafast DNA Dynamics: Characterization of a DNA: APE1 Complex. *Biophys. J.* **2005**, *89*, 4129-4138.

(59) Zhong, D.; Pal, S. K.; Zewail, A. H. Femtosecond studies of Protein-DNA Binding and Dynamics: Histone 1. *Chem.Phys.Chem* **2001**, *2*, 219-227.

(60) Duboué-Dijon, E.; Fogarty, A. C.; Hynes, J. T.; Laage, D. Dynamic Disorder in the DNA Hydration Shell. *J. Am. Chem. Soc.* **2016**, *138*, 7610-7620.

(61) Vega, M. C.; Garcia Saez, I.; Aymami, J.; Eritja, R.; Van der Marel, G. A.; Van Boom, J. H.; Rich, A.; Coll, M. Three-Dimensional Crystal Structure of the A-Tract DNA Dodecamer d(CGCAAATTTGCG) Complexed with the Minor-Groove-Binding Drug Hoechst 33258. *Eur. J. Biochem*. **1994,** *222*, 721-726.

(62) Pjura, P. E.; Grzeskowiak, K.; Dickerson, R. E. Binding of Hoechst 33258 to the Minor Groove of B-DNA. *J. Mol. Biol.* **1987,** *197*, 257-271.

(63) Berendsen, H. J. C.; Grigera, J. R.; Straatsma, J. R.The missing term in effective pair potentials. *J. Phys. Chem.* **1987**, *91*, 6269–6271.

(64) Aqvist, J. Ion Water Interaction Potentials derived from Free Energy Perturbation Simulations. *J. Phys. Chem* **1990**, *94*, 8021-8024.

(65) Smith, D. E.; Dang, L. X. Computer Simulations of NaCl Association in Polarizable Water. *J. Chem. Phys*. **1994**, *100*, 3757-3766.

(66) Uberuaga, B. P.; Anghel, M.; Voter, A. F. Synchronization of Trajectories in Canonical Molecular-Dynamics Simulations: Observation, Explanation, and Exploitation. *J. Chem. Phys.* **2004**, *120*, 6363-6374.

(67) Case, D. A.; Babin, V.; Berryman, J. T.; Betz, R. M.; Cai, Q.; Cerutti, D. S.; Cheatham, T. E. III; Darden, T. A.; Duke, R. E.; Gohlke, H.; Goetz, A. H.; Gusarov, S.; Homeyer, N.; Janowski, P.; Kaus, J.; Kolossváry, I.; Kovalenko, A.; Lee, T. S.; LeGrand, S.; Luchko, T.; Luo, R.; Madej, B.; Merz, K. M.; Paesani, F.; Roe, D. R.; Roitberg, A.; Sagui, C.; Salomon-Ferrer, R.; Seabra, G.; Simmerling, C. L.; Smith, W.; Swails, J.; Walker, R. C.;Wang, J.; Wolf, R. M.; Wu, X.; P.A. Kollman, P. A. *AMBER 14*, University of California, San Francisco, **2014**.

(68) Ryckaert, J. P.; Ciccotti, G.; Berendsen, H. J. C. Numerical integration of the Cartesian Equations of Motion of a Systewith Constraints: Molecular Dynamics of n-Alkanes. *J. Comput. Phys.* **1977**, *23*, 327-341.

(69) Darden, T.; York, D.; Pedersen, L. Particle Mesh Ewald: An N·log(N) Method for Ewald Sums in Large Systems. *J. Chem. Phys.* **1993**, *98*, 10089.

(70) Humphrey, W.; Dalke, A.; Schulten, K. VMD: Visual Molecular Dynamics. *J. Mol. Graphics* **1996**, *14*, 33-38

(71) Pettersen, E. F.; Goddard, T. D.; Huang, C. C.; Couch, G. S.; Greenblatt, D. M.; Meng, E. C.; Ferrin, T. E. UCSF Chimera—A Visualization System for Exploratory Research and Analysis. *J. Comput. Chem.* **2004**, *25*, 1605-1612.

(72) Gorner, H. Direct and Sensitized Photoprocesses of bis-Benzimidazole Dyes and the Effects of Surfactants and DNA. *Photochem. Photobiol.* **2001**, *73***,** 339–348.

(73) Breusegem, S. Y.; Clegg, R. M.; Loontiens, F. G. Base-Sequence Specificity of Hoechst 33258 and DAPI Binding to Five $(A/T)_4$ DNA Sites with Kinetic Evidence for More than One High-Affinity Hoechst 33258-AATT Complex. *J. Mol. Biol.* **2002**, *315*, 1049−1061.

(74) Vlieghe, D.; Sponer, J.; Meervelt, L. V. Crystal Structure of d(GGCCAATTGG) Complexed with DAPI Reveals Novel Binding Mode. *Biochemistry* **1999**, *38*, 16443−16451.

(75) Fennell, C. J.; Gezelter, J. D. Is the Ewald Summation Still Necessary? Pairwise Alternatives to the Accepted Standard for Long-Range Electrostatics. *J. Chem. Phys.* **2006**, *124*, 234104.

(76) Perez, A.; Marchan, I.; Svozil, D.; Sponer, J.; Cheatham, T. E. 3rd, Laughton, C. A.; Orozco, M. Refinement of AMBER Force Field for Nucleic Acids: Improving the Description of α/γ Conformers. *Biophys. J.* **2007**, *92*, 3817-3829.

Chapter 5

Effect of T·T-Mismatch on Solvation Dynamics in the Minor Groove of DNA

The preceding chapter discussed the results of solvation dynamics in the minor groove of Watson-Crick duplex-DNA, created by two different A_nT_n rich sequences. The power-law solvation dynamics probed by groove-bound Hoechst were shown to be different in the DNA with two central A_nT_n sequences. Direct comparison of TRFSS experiment to MD simulations provided the intricate details of the dynamics in the two DNA systems, showing that it is either the local DNA or the water motions that control the dispersed solvation dynamics in the minor groove of DNA created by two different A_nT_n sequences. In this chapter, TRFSS results of two popular minor groove binders, Hoechst and DAPI, are reported which show that these grove-binders can sense the effect of local DNA damage (a T·T mismatch base-pair) introduced in the minor groove of DNA near the ligand binding site. The results presented here will clearly show that TRFSS experiments are sensitive enough to capture the effect of local distortions of a mismatch base-pair to the local collective solvation dynamics in the minor groove of DNA.

5.1. Introduction

Base mismatch in DNA is a type of DNA damage (or defect) in which two non-complementary bases are paired within the stacks of normal Watson-Crick base-pairs of duplex DNA.[1] Such mismatches are associated with 10-30% of spontaneous cancer in various tissues and in some of hereditary cancers like colorectal one.[2,3] DNA mismatches can arise from incorrect incorporation of bases during heteroduplex formation through recombination,[4] DNA replication,[5] as well as from harsh effect of mutagenic chemicals, radiation and spontaneous deamination.[6]

DNA mismatches are unwanted for genomic stability, which get quickly corrected by mismatch repair enzymes post replication.[6,7] MutS in *E. coli* (and homologous MutSα proteins in humans) plays vital role in the first step of such DNA mismatch recognition, followed by repair of the mismatch involving other proteins.[5-8] DNA mismatches can form in purine-purine and pyrimidine-pyrimidine (transversion) as well as in purine-pyrimidine (transduction) base combinations. Several earlier studies showed that these mismatches induce local structural changes in DNA double helix which are different for different types of mismatches,[9-12] although such local changes are found to depend on neighbouring canonical base-pair sequence in the DNA.[11,13,14] Extensive exploration toward this end has happened over past decades, using both experiments and computer simulation, to understand how local structural changes at/near mismatch sites provide the cue to repair enzymes for mismatch recognition.[9-19] In fact, it has been shown that purine-pyrimidine (G·T) mismatches are better repaired compared to only purine-purine or pyrimidine-pyrimidine ones by the repair proteins.[18] Higher repair efficiencies of purine-purine mismatches compared to pyrimidine-pyrimidine ones are also reported.[10,11] Recent simulation study, however, indicated that it is rather difficult to find a simple correlation between only structural changes of mismatch sites and the differential efficiencies of mismatch recognition by repair enzymes.[16]

Actually, most of the previous studies focused on measuring the local structural changes of mismatched bases *per se* – so as to find the clue for differential mismatch repair efficiency of repair enzymes, but did not focus much on the effect of such structural changes in the surrounding water and ion environment and their collective dynamics, which are also believed to be important for the mismatch recognition by repair enzymes. This chapter focuses on such local collective dynamics of water, DNA and ions from ~100 fs to 10 ns, measured near a mismatch site in the AT-rich minor groove of DNA using two groove binders, and compare the same with the dynamics measured in the minor groove of normal-DNA. The results presented here show that a single T·T mismatch base-pair inside DNA drastically induces the collective dynamics near the mismatch site, compared to that in normal-DNA. Such changes in dynamics, introduced by the base-mismatch in the *minor groove* of DNA, may have vital importance in the mismatch recognition by enzymes and in subsequent repair mechanism, because repair enzymes (MutS in *E. coli.* and MSH6 in humans) are found to bind through intercalation of phenylalanine and hydrogen bonding of glutamate residues from the *minor groove* side.[20,21]

X-ray crystallography[22,23] and NMR spectroscopy[9,11,24,25] have been widely used to characterize the structural/dynamical changes of different mismatches in duplex DNA. Brown *et al.* reported the first X-ray crystal structure of duplex DNA containing G·T mismatch, indicating the importance of G·T wobble motion for the mismatch recognition by enzymes.[22] Subsequently, several other X-ray and NMR studies reported the structural/dynamical aspects of other mismatches and their effects on overall DNA structures.[9,11,22-25] All these studies found minimal effect of mismatch on the global conformation of DNA double helix. Interestingly, however, NMR studies found that different mismatches have different base-pair lifetimes – with G·G, A·A and C·C having longer lifetimes than T·T mismatch.[9]

Time-resolved fluorescence anisotropy decay of 2-aminopurine (2-AP: an adenine analog), opposite different mismatched bases and base-pairs, has been utilized to follow the structural dynamics of mismatched bases/base-pairs.[26,27] While the overall rotational dynamics of whole DNA, probed by 2-AP, was found to be insensitive to mismatch type, the fast internal local rotational motions of 2-AP opposite/near mismatch sites were found to vary depending on the mismatch type – indicating that the alteration of this motional dynamics may be used as signal by repair enzymes for the differential mismatch recognition.[26,27] Recent fluorescence correlation spectroscopy (FCS) study also showed that a single mismatched base can spontaneously flip out of DNA double helix with long extra-helical lifetime.[15] However, all these studies focused on local structural/dynamical changes of mismatched bases *per se*.

Much of the understanding of structure and dynamics of DNA mismatches can be obtained from molecular dynamics (MD) simulation studies, although only few are reported in literature. MD simulation results have been compared for normal and mismatched-base containing DNA to discern the local structural dynamics of mismatched bases and their effect on helical parameters of DNA such as rise, twist, roll, tilt and base-pair opening – all of which showed differences in mismatched-DNA compared to those in normal-DNA.[16,18] Simulation on DNA containing T·T mismatch found that T·T wobbling is dependent on the nearest neighbour canonical sequence, and there exists three-centred H-bonds at the mismatch site.[19] More recent simulation, together with free-energy profiling of DNA-bending using umbrella sampling, found that DNA containing purine-pyrimidine mismatches are least destabilizing, followed by intermediately destabilizing DNA with purine-purine, and most destabilizing with pyrimidine-pyrimidine mismatches.[10] The ease of bending in such DNA was found partially correlate to the binding affinity of MutS.[14] Simulation with selective integrated tempering sampling (SITS) found that flipping of single mismatched base has much lower free energy cost than simultaneous flipping of both bases.[17] Nonetheless, these simulations were rather short and mainly focused on the structural dynamics of mismatched base-pairs in DNA.

Recently, Rossetti *et al*. reported very long simulation and through analysis of trajectories of DNA containing all possible mismatches, together with NMR studies, to conclude that it is rather hard to find a simple correlation between only structural dynamics of mismatched base-pairs and efficiencies of mismatch recognition by repair enzymes, except for some general correlation between overall breathing/structural changes in DNA and the relative mismatch recognition by MutS.[16] However, most importantly, this study showed that the mismatched bases induce significant alteration in the surrounding ion environment, and (possibly) hydration structure, near the mismatch sites.[16] This study also indicated that the transfer of signal to the repair enzymes possibly occur through-space involving surrounding water and ions in the groove.[16] This is because, changes in water and ion environment are intimately connected to the local conformational changes in DNA. In fact, the hypothesis that – variation in local DNA motion, coupled to surrounding water and ion dynamics, near mismatch sites may be more important than the structural changes of mismatched bases *per se* for mismatch recognition – is rational because there remains strong electrostatic coupling among negatively charged DNA and the surrounding positively charged counterions and dipolar water.

The hypothesis that mismatched base-pair affects the local dynamics in DNA is tested in this chapter, which looks at the changes in the collective dynamics of DNA, water and Na^+ counterions near a T·T mismatch site in the AT-rich minor groove of DNA. The collective solvation dynamics is measured by monitoring time-resolved fluorescence Stokes shifts (TRFSS) of two popular minor groove binders, Hoechst 33258 and DAPI, and compared the same with the dynamics measured in the minor groove of normal DNA over five decades of time from 100 fs to 10 ns. Monitoring the Hoechst and DAPI (ligands) fluorescence and their time evaluation, results show that fluorescence properties of the ligands are affected significantly in the minor groove containing T·T mismatch, as compared to minor groove of normal-DNA. More importantly, it is found that the nature of dynamic Stokes shifts of Hoechst and DAPI are somewhat different in the minor groove of normal-DNA; however, introduction of T·T mismatch in the minor groove gives rise to very similar Stokes shift dynamics, as probed by both minor groove binders, which follow a single power-law relaxation (with exponent ~0.23-0.24) over five decades of time from ~100 fs to 10 ns. Fluorescence anisotropy decays of the ligands bound to mismatched- and normal-DNA are found to be nearly identical for both ligands, which originate from overall rotational motion of the DNA/ligand complexes. This suggests that Stokes shift dynamics and their changes in mismatched-DNA, compared to normal-DNA, originate purely from relaxation of electrostatic interaction energy of the ligands with surrounding charged/dipolar molecules, and not from any internal local rotational motion of the probe-ligands. These results are significant because the very similar Stokes shift dynamics probed by both minor groove binders in T·T mismatch containing DNA (T·T–DNA), despite their differences in normal-DNA, may actually indicate that incorporation of single base-mismatch induces unique coupled dynamics, for a given flanking canonical base-sequence, in the minor groove of DNA. Such collective dynamics in the minor groove may have important role in the mismatch recognition of repair enzymes and subsequent repair mechanism, because repair enzymes bind to the mismatched-site from the minor groove side.[20,21]

5.2. Materials and Methods

DNA minor groove binders, DAPI (4',6-diamidino-2-phenylindole, dilactate) and Hoechst 33258 (2′-(4-hydroxyphenyl)-5-(4-methyl-1-piperazinyl)-2,5′-bi(1H-benzimidazole) trihydrochloride hydrate) were purchased from Sigma-Aldrich, and were used without further purification (Figure 5.1A). Self-complementary normal (14-mer) DNA and T·T–DNA (13-mer) oligonucleotides of sequences 5'-CGCGCAATTGCGCG-3' and 5'-CGCGCATTGCGCG-3', respectively, were from Integrated DNA Technologies. Solvents were from Spectrochem (UV-grade) and Merck (HPLC-grade). B-form DNA duplexes were prepared by re-suspending single-stranded oligonucleotides in buffer of 100 mM sodium phosphate with 50 mM NaCl of pH 7, and annealing them from 95°C to room temperature (25°C) over ~5 hours. Formation of double-stranded B-DNA was confirmed by circular dichroism (CD) spectra measured using a CD spectrometer. All samples were prepared in HPLC grade water (Merck). All experiments were performed with concentration ratios of

[Ligand]/[DNA] of 1:5 for normal-DNA and 1:25 for T·T–DNA where Hoechst and DAPI fluorescence reach saturation, such that nearly all ligands remain bound to the DNA (see Figure 5.2A). Fluorescence decays were measured at magic angle using TCSPC and UPC, and anisotropy decays were measured in TCSPC technique (see chapter 3 for details). UPC measurements were carried out at concentrations; [DAPI] or [Hoechst] = 20 μM and [DNA] = 100 μM for normal-DNA, and [DAPI] or [Hoechst] = 20 μM and [DNA] = 500 μM for T·T–DNA. TCSPC measurements were carried out with samples of concentrations, [DAPI] or [Hoechst] = 3 μM and [DNA] = 15 μM for normal-DNA, and [DAPI] or [Hoechst] = 3 μM and [DNA] = 75 μM for T·T–DNA.

5.3. Results and Discussion

5.3.1. CD Spectroscopy: Conformation of Normal- and T·T-DNA

Right handed B-form structures of normal- and T·T–DNA in absence and presence of the minor groove binders (Hoechst and DAPI: Figure 5.1A) were confirmed from the CD spectra. Figure 5.1B shows the CD spectra of bare normal- and T·T–DNA (15 mM) having characteristic negative peak near ~255 nm, confirming that both DNA have B-form structures. The effect of ligand binding to the structures of DNA and the induced-CD of ligands inside DNA

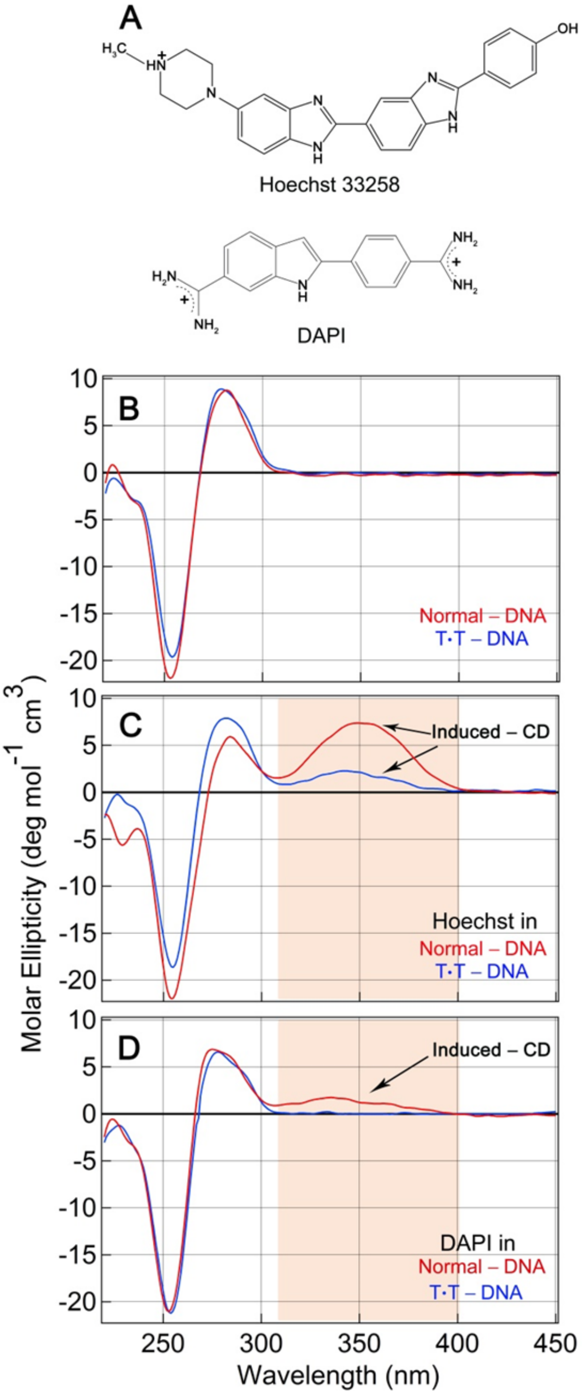

Figure 5.1: (A) Molecular structures of Hoechst 33258 and DAPI. (B) Circular dichroism (CD) spectra of 14-mer normal- and 13-mer T·T–DNA (15 mM), showing characteristic negative peak ~255 nm confirming right handed B-form DNA. See figure for legends. (C) CD spectra of normal- and T·T–DNA (15 mM) in presence of Hoechst (15 mM). Spectra show clear induced CD of Hoechst with peak near 350 nm. (D) CD spectra of normal- and T·T–DNA (15 mM) in presence of DAPI (15 mM). Spectrum in normal-DNA show induced CD of DAPI with peak near 350 nm, although induced CD of DAPI is nearly absent in T·T–DNA. See text for details.

were also studied. Figure 5.1C shows the CD spectra of Hoechst (15 mM) in normal- and T·T–DNA (15 mM). It can be seen that binding of Hoechst retains the characteristics of right handed B-form of DNA. Moreover, Hoechst shows clear induced-CD spectra with peaks ~350 nm upon binding to the minor grooves of normal- and T·T–DNA. The lower amount of induced-CD signal in T·T–DNA may be attributed to the slight conformational change and/or environmental effect on the excitation probability of ligand in T·T–DNA, compared to those in normal–DNA (see chapter 3 for details). Figure 5.1D plots the CD spectra of DAPI (15 mM) in normal- and T·T–DNA (15 mM), which again show that DAPI also retains the B-form of normal- and T·T–DNA. It is however seen that induced-CD signal for DAPI in normal DNA is small while that in the T·T–DNA is negligible. This difference in induced CD can arise from conformational or environmental changes, similar as observed in case of Hoechst. However, DAPI has been shown to bind to the minor groove of DNA containing T.T mismatch with negligible structural changes, compared to that in normal-DNA.[28] Thus, it may be that the effect of environment on excitation probability is more pronounced on the induced CD of ligands binding to T·T–DNA. Overall, it is seen that the right handed B-form of normal and T·T–DNA remains same upon ligand binding.

5.3.2. Steady State Fluorescence Spectra: Effect of T·T–Mismatch

Hoechst and DAPI are widely used as fluorescent markers (ligands) for biochemical, cytochemical and fluorescence imaging studies.[29,30] Both Hoechst and DAPI show very low fluorescence quantum yield in bulk water, but their quantum yields are enhanced by several folds upon binding to DNA minor groove.[31,32] These ligands preferentially bind to minor grooves having A_nT_n-rich sequences, which sit iso-helically in the floor of the minor groove through strong (bifurcated) hydrogen bonds as well as electrostatic and van der Waals interactions with DNA.[33,34] In water, the fluorescence quantum yields of Hoechst and DAPI are very low (~0.015 - 0.046) which arise from non-radiative processes, possibly involving excited-sate proton transfer and/or rotation of flexible bonds between aromatic rings.[31,32] On binding to minor grooves of DNA the fluorescence signal of these ligands increases several fold, which occurs due to suppression of the non-radiative pathways. It has been shown that the binding affinity, fluorescence quantum yields of these ligands as well as the dynamics probed by such ligands depend on base-sequence near their binding site.[35-37] However, it is not known how the binding affinity and static/dynamic fluorescence properties of these ligands change upon incorporation of a mismatched base-pair in the minor groove near their binding sites. In this context, two natural questions arise: (1) whether the changes in the static and dynamic fluorescence of these ligands are at all sensitive to introduction of a base-mismatch near their binding site or not? (2) If so then what is the effect of base-mismatch on the local dynamics sensed by these ligands?

Figure 5.2A shows the titration of ligands' fluorescence with normal– and T·T–DNA, where fluorescence signals of ligands were monitored keeping their concentration constant and varying the DNA amount. It is clear from this plot that binding affinities of the ligands decrease due to introduction of T·T mismatch in the minor groove of DNA: the 50% signal increment occurs at DNA/ligand ratios of ~1 and ~2 for DAPI in normal- and T·T–DNA, respectively, while those ratios are ~1 and ~4.6 for Hoechst in normal- and T·T–DNA, respectively. Consequently, the saturation of ligands' fluorescence occurs at lower and higher DNA concentrations in normal- and T·T–DNA, respectively. Thus, DNA/ligand ratios used in the final samples for time-resolved measurements are different for normal- and T·T–DNA.

Figure 5.2B compares the corrected fluorescence spectra of Hoechst and DAPI in normal- and T·T–DNA (at DNA concentrations where ligands' fluorescence saturate) and also in buffer. Upon binding to minor groove of normal–DNA, Hoechst and DAPI show significant fluorescence signal enhancement of ~160 and ~40 times, respectively, compared to that in buffer. However, the increments become ~36 and ~29 times when Hoechst and DAPI are bound to the T·T–DNA, respectively, compared to buffer. The spectral peaks of Hoechst in buffer, normal–DNA and T·T–DNA are found to be at ~515 nm, ~457 nm and ~480 nm, respectively, while those for DAPI are found at ~490 nm, ~463 nm and ~463 nm, respectively (Figure 5.2C). The Hoechst and DAPI spectra are blue shifted by ~58 nm and ~27 nm, respectively, when bound to normal-DNA, compared to those in buffer. This indicates that interior of minor groove of normal-DNA is less polar compared to bulk water. The solvent polarity dependent spectral shifts are found to be larger for Hoechst compare to DAPI (Figure 5.3). Importantly,

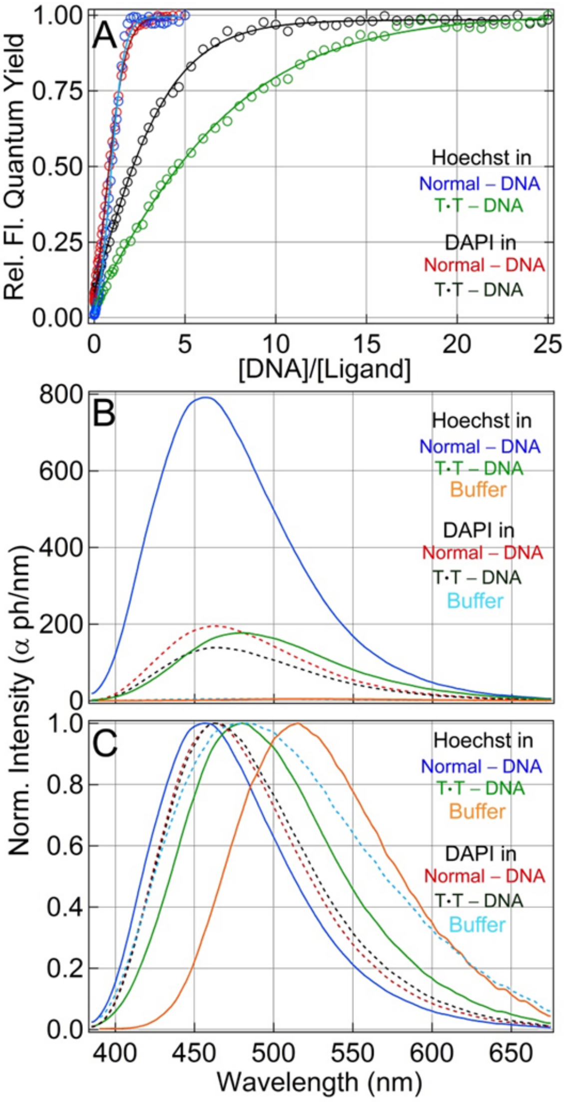

Figure 5.2: (A) Titration of ligands with normal- and T·T–DNA, in which fluorescence signals of ligands are monitored keeping their concentration constant and varying the DNA concentration. Ligands show lower binding affinity to T·T–DNA, compared to normal-DNA. (B) Corrected relative fluorescence spectra of Hoechst and DAPI in buffer and bound to minor grooves of normal- and T·T–DNA. Relative changes in fluorescence indicate ligands sense different local environments in the three systems (buffer, normal- and T·T–DNA). (C) Same spectra normalized to one, showing the relative peak shifts. See text for details.

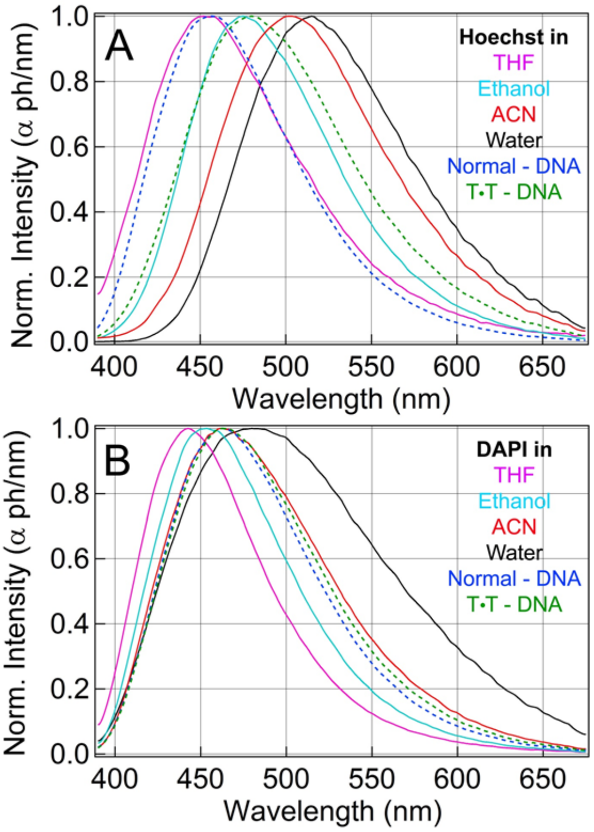

Figure 5.3: Solvent (polarity) dependent spectral shifts of (A) Hoechst and (B) DAPI. Spectra of Hoechst (A) and DAPI (B) in normal- and T·T–DNA are also included for comparison. It is seen Hoechst senses local environment in normal-DNA that is similar to tetrahydrofuran (THF) while that in T·T–DNA is in-between ethanol and acetonitrile (ACN), with a bit more toward ethanol (A). DAPI senses environment in normal and T·T–DNA which is similar to that in-between ethanol and acetonitrile (ACN), with a bit more like ACN (B); the spectrum in T·T–DNA also gets broadened due to local environmental change. The solvent dependent spectral shifts are found to be larger for Hoechst than DAPI.

however, it is found that upon binding to the T·T–DNA, Hoechst spectrum shifts toward longer wavelength by ~23 nm compared to that in normal-DNA; although, DAPI spectral peak remains same in T·T–DNA except small spectral broadening, compared to that in normal-DNA. Comparison of the fluorescence spectra of Hoechst and DAPI in DNA and in common solvents shows that introduction of T·T mismatch induces relatively more polar environment around the ligands inside T·T–DNA, compared to normal-DNA, which more-or-less lies in-between the polarity of ethanol and acetonitrile (see Figure 5.3). This occurs possibly because of change in hydration level in the T·T–DNA due to wobbling of T·T base-pair which may allow water penetration near the ligand binding site. The decrease in ligands' fluorescence signals in T·T–DNA, compared to normal one, also refers to a similar effect of local polarity change. Thus, the steady state fluorescence spectra clearly show that introduction of a single mismatched base-pair near the binding site of minor groove binders significantly alters the static fluorescent properties of the ligands. Hence, minor groove binders are good reporters for mismatch recognition, at least for the T·T mismatch studied here. In fact, the next chapter will show that ligand fluorescence depends significantly on other mismatches introduced in the minor groove of DNA as well.

5.3.3. Fluorescence Decays: Effect of T·T–Mismatch

The time-resolved fluorescence data of ligands in normal- and T·T–DNA are now compared to see the effect of mismatch on fluorescence decays of the minor groove binders. Actually, to monitor the effect of T·T mismatch on collective (solvation) dynamics over

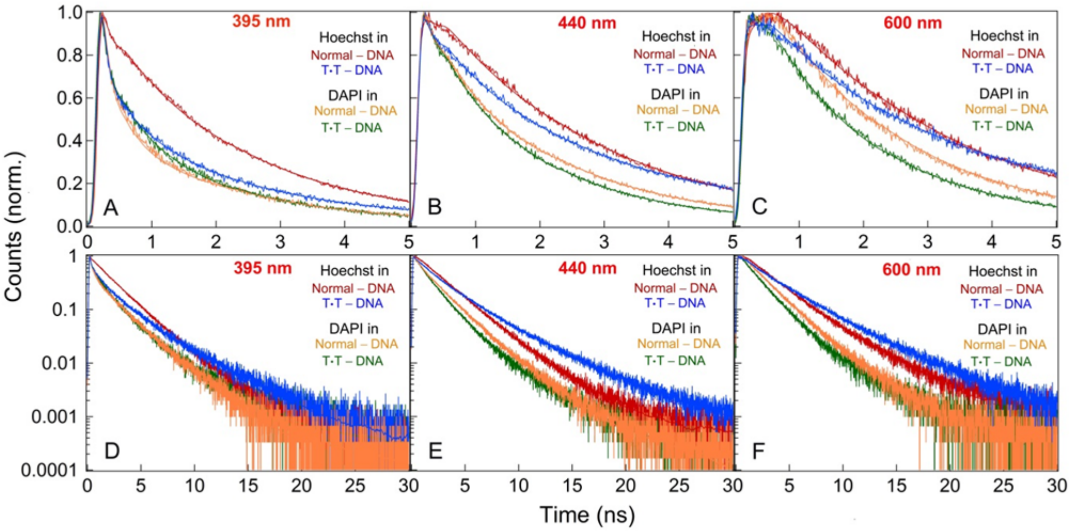

Figure 5.4: Fluorescence decays of Hoechst and DAPI bound to minor groove of normal- and T·T–DNA, measured in TCSPC at blue-side (395 nm), near peak (440 nm) and red-side (600 nm) of the fluorescence spectra. (A) – (C) Decays in short time-range upto 5 ns, and (D) – (F) decays in the full time-range plotted in semi-log scale. Lines through raw decays are fits using sum of 3-4 exponentials. Data show substantial effect of T·T mismatch, compare to normal-DNA. See text for details.

broad time range, we measured wavelength dependent fluorescence decays of Hoechst and DAPI in the minor grooves of normal- and T·T–DNA using UPC and TCSPC techniques. Total 20–22 fluorescence decays were measured in UPC and TCSPC for each DNA/ligand sample. The raw decays follow characteristic features of solvation dynamics, showing fast-decay at shorter wavelengths, fast-rise (or decay) followed by slow decay near peak wavelengths, and slow-rise followed by slow-decay at longer wavelengths. These decays were fitted using sum of 3-4 exponentials, and the fitted parameters were used in the re-construction of TRES following procedures reported earlier (see chapter 3 for details).

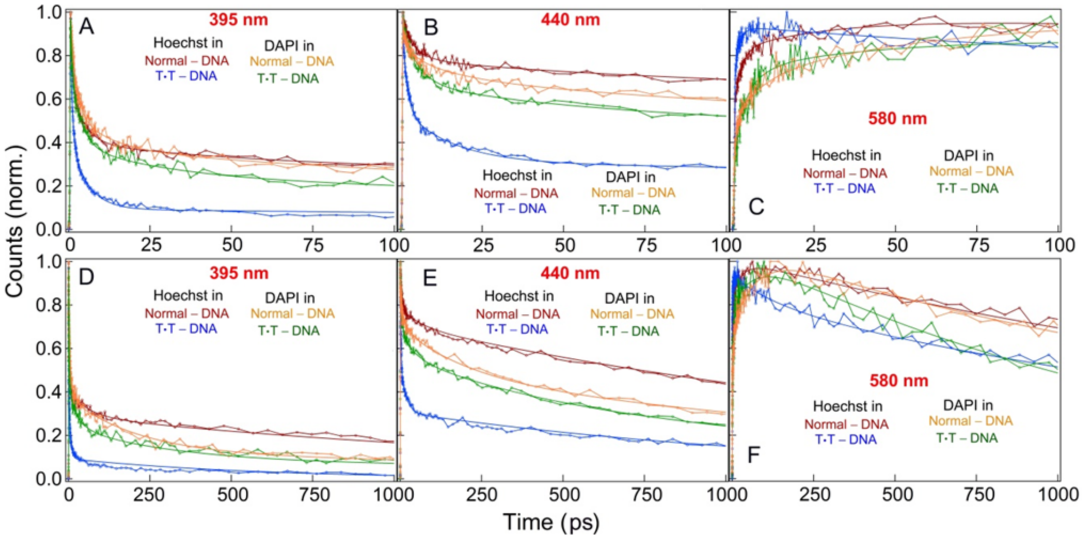

Figure 5.5: Fluorescence decays of Hoechst and DAPI bound to minor groove of normal- and T·T–DNA, measured in UPC at blue-side (395 nm), near peak (440 nm) and red-side (580 nm) of the fluorescence spectra. (A) – (C) Decays in short time-range upto 100 ps, and (D) – (F) decays in the longer time-range upto 1000 ps. Lines through raw decays are fits using sum of 3-4 exponentials.

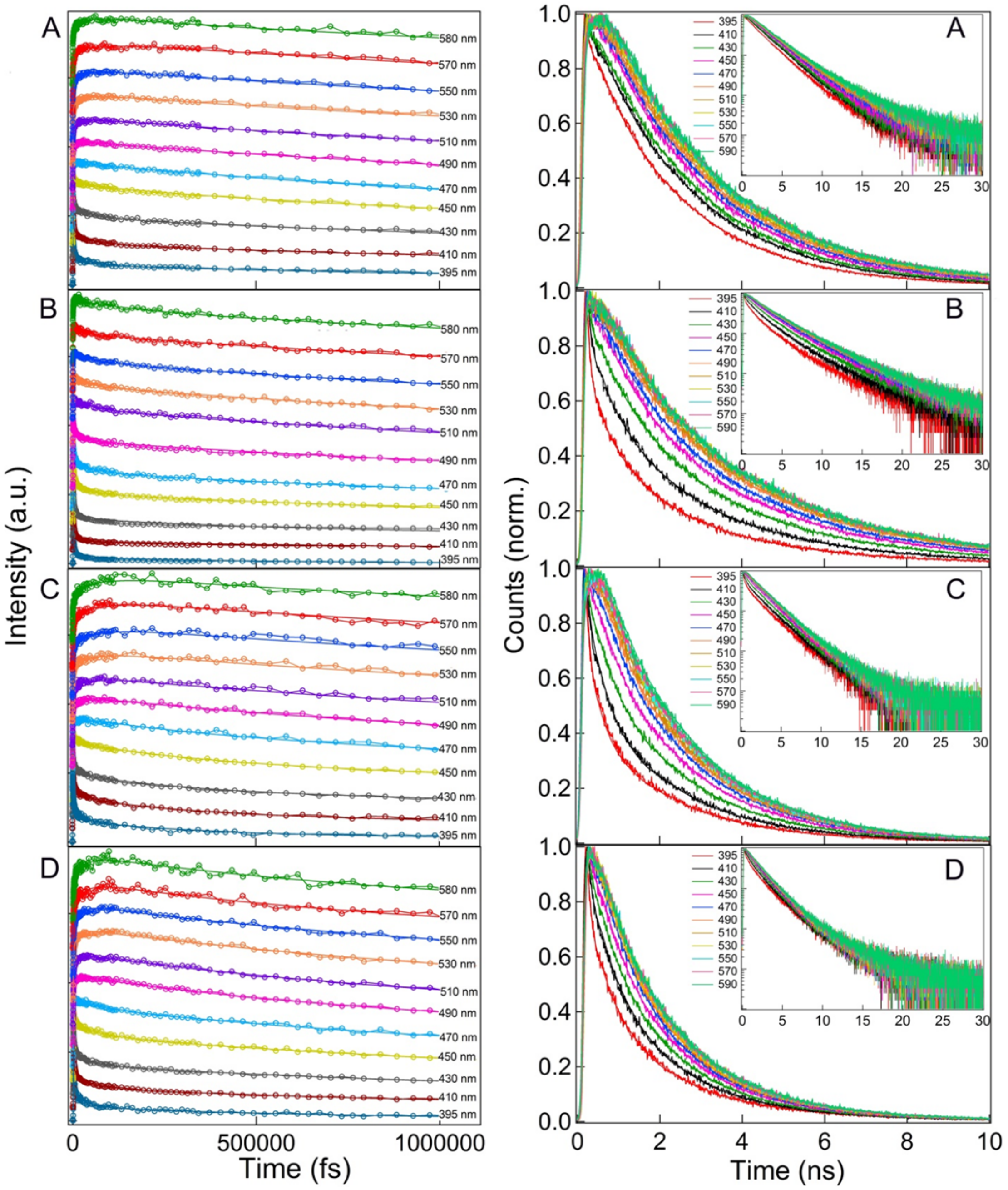

Figure 5.6: Wavelength dependent fluorescence decays (with fits) of Hoechst bound to minor grooves of (A) normal-DNA and (B) T·T–DNA and those of DAPI bound to minor groove of (C) normal-DNA and (D) T·T–DNA, collected using UPC (left panel) and TCSPC (right panel). The decays show characteristic trend of solvation dynamics, that is, fast decay in blue-side, fast rise/decay followed by slow decay in peak region and slow rise followed by slow decay in red region of fluorescence spectra. Total 11 decays, out of 20-22 decays, covering entire fluorescence spectra of Hoechst in DAPI in respective DNA-systems are plotted here to minimize clumsiness. Fits to the raw data using sum of 3-4 exponential decays are also included in the figures (solid lines through raw data).

Figure 5.4 compares the decays of Hoechst and DAPI in normal- and T·T–DNA at shorter, peak and longer wavelengths measured in TCSPC (see Figure 5.6 for other decays). Comparison shows distinct effect of T·T mismatch on the decay patterns, compared to those in normal-DNA. The effect is relatively stronger on Hoechst decays. As can be seen in Figure 5.4, for Hoechst, decays at most wavelengths in T·T–DNA are faster in the short time-scales and slower in long times, compared to those in normal-DNA. The effect is somewhat smaller in case of DAPI in T·T–DNA for which at shorter wavelengths the decays are similar while they are mostly faster in longer wavelengths. These raw fluorescence decays suggest that there could be substantial difference in nanosecond solvation dynamics of Hoechst and DAPI in the minor groove of T·T–DNA compared to that in the minor groove of normal-DNA.

Figure 5.5 compares the raw fluorescence decays in faster time-scales, measured in UPC setup (see Figure 5.6 for other decays). A similar effect of T·T mismatch on the femtosecond decay patterns is also observed on the Hoechst and DAPI decays. Again, a larger effect of mismatch on Hoechst decays is observed compared to DAPI decays in this time-range. Nevertheless, the quantitative effect of mismatch on the solvation dynamics is captured in the dynamic Stokes shifts (i.e., average frequency shifts) of the ligands as discussed below.

5.3.4. Comparison of Ligands' Dynamics in Normal–DNA

It was not known whether the solvation dynamics from femtoseconds to nanoseconds in the minor groove of normal-DNA, probed by two most popular minor groove binders Hoechst and DAPI, are similar or not, particularly in the minor groove created by the central –AATTG– sequence which is used in this study. This test is important because dynamics probed by minor groove binder (DAPI) was earlier shown to depend on the base-sequence near the binding site.[37] It is seen here that the Stokes shift dynamics from ~100 fs to 10 ns, probed by Hoechst and DAPI, in the minor groove of normal-DNA are somewhat different, especially in the longer times, although power-law relaxation (of exponent ~0.15) in the initial time-decades remains similar for both probes. Previously, Stokes shift dynamics of Hoechst in minor groove of duplex DNA was reported by Zewail and co-workers, measured by UPC, showing bi-exponential relaxation till 100 ps.[39] Furthermore, Pal and co-workers reported nanosecond solvation dynamics of Hoechst (and DAPI) in minor groove of DNA, measured using TCSPC, again showing bi-exponential decay till ~5 ns.[40] However, Furse and Corcelli simulated the dynamics of Hoechst in minor groove of DNA, same system as Zewail and co-workers,[39] and reported dispersed solvation correlation function till ~7 ns which show nearly linear dependence with time in log-log plot (like power-law).[47] On the other hand, Sen and co-workers reported the experimental Stokes shift dynamics of DAPI inside minor groove of normal-DNA (of central –AATTG– sequence) from ~100 fs to 10 ns and showed that the dynamics follow a power-law (of exponent ~0.15) till ~100 ps, but beyond this time the dynamics converge rapidly to equilibrium near 10 ns following bi-exponential relaxation.[43,44]

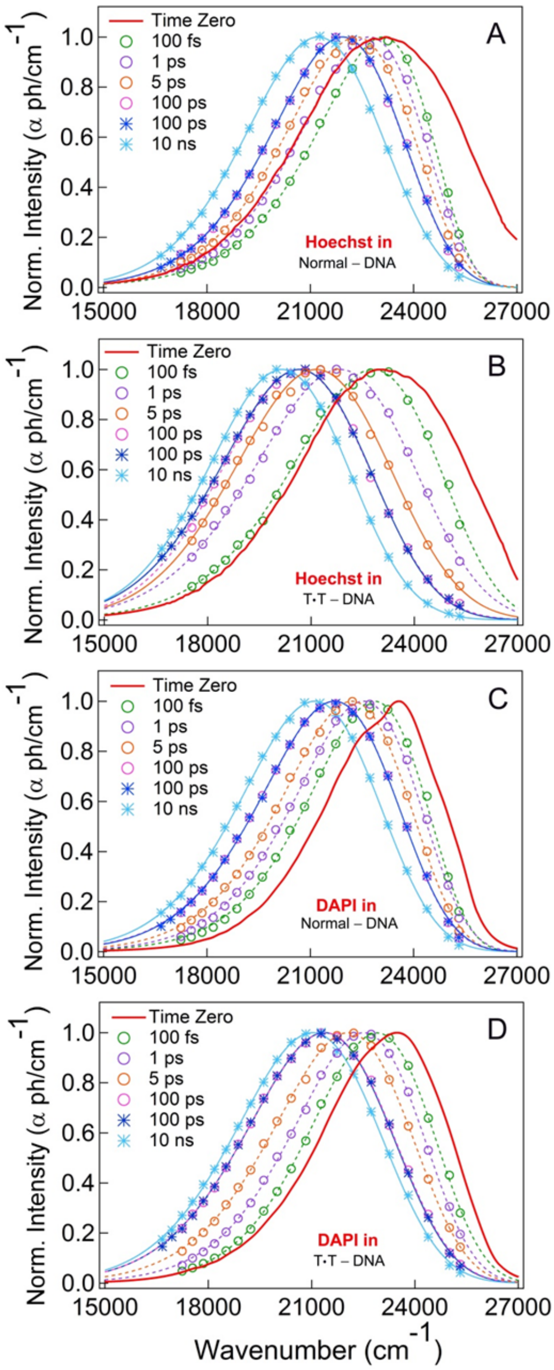

Figure 5.7: Time-resolved emission spectra (TRES) of Hoechst bound to minor grooves of (A) normal-DNA and (B) T·T–DNA, and of DAPI bound to minor grooves of (C) normal-DNA and (D) T·T–DNA, constructed from fluorescence decays measured in UPC (circles) and TCSPC (stars). Matching of TRES from UPC and TCSPC at common time-point (100 ps) are also shown in figures. Colored dashed and solid lines denote log-normal fits to the TRES data. Red solid-line spectra are time-zero glass-spectra of the respective samples measured in dry-ice/acetone mixture at –78 °C (see main manuscript for details).

Figure 5.7 plots the TRES (along with time-zero spectra) of Hoechst and DAPI in normal- and T·T–DNA constructed using methods described in chapter 3. Figure 5.8A compares the ‘absolute’ dynamic Stokes shifts of Hoechst in the minor groove of normal-DNA over five decades in time from ~100 fs to 10 ns (measured here) with the dynamics probed by DAPI in the DNA of same sequence reported earlier by Sen and co-workers.[55,56] Previously, Sen *et al*. showed that DAPI dynamics in normal-DNA can be modelled with a power-law (of exponent ~0.15), multiplied with bi-exponential decay function.[43] Here, the Hoechst absolute dynamic Stokes shifts data in normal-DNA could be modelled using a single power-law (equation 5.1) over a broad time-range.

$$S(t) = S_\infty\left[1-\left(1+\frac{t}{t_0}\right)^{-n}\right] \qquad (5.1)$$

Fit extracts power-law exponent of ~0.15 (see Table 5.1 for comparison of fitted parameters). One should note here that the extracted S_∞ value from fit using equation 5.1 is higher than the Stokes shift measured at highest time-point of the window (10 ns). This fit indicates that the power-law dynamics continue beyond the longest measured time-window (i.e., 10 ns), although we see faster relaxation beyond ~7 ns. Figure 5.8B plots the solvation correlation functions, $C(t)$, calculated from the absolute Stokes shift data in Figure 5.8A taking $S_\infty = S(10 \text{ ns})$ as; $C(t)$

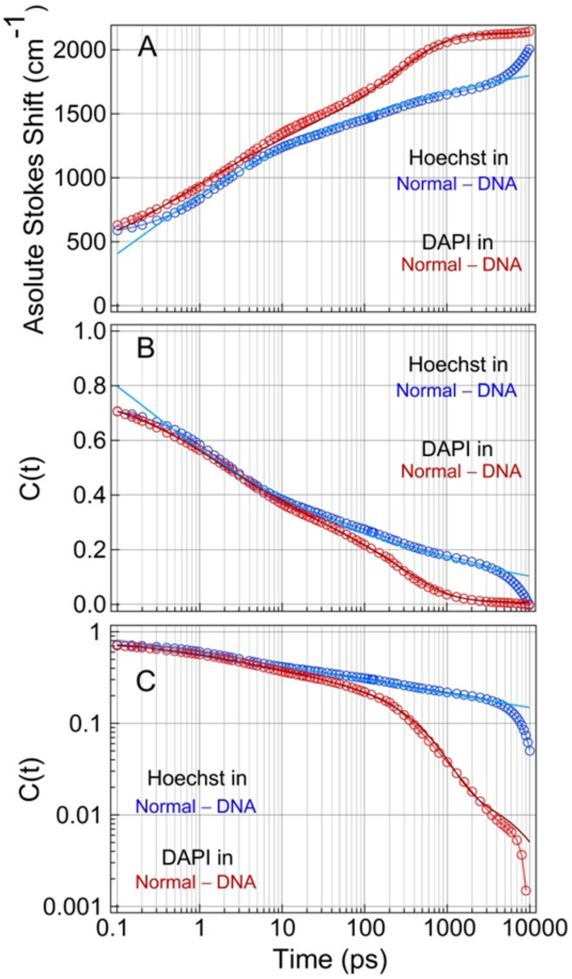

Figure 5.8: (A) Comparison of 'absolute' Stokes shifts of Hoechst and DAPI in the minor groove of normal-DNA[39,55,56] measured over five decades of time from 100 fs to 10 ns. (B) Comparison of solvation correlation function, $C(t)$ of Hoechst and DAPI in normal-DNA, constructed from Stokes shift data in (A) as, $C(t) = (S(10\ \text{ns}) - S(t))/S(10\ \text{ns})$ and (C) as $C(t) = (S_\infty - S(t))/S_\infty$ using fitted S_∞. Plots include fits to the data using either a single power-law or power-law multiplied with sum-of-two exponentials. The correlation functions, $C(t)$, calculated using S_∞ extracted from the fits to data in (A), are included in the SI (Figure S4). See text for details.

= (S(10 ns) − $S(t)$)/S(10 ns)). This estimation of $C(t)$, however, does not allow the time-correlation function to continue beyond the longest TRES (at 10 ns) and forces the power-law relaxation converge to zero at 10 ns. Otherwise, one can also construct $C(t)$ using the fitted S_∞ value as; $C(t) = (S_\infty - S(t))/S_\infty$), to allow the power-law dynamics continue beyond the measured time-window (Figure 5.8C). Nevertheless, guessing the exact S_∞ for calculating solvation correlation function in a complex system like DNA is rather hard, and has been a subject of discussion in previous studies.[37,48] It is, thus, difficult to suggest which method is right and which is wrong, because Stokes shifts may converge at different values of S_∞ (and at different times) for different DNA systems. However, comparing the features of experimental Stokes shifts (measured here) and the simulated solvation correlation function of Hoechst in minor groove reported by Furse and Corcelli,[47] we conclude that $S_\infty = S$(10 ns) may be a better choice because simulated $C(t)$ in this DNA/ligand system shows convergence within this time-range. Nevertheless, it can be seen in Figure 5.8 that the dynamics probed by Hoechst and DAPI in the minor groove of normal-DNA show similar power-law behaviour till ~50 ps, but beyond this time DAPI dynamics converge rapidly to equilibrium near 10 ns. However, Hoechst dynamics continue the same power-law relaxation till ~7 ns, beyond which there is also some deviation with apparent faster dynamics. In fact, the feature of experimentally measured dispersed Stokes shift dynamics (and $C(t)$) of Hoechst in the minor groove of normal-DNA is found to be similar to the simulated dynamics of Hoechst in minor groove reported by Furse and Corcelli.[47] However, comparison of experimental and simulation data for DAPI

Table 5.1: Parameters obtained from fits of absolute Stokes shifts using power-law and power-law multiplied to bi-exponential relaxation.

System	S_∞ (cm^{-1})	t_0 (ps)	Power-law exponent *(n)*	a_1	τ_1 (ps)	a_2	τ_2 (ns)
DAPI/ Normal−DNA[†]	2140	0.09	0.15	0.76	460	0.05	**6.0**
Hoechst/ Normal−DNA	2111	0.05	0.15	–	–	–	–
DAPI/ T·T–DNA	2361	0.18	0.23	–	–	–	–
Hoechst/ T·T–DNA	2997	0.09	0.24	–	–	–	–

[†] Data taken from ref. 39.

could not be made because of non-availability of simulation data in this system. These experimental and simulation data confirm that the dynamics probed by Hoechst in the minor groove of normal-DNA indeed show dispersed (power-law) relaxation over broad time-range, and not multi-exponential relaxations as perceived earlier.[49,52] Thus, very long measurement time-window (both in experiment and simulation) is essential for capturing full dynamics in DNA. Comparison of dynamics data in Figure 5.8 clearly suggests that solvation dynamics in DNA minor groove is a complex process which depends on the probe structure, at least for the DNA sequence used here. Speculating the possible origin of such deviations in the dynamics probed by Hoechst and DAPI in normal-DNA is difficult, except that it is believed the relative contributions from motions of water, counterions and DNA-parts may contribute differently to the collective dynamics probed by Hoechst and DAPI in the same minor groove of normal-DNA. This needs further exploration with extensive MD simulations, similar as performed earlier.[45,48-50]

5.3.5. Comparison of Ligands' Dynamics in Minor Groove of T·T-DNA

One natural question immediately arises; what happens to the dynamics when a mismatch is introduced near the binding site of the minor groove binders? It has been seen above that introduction of a T·T mismatch in the minor groove substantially changes the fluorescence properties of the ligands, although to different extents in the relative quantum yields and peak shifts of Hoechst and DAPI spectra as well as their fluorescence decays. This may indicate that dynamics probed by these ligands may also be different in T·T–DNA. To the surprise, it is however seen that both ligands in the minor groove of T·T–DNA sense similar solvation response.

Figure 5.9A compares the absolute Stokes shifts of Hoechst and DAPI in the minor groove of T·T–DNA. Both data could be nicely fitted with a single power-law (equation 5.1) over nearly the entire measurement time-range. We see that total observable absolute Stokes shift of Hoechst is larger (2997 cm^{-1}) compared to that of DAPI (2361 cm^{-1}) in the

T·T–DNA (Table 5.1). This is in line with the fact that environment dependent spectral shifts of Hoechst are larger than that of DAPI (see Figure 5.3). The fits to Hoechst and DAPI data using equation 5.1 extract similar power-law exponent of ~0.23 (for DAPI) - 0.24 (for Hoechst) (see Table 1). Figure 5.9B constructs the solvation correlation functions, $C(t)$, from the absolute Stokes shift data as; $C(t) = (S(10\text{ ns}) - S(t))/S(10\text{ ns})$ in T·T–DNA. $C(t)$ using the fitted S_∞ (Table 1) are also calculated, which allows the power-law to continue beyond the measured time-window and plotted in Figure 5.9C. The solvation dynamics probed by both ligands in the minor groove of T·T–DNA show very similar power-law relaxation with exponent ~0.23-0.24 over nearly the entire five decades. This result is significantly important because it shows that introduction of a T·T mismatch in the minor groove induces *similar* collective (power-law) dynamics around the mismatch site, for a given canonical base sequence flanking the mismatch, which is probed by both minor groove binders, despite the fact that these ligands sense different dynamics in the minor groove of normal-DNA. The *similar* power-law dynamics, but not distinct time-scale(s), induced by T·T mismatch suggests that the overall collective dynamics remains dispersed around the mismatch site, despite that T·T base-pair was shown to have distinct lifetime in previous NMR study.[9]

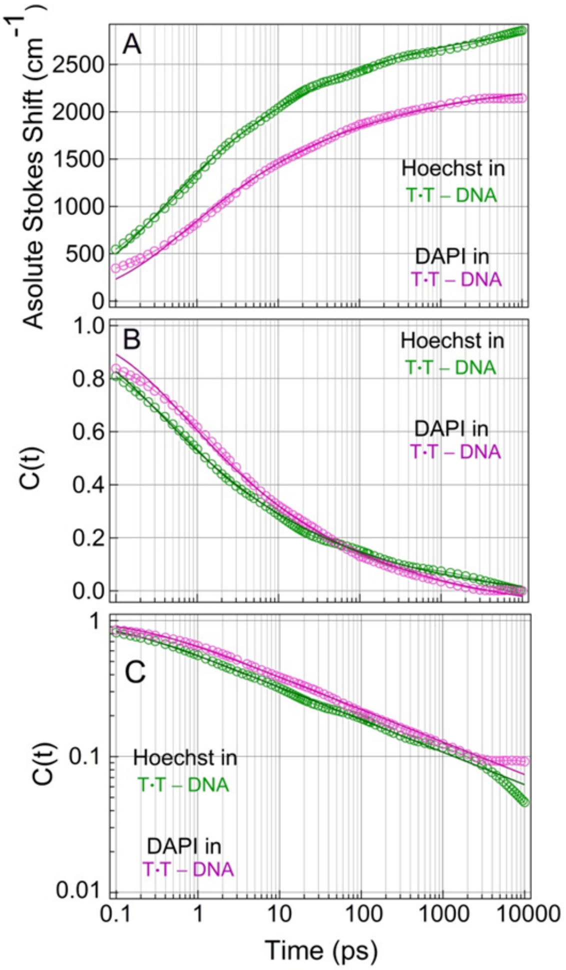

Figure 5.9: (A) Comparison of 'absolute' Stokes shifts of Hoechst and DAPI in the minor groove of T·T–DNA measured over five decades of time from 100 fs to 10 ns. (B) Comparison of solvation correlation function, $C(t)$ of Hoechst and DAPI in T·T–DNA, constructed from Stokes shift data as, $C(t) = (S(10\text{ ns}) - S(t))/S(10\text{ ns})$ and (C) as $C(t) = (S_\infty - S(t))/S_\infty$ using fitted S_∞. Plots include fits to the data using a single power-law relaxation. The correlation functions, $C(t)$, calculated using S_∞ extracted from the fits to data in (A). Both ligands show very similar power-law dynamics (of exponent 0.23-0.24) in T·T–DNA over the entire time-range. See text for details.

5.3.6. Fluorescence Anisotropy Decay: No Effect of T·T–Mismatch

The effect of internal rotational motion of mismatched bases on the motions of probe-ligands can be characterized by performing time-resolved fluorescence anisotropy experiments. Earlier, adenine analog, 2-AP, was used to monitor the internal motions of mismatched bases and base-pairs to find their characteristic internal dynamics in DNA.[26,27] An important test is done here too – so as to find whether the internal wobbling motion of T·T mismatch has any direct role on the slow solvation dynamics through modifying probe-ligands' internal motions or not. This way, one can make sure if the changes in slow solvation dynamics in mismatched-DNA, compared to normal-DNA, is a direct manifestation of the probes' rotation/internal motion or not. In fact, it has been shown earlier that internal rotational dynamics of protein-segments can have direct correlation to the solvation response at different probe-sites inside the protein, suggesting direct coupling of protein segmental motions to solvation dynamics.[52] To discern such possibility, we measured rotational anisotropy decays of Hoechst and DAPI in normal- and T·T–DNA. Figure 5.10 plots four anisotropy decays of the two ligands in normal- and T·T–DNA, measured in TCSPC setup. This plot shows almost identical anisotropy decays of both probes in both normal- and T·T–DNA, suggesting that there is no effect of incorporation of T·T mismatch on the rotational/internal dynamics of probe-ligands. The overall anisotropy decays could be fitted well with a single exponential time-constant of ~3.9 ns which arises from the overall rotational tumbling of the ligand/DNA complexes. Thus, the solvation responses of the ligands in both normal- and T·T–DNA arise purely from the relaxation of electrostatic interaction energy of the ligands with surrounding charged/dipolar molecules, and that the ligands are bound strongly enough to the grooves of normal- and T·T–DNA to tumble together with the whole DNA molecule. In fact, previous NMR study showed that DAPI tightly binds to the minor groove of T·T containing DNA in a similar fashion as that bound in normal-DNA, allowing the mismatched thymines to adopt a wobble base-pair conformation.[28] However, no such structural information is available for Hoechst bound to T·T–DNA. Nevertheless, the CD spectra suggest that both ligands bind to the normal- and

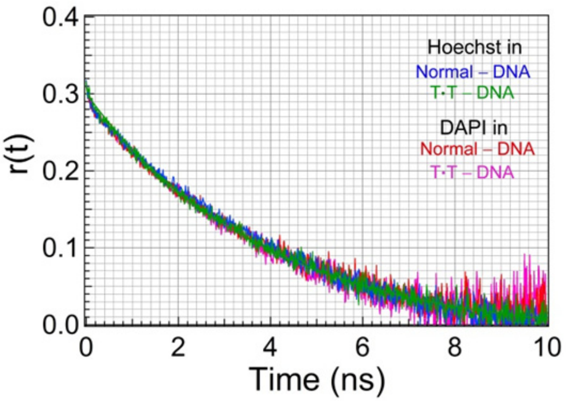

Figure 5.10: Rotational anisotropy decays of Hoechst and DAPI in the minor grooves of normal- and T·T–DNA measured in TCSPC. All anisotropy decays could be fitted with a single exponential decay of time-constant ~3.9 ns, which arises from the overall rotational motions of the DNA/ligand complexes. This suggests that internal wobbling motion of T·T mis-pair has no direct effect on the slow solvation dynamics through modifying probes' internal rotational motions. See text for details.

T·T–DNA, keeping the right-handed B-conformation of the DNA intact (see Figures 5.1C and 5.1D).

5.3.7. Origin of Dispersed Dynamics in T·T-DNA

What is the origin of dispersed power-law dynamics in T·T–DNA? The exact answer to this question requires extensive exploration of these DNA/ligand systems using large-scale MD simulation. As shown in previous chapter, MD simulation remains a key methodology for quantitative explanation of the experimental Stokes shift dynamics. In fact, much of the current understanding about Stokes shift dynamics in DNA came from simulations,[45,47-50] which is clearly shown in previous chapter 4 and also in chapter 7. However, the ability of such simulation methods to quantify the experimental results, especially in long times, remains challenging. Questions have been raised on the interpretation of complex correlated dynamics of constituent molecules in DNA systems.[45,47-50] Nevertheless, the success of interpreting experimental results through comparison of simulated dynamics to TRFSS results in DNA has just begun,[45,47-50] including those results discussed in chapter 4 and chapter 7, which started upgrading our knowledge about the complex solvation dynamics in DNA.

This chapter showed that dynamics of Hoechst in the minor groove of normal-DNA can be depicted by a single power-law relaxation – a feature which is found to be similar to the previous simulation data of Furse and Corcelli.[47] Moreover, decomposition analysis of individual component's contribution to the overall dynamics sensed by Hoechst in normal DNA, reported earlier by Furse and Corcelli, was shown to be dominated by DNA motion rather than the water and counterion motions, especially in longer times.[49] Along this line, one possibility could be that the power-law dynamics seen in T·T–DNA is also originating from mainly the local DNA motions, including wobbling of mismatched T·T base-pair.

However, two important observations were made in the steady state fluorescence spectra (Figure 5.2) and Stokes shift dynamics (Figures 5.8 and 5.9): (1) Hoechst spectrum is significantly red-shifted (by ~23 nm) with lower quantum yield and DAPI spectrum is broadened with lower quantum yield in T·T–DNA, compared to those in normal-DNA. (2) Stokes shifts dynamics is faster in T·T–DNA (power-law exponent of ~0.23-0.24) compared to that in normal-DNA (power-law exponent of ~0.15). These observations indicate that the local environment sensed by the ligands in T·T–DNA is more polar compared to normal-DNA. More so, the overall dispersed dynamics in T·T–DNA is faster than in normal-DNA.

The large changes in static and dynamic features of ligands' fluorescence seem difficult to originate from only the structural changes of mismatched bases in the minor groove; rather, this may be arising from the collective effects/motions of mismatched base-pair and electrostatically perturbed surrounding water and counterions. Also, as shown above, internal motions of T·T mismatch do not induce any extra rotations in probe-ligands which can contribute to the slow dynamics. These are the indications that suggest the ligands possibly access more number of water molecules when bound in the minor groove of T·T–DNA, compared to that in normal-DNA. One may argue at this point that counterion motion can also control the slow dynamics. In fact, using mode-coupling theory, Bagchi suggested that collective ion motions can dictate the power-law solvation dynamics in native DNA.[51] Moreover, through decomposition of simulated solvation correlation function, Sen *et al*. also showed that counterion dynamics in native DNA can contribute moderately to dictate overall dynamics in long times.[48] However, binding of minor groove binders to DNA displaces ions from the groove, keeping the strongly bound water molecules to the groove partially intact.[33,34] In fact, Furse and Corcelli showed Hoechst dynamics in minor groove of normal-DNA sense nearly zero contribution from counterion dynamics.[49] Furthermore, through comparison of counterion-dependent experimental Stokes shifts dynamics of DAPI in normal-DNA Sen and co-workers showed that DAPI does not sense the counterions' motions when bound inside the minor groove.[44] Recently, it has been also shown through decomposition of simulated solvation correlation function that contribution of counterion dynamics remains negligible in the overall dynamics probed by DAPI in the groove of G-quadruplex DNA, where mainly water and DNA motions dictate the power-law dynamics in longer times.[45] In fact, the di-cationic DAPI and mono-cationic Hoechst should actually screen the positively charged Na^+ counterions coming close to the ligands' binding sites. Hence, one would not expect to observe large ion contribution to the total dynamics sensed by Hoechst and DAPI in the minor grooves of normal- and T·T–DNA. In fact, it is likely that the wobbling motion of T·T mis-pair may actually involve larger number of nearby motional water molecules, compared to that by normal matched base-pairs. Thus, it seems plausible that the perturbed water motion, coupled to local T·T wobbling and motion of nearby DNA parts, may be responsible for the dispersed power-law solvation dynamics in T·T–DNA, as sensed by the groove-bound ligands. Nevertheless, the exact origin of the dispersed dynamics in T·T–DNA can only be quantified through extensive MD simulations.

At this juncture, one valid question still remains – how far the ligand binding to minor groove of mismatched-DNA perturbs the local hydration and ion environment? If the environment is perturbed then the *actual* collective dynamics of water, ions and DNA in *bare* mismatched-DNA, sensed by repair enzymes prior to DNA binding, may not be seen by probe-ligands bound to the mismatched site. It is true that binding of ligands to minor groove displaces most of groove-bound water and ions.[39,43,49] Thus, local environment is certainly disturbed by the ligand binding to the mismatched site, compared to that in *bare* mismatched-DNA. However, similar may be the situation which remains in the DNA/enzyme (MutS and MSH6) complexes where parts of proteins (phenylalanine and glutamate) interact with the mismatched base-pair through intercalation and (bifurcated) hydrogen-bonding from the minor groove side, with water molecules stabilize a Mg^{2+} ion near the binding site.[20,21,53] Previous NMR study found that DAPI tightly binds to the T·T mismatch in the minor groove of DNA in similar fashion as that in the normal-DNA, allowing the mismatched thymines to adopt wobble base-pair conformation.[28] Similar is the case may be also for Hoechst in T·T–DNA, although no structural data is available. Thus, the changes in the static and dynamic fluorescent properties of the minor groove binders in T·T–DNA observed here, compared to normal-DNA, are the *relative* effects that the probes sense which arise due to the presence of T·T mis-pair in the DNA. Hence, the changes in Stokes shift dynamics measured by ligands in T·T–DNA, compared to normal-DNA, depict the effect of T·T-mismatch that induces dispersed collective dynamics of water and DNA-parts (with ion-contribution possibly being negligible), when probed by the minor groove binders.

5.3.8. Role of Collective Solvation Dynamics in Signal Transfer to Repair Enzymes

It has been proposed earlier based on MD simulation that signal from the mismatched site to the repair enzyme may be transferred through-space, mediated by surrounding environment (mainly water and ions).[16] Based on present data, it may be proposed that the collective dynamics of the local environment (molecules within ~10-15 Å from probe-site[45,48,49]) near the mismatch base-pair may be more important than only the structural changes of mismatched base-pair for the mismatch recognition by enzymes and subsequent repair mechanism. In fact, the strong electrostatic coupling among DNA-parts, water and counterions in the groove is unavoidable, which is actually sensed by the repair enzymes at physiological condition. Moreover, it is clearly pointed out by Rossetti *et al*. that specific signal from mismatched base-pair is very low in strength which is rather difficult to separate from the thermal noise.[16] In fact, several room temperature (equilibrium) MD simulations in normal native DNA and DNA/ligand complexes found strong electrostatic coupling among constituent molecules which gives rise to similar amplitudes of Coulombic interaction energy fluctuations of water, DNA and counterions at a probe-site near/inside DNA.[45,47,48,50] Such long-range Coulombic interactions would play the most important role, compared to other non-bond interactions, at the first step of the mismatch recognition by repair

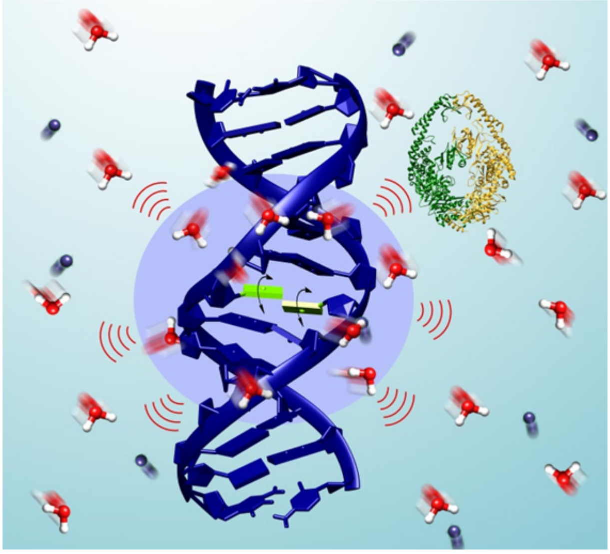

Figure 5.11: A representative cartoon showing the possible way of communication between mismatched site/region in DNA and the repair enzyme through recognition of the collective dynamics of water, DNA-parts and counterions prior to physically binding to the DNA. See text for discussion.

enzyme when the enzyme comes close to the mismatch site (within the few layers of solvation), prior to physically bonding DNA. Thus, the incoming enzyme may sense similar strengths of energy fluctuations from the water, counterions and DNA-parts as well as their collective dynamics, and the enzyme may not be able to single out the fluctuations and dynamics of only the mismatch base-pair, if they are not significantly different from those of water and counterions. It is also expected that larger fluctuations of mismatched base-pairs would result in stronger perturbation to the nearby water and counterions. Such effects on surrounding environment by different types of mismatched base-pairs are likely to be different which would then act as cues for the differential mismatch recognition by repair enzymes. Thus, the effects of water and counterion dynamics in-and-around the mismatch site can not be neglected when explaining the possible mechanism of DNA mismatch recognition by enzymes and subsequent mismatch repair. A cartoon showing the possible way of communication between the mismatched site/region in DNA and the repair enzyme is included in Figure 5.11.

It is, however, noted that the present T·T–DNA/ligand systems resemble more to the T·T–DNA/enzyme complex,[20,21,53] where perturbation to the minor groove width and local dielectric environment are inevitable because binding of ligands to minor groove is favoured by the partial displacement of groove-bound water and ions, leading to entropic contribution to the binding energy.[34,35] Thus the measured dynamics of electrostatic interaction energy of minor groove binders may not be reflecting the actual collective dynamics of mismatched base-pair and local water and ions in *bare* mismatched-DNA. Nevertheless, as pointed out in previous section, the comparison of data in normal- and T·T–DNA reveals the relative effects of the T·T mismatch, where the local hydration dynamics and motions of DNA-parts may be controlling the collective dynamics near the mismatched site. Thus, the static and dynamic properties studied here may be similar to those prevailing in the DNA/enzyme complexes. Covalently attached base-stacked fluorescent probes to DNA with long excited state lifetime, together with large-scale MD simulations, may be useful for measuring the exact effects of mismatched base/base-pairs on the collective solvation dynamics in the grooves of mismatch-DNA, which may resemble more to the *bare* mismatched DNA.

5.4. Conclusion

This chapter showed that introduction of a T·T mismatch inside the minor groove of DNA induces dispersed local Stokes shifts dynamics from ~100 fs to 10 ns that follow power-law relaxation with exponent ~0.23-0.24, for a given canonical base-pair sequence flanking the mismatched base-pair, when probed by two popular minor groove binders, Hoechst and DAPI. These ligands however sense somewhat different Stokes shifts dynamics in the minor groove of normal-DNA. Comparing the steady-state fluorescence properties, it has been shown that introduction of T·T mismatch induces a local dielectric environment in mismatched-DNA that is more polar than that in normal-DNA, as sensed by the minor groove binders. Anisotropy decays of ligands in normal- and T·T–DNA confirmed that introduction of T·T mismatch does not induce any local rotational motions in the probe-ligands, such that they can contribute to the slow dispersed solvation dynamics in the T·T–DNA.

The power-law solvation dynamics seen in T·T–DNA, for the given flanking canonical base-sequence, indicates that the probe-ligands do not sense any particular (exponential) dynamics specific to the T·T wobbling and/or their motion between intra- and extra-helical conformations. Instead, based on static and dynamic data, it seems that local water dynamics play important role to define the dispersed collective dynamics without any specific time-component. This may be the reason why T·T mismatch is not well recognized and repaired by the repair enzymes compared to purine-pyrimidine and purine-purine mismatches.[7,15] It is however possible that different mismatches would induce different levels of perturbations to the nearby water and counterions, which may then lead to different collective motions of water, DNA and counterions. More so, the canonical base-sequence flanking the mismatch site is also shown to affect the ability of repair enzymes to detect the mismatched base-pairs.[54,55] In fact, such an elaborate study using all possible mismatches (total 8 mismatches plus normal DNA) in a different canonical base-pair sequence flanking the mismatches is discussed in the next chapter 6. It will be shown in next chapter that different mismatch base-pairs affect the local collective dynamics differently which correlate well to the differential mismatch recognition/repair efficiency by the repair proteins. Nevertheless, the present chapter showed that dynamic Stokes shift experiment has tremendous capability to unravel the complex dynamical features induced by a single mismatched base-pair inside DNA minor groove, which is further explored in the next chapter on DNA with all possible mismatches and a different canonical base-sequence flanking the mismatch sites.

Reference

(1) Modrich, P. DNA Mismatch Correction. *Annu. Rev. Biochem.* **1987**, *56*, 435-466.

(2) Kolodner, R. D. Mismatch Repair: Mechanisms and Relationship to Cancer Susceptibility. *Trends Biochem. Sci*. **1995**, *20*, 397-401.

(3) Renkonen, E. Altered Expression of MLH1, MSH2, and MSH6 in Predisposition to Hereditary Nonpolyposis Colorectal Cancer. *J. Clin. Oncol.* **2003**, *21*, 3629-3637.

(4) Bhattacharyya, A.; Lilley, D. M. Single Base Mismatches in DNA. Long- and Short-Range Structure Probed by Analysis of Axis Trajectory and Local Chemical Reactivity. *J. Mol. Biol.* **1989**, *209*, 583-597.

(5) Goodman, M. F.; Creighton, S.; Bloom, L. B.; Petruska, J. Biochemical Basis of DNA-Replication Fidelity. *Crit. Rev. Biochem. Mol. Biol.* **1993**, *28*, 83-126.

(6) Kunz, C.; Saito, Y.; Schar, P. DNA Repair in Mammalian Cells: Mismatched Repair: Variations on a Theme. *Cell. Mol. Life Sci.* **2009**, *66*, 1021–1038.

(7) Kunkel, T. A.; Erie, D. A. DNA Mismatch Repair. *Annu. Rev. Biochem.* **2005**, *74*, 681-710.

(8) Schofield, M. J.; Hsieh, P. DNA Mismatch Repair: Molecular Mechanisms and Biological Function. *Annu. Rev. Microbiol.* **2003**, *57*, 579-608.

(9) Bhattacharya, P. K.; Cha, J.; Barton, J. K. ^{1}H NMR Determination of Base-Pair Lifetimes in Oligonucleotides Containing Single Base Mismatches. *Nucleic Acids Res.* **2002**, *30*, 4740-4750.

(10) Tikhomirova, A.; Beletskaya, I. V.; Chalikian, T. V. Stability of DNA Duplexes Containing GG, CC, AA, and TT Mismatches. *Biochemistry* **2006**, *45*, 10563-10571.

(11) Peyret, N.; Seneviratne, P. A.; Allawi, H. T.; SantaLucia, J. Nearest-Neighbor Thermodynamics and NMR of DNA Sequences with Internal A.A, C.C, G.G, and T.T Mismatches. *Biochemistry* **1999**, *38*, 3468-3477.

(12) Sharma, M.; Predeus, A. V.; Mukherjee, S.; Feig, M. DNA Bending Propensity in the Presence of Base Mismatches: Implications for DNA Repair. *J. Phys. Chem. B* **2013**, *117*, 6194-6205.

(13) Ke, S. H.; Wartell, R. M. Influence of Nearest Neighbor Sequence on the Stability of Base Pair Mismatches in Long DNA: Determination by Temperature-Gradient Gel Electrophoresis. *Nucleic Acids Res.* **1993**, *21*, 5137-5143.

(14) Allawi, H. T.; SantaLucia, J. Nearest-Neighbor Thermodynamics of Internal A.C Mismatches in DNA: Sequence Dependence and pH Effects. *Biochemistry* **1998**, *37*, 9435-9444.

(15) Brown, J.; Brown, T.; Fox, K. R. Affinity of Mismatch-Binding Protein MutS for Heteroduplexes Containing Different Mismatches. *Biochem. J.* **2001**, *354*, 627-633.

(16) Rossetti, G.; Dans, P. D.; Gomez, P. I.; Ivani, I.; Gonzalez, C.; Orozco, M. The Structural Impact of DNA Mismatches. *Nucleic Acids Res.* **2015**, *43*, 4309-4321.

(17) Yin, Y.; Yang, L.; Zheng, G.; Gu, C.; Yi, C.; He, C.; Gao, Y. Q.; Zhao, X. S. Dynamics of Spontaneous Flipping of a Mismatched Base in DNA Duplex. *Proc. Natl. Acad. Sci. U.S.A.* **2014**, *111*, 8043-8048.

(18) Isaacs, R. J.; Spielmann, H. P. Insight into G-T mismatch Recognition using Molecular Dynamics with Time-Averaged Restraints Derived from NMR Spectroscopy. *J. Am. Chem. Soc.* **2004**, *126*, 583-590.

(19) Gantchev, T. G.; Cecchini, S.; Hunting, D. J. Dynamic Conformational States of DNA Containing T.T or BrdU.T Mispaired Bases: Wobble H-bond Pairing versus Cross-Strand Inter-Atomic Contacts. *J. Mol. Model* **2005**, *11*, 141-159.

(20) Lamers, M. H.; Perrakis, A.; Enzlin, J. H.; Winterwerp, H. H. K.; Wind, N. D.; Sixma, T. K. The Crystal Structure of DNA Mismatch Repair Protein MutS Binding to a G·T Mismatch. *Nature* **2000**, *407,* 711-717.

(21) Natrajan, G.; Lamers, M. H.; Enzlin, J. H.; Winterwerp, H. H. K.; Perrakis, A.; Sixma, T. K. Structures of Escherichia Coli DNA Mismatch Repair Enzyme MutS in Complex with Different Mismatches: A Common Recognition Mode for Diverse Substrates. *Nucleic Acids Res.* **2003**, *31*, 4814-4821.

(22) Brown, T.; Kennard, O.; Kneale, G.; Rabinovich, D. High Resolution Structure of a DNA Helix Containing Mismatched Base Pairs. *Nature* **1985**, *315*, 604-606.

(23) Hunter, W. N.; Brown, T.; Kennard, O. Structural Features and Hydration of a Dodecamer Duplex containing two CA Mispairs. *Nucleic Acids Res.* **1987**, *15*, 6589-6606.

(24) Allawi, H. T.; SantaLucia, J. Jr. NMR Solution Structure of a DNA Dodecamer Containing Single G ·T Mismatches. *Nucleic Acids Res.***1998**, *26*, 4925-4934.

(25) Gervais, V.; Cognet, J. A. H.; LeBret, M.; Sowers, L. C.; Fazakerley, G. V. Solution Structure of two Mismatches A.A and T.T in the K-ras Gene Context by Nuclear Magnetic Resonance and Molecular Dynamics. *Eur. J. Biochem.* **1995**, *228*, 279-290.

(26) Guest, C. R.; Hochstrasser, R. A.; Sowers, L. C.; Millar, D. P. Dynamics of Mismatched Base Pairs in DNA. *Biochemistry* **1991**, *30*, 3271-3279.

(27) Nag, N.; Rao, B. J.; Krishnamoorthy, G. Altered Dynamics of DNA Bases Adjacent to a Mismatch: A Cue for Mismatch Recognition by MutS. *J. Mol. Biol.* **2007**, *374*, 39-53.

(28) Trotta, E.; Paci, M. Solution Structure of DAPI Selectively Bound in the Minor Groove of a DNA T ·T Mismatch-Containing Site: NMR and Molecular Dynamics Studies. *Nucleic Acids Res.* **1998**, *26*, 4706-4713.

(29) Zimmer, C.; Wahnert, U. Nonintercalating DNA-Binding Ligands: Specificity of the Interaction and Their Use as Tools in Biophysical, Biochemical and Biological Investigations of the Genetic Material. *Prog. Biophys. Mol. Biol.* **1986**, *47*, 31-112.

(30) Bardhan, R.; Lal, S.; Joshi, A.; Halas, N. J. Theranostic Nanoshells: From Probe Design to Imaging and Treatment of Cancer. *Acc. Chem. Res.* **2011**, *44*, 936-946.

(31) Szabo, A.; Krajcarski, D.; Cavatorta, P.; Masotti, L.; Barcellona, M. Excited State pKa Behaviour of DAPI. A Rationalization of the Fluorescence Enhancement of DAPI in DAPI-Nucleic Acid Complexes. *Photochem. Photobiol*. **1986**, *44*, 143-150.

(32) Gorner, H. Direct and Sensitized Photoprocesses of Bis-benzimidazole Dyes and the Effects of Surfactants and DNA. *Photochem. Photobiol.* **2001**, *73*, 339-348.

(33) Vega, M. C.; Saez, I. G.; Aymami, J.; Eritja, R.; Marel, G. A. V. D.; Boom, J. H. V.; Rich, A.; Coll, M. Three-Dimensional Crystal Structure of the A-tract DNA Dodecamer d(CGCAAATTTGCG) Complexed with the Minor-Groove-Binding Drug Hoechst 33258. *Eur. J. Biochem.* **1994**, *222*, 721-726.

(34) Larsen, T. A.; Goodsell, D. S.; Cascio, D.; Grzeskowiak, K.; Dickerson, R. E. The Structure of DAPI Bound to DNA. *J. Biomol. Struct. Dyn.* **1989**, *7*, 477-791.

(35) Breusegem, S. Y.; Clegg, R. M.; Loontiens, F. G. Base-Sequence Specificity of Hoechst 33258 and DAPI Binding to Five $(A/T)_4$ DNA Sites with Kinetic Evidence for more than one High-Affinity Hoechst 33258-AATT Complex. *J. Mol. Biol.* **2002**, *315*, 1049-1061.

(36) Vlieghe, D.; Sponer, J.; Meervelt, L. V. Crystal Structure of d(GGCCAATTGG) Complexed with DAPI Reveals Novel Binding Mode. *Biochemistry* **1999**, *38*, 16443-16451.

(37) Verma, S. D.; Pal, N.; Singh, M. K.; Sen, S. Sequence-Dependent Solvation Dynamics of Minor-Groove Bound Ligand inside Duplex-DNA. *J. Phys. Chem. B* **2015**, *119*, 11019-11029.

(38) Brauns, E. B.; Madaras, M. L.; Coleman, R. S.; Murphy, C. J.; Berg, M. A. Measurement of Local DNA Reorganization on the Picosecond and Nanosecond Time Scales. *J. Am. Chem. Soc.* **1999**, *121*, 11644-11649.

(39) Pal, S. K.; Zhao, L.; Zewail, A. H. Water at DNA Surfaces: Ultrafast Dynamics in Minor Groove Recognition. *Proc. Natl. Acad. Sci. U.S.A.* **2003**, *100*, 8113-8118.

(40) Banerjee, D.; Pal, S. K. Dynamics in the DNA Recognition by DAPI: Exploration of the Various Binding Modes. *J. Phys, Chem. B* **2008**, *112*, 1016-1021.

(41) Andreatta, D.; Sen, S.; Pérez Lustres, J. L.; Kovalenko, S. A.; Ernsting, N. P.; Murphy, C. J.; Coleman, R. S.; Berg, M. A. Ultrafast Dynamics in DNA: "Fraying" at the end of the Helix. *J. Am. Chem. Soc.* **2006**, *128*, 6885-6892.

(42) Andreatta, D.; Pérez Lustres, J. L.; Kovalenko, S. A.; Ernsting, N. P.; Murphy, C. J.; Coleman, R. S.; Berg, M. A. Power-Law Solvation Dynamics in DNA over Six Decades in Time. *J. Am. Chem. Soc.* **2005**, *127*, 7270-7271.

(43) Pal, N.; Verma, S. D.; Sen, S. Probe Position Dependence of DNA Dynamics: Comparison of the Time-Resolved Stokes Shift of Groove-Bound to Base-Stacked Probes. *J. Am. Chem. Soc.* **2010**, *132*, 9277-9279.

(44) Verma, S. D.; Pal, N.; Singh, M. K.; Sen, S. Probe Position-Dependent Counterion Dynamics in DNA: Comparison of Time-Resolved Stokes Shift of Groove-Bound to Base-Stacked Probes in the Presence of Different Monovalent Counterions. *J. Phys. Chem. Lett.* **2012**, *3*, 2621-2626.

(45) Pal, N.; Shweta, H.; Singh, M. K.; Verma, S. D.; Sen, S. Power-Law Solvation Dynamics in G‑Quadruplex DNA: Role of Hydration Dynamics on Ligand Solvation inside DNA. *J. Phys. Chem. Lett.* **2015,** *6*, 1754-1760.

(46) Singh, M. K.; Shweta, H.; Sen, S. Dispersed Dynamics of Solvation in G-Quadruplex DNA: Comparison of Dynamic Stokes Shifts of Probes in Parallel and Antiparallel Quadruplex Structures. *Methods Appl. Fluoresc.* **2016**, *4*, 034009.

(47) Furse, K. E.; Corcelli, S. A. Dynamic Signature of Abasic Damage in DNA. *J. Am. Chem. Soc.* **2011**, *133*, 720-723.

(48) Sen, S.; Andreatta, D.; Ponomarev, S. Y.; Beveridge, D. L.; Berg, M. A. Dynamics of Water and Ions Near DNA: Comparison of Simulation to Time-Resolved Stokes-Shift Experiments. *J. Am. Chem. Soc.* **2009**, *131*, 1724-1735.

(49) Furse, K. E.; Corcelli, S. A. The Dynamics of Water at DNA Interface: Computational Study of Hoechst-33258 Bound to DNA. *J. Am. Chem. Soc.* **2008**, *130*, 13103-13109.

(50) Pal, S.; Maiti, P. K.; Bagchi, B.; Hynes, J. T. Multiple Time Scales in Solvation Dynamics of DNA in Aqueous Solution: The Role of Water, Counterions, and Cross-Correlations. *J. Phys. Chem. B* **2006**, *110*, 26396-26402.

(51) Bagchi, B. Anomalous Power Law Decay in Solvation Dynamics of DNA: A Mode Coupling Theory Analysis of Ion Contribution. *Mol. Phys.* **2014**, *112*, 1-9.

(52) Jha, A.; Ishii, K.; Udgaonkar, J. B.; Tahara, T.; Krishnamoorthy, G. Exploration of the Correlation Between Solvation Dynamics and Internal Dynamics of a Protein. *Biochemistry* **2011**, *50*, 397-408.

(53) Fukui, K. DNA Mismatch Repair in Eukaryotes and Bacteria. *J. Nucleic Acids*, **2010**, *2010*, 1231-1264.

(54) Fazakerley, G. V.; Quignard, E.; Woisard, A.; Guschlbauer, W.; Marel, G. A. V. D.; Boom, J. H. V.; Jones, M.; Radman, M. Structures of Mismatched Base Pairs in DNA and Their Recognition by the Escherichia Coli Mismatch Repair System. *EMBO J.* **1986**, *5*, 3697-3703.

(55) Hoffman, P. D.; Wang, H.; Lawrence, C. W.; Iwai, S.; Hanaoka, F.; Hays, J. B. Binding of MutS Mismatch Repair Protein to DNA Containing UV Photoproducts, "Mismatched" Opposite Watson–Crick and Novel Nucleotides, in Different DNA Sequence Contexts. *DNA Repair* **2005**, *4*, 983-993.

Chapter 6

Differential Effects of Mismatched Base-Pairs on Solvation Dynamics in Minor Groove of DNA

The preceding chapter showed that minor groove binders are good reporters for detecting the presence of mismatched base-pairs inside the minor groove of DNA. More so, they nicely depict the changes in local solvation dynamics induced by introduction of a mismatched base-pair near their binding sites. Thus, chapter 5 proved that minor grooves can be used to probe the effect of mismatch on the solvation dynamics in DNA. This chapter now elaborates on showing the sensitivity of the fluorescence properties of such minor groove binders (viz. DAPI here) in the AT-rich minor groove of DNA having different types (possible eight types) of mismatches introduced at the same place in the minor groove created by the AT-rich sequence. Data presented in this chapter clearly show that DAPI can nicely sense the differential collective solvation dynamics induced by different types of mismatches, which correlate well with the relative efficiencies of these mismatches recognition and repair by MutS.

6.1. Introduction

It is well known that different mismatches are recognized and repaired by enzymes with varying efficiencies.[1-5] This clearly suggests that the different types of mismatches have their characteristic properties (both static and dynamic) which may affect their immediate local environment also differently.[6] As pointed out in last chapter, it is believed that because different mismatches have their inherent static and dynamic properties, they will perturb their local environment at different levels, which will possibly lead to the differential local collective dynamics of water, ions and DNA. This is the focus of current chapter which will clearly show that indeed the different types of base-pair mismatches induce different local solvation dynamics in minor groove of DNA, for a given neighbouring canonical base-sequence flanking the mismatch sites, when probed by the minor groove binder, DAPI, in AT-rich minor groove of DNA. More importantly, it is observed that the relative changes in solvation dynamics around different mismatched base-pairs correlate well to the relative mismatch recognition and repair by enzyme, MutS.[7-10] The present study shows for the first time that collective solvation dynamics of around the mismatch sites, rather than only the local structural changes of mismatched base-pairs, are modulated in such ways that they may provide important cues to the repair enzymes for their differential mismatch recognition and repair mechanism.

Earlier molecular biology experiments, biophysical and biochemical studies showed that different DNA mismatches are recognized and repaired with different efficiencies, although the efficiencies were found to be also dependent on the neighbouring canonical base sequences.[7-12] Moreover, several deviations in the relative mismatch repair efficiencies were also reported.[7-10] In an early study, Radman and co-workers through genetic analysis of progeny phases of mismatched-DNA transfected *E. coli* found that among eight possible mismatches, C·T, C·C and A·G are less repaired by the enzymes compared to other types of mismatches.[7] In similar time, another study by Fritz and co-workers reported that methyl-directed DNA mismatch-repair in *E. coli* is strongly dependent on the mismatched base/base-pair types – such that there are three classes of efficiencies of repair which can be categorized as: high efficiency of repair for T·G (or G·T), C·A and G·G, intermediate efficiency for A·A, and low efficiencies for G·A (or A·G), C·C, C·T (or T·C) and T·T base-mismatches.[8] On the other hand, Brooks and co-workers found that among 12 different types of mismatch-containing M13 phase DNA the relative efficiency of mismatch repair changes by ~4 fold between the most and least effectively repaired mismatches.[9] They however found that C·A and T·C (or C·T) mismatches are repaired most compared to others, and such repair efficiencies vary with mismatch orientation.[9] Through in vitro bandshift assay analysis, Fox and co-workers found that the binding affinity of MutS to different base-pair mismatches changes from high to low as: G·T > G·G > A·A ≈ T·T ≈ T·C > C·A > G·A > C·C; however, such affinities are also affected by the neighbouring canonical base-pairs sequence.[10] A general conclusion can be made from most of these studies that purine-pyrimidine mismatches are most efficiently recognized and repaired by enzymes (with highest efficiency for G·T), followed by the purine-purine mismatches, and least efficiently recognized and repaired are the pyrimidine-pyrimidine mismatches.

Several other biophysical studies indirectly suggested the possible connections between the relative local structural changes near the mismatched sites and the relative recognition and repair of different types of mismatches by MutS.[13-19] NMR spectroscopic study found that different mismatches show different base-pair lifetimes and the order of such lifetimes follow a sequence: G·G > A·A > C·C > T·T,[15] which more-or-less follow the sequence of relative mismatch recognition and repair by enzymes. A new approach of diffusion-decelerated fluorescence correlation spectroscopic (ddFCS) study recently showed that extra-helical flipping rate of G·T mismatch is much smaller compared to T·T and C·T mismatches.[16] In fact, this work suggested that because of direct hydrogen-bond formation between G and T in G·T mismatch, the base-pair mostly stay intra-helical conformation whose lifetime is nearly ~60 times higher compared to those of T·T and C·T mismatches. This study, thus correlates the drastically different kinetic features of G·T mismatch to its most efficient recognition and repair by enzymes.[16] Earlier, time-resolved fluorescence anisotropy decay of 2-aminopurine (2-AP) also showed that the fast internal local rotational motions of 2-AP opposite/near mismatch sites vary depending on the mismatch type, which indirectly indicates that the alteration of this motional dynamics may be vital for the differential mismatch recognition.[17,18] MD simulations also came in handy to predict the possible mechanistic route for differential mismatch recognition and repair through indirect measures. MD simulation, along with free-energy profiling of DNA-bending, found that DNA containing purine-pyrimidine mismatches are least destabilizing, followed by intermediately destabilizing DNA with purine-purine, and most destabilizing with pyrimidine-pyrimidine mismatches.[19] The easily bend mismatches in DNA are predicted to be repaired efficiently by MutS. Simulation with selective integrated tempering sampling (SITS) also found that the free energy of flipped out conformation of G·T is higher than the T·T mismatch, which may also be another reason why G·T is better repaired compared to any other mismatches.[16]

Nevertheless, recent large-scale MD simulation with free-energy calculations, together with NMR study, by Rossetti *et al*. suggested that it is rather difficult to find a simple correlation between the structural changes of different mismatched base-pairs and the efficiencies of these mismatches' recognition by repair enzymes, except for some general correlation that overall breathing/structural changes in purine-purine mismatches are larger compared to those in pyrimidine-pyrimidine mismatches in DNA.[6] More so, this extensive simulation on all possible mismatches did not find any specific structural features of G·T and C·A which are substantially different compared to other mismatches – so as to predict why these mismatches are best recognized and repaired among all. In fact, the helical bend, breading percentage, etc. of these two mismatches were found to be of similar orders as in T·T mismatch that is much less efficiently repaired. However, importantly, this study showed that the mismatched bases actually induce significant alteration in the surrounding ion environment, and (possibly) hydration structure, near the mismatch sites.[6] This study indeed showed very high local ion accumulation (~5 mM) in the vicinity of G·T and C·A mismatches compared to matched and other mismatched pairs. Based on these observations, this study indicated that the transfer of signal to the repair enzymes possibly occur through-space, involving surrounding water and ions in the groove.[6] As indicated in the chapter 5, such interconnected effects (both static and dynamic) of mismatched pairs and surrounding water and ions may be more important for the mismatch recognition and repair mechanism.

This hypothesis is tested in this chapter by measuring the collective solvation dynamics of DNA, water and Na^+ counterions near *eight* possible mismatches and a normal matched DNA in the AT-rich minor groove of DNA. The dynamics is measured by monitoring the time-resolved fluorescence Stokes shifts (TRFSS) of the minor groove binder, DAPI, and compared among all such DNA systems over five decades of time from 100 fs to 10 ns. Results show that in all cases the underlying Stokes shift dynamics follow similar power-law relaxation, multiplied with single or double exponential relaxations in most of these DNA systems, except T·T-DNA which follow only a single power-law over entire five decades of time. The relative variations in the values of extra exponential relaxations are found to nicely correlate to the differential mismatches' recognition and repair by enzymes as reported earlier,[7-12] with only one exception. Fluorescence anisotropy decays from femtoseconds to nanoseconds time-range of DAPI bound to mismatched- and normal-DNA are found to be nearly identical, which suggests that Stokes shift dynamics and their changes in mismatched- and normal-DNA originate purely from relaxation of electrostatic interaction energy of the ligand with surrounding charged/dipolar molecules, and not from any internal local rotational motion of the probe-ligand. Thus, the collective solvation dynamics in the minor grooves containing mismatched base-pairs seem to play important role in the mismatch recognition of repair enzymes and in the subsequent repair mechanism.

The present study chooses DAPI over Hoechst (used in chapter 5) as the probe-ligand for several reasons: (1) DAPI is small enough (compared to Hoechst) which shall occupy only a few bases (typically 3-bases) near the mismatch site – such that it can report changes of very local effects; (2) DAPI is much more photo-stable compared to Hoechst; – DAPI can sustain high femtosecond laser power excitation for very long time without photo-bleaching compared to that of Hoechst; (3) Changes in solvation dynamics features measured by DAPI in normal- and T·T-DNA, seen in chapter 5, are drastic compared to that probed by Hoechst; – DAPI dynamics changes from power-law multiplied with bi-exponential relaxation in normal-DNA to single power-law dynamics in T·T-DNA (chapter 5). The present study also uses a different canonical base-pair sequence flanking the mismatched site (5′-GGCGCAA**X**TGCGCGG-3′), compared to that used in the study of chapter 5 (5'-CGCGCA**T**TGCGCG-3') – so that they show the effect of flanking base-sequence on the overall dynamics, at least for T·T-DNA.

6.2. Materials and Methods

DAPI was from Sigma-Aldrich, used without further purification. 15-mer DNA oligonucleotides of sequences 5′-GGCGCAA**X**TGCGCGG-3′ (**X**: mismatch position), and their complementary sequences were from Integrated DNA Technologies. B-form DNA duplexes were prepared by re-suspending single-stranded (both strands) oligonucleotides in buffer of 100 mM sodium phosphate with 50 mM NaCl of pH 7, and annealing them from 95°C to room temperature (25°C) over ~5 hours. Formation of double-stranded B-DNA was confirmed by circular dichroism (CD) spectra measured using a CD spectrometer. All samples were prepared in HPLC grade water (Merck). All experiments were performed with concentration ratios of [Ligand]/[DNA] of 1:5 for normal-DNA and 1:25 for mismatched–DNA where enhancement of DAPI fluorescence is saturated, such that nearly all ligands remain bound to the DNA (see Figure 6.2A). Fluorescence decays were measured at magic angle using TCSPC and UPC techniques. To cover a broad range of anisotropy decays, both UPC and TCSPC techniques were used (see chapter 3 for details). UPC measurements were carried out at concentrations; [DAPI] = 20 μM and [DNA] = 100 μM for normal-DNA, and [DAPI] = 25 μM and [DNA] = 625 μM for all mismatched–DNA, except for G·T mismatch [DAPI] = 30 µM and [DNA] = 750 µM, and for G·G mismatch [DAPI] = 40 µM and [DNA] = 1000 µM. TCSPC measurements were carried out with samples of concentrations, [DAPI] = 3 µM and [DNA] = 15 µM for normal-DNA, and [DAPI] = 3 µM and [DNA] = 75 µM for mismatched–DNA.

6.3. Results and Discussion

6.3.1. CD Spectroscopy: Conformation of Normal- & Mismatched-DNA

Right handed B-form structures of normal- and mismatched–DNA were confirmed from the CD spectra. Figure 6.1 shows the CD spectra of bare normal- and all eight mismatched–DNA (all 15 mM), which show characteristic negative peak near ~255 nm, confirming have B-DNA structures. However, the effect of ligand binding to the structures of DNA and the induced-CD of ligands inside DNA were not measured here, considering that all mismatched DNA structures would show B-form also in the ligand-bound form, as seen in the last chapter 5.

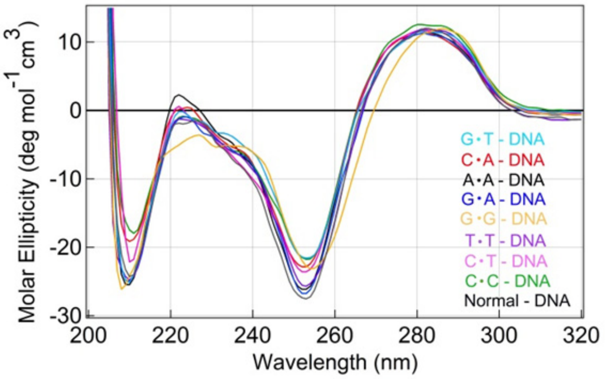

Figure 6.1: Circular dichroism (CD) spectra of 15-mer eight mismatched–DNA and normal-DNA (all 15 mM), showing characteristic negative peak ~255 nm confirming right handed B-form DNA. See figure for legends.

6.3.2. Steady-State Fluorescence Spectra: Effect of Different Mismatches

Upon binding to minor grooves of normal- and mismatched-DNA the fluorescence signal of DAPI increase several folds, but with varying amounts, which occurs due to suppression of the non-radiative pathways. However, it is not known how the binding affinity and static/dynamic fluorescence properties of DAPI change upon binding to different mismatches inside the minor groove of DNA.

Figure 6.2 shows the titrations of DAPI fluorescence with all mismatched- and normal–DNA, in which fluorescence signals of DAPI were monitored keeping its concentration constant and varying the DNA amount. It is clear from these plots that binding affinities of DAPI varies with the types of mismatches in the minor groove of DNA. The 50% signal increment occurs at [DNA]/[ligand] ratios that significantly vary among the mismatched-DNA/ligand systems. Table 6.1 includes the [DNA]/[ligand] ratios where the fluorescence signal of DAPI reaches 50% in respective samples. However,

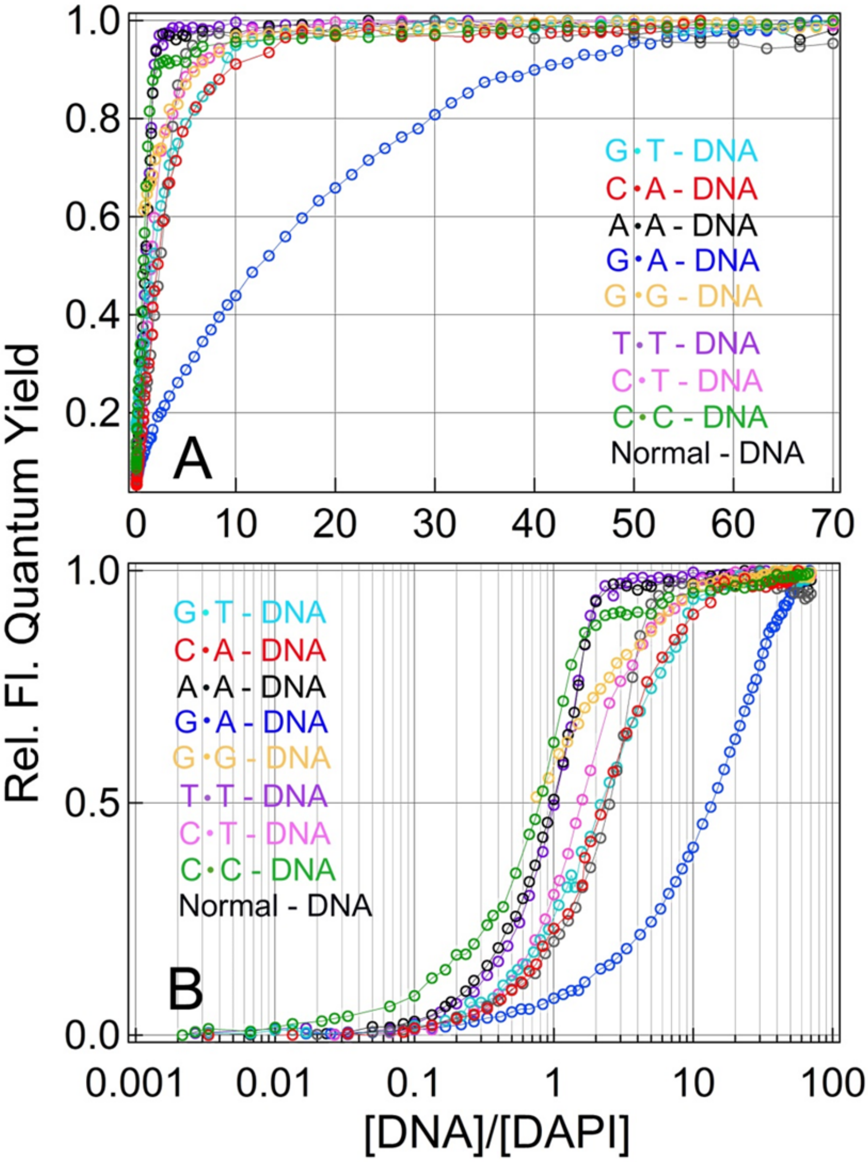

Figure 6.2: Titration of DAPI with normal- and all mismatched–DNA, in which fluorescence signal of DAPI are monitored keeping its concentration constant and varying the DNA concentration. Plots show (normalized) relative quantum yield change of DAPI in all DNA samples in linear scale (A) and semi-log scale (B).

there was no trend found in this binding affinity of DAPI toward different mismatched-DNA, which can be correlated to the differential mismatch repair efficiencies by enzymes. For G·G–DNA, the binding at 50% signal could not be detected properly primarily because of the fact that DAPI fluorescence increases merely by ~1.7 in G·G–DNA compared to that in buffer. Thus, titration of DAPI with G·G–DNA could not be completed fully because of large background signal of free DAPI in solution. Nevertheless, the titration curve for G·G–DNA does show some changes of fluorescence intensity upon gradual increase of DNA amount (see Figure 6.2).

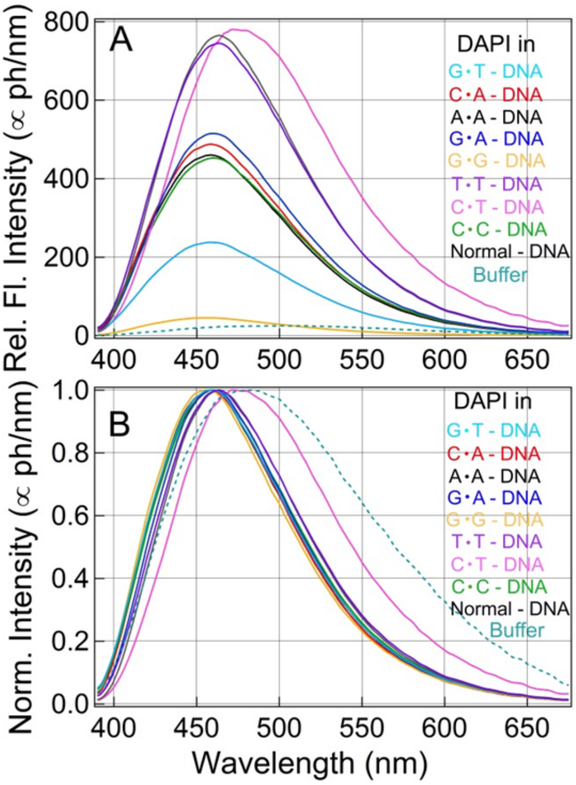

Figure 6.3: (A) Corrected relative fluorescence spectra of DAPI in buffer and bound to minor grooves of normal- and mismatched–DNA. Relative changes in fluorescence indicate ligands sense different local environments in these systems. (B) Same spectra intensity normalized to one, showing the relative peak shifts. See text for details.

Figure 6.3A compares the corrected fluorescence spectra of DAPI in normal- and all eight mismatched–DNA (at DNA concentrations where DAPI fluorescence signal saturate), and also in buffer. Upon binding to minor groove of most of normal- and mismatched-DNA, DAPI fluorescence significantly enhances, except in G·G–DNA possibly because of quenching of DAPI fluorescence due to high electron transfer from electron-rich guanines and electron deficient DAPI. The relative fluorescence intensity changes of DAPI in all mismatched and normal-DNA, compared to that in buffer, are included in Table 6.1. It can be seen from the table that in most DNA systems DAPI fluorescence increases by ~18-30 folds, except that in G·G– and G·T–DNA where fluorescence enhancements are only ~1.7 and ~9.5 times, respectively. Again, this trend of fluorescence enhancement of DAPI in different mismatched-DNA could not predict any relation of static fluorescence properties of DAPI to the relative mismatch recognition and repair of mismatches by MutS reported earlier.[7-12]

Figure 6.3B plots the spectra of DAPI in all DNA samples in the intensity normalized form to compare their relative peak shifts. The peak positions of DAPI in all DNA samples are also included in Table 6.1. It is interesting to note that in most DNA samples DAPI show peaks within 459 nm – 463 nm, except in C·T– and G·G–DNA. The spectrum is seen to be highly red-shifted in C·T–DNA (475 nm) compared to others, although it is still ~5 nm blue-shifted compared to that in buffer, suggesting that DAPI senses less polar environment in C·T–DNA, compared to buffer, but more polar environment in C·T–DNA compared to those in the minor grooves of other DNA (see also discussion in chapter 5 for comparison of spectral shifts of DAPI in various solvents of different dielectric constants). Also, the spectrum in C·T–DNA is broadened compared to others that show nearly similar full width at half maxima (fwhm). Surprisingly, however, DAPI shows most blue shifted spectrum (peak at ~456 nm) in G·G–DNA, suggesting that DAPI senses the most non-polar environment in G·G–DNA among all the DNA samples tested here. However, the quantum

Table 6.1: Parameters obtained from steady-state fluorescence of DAPI in mismatched- and normal-DNA.

System	[DNA]/[DAPI] @ 50% Fl. Intensity	Relative Fl. Change	Spectral Peak (nm)
G·T	2.2	9.5	459
C·A	2.5	19.5	459
A·A	1.0	18.4	459
G·A	13.4	20.6	460
G·G	—	1.7	456
T·T	1.0	29.8	463
C·T	1.6	31.2	475
C·C	0.9	18.0	460
Normal	2.5	30.6	463
Buffer	—	1.0	480

yield of DAPI is the minimum in G·G–DNA. This contradicting behaviour thus suggests that fluorescence properties of DAPI in G·G–DNA are significantly altered by the presence of two (electron-rich) guanines near the binding site of (electron-deficient) DAPI in the minor groove, which do not follow a simple reasoning to explain the static fluorescence data. Nevertheless, it is seen from Figures 6.2, 6.3 and Table 6.1 that DAPI fluorescence shows significant alterations in the minor groove of DNA because of the presence of various types of mismatched base-pairs near DAPI's binding site. However, again, no specific trend in DAPI spectral shifts in different mismatched- and normal-DNA is observed which can be correlated to the differential mismatch recognition and repair mechanism by MutS (or its analogues in human).[7-12]

6.3.3. Fluorescence Decays: Effect of Different Mismatches

The time-resolved fluorescence data of DAPI in normal- and all mismatched–DNA are compared to see the effect of the mismatches on fluorescence decays in the minor grooves of DNA. To monitor the effect of all such mismatches on collective (solvation) dynamics over broad time range, extensive data on wavelength dependent fluorescence decays of DAPI in the minor grooves of normal- and mismatched–DNA using UPC and TCSPC techniques were collected (total 9 samples, including 8 mismatched-DNA and one normal-DNA). Total 20–22 fluorescence decays were measured in UPC and TCSPC for each DNA/DAPI sample, totalling ~180 decays in UPC and ~198 decays in TCSPC. All raw fluorescence decays in each sample followed characteristic features of solvation dynamics, showing fast-decay at shorter wavelengths, fast-rise (or decay) followed by slow decay near peak wavelengths, and slow-rise followed by slow-decay at longer wavelengths. These decays were fitted using sum of 3-4 exponentials, and the fitted parameters were used in the re-construction of TRES following procedures discussed in chapter 3. It is, however, found that due to very low quantum yield of DAPI in G·G–DNA (only ~1.7 time

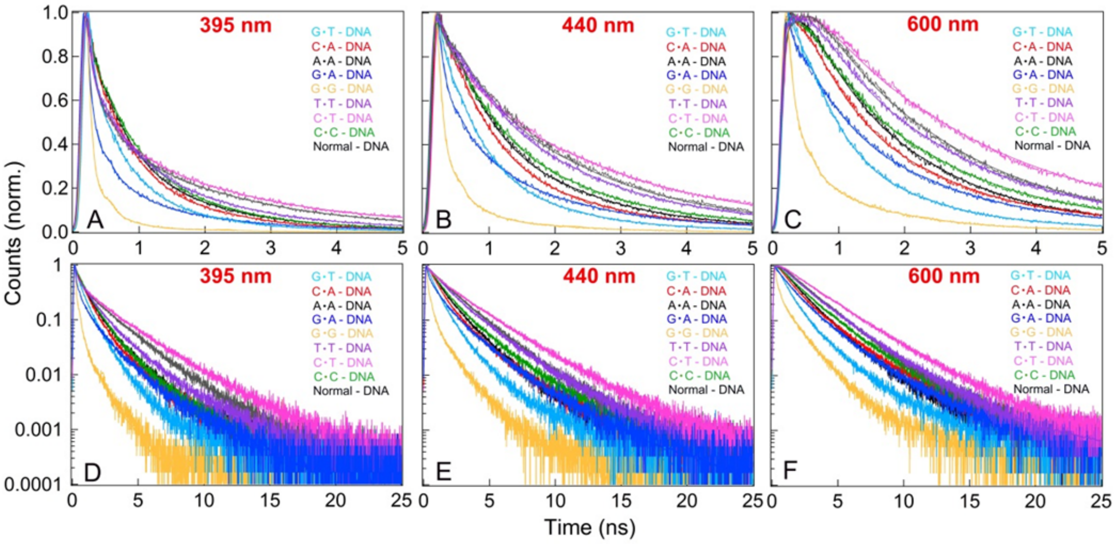

Figure 6.4: Fluorescence decays of DAPI bound to minor grooves of normal- and eight mismatched–DNA, measured in TCSPC at blue-side (395 nm), near peak (440 nm) and red-side (600 nm) of the fluorescence spectra. (A) – (C) Decays in short time-range upto 5 ns, and (D) – (F) decays in the full time-range plotted in semi-log scale. Lines through raw decays are fits using sum of 3-4 exponentials.

of buffer), the wavelength decays were much faster compared to those in other DNA samples. Nevertheless, these wavelength-dependent decays were analysed further to construct the TRES and subsequently obtain the Stoke shift data.

Figure 6.4 compares the decays of DAPI in normal- and all eight mismatched–DNA at shorter, peak and longer wavelengths, measured in TCSPC (see Figure 6.6 for other decays). Comparison shows distinct effects of different mismatches on the decay patterns, compared to those in normal-DNA. The relative (average) decay time-constants in different

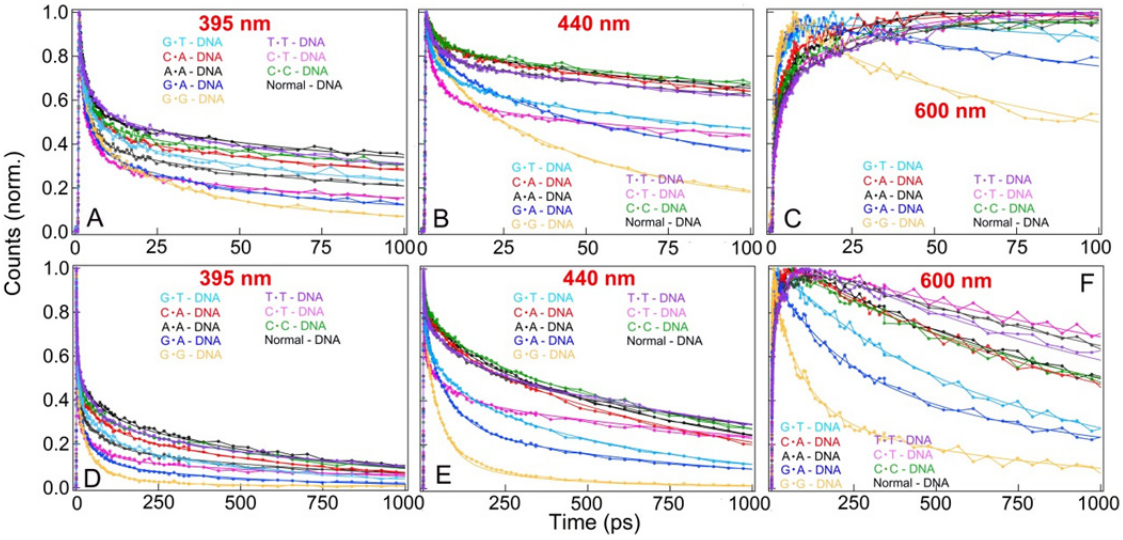

Figure 6.5: Fluorescence decays of DAPI bound to minor grooves of normal- and eight mismatched–DNA, measured in UPC at blue-side (395 nm), near peak (440 nm) and red-side (580 nm) of the fluorescence spectra. (A) – (C) Decays in short time-range upto 100 ps, and (D) – (F) decays in the longer time-range upto 1000 ps. Lines through raw decays are fits using sum of 3-4 exponentials.

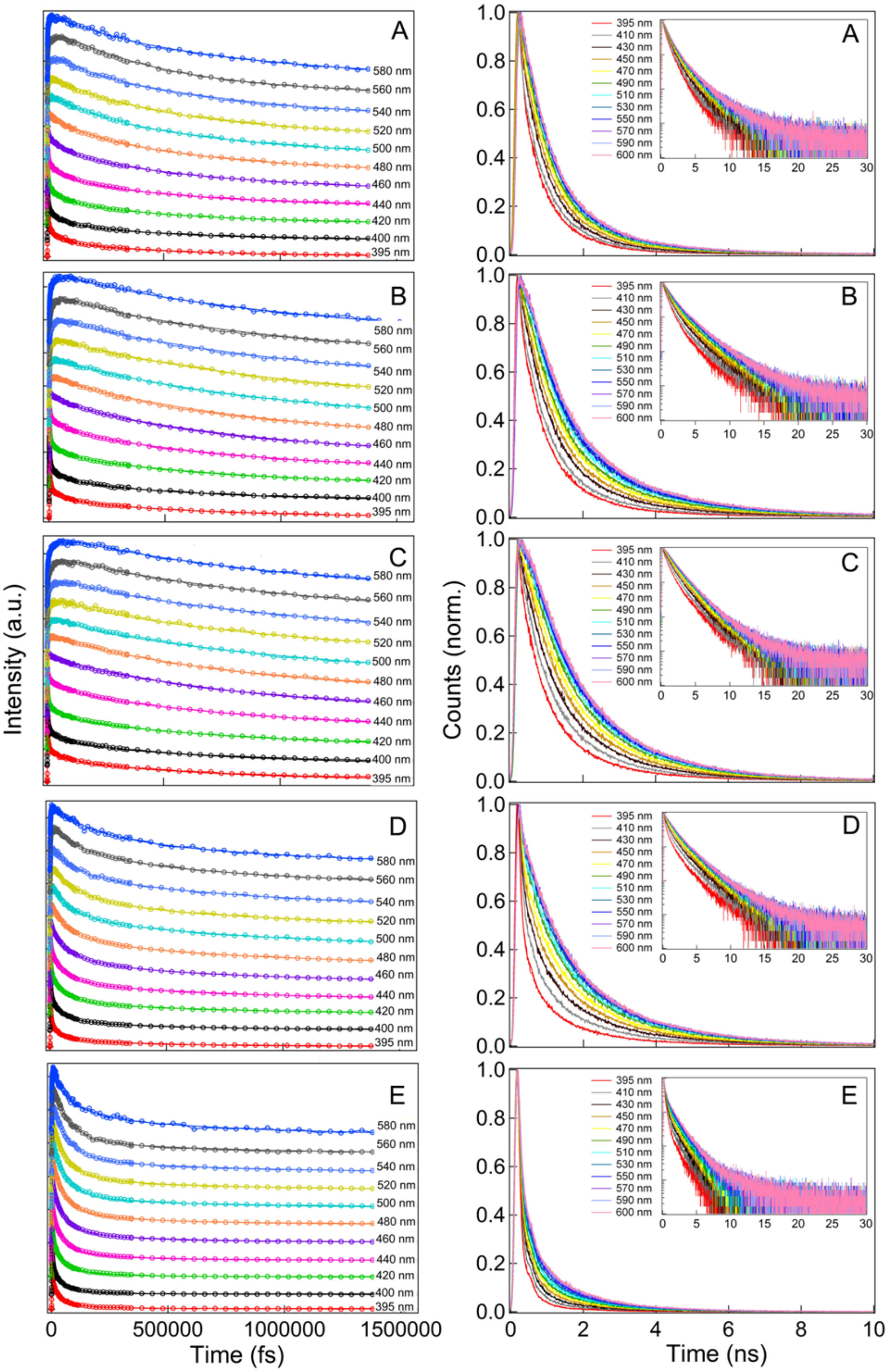

Figure 6.6a: Wavelength dependent fluorescence decays (with fits) of DAPI, measured in UPC (panels in left) and TCSPC (panels in right) setups, when bound to minor grooves of (A) G·T–DNA, (B) C·A–DNA, (C) A·A–DNA, (D) G·A–DNA, (E) G·G–DNA. Total 11 decays, out of 20-22 decays, covering entire fluorescence spectra of DAPI in respective DNA systems are plotted here to minimize clumsiness. Fits to raw data using sum of 3-4 exponential decays are included in the figures (solid lines through raw data).

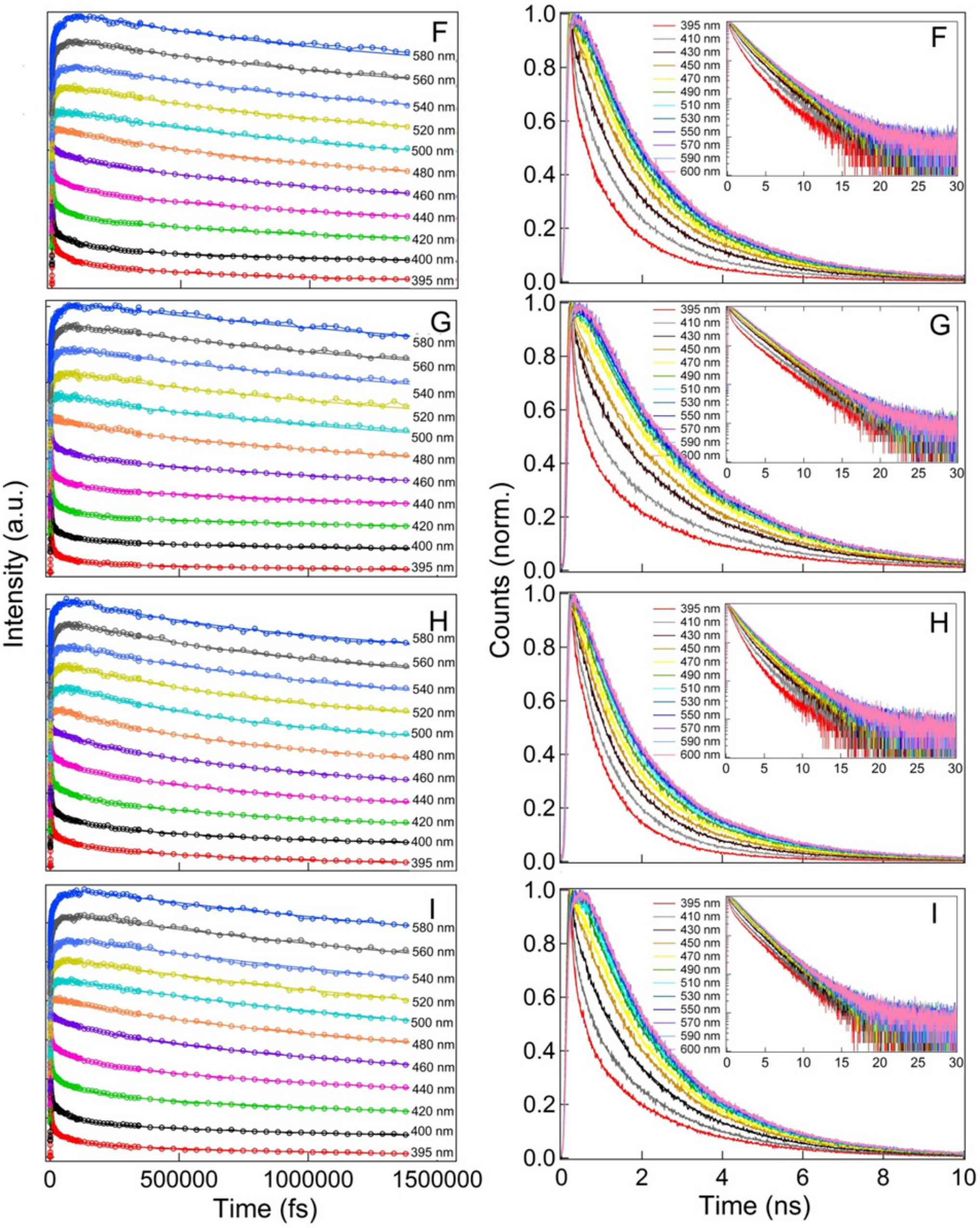

Figure 6.6b: Wavelength dependent fluorescence decays (with fits) of DAPI, measured in UPC (panels in left) and TCSPC (panels in right) setups, when bound to minor grooves of (F) T·T–DNA, (G) C·T–DNA, (H) C·C–DNA, (I) normal–DNA. Total 11 decays, out of 20-22 decays, covering entire fluorescence spectra of DAPI in respective DNA systems are plotted here to minimize clumsiness. Fits to raw data using sum of 3-4 exponential decays are included in the figures (solid lines through raw data).

DNA samples follow similar trend as that found in the steady-state fluorescence properties of DAPI in all these DNA samples. As can be seen, the DAPI decays in G·G–DNA are the fastest among all DNA samples, suggesting similar trend as observed in static fluorescence results. These raw fluorescence decays indeed suggest that there could be substantial differences in nanosecond solvation dynamics in the minor grooves of mismatched–DNA, compared to that in the minor groove of normal-DNA, as probed by the groove-bound DAPI. Figure 6.5 compares the raw fluorescence decays in faster time-scales, measured in UPC setup (see Figure 6.6 for other decays). A similar effect of the mismatched base-pairs on the femtosecond decay patterns is also observed on the DAPI decays. Nevertheless, the quantitative effect of mismatch on the solvation dynamics is captured in the dynamic Stokes shifts (i.e., average frequency shifts) of the minor groove binder as discussed below.

6.3.4. Comparison of Solvation Dynamics in All Mismatched- and Normal-DNA

Figure 6.7 plots the TRES (along with time-zero spectra) of DAPI in normal- and all mismatched–DNA, constructed from UPC and TCSPC decay data following the methods

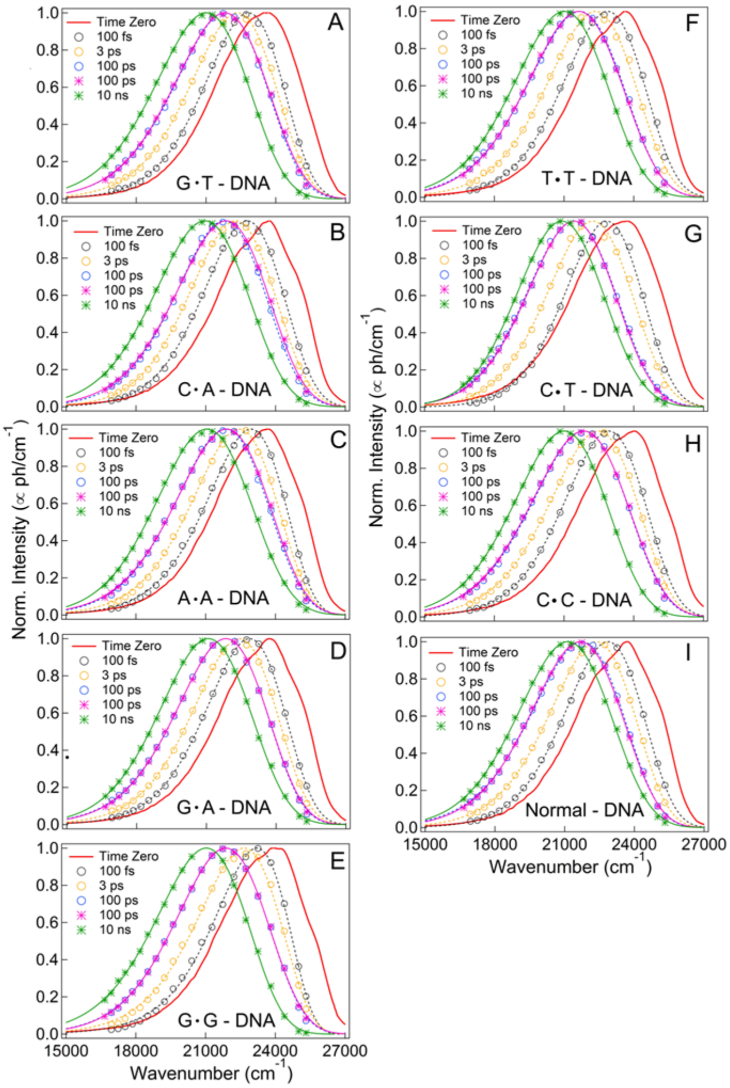

Figure 6.7: Time-resolved emission spectra (TRES) of DAPI bound to minor grooves of normal-DNA and all eight mismatched–DNA constructed from UPC data (circles) and TCSPC data (stars). TRES from UPC and TCSPC at 100 ps is shown in figures. Dashed and solid lines are log-normal fits to TRES. Red solid-line spectra are time-zero glass-spectra. Legends are included in the respective figures.

described in chapter 3. TRES shows proper spectral shift with time, suggesting that DAPI captures the dynamic Stokes shifts in all DNA samples studied here over entire five decades in time from 100 fs to 10 ns.

Figure 6.8A compares the 'absolute' dynamic Stokes shifts of DAPI in the minor grooves of all mismatched-DNA and normal-DNA over five decades in time from ~100 fs to 10 ns. The raw Stokes shift data show nearly smooth variation (like power-law) till ~100 ps in most DNA samples, beyond which exponential type relaxations are found to be originating in most samples. The Stokes shift dynamics in T·T–DNA, however, show very smooth variation over entire time-decades, indicating a single power-law type relaxation in this T·T–DNA, similar as observed in chapter 5 with another flanking canonical base-sequence near the T·T mismatch site (see below for details). The Stokes shift data could be well fitted with mainly three types of functions: a single power-law (equation 6.1), a power-law multiplied with a single exponential relaxation (equation 6.2), and a power-law multiplied with bi-exponential relaxation (equation 6.3) as,

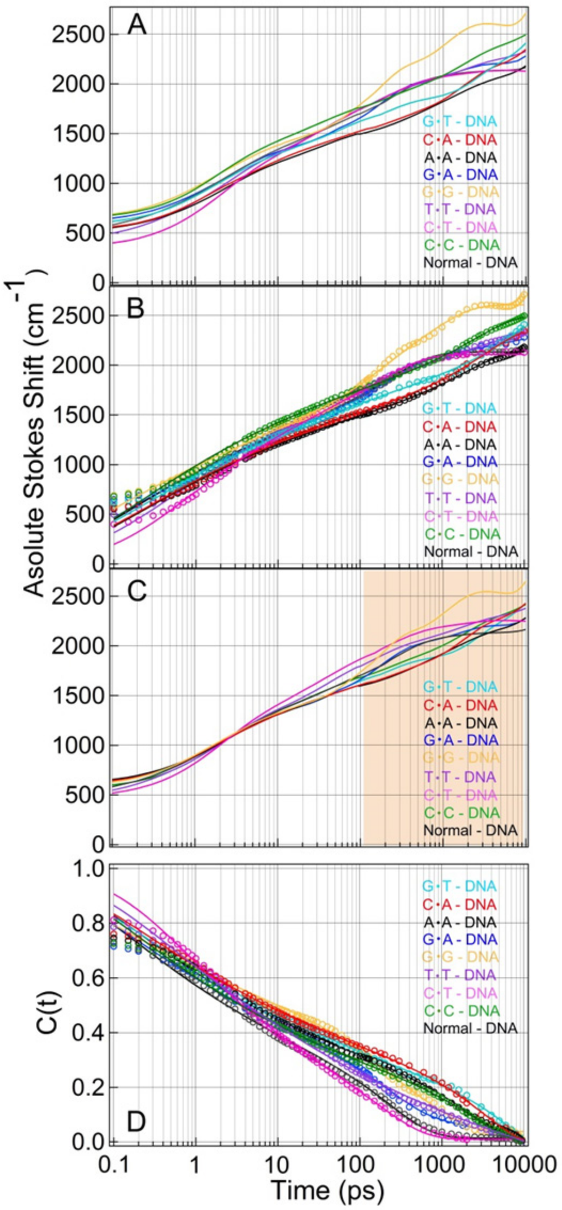

Figure 6.8: (A) Comparison of 'absolute' Stokes shifts of DAPI in the minor grooves of normal-DNA and eight mismatched-DNA. (B) Fits to the Stokes shift data using equations 6.1, 6.2 and 6.3. (C) Comparison of raw Stokes shifts after shifting them to merge in the initial time-decades, showing clear differences in the (exponential) dynamics in longer times (> 100 ps) – shaded portion. (D) Comparison of solvation correlation function, $C(t)$ of DAPI in normal- and mismatched DNA, constructed as, $C(t) = (S(10\text{ ns}) - S(t))/S(10\text{ ns})$.

$$S(t) = S_\infty\left[1 - \left(1 + \frac{t}{t_0}\right)^{-n}\right] \qquad (6.1)$$

$$S(t) = S_\infty\left[1 - \left(1 + \frac{t}{t_0}\right)^{-n} \times \mathrm{e}^{-\mathrm{t}/\tau_1}\right] \qquad (6.2)$$

$$S(t) = S_\infty\left[1 - \left(1 + \frac{t}{t_0}\right)^{-n} \times \left(a\mathrm{e}^{-\mathrm{t}/\tau_1} + (1-a)\mathrm{e}^{-\mathrm{t}/\tau_2}\right)\right] \qquad (6.3)$$

where S_∞ is the Stokes shift at $t = \infty$, t_0 is the time where power-law starts converging toward zero at $t = 0$, n is the power exponent, τ_i's are exponential time-constants, and a is the fraction of time-component. The plateau of Stokes shifts in the initial times (<~300 fs) arises because of limited time-resolution of the UPC setup (~250 fs). However, fits extracted power-law relaxations in this lower time range, leading to some deviations of the fits and the raw data below ~300 fs. Similar as seen in chapter 5, the Stokes shifts dynamics in T·T–DNA could again be nicely modelled with the equation 6.1, showing single power-law dynamics of exponent ~0.1. This power-law exponent (~0.1) is different than that obtained in chapter 5 (power-law exponent ~0.23) for a different canonical sequence flanking the T·T mismatch. This shows the direct effect of flanking sequence on the local solvation dynamics in the minor groove containing the T·T mismatched base-pair. More discussion on this is given below (section 6.3.5). The Stokes shifts dynamics of DAPI in G·T–, C·A–, A·A–, C·T–, C·C–, and normal–DNA could be well fitted to equation 6.2 which incorporate an extra (multiplicative) exponential relaxation in longer times together with the power-law. The Stokes shifts data in G·A– and G·G–DNA, however, could only be fitted with equation 6.3 that incorporates bi-exponential relaxation, multiplied to power-law, that model the long-time dynamics. Figure 6.8B combines the raw Stokes shifts data and the corresponding fits, while Figure 6.8C shows the Stokes shift data shifted to match the initial time-decades – so as to clearly show the differences in the exponential relaxations in longer times (> 100 ps). All the fitted parameters are included in Table 6.2. It can be seen that the dynamics in initial time-decades in the mismatched- and normal-DNA follow power-law with exponents that varies with small amount (~0.10 – 0.16) among most of the DNA-samples, except that in C·T–DNA which follow a faster power-law of exponent ~0.23. This observation is in line with the fact that DAPI senses most polar environment in the minor groove containing C·T–mismatch (see Figure 6.2), which may actually suggest that more water penetration near the DAPI binding site in C·T–DNA. Figure 6.8D plots the solvation correlation functions, $C(t)$, calculated from the absolute Stokes shift data in Figure 6.8A taking $S_\infty = S(10\text{ ns})$ as; $C(t) = (S(10\text{ ns}) - S(t))/S(10\text{ ns})$).

Table 6.2: Parameters obtained from fits to absolute Stokes shifts using equations 6.1, 6.2 and 6.3.

System	S_∞ (cm^{-1})	t_0 (ps)	Power-law exponent (n)	a	τ_1 (ns)	(1-a)	τ_2 (ns)	$<\tau>$ (ns)
G·T	2792	0.03	0.10	1	16.10	—	—	**16.10**
C·A	2392	0.03	0.12	1	4.60	—	—	**4.60**
A·A	2153	0.04	0.14	1	2.80	—	—	**2.80**
G·A	2233	0.02	0.14	0.65	0.28	0.35	2.88	**1.19**
G·G	2570	0.02	0.11	0.39	0.22	0.61	1.29	**0.87**
T·T	3271	0.06	0.10	—	—	—	—	—
C·T	2108	0.18	0.23	1	0.32	—	—	**0.32**
C·C	2509	0.04	0.15	1	3.67	—	—	**3.67**
Normal	2133	0.03	0.16	1	0.35	—	—	**0.35**

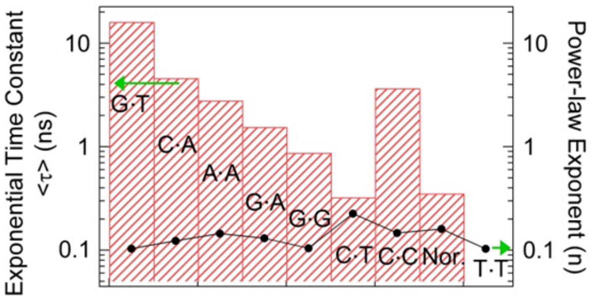

Figure 6.9: Graph plotting the relative values of average exponential relaxations (bars) and power-law exponent extracted from fits in respective mismatched- and normal-DNA. See also Table 6.2. See figure for legends and text for detailed discussion.

Comparison of dynamics data in Figure 6.8 (and Table 6.2) clearly shows that there are substantial differences in the exponential relaxations in longer times among the different mismatched base-pairs, although the dynamics remains very dispersed (power-law relaxation) in the initial time-decades till ~100 ps. The big question is now – whether such changes in the collective solvation dynamics of DNA, water and (possibly) ions around the mismatched sites in the minor groove of DNA correlate to the respective mismatch recognition and repair by the MutS (and its analogue) as reported earlier or not.[7-12] It is clear from Table 6.2 that the dispersed power-law dynamics in the initial time-decades do not change much among the different mismatched-DNA, and thus, no correlation of this power-law to the differential repair efficiencies is observed.

However, it is found that the (average) exponential relaxations are significantly varied among the different mismatches. Figure 6.9 plots the (average) exponential relaxation time-constants in the mismatched- and normal-DNA, together with the power-law exponents, found in the dynamics of respective systems. (Dynamics in T·T–DNA show pure power-law relaxation, hence, only the power-law exponent is plotted in Figure 6.9 for this system.) From most of earlier studies, as discussed in the introduction, it was found that purine-pyrimidine mismatches are most efficiently recognized and repaired by enzymes (with highest efficiency for G·T), followed by the purine-purine mismatches, and least efficiently recognized and repaired are the pyrimidine-pyrimidine mismatches.[7-12] It was also clearly noticed that G·T–mismatch is recognized and repaired the most among all mismatch types.[1,5,7-12] Interestingly, in Figure 6.9 it is observed that the exponential relaxation is very slow (16.1 ns) in G·T–DNA which is substantially different compared to those in other mismatched-DNA. The next highest time-constant of exponential relaxation is found in C·A–DNA, which was also shown to be repaired by MutS with similar efficiency as that of G·T–mismatch.[7-12] These two purine-pyrimidine mismatched pairs are most efficiently recognized and repaired by the enzymes, which also show here the exponential relaxations that are significantly higher compared those found in other mismatch types. As discussed in chapter 5, it is believed that different mismatch types can have different local structural dynamics which may, in turn, perturb the nearby water and ion environment in such a way that the collective solvation dynamics of all these components may be playing a bigger role, compared to only the local structural changes, to provide the signals to the mismatch repair protein-system. From present data, it seems the (slow) exponential solvation relaxations may directly provide the cues to the mismatch repair proteins. The purine-purine mismatches were also shown to be repaired with moderate efficiency by the repair enzymes. It is found in Figure 6.9 (and Table 6.2) that the time-constants of exponential relaxations are faster in case of A·A– and G·A–mismatches, however, somewhat smaller value is observed for G·G–mismatch because DAPI in G·G–DNA shows very low fluorescence quantum yield and lifetime – such that the dynamics in longer time-range could not be extracted completely. On the other hand, the pyrimidine-pyrimidine mismatches such as T·T– and C·T–DNA show either a single power-law (in T·T–DNA) or very small time-constant for the (multiplied) exponential relation (in C·T–DNA). In fact, the exponential time-constant (0.32 ns) is found to be very similar to that found in normal-DNA (0.35 ns). The single power-law seen in T·T–DNA is also in accordance with the results presented in previous chapter 5. Thus, it seems the faster exponential solvation relaxations are not well recognized as signals by the repair enzymes.

The dynamics in C·C–DNA, however, seen to be way off from the trend because DAPI in C·C–DNA shows slow exponential relaxation (3.67 ns) that is similar to the relaxation found in C·A–DNA. This is a clear deviation that does not match with the repair efficiency of MutS,[7,8] as it was reported in most of earlier studies that C·C–mismatch is least recognized and repaired by the enzymes.[7,8] This indicates that there may be other competing processes that are important for the recognition of this mismatch, which doesn’t allow MutS to efficiently repair the C·C–mismatch. Previous MD simulation study also found that the C·C–DNA does not follow the trend similar as others because the bending free-energy of C·C–mismatch are relatively low which would allow MutS (and other analogues) to repair this mismatch efficiently.[19] A similar trend is also found in the present study in terms of local solvation dynamics near this C·C–mismatch. All these results clearly indicate that there may be other competing factors which ultimately determine the efficiency of C·C–mismatch repair by the enzymes in physiological conditions. Nevertheless, the present results strongly suggest that it is the collective solvation dynamics of the local environment around the mismatch-sites (within ~10 – 15 Å) which provide important cues to the mismatch repair enzymes.

At this stage, it is not clear that which component (or with collective response of components) is responsible for the extra exponential relaxations observed in experiment for most of the mismatched-DNA. Certainly, large-scale MD simulation, together with calculations of solvation correlation functions, will be useful to explain the origin of the relaxations which seem important for mismatch recognition and repair. However, as discussed in the introduction, recent MD simulation did show that mismatched base-pairs induce significant alteration in the surrounding ion environment, possibly also the local hydration, particularly in G·T– and C·A–DNA. Thus, it may be possible that such changes in local hydration and ion environment, together with the specific DNA-mismatch motions, allow differential solvation dynamics around different mismatched base-pairs – such that these collective responses are differentially sensed by the repair enzymes.

6.3.5. Effect of Neighboring Canonical Sequence: T·T–DNA

It has been clearly documented in literature that the efficiency of mismatch recognition also depends on the canonical base-sequence flanking the mismatch-site.[7-9,20,21] To see such effects, the dynamic Stokes shifts of DAPI near T·T–mismatch introduced in the minor groove with two different flanking sequences, *Seq-1*: 5'-**CGCGCA**T**TGCGCG**-3' (chapter 5), *Seq-2*: 5′-**GGCGCAA**T**TGCGCGG**-3′ (this chapter), are compared in Figure 6.10. It is readily seen that although the overall dynamics remain dispersed showing single power-law relaxation over five decades in both minor grooves of T·T–DNA, the power-law exponent changes substantially from 0.23 in *Seq-1* to 0.10 in *Seq-1*, given the fact that in most of normal- and mismatched-DNA the power-law exponent remains similar (~0.10 – 0.16). This result clarifies that the neighbouring base-sequence near the mismatch-site does induce significant effect on the local solvation dynamics in DNA around the mismatch-site.

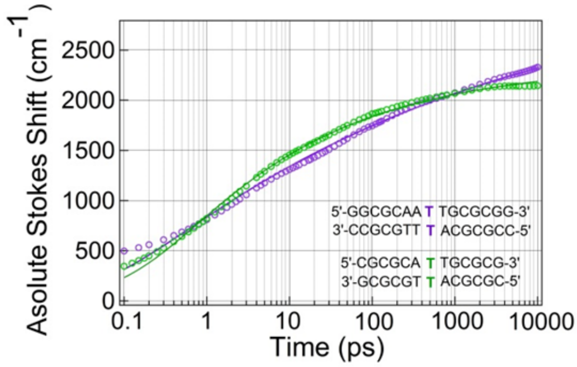

Figure 6.10: Comparison of 'absolute' Stokes shifts of DAPI (with single power-law fits) in the minor grooves of T·T-DNA with two different neighboring canonical sequences. For sequence see legends.

6.3.6. Fluorescence Anisotropy Decay: No Effect of Mismatches

One very important checking is needed at this stage to see if the extra exponential relaxations are originating from any internal rotational motions of probe-DAPI or not. The effect of mismatched bases on the internal motions of probe-DAPI can be characterized by performing time-resolved fluorescence anisotropy experiments, similar as done in the last chapter. This way, one can find if changes in the exponential solvation relaxations in mismatched-DNA are the direct effects of the probe's rotation/internal motion or not. To check this possibility we measured rotational anisotropy decays of DAPI in normal- and all eight mismatched–DNA using both TCSPC and UPC techniques. Both techniques were used because it was needed to also see if any rotational internal dynamics is originating in the probe-ligand in longer as well as shorter (femtosecond) time-scales or not. Figure 6.11 compares the anisotropy decays of DAPI in normal- and mismatched–DNA, measured in UPC (Figure 6.11A) and TCSPC (Figure 6.11B) setups. The UPC data capture the initial anisotropy decays that start from $r(t)$ = 0.4, while the rest of anisotropy decays after $r(t)$ = 0.3 in longer times is captured in TCSPC setup. Thus, combining data from both setups, the full anisotropy decays of DAPI in different DNA samples are captured here. These plots show almost identical anisotropy decays of DAPI in DNA samples, both in faster and longer time-scales, suggesting that there is no effect of incorporation of the mismatches on the rotational/internal dynamics of probe-DAPI. Thus, the solvation responses of DAPI in normal- and mismatched–DNA arise purely from the relaxation of electrostatic interaction energy of the ligand with surrounding charged/dipolar molecules, and that the ligand is bound strongly to the groove to tumble together with whole DNA molecule.

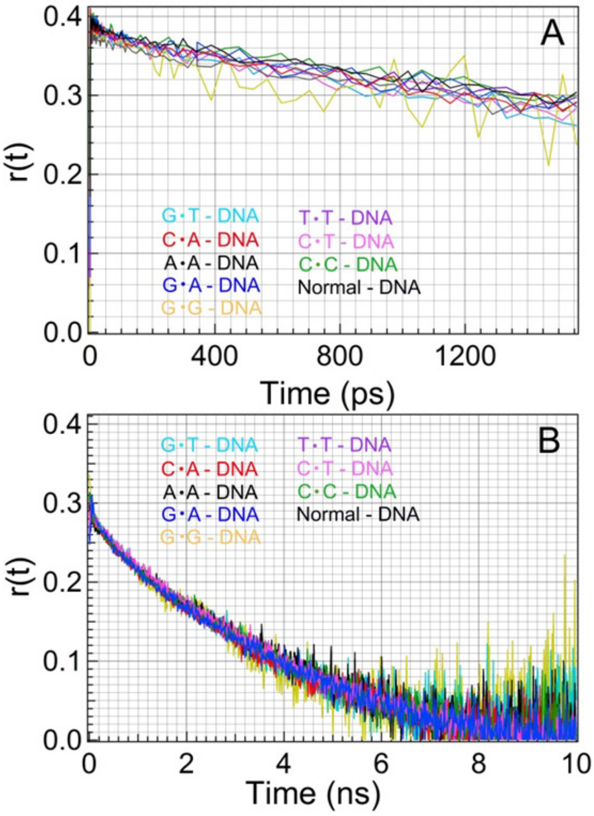

Figure 6.11: Rotational anisotropy decays of DAPI in the minor grooves of normal- and eight mismatched–DNA, measured in UPC (A) and TCSPC (B) setups. The UPC data captures the initial anisotropy decays that start from 0.4, while the rest of anisotropy decays after $r(t)$ = 0.3 in longer times is captured in TCSPC setup.

6.4. Conclusion

This chapter showed that introduction of different mismatches inside the minor groove of DNA induce Stokes shifts dynamics from ~100 fs to 10 ns that follow power-law or power-law multiplied to exponential relaxation, for the given canonical base-pair sequence flanking mismatched base-pairs. The extra exponential relaxation time-components are found to correlate very well to the differential efficiencies of mismatch recognition and repair by MutS (and its analogues in human).[1-5,7-12] It is clearly showed that the purine-pyrimidine mismatch base-pairs (G·T and C·A) induce slower exponential relaxations, with G·T–mismatch showing the slowest relaxation, compared to others (see Figure 6.9). These mismatches are shown to be repaired best among all by MutS, with G·T being more efficiently repaired. Earlier reports also showed purine-purine mismatches are repaired with moderate efficiency. In the same line, A·A– and G·A–mismatches are found to induce faster exponential relaxations compared to the purine-pyrimidine mismatches, although in G·G–mismatch the slower exponential component could not be extracted fully due to very low fluorescence quantum yield and much faster lifetime of DAPI in this DNA. The pyrimidine-pyrimidine mismatches, however, show either very fast extra exponential relaxation (in C·T–DNA) or only dispersed power-law (in T·T–DNA), similar as found in normal DNA. These mismatches were found to be repaired with low efficiency by MutS. The only exception found is with C·C–DNA which also showed very slow exponential relaxation, although this mismatch was reported to be repaired by MutS with least efficiency. Thus, it is believed that there may be other factors that control the mismatch repair efficiency, at least for this mismatch. These results are significantly important because it shows that the slower collective dynamics of the local environment around the mismatch-sites seem to provide important cues to the repair enzymes for the repair mechanism. As pointed out in chapter 5, it is believed that different mismatches would have different levels of perturbations to the surrounding water and ions, as also seen in recent MD simulation study,[6] which would then define the local collective solvation dynamics that are sensed by the incoming repair enzymes to differentiate the mismatch types. The current results point directly to such a situation. However, it is still not clear which component/components define such local dynamics in the slower time scales (slower than 100 ps) which induce the differential solvation dynamics around the different mismatches. Extensive MD simulations with correlation function calculations and decomposition of components' contributions are needed to fully understand the origin of the differential dynamics in mismatched-DNA, especially in longer nanoseconds time scales. Nevertheless, chapter 5 and this present chapter clearly showed that dynamic Stokes shift experiments have tremendous capability to unravel the complex dynamical features induced by a single mismatched base-pair inside DNA minor groove. Thus, further similar experiments on other base-sequences as well as extensive MD simulations would help tremendously to shed new light on the understanding of DNA-mismatch recognition and repair by enzymes in vivo.

Reference

(1) Modrich, P. DNA Mismatch Correction. *Annu. Rev. Biochem.* **1987**, *56*, 435-466.

(2) Kunz, C.; Saito, Y.; Schar, P. DNA Repair in Mammalian Cells: Mismatched Repair: Variations on a Theme. *Cell. Mol. Life Sci.* **2009**, *66*, 1021-1038.

(3) Kunkel, T. A.; Erie, D. A. DNA Mismatch Repair. *Annu. Rev. Biochem.* **2005**, *74*, 681-710.

(4) Schofield, M. J.; Hsieh, P. DNA Mismatch Repair: Molecular Mechanisms and Biological Function. *Annu. Rev. Microbiol.* **2003**, *57*, 579-608.

(5) Fukui, K. DNA Mismatch Repair in Eukaryotes and Bacteria. *J. Nucleic Acids* **2010**, *2010*, 1231-1264.

(6) Rossetti, G.; Dans, P. D.; Gomez, P. I.; Ivani, I.; Gonzalez, C.; Orozco, M. The Structural Impact of DNA Mismatches. *Nucleic Acids Res.* **2015**, *43*, 4309-4321.

(7) Dohet, C.; Wagner, R.; Radman, M. Repair of Defined Single Base-Pair Mismatches in Escherichia Coli. *Proc. Nat. Acad. Sci. USA* **1985**, *82*, 503-505.

(8) Kramer, B.; Kramer, W.; Fritz, H. J. Different Base/Base Mismatches are Corrected with Different Efficiencies by the Methyl-Directed DNA Mismatch-Repair System of E. coli. *Cell* **1984**, *38*, 879-887.

(9) Varlet, I.; Radman, I.; Brooks, P. DNA Mismatch Repair in Xenopus Egg Extracts: Repair Efficiency and DNA Repair Synthesis for all Single Base-Pair Mismatches. *Proc. Nat. Acad. Sci. USA* **1990**, *87*, 7883-7887.

(10) Brown, J.; Brown, T.; Fox, K. R. Affinity of Mismatch-Binding Protein MutS for Heteroduplexes containing Different Mismatches. *Biochem. J.* **2001**, *354*, 627-633.

(11) Schaaper, R. M. Base Selection, Proofreading, and Mismatch Repair during DNA Replication in Escherichia coli. *J. Biol. Chem.* **1993**, *268*, 23762-23765.

(12) Brown, T.; Hunter, W. N. Non-Watson-Crick Base Associations in DNA and RNA Revealed by Single Crystal X-Ray Diffraction Methods: Mismatches, Modified Bases, and Nonduplex DNA. *Biopolymers* **1997**, *44*, 91-103.

(13) Tikhomirova, A.; Beletskaya, I. V.; Chalikian, T. V. Stability of DNA Duplexes Containing GG, CC, AA, and TT Mismatches. *Biochemistry* **2006**, *45*, 10563-10571.

(14) Peyret, N.; Seneviratne, P. A.; Allwai, H. T.; SantaLucia, J. Jr. Nearest-Neighbor Thermodynamics and NMR of DNA Sequences with Internal A·A, C·C, G·G, and T·T Mismatches. *Biochemistry*, **1999**, *38,* 3468–3477.

(15) Bhattacharya, P. K.; Cha, J.; Barton, J. K. ^{1}H NMR Determination of Base-Pair Lifetimes in Oligonucleotides Containing Single Base Mismatches. *Nucleic Acids Res.* **2002**, *30*, 4740-4750.

(16) Yin, Y.; Yang, L.; Zheng, G.; Gu, C.; Yi, C.; He, C.; Gao, Y. Q.; Zhao, X. S. Dynamics of Spontaneous Flipping of a Mismatched Base in DNA Duplex. *Proc. Nat. Acad. Sci. U.S.A.* **2014**, *111*, 8043-8048.

(17) Guest, C. R; Hochstrasser, R. A.; Sowers, L. C.; Millar, D. P. Dynamics of Mismatched Base Pairs in DNA. *Biochemistry* **1991**, *30*, 3271-3279.

(18) Nag, N.; Rao, B. J.; Krishnamoorthy, G. Altered Dynamics of DNA Bases Adjacent to a Mismatch: A Cue for Mismatch Recognition by MutS. *J. Mol. Biol.* **2007**, *374*, 39-53.

(19) Sharma, M.; Predeus, A. V.; Mukherjee, S.; Feig, M. DNA Bending Propensity in the Presence of Base Mismatches: Implications for DNA Repair. *J. Phys. Chem. B* **2013**, *117*, 6194-6205.

(20) Joshi, A.; Rao, B. J. MutS Recognition: Multiple Mismatches and Sequence Context Effects. *J. Biosci.* **2001**, *26*, 595-606.

(21) Fazakerley, G. V.; Quignard, E.; Woisard, A.; Guschlbauer, W.; Marel, G. A. V. D.; Boom, J. H. V.; Jones, M.; Radman, M. Structures of Mismatched Base Pairs in DNA and Their Recognition by the Escherichia coli Mismatch Repair System. *EMBO J.* **1986**, *5*, 3697-3703.

Chapter 7

Solvation Dynamics in G-quadruplex DNA

The last three chapters presented extensive TRFSS experimental and MD simulation results on Watson-Crick normal and mismatch-incorporated duplex-DNA. The TRFSS results as well as direct comparison of TRFSS experiments to simulation have allowed obtaining unprecedented details of the nature of solvation dynamics in the minor grooves of normal- and mismatched-DNA. It was shown that TRFSS experiments and MD simulations have tremendous power to explain the dynamics of solvation in DNA. These results clearly showed that *power-law* solvation dynamics is intrinsic to duplex-DNA, although such dispersed dynamics may have different origin. More so, it was shown that such power-law dynamics can be modulated to exponential type relaxations in nanosecond time-scales by different base-pair mismatches introduced in the minor groove of duplex DNA. Now, this chapter (and chapter 8) elaborates on similar TRFSS and MD simulation studies performed first time on the higher order G-quadruplex DNA structures. Results will show that solvation dynamics in such G-quadruplex DNA remain similar as found in Watson-Crick duplex-DNA, showing dispersed power-law dynamics over several decades of time.

7.1. Introduction

G-quadruplex structures are higher order DNA structures that are formed by the self-assembly of DNA sequences that are guanine-rich in presence of monovalent cations such as Na^+ or K^+ and/or small molecules.[1-7] These structures are formed by the association of four guanine bases that are held together by Hoogsteen-type hydrogen bonds, forming a planar structure called guanine-tetrads. Multiple guanine tetrads stack on top of each other giving rise to unusual DNA structure called G-quadruplex.[1-7] In human genome, G-quadruplex structures are found at the end of chromosomes, i.e., telomeric ends as well as in promotor regions.[8,9] During the process of normal cell division, shortening of telomere occurs which leads to apoptosis and ultimately cell death. However, in cancer cells, overexpression of telomerase catalyzes elongation of telomere which leads to abnormal cell division.[10] G-quadruplex DNA structures are found to inhibit the catalytic activity of telomerase, thus blocking uncontrolled division of cells.[11] Therefore, these structures have attracted huge attention for its therapeutic activity as a target for anticancer drugs to stop telomerase activity.[7,10,12-14] Formation of quadruplex structures in vitro,[1-4,11,15] as well as in human cells[5] has initiated tremendous research to develop ligands which can specifically recognize and target these structures for efficient anti-tumor effects.[6,7]

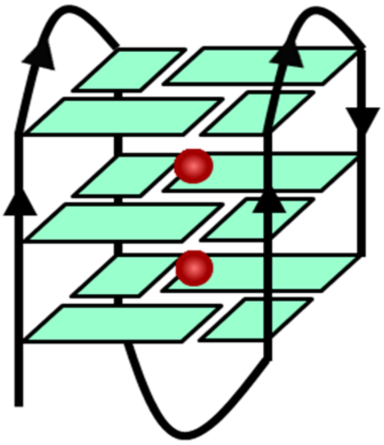

Figure 7.1: Schematic representation of antiparallel G-quadruplex DNA.

G-quadruplex DNA (GqDNA) possesses high structural diversity and shows various structural topologies in solution based on ion environment and/or induced by small molecules.[2-4,6,15,16] More importantly, it is found that structural polymorphism is drastically induced by the change in local hydration/solvation state,[17,18] thus affecting the binding of ligands to these structures.[19] However, regardless of large sum of structural data on quadruplex-ligand complexes,[1,6,7,15,17,18] dynamics of water and ions in-and-around quadruplex DNA and their role in stabilizing the local solvation around a ligand bound inside GqDNA still remains unknown.

Though DNA differs from proteins in many ways, there exists similarity in their underlying dynamical features. Significant attempts have been made to understand the dynamics in DNA and proteins through interplay between experiments,[20-32] theory[33] and simulations.[34-50] Dynamics in biological macromolecules extend in time >10 ps,[20-32] while the dynamics in simple water completes within few picoseconds.[51] It has been found that DNA and proteins show non-exponential and dispersed dynamical feature that extends in several decades of time, following logarithmic,[45,46] stretched-exponential[44] or even power-law[27-30,35,38,46,47] relaxation in many cases. Explaining such slow and dispersed dynamics remains difficult due to strong coupling between the components of biomolecular solution i.e., ions, water and biomolecule. Thus, questions concerning the origin of such dynamics still remain; whether the dynamics of ion or water or biomolecules or the coupled motion of these components controls the dynamics in biomolecules.[20,34-41] Nevertheless, solvation dynamics studies in DNA are still limited as compared to proteins and are mainly focussed only on duplex-DNA.[22-38] Dynamics of solvation in other higher order DNA structures such as G-quadruplex DNA has never been explored earlier.

This chapter interrogates the dynamic Stokes shifts of ligand (DAPI: 4′6,-diamidino-2-phenylindole) in antiparallel GqDNA (Figure 7.1) through direct comparison of TRFSS experiments to MD simulation and to the previous TRFSS data in duplex-DNA.[27,28] It has been found that ligand solvation in GqDNA shows power-law relaxation added with fast exponential feature from ~100 fs to 10 ns. Simulation results on same DAPI-GqDNA complex of 65 ns show that motion of water molecules governs the fast relaxation, while both water and DNA motions contribute equally to the slow dispersed power-law dynamics.[52] Contribution from ions was found to be insignificant. Moreover, broadly distributed residence time and sublinear mean-square displacements (MSDs) of water molecules near the binding site of the ligand indicate that such slow and dispersed solvation dynamics can be directly related to the subdiffusive motion of perturbed water near GqDNA.[52]

7.2. Materials and Methods

DAPI was from Sigma-Aldrich, HPLC-purified single-stranded human telomeric 22-mer 5'-AGGG(TTAGGG)3-3' DNA oligonucleotide was also from Sigma-Aldrich. GqDNA samples were prepared in HPLC grade water (H_2O; Merck) and in deuterium oxide (D_2O; Sigma Aldrich). Anti-parallel GqDNA was prepared in 10 mM Tris-HCl buffer of pH 7.2 with 100 mM NaCl in H_2O by annealing DNA from 95°C to 25°C for ~5 hours. For GqDNA prepared in D_2O, pH was maintained at 7.2 by adding orthophosphoric acid. Human telomeric DNA sequence takes antiparallel structure in presence of NaCl with two lateral loops and one diagonal loop.[1,3] The structures were confirmed by taking CD spectra (Figure 7.2).

Before making DAPI/GqDNA samples for measurements, binding kinetics of DAPI to GqDNA was monitored by titrating varying concentration of GqDNA and keeping DAPI concentration constant. Figure 7.3 shows the binding kinetics of DAPI with GqDNA showing changes in fluorescence signal with GqDNA concentration. From this data, we chose [GqDNA]:[DAPI] ratio where DAPI fluorescence saturates. For UPC measurements, DAPI concentration was kept at 20 µM and GqDNA at 1.3 mM ([GqDNA]:[DAPI] = 65:1), whereas for TCSPC measurements DAPI and GqDNA concentrations were 3 µM and 195 µM, respectively ([GqDNA]:[DAPI] = 65:1).

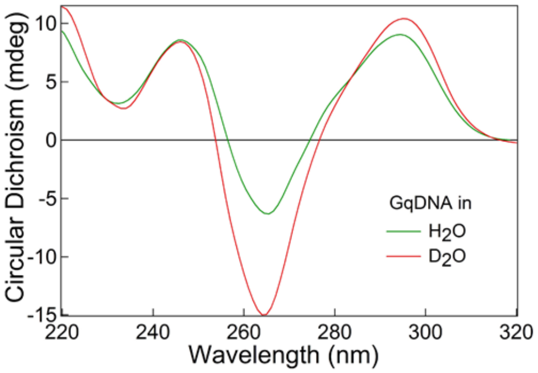

Figure 7.2: CD spectra showing formation of anti-parallel G-quadruplex DNA in H_2O buffer (green) and D_2O (red). The negative peak at ~265 nm and positive peak at ~245 nm indicate the typical signature of anti-parallel G-quadruplex structure formation.

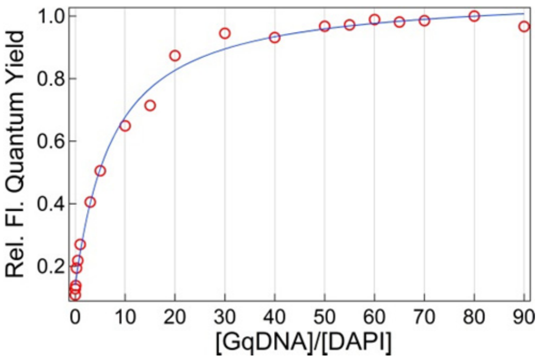

Figure 7.3: Binding kinetics of DAPI to anti-parallel GqDNA in H_2O-buffer. The line through points is a guide to eye.

7.3. Results: Experiments

7.3.1. Steady State Fluorescence Data

Upon binding to GqDNA, DAPI fluorescence increases by ~8 times and the emission spectrum shifts by ~2 nm relative to buffer. Fluorescence of DAPI increases ~12 times and the spectrum shifts towards blue-side by ~10 nm upon binding to GqDNA prepared in D_2O (Figure 7.4). These results suggest local hydration plays important role on DAPI binding to GqDNA. The larger blue shift in D_2O indicates lower polarity inside GqDNA in D_2O compared to H_2O.

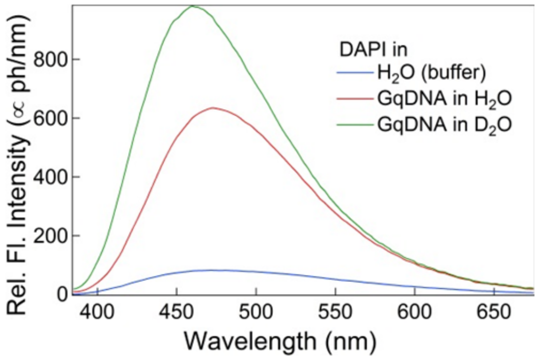

Figure 7.4: Steady-state fluorescence spectra of DAPI in bulk water (buffer; blue), and bound to anti-parallel GqDNA prepared in H_2O-buffer (red) and in D_2O (green).

7.3.2. Binding Constant of DAPI to GqDNA

The binding constant (K) of DAPI to GqDNA in H_2O was calculated by measuring rotational anisotropy decays of DAPI/GqDNA complex at various GqDNA concentrations using TCSPC technique. Anisotropy decays were collected for 19 samples with varying concentration of GqDNA from 0 μM to 300 μM with a constant DAPI of 3 μM. Figure 7.5A shows (few) anisotropy decays. The decays were fitted (globally) to bi-exponential function (equation 7.1) having two rotational time-constants; for free (τ_f) and bound (τ_b) DAPI.

$$r(t) = r_0\left[a_f^r \exp\left(-\frac{t}{\tau_f^r}\right) + a_b^r \exp\left(-\frac{t}{\tau_b^r}\right)\right] \tag{7.1}$$

where a_f^r and a_b^r are contributions of free and bound DAPI, τ_f^r (= 0.26 ns) and τ_b^r (= 2.7 ns) are the corresponding time-constants. Intensity weighted fractions, a_f^r and a_b^r, are written in terms of binding constant (K) as,

$$a_f^r = \frac{1}{1+(F_b/F_f)K[\mathrm{GqDNA}]} \tag{7.2a}$$

$$a_b^r = \frac{(F_b/F_f)K[\mathrm{GqDNA}]}{1+(F_b/F_f)K[\mathrm{GqDNA}]} \tag{7.2b}$$

where F_b and F_f are fluorescence intensities of bound and free DAPI, respectively. The variations of a_f^r and a_b^r with [GqDNA] are shown in Figure 7.5B. The binding constant (K) was determined to be 2.7 × 10^5 M^{-1} by fitting the variation of a_f^r or a_b^r using equation 7.2 (see Figure 7.5B).

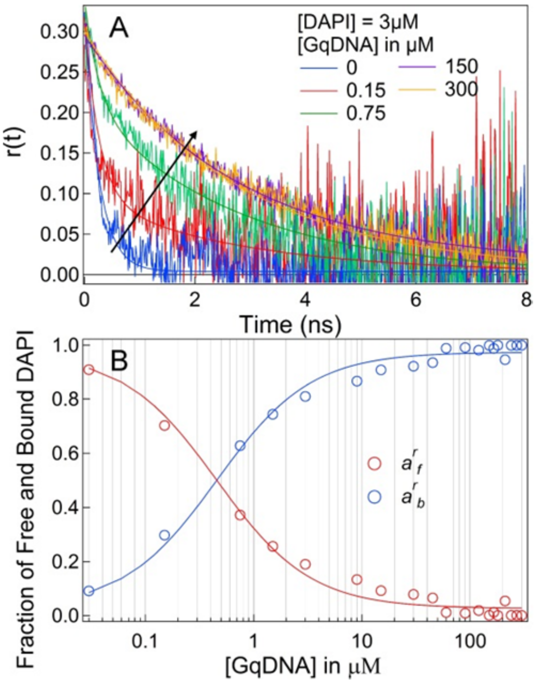

Figure 7.5: (A) Fluorescence anisotropy decays of DAPI in GqDNA. (B) Variations of free (red) and bound (blue) fractions of DAPI to GqDNA at different [GqDNA].

7.3.3. Fluorescence Decays

Total 19 fluorescence decays in UPC and 22 decays in TCSPC were collected at magic-angle polarization with interval of 10 nm, covering full fluorescence spectra. Measured decays in UPC and TCSPC in H_2O and D_2O are shown in Figure 7.6. The fluorescence decays of DAPI-GqDNA complex in D_2O are slower in longer-times and moderately slower in fast time-scales, compared to that of GqDNA in H_2O.

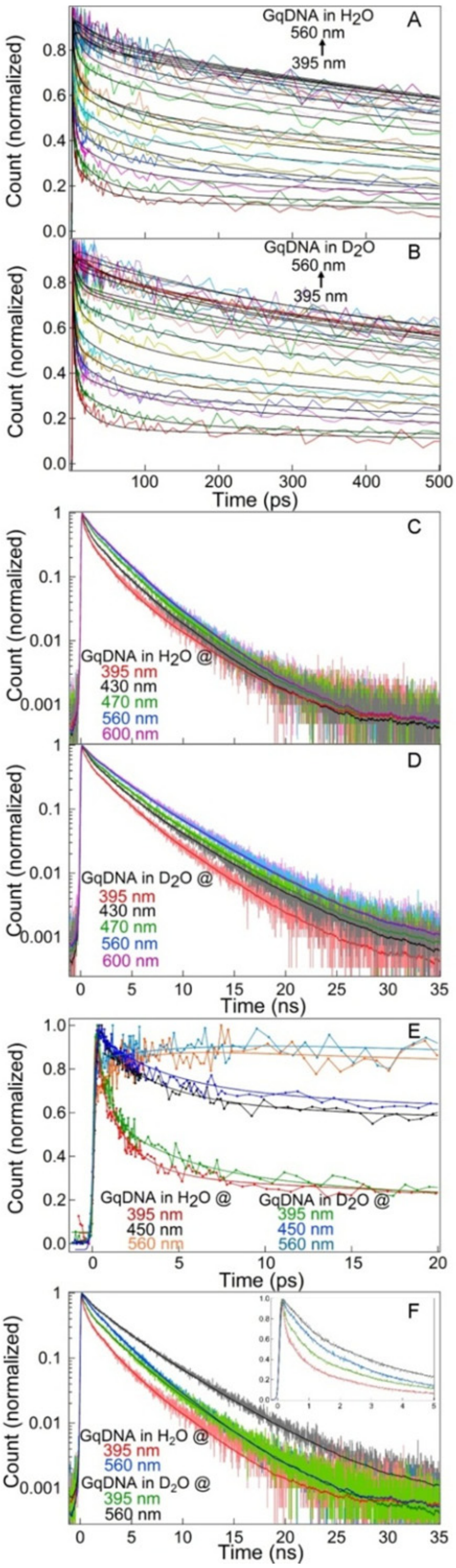

Figure 7.6: Fluorescence decays measured in UPC and TCSPC: UPC data of DAPI/GqDNA in H_2O-buffer (A) and D_2O (B), and TCSPC data for GqDNA in H_2O-buffer (C) and D_2O (D). Only few raw TCSPC data are shown to minimize clumsiness.

7.3.4. Time-Resolved Fluorescence Stokes Shifts

Figure 7.7 shows the TRES of DAPI in GqDNA prepared in H_2O and D_2O from 100 fs to 10 ns. The time-zero glass spectra were measured for GqDNA samples by freezing them at -78°C (195 K) to form glass and are included in the TRES plot. TRFSS of DAPI bound to 22-mer (5′AGGG(TTAGGG)3-3′) human telomeric antiparallel GqDNA[1] in H_2O and D_2O buffer from 100 fs to 10 ns shows that rate of Stokes shift in both samples are slow and dispersed along with a faster relaxation below ~5 ps (Figure 7.8A). The dynamic Stokes shift data of DAPI bound to GqDNA in both, H_2O and D_2O samples were modelled with a power-law summed with exponential relaxation as

$$S(t) = S_{\infty}\left[a\left(1-\left(1+\frac{t}{t_0}\right)^{-n}\right)+b\left(1-e^{-t/\tau}\right)\right] \tag{7.3}$$

The fit extracted slow dynamics as power-law relaxation of exponent 0.16 and fast exponential relaxation of 2 ps for H_2O buffer sample, whereas a more dispersed power-

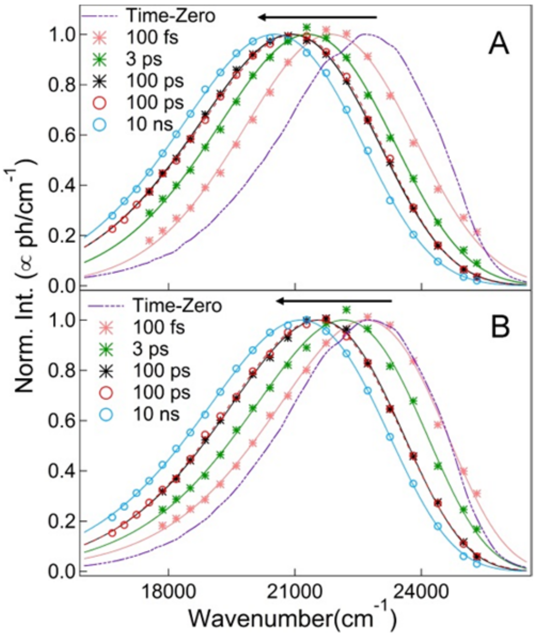

Figure 7.7: Time-resolved emission spectra (TRES) of DAPI in GqDNA prepared in H_2O buffer (A) and D_2O (B), constructed from UPC (star) and TCSPC (circle) data. TRES matching of UPC and TCSPC is shown at common time-point of 100 ps. Dashed and solid lines through points show log-normal fits to data. Purple dotted curves denote the time-zero glass spectra of samples measured at -78 °C.

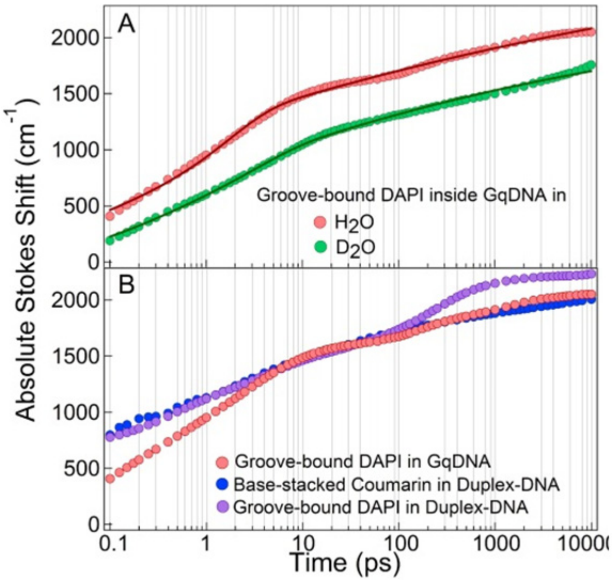

Figure 7.8: (A) Comparison of absolute Stokes shifts of DAPI bound to GqDNA prepared in H_2O buffer (pink) and D_2O (green). Lines through points show fits using eq. 1. (B) Comparison of “absolute” Stokes shift of DAPI in GqDNA (green) to previous Stokes shift data of DAPI (purple) and coumarin (blue) in duplex-DNA. The duplex-DNA data are shifted vertically to match with GqDNA data.

law relaxation of exponent 0.09 and exponential relaxation of 3.7 ps for D_2O buffer sample was observed. Note that the dynamics in pure water completes within ~1 ps[51] while the diffusive dynamics of water near biomolecule surface slowdown by a factor of only 2-3 compared to pure water.[43] Hence, the exponential time-constant of 2 ps obtained for H_2O sample was attributed to interfacial-water dynamics near GqDNA. This was confirmed from the D_2O effect on the dynamics and MD simulation (see below). In fact, retardation in dynamics on replacing H_2O with D_2O by a factor of ~1.4 in duplex-DNA was observed by Ernsting *et al.*[25] Similar D_2O effect on dynamics infers that water contributes substantially to the overall solvation dynamics in GqDNA.

Several TRFSS studies with probes bound to minor grooves or covalently attached inside duplex-DNA have been performed which showed that DNA dynamics extends to several decades of time following stretched-exponential or logarithmic or power-law relaxation.[22-32] Absolute Stokes shift of DAPI in GqDNA was compared with the previously reported data of groove-bound DAPI and base-stacked coumarin in duplex-DNA (Figure 7.8B).[27,28] It can be seen that in times >5 ps the power-law dynamics probed by DAPI in GqDNA is similar to the dynamics probed by coumarin in duplex-DNA,[22,23] but differs from DAPI in duplex-DNA.[24] Moreover, at times <5 ps, distinct fast relaxation appears in GqDNA which is absent in case of duplex-DNA.[27,28] This can be a direct reflection of loosely bound DAPI in GqDNA[52] (binding constant ~2.7 x 10^5 M^{-1}) compared to duplex-DNA which may result into a condition where DAPI is exposed towards water to probe both the fast and slow (perturbed) water dynamics near GqDNA, compared to buried DAPI and coumarin inside duplex-DNA (Figure 7.8B).[27,28]

Although TRFSS experiments showed dispersed dynamics in GqDNA, it is still very difficult to assign such dynamics to components of DNA solution. MD simulation provides direct route to interpret the complex TRFSS dynamics.[34-38] Hynes, Bagchi and co-workers found slow dynamics in duplex-DNA simulation which was attributed to water and ion motions, but could not capture long time (nanosecond) dynamics as the simulation was not long enough.[34] Sen et al. compared time resolved Stokes shift of coumarin and simulated electric field correlation in duplex-DNA and found that both the data are in excellent agreement with each other.[35] This study also shows that water motion governs the slow power-law dynamics in duplex-DNA. However, Furse and Corcelli performed simulation on Hoechst bound to the groove of duplex-DNA, similar to the experiment of Zewail and found that it is not the motion of water or ions, but DNA controls the slow dynamics till 350 ps.[36,37] These results indicate that regardless of slow dispersed power-law dynamics observed in duplex-DNA, explanation of such complex dynamics remains difficult.[34-38]

To explain and quantify the dispersed solvation dynamics in GqDNA, MD simulation of 65 ns was performed on docked DAPI/GqDNA system. The TRFSS result in H_2O-buffer was directly compared to the simulated Stokes shift dynamics to explain the complex dynamics in GqDNA. The details are provided in the next section.

7.4. Simulation Methods, Results and Discussion

MD simulation has excellent capability to provide intricate details of dynamics measured in experiments, including the contributions of individual components of complex biomolecular systems. An equilibrium MD simulation of 65 ns was performed on a docked DAPI-GqDNA complex in AMBER-12[52] using *parm99* force field and TIP3P water molecules – so as to quantify the dynamics seen in TRFSS experiments. Simulation results were directly compared with the experimental data. All simulations were performed on a workstation with 16 CPU-cores using SANDER module of AMBER-12.

7.4.1. Molecular Docking

Three dimensional coordinates (X-ray or NMR structural data) of DAPI bound to GqDNA is not available in literature. Therefore, molecular docking of DAPI in human telomeric antiparallel G-quadruplex DNA (PDB entry 143D)[1] was performed using AUTODOCK 4.2[53]. The NMR structure of human telomeric GqDNA (143D) does not contain central Na^+ ions that govern the stability of guanine quartet. Thus, two Na^+ ions were introduced manually in between three G-stacks of quadruplex DNA to provide stability to the system. Before docking DAPI onto quadruplex structure and proceeding towards MD simulation, the position of these two central Na^+ ions were equilibrated through several steps of minimization, equilibration and production runs. The procedure is briefly discussed below.

After introducing two central ions, negative charge of DNA was neutralized by additional 19 Na^+ ions which were added through LEAP module of AMBER-12. Aqvist parameters were used for Na^+ ions.[54] TIP3P water molecules (4767) were used to solvate the system using a buffer of 10 Å from DNA in each direction.[55] Solvated DAPI-GqDNA system was minimized using *parm*99 force-field in AMBER-12 at different steps: During initial 10000 steps of minimization, both DNA and central ions were kept fixed with a restraint of 300 kcal mol^{-1} $Å^{-2}$. The restraint on DNA was removed gradually by decreasing it from 200 kcal mol^{-1} $Å^{-2}$ to 100, 50 and 10 kcal mol^{-1} $Å^{-2}$ in further 10000 steps of minimization each, while the restraint on central Na^+ ions were kept fixed at 300 kcal mol^{-1} $Å^{-2}$. This was followed by reducing the restraint on central ions in steps of 10000 each down to 200, 100, 50, and 10 kcal mol^{-1} $Å^{-2}$. Final step was executed by performing 10000 steps of restraint free minimization of entire system. After minimization, position stability of ions in guanine quartets was confirmed by measuring the distance between the two central Na^+ atoms which were found to be residing at their desired position of 3.5 Å (± 0.2) apart, inside the G-stacks of quadruplex DNA. This final structure was then subjected to 20 ps of equilibration in NVT ensemble with a restraint of 50 kcal mol^{-1} $Å^{-2}$ on quadruplex DNA and central Na^+ ions. Further, the system was heated to production temperature from 0 K to 300 K in NVT ensemble. The restraint on central ions was reduced to 30 kcal mol^{-1} $Å^{-2}$ and then removed in 20 ps of NVT equilibration each. DNA restraint was then reduced to 30 kcal mol^{-1} $Å^{-2}$ and finally released in next 20 ps of NVT equilibration. Proper density of the system was maintained by 100 ps of equilibration in NPT ensemble which was then followed by next 50 ps of run in NVT ensemble. Afterwards, the system was subjected to 1.5 ns of equilibration in 3 steps of 500 ps each in NVE ensemble. Finally, production simulation of 1 ns at 300 K in NVE ensemble was performed to obtain the PDB structure of the G-quadruplex DNA with two central ions. Water molecules and neutralizing ions were removed from this final PDB structure keeping the two central ions intact, to which the DAPI was docked using AUTODOCK 4.2.

Prior to docking DAPI onto GqDNA, the initial step requires merging all non-polar hydrogens of DNA with their corresponding carbons using AutoDock-tools followed by assigning the corresponding atomic charges. The dimension of active box was defined as 42 × 42 × 42 Å with 0.375 Å of grid spacing and placed at the centre of the quadruplex structure. Docking calculations were based on lamarckian genetic algorithm following standard protocol.[53] Total of 2500000 energy evaluations were performed with a population of random individuals (population size: 150). Mutation rate was 0.02 for a maximum number of 27000 generations. Fifty conformations were run to find the binding site of DAPI which were clustered according to the root mean-square criterion of 0.5Å. Based on fifty

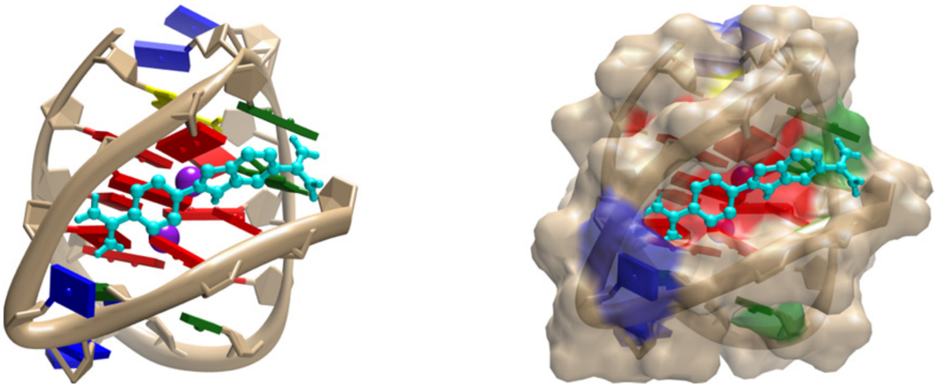

Figure 7.9: Cartoon showing most stable binding site of DAPI inside groove of anti-parallel GqDNA (PDB entry 143D) obtained from docking study using Autodock-4.2. Left: DNA represented in ribbon mode. Right: Showing the molecular surface of DNA along with DAPI.

runs, the most stable conformation with lowest energy was chosen, where DAPI was bound to one of the narrower groove of quadruplex DNA (Figure 7.9).

7.4.2. Molecular Dynamics Simulation

The final docked DAPI/GqDNA complex was used (Figure 7.9) to perform MD simulation using *parm99* force field in AMBER-12. The atomic charges and standard force-field parameters for DAPI were obtained from earlier study of Sponer and co-workers.[50] Simulation was performed following the standard protocol suggested by Furse and Corcelli[38,56] as well as Sponer and co-workers.[50]

MD simulations were carried out by solvating the DAPI/GqDNA complex with 4940 TIP3P water molecules that extend upto 10 Å from the DNA on each side resulting into a rectangular box of 56 × 59 × 60 Å. DAPI-DNA complex was charge neutralized by adding 17 Na^+ ions (Note here that the docked structure contained two central ions and DAPI itself contains two positive charges, thus a total of only 17 Na^+ ions were required for total charge neutrality of the system). This DAPI/DNA system contains a total of 15592 atoms (Figure 7.10). System is relaxed prior to MD through energy minimization using steepest decent and conjugate gradient algorithms.

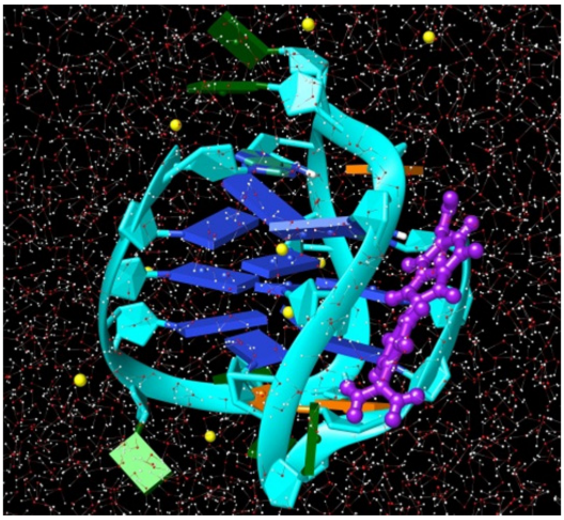

Figure 7.10: Snapshot of simulation box consisting water (white-red dots), ions (yellow spheres) and DAPI (purple ball-and-stick) inside groove of anti-parallel GqDNA. GqDNA is represented as; sugar-phosphate backbone – cyan, G – blue, A – orange, and T – green.

During initial 10000 steps of energy minimization the DAPI-quadruplex system and ions were restrained with a force constant of 300 kcal mol^{-1} Å^{-2} and water molecules were minimized without any restraint. This was followed by restraint free energy minimization of 10000 steps to relax the entire system. After energy minimization, the entire system was subjected to several steps of equilibration process. First step of equilibration was performed in NVT ensemble for 50 ps by restraining DAPI-quadruplex complex and two central ions by a force constant of 50 kcal mol^{-1} Å^{-2}, while water and outside 17 ions were kept free. In the same step, the system was heated over the course of 50 ps and temperature of the system was raised from 0 to 300 K using Langevin temperature control.[57] The restraint on DAPI-quadruplex complex and two central ions was reduced down to 30 kcal mol^{-1} Å^{-2} in next 50 ps NVT ensemble. Further, 50 ps equilibration of the entire system was performed without any restraint in NVT simulation. Once the system is heated to production temperature and equilibrated properly, the density of the system was maintained by running another 100 ps of simulation in NPT ensemble. This equilibration process was extended by two cycles of 50 ps of NVT and 50 ps NVE runs. This was followed by final equilibration of the system by running 2 ns of simulation in NVE ensemble. All atom 65 ns of production simulations were performed in NVE ensemble where the DAPI-DNA complex was kept fully flexible. SHAKE algorithm[58] was used to treat covalent bonds containing hydrogen atoms and particle-mesh Ewald (PME) sum for treating long range electrostatic interactions.[59] The simulation step size was 2 fs. Trajectories over entire 65 ns of production run were saved at every 200 fs. Static picture representing the typical simulated system is given in Fig. 6.12. Analysis of the MD trajectories was done using codes written in FORTRAN-90 and IGOR Pro software. VMD[60] and Chimera[61] were used for trajectory visualization and picture making.

7.4.3. Structural Analysis of DAPI/GqDNA Complex

Occupancies of hydrogen bonds (H-bonds) formed between DAPI and GqDNA over entire simulation run have been calculated. Result showed that there are four long lived H-bonds that keep the DAPI intact in the grooves of GqDNA (Figure 7.11B). DAPI structure with their atom numbers is represented in (Figure 7.11A). A strong hydrogen bond between H32 atom of indole-amidinium ring of DAPI and O2P of G14 in GqDNA with occupancy of 92.1% and H-bond length of 2.90 Å was found over the entire simulation run. It was also found that the same atom (H32) forms another H-bond with O3′ of A13 of GqDNA with occupancy of 32.2% and H-bond length of 3.06 Å. H-bond was formed between atom H52 attached to amidinium group in phenyl ring of DAPI and O2P of G16 of GqDNA with 48% occupancy and H-bond length of 2.78 Å. Atom H42 of DAPI was found to be hydrogen bonded to O2P of G16 of GqDNA with 47.8% occupancy (H-bond length of 2.78 Å). However, the strong bifurcated H-bond at the –NH site of indole ring in DAPI as reported in duplex-DNA was not observed in this case. Thus, larger groove-width and absence of strong bifurcated H-bonds lead to weaker binding of DAPI to antiparallel GqDNA as compared to that in duplex DNA. Apart from these direct H-bonds, several intermittent H-bonds mediated by water molecules are also formed between DAPI and GqDNA. Analysis of the MD trajectories shows that water molecules reside for more than 3 ns at four different hydration sites (I, II, III, IV) of DAPI-GqDNA interface near N2@G15, O4′@G15, O2P@G16 and O2P@G20 atoms of GqDNA (Figure 7.11C). Sites I, II and IV show few water exchange, while site III remained occupied by a water molecule with only one water exchange over the entire 65 ns of simulation. Beside these hydrogen bonds, the electrostatic interaction between negatively charged phosphate groups of GqDNA and positively charged amidinium moieties of DAPI also adds to the stability of DAPI inside the groove of GqDNA. To confirm the stable position of DAPI inside GqDNA the distance between centre-of-masses of DAPI and two central Na⁺ ions was calculated over 65 ns, which show average distance of ~11.45 Å (Figure 7.11D).

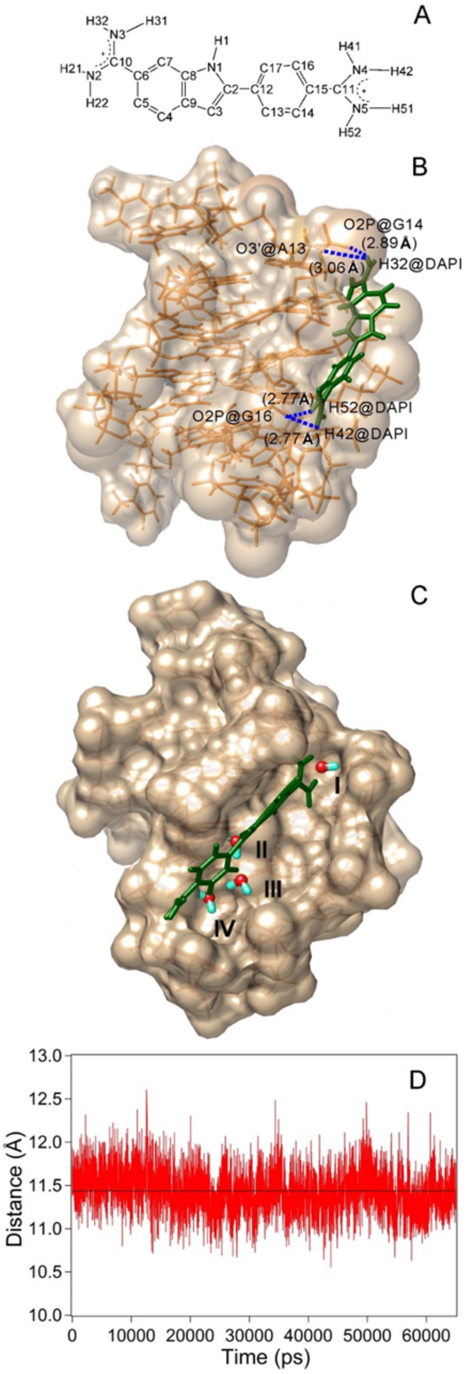

Figure 7.11: (A) Molecular structure of DAPI showing atom numbers. Hydrogen atoms attached to only nitrogen atoms are shown. (B) DAPI-GqDNA structure showing most stable hydrogen bonds between DAPI and GqDNA. The H-bond distances and respective atom numbers are also shown in the picture. (C) Cartoon showing the four high residency hydration sites near interface of DAPI and GqDNA (see text for details). (D) Distance of and DAPI (center-of-mass) relative to the center-of-mass of the two central Na^+ ions over entire 65 ns simulation. Plot confirms that location of DAPI remains fixed (within ± 0.5Å) inside the groove of GqDNA.

7.4.4. Electrostatic Interaction Energy Fluctuations and Solvation Correlation Function

For direct comparison of experimental results with simulation, electrostatic interaction energy of DAPI with charged/dipolar molecules in its surrounding was calculated from the MD trajectories. Damped Shift Force (DSF)[62] sum method is used to calculate the electrostatic interaction energy of DAPI with the surrounding water molecules, ions and DNA, similar as used in earlier simulation studies of duplex-DNA.[38,56,74] Effects of long range electrostatic interactions among atoms of the system are efficiently included by DSF sum method.[62] Furse and Corcelli have validated this method for calculating electrostatic interaction and energy and solvation correlation functions of probe in duplex-DNA.[38,56,74] The electrostatic interaction energy using DSF method is calculated as follows.

$$E(t) = \sum_{m=1}^{N_{solute}} q_m \sum_{n=1}^{N_{solvent}} q_n \left[\begin{array}{c} \frac{erfc(\alpha r)}{r} - \frac{erfc(\alpha R_c)}{R_c} + \\ \left(\frac{erfc(\alpha R_c)}{R_c^2} + \frac{2\alpha}{\sqrt{\pi}} \frac{exp(-\alpha^2 R_c^2)}{R_c} \right)(r - R_c) \end{array} \right] \qquad (7.4)$$

where, q_m is the charge of m^{th} atom of the solute (here, ground-state DAPI charges), q_n is the charge of the n^{th} solvent atom, r is the interatomic distance between q_m and q_n, R_c is the cut-off radius ($r \leq R_c$) and α is the damping factor that controls the convergence of the Coulomb sum over distance. In this work, R_c is defined as 26 Å (half of the box size) and α is chosen as 0.2 Å^{-1} (similar as used in simulation of duplex DNA).[38,56,74] The electrostatic interaction energy of DAPI with water, DNA, ions and total system has been calculated over entire 65 ns of simulation and are plotted in (Figure 7.12A). The plot shows large DNA and water energies which are strongly anti-correlated to each other. Contribution of ion is however, found to be small. Total interaction energy fluctuation was then used to calculate the total equilibrium solvation correlation function, $C_{simu}(t)$, as,[34]

$$C_{simu}(t) = \frac{\langle \Delta E(0) \Delta E(t) \rangle_g}{\langle \Delta E(0)^2 \rangle_g} \qquad (7.5)$$

where $\Delta E(t) = (E(t) - \langle E(t) \rangle)_g$, is fluctuation in interaction energy of (ground-state) DAPI charges and partial charges of DNA, ions and water molecules relative to average energy.

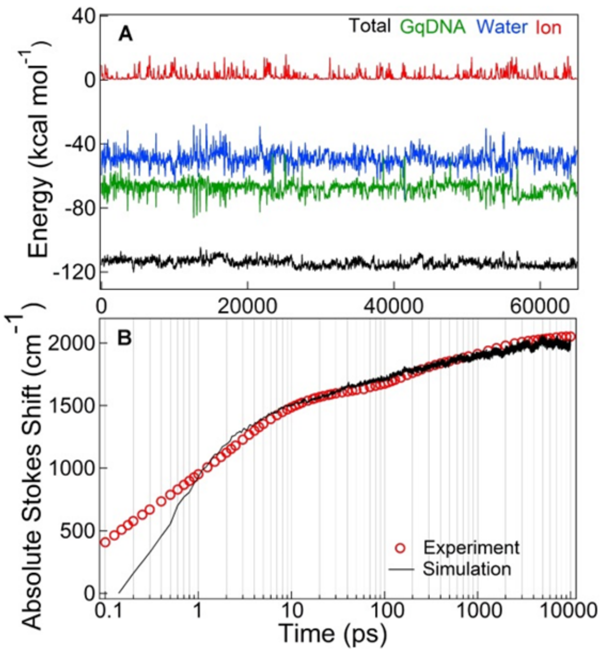

Figure 7.12: (A) Electrostatic interaction energy of DAPI with ions (red), water (blue), DNA (green) and total system (black) over 65 ns simulation calculated using DSF sum. Energies are calculated at 0.1 ps step. Energy fluctuations are smoothed with 50 ps running average for clarity in representation. (B) Comparison of "absolute" Stokes shifts of DAPI in GqDNA obtained from experiment and simulation. Limited time-resolution of UPC setup (~270 fs) could not allow for extraction of dynamics by ~450 cm^{-1} at 100 fs, which leads to the deviation between experimental and simulation data below ~600 fs (see text for details).

Solvation correlation functions calculated from equilibrium simulation, $C_{simu}(t)$, can be compared directly to the non-equilibrium correlation function measured experimentally, $C_{expt}(t)$, within linear response approach.[34,35] However, comparison of experimental and simulation data is not straightforward as $C_{simu}(t)$ includes ~60-80% of fast inertial component which is absent in the experimentally measured dynamic Stokes shifts. Thus, for comparison, simulated absolute Stokes shift was calculated from the simulated correlation function as,[35]

$$S(t) = \delta S_0 + s[1 - C_{simu}(t)] \tag{7.6}$$

where, δS_0 is the inertial component and s is the total Stokes shift (simulated). Comparison of experimental and simulation absolute Stokes shift is plotted in Figure 7.12B. Matching of both the data is extremely good beyond ~600 fs which requires δS_0 = -5338 cm^{-1} and s = 7400 cm^{-1}. This indicates that inertial contribution (δS_0) of ~72% is subtracted from the total Stokes shift (simulated) for comparison to experimental data. It can be noted here that full extraction of dynamics in experimentally measured Stokes shift is limited by 450 cm^{-1} at 100 fs due to limited time resolution of UPC setup (~270 fs) which leads to deviation in both data below ~600 fs (Figure 7.12B). Nonetheless, the agreement between experimental and simulated data (beyond ~600 fs) not only validates linear response theory,[63] but also confirms that the starting docked DAPI-GqDNA structure and simulation methodology used were correct. The absolute Stokes shift obtained from the simulated energy correlation function using equation 7.6 was fitted with a power law added with two exponential functions. The fit extracts power law relaxation (n = 0.14) with exponential time constant of 1.8 ps (similar as found in experiment) and another of 0.45 ps (Figure 7.13). Due to limited time resolution (~270 fs) of the experimental (UPC) setup, the fast component of 0.45 ps seen in simulation could not be resolved accurately in experimental Stokes shift data.

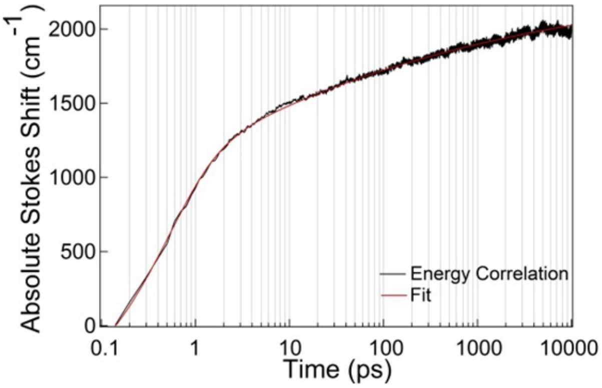

Figure 7.13: Absolute Stokes shift of DAPI in G-quadruplex DNA obtained from energy correlation function calculated from simulation trajectories (black line), fitted with power-law summed with two exponential relaxations (red line).

7.4.5. Origin of Slow Dynamics

To find the origin of slow power-law relaxation and exponential dynamics, $C_{simu}(t)$ has been decomposed into partial correlations of DNA, ions and water molecules using linear response decomposition (LRD) method.[40] Within LRD method, $C_{simu}(t)$ is expressed as sum of partial correlations functions of individual components as [36-41]

$$C_{simu}(t) = \sum_i \frac{\langle \Delta E_i(t)\Delta E(0)\rangle}{C(0)} \qquad (7.7)$$

where i indicates individual component (i.e. water, ions and DNA proper) and *C(0)* is the total correlation at zero time. The partial correlations of DNA, ions, water molecules and total correlation are plotted in Figure 7.14A. It has been found that the fast exponential relaxation below ~10 ps is governed by water, whereas, both water and DNA contributes equally to the power-law relaxation in longer times. Such behaviour is also indicated by the strong anti-correlation between DNA and water energy (Figure 7.15) Signal-to-noise ratios in decomposed DNA and water correlation is not satisfactory beyond ~1 ns which requires averaging over many simulation runs to improve the quality of decomposed data. However, signal-to-noise ratio for total correlation is good in the longer times that matches well with the experimental data (Figure 7.12B). Plots (Figure 7.14A) show that water contributes ~65% to the overall dynamics followed by contributions from DNA proper that shows nearly a power-law relaxation, whereas, the dynamic contribution from ion is almost negligible over the entire time range.

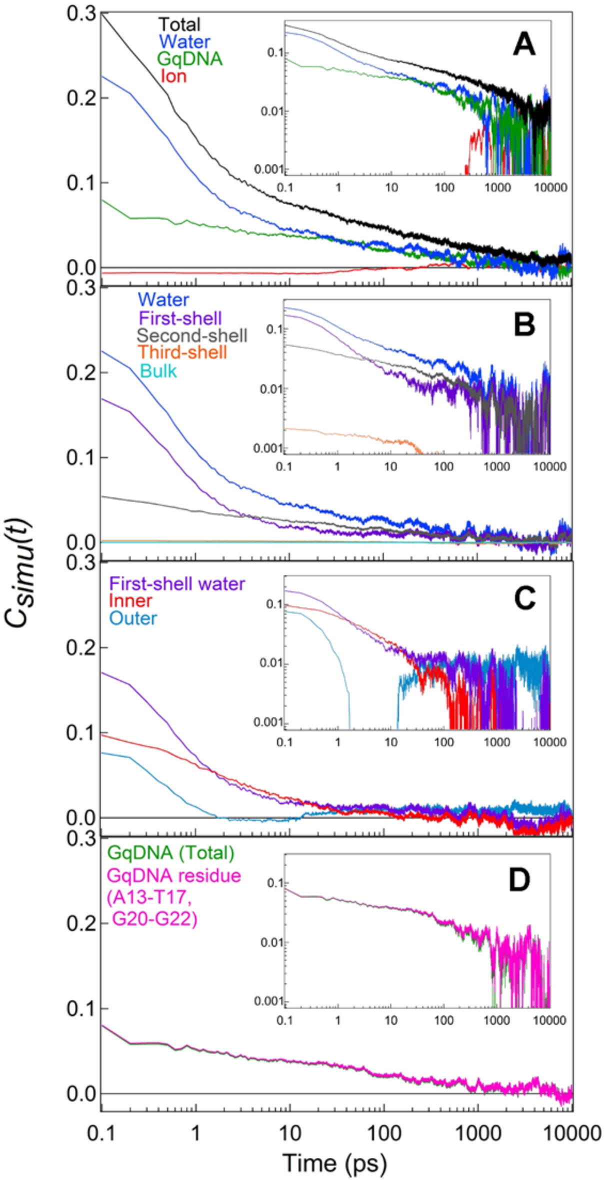

Figure 7.14: Linear response decomposition (LRD) of total simulated correlation (black) into water (blue), DNA (green) and ion (red) correlations. (B) Spatial decomposition of water into first (within 4 Å), second (within 4 – 8 Å), third (within 8 – 12 Å) solvation shells, and bulk (>8 Å) around DAPI. Power-law type relaxation originates from second-shell water, while the fast relaxation together with long tail of slow dynamics originates from first-shell water. (C) Spatial decomposition of first-shell water into *inner* (within 7.5 Å of DNA) and *outer* (beyond 7.5 Å of DNA) water that approximately separate the fast and slow relaxations of first-shell water-correlation, respectively. (D) Correlation from DNA parts (A13 – T17 and G20 – G22) that defines the DNA-correlation.

Spatial decomposition of water shell and DNA parts has been performed using LRD method in order to find the range of interaction of water molecules and DNA with ligand. Water shell is decomposed into first-, second-, third solvation shell and bulk water based on the criteria that oxygen atom of any water molecule that falls within a region of 4 Å from any atom of DAPI forms first solvation shell. Similarly, water within shell of radii 4-8 Å, 8-12 Å and >12 Å forms second solvation shell, third solvation shell and bulk water, respectively.

Contribution from the water molecules of respective shells are plotted in Figure 7.14B. It shows that the water molecules within 4 Å governs the fast exponential relaxation as well as long tail of slow dynamics and contributes to 62% of the total water contribution. More importantly, the water molecules residing in second shell shows nearly a single power-law relaxation (similar to DNA) and contributes to 37% of total water contribution. However, contribution of water molecules within third-shell and beyond is negligible. First-shell water molecules were further decomposed into its contributions from inner and outer water molecules based on LRD method in order to discern the contribution from the water molecules of the first shell that reside near and those reside away from the GqDNA molecule (Figure 7.14C). All those first shell water molecules around DAPI whose oxygen atoms fall within a

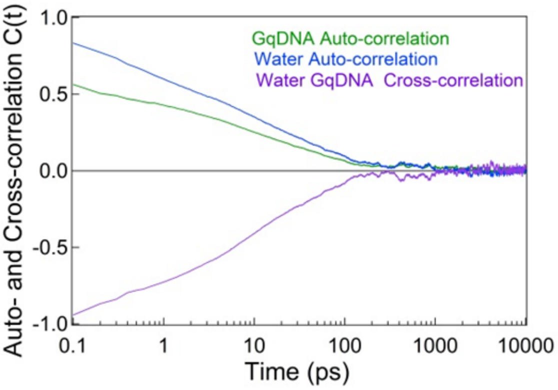

Figure 7.15: Auto- and cross-correlations of water and DNA energy fluctuations. The large negative cross-correlation between water and DNA energy suggest the cross-talk between water and DNA.

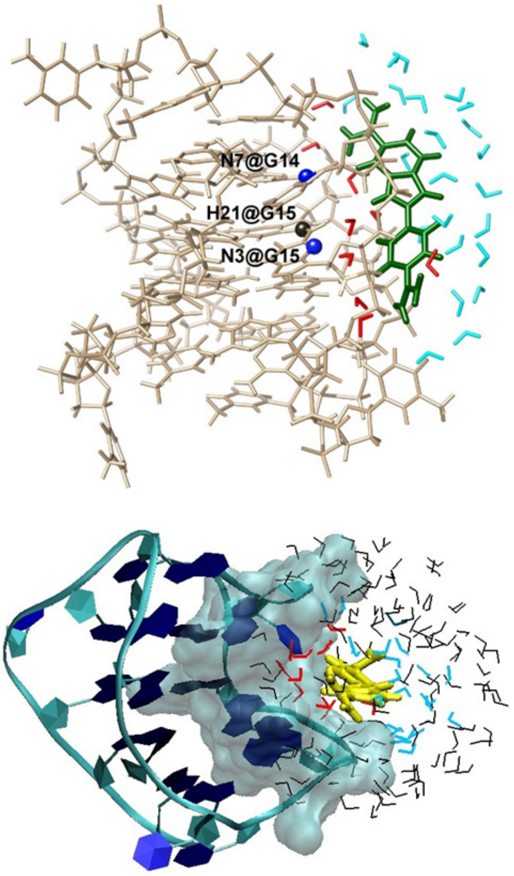

Figure 7.16: DAPI-GqDNA complex with first solvation shell water molecules around DAPI. The *inner* (red) and *outer* (cyan) water molecules of the first-shell were separated by finding those water oxygen-atoms that come within 7.5 Å from DNA atoms: N7@G14, H21@G15 and N3@G15 shown in blue and black. Lower panel: The part of DNA that defines DNA-correlation is shown as molecular surface. It is found that materials (water and DNA-parts) within ~9 Å of DAPI control the total dynamics in GqDNA.

region of 7.6 Å from N7@G14, H21@G15 and N3@G15 atoms of GqDNA were defined as inner water and the remaining first shell water molecules are termed as outer water (Figure 7.16). It was found that over entire simulation run, ~9 inner water molecules and ~28 outer water molecules on average come near DAPI, and the fast and slow relaxation in the first-shell water correlation can be approximately attributed to these outer and inner water molecules, respectively (see Figure 7.14C). Moreover, spatial decomposition of DNA showed that DNA parts consisting of A13-A17 and G20-G22 that come within a region of 9 Å from DAPI, govern the DNA correlation (Figure 7.14D). A cartoon representing DNA parts and water molecules that control the total dynamics in GqDNA is shown in Figure 7.16.[52]

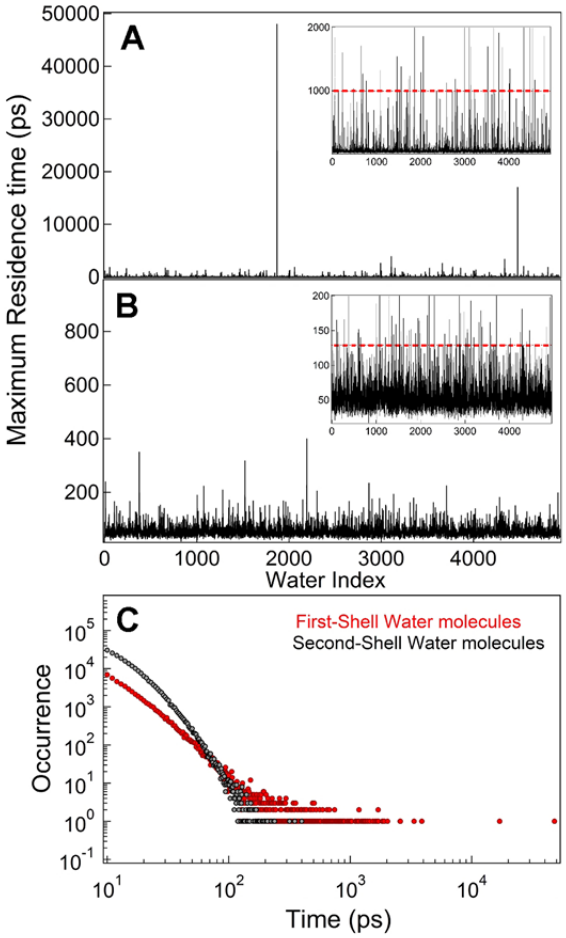

Figure 7.17: Maximum residence times of all 4940 water molecules that visit first solvation shell (A) and second solvation shell (B). The red dotted lines in insets show the lower limit above which the water molecules were considered for mean square displacement (MSD) calculations. (C) Distribution of residence times of all water molecules in first (red) and second (gray) solvation shells. The tails of distributions show linear dependence with time in log-log plot.

7.4.6. Sub-Diffusive Motion of Water near GqDNA

It is difficult to provide a clear explanation to the dispersed solvation dynamics in biomolecules, therefore an attempt has been made to explain these anomalous dynamics in biomolecules by adopting various theoretical approaches.[42-46,64-70] It has been found that the anomalous solvation dynamics in the proximity of biomolecules can be related to the nature of diffusion of water on the fractal geometry of biomolecules and/or on the rugged potential energy landscape formed by the biomolecules.[43,46] Various other approaches to explain such behavior such as molecular jump water reorientation model[42,70] and mode-coupling theory (MCT)[64] have also been proposed. Motion of water molecules on the rugged potential surface results into a situation where the distribution of residence times of nearby water molecules show power-law tail, indicating that the trapping times of water molecules in local minima across the rugged potential surface is broadly distributed.[43,46] In such cases, the mean square displacement (MSD) of water in the vicinity of biological macromolecules follows sublinear diffusion as, $\langle \Delta r(t)^2 \rangle \approx A\, t^{\alpha}$ with $\alpha < 1$.[43,44,66-69]

Residence time for the water molecules that come within first and second solvation shells around DAPI has been calculated. In this case, residence time was defined as a time during which each water molecule resides in a solvation shell for a minimum 1 ps. It is found that both the first and the second shells are visited by all 4940 water molecules some time or the other within the entire course of simulation. Maximum residence times for all 4940 water molecules in first and second solvation shells are plotted in Figures 7.17A, 7.17B. It is very interesting to note that there are several water molecules which reside in first shell with a residence time >1 ns and many in second shell with residence time >100 ps (Figures 7.17A, 7.17B). The residence time of water molecules at four hydration sites near DAPI/GqDNA interface was found to be even >3 ns (see Figure 7.11C). Distribution of residence times of water molecules in the first and second shells show power-law response in longer times. Such power-law behaviour may indicate that GqDNA perturbs motion of hydration water in such a way that it leads to broadly distributed activation barriers for water molecules to exchange between different sites, thus resulting into relaxation times of solvent molecules that are widely dispersed (see Figure 7.19 below). In order to check the sublinear (translational) diffusion of water, MSD (time averaged) of water molecules residing in first solvation shell for more than 1 ns was calculated. The result shows that MSD follows $\sim t^{0.91}$ illustrating sublinear diffusion (Figure 7.18A). Small deviation from normal diffusion ($\alpha = 1$) may indicate that most of the first shell water molecules are mobile and responsible for the fast exponential relaxation (~2 ps). In fact, it was found that a subset of water molecules residing in first solvation shell follows MSD of $\sim t^{0.43}$ which explains the origin of the slow tail of dynamics of the first-shell water correlation (Figure 7.18A). Theoretical modelling of biological system involves population splitting of diffusion particles.[66-69,71] For example, using

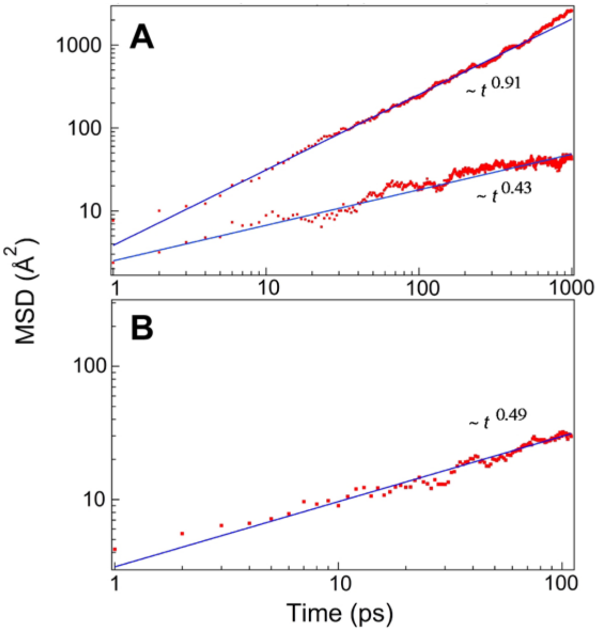

Figure 7.18: Mean square displacements (MSD) of first-shell (A) and second-shell (B) water molecules which are chosen based on the residence times > 1 ns and >110 ps, respectively (see insets in A and B). MSD was calculated at 1 ps step. First-shell water molecules show sublinear diffusion with MSD $\sim t^{0.91}$, while a subset of these water molecules shows MSD $\sim t^{0.43}$. Second-shell water show sublinear diffusion with MSD $\sim t^{0.49}$.

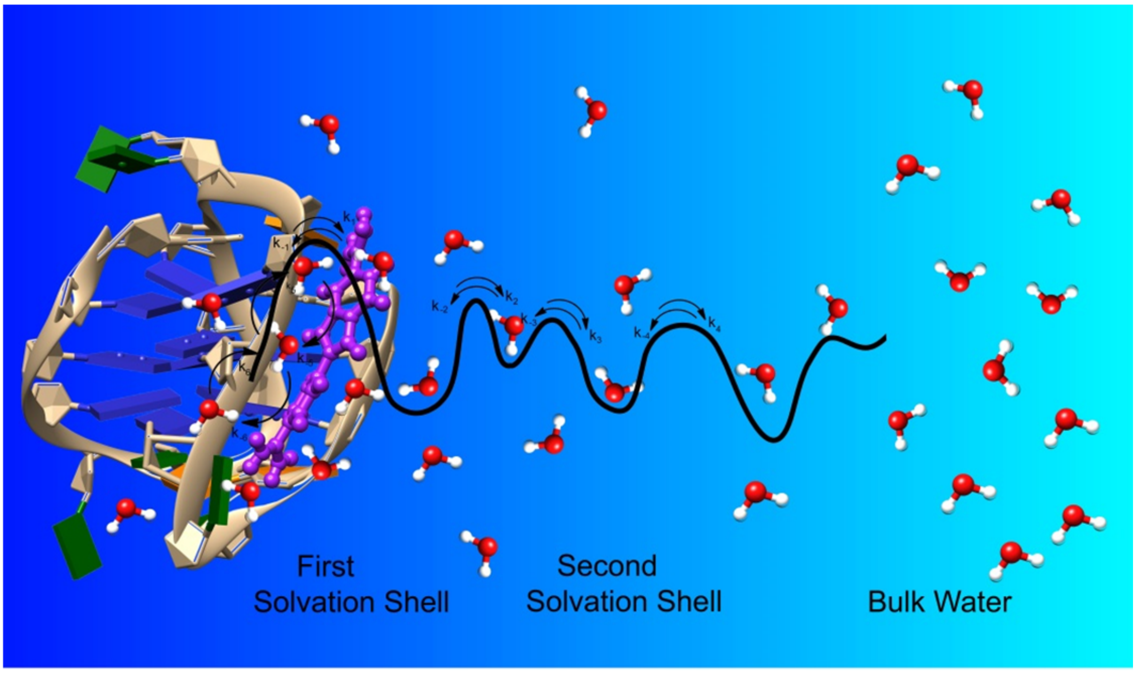

Figure 7.19: Representative cartoon depicting the situation of perturbed water molecules on rugged potential surface near DNA. Water with broad distribution of residence times can have different trapping times at local minima and different exchange rates k_i's between minima on the rugged potential surface, which can ultimately lead to the observed dispersed (power-law) solvation dynamics in DNA.

aging renewal theory, it has been shown that for processes which are non-stationary, time aging can induce splitting of the population of diffusing particles based on their mobility.[69,71] Sub-diffusive motion of water molecules at lipid membrane surface has been shown to exhibit such aging effect.[72] Similar situation of population splitting of diffusing water molecules seems to hold in the present GqDNA system as well. MSD of second-shell water molecules with residence time >110 ps follows $\sim t^{0.49}$ showing highly sublinear behavior (Figure 7.18B). Based on the above results and observations, it is concluded that water molecules may have different trapping times on the rugged potential surface showing broad distribution of the residence time, thus resulting into the dispersed power-law solvation dynamics in GqDNA. A representative cartoon showing similar (possible) situation of the water molecules near GqDNA is presented in Figure 7.19.

7.4.7. DNA Force-Field Dependence of Solvation Correlation Function

Three different DNA force-fields (*parm99, parmbsc0* and *parmbsc0*$_{\chi OL4}$) were used earlier to model antiparallel GqDNA in solution – so as to capture its structural and dynamical properties accurately.[73] The new refined force field for nucleic acids (*parmbsc0*$_{\chi OL4}$) with proper parameterization has been proposed to model the X-ray structure of antiparallel GqDNA in a better way as compared to other DNA force fields.[73] However, it is rather difficult to indicate which force field will reproduce solvation dynamics in GqDNA.

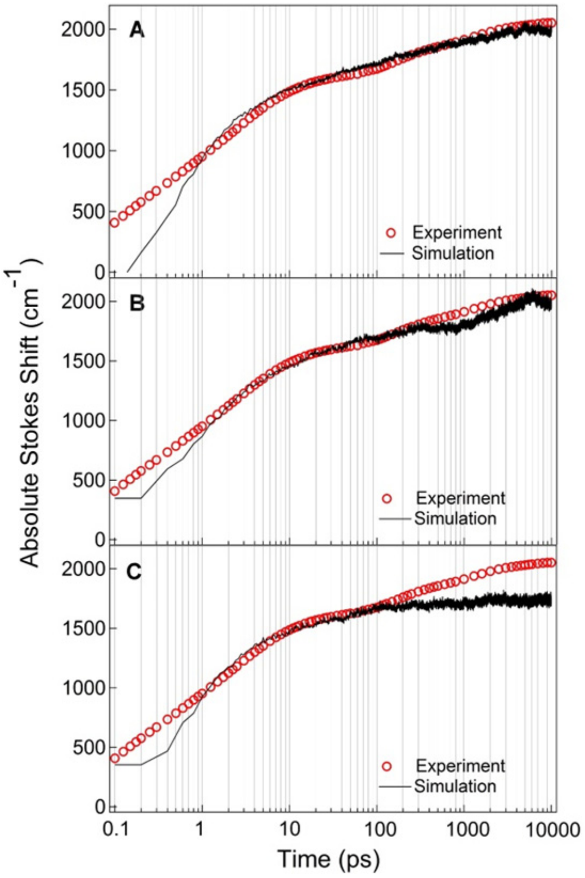

Figure 7.20: Comparison of “absolute” Stokes shift obtained from TRFSS experiment and calculated from simulation using force-fields: (A) *parm99* (B) *parmbsc0* and (C) *parmbsc0*$_{\chi OL4}$. The best matching is found with *parm99* force-field. Hence the data obtained with this force field are presented in the manuscript.

Therefore, all the three force fields have been tested separately in order to reproduce the solvation dynamics in GqDNA observed experimentally. It was found that among the given force fields, *parm99* reproduces experimental solvation dynamics in GqDNA, probed by groove-bound DAPI, more accurately as compared to other two force fields. Comparison of experimental and simulated “absolute” Stokes shifts of DAPI using the three force fields is shown in (Figure 7.20). Further studies are required to explore the reason behind such discrepancies among the results obtained from using these three force fields.

7.4.8. Reproducibility of Simulation data using *parm99* Force Field

Reproducibility of simulation results was checked by performing a separate set of 50 ns MD simulation which was started from a different equilibrated structure (at 3 ns) and trajectories were saved at every 200 fs. Fluctuation of electrostatic interaction energy calculated between DAPI and the surrounding water molecules, ions and DNA using DSF sum method is shown in Figure 7.21A. It has been found that the relative energy contribution of individual component and total system over entire 50 ns of the run is very similar to the first set of 65 ns simulation (Figure 7.12A). Simulated absolute Stokes shift was calculated from the energy correlation function of the second MD run of 50 ns and compared to the experimental result that matches extremely well (Figure 7.21B). Total energy correlation of the system was decomposed into its individual components of water, DNA and ions based on linear response decomposition method (Figure 7.21C). The dynamic contributions obtained from individual components of second set of MD to the total dynamics were found to be similar as seen in first set of MD simulation.

Research in the field of G-quadruplex DNA is developing rapidly as it acts as a target for anticancer drugs. Thus, potential to target these quadruplex structures with ligands for effective cancer therapy requires detail understanding of the drug solvation inside DNA.

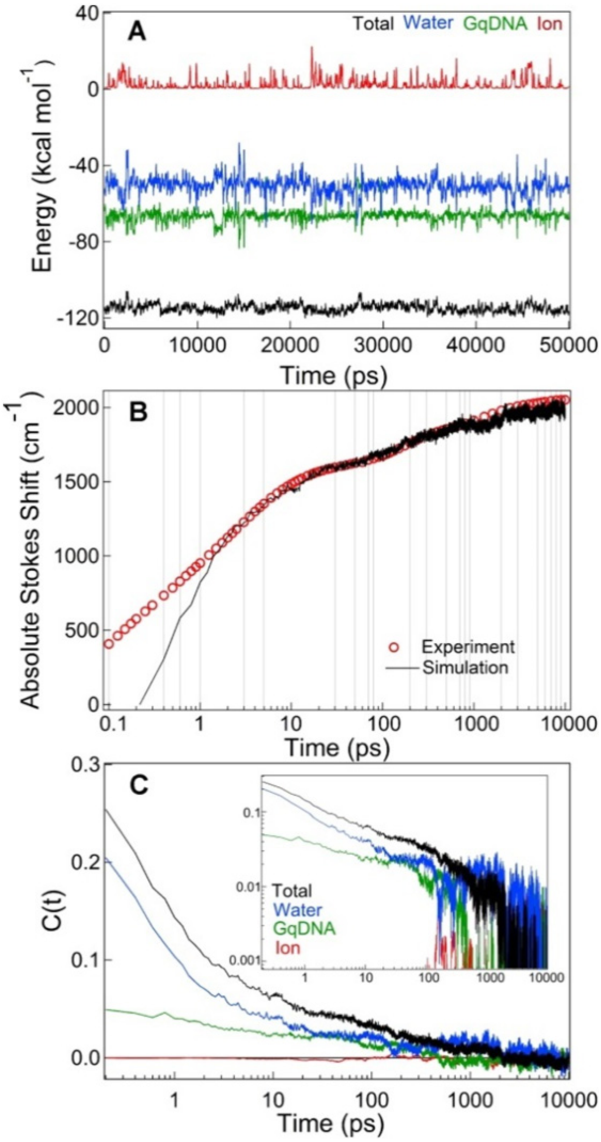

Figure 7.21: Reproducibility of simulation results: (A) Contributions of interaction energy of DAPI with ions (red), water (blue), DNA (green) and total (black) over 50 ns simulation run, calculated using DSF sum. Energies are calculated at 0.2 ps step, smoothed with 50 ps running average. Similar to the other run, the anti-correlation between water and DNA is very strong over entire 50 ns. (B) Direct comparison of absolute Stokes shifts of DAPI in GqDNA obtained from experiment and second-set of simulation run. Matching of two data is extremely good in times > ~1 ps. This is because of the lower time resolution (0.2 ps) of simulation data points compared to the other set of data. (C) Linear response decomposition of total energy correlation into individual components, i.e., water, ions and DNA. As seen in Figure 8 in main manuscript, we find similar features for the individual correlations calculated from the second-set of simulation run.

Such a study is presented in this chapter by directly comparing the TRFSS experimental and simulation results. These results reveal that water near biomolecules (hydration water) plays very crucial role in solvating ligand inside GqDNA. Dispersed relaxation of water molecules showing power-law feature near GqDNA may hold important biological impacts that can be related to the interaction of dipolar/charged molecules with DNA. The slow hydration dynamics around DNA may actually participates directly in capturing macromolecules and (dipolar/charged) ligands from bulk and solvating them in between DNA bases or near/inside DNA grooves. In fact, drug binding to duplex-DNA was found to be facilitated by the dynamics of water uptake/release.[75] Such dispersed dynamics of hydration play direct role in defining processes that occurs on complex free-energy surface.[75] Moreover, the telomeric ends of DNA that are exposed toward cellular water may further facilitate the functioning and interaction of GqDNA with drugs. Nevertheless, further combined experimental and simulation studies are required for complete understanding of dispersed dynamics in DNA, such as the effect of GqDNA and ligand structures on the solvation response inside GqDNA. The next chapter sheds light on such effects on solvation response in GqDNA.

Reference

1. Wang, Y.; Patel, D. J. Solution Structure of the Human Telomeric Repeat d[AG3(T2AG3)$_3$] G-tetraplex. *Structure* **1993**, *1*, 263-282.
2. Balasubramanian, S.; Hurley, L. H.; Neidle, S. Targeting G-quadruplexs in Gene Promoters: A Novel Anticancer Strategy. *Nat. Rev. Drug Discov.* **2011**, *10*, 261-275.
3. Verma, S. D.; Pal, N.; Singh, M. K.; Shweta, H.; Khan, M. F.; Sen, S. Understanding Ligand Interaction with Different Structures of G-Quadruplex DNA: Evidence of Kinetically Controlled Ligand Binding and Binding-Mode Assisted Quadruplex Structure Alteration. *Anal. Chem.* **2012**, *84*, 7218-7226.
4. Agarwal, T; Roy, S; Kumar, S; Chakraborty, T. K.; Maiti, S. In the Sense of Transcription Regulation by G-Quadruplexs: Asymmetric Effects in Sense and Antisense Strands. *Biochemistry* **2014**, *53*, 3711-3718.
5. Biffi, G.; Tannahill, D.; McCafferty, J.; Balasubramanian, S. Quantitative Visualization of DNA G-Quadruplex Structures in Human Cells. *Nat. Chem.* **2013**, *5*, 182-186.
6. Jain, A. K.; Bhattacharya, S. Interaction of G-Quadruplexs with Nonintercalating Duplex-DNA Minor Groove Binding Ligands. *Bioconjugate Chem.* **2011**, *22*, 2355-2368.
7. Monchaud, D.; Teulade-Fichou, M. P. A Hitchhiker's Guide to G-quadruplex Ligands. *Org. Biomol. Chem.* **2008**, *6*, 627-636.
8. Huppert, J. L.; Balasubramanian, S. Prevalence of Quadruplexes in the Human Genome. *Nucleic Acids Res.* **2005**, *33*, 2908-2916.
9. Huppert, J. L.; Balasubramanian, S. G-Quadruplexes in Promoters throughout the Human Genome. *Nucleic Acids Res.* **2007**, *35*, 406-413.
10. Neidle, S.; Parkinson, G. Telomere Maintenance as a Target for Anticancer Drug Discovery. *Nat. Rev. Drug Discovery*, **2002**, *1*, 383-393.
11. Zehlar, A. M.; Williamson, J. R.; Cech, T. R.; Prescott, D. M. Inhibition of Telomerase by G-Quartet DNA Structures. *Nature*, **1991**, *350*, 718-720.
12. Ou, T.; Lu, Y.; Tan, J.; Huang, Z.; Wong, K.; Gu, L. G-Quadruplexes: Targets in Anticancer Drug Design. *ChemMedChem* **2008**, *3*, 690-713.
13. Neidle, S. The structures of quadruplex nucleic acids and their drug complexes. *Curr. Opin. Struct. Biol*. **2009**, *19*, 239-250.
14. Oganesian, L.; Bryan, T. M. Physiological Relevance of Telomeric G-Quadruplex Formation: A Potential Drug Target. *BioEsaays* **2007**, *29*, 155-165.
15. Neidle, S. The Structures of Quadruplex Nucleic Acids and their Drug Complexes. *Curr. Opin. Struct. Biol.* **2009**, 19, 239-250.
16. Neidle, S.; Parkinson, G. Telomere Maintenance as a Target for Anticancer Drug Discovery. *Nat. Rev. Drug Discov.* **2002**, *1*, 383-393.
17. Miller, M. C.; Buscaglia, R.; Chaires, J. B.; Lane, A. N.; Trent, J. O. Hydration is a Major Determinant of the G-Quadruplex Stability and Conformation of the Human Telomere 3′ Sequence of d(AG3(TTAG3)$_3$). *J. Am. Chem. Soc.* **2010**, *132*, 17105-17107.
18. Heddi, B.; Phan, A. T. Structure of Human Telomeric DNA in Crowded Solution. *J. Am. Chem. Soc.* **2011**, *133*, 9824-9833.
19. Chen, Z.; Zheng, K.; Hao, Y.; Tan, Z. Reduced or Diminished Stabilization of the Telomere G-Quadruplex and Inhibition of Telomerase by Small Chemical Ligands under Molecular Crowding Condition. *J. Am. Chem. Soc.* **2009**, *131*, 10430-10438.
20. Li, T.; Hassanali, A. A.; Kao, Y.-T.; Zhong, D.; Singer, S. J. Hydration Dynamics and Time Scales of Coupled Water-Protein Fluctuations. *J. Am. Chem. Soc.* **2007**, *129*, 3376-3382.
21. Chang, C. –W.; He, T. –F.; Guo, L.; Stevens, J. A.; Li, T.; Wang, L.; Zhong, D. Mapping Solvation Dynamics at the Function Site of Flavodoxin in Three Redox States. *J. Am. Chem. Soc.* **2010**, *132*, 12741-12747.
22. Brauns, E. B.; Madaras, M. L.; Coleman, R. S.; Murphy, C. J.; Berg, M. A. Measurement of Local DNA DNA Reorganization on the Picosecond and Nanosecond Time Scales. *J. Am. Chem. Soc.*, **1999**, *121*, 11644-11649.
23. Pal, S. K.; Zhao, L.; Zewail, A. H. Water at DNA Surfaces: Ultrafast Dynamics in Minor Groove Recognition. *Proc. Natl. Acad. Sci. U.S.A.* **2003**, *100*, 8113-8118.
24. Pal, S. K.; Zhao, L.; Xia, T.; Zewail, A. H. Site- and Sequence-Selective Ultrafast Hydration of DNA. *Proc. Natl. Acad. Sci. U.S.A.* **2003**, 100, 13746-13751.

25. Dallmann, A.; Pfaffe, M.; Mügge, C.; Mahrwald, R.; Kovalenko, S. A.; Ernsting, N. P. Local THz Time Domain Spectroscopy of Duplex DNA via Fluorescence of an Embedded Probe. *J. Phys. Chem. B* **2009**, *113*, 15619-15628.
26. Banerjee, D.; Pal, S. K. Dynamics in the DNA Recognition by DAPI: Exploration of the Various Binding Modes. *J. Phys, Chem. B* **2008**, *112*, 1016-1021.
27. Andreatta, D.; Sen, S.; Pérez Lustres, J. L.; Kovalenko, S. A.; Ernsting, N. P.; Murphy, C. J.; Coleman, R. S.; Berg, M. A. Ultrafast Dynamics in DNA: "Fraying" at the End of the Helix. *J. Am. Chem. Soc.* **2006**, *128*, 6885-6892.
28. Andreatta, D.; Pérez Lustres, J. L.; Kovalenko, S. A.; Ernsting, N. P.; Murphy, C. J.; Coleman, R. S.; Berg, M. A. Power-Law Solvation Dynamics in DNA over Six Decades in Time. *J. Am. Chem. Soc.* **2005**, *127*, 7270-7271.
29. Pal, N.; Verma, S. D.; Sen, S. Probe Position Dependent of DNA Dynamics: Comparison of the Time-Resolved Stokes Shift of Groove-Bound to Base-Stacked Probes. *J. Am. Chem. Soc.* **2010**, *132*, 9277-9279.
30. Verma, S. D.; Pal, N.; Singh, M. K.; Sen, S. Probe Position-Dependent Counterion Dynamics in DNA: Comparison of Time-Resolved Stokes Shift of Groove-Bound to Base-Stacked Probes in the Presence of Different Monovalent Counterions. *J. Phys. Chem. Lett.*, **2012**, *3*, 2621-2626.
31. Sen, S.; Gearheart, L. A.; Rivers, E.; Liu, H.; Coleman, R. S.; Murphy, C. J.; Berg, M. A. Role of Monovalent Counterions in the Ultrafast Dynamics of DNA. *J. Phys. Chem. B* **2006**, *110*, 13248-13255.
32. Sajadi, M.; Furse, K. E.; Zhang, X. –X.; Dehmel, L.; Kovalenko, S. A.; Corcelli, S. A.; Ernsting, N. P. Detection of DNA-Ligand Binding Oscillations by Stokes-Shift Measurements. *Angew. Chem. Int. Ed.* **2011**, *50*, 9501-9501.
33. Manucs 38
34. Pal, S.; Maiti, P. K.; Bagchi, B.; Hynes, J. T. Multiple Time Scales in Solvation Dynamics of DNA in Aqueous Solution: The Role of Water, Counterions, and Cross-Correlations. *J. Phys. Chem. B* **2006**, *110*, 26396-26402.
35. Sen, S.; Andreatta, D.; Ponomarev, S. Y.; Beveridge, D. L.; Berg, M. A. Dynamics of Water and Ions Near DNA: Comparison of Simulation to Time-Resolved Stokes-Shift Experiments. *J. Am. Chem. Soc.* **2009**, *131*, 1724-1735.
36. Furse, K. E.; Corcelli, S. A. The Dynamics of Water at DNA Interfaces; Computational Studies of Hoechst 33258 Bound to DNA. *J. Am. Chem. Soc.* **2008**, *130*, 13103-13109.
37. Furse, K. E.; Corcelli, S. A. Molecular Dynamics Simulation of DNA Solvation Dynamics. *J. Phys. Chem. Lett.* **2010**, *1*, 1813-1820.
38. Furse, K. E.; Corcelli, S. A. Dynamical Signature of Abasic Damage in DNA. *J. Am. Chem. Soc.* **2011**, *133*, 720-723.
39. Halle, B.; Nilsson, L. Does the Dynamic Stokes Shift Report on Slow protein Hydration Dynamics? *J. Phys. Chem. B* **2009**, *113*, 8210-8213.
40. Nilsson, L.; Halle, B. Molecular Origin of Time-Dependent Fluorescence Shifts in Proteins. *Proc. Natl. Acad. Sci. U.S.A.* **2005**, *102*, 13867-13872.
41. Golosov, A. A.; Karplus, M. Probing Polar Solvation Dynamics in Proteins; A Molecular Dynamics Simulation Analysis. *J. Phys. Chem. B* **2007**, *111*, 1482-1490.
42. Sterpone, F.; Stirnemann, G.; Laage, D. Magnitude and Molecular Origin of Water Slowdown Next to a Protein. *J. Am. Chem. Soc.* **2012**, *134*, 4116-4119.
43. Pizziutti, F.; Marchi, M.; Sterpone, F. Rossky, P. J. How Protein Surfaces Induce Anomalous Dynamics of Hydration Water. *J. Phys. Chem. B* **2007**, *111*, 7584-7590.
44. Bizzarri, A. R.; Cannistraro, S. Molecular Dynamics of Water at the Protein-Solvent Interface. *J. Phys. Chem. B* **2002**, *106*, 6617-6633.
45. Lagi, M.; Baglioni, P.; Chen, S. -H. Logarithmic Decay in Single-Particle Relaxation of Hydrated Lysozyme Powder. *Phys. Rev. Lett.* **2009**, *103*, 108102.
46. Kämpf, K; Klameth, F.; Vogel, M. Power-law and Logarithmic Relaxations of Hydrated Proteins: A Molecular Dynamics Simulation Study. *J. Chem. Phys.* **2012**, *137*, 205105.
47. Volk, M.; Kholodenko, Y.; Lu, H. S. M.; Gooding, E. A.; DeGrado, W. F.; Hochstrasser, R. M. Peptide Conformational Dynamics and Vibrational Stark effects Following Photoinitiated Disulfide Cleavage. *J. Phys. Chem. B* **1997**, *101*, 8607-8616.
48. Li, T. Validity of Linear Response Theory for Time-Dependent Fluorescence in *Staphylococcus* Nuclease. *J. Phys. Chem. B* **2014**, *118*, 12952-12959.
49. Case, D. A. et al. (2012) AMBER 12, University of California, San Francisco.

50. Spackova, N.; Cheatham III, T. E.; Ryjacek, F.; Lankas, F.; Meervelt, L. v.; Hobza, P.; Sponer, J. Molecular Dynamics Simulation and Thermodynamics Analysis of DNA-Drug Complexes. Minor Groove Binding between 4′,6-Diamidino-2-phenylindole and DNA Duplexes in Solution. *J. Am. Chem. Soc.* **2003**, *125*, 1759-1769.
51. Jimenez, R.; Fleming, G. R.; Kumar, P. V.; Maroncelli, M. Femtosecond Solvation Dynamics of Water. *Nature* **1994**, *369*, 471-473.
52. Pal, N.; Shweta, H.; Singh, M.K.; Verma, S. D.; Sen, S. Power-Law Solvation Dynamics in G-quadruplex DNA: Role of Hydration Dynamics on Ligand Solvation inside DNA. *J. Phys. Chem. Lett.* **2015**, *6*, 1754-1760.
53. Morris, G. M.; Goodsell, D. S.; Halliday, R. S.; Huey, R.; Hart, W. E.; Belew, R. K.; Olson, A. J. Automated Docking using a Lamarckian Genetic Algorithm and an Empirical Binding Free Energy Function. *J. Comput. Chem.* **1998**, *19*, 1639-1662.
54. Aqvist, J. Ion-Water Interaction Potentials Derived from Free Energy Perturbation Slmulations. *J. Phys Chem.* **1990**, *94*, 8021-8024.
55. Jorgensen, W. L.; Chandrasekhar, J.; Madura, J. D.; Impey, R. W.; Klein, M. L. Comparison of Simple Potential Functions for Simulating Liquid Water. *J. Chem. Phys.* **1983**, *79*, 926.
56. Furse, K. E.; Corcelli, S. A. Effects of Long-Range Electrostatics on Time-Dependent Stokes Shift Calculations. *J. Chem. Theory Comput.* **2009**, *5*, 1959-1567.
57. Uberuaga, B. P.; Anghel, M.; Voter, A. F. Synchronization of Trajectories in Canonical Molecular-Dynamics Simulations: Observation, Explanation, and Exploitation. *J. Chem. Phys.* **2004**, *120*, 6363-74.
58. Ryckaert, J. P.; Ciccotti, G.; Berendsen, H. J. C. Numerical Integration of the Cartesian Equations of Motion of a System with Constraints: Molecular Dynamics of n-Alkanes. *J. Comput. Phys.* **1977**, *23*, 327-341.
59. Darden, T.; York, D.; Pedersen, L. Particle Mesh Ewald: An *N*.Log(*N*) Method for Ewald Sums in Large Systems. *J. Chem. Phys.* **1993**, *98*, 10089-10092.
60. Humphrey, W.; Dalke, A.; Schulten, K. VMD: Visual Molecular Dynamics. *J. Mol. Graphics* **1996**, *14*, 33-8.
61. Pettersen, E. F.; Goddard, T. D.; Huang, C. C.; Couch, G. S.; Greenblatt, D. M.; Meng, E. C.; Ferrin, T. E. UCSF Chimera -- A Visualization System for Exploratory Research and Analysis. *J. Comput. Chem.* **2004**, *25*, 1605-12.
62. Fennell, C. J.; Gezelter, J. D. Is the Ewald Summation Still Necessary? Pairwise Alternatives to the Accepted Standard for Long-Range Electrostatics. *J. Chem. Phys.* **2006**, *124*, 234104.
63. Kubo, R. The Fluctuation-Dissipation Theorem. *Rep. Prog. Phys.* **1966**, *29*, 255-284.
64. Bagchi, B. Anomalous Power Law Decay in Solvation Dynamics of DNA: A Mode Coupling Theory Analysis of Ion Contribution. *Mol. Phys.* **2014**, *112*, 1-9.
65. Frauenfelder, H.; Sligar, S. G.; Wolynes, P. G. The Energy Landscapes and Motions of Proteins. *Science* **1991**, *254*, 1598 – 1603.
66. Metzler, R.; Jeon, J, -H.; Cherstvy, A. G.; Barkai, E. Anomalous Diffusion Models and their Properties: Non-Stationary, Non-Ergodicity, and Ageing at the Centenary of Single Particle Tracking. *Phys. Chem. Chem. Phys.* **2014**, *16*, 24128 – 24164.
67. Schulz, J. H. P.; Barkai, E.; Metzler, R. Aging Effects and Population Splitting in Single-Particle Trajectory Averages. *Phys. Rev. Lett.* **2013**, *110*, 020602.
68. Cherstvy, A. G.; Metzler, R. Population Splitting, Trapping, and Non-Ergodicity in Heterogeneous Diffusion Processes. *Phys. Chem. Chem. Phys.* **2013**, *15*, 20220 – 20235.
69. Shin, J.; Cherstvy, A. G.; Metzler, R. Kinetics of Polymer Looping with Macromolecular Crowding: Effects of Volume Fraction and Crowder Size. *Soft Matter* **2015**, *11*, 472 – 488.
70. Laage, D.; Hynes, J. T. A Molecular Jump Mechanism of Water reorientation. *Science* **2006**, *311*, 832-835.
71. Bel, G.; Barkai, E. Weak Ergodicity Breaking in the Continuous-Time Random Walk. *Phys. Rev. Lett.* **2005**, *94*, 240602.
72. Yamamoto, E.; Akimoto, T.; Yasui, M.; Yasuoka, K. Origin of Subdiffusion of Water Molecules on Cell Membrane Surfaces. *Sci. Rep.* **2014**, *4*, 4720.
73. Krepl, M.; Zgarbova, M.; Stadlbauer, P.; Otyepka, M. Banas, P.; Kova, J.; Cheatham, III, T. E.; Jurecka, P.; Sponer, J. Reference Simulations of Noncanonical Nucleic Acids with Different χ-Variants of the AMBER Force Field: Quadruplex DNA, Quadruplex RNA and Z-DNA. *J. Comp. Theory Comput.* **2012**, *8*, 2506-2520.

74. Furse, K. E., Lindquist, B. A., Corcelli, S. A. Solvation Dynamics of Hoechst 33258 in Water: An Equilibrium and Nonequilibrium Molecular Dynamics Study. *J. Phys. Chem. B* **2008**, *112*, 3231-3239.
75. Mukherjee, A.; Lavery, R.; Bagchi, B.; Hynes, J. T. On the Molecular Mechanism of Drug Intercalation into DNA: A Simulation Study of Intercalation Pathway, Free Energy, and DNA Structural Changes. *J. Am. Chem. Soc.* **2008**, *130*, 9747-9755.

Chapter 8

Solvation Dynamics in G-quadruplex DNA: Dependence on Quadruplex and Ligand Structures

The previous chapter showed that solvation dynamics in anti-parallel G-quadruplex DNA (GqDNA) is dispersed which follow power-law dynamics (summed with exponential relaxation). Direct comparison of TRFSS results to MD simulation showed matching of experimental and simulation results extremely well. Deuterium effect on experimental solvation response and decomposition of total simulated solvation correlation function into dynamics of individual components clearly showed that perturbed water, together with local DNA motion, defines the dispersed power-law dynamics in anti-parallel GqDNA. However, it is not known how such dynamics depend on the GqDNA and ligand structures as well as ligand binding positions and modes to different GqDNA. This chapter sheds light on such important questions, showing that there are only minimal effects of these parameters on solvation response inside GqDNA which eventually lead to dispersed power-law solvation response in different GqDNA structures.

8.1. Introduction

Self-assembly of repetitive guanine rich sequences leads to formation of non-canonical G-quadruplex structures (GqDNA) in presence of cations such as Na^+ or K^+. Formation of quadruplex structures are also induced by ligands (small molecules).[1-4] As discussed in previous chapter, stability to such non-canonical structures is provided by Hoogsteen-type hydrogen bonds formed between guanine, thus adopting several topological form such as parallel, anti-parallel, hybrid, etc. (Figure 8.1).[1-4] Studies have indicated that quadruplex DNA can be formed in the promotor region of many oncogenes and at the telomeric ends.[1-3] Quantitative visualization of such structures inside human cells have been reported by recent studies.[5] Due to their utility as a promising target for anti-cancer drug, quadruplex structures have attracted tremendous attention of late with an aim to synthesize and develop ligands which can specifically target such DNA forms. Furthermore, various ligands with specific selectivity towards quadruplex structure have been used to explore structural changes and reactivity of these forms,[6,7] and also to find their importance in several label-free assays in order to monitor exonuclease activity,[8] protein tyrosine kinase[9] and helicase activity.[10] In comparison to duplex-DNA, quadruplex DNA is structurally more diverse. Moreover, recent studies have shown that alteration in local solvation/hydration have severe impacts on the structure of quadruplex DNA,[11,12] as well as on the binding affinity of ligands towards them.[13] However, hydration/solvation

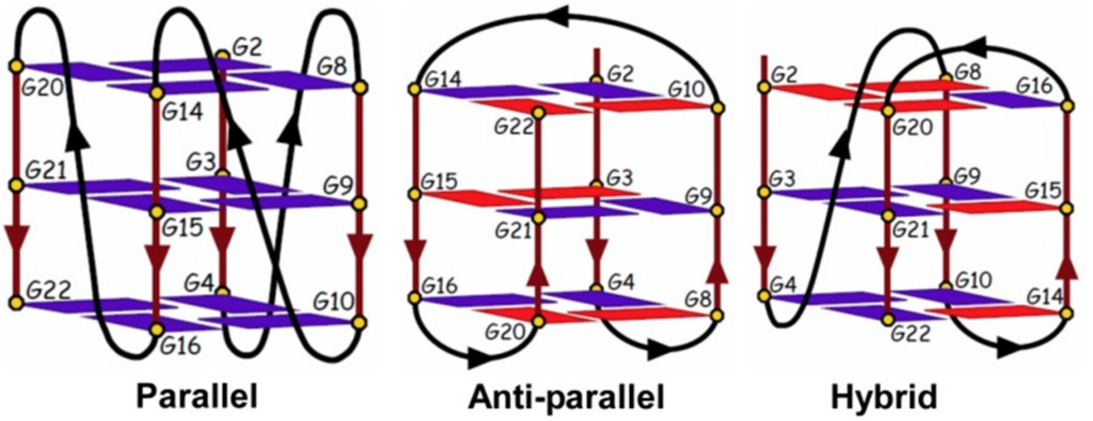

Figure 8.1: Schematic representation of various G-quadruplex structures formed in presence of different ions and small molecules (ligands). Loops of these structures are coloured in black, whereas syn- and anti-guanines are coloured in red and violet, respectively.

dynamics around quadruplex DNA was not much explored till recently by our research group.[31] Previous chapter discussed these results on solvation dynamics of groove bound ligand (DAPI) to antiparallel human telomeric GqDNA. This study showed that the dynamics in antiparallel GqDNA follows a power-law relaxation added with fast exponential relaxation over five decades of time (from 100 fs to 10 ns), showing similar dynamics as seen in duplex-DNA. Directly comparing the experimental and MD simulation results and decomposing the energy correlation functions (simulated) revealed that the dispersed solvation dynamics in GqDNA is controlled by water molecules, including parts of DNA, that come within a region of ~9 Å of DAPI.[31] However, it is still not known how the probe structures and locations as well as different GqDNA structures affect the hydration/solvation dynamics in different GqDNA structures.

This chapter tackles these issues by measuring the solvation dynamics in parallel c-Myc (*mPu22*) G-quadruplex DNA, probed by non-covalently attached ligand, Hoechst from 100 fs to 10 ns,[32] and comparing the same with the previous dynamic Stokes shifts of groove bound DAPI to the antiparallel human telomeric (*hTelo22*) quadruplex DNA discussed in the preceding chapter.[31] It has been found that the dynamic Stokes shift of Hoechst in parallel GqDNA follows power-law relaxation, summed with an exponential relaxation of 2 ps. The two ligand/GqDNA systems follow a power-law relaxation with only small difference in the power law exponents. Data shows an exponent of 0.06 for Hoechst/parallel GqDNA complex, whereas 0.16 for DAPI/antiparallel GqDNA complex.[32] Tight binding of Hoechst to parallel GqDNA is confirmed by steady state fluorescence and time-resolved anisotropy decay measurements, which shows a binding constant of ~1 x 10^5 M^{-1}. An equilibrium 50 ns simulation performed using docked Hoechst in parallel GqDNA shows that Hoechst binds near G13 and G4 residues of the outer G-tetrads through end stacking. Binding of Hoechst in parallel *mPu22* GqDNA was found to be different from the groove binding of DAPI in anti-parallel *hTelo22* GqDNA. Based on the previous experimental and simulation results,[31] the fast exponential relaxation of 2 ps has been assigned to the motion of water molecules that are weakly perturbed by parallel *mPu22* GqDNA, whereas, the coupled dynamics of DNA part and water molecules in the proximity of Hoechst inside parallel GqDNA control the power-law relaxation.[32]

8.2. Materials and Methods

8.2.1. Experimental Methods

Hoechst 33258 (bisbenzimide) was from Sigma-Aldrich and used without further purification (Figure 8.2A). Desalted 22-mer single stranded c-Myc (*mPu22*) DNA of sequence 5'-TGAGGGTGGGGAGGGTGGGGAA-3' was from Integrated DNA Technology (IDT). G-quadruplex samples were made by annealing 22-mer oligonucleotide in Tris-HCl buffer (10 mM) of *p*H 7.2 in presence of 100 mM KCl from 95 °C to room temperature (25 °C) over duration of ~5 hours. CD spectrum obtained for the sample confirms the formation of parallel quadruplex structure (Figure 8.2B) which shows negative peak at ~243 nm and a sharp dominant positive peak at ~265 nm.[14]

Prior to Hoechst/GqDNA sample preparation for time-resolved measurements, binding kinetics of ligand (Hoechst) to parallel *mPu22* GqDNA structure was checked by titrating parallel *mPu22* GqDNA against Hoechst of constant concentration (Figure 8.3B). A ratio of 50:1 for [*mPu22*]/[Hoechst] sample was chosen for time-resolved measurements where Hoechst fluorescence nearly saturates (see Figure 8.3). It is expected that all of the Hoechst molecules are bound to parallel quadruplex structure at this ratio. Concentration of Hoechst and *mPu22* GqDNA was kept at 20 µM and 1 mM, respectively for measurement in UPC, whereas the concentrations of Hoechst was kept at 1 µM and *mPu22* was kept at 50 µM for TCSPC measurements. Two other samples of [mPu22]/[Hoechst] = 80:1 and 45:1 were used to check the concentration dependence on measured fluorescence decays. Fluorescence decays were identical for both these ratios, indicating that either all the ligands (Hoechst) are bound to *mPu22* GqDNA, or the presence of small fraction of free dye (if any) doesn't

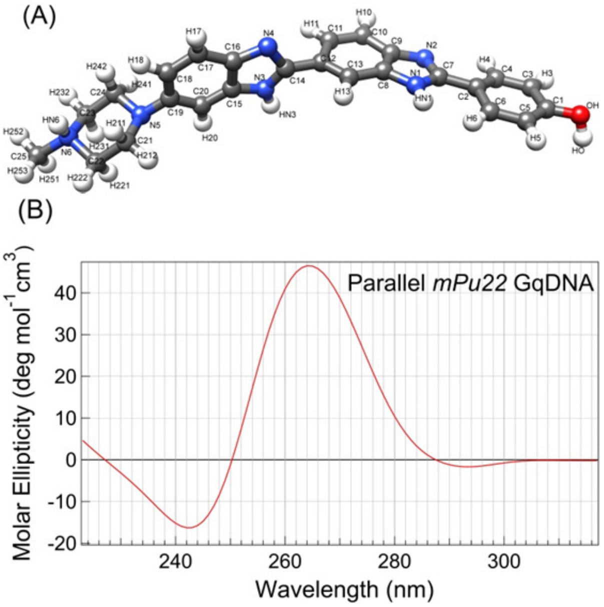

Figure 8.2: (A) Representation of Hoechst 33258 structure with atom names. (B) Formation of parallel GqDNA by mPu22 sequence in ionic condition of 100 mM KCl is confirmed by CD spectroscopy.

have any effect on the overall decay of Hoechst-DNA complex. To cover broad time-range of dynamics, fluorescence decays of the sample were collected in UPC and TCSPC setups. Finally, the TRES and dynamic Stokes shifts from 100 fs to 10 ns of the ligand bound to parallel GqDNA were calculated following procedures discussed in chapter 3.

8.2.2. Simulation Methods

8.2.2.1. Molecular Docking

Because of the absence of NMR/crystal structure of Hoechst/*mPu22* complex, Hoechst was docked onto parallel *Pu24* quadruplex structure obtained from protein data bank (PDB id 2A5P)[15] using AutoDock 4.2 before running 50 ns of equilibrium simulation.[16] AutoDock Tools (ADT) assign Gasteiger charges to *Pu24* GqDNA structure after merging the nonpolar hydrogen with their corresponding carbons. Rotatable bonds of ligand were detected by ADT and Gasteiger charges were assigned. Autogrid creates an active box of 40 Å x 40 Å x 40 Å based on a grid spacing of 0.375 Å, placed at the center of quadruplex structure. Lamarkian genetic algorithm was used for docking calculation. A population of random individual (population size: 150) was used with 2500000 energy evaluations. Mutation rate of 0.02 and a maximum number of 27000 generations were used. Fifty independent conformations were performed for Hoechst binding to *Pu24* quadruplex structure. Resulting positions were clustered based on root mean square criterion of 0.5 Å. Finally, the lowest free energy conformation obtained from the docking was used to perform 50 ns of simulation.

8.2.2.2. Molecular Dynamics Simulation

MD simulation on final docked Hoechst/*mPu22* GqDNA system had been carried out using standard force field for nucleic acids (*Parm99+bsc0*) in AMBER-14.[17] Atomic (ground state) charges and molecular mechanic force field parameters for Hoechst were taken from a previous study.[18] Since the PDB of *Pu24* structure contains one inosine in the central position of the sequence instead of guanine, thus inosine was modelled with the force field parameters obtained from an earlier study by Lankas.[19] Cubic box of TIP3P (8077) water molecules was used to solvate Hoechst/*mPu22* complex with a buffer extending upto 10 Å in each direction from GqDNA structure. Charge of entire Hoechst GqDNA complex was neutralized by adding 22 K^+ ions. This Hoechst-GqDNA system contains 25092 atoms. After the system was solvated and charge neutralized, it was subjected to 10000 steps of energy minimization using steepest decent as well as conjugate gradient algorithms keeping Hoechst/GqDNA system and counter-ions fixed with a restraint of 300 kcal mol^{-1} $Å^{-2}$, followed by restraint free energy minimization of the system for another 10000 steps. The entire system was heated from 0 K to 300 K using Langevin temperature[20] control in NVT ensemble for 50 ps, keeping a restraint of 25 kcal mol^{-1} $Å^{-2}$ on GqDNA and Hoechst.

Proper density of the system was maintained by running simulation of 20 ps with a restraint of 25 kcal mol^{-1} $Å^{-2}$ on GqDNA and Hoechst in NPT ensemble. The restraint on Hoechst GqDNA complex was reduced from 25 kcal mol^{-1} $Å^{-2}$ to 5 kcal mol^{-1} $Å^{-2}$ in next four cycles of 20 ps simulation in NPT ensemble. Further the system was equilibrated with 150 ps of simulation in NVT ensemble. This was followed by another 50 ps simulation in NVE ensemble. Final equilibration of the system was performed by running 2 ns of simulation in NVE ensemble. After the system was minimized and equilibrated properly, it was subjected to 50 ns of all atom production simulation using ground state charges of Hoechst molecules, where the entire system was kept flexible, using CPU codes of *pmemd* modules in AMBER-14. SHAKE algorithm was used to treat the covalent bonds containing hydrogen atoms, whereas particle-mesh Ewald (PME) were used to take proper care of long range electrostatic interactions.[21] Step size of simulation was kept at 2 fs and the trajectories were updated at an interval of 1 ps. CPPTRAJ of AMBER-14 and Igor Pro software were used for the final analysis of the MD trajectories. Chimera[34] and VMD[33] were used for figures preparation and visualization of the MD trajectories.

8.3. Results and Discussions

8.3.1. Steady-State Fluorescence Data

Steady-state fluorescence spectra of Hoechst/*mPu22* were collected by exciting the sample at 375 nm. Quinine sulphate is used as standard to correct fluorescence spectra.[22] Steady-state fluorescence spectra give the first-hand information about the local interaction of solute with the charged molecules in complex environment. Non-radiative processes involving rotation along the bisbenzimide linkage results in very low fluorescence quantum yield of Hoechst in water (~0.034).[23] On binding to parallel *mPu22* GqDNA, fluorescence intensity of Hoechst increases ~80 folds, compared to buffer, resulting into blue spectral shift by ~32 nm. Relative fluorescence spectra of Hoechst bound to *mPu22* GqDNA structure and in buffer are shown in Figure 8.3A, whereas the result of titration of Hoechst with varying concentration GqDNA is plotted in Figure 8.3B. These results illustrate that local environment inside DNA is critical for enhancing and shifting the fluorescence of Hoechst upon binding to parallel GqDNA. Similar effect was seen in case of Hoechst/c-Myc GqDNA complex earlier,[24] though the change in quantum yield was lower than that found in the present case.

8.3.2. Binding Constant of Hoechst to *mPu22* GqDNA

Hoechst binds to parallel *mPu22* GqDNA structure with a binding constant (K_b) of 1 x 10^5 M^{-1} which is calculated by fitting the binding isotherm of Hoechst to parallel quadruplex structure utilizing a kinetic model given by Maiti *et al.* (see Figure 8.3B)[24] Hoechst binds to *mPu22* with an affinity smaller than that reported for Hoechst in human c-Myc DNA.[24] However, binding constant (K_b) of Hoechst to *mPu22* is very similar to the one reported for DAPI in antiparallel *hTelo22* structure (2.7 x 10^5 M^{-1}).[31]

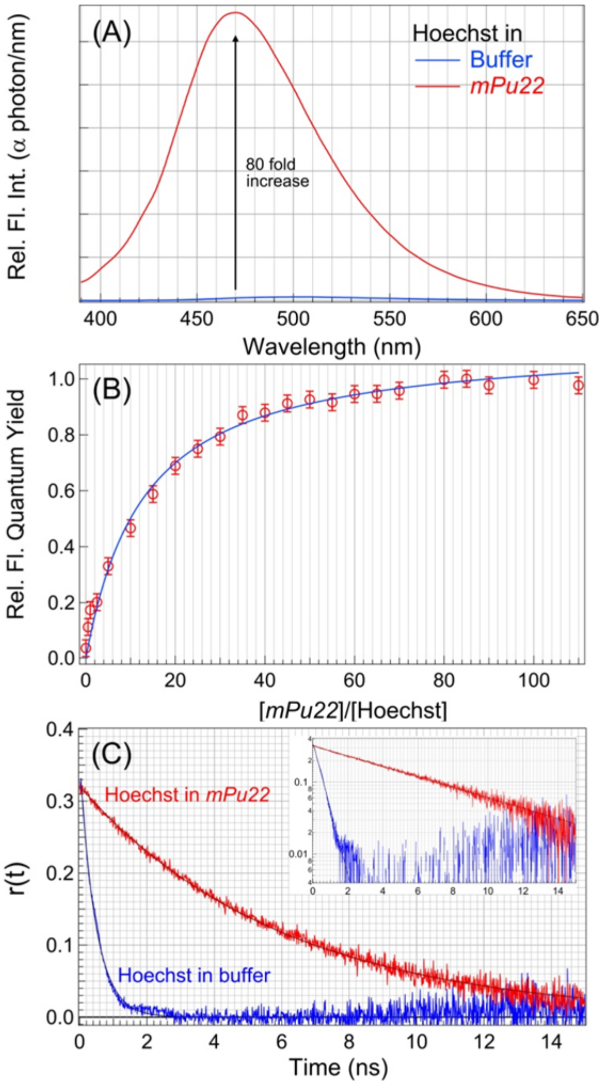

Figure 8.3: (A) Fluorescence spectra (corrected) of Hoechst bound to parallel *mPu22* GqDNA (red) and in buffer (blue). Fluorescence intensity of Hoechst increases ~80 folds upon binding to mPu22 along with shift in spectra towards blue side by ~32 nm. (B) Binding isotherm of end-stacked Hoechst to parallel GqDNA obtained by titrating constant concentration of Hoechst (1 μM) against varying concentration of GqDNA. The data is fitted using the kinetic model proposed by Maiti *et al.* which is shown by lines through the data points.[64] Hoechst binds to parallel mPu22 by a binding constant of 1×10^5 M^{-1}. Error bars shown in the plots are obtained by repeated measurements at few concentration ratios. (C) Anisotropy decays measured for Hoechst bound to *mPu22* GqDNA (red) and free Hoechst in buffer (blue). Anisotropy decay is modelled with single exponential shown by line through data. Inset shows semi-log plot indicating pure single exponential decays.

8.3.3. Fluorescence Anisotropy Decay

Direct information about fluorophore binding to a macromolecule can be extracted from fluorescence anisotropy decay. Anisotropy decays for Hoechst bound to parallel *mPu22* GqDNA structure and in buffer were measured by exciting the sample at 375 nm using TCSPC setup. Fluorescence anisotropy decay (Figure 8.3C) confirms the tight binding of Hoechst to *mPu22*. Anisotropy decay of free Hoechst in buffer and Hoechst/*mPu22* complex can be very well modeled with an exponential decay function which shows a rotational time constant of 0.47 ns and 6 ns for Hoechst in buffer and Hoechst/mPu22 complex, respectively (Figure 8.3C). Anisotropy decay of Hoechst/*mPu22* complex doesn't show any fast component which rules out the possibility of contribution from free dye. It also reveals that Hoechst binds to *mPu22* in such a way that it doesn't give rise to any fast local rotational motion that could affect the anisotropy decay at least within the measured time window using TCSPC setup.

Hydrodynamic radii of Hoechst

and Hoechst/DNA complex were calculated using rotational time constant through Stokes-Einstein-Debye relation assuming spherical shapes of dye and dye-DNA complex[22] as,

$$R_h = \sqrt[3]{\frac{3kT\tau_R}{4\pi\eta}} \tag{8.1}$$

where T is absolute temperature, k is Boltzmann's constant, and η is the solvent viscosity. The hydrodynamic radius for free Hoechst and Hoechst *mPu22* complex are found to be ~8 Å and ~19 Å, respectively. These sizes are in agreement with the sizes of Hoechst and Hoechst *mPu22* complex (approximately) obtained from physical sizes of the systems obtained in MD simulation.

8.3.4. Binding site of Hoechst in *mPu22*

Phan *et al.* reported the possible binding site of Hoechst to human c-Myc promoter (*Pu24*) GqDNA structure in the solution NMR.[25] Monitoring the broadening and shifting of the signal from imino proton of guanine, which is present near the binding site of Hoechst, they suggested that several stacking configurations near G13 residue of *Pu24* structure keeps Hoechst intact to the parallel *Pu24* GqDNA.[25] However, the structure of Hoechst bound to *Pu24* was not available, therefore Hoechst was docked to the *Pu24* GqDNA structure obtained from protein data bank (PDB id. 2A5P). The most energetically stable configuration of Hoechst/GqDNA complex was further used to run 50 ns of production simulation in AMBER-14. (Note here that the presence of two additional guanines residues at the end of *Pu24* is the only difference between the base sequences of the two structures; *Pu24* and *mPu22*. Since these two guanines are located far away from the binding site of Hoechst, thus their presence did not affect Hoechst binding.) Simulation result shows that Hoechst end-stacks to *Pu24* near G4, G8, G13 and G17 residues of outer G-tetrad (Figure 8.4). In fact it was observed that imidazole ring which is linked to phenol part of Hoechst stacks over G13 as anticipated from experiment,[25] whereas, the benzimidazole ring of Hoechst connected to piperazine ring resides near G4 and is found to be rotated in a way such that it occupies a plane perpendicular to the rest of the Hoechst structure. It was also observed that piperazine ring is not in plane with the attached benzimidazole ring; rather it is deviated as shown in Figure 8.4. However, the entire Hoechst structure was found to be shifted towards the G17 residue of the same G-tetrad after ~ 30 ns of simulation. This may indicate that Hoechst binds near the outer G-tetrad of *Pu24* GqDNA structure with multiple stacking conformations as anticipated by the NMR results.[25] Nevertheless, Hoechst structure (RMSD) was found to be similar throughout the simulation (Figure 8.5). It was also found that the indole ring of the Hoechst stays in a plane almost parallel to the outer G-tetrad of GqDNA throughout the entire 50 ns simulation. Hydrogen bonds (H-bonds) provide stability to Hoechst which are formed between *Pu24* GqDNA structure and

Hoechst: O6 atom of G13 is H-bonded to HN3 atom of imidazole nitrogen (N3) of dye with an occupancy of ~ 88%, O2P atom of G17 forms H-bond with an occupancy of ~ 33% to HO group of Hoechst, HN1 atom of imidazole nitrogen (N1) shows a H-bond formed with O5′ and O4′ atoms of T1 with an occupancy of ~ 31% and ~ 21%, respectively. It is also H-bonded to N7 atom of A3 with ~30% occupancy (see Figure 8.4A). The presence of H-bonds, together with electrostatic interactions and π-stacking, facilitate tight binding of Hoechst to the parallel GqDNA.

Numbers of water molecules in first, second and third solvation shells of Hoechst were calculated as those water molecules that come within 4 Å, 4 Å to 8 Å and 8 Å to 12 Å from any atom of Hoechst, respectively. The average numbers of water molecules occupying the first, second and third hydration shells has been found to be ~45, ~209 and ~590, respectively. Thus, due to presence of large number of water molecules, Hoechst remains highly hydrated in the parallel quadruplex structure. Moreover, it also indicates that probably hydration dynamics plays vital role in stabilizing Hoechst inside parallel *mPu22* GqDNA structure, similar as found in previous chapter in case of groove-bound DAPI in antiparallel *hTelo22* GqDNA.

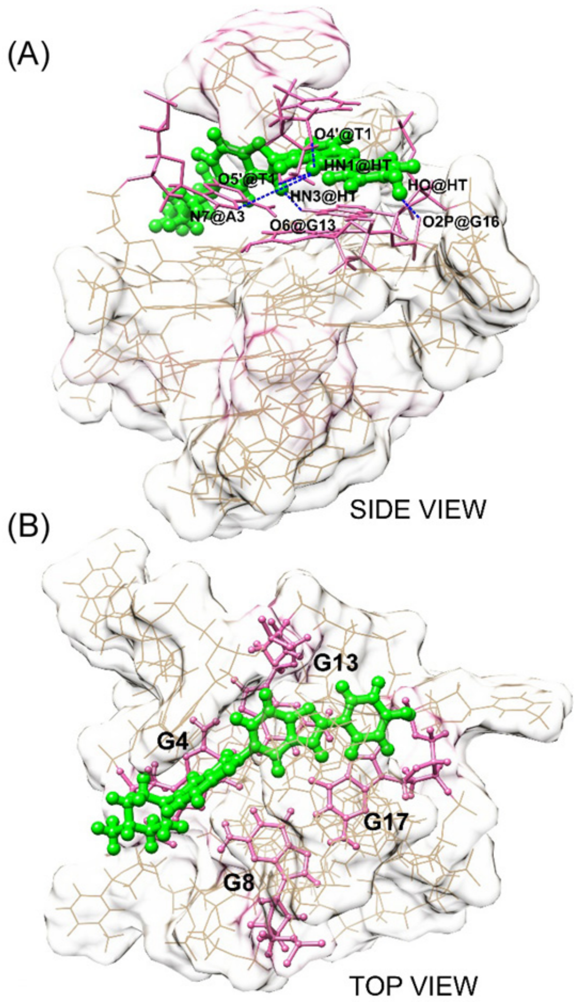

Figure 8.4: (A) Cartoon representing Hoechst binding site within *mPu22* quadruplex structure, stability to which is provided by formation of hydrogen bonds between *mPu22* and Hoechst (see side view). (B) Hoechst binds to parallel GqDNA through end-stacking to one of the outer G-tetrad formed by G4, G8, G13 and G17 near G13 and G4.

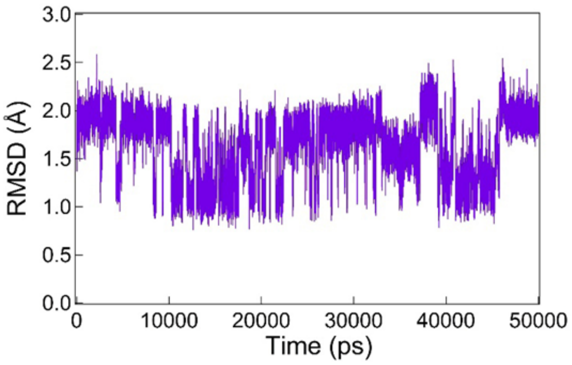

Figure 8.5: Root mean square deviation (RSMD) of Hoechst bound to parallel quadruplex structure over entire 50 ns simulation.

8.3.5. Time-Resolved Fluorescence Data

Fluorescence decays of end-stacked Hoechst in parallel *mPu22* GqDNA at different wavelengths, distributed over entire steady-state spectrum, were collected in UPC and TCSPC techniques to monitor dynamic Stokes shifts from ~100 fs to 10 ns. Figure 8.6 shows the fluorescence decays along with their multi-exponential decays fits, measured using TCSPC and UPC techniques. Decays exhibit fast decay at the shorter wavelengths, rise followed by decay at longer wavelengths. Fluorescence decays were fitted with the sum of three exponentials. TRES constructed using the fitted parameters obtained from the wavelength dependent decays of UPC and TCSPC, using steady state spectrum (as described in chapter 3), were combined to cover broad range of time from ~100 fs to 10 ns (Figure 8.7A). TRES shown in Figure 8.7A also includes time-zero spectrum of the sample measured at -78 ˚C. It can be clearly seen that due to limited temporal resolution of UPC setup (~270 fs), even at 100 fs diffusive solvation dynamics cannot be fully extracted relative to the time-zero glass spectrum. Merging of the TRES from 100 fs to 300 ps obtained through UPC and ~30 ps to 10 ns obtained by TCSPC setup give rise to the similar dynamic Stokes shifts in the overlapped time range. Figure 8.7B shows excellent overlapping of the Stokes shift (1st moment frequency shift) within the common time points (from ~30 ps to ~300 ps), obtained from both techniques. However, the Stokes shifts at the time points <~100 fs for UPC data and <~30 ps for TCSPC data were not reliable because of the limited time resolutions of these techniques.

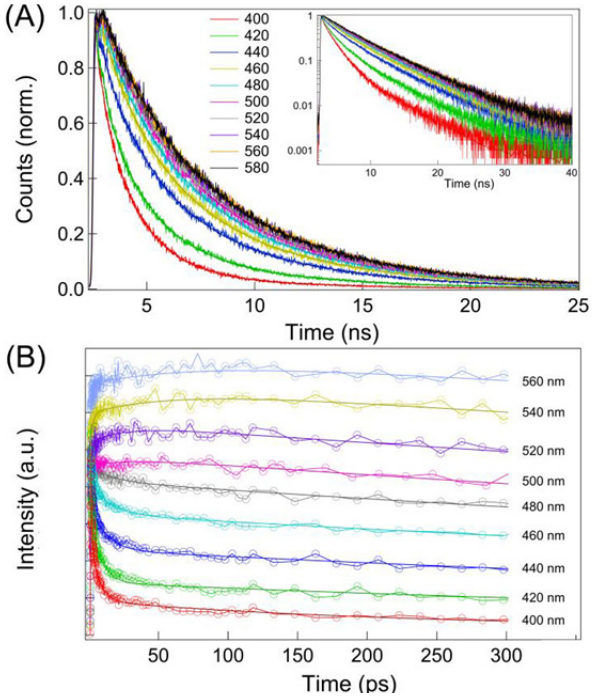

Figure 8.6: (A) Fluorescence decays of end stacked Hoechst to *mPu22* GqDNA at different wavelength measured using time-correlated single photon counting (TCSPC) technique. Decays were fitted by sum of three exponentials indicated by the lines through data. Inset shows semi-log plot of same data. To minimise clumsiness, only 10 out of 20 measured decays are shown. (B) Wavelength dependent decays collected using fluorescence up-conversion (UPC) technique. Decays were modelled with sum of three exponentials.

8.3.6. Comparison of dynamic Stokes Shifts in Parallel and Antiparallel GqDNA

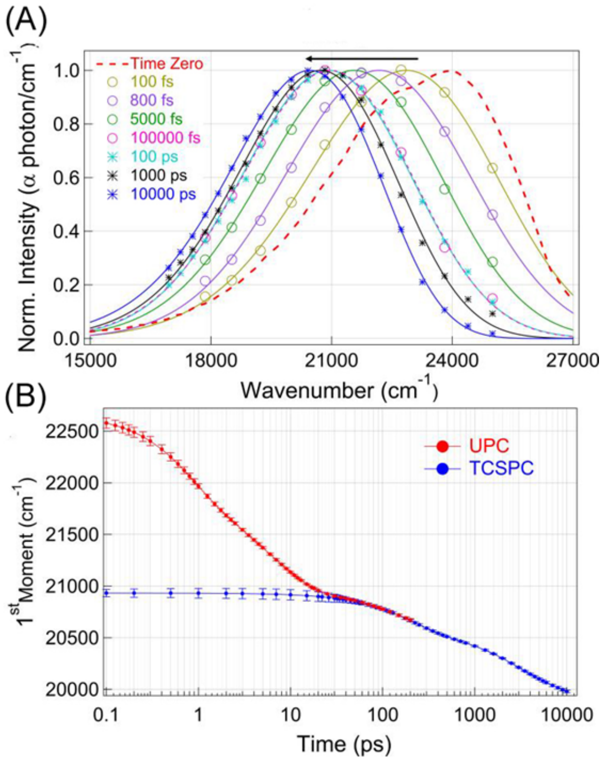

Figure 8.7: (A) Time-resolved emission spectra of end-stacked Hoechst to parallel quadruplex DNA from 100 fs to 10 ns obtained from UPC and TCSPC data. Time-zero glass spectrum measured at -78 °C is also plotted. (B) First-moment frequency shifts of TRES obtained from TCSPC (blue) and UPC (red), showing overlap of TCSPC and UPC data at common time-points. Repeated measurements of Hoechst-mPu22 GqDNA dynamics in TCSPC and UPC setups give the estimated error bars (±SD).

'Absolute' Stokes shift of end-stacked Hoechst in parallel GqDNA structure was calculated using equation 3.24 (see chapter 3) and compared with the absolute Stokes shift of groove bound DAPI in antiparallel *hTelo22* GqDNA structure (Figure 8.8A). The plots show that, relative to time zero spectrum, the total Stokes shift of end-stacked Hoechst in parallel GqDNA is larger (2785 cm^{-1}) as compared to groove bound DAPI in antiparallel GqDNA (2051 cm^{-1}) from 100 fs to 10 ns. Figure 8.8B shows comparison of solvation correlation function C(t) of both, Hoechst/*mPu22* and DAPI/*hTelo22* systems, constructed using the absolute Stokes shifts in Figure 8.8A as,

$$C(t) = \frac{S(10\ ns) - S(t)}{S(10\ ns)} \qquad (8.2)$$

The difference in the absolute Stokes shift of both the system could have arisen from the characteristic feature of the ligands, because environment polarity dependent spectral shifts of Hoechst are larger than that of DAPI (discussed in chapter 5). Also, different local environments experienced by end-stacked Hoechst and groove-bound DAPI in parallel *mPu22* and antiparallel *hTelo22* structure, respectively, can give rise to such differences in the total dynamic Stokes shifts. It can also be seen from Figure 8.8 that in comparison to the Stokes shifts of DAPI in antiparallel structure at longer times, Hoechst shows a bit more stretched rate of Stokes shifts in parallel GqDNA structure.[32] The Stokes shifts of end-stacked Hoechst to parallel GqDNA structure was fitted with a power-law added to an exponential relaxation, similar as used to model groove bound DAPI data in previous study.[31]

$$S(t) = S_{\infty}\left[a\left(1-\left(1+\frac{t}{t_0}\right)^{-n}\right)+b\left(1-e^{-t/\tau}\right)\right] \qquad (8.3)$$

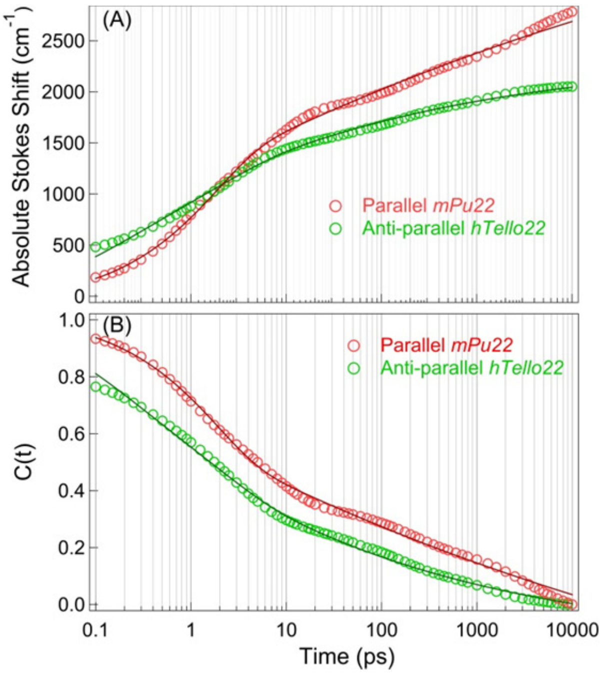

Figure 8.8: (A) Absolute Stokes shifts of Hoechst end-stacked to parallel GqDNA is compared to that of DAPI groove bound to antiparallel *hTelo22* GqDNA as reported in earlier study. Fits to data is represented by lines through points. Hoechst in parallel *mPu22* shows larger Stokes shift (2785 cm^{-1}) than that of DAPI in antiparallel *hTelo22* (2051 cm^{-1}) at least within the measured time-window. (B) Comparison of solvation correlation functions of the two quadruplex systems constructed from absolute Stokes shifts is shown.

The fit to Hoechst/*mPu22* data using equation 8.3 extracts S_∞ = 4750 cm^{-1}, t_0 = 90 fs, a = 0.86, n = 0.06, b = 0.14 and τ = 2 ps. The obtained parameters reveal that the solvation dynamics around Hoechst in parallel GqDNA also shows dispersed dynamics that follow power-law relaxation of exponent 0.06, summed with exponential relaxation of 2 ps. Dynamics of solvation in neat water completes within ~1 ps,[26] such hydration dynamics around biomolecular surface gets retarded by a factor of 2-3.[27] The fast exponential time constant of 2 ps obtained for Hoechst/*mPu22* system was found to be similar as in the previously discussed groove-bound DAPI to antiparallel GqDNA system (chapter 7).[31] In fact, previous MD simulation results on DAPI/*hTelo22* system showed that the fast exponential relaxation of 2 ps originates from the motion of water molecules of first solvation shell that come within a region of 4 Å from DAPI.[31] The present case of Hoechst/*mPu22* system is expected to show similar effects; thus, time component of 2 ps was assigned to the weakly perturbed dynamics of interfacial water molecules around Hoechst by parallel GqDNA structure.[32] Importantly, from MD simulation trajectories, it was found that end-stacked Hoechst inside *mPu22* has access to large number of water molecules (~45, ~209, ~580 in the first, second and third solvation shells, respectively), whereas the water molecules that come near groove-bound DAPI in antiparallel *hTelo22* GqDNA structure were somewhat smaller in number (~34, ~56, and ~103 in first, second and third shell, respectively: chapter 7).[31] Regardless of the differences in the number of water molecules, the result suggests that the hydration layers around Hoechst/*mPu22* complex were perturbed by *mPu22* structure in a way similar to DAPI/*hTelo22* GqDNA system, (possibly) showing similar relaxation of water molecules near the GqDNA.[32]

However, a subtle difference in the power-law exponent is seen in both the cases: end-stacked Hoechst in parallel *mPu22* GqDNA shows power-law exponents of 0.06,[32] whereas groove bound DAPI in *hTelo22* GqDNA shows exponent of 0.16.[31] However, previous MD simulation on groove-bound DAPI in antiparallel *hTelo22* structure and decomposition of the total (simulated) energy correlation into its contributions from individual components shows that the coupled dynamics of water molecules and parts of DNA that reside within a region of ~ 9 Å of DAPI control the slow dispersed power-law dynamics. Simulated energy correlation for Hoechst/*mPu22* GqDNA system were not calculated due to limited simulation length; but based on previous observation of DAPI/*hTelo22* GqDNA system, it was anticipated that perturbed motion of water molecules and parts of DNA near binding site of Hoechst may govern the slow dispersed power-law dynamics in Hoechst/*mPu22* system as well.[32] However, complex coupling of perturbed water motion and backbone of DNA, along with the dynamics of flexible loops connecting G-tetrads and its unpaired DNA bases, may also be the reason behind the (subtle) differences in the power-law exponents of the two systems. In fact, comparing the binding sites of Hoechst and DAPI in the two different quadruplex structures reveals that parts of DNA loops connecting the G-tetrads and its unpaired DNA bases stay closer to end-stacked Hoechst as compared to groove-bound DAPI in antiparallel GqDNA.[32] Thus, it is believed that the dynamics of unpaired DNA bases along with these DNA loops may also contribute to the coupled dynamics of water and DNA when probed by Hoechst, which may eventually affect the power-law dynamics as seen in case of Hoechst in parallel GqDNA system.[32]

Finally, it should be noted that Figure 8.8 shows comparison of dynamic Stokes shifts of Hoechst and DAPI in two different (parallel and antiparallel) GqDNA, instead of using the same probe molecule in both systems. This was done because of the low binding affinity of DAPI to parallel/hybrid quadruplex structures which result into small changes in the fluorescence quantum yield. Nevertheless, this comparison helped to examine any significant effect induced by ligand structure, if any, on the solvation dynamics in different GqDNA systems. In fact, solvation response shown by both the probes (DAPI and Hoechst) in pure water ~1 ps.[31,28] In accordance with theory of solvation, which states that as long as the dipolar properties of structurally different solvation ligands do not vary much, both probes would show a similar solvation response.[29,30] This is the case with Hoechst and DAPI. Hence, it is expected that the probe structures have insignificant effect on the overall dynamics in two quadruplex structures; instead the quadruplex structures and position of the probes should play the significant role in influencing the overall dynamics in GqDNA systems. Nevertheless, comparing the dynamic Stokes shifts of two probes, it is clear that these factors may have only subtle effect on overall solvation dynamics in different GqDNA systems, which ultimately give rise to dispersed power-law solvation response extending over broad time-range.

8.4. Conclusion

Current study on parallel and antiparallel GqDNA structures using two different probes clearly indicated that solvation dynamics in both the structures inherently follow a power-law, showing similar dynamics from 100 fs to 10 ns. However, unlike in duplex-DNA, different quadruplex structures are found to show similar dynamics of solvation irrespective of probe-positions (groove-bound vs. end-stacked). It may perhaps specify that in different quadruplex structures the site-specific characteristics of DNA hydration dynamics are not altered much, which ultimately gets revealed in the Stokes shifts dynamics of different ligands bound to different quadruplex structures at different positions.

The results presented in this part -I of the thesis comprised of exploration of solvation dynamics in various duplex and quadruplex DNA systems. The vast amount of results presented here suggested several important dynamical aspects in DNA, which provided several new insights about DNA solvation:

(1) It is clearly confirmed that the dynamics of solvation in DNA is highly dispersed which mainly follow power-law relaxation over broad time-range that can extend over several decades.

(2) It is shown through deuterium effect and simulation studies that power-law dynamics can actually originate from very slow motions of perturbed water molecules near the probe site inside DNA groove.

(3) There is substantial effect of base-sequence on the minor groove solvation, which can significantly induce the relative contributions of perturbed water and DNA motions into the overall dynamics. It is *not* always true that groove binders are mainly solvated by slow motions of DNA parts, instead that situation actually depends on the local DNA sequence which ultimately dictate the very slow and dispersed hydration dynamics in the grooves of DNA.

(4) The highly dispersed power-law dynamics can be significantly modulated by the introduction of mismatched base-pairs near the probe site, which ultimately allow one to assign characteristic effects of mismatches on the overall local collective solvation dynamics in DNA. Such collective dynamics may be of extreme importance in the context of mismatch recognition and repair by enzymes in vivo.

(5) Solvation response in higher order G-quadruplex DNA structures is also highly dispersed which also shows power-law relaxation of similar kind as seen in duplex-DNA. More so, such dispersed dynamics is shown to be affected barely by the quadruplex structure (antiparallel or parallel) and/or probe structures and/or probe positions (groove-bound vs. end-stacked).

(6) In all cases, counter-ion motions are found to be (or predicted to be) minimally affecting the overall solvation response in DNA grooves when probed by

ligands bound to the grooves. It is found that either the motion of water molecules or DNA parts or the collective motion of water and DNA parts mainly control the dispersed solvation response over broad time-range. The relative contributions of these are modulated by the DNA base sequence and the mismatch introduced.

References

1. Murat, P.; Balasubramanian, S. Existence and Consequences of G-Quadruplex Structures in DNA. *Curr. Opin. Genet. Dev.* **2014**, *25*, 22-29.
2. Maji, B.; Bhattacharya, S. Advances in the Molecular Design of Potential Anticancer Agents via Targeting of Human Telomeric DNA. *Chem. Commun.* **2014**, *50*, 6422.
3. Neidle, S. The Structures of Quadruplex Nucleic Acids and Their Drug Complexes. *Curr. Opin. Struct. Biol.* **2009**, *19*, 239-250.
4. Verma, S. D.; Pal, N.; Singh, M. K.; Shweta, H.; Khan, M. F.; Sen, S. Understanding Ligand Interaction with Different Structures of G-Quadruplex DNA: Evidence of Kinetically Controlled Ligand Binding and Binding-Mode Assisted Quadruplex Structure Alteration. *Anal. Chem.* **2012**, *84,* 7218-7226.
5. Biffi, G.; Tannahill, D.; McCafferty, J. Balasubramanian, S. Quantitative Visualization of DNA G-Quadruplex Structures in Human Cells. *Nat. Chem.* **2015**, *5,* 182-186.
6. Bhasikuttan, A. C.; Mohanty, J. Targeting G-Quadruplex Structures with Extrinsic Fluorogenic Dyes: Promising Fluorescence Sensors. *Chem. Commun.* **2015**, *51*, 7581-7597.
7. Debnath, M.; Ghosh, S.; Panda, D.; Bessi, I.; Schwalbe, H.; Bhattacharyya, K.; Dash, J. Small Molecule Regulated Dynamic Structural Changes of Human G-Quadruplexes. *Chem. Sci.* **2016,** *7*, 3279-3285.
8. Leung, C. H.; Chan, D. S. H.; Man, B. Y. W.; Wang, C. J.; Lam, W.; Cheng, Y. C.; Fong, W. F.; Hsiao, W. W. L.; Ma, D. L. A Simple and Convenient G-Quadruplex-Based Turn-on Fluorescence Assay for 3′ → 5′ Exonuclease Activity. *Anal. Chem.* **2011**, *83,* 463-466.
9. Lin, S.; Gao, W.; Tian, Z.; Yang, C.; Lu, L.; Mergny, J. L.; Leung, C. H. Ma, D. L. Luminescence Switch-on Detection of Protein Tyrosine Kinase-7 Using a G-Quadruplex-Selective Probe. *Chem. Sci*. **2015**, *6*, 4284-4290.
10. Leung, K. H.; He, H. J.; He, G.; Zhong, H. J.; Lin, S.; Wang, Y. T.; Ma, D. L. Leung, C. H. Label-Free Luminescence Switch-on Detection of Hepatitis C Virus NS3 Helicase Activity Using a G-Quadruplex-Selective Probe. *Chem. Sci.* **2015**, *6*, 2166-2171.
11. Miller, M. C.; Buscaglia, R.; Chaires, J. B.; Lane, A. N.; Trent, J. O. Hydration is a Major Determinant of the G-Quadruplex Stability and Conformation of the Human Telomere 3′ Sequence of d(AG3(TTAG3)$_3$). *J. Am. Chem. Soc.* **2010**, *132*, 17105-17107.
12. Heddi, B.; Phan, A. T. Structure of Human Telomeric DNA in Crowded Solution. *J. Am. Chem. Soc.* **2011**, *133*, 9824-9833.
13. Chen, Z.; Zheng, K.; Hao, Y.; Tan, Z. Reduced or Diminished Stabilization of the Telomere G-Quadruplex and Inhibition of Telomerase by Small Chemical Ligands Under Molecular Crowding Condition. *J. Am. Chem. Soc.* **2009**, *131*, 10430-10438.
14. Phan, A. T.; Modi, Y. S.; Patel, D. J. Propeller-Type Parallel-Stranded G-Quadruplexes in the Human C-MYC Promoter *J. Am. Chem. Soc.* **2004**, *126,* 8710–8716.
15. Phan, A. T.; Kuryavyi, V.; Gaw, H. Y.; Patel, D. J. Small-Molecule Interaction with a Five-Guanine-Tract G-Quadruplex Structure From Human MYC Promoter. *Nat. Chem. Biol*. **2005**, *1*, 167–173.
16. Morris, G. M.; Goodsell, D. S.; Halliday, R. S.; Huey, R.; Hart, W. E.; Belew, R. K.; Olson, A. J. Automated Docking Using a Lamarckian Genetic Algorithm and An Empirical Binding Free Energy Function. *J. Comput. Chem.* **1998**, *19*, 1639-1662.
17. Case, D. A.; Babin, V.; Berryman, J. T.; Betz, R. M. Cai, Q.; Cerutti, D. S.; Cheatham, T. E.; Darden, T. A.; Duke, R. E.; Gohlke, H.; Goetz, A. W.; Gusarov, S.; Homeyer, N.; Janowski, P.;

Kaus, J. Kolossváry, I.; Kovalenko, A.; Lee, T. S.; LeGrand, S.; Luchko, T.; Luo, R.; Madej, B.; Merz, K. M.; Paesani, F.; Roe, D. R.; Roitberg, A.; Sagui, C.; Salomon-Ferrer, R.; Seabra, G.; Simmerling, C. L.; Smith, W.; Swails, J.; Walker, R. C.; Wang, J. Wolf, R. M.; Wu, X. Kollman, P. A. *AMBER 14*, University of California, San Francisco **2014.**

18. Ryckaert, J. P.; Ciccotti, G.; Berendsen, H. J. C. Numerical Integration of the Cartesian Equations of Motion of a System with Constraints: Molecular Dynamics of n-Alkanes. *J. Comput. Phys.* **1977**, *23*, 327-341.
19. Lankas, F.; Cheatham III, T. E.; Spackova, N.; Hobza, P.; Langowski, J.; Sponer, J. Critical Effect of the N2 Amino Group on Structure, Dynamics, and Elasticity of DNA Polypurine Tracts. *Biophys. J.* **2002**, *82*, 2592.
20. Uberuaga, B. P.; Anghel, M. Voter, A. F. Synchronization of Trajectories in Canonical Molecular-Dynamics Simulations: Observation, Explanation, and Exploitation. *J. Chem. Phys.* **2004**, *120*, 6363-6374.
21. Darden, T.; York, D.; Pedersen, L. Particle Mesh Ewald: An *N*.Log(*N*) Method for Ewald Sums in Large Systems. *J. Chem. Phys.* **1993**, *98*, 10089-10092.
22. Lakowicz, J. R. *Principles of Fluorescence Spectroscopy,* 3rd Edition, Springer, USA, **2000**.
23. Härd, T.; Fan, P.; Kearns, D. R. A Fluorescence Study of the Binding of Hoechst 33258 and DAPI to Halogenated DNAs. *Photochem. Photobiol.* **1990**, *51*, 77-86.
24. Maiti, S.; Chaudhury, N. K.; Chowdhury, S. Hoechst 33258 Binds to G-quadruplex in the Promoter Region of Human C-MYC. *Biochem. Biophys. Res. Comm.* **2003**, *310*, 505-512.
25. Phan, A. T.; Kuryavyi, V.; Gaw, H. Y.; Patel, D. J. Small-Molecule Interaction With a Five-Guanine-Tract G-Quadruplex Structure From Human MYC Promoter. *Nat. Chem. Biol*. **2005**, *1*, 167-173.
26. Jimenez, R.; Fleming, G. R.; Kumar, P. V.; Maroncelli, M. Femtosecond Solvation Dynamics of Water. *Nature* **1994**, *369*, 471-473.
27. Sterpone, F.; Stirnemann, G.; Laage, D. Magnitude and Molecular Origin of Water Slowdown Next to a Protein *J. Am. Chem. Soc.* **2012**, *134*, 4116-4119.
28. Furse, K. E.; Lindquist, B. A.; Corcelli, S. A. Solvation Dynamics of Hoechst 33258 in Water: An Equilibrium and Nonequilibrium Molecular Dynamics Study. *J. Phys. Chem. B.* **2008**, *112*, 3231.
29. Maroncelli, M.; Castner, E. W.; Webb, S. P.; Fleming, G. R. *Ultrafast phenomena*, Springer, New York, USA, **1986**.
30. Kremer, F.; Schönhals, A. *Broadband dielectric spectroscopy*, Chapter 15, Springer, New York, USA, **2003.**
31. Pal, N.; Shweta, H.; Singh, M.K.; Verma, S. D.; Sen, S. Power-Law Solvation Dynamics in G-quadruplex DNA: Role of Hydration Dynamics on Ligand Solvation Inside DNA. *J. Phys. Chem. Lett.* **2015**, *6*, 1754-1760.
32. Singh, M. K.; Shweta, H.; Sen, S. Dispersed Dynamics of Solvation in G-quadruplex DNA: Comparison of Dynamics Stokes Shifts of Probes in Parallel and Antiparallel Quadruplex Structures. *Methods Appl. Fluoresc.* **2016**, *4*, 034009.
33. Humphrey, W.; Dalke, A.; Schulten, K. VMD: Visual Molecular Dynamics. *J. Mol. Graphics* **1996**, *14*, 33-38.
34. Pettersen, E. F.; Goddard, T. D.; Huang, C. C.; Couch, G. S.; Greenblatt, D. M.; meng, E. C.; Ferrin, T. E. UCSF Chimera -- A Visualization System for Exploratory Research and Analysis. *J. Comput. Chem.* **2004**, *25*, 1605-1612.

Part II

Study of Location Dependent Polarity and Hydration at Lipid/Water Interfaces

Chapter 9

Static and Dynamic Properties of Lipid Membrane: An Overview

9.1. Introduction

Lipid membrane, a double layered bio-interface, acts as a containment of biological cells and forms matrix which separates the living cells from the outside environment. Certainly, DNA is considered as an "eternal molecule" of life due to its vital significance in life's processes; likewise, membrane can be termed as an "eternal structure" due to its contribution to cell viability.[1] Structural component of biological lipid-membrane provides permeability barrier that defines the boundaries of cells and subcellular organelles through which communication between intra- and extra-cellular environments is established so as to perform various essential biochemical processes at molecular level. Thus, involvement of chemical and physical properties of membranes in interacting with its surroundings and initiating most cellular processes makes lipid very dynamic relative to cellular processes, rather than just marking a static barrier. The puzzle around biological lipid-membrane started with its very discovery in late 1890s by British physiologist Charles Ernest Overton who termed it as "lipoids".[2] However, following the subsequent ground-works of Irwin Langmuir (an American chemist), Gorter and Grendel[3] (physiologists from Holland), Danielli[4] (an English physiologist), Davson[4] (British biologist) and Robertson[5,6] (American chemist); Singer and Nicolson[7] came up with the famous "Fluid Mosaic Model" of cell membrane in 1972, opening a new era in science. However, this simplified model had been challenged by the hypothesis of lipid rafts within membrane, formulated by Simons and Ikonen.[8] Membrane consists of number of different lipid molecules which include phospholipids, glycerolipids, sphingolipids and cholesterol.[9-11] Mixing of these molecules within membranes presumably becomes highly non-uniform which gives rise to formation of micrometer to nanometer sized domains called lipid rafts.[12-15] These lipid-rafts have been suggested to participate in many important cellular processes, such as protein trafficking and aggregation, membrane fusion and signal transduction. On the other hand, changes in expression levels of individual lipid species have been implicated to relate to many diseases, including diabetes, cancers, Alzheimer's disease, HIV entry, and atherosclerosis.[16,17] It is also well documented that changes in the viscosity of cell-membrane can affect the activity of membrane-bound proteins, which in turn lead to disorders at the cellular and organismal level.[18,19] For instance, cardiovascular diseases[20], cell malignancy[21,22], Alzheimer's disease[23], diabetes[24], hypertension[25] and aging[26] are the disorders that associate with the change in membrane viscosity. Membranes are also important for regulating cellular processes like signal transduction, membrane-protein trafficking, neurotransmission, etc. Besides, membranes play crucial role in the processes like membrane budding (exocytosis and endocytosis), adhesion, fusion and fission, protein targeting, pore formation, surface pattering etc.[2]

All the above processes within lipid membrane are directly linked to the normal (or abnormal) functioning of cells. However, at molecular level, these biochemical processes are controlled by the basic chemical phenomena like electron, proton and ion transfer from one site to another, as well as the (non-covalent) molecular interactions and transportation of (bio)-molecules like proteins, DNA and small molecules (drugs) within/through the lipid membrane. Most importantly, these molecular phenomena critically depend on the physicochemical properties of lipid membrane such as composition, environment polarity, surface tension, rotational mobility, extent of water penetration, fluidity, chain ordering, etc. – all of which are dependent on the '*depth*' across the lipid/water interface and within the bilayer.[27-32] For example, anisotropic changes in membrane organization were found to be different when monitored at different positions (depths) across the cell-membrane of adult rat-liver.[33] The organization and dynamics of hippocampal membranes are also found to be depth-dependent.[34] In fact, polarity and viscosity profiles across the lipid/water interface are the key determinant for interaction with and insertion of various biomolecules and small molecules in the lipid bilayer.[35,36] These interactions are affected by the depth-dependent hydration state, proton activity, hydrogen bond availability, dynamics and ordering of lipids across the lipid/water interface.[28-32] The depth-dependent polarity profile at lipid interface can result from the depth-dependent distribution of water at the interface. Similarly, viscosity (and rigidity) inside lipid bilayer can change upon going from the bulk water-phase into the hydrophobic chain-region. The depth-dependent static properties are also presumably linked to the local dynamics inside lipid bilayer. In fact, local static and dynamic properties in any biomolecule bridge the gap between the structure and function of that biomolecule. Hence, characterization of static and dynamic properties at different depths (within few Angstroms apart) across lipid/water interface is vital for understanding the basis of all biochemical processes that occur at the membrane interfaces. Nevertheless, despite the availability of large sum of information on structure, phase and dynamics of lipid membranes, clear depth-dependent static and dynamic properties such as changes in static polarity, solvation dynamics, resonance energy transfer efficiencies etc. at lipid/water interfaces at their molecular length-scale is still unavailable. This part of the thesis will present a comprehensive understanding on how such static polarity can vary at different depths across lipid/water interface based on the lipid bilayer fluidity/rigidity. Such studies have been performed using a series of suitably tailored (synthesized) fluorescent molecules of different hydrophobicity that stay at different depths across the lipid-bilayer interface within few Angstroms apart, acting like *Molecular Rulers*.

Various techniques such as SHG,[37,38,39] SFG,[40-43] EPR,[44,45,46] ESR,[47,48] NMR,[49,50] 3PEPS,[51] X-ray and neutron diffraction,[52,53,54,55] fluorescence spectroscopy[56-58,61-64] have been employed to study the structure, organization, dynamics, heterogeneity, mobility, local polarity of lipid bilayer experimentally. Among them, fluorescence spectroscopy has been evolved as a unique technique for its high sensitivity, which has been widely used to study static and dynamic properties of lipid membranes. On the other hand, molecular dynamics (MD) simulations have contributed immensely to upgrade the knowledge about the complex membrane structure and dynamics as well as the interactions of small molecules, their location and orientation within lipid membrane.[59,60,65-67] Such information is difficult to obtain from only experiments. In fact, elaborate understanding of static and dynamic properties of biomolecules is now possible by directly comparing MD simulation results with fluorescence spectroscopic results, although such studies on lipid membrane are almost non-existent. This part of the thesis will discuss such combination of simulation and experiments to understand the depth-dependent static solvation properties across lipid/water interface of gel- and fluid-phases of lipid bilayers simultaneously.

This chapter will briefly discuss the evolution of study of static and dynamic properties at lipid/water interfaces – so as to compile the existing understanding of the interfaces, especially of lipid bilayer and water. However, before discussing the static and dynamical results, section 9.2 will first provide brief general perspective on lipid/water interface that is found to be important for biological functions. Sections 9.3 and 9.4 will give brief discussion about phase behaviour of lipid membrane and about synthetic lipids, followed by model lipid membranes which are used to mimic biological membrane. Section 9.5 will then discuss the molecular probes that have been used already to study static and dynamics properties of membrane interfaces. Sections 9.6 will be mainly focussed on static and dynamic studies especially at water/lipid interfaces, and section 9.7 is on earlier MD simulation studies on such interfaces.

9.2. Interface: A General Perspective

Interfaces are ubiquitous. The physical and chemical properties of various air/liquid, liquid/liquid, liquid/solid, air/solid interfaces are generally different from that of the bulk media which constitute the interface. Asymmetry of forces that acts on the atoms and molecules of these interfaces gives rise to its distinct characteristics.[68] This asymmetry defines the unique structure, chemical composition, polarity, and transport properties of the interfaces. Various vital elementary processes in nature takes place at these interfaces. For examples; uptake and reactions of pollutants at air/water (at surface of water droplets) and air/solid (on ice particles) interfaces in the atmosphere,[70,71,72] phase transfer catalysis as well as ion-,[69,73,74,75] electron-, proton-transfer reactions at liquid/liquid and liquid/membrane interfaces.[69,76,77] However, despite the scientific and practical significance, chemical and physical understanding of these interface is still very limited,

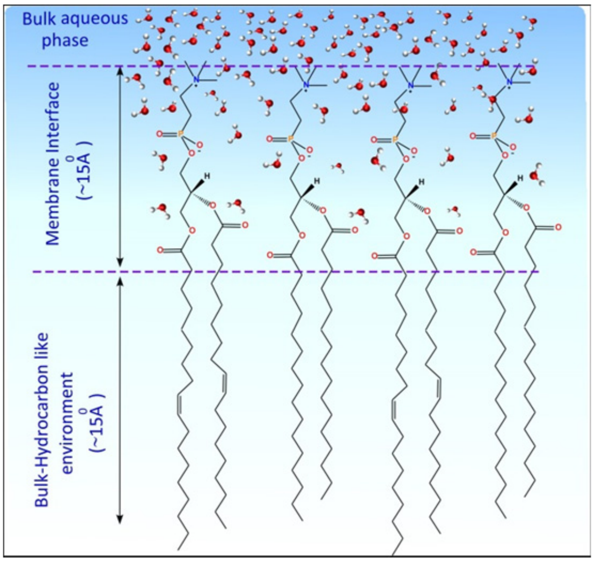

Figure 9.1: Schematic representation of lipid/water interfaces.

because the interface regions are only few angstroms wide which are hard to characterize at their molecular length-scale by conventional experimental methods. Nonetheless, interface selective linear and nonlinear optical spectroscopic techniques such as SHG, SFG and TIRF have been widely used to probe interfacial properties such as polarity, solvent relaxation, pH, solute positions and activities etc.[37,38,40,41,78-80] Nonlinear electronic SHG and SFG techniques have been successfully employed to understand the depth-dependent as well as molecular orientation-dependent polarity at various neutral and charged air/liquid and liquid/liquid interfaces. Vibrational SHG and SFG techniques, on the other hand, have unfolded the unique character of interfacial water at the air/water interface as well as of other interfaces.[81-83] In recent times, phase-sensitive SHG and SFG techniques have also been developed and employed to characterize the absolute orientations of molecules at various interfaces.[41,88-90] However, despite having interface selectivity, these techniques remains expensive and difficult to implement for studying interfaces, especially the buried interfaces which mostly occur in biological membranes. Beside optical techniques, computer simulations have been employed to explore structural and dynamical aspects of lipid bilayers. Due to its accessibility to time and length scale down to atomic level, MD simulations can be utilized to create detailed picture of various interfaces at molecular level, providing insights into relatively slow translation, diffusion and molecular reorientation of water and other molecules at interfaces.[84-87,91,92]

In biology, the most important interface is the lipid/water interface. These interfaces function as barriers between outside environment and the living cells. The basic building blocks of biological interfaces are the phospholipids. These interfaces also contain a large number of proteins, cholesterols and other molecules embedded inside the phospholipid bilayer (membrane). The lipid molecules consist of charged/zwitterionic head-groups and hydrophobic hydrocarbon tails. The hydrophobic effect causes these lipids to form bilayers consisting of two sheets (leaflets) of lipids with their hydrophobic tails facing towards each other and the hydrophilic parts facing outside environment or cytoplasm inside cell. These hydrophilic head-groups form an interface with the aqueous environment on both sides of bilayer. Typically, the hydrophobic core (within a single leaflet) is ~15 Å thick, while the lipid/water interface region extends upto ~15 Å. The lipid/water interface region is defined between an internal plane (the water–hydrocarbon interface) and an external plane (the slipping plane in contact with the bulk aqueous phase) as shown in Figure 9.1. At these interfaces water molecules permeate into the head-group regions of phospholipid bilayer with a steeply decreasing concentration as one proceeds toward the inner hydrophobic region of the bilayer. There is no sharp border between the hydrophobic lipid-core and the hydrophilic water as the interface region provides a zone of gradually changing hydrophobicity, although in many occasion it is defined by the Gibbs dividing surface. However, it is still not known how this hydrophobicity changes gradually at lipid/water interface, which will be presented in this part-II of thesis. The majority of the water molecules reside in the polar head-group region of lipid bilayer through H-bonds to the phosphate groups, along with a smaller fraction bound to the carbonyl groups located deeper in the bilayer. These water molecules play vital role in controlling the interactions and solvation of various biomolecules and small molecules (drugs) at the lipid/water interface.

9.3. Phase Behaviour of Lipid Membrane

The relative mobility of lipid molecules is among the most significant characteristics possessed by lipid bilayers. Depending on hydration, temperature, pressure, and structural features of lipid, including hydrocarbon tails length and composition of head-group, mobility of phospholipids varies. This response due to change in the fluidity of phospholipids is known as phase behaviour of lipid membranes. For phospholipids, the phase formed at low-temperature is a sub-gel L_c phase, which is represented by highly ordered hydrocarbon chains that are tilted relative to the normal of bilayer surface (Figure 9.2).[93] Characteristic temperature results into transition (melting) of bilayer, which acquires several phases depending on how the head-group are interacting. Upon heating, the sub-gel phase is transformed to a lamellar gel phase. Gel phase can adopt L_β (for example in phosphatidylethanolamines) or $L_{\beta'}$ phase (for example in phosphatidylcholines) based on the structural composition of the head-group as shown in Figure 9.2. In these gel phases, the bilayer has access to more number of water molecules which keeps it more hydrated

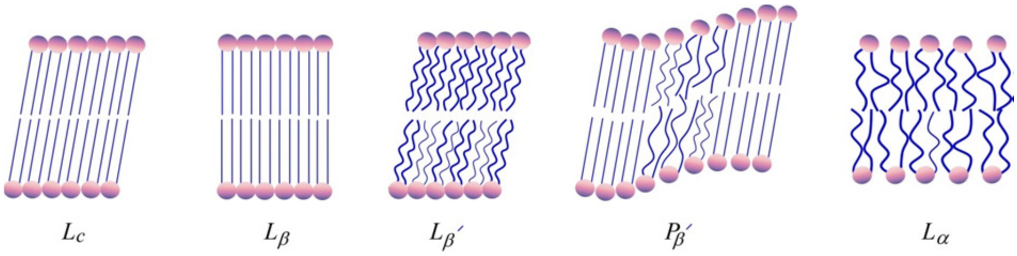

Figure 9.2: Cartoons of various lipid phases. Filled circle represent a hydrophilic headgroup and lines represents hydrophobic tail of lipids.

compared to L_c phase. The hydrocarbon tails exhibits a highly ordered structure, but less than that in L_c phase. Lipid tail in L_β phase stays in highly ordered configuration parallel to normal of lipid bilayer, whereas it is tilted relative to bilayer normal in $L_{\beta'}$ phase (Figure 9.2).

At characteristic temperature, lipid bilayer undergoes transition from gel phase to the L_α phase, known as fluid or liquid crystalline phase, where the hydrocarbon tails of bilayer remains disordered (see Figure 9.2). Physiologically, L_α phase is the most significant phase. Many lipids get transformed from the ordered gel phase to the disordered fluid (liquid crystalline) phase in two steps: The initial step includes transition from the ordered gel phase to a pre-transition state called as rippled phase $P_{\beta'}$, followed by the melting of bilayer from the $P_{\beta'}$ to the disordered L_α phase in the second step. Pre-transition phase (rippled-phase) is characterized by unusual swelling of the membrane and a long-wavelength rippling of the lipid bilayer. The hydrocarbon tails are ordered and tilted with respect to the bilayer normal. The temperature interval between the pre-transition and the main transition decreases with increasing chain length. The rippled phase is only observed in bilayers containing PCs, of which the low-temperature phase is the $L_{\beta'}$. Phosphatidylethanolamines (PEs) and glucolipids, which exhibit L_β phase at low-temperature do not display a pre-transition state.[94] However, bio-membranes are generally composed of lipid mixtures such as phospholipids, glycerolipids, sphingolipids, cholesterol, and minor components like lysolipids, glycolipids and cerebrosides. As a result of selective interactions among cholesterol, sphingolipids and membrane proteins, lipids within one layer can congregate (or laterally phase segregate) to create lipid domains and raft.[9] In bio-membrane or multi-component model membranes ($n > 2$), this selective interactions give rise to microscopically separated fluid membrane phases, such as liquid-ordered (L_o) phase which is supplemented by cholesterol and saturated (sphingo-) lipids in a highly condensed state, and the liquid-disordered (L_d) phase which is enriched by disordered state of unsaturated glycerophospholipid. Thus, the long-established illustration of the membrane using mixture of liquid crystalline (fluid) and gel phases was replaced by a perspective of complex system which is described as the combination of liquid ordered (L_o) and disordered (L_d) phases, containing saturated and unsaturated lipids together with cholesterol.

9.4. Synthetic Lipids

Vesicles formed by lipids, especially phospholipids, are mainly utilized as experimental model to mimic biological membrane. Two types of phospholipids that are mainly used for making liposomes can be classified into natural and synthetic phospholipids. Phosphatidylcholine (PC), also known as lecithin, is the most common natural phospholipid which can be extracted from vegetable (soybean) or animal (hen egg) sources. Other natural phospholipids include phosphatidylserine (PS) and

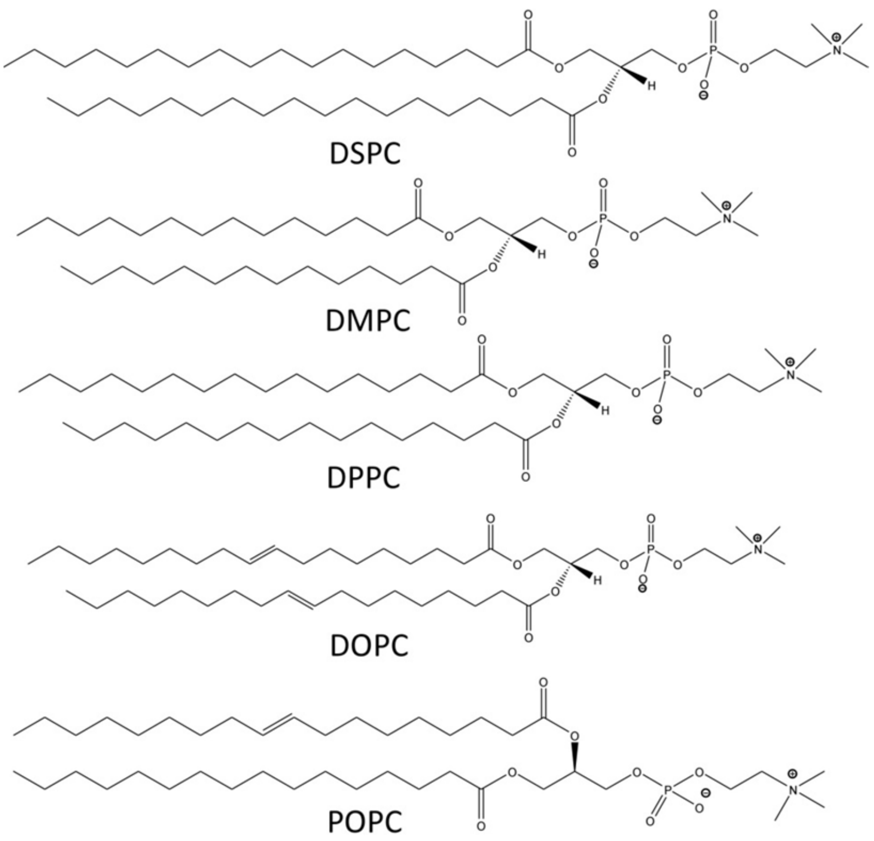

Figure 9.3: Molecular structures of synthetic phospholipids.

phosphatidylethanolamine (PE). However, these natural lipids show differences in acyl chain types depending upon the sources. Moreover, these phospholipids are highly heterogeneous with respect to their fatty acid chains and usually have a high degree of polyunsaturation, which affect the pure liposome formation. Advantage of using synthetic phospholipids lies in fact that composition of fatty acids can be tailored according to specific needs. For example, length of acyl chain and degree of unsaturation can be tailored in synthetic PCs in order to get required bilayer characteristics (i.e. desired gel-transition temperature (T_m), rigidity, etc.), together with low sensitivity to oxidation. Hence, bilayer/vesicle formed by a single synthetic phospholipid can act as ideal membrane-model systems to mimic the characteristics of membrane of interest. Some of the commonly used synthetic phospholipids are 1,2-distearoyl-*sn*-glycero-3-phosphocholine (DSPC), dimyristoyl-phosphatidylcholine (DMPC), 1-palmitoyl-2-oleoyl-2-sn-glycero-3-phosphocholine (POPC), 1,2-dioleoyl-sn-glycero-3-phosphocholine (DOPC), 1,2-dipalmitoyl-sn-glycerol-3-phosphocholine (DPPC), etc. Structural representations of these widely used PCs are given in Figure 9.3. Depending on the nature of phospholipids, the constructed lipid bilayer of liposomal vesicles can exist in various lipid phases such as fluid or gel phase at ambient temperature as described in previous section. Numerous factors such as lipids alkyl hydrocarbon chain length and degree of saturation can tune the phase transition temperatures of synthetic phospholipids. For example, carbon chain length of 1,2-dipalmitoyl-sn-glycerol-3-phosphocholine (DPPC) is C16 with phase transition temperature of 41°C, whereas, carbon chain length of 1,2-dioleoyl-sn-glycero-3-phosphocholine (DOPC) is C18 and has a phase transition temperature of -17°C. Thus, at room temperature, DOPC and DPPC form fluid- and gel-phase, respectively. The next chapter sheds light on the depth-dependent static properties at lipid/water interface in vesicles prepared at room temperature with these DOPC and DPPC lipids in their fluid- and gel-phase, respectively, and explored using experimental and simulation methods.

9.4.1. Artificial Model System for Cell Membrane

Naturally occurring lipids possess diverse molecular structure and complex composition. Thus, simplified model systems of biological membranes are useful for investigating the properties and roles of individual components of the membrane in biological functions. Supported lipid bilayer, lipid monolayer and liposomes have been the most widely used model membrane systems for the characterization of a biological membrane. Brief discussion on compositions and structure of these systems are provided below for completeness.

9.4.1.1. Supported Lipid Bilayers

Supported lipid bilayers (SLBs) are bilayer structures sitting on smooth solid surfaces like mica or silicon. SLBs can be formed by various means that generally includes fusion of lipid vesicles onto smooth solid supports or can be formed by techniques such as Langmuir-Blodgett (LB) or by a combination of the LB with Langmuir-Schaeffer (LS) techniques.[95-98] Variation in morphology, structure and surface chemistry of SLBs as well as their interactions with drugs and drug delivery systems have been explored using various techniques, such as scanning electron microscopy, X-ray scattering, transmission electron microscopy, Fourier transform infrared resonance (FTIR), atomic force microscopy (AFM), and X-ray photoelectron spectroscopy. All these studies have provided vital information about the molecular interactions at lipid bilayers.[99,100]

9.4.1.2. Lipid Monolayers

Langmuir film balance is used widely to form lipid monolayers at the air/water interface. Biological conditions for these lipid monolayers are imitated by choosing various parameters such as temperature, sub-phase and lipid composition.[101,102] Moreover, lipid monolayers are homogeneous, stable and very well-defined two-dimensional systems with planar geometry. Thus, the interactions of lipids with drugs and drug delivery systems can be explored using lipid monolayers by monitoring the changes in surface pressure in presence and absence of the additives. However, apart from measuring surface pressure, morphological changes in lipids at the air-water interface can also be studied through Brewster angle microscopy,[103] which allows *in situ* study of the two-dimensional Langmuir monolayers at the air/water interface.

9.4.1.3. Liposomes

It has already been discussed that phospholipids are the basic elementary unit of cellular membranes. Amphiphilicity is the key feature that assigns the driving force to lipid molecules as soon as it comes in contact with water, to self-assemble into monolayer and bilayer, with its hydrophilic head-group being hydrated with the interfacial water molecules. When lipids are (with appropriate packing parameter for vesicle formation) dissolved in water, they organize themselves in order to form closed spherical structures known as lipid vesicles or liposomes.[104] The interior and exterior part of these spherical structures are made up of water molecules, and lipid bilayer marks the boundary that separates the inner and outer aqueous phases. In the case of only one lipid bilayer encapsulating the aqueous core, the vesicles are classified into small, large and giant unilamellar vesicles (SUVs, LUVs or GUVs, respectively), while in the case of many concentric bilayers one defines the liposomes as large multilamellar vesicles (MLVs) having onion-like structure. The classifications of liposomes based on size and number of membrane (lamellarity) are summarized in Table 9.1.

Because of the underlying similarity with the cell membrane, vesicles have been used extensively to model lipid membrane – so as to understand various physical properties of these membranes. Vesicles represent natural environment as compared to supported bilayers and monolayers as they do not have any solid surface or other interface to induce

Table 9.1: Classification of vesicle based on size and lamellarity.

Vesicle Type (Abbreviation)	Diameter	No. of Lipid Bilayer
Small Unilamellar Vesicle (SUV)	20-100 nm	One
Large Unilamellar Vesicle (LUV)	> 100 nm	One
Giant Unilamellar Vesicle (GUV)	> 1 μm	One
Oligolamellar Vesicle (OLV)	0.1 - 1 μm	5 (approx.)
Multilamellar Vesicle (MLV)	> 0.5 μm	5 - 25
Multivesicular Vesicle (MV)	> 1 μm	Multi compartmental structure

perturbation. These lipid vesicles are extensively used to study topology, shape fluctuations, phase behaviour, permeability, fission and fusion of membranes. Moreover, vesicles can be formed with varying sizes, thus, give an advantage to choose membrane model which can resemble biologically relevant features. This thesis reports results obtained with SUVs of DOPC and DPPC as a model membrane systems.

9.5. Molecular Probes for Studying Lipid Membrane

Probing the structure, dynamics, phase, hydration, conformation and function of lipid membranes remains an experimental challenge due to highly organized complex nature of membranes. Many experimental methods such as NMR, ESR, EPR, SFG and fluorescence techniques have been employed to scan these properties of lipid membranes.[37-50,56-58] Among them, fluorescence methods have been quite promising primarily due to the fact that the properties such as quantum yield, spectral position, lifetime, etc. of many chromophores are sensitive and responsive to their immediate surrounding environment. Moreover, the ultimate sensitivity of fluorescence spectroscopy can eventually reach down to single molecule level. Furthermore, ample information can be extracted from these fluorescence techniques when the chromophores are specifically positioned at a defined site of interest within the lipid membrane. Lipid molecules do not have intrinsic fluorescence properties, thus incorporation of fluorescent probes at different location inside lipid membranes are needed – so as to acquire knowledge concerning the site specific properties of these membranes. These membrane probes can be broadly classified into four main groups based on their structural and functional properties as: lipid probe-derivatives, molecular rotor, lipophilic probes and solvatochromic probes. Brief descriptions of these probes are given below.

9.5.1. Lipid Probe-Derivatives

Most common approach to obtain a fluorescent membrane probe is to label a lipid (either cholesterol or phospholipid) with a fluorescent moiety.[105] Membrane probes of this class are known as fluorescently label lipid or lipid probe-derivative. Phospholipids are most versatile molecules that are used as fluorescent membrane probes as they can be labelled at different sites including acyl chain or at the polar head group. Labelling at the polar head group is generally done for phosphatidyl ethanolamine (PE). Some of such fluorescently label lipid probe-derivatives are shown in Figure 9.4.

9.5.2. Molecular Rotor

The molecular rotors belong to the group of membrane fluorophores that show large variation in their fluorescence quantum yield depending on their intramolecular rotation

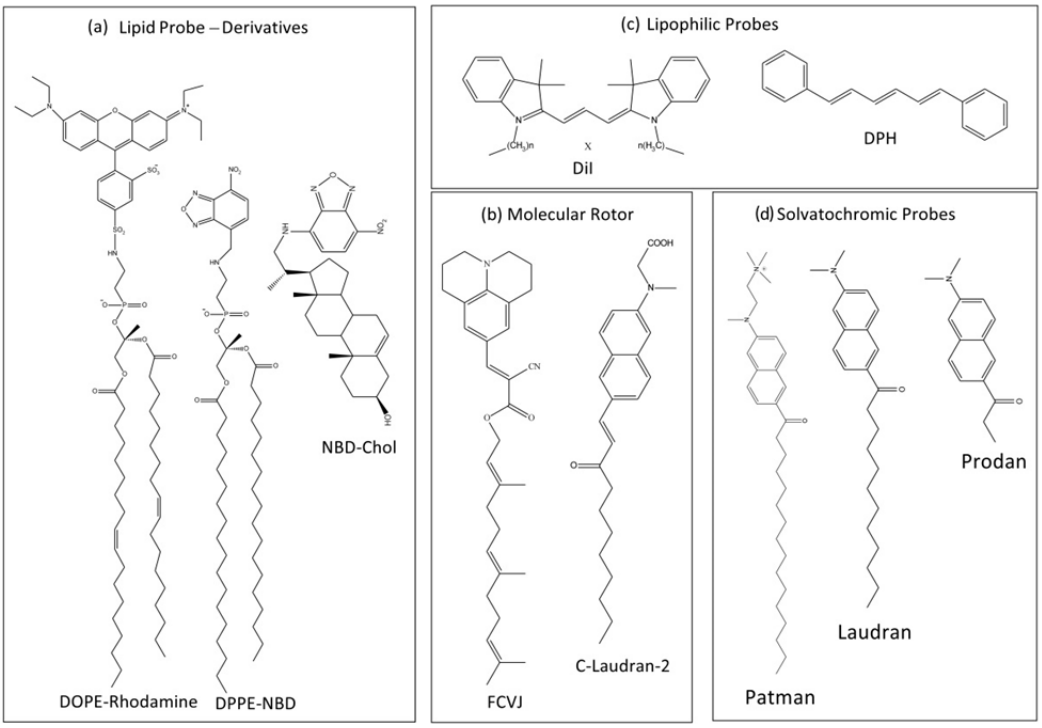

Figure 9.4: Molecular Probes for membrane studies.

(typically at C=C) based on the viscosity of the local environment.[106] In viscous media these intramolecular rotation get slowed down which is directly reflected in their increased fluorescence quantum yield. Molecular rotors being incorporated into lipid membranes monitor the local micro-viscosity within membrane. FCVJ and c-Laudran-2 are typical examples of these probes which are represented in Figure 9.4.

9.5.3. Lipophilic Probes

Dyes with sufficiently high lipophilic properties can be used as an alternative to fluorescently labelled lipids, as they can stay at different positions within lipid membrane. These membrane probes are classified as lipophilic probes which have two different classes: polycyclic aromatic hydrocarbons (PAH dyes) and dyes bearing long-chain hydrocarbons (LCH dyes). Alkylated cyanine and rhodamine dyes are typical representatives of the LCH dyes. Cyanine dyes, such as DiI and DiO bear two hydrocarbon chains along with a net positive charge, so as to structurally match with lipid molecules. Some of these amphiphilic probes are shown in Figure 9.4.

9.5.4. Solvatochromic Probes

Solvatochromic probes are the most established environment sensitive probes for studying the local solvation properties of various physicochemical and biological systems. These solvatochromic probes show strong alteration in their dipole moments upon optical excitation to higher excited states. The dipole-dipole and specific (H-bonding) interactions of these probes with the dipolar/charged molecules of its surrounding alter the interaction energy of probes, thus changing their electronic transitions, which results into shifting of their absorption and emission spectra depending on local solvation and specific interactions. Such properties, in combination with time-resolved fluorescence techniques, can also be used to explore the local solvation dynamics of complex molecular systems.

Several such probes have been used to study the static and dynamic solvation properties in lipid membrane, which include Laurdan, Prodan, Patman, coumarin, NBD, etc. (Figure 9.4). However, the static and dynamic properties of lipid/water interfaces explored in chapter 10 has been probed by solvatochromic fluorescent molecules which are synthesized by attaching alkyl chains of different lengths to a (polar) solvatochromic 4-aminophthalimide (4-AP) moiety – so as to create a homologous series of 4AP-C*n* molecules with systematically varying hydrophobicity that can stay at different depths across the lipid/water interface. Such probes act similar as solvatochromic fluorescent *molecular rulers*. The 4-AP molecule is widely used as solvatochromic molecule to study local solvation and its dynamics in many biomolecular and physicochemical systems. However, this molecule has never been used for studying the solvatochromic properties of water/lipid interfaces. The discussion in chapter 10 will show that these synthesized probes are far superior to most of existing solvatochromic fluorescent and ESR probes, which can be used to study solvation properties of lipid/water interfaces of different lipid phases simultaneously.

9.6. Static and Dynamic Properties of Lipid Membrane

Membranes are complex, two-dimensional anisotropic assemblies of lipids and protein, which play vital role in many cellular functions.[27,107-109] Water, apart from lipids and proteins forms one of the most critical constituents of membrane. Various static and dynamic properties of membrane are determined by water molecules which play significant role in the interactions of membrane with other components in its surrounding, thereby fine-tuning abundance of cellular processes during cell cycle. Water in the close proximity of membrane interfaces shows varying properties based on their site across the membrane/water interface, thus defining the depth-dependent static and dynamic properties of lipid membranes.[27-32,35,36] In fact, it has been found that distribution of water molecules from bulk toward lipid hydrophobic core does not decrease in a continuous manner. Instead, the dynamic properties of water molecules above ~4 nm of lipid-surface resemble to that of bulk water, and number of water molecules around lipid head group and near the boundary of acyl chain region decreases by 2-3 and 6-7 fold, respectively,[110] which eventually give rise to depth-dependent variation in static and dynamic solvation and molecular properties at the lipid/water interfaces. Diffusive motion of water molecules changes drastically depending on such depth inside lipid bilayer. It has been found that the water molecules show sublinear diffusion near lipid membranes instead of normal diffusion like in bulk.[117] Depending upon distribution site of water molecules near membranes, water molecules can be categorized as, bulk type water, near-interfacial water, water strongly bound to head-groups of lipids, and buried water molecules which penetrate deep inside the hydrophobic acyl chain.[111-114] Such classification of water molecules was made based on the degree of their mobility, which was determined through several experimental techniques such as ESR, NMR, ESR, IR methods, incoherent neutron scattering and electrical conductivity measurements or calculated via MD simulations.[111,113-114,115,116,147] It has been shown through NMR data that the mobility of water molecules strongly bound to the membrane is 100 folds slower than that of bulk water.[116,118]

While understanding the static and dynamic solvation at lipid/water interface is essential to illustrate the local dielectric properties of lipid interfaces, acquiring knowledge about the molecular interactions at lipid/water interfaces is vital to explain the significant biological processes. Hence, details of biophysical processes occurring at membrane surface can be elucidated by deeper understanding of how static and dynamic properties such as solvation, pH, rigidity, molecular interactions etc. changes at different depths of molecular length-scale at the lipid/water interfaces formed by different lipid molecules and lipid phases.

9.6.1. Polarity of Lipid/Water Interface

Molecular recognition plays a critical role in sustaining life on earth. Thus, molecular interactions at and with membrane interfaces are of paramount significance. The differential partitioning of water molecules into the hydrophilic polar head-group region and hydrophobic carbon tail of lipid membrane leads to drastic variation in hydration and polarity profiles across the lipid/water interface. Physicochemical characteristics of the lipid bilayer are defined by two fundamental factors: polarity and hydration. These two parameters are strongly correlated, which exhibit gradient across the water/lipid interface. In general, the hydrophobic region of bilayer shows very low polarity and hydration, and are high at the bilayer/water interface region.[119] The heterogeneity in hydration is evidenced by the MD simulation studies which revealed a complex distribution and polarization of water molecules along the normal to the membrane surface, and pronounced water penetration into the hydrophobic–hydrophilic boundary of the bilayer, defining the complex polarity profile across lipid/water interface.[65] These effects are thus responsible for the formation of distinct gradients of electric fields such as dipole and surface potentials across lipid membrane.[120,121] Various biological processes within and across lipid membranes such as ion conductance, membrane transport, insertion and translocation of proteins and other molecules are governed by hydration, polarity and electric potential gradient across the interfaces.[122,123] Hence, illustration of such properties at precise depths of lipid/water interface is particularly important for understanding the membrane functions. In fact, studies in this part of thesis will show the existence of distinct polarity profiles of lipid/water interfaces, formed by different phases of lipid bilayer.

Classically, Onsager function of dielectric constant (ε) is used to approximate polarity.[124,125] It is based on the relative mobility of polar groups and polar molecules at the bilayer interface.[48,126,127] Several methods such as ESR, fluorescence, IR spectroscopy, X-ray, neutron diffraction and NMR have been employed to determine the hydration and polarity, inside the membrane.[49,51,128-130] Among them, fluorescence spectroscopy stands out to be the most popular technique to measure the polarity using solvatochromic fluorescent probes from their spectral shifts, calculated through various polarity scaling such as $E_T(30)$, Δf, etc.

CW-ESR and pulsed ESR spectroscopy were used to monitor the complete depth-dependent polarity profile of hydrocarbon region of lipid membrane using spin-labelled fatty acids (doxyl-stearates) or spin-labelled phospholipids having nitroxide moiety linked to different sites along the alkyl chains.[48,131,132] Marsh studied polarity and permeation profile in lipid of spin-labelled phospholipids with the nitroxide moiety attached at 12 different carbon positions of one of the alkyl chains, using EPR spectroscopy.[44,45] It has been found that the isotropic hyperfine splitting constant (a_0^N) depends on the position of spin label along the alkyl chain. Polarity profiles were characterized based on the spin-label measurements of membranes formed by different lipid molecules and it was found that the polarity profile shows sigmoidal pattern. Thus, the polarity profile across the whole hydrophobic region of the bilayer was found to be trapezoidal in shape.[44,45] Similar shape was also observed in ESR measurements using frozen samples by Hyde and co-workers.[48] Several groups have also shown that membrane like microsome, myelin and chromaffin granule membranes, exhibits similar trapezoidal shape of the polarity profile in accordance with the model membranes.[46] However, it should be noted that all these studies have determined the polarity profile of alkyl chain region of the lipid bilayers, and not of the lipid/water interface region.

Several attempts have been made to develop methods for measuring water penetration into the membranes based on fluorescence.[126,133] Chattopadhyay and co-workers measured the red edge excitation shift (REES) of the fluorescent probe, 7-nitrobenz-2-oxa-1,3-diazol-4-yl (NBD), which was localized near the membrane/water interface when bound at the head-group of phosphatidylethanolamine (NBD-PE), whereas, the probe resides deeper inside the membrane when bound to cholesterol (NBD-cholesterol).[133] It was shown that NBD-PE exhibited much stronger REES relative to the NBD-cholesterol, indicating the effect of water interaction with NBD at the membrane/water interface. In the gel phase, no such significant change in REES of the NBD-PE was observed compared to that in fluid phase, while NBD-cholesterol in gel phase did not show REES effect at all. This observation was attributed to the more compact arrangement of the fatty acid chains in the gel phase and the absence of water deeper inside the membrane.

Recent attempts by Klymchenko and co-workers based on the introduction of the 3-hydroxyflavone derivatives (F2N8 and F4N1 probes) anchored to lipid bilayer at relatively well determined depths were presented, where F4N1 probe is located deeper in the membrane than F2N8.[126] They were able to probe both polarity and hydration inside bilayer membrane by estimating the two-band fluorescence spectra of the H-bonded and H-free forms, while the relative contributions of these two forms determined the local hydration. However, the absolute values obtained from these two probes could not be compared due to different interactions of probes with environment. These results are in line with the ESR data, indicating that the hydration contributes strongly to the bilayer polarity. Klymchenko and co-workers also explored hydration and fluidity at the interface of liquid-ordered and gel phase lipid bilayer with same hydration probe (3-hydroxyflavone derivatives) and fluidity probe (diphenylhexatriene derivative). [126]

Fluorescent lipid probes such as anthroyl fatty acids and LAURDAN have also been used to probe local polarity inside membrane.[134] On the other hand, Hemminga and co-workers used AEDANS [N-(iodoacetylaminoethyl)-5-napthylamine- 1-sulphonic acid]-labelled cysteine mutants of M13 major coat protein, incorporated in lipid bilayers, to determine transmembrane polarity with considerable success.[135] More recently, Carney *et al.* have also used fluorescence maxima of site-specific tryptophan mutants to determine the polarity of transmembrane segments of the mechano-sensitive ion channel, MscL.[136]

From all these above studies it is clear that different groups have developed different methods to measure environment polarity in membranes. However, the complete polarity profiling at molecular length scale, especially across the lipid/water interfaces, is yet to be pictured. This provides the main motivation to explore the depth-dependent polarity and hydration at lipid/water interfaces of lipids in different phases.

9.7. Molecular Dynamics Simulation in Lipid Membrane

The inherent complex nature of lipid membranes remains the primary cause for difficulties in developing simple models for membranes that can be used to visualize these systems *in silico* and interpret the experimental results. With improved approximations, parameterization and continuous development of models for lipid membranes, computer simulation methods such as molecular dynamics and Monte Carlo simulations have been employed to understand the structural, dynamical and hydration properties of these systems.[29,137,138] In fact, a large amount of critical information about the structure and dynamics of lipid membranes at molecular level have been emerged from simulation studies, although compared to proteins, lipid membranes are less explored.

In 1988, Egberts and Berendsen performed the first molecular simulation on bilayer, which contained a mixture of fatty acids and ternary alcohol solvated with water molecules.[139] Full atomistic molecular simulations of solvated phospholipid bilayers were conducted in the early nineties. Experimental studies on osmotic stress demonstrated the significance of interfacial water molecules in the proximity of membranes as well as the hydration force that governs the membrane and its interfaces.[140] The extent of these hydration forces are extended to a region between ~0.4 and ~0.9 nm, when the lipid membrane squeezes only 2 – 3 layers of interfacial water molecules. Simulation studies by Essmann *et al.*[141] showed well agreement of hydration forces with the conclusions of McIntosh and Simon.

Berkowitz and co-workers performed MD simulations to determine density of water at the interface of membrane/water. It was found that, proper equilibration of water density shows existence of oscillations and layering of water molecules around membrane interface.[114] They concluded the existence of intrinsic water layer that can incorporate into the head-group region. In fact, presence of water layers around phospholipid bilayers were also reported in experimental findings.[142] Pasenkiewitz-Gierula *et al.* have performed simulation studies in order to explore the hydrogen bonding networks of water molecules in the vicinity of DMPC bilayer.[143] Because these simulations were performed with limited statistics, Lopez *et al.*[29] re-examined the water network around DMPC bilayer. They observed that hydrogen bonding probability of ester oxygen atoms is lower than that of carbonyl oxygen atoms of lipid bilayer. They also found that phosphate group of lipid bilayers have large access to water molecules, as a result oxygen atoms of water get strongly engaged in hydrogen bond formation. The oxygen atom which is double bonded to the phosphorous atom shows highest probability (74%) for hydrogen bonding, while the oxygen atom single bonded to phosphorous atom shows a lower probability of 18 - 27%. It was also observed that lipid molecules employ hydrogen bonding bridges which provide structural strengthening to membrane/water interface. In general, they inferred that the structure, stability and dynamics of lipid/water interfaces are determined by the combination of several factors that include hydrogen bonded bridges and charge-pair interactions. They further reported on the translational diffusion motion of water molecules distributed next to the lipid surface and found it to be slower than the bulk water. For example, the water molecules associated with the oxygen atoms of head-groups show diffusion coefficient of ~2.0×10^{-7} cm^2/s, while the water molecules in the bulk exhibit faster diffusion coefficient by 2 orders of magnitude (~4×10^{-5} cm^2/s). Moreover, many MD simulation studies have shown reduced lateral diffusion coefficient for water molecules residing around the lipid/water interface. More recent simulation studies have confirmed slow translational dynamics of water molecules at the interface of DPPC bilayer.[144] Further, this simulation shows that motion of water molecules is not simply diffusive, rather it exhibits a ballistic feature at short time scales (within 40 fs), whereas, the interfacial water molecules shows sub-diffusive character at longer time scales within 5 ps.[144]

Simulation studies performed by Bhide and Berkowitz show that the water molecules trapped in the pockets created by polar head-groups of lipid bilayer resulted into a long-time component due to its reorientional relaxation which gets slowed down by a factor of ~100 compared to bulk water.[145] When the simulations were performed with frozen lipid groups, the relaxation of water molecules slowed down by a factor ~30-40 due to coupling between motion (slow) of the headgroups and motion of water molecules.[144] They further observed that most of the water molecules interchange quickly between various regions of interface showing few times larger orientational relaxation time, compared to bulk. Earlier, it was believed that orientational relaxation of water molecules occurs through rotational diffusion, but recent studies by Laage and Hynes have shown that such relaxation of water molecules takes place through the molecular jump mechanism (MJM), where water jumps to switch hydrogen bonding partners.[146] Berkowitz and co-workers, through simulation studies have shown that MJM is also applicable to the orientational motion of water molecules at the interface of lipids.[147] They reported that, with decrease in lipid hydration the decay time of the orientational correlation function increases, similar to that observed by Zhao *et al*. in the nonlinear ultrafast spectroscopic experiment.[116] Thus, MD simulation has successfully been used to study dynamics of interfacial water. Many more MD simulations have been performed to elucidate multicomponent bilayer system even in presence of cholesterol (detail literature survey of such studies has not been included here).

Most recently, Ladokhin and co-workers have extracted quantitative information on membrane penetration by combination MD simulation and depth-dependent fluorescence quenching experiments.[148] Use of fluorescence probes in membrane biophysics is widespread due to its sensitivity and versatility. Proper interpretation of data obtained from fluorescence techniques requires precise knowledge about the location, orientation, dynamics and stability of probe in lipid membrane. Thus, in cases, behaviour of these probes incorporated in the bilayer is often poorly understood. Not only that, it is still unknown how the number of hydration water varies around probes placed at different depths across the lipid/water interface as well as how the orientation of probe molecules controls the exposure of these probes to water molecules. Molecular dynamics simulations present a convenient way to address such issues, which have been used in chapter 10 to explore intricate details of probe hydration at lipid/water interfaces, complementing the experimental observations.

9.8. Conclusion

It is now well-established that the static and dynamic properties of lipid bilayer and its interfaces control structure and functions of lipid membranes. However, the endeavour to arrive on a unified picture of the depth-dependent static and dynamic properties and molecular interactions at lipid/water interfaces is still in its nascent state. Nonetheless, this endeavour has triggered numerous experimental and simulations studies on membrane and their interfaces that have unravelled knowledge regarding the complexity of the structure and dynamics in these systems. However, questions remain – how the lipid bilayers interact among themselves and with other small molecules (drug or anesthesia)? How these interactions depend on the interfacial properties of bilayer and structure of drug? How such interactions depend on lipid phases – gel, fluid and other phases? It is obvious from above discussion that explanation of how the static and dynamic properties of membrane interfaces differ at different depths of molecular length-scale as well as their implications in drug-membrane interactions, membrane-protein and membrane-membrane fusion has not been obtained properly. The primary objective of the work presented in chapter 10 is to study the molecular interactions of lipid bilayer with small molecules of different hydrophobicity, and quantify the local dielectric environments at different depths across lipid/water interface that differs in sub-nanometre scale. The next chapter will indeed show some unusual static solvation properties at lipid/water interfaces, which are characterized by a series of newly synthesized fluorescent molecules, which were never been used in context of lipid membrane studies, that act as *Molecular Rulers* to scan the interface in sub-nanometre (relative) scale.

Reference

1. Hulbert, A. J. Life, Death and Membrane Bilayers. *J. Exp. Biol.* **2003,** *206*, 2303-2311.
2. Stillwell, W. *An Introduction to Biological Membranes*. Elsevier: San Diego, CA, USA, **2013**.
3. Gorter, E.; Grendel, F. On Bimolecular Layers of Lipoids on the Chromocytes of the Blood. *J. Exp. Med.* **1925**, *41*, 439-443.
4. Davson, H. A.; Danielli, J. F. A Contribution to the Theory of Permeability of Thin Films. *J. Cell. Comp. Physiol.* **1935**, *5* 495-508.
5. Robertson, J. D. New Observations on the Ultrastructure of the Membranes of Frog Peripheral Nerve Fibers. *J. Cell. Biol.* **1957,** *3,* 1043-1048.
6. Robertson, J. D. Granulo-Fibrillar and Globular Substructure in Unit Membranes. *Ann. N. Y. Acad. Sci.* **1966**, *137*, 421-440.
7. Singer, S. J.; Nicolson, G. L. The Fluid Mosaic Model of the Structure of Cell Membranes. *Science* **1972**, *175*, 720-731.
8. *Simons, K.; Ikonen, E.* Functional Rafts in Cell Membrane. *Nature* **1997**, *387*, 569-572.
9. Van Meer, G.; Voelker, D. R.; Feigenson, G. W. Membrane Lipids: Where They Are and How They Behave. *Nat. Rev. Mol. Cell. Biol.* **2008**, *9*, 112-124.
10. Sampaio, J. L.; Gerl, M. J.; Klose, C.; Ejsing, C. S.; Beug, H. Simons, K.; Shevchenko, A. Membrane Lipidome of an Epithelial Cell Line. *Proc. Natl. Acad. Sci. U.S.A.* **2011**, *108*, 1903-1907.
11. Klose, C.; Surma, M. A.; Simons, K. Organellar Lipidomics--Background and Perspectives. *Curr. Opin. Cell. Biol.* **2013**, *25*, 406-413.
12. Engelman, D. M. Membranes are More Mosaic than Fluid. *Nature* **2005**, *438*, 578-580.
13. Lingwood, D.; Simons, K. Lipid Rafts as a Membrane-Organizing Principle. *Science* **2010**, *327*, 46-50.
14. Baumgart, T.; Hammond, A. T.; Sengupta, P.; Hess, S. T.; Holowka, D. A.; Baird, B. A.; Webb, W. W. Large-Scale Fluid/Fluid Phase Separation of Proteins and Lipids in Giant Plasma Membrane Vesicles. *Proc. Natl. Acad. Sci. U.S.A.* **2007**, *104*, 3165-3170.
15. Kaiser, H. J.; Lingwood, D.; Levental, I.; Sampaio, J. L.; Kalvodova, L.; Rajendran, L.; Simons, K. Order of Lipid Phases in Model and Plasma Membranes. *Proc. Natl. Acad. Sci. U.S.A.* **2009**, *106*, 16645-16650.
16. Van Meer, G. Cellular Lipidomics. *EMBO J.* **2005**, *24*, 3159-3165.

17. Holthuis, J. C. M.; Menon, A. K. Lipid Landscapes and Pipelines in Membrane Homeostasis. *Nature* **2014**, *510*, 48-57.
18. Shinitzky, M. *Physiology of Membrane Fluidity*. CRC Press; Boca Raton, FL, **1984**.
19. Luby-Phelps, K. Cytoarchitecture and Physical Properties of Cytoplasm: Volume, Viscosity, Diffusion, Intracellular Surface Area. *Int. Rev. Cytol.* **2000**, *192*, 189-221.
20. Luneva, O. G.; Brazhe, N. A.; Maksimova, N. V.; Rodnenkov, O. V.; Parsina, E. Y.; Bryzgalova, N. Y.; Maksimov, G. V.; Rubin, A. B.; Orlov, S. N.; Chazov, E. I. Ion Transport, Membrane Fluidity and Haemoglobin Conformation in Erythrocyte from Patients with Cardiovascular Diseases: Role of Augmented Plasma Cholesterol. *Pathophysiology* **2007,** *14*, 41-46.
21. Goodwin, J. S.; Drake, K. R.; Remment, C. L.; Kenworthy, A. K. Ras Diffusion is Sensitive to Plasma Membrane Viscosity. *Biophys. J.* **2005**, *89*, 1398-1410.
22. Dibner, M. D.; Ireland, K. A.; Koerner, L. A.; Dexter, D. L. Polar Solvent-Induced Changes in Membrane Lipid Lateral Diffusion in Human Colon Cancer Cells. *Cancer Res.* **1985**, *45*, 4998-5003.
23. Hou, X.; Richardson, S. J.; Aguilar, M. I.; Small, D. H. Binding of Amyloidogenic Transthyretinto the Plasma Membrane Alters Membrane Fluidity and Induces Neurotoxicity. *Biochemistry* **2005**, *44*, 11618-11627.
24. Ahn, J. H.; Kim, T. Y.; Kim, Y. J.; Han, M. W.; Yoon, T. H.; Chung, J. W. Lipo-Prostaglandin E1 in Combination with Steroid Therapy is Effective for Treatment of Sudden Sensorineural Hearing Loss in Korean Patients with Type 2 Diabetes. *Diabetic Med.* **2006**, *23*, 1339-1343.
25. Kearney-Schwartz, A.; Virion, J. M.; Stoltz, J. F.; Drouin, P.; Zannad, F. Haemorheological Disturbances in Hypertensive type 2 Diabetic Patients--Influence of Antihypertensive Therapy. *Fundam. Clin. Pharmacol.* **2007**, *21*, 387–396.
26. Bosman, G. J. C. G. M.; Bartholomeus, I. G. P.; de Grip, W. J. Alzheimer's Disease and Cellular Aging: Membrane-Related Events as Clues to Primary Mechanisms. *Gerontology.* **1991**, *37*, 95–112.
27. Disalvo, E. A.; Lairion, F.; Martini, F.; Tymczyszyn, E.; Frias, M.; Almaleck, H.; Gordillo, G. J. Structural and Functional Properties of Hydration and Confined Water in Membrane Interfaces. *Biochim. Biophys. Acta* **2008**, *1778*, 2655-2670.
28. Haldar, S.; Chaudhuri, A.; Chattopadhyay, A. Organization and Dynamics of Membrane Probes and Proteins Utilizing the Red Edge Excitation Shift. *J. Phys. Chem. B* **2011**, *115*, 5693-5706.
29. Lopez, C. F.; Nielsen, S. O.; Klein, M. L.; Moore, P. B. Hydrogen Bonding Structure and Dynamics of Water at the Dimyristoylphosphatidylcholine Lipid Bilayer Surface from a Molecular Dynamics Simulation. *J. Phys. Chem.* B **2004**, *108*, 6603-6610.
30. Filipe, H. A. L.; Moreno, M. J.; Loura, L. M. S. Interaction of 7-Nitrobenz-2-oxa-1,3-diazol-4-yl-Labeled Fatty Amines with 1-Palmitoyl, 2-Oleoyl-sn-glycero-3-phosphocholine Bilayers: A Molecular Dynamics Study. *J. Phys. Chem. B*. **2011**, *115*, 10109-10119.
31. Jämbeck, J. P. M.; Lyubartsev, A. P. Derivation and Systematic Validation of a Refined All-Atom Force Field for Phosphatidylcholine Lipids. *J. Phys. Chem. B* **2012**, *116*, 3164-3179.
32. Kraszewska, J. B.; Kraszewski, S.; Ramseyer, C. Will C-Laurdan Dethrone Laurdan in Fluorescent Solvent Relaxation Techniques for Lipid Membrane Studies? *Langmuir* **2013**, *29*, 1174-1182.
33. Revathi, C. J.; Chattopadhyay, A.; Srinivas, U. K. Change in Membrane Organization Induced by Heat Shock. *Biochem. Mol. Biol. Int.* **1994**, *32*, 941-950.
34. Singh, P.; Tarafdar, P. K.; Swamy, M. J.; Chattopadhyay, A. Organization and Dynamics of Hippocampal Membranes in a Depth-Dependent Manner: An Electron Spin Resonance Study. *J. Phys. Chem. B* **2012**, *116*, 2999-3006.
35. Cladera, J.; O'Shea, P. Intramembrane Molecular Dipoles Affect the Membrane Insertion and Folding of a Model Amphiphilic Peptide. *Biophys. J.* **1998**, *74*, 2434-2442.
36. Voglino, L.; McIntosh, T. J.; Simon, S. A. Modulation of the Binding of Signal Peptides to Lipid Bilayers by Dipoles Near the Hydrocarbon-Water Interface. *Biochemistry* **1998**, *37*, 12241-12252.
37. Salafsky, J. S.; Eisenthal, K. B. Second Harmonic Spectroscopy: Detection and Orientation of Molecules at a Biomembrane Interface. *Chem. Phys. Lett.* **2000**, *319*, 435-439.

38. Yan, E. C. Y.; Eisenthal, K. B. Effect of Cholesterol on Molecular Transport of Organic Cations across Liposome Bilayers Probed by Second Harmonic Generation. *Biophys. J.* **2000**, *79*, 898-903.
39. Nguyen, T. T.; Sly, C. L.; Conboy, J. C. Comparison of the Energetics of Avidin, Streptavidin, NeutrAvidin, and Anti-biotin Antibody Binding to Biotinylated Lipid Bilayer Examined by Second-Harmonic Generation. *Anal. Chem.* **2012**, *84*, 201-208.
40. Chen, X.; Hua, W.; Huang, Z.; Allen, H. C. Interfacial Water Structure Associated with Phospholipid Membranes Studied by Phase-Sensitive Vibrational Sum Frequency Generation Spectroscopy. *J. Am. Chem. Soc.* 2010, 132, 11336-11342.
41. Mondal, J.; Nihonyanagi, S.; Yamaguchi, S.; Tahara, T. Three Distinct Water Structures at a Zwitterionic Lipid/Water Interface Revealed by Heterodyne-Detected Vibrational Sum Frequency Generation. *J. Am. Chem. Soc.* **2012**, *134*, 7842-7850.
42. Walker, R. A.; Conboy, J. C.; Richmond, G. L. Molecular structure and ordering of phospholipids at a liquid-liquid interface. *Langmuir*, **1997**, *13*, 3070-3073.
43. Smith, K. A.; Conboy, J. C. A Simplified Sum-Frequency Vibrational Imaging Setup Used for Imaging Lipid Bilayer Arrays. *Anal. Chem.* **2012**, *84*, 8122-8126.
44. Marsh, D. Polarity and Permeation Profiles in Lipid Membranes. *Proc. Natl. Acad. Sci. U.S.A.* **2001**, *98*, 7777-7782.
45. Marsh, D.; Kurad, V. A. High-Field Electron Spin Resonance of Spin Labels in Membranes. *Chem. Phys. Lipids* **2002**, *116*, 93-114.
46. Griffith, O. H.; Dehlinger, P. J.; Van, S. P. J. Shape of the Hydrophobic Barrier of Phospholipid Bilayers (Evidence for Eater Penetration in Biological Membranes). *Membrane Biol.* **1974**, *15*, 159-192.
47. Borbat, P.; Costa-Filho, A.; Earle, K.; Moscicki, J.; Freed, J. Electron Spin Resonance in Studies of Membranes and Proteins. *Science* **2001,** *291*, 266-269.
48. Subczynski, W. K.; Wisniewska, A.; Yin, J. J.; Hyde, J. S. Hydrophobic Barriers of Lipid Bilayer Membranes Formed by Reduction of Water Penetration by Alkyl Chain Unsaturation and Cholesterol. *Biochemistry* **1994**, *33*, 7670-7681.
49. Volke, F.; *Eisenblätter*, S.; Klose, G. Hydration Force Parameters of Phosphatidylcholine Lipid Bilayers as Determined from 2H-NMR Studies of Deuterated Water. *Biophys. J.* **1994**, *67*, 1882-1887.
50. Hsieh, C. H.; Wu, W. G. Structure and Dynamics of Primary Hydration Shell of Phosphatidylcholine Bilayers at Subzero Temperatures. *Biophys. J.* **1996,** *71*, 3278-3287.
51. Bürsing, H.; Ouw, D.; Kundu, S.; Vöhringer, P. Probing Solvation Dynamics in Liquid Water and at Phospholipid/Water Interfaces with Femtosecond Photon-Echo Spectroscopies. *Phys. Chem. Chem. Phys.* **2001**, *3*, 2378-2387.
52. Simon, S. A.; McIntosh, T. J.; Latorre, R. Influence of Cholesterol on Water Penetration into Bilayers. *Science* **1982**, *216*, 65-67.
53. Rheinstadter, M. C.; Seydel, T.; Salditt, T. Nanosecond Molecular Relaxations in Lipid Bilayers Studied by High Energy-Resolution Neutron Scattering and in situ Diffraction. *Phys. Rev. E* ***2007***, *75*, 011907.
54. Milhaud, J. New Insights into Water-Phospholipid Model Membrane Interactions. *Biochim. Biophys. Acta* **2004**, *1663*, 19-51.
55. Nagle, S. T.; Nagle, J. F. Lipid bilayers: Thermodynamics, Structure, Fluctuations, and Interactions. *Chem. Phys. Lipids* **2004**, *127*, 3-14.
56. Lu, W.; Kim, J.; Qiu, W.; Zhong, D. Femtosecond Studies of Tryptophan Solvation: Correlation Function and Water Dynamics at Lipid Surfaces. *Chem. Phys. Lett.* **2004**, *388*, 120-126.
57. Bacia, K.; Kim, S.; Schwille, P. Fluorescence Cross-Correlation Spectroscopy in Living Cells. *Nature Methods* **2006**, *3*, 83-89.
58. Halder, S.; Chaudhuri, A.; Chattopadhay, A. Organization and Dynamics of Membrane Probes and Proteins Utilizing the Red Edge Excitation Shift. *J. Phys. Chem. B* **2011**, *115*, 5693-5706.
59. Lyubartsev, A. P.; Rabinovich, A. L. Recent Development in Computer Simulations of Lipid Bilayers. *Soft Matter* **2011**, *7*, 25-39.
60. Eisenthal, K. B. Equilibrium and Dynamic Processes at Interfaces by Second Harmonic and Sum Frequency Generation. *Annu. Rev. Phys. Chem.* **1992**, *43*, 627-641.

61. Ito, N.; Arzhantsev, S.; Heitz, M.; Maroncelli, M. Solvation Dynamics and Rotation of Coumarin 153 in Alkylphosphonium Ionic Liquids. *J. Phys. Chem. B* **2004**, *108*, 5771-5777.
62. Andreatta, D.; Lustres, J. L. P.; Kovalenko, S. A.; Ernsting, N. P.; Murphy, C. J.; Coleman, R. S.; Berg, M. A. Power-Law Solvation Dynamics in DNA over Six Decades in Time. *J. Am. Chem. Soc.* **2005**, 127, 7270–7271.
63. Jimenez, R.; Fleming, G. R.; Kumar, P. V.; Maroncelli, M. Femtosecond Solvation Dynamics of Water. *Nature* **1994**, *369*, 471-473.
64. Pal, S. K.; Peon, J.; Zewail, A. H. Biological Water at the Protein Surface: Dynamical Solvation Probed Directly with Femtosecond Resolution. *Proc. Natl. Acad. Sci. U.S.A.* **2002**, *99*, 1763-1768.
65. Zhou, F.; Schulten, K. Molecular Dynamics Study of a Membrane-Water Interface. *J. Phys. Chem*. **1995**, *99*, 2194-2207.
66. Lipinski, C. A.; Lombardo, F.; Dominy, B. W.; Feeney, P. J. Experimental and Computational Approaches to Estimate Solubility and Permeability in Drug Discovery and Development Settings. *Adv. Drug Delivery Rev.* **2001**, *46*, 3-26.
67. Henin, Y.; Gouyette, C.; Schwartz, O.; Debouzy, J. C.; Neumann, J. M.; Huynh-Dinh, T. Lipophilic Glycosyl Phosphotriester Derivatives of AZT: Synthesis, NMR Transmembrane Transport Study and Antiviral Activity. *J. Med. Chem*. **1991**, *34*, 1830-1837.
68. Eisenthal, K. B. Equilibrium and Dynamic Processes at Interfaces by Second Harmonic and Sum Frequency Generation. *Annu. Rev. Phys. Chem.* **1992**, *43*, 627-661.
69. Berg, J. M.; Tymoczko, J. L.; Stryer, L. *Biochemistry*, 7th ed., Freeman, New York, **2012**.
70. Charles, E.; Kolb, L. R.; Williams, J. T. J.; Douglas, R. W.; Paul, D. Mass Accommodation and Chemical Reactions at Gas-Liquid Interfaces. *Chem. Rev.* **2006,** *106*, 1323-1354.
71. Tanaka, S.; Yamanaka, K.; Hashimoto, Y. *The Chemistry of Acid Rain: Sources and Atmospheric Processes*; Johnson, R. W., Gordon, G. E., Eds.; American Chemical Society Symposium Series 349; American Chemical Society: Washington, DC, **1987**.
72. Finlayson-Pitts, B. J.; Pitts, J. N. Jr. *Chemistry of the Upper and Lower Atmosphere*; Academic Press: San Diego, CA, **2000**.
73. Starks, C. M.; Liotta, C. L.; Halpern, M. *Phase Transfer Catalysis*; Chapman & Hall: New York, **1994**.
74. Campbell, C. J.; Rusling, J. F. Electrochemical Phase Transfer Catalysis in Microemulsions: Carbene Formation. *Langmuir* **1999**, *15*, 7416-7417.
75. Makosza, M. Phase-Transfer Catalysis. A General Green Methodology in Organic Synthesis. *Pure Appl. Chem.* **2000**, *72*, 1399-1403.
76. Volkov, A. G., Deamer, D. W., Eds.; *Liquid-Liquid Interfaces*; CRC press: Boca Raton, FL, **1996**.
77. Volkov, A. G., Ed.; *Interfacial Catalysis*; Marcel Dekker: New York, **2003**.
78. Wang, H.; Borguet, E.; Eisenthal, K. B. Generalized Interface Polarity Scale Based on Second Harmonic Spectroscopy. *J. Phys. Chem. B* **1998**, *102*, 4927-4932.
79. Wang, H.; Borguet, E.; Eisenthal, K. B. Polarity of Liquid Interfaces by Second Harmonic Generation Spectroscopy. *J. Phys. Chem. A* **1997**, *101*, 713-718.
80. Ishizaka, S.; Kim, H.; Kitamura, N. Time-Resolved Total Internal Reflection Fluorometry Study on Polarity at a Liquid/Liquid Interface. *Anal. Chem.* **2001**, *73*, 2421-2428.
81. Steel, W. H.; Walker, R. A. Measuring Dipolar Width Across Liquid–Liquid Interfaces with 'Molecular Rulers'. *Nature* **2003**, *424*, 296-299.
82. Steel, W. H.; Walker, R. A. Solvent Polarity at an Aqueous/Alkane Interface: The effect of Solute Identity. *J. Am. Chem. Soc*. **2003**, *125*, 1132-1133.
83. Sen, S.; Yamaguchi, S.; Tahara, T. Different Molecules Experience Different Polarities at the Air/Water Interface. *Angew. Chem. Int. Ed.* **2009**, *48*, 6439-6444.
84. Benjamin, I. Static and Dynamic Electronic Spectroscopy at Liquid Interfaces. *Chem. Rev.* **2006**, *106*, 1212-1233.
85. Eisenthal, K. B. Liquid Interfaces Probed by Second-Harmonic and Sum-Frequency Spectroscopy. *Chem. Rev*. **1996**, *96*, 1343-1360.
86. Michael, D.; Benjamin, I. Structure, Dynamics, and Electronic Spectrum of N,N′-Diethyl-p-nitroaniline at Water Interfaces. A Molecular Dynamics Study. *J. Phys. Chem. B* **1998**, *102*, 5145-5151.
87. Benjamin, I. Solvent Effects on Electronic Spectra at Liquid Interfaces. A Continuum Electrostatic Model. *J. Phys. Chem. A* **1998**, *102*, 9500-9506.

88. Watanabe, H.; Yamaguchi, S.; Sen, S.; Morita, A.; Tahara, T. “Half-Hydration” at the Air/Water Interface Revealed by Heterodyne-Detected Electronic Sum Frequency Generation Spectroscopy, Polarization Second Harmonic Generation, and Molecular Dynamics Simulation. *J. Chem. Phys.* **2010**, *132*, 144701.
89. Yamaguchi, S.; Watanabe, H.; Mondal, A.K.; Tahara, T. "Up" versus "Down" Alignment and Hydration Structures of Solutes at the Air/Water Interface Revealed by Heterodyne-Detected Electronic Sum Frequency Generation with Classical Molecular Dynamics Simulation. *J. Chem. Phys*. **2011**, *135*, 194705.
90. Sing, P.; Nihonyanagi, S.; Yamaguchi, S.; Tahara, T. Interfacial Water in the Vicinity of a Positively Charged Interface Studied by Steady-State and Time-Resolved Heterodyne-Detected Vibrational Sum Frequency Generation. J. Chem. Phys. 2014, 141, 18C527.
91. Berkowitz, M. L.; Bostick, D. L.; Pandit, S. Aqueous Solutions Next to Phospholipid Membrane Surfaces: Insights from Simulations. *Chem. Rev*. **2006,** *106*, 1527-1539.
92. Berkowitz, M. L.; Vacha, R. Aqueous Solutions at the Interface with Phospholipid Bilayers. *Accounts Chem. Res. **2012**, 45, 74-82.*
93. Koynova, R.; Caffrey, M. Phases and Phase Transitions of the Phosphatidylcholines. *Biochim. Biophys. Acta* **1998**, *1376*, 91-145.
94. Heimburg, T. A Model for the Lipid Pretransition: Coupling of Ripple Formation with the Chain-Melting Transition. *Biophys. J.* **2000**, *78*, 1154-1165.
95. Clausell, A.; Busquets, M. A.; Pujol, M.; Alsina, A.; Cajal, Y. Polymyxin B-Lipid Interactions in Langmuir-Blodgett Monolayers of Escherichia Coli Lipids: A Thermodynamic and Atomic Force Microscopy Study. *Biopolymers* **2004**, *75*, 480-490.
96. Ihalainen, P.; Peltonen, J. Covalent Immobilization of Antibody Fragments onto Langmuir−Schaefer Binary Monolayers Chemisorbed on Gold. *Langmuir* **2002**, *18*, 4953-4962.
97. Hughes, A. V.; Howse, J. R.; Dabkowska, A.; Jones, R. A.; Lawrence, M. J.; Roser, S. J. Floating Lipid Bilayers Deposited on Chemically Grafted Phosphatidylcholine Surfaces. *Langmuir* **2008**, *24*, 1989-1999.
98. Liu, J.; Conboy, J. C. Structure of a Gel Phase Lipid Bilayer Prepared by the Langmuir−Blodgett/Langmuir-Schaefer Method Characterized by Sum-Frequency Vibrational Spectroscopy. *Langmuir* **2005**, *21*, 9091-9097.
99. Giocondi, M. C.; Le Grimellec, C. Temperature Dependence of the Surface Topography in Dimyristoylphosphatidylcholine/Distearoylphosphatidylcholine Multibilayers. *Biophys. J.* **2004**, *86*, 2218-2230.
100. Shaw, J. E.; Slade, A.; Yip, C. M. Simultaneous in situ Total Internal Reflectance Fluorescence/Atomic Force Microscopy Studies of DPPC/dPOPC Microdomains in Supported Planar Lipid Bilayers. *J. Am. Chem. Soc.* **2003**, *125*, 11838-11839.
101. Brezesinski, G.; Mohwald, H. Langmuir Monolayers to Study Interactions at Model Membrane Surfaces. *Adv. Colloid Interface Sci.* **2003**, *100-102*, 563–584.
102. Marsh, D. Intrinsic Curvature in Normal and Inverted Lipid Structures and in Membranes. *Biophys. J.* **1996**, *70*, 2248-2255.
103. Amado, E.; Kerth, A.; Blume, A.; Kressler, J. Infrared Reflection Absorption Spectroscopy Coupled with Brewster Angle Microscopy for Studying Interactions of Amphiphilic Triblock Copolymers with Phospholipid Monolayers. *Langmuir* **2008**, *24*, 10041-10053.
104. Sessa, G.; Weissmann, G. Phospholipid Spherules (liposomes) as a Model for Biological Membranes. *J. Lipid Res.* **1968**, *9*, 310-318.
105. Maier, O., Oberle, V.; Hoekstra, D. Fluorescent Lipid Probes: Some Properties and Applications (A Review). *Chem. Phys. Lipids* **2002**, *116*, 3-18.
106. Haidekker, M. A.; Theodorakis, E. A. Molecular Rotors--Fluorescent Biosensors for Viscosity and Flow. *Org. Biomol. Chem.* **2007**, *5*, 1669-1678.
107. Lingwood, D.; Simons, K. Lipid Rafts as a Membrane-Organizing Principle. *Science* **2010**, *327*, 46-50.
108. Cherepanov, D. A.; Junge, W.; Mulkidjanian, A. Y. Proton Transfer Dynamics at the Membrane/Water Interface: Dependence on the Fixed and Mobile pH Buffers, on the Size and Form of Membrane Particles, and on the Interfacial Potential Barrier. *Biophys. J.* **2004**, *86*, 665–680.
109. Zhang, Z.; Huang, L.; Shulmeister, V. M.; Chi, Y. I.; Kim, K. K.; Hung, L. W.; Crofts, A. R.; Berry, E. A.; Kim, S. H. Electron Transfer by Domain Movement in Cytochrome BC 1. *Nature* **1998**, *392*, 677-684.

110. Kausik, R.; Han, S. Dynamics and State of Lipid Bilayer-Internal Water Unraveled with Solution State 1H Dynamic Nuclear Polarization. *Phys. Chem. Chem. Phys*. **2011**, *13*, 7732–7746.
111. Marrink, S.; Berendsen, H. Simulation of Water Transport Through a Lipid Membrane. *J. Phys. Chem.* **1994**, *98*, 4155-4168.
112. Rosso, L.; Gould, I. Structure and Dynamics of Phospholipid Bilayers using Recently Developed General All-Atom Force Fields. *J. Comput. Chem*. **2008**, *29*, 24-37.
113. Nagle, J.; Mathai, J.; Zeidel, M.; Tristram-Nagle, S. Theory of Passive Permeability Through Lipid Bilayers. *J. Gen. Physiol*. **2008**, *131*, 77-85.
114. Bhide, S.; Berkowitz, M. Structure and Dynamics of Water at the Interface with Phospholipid Bilayers. *J. Chem. Phys*. **2005**, *123*, 224702.
115. Damodaran, K. V.; Merz,K. M. Jr. Head Group- Water Interaction in Lipid Bilayers: A Comparison Between DMPC- and DLPE- Based Lipid Bilayers. *Langmuir* **1993**, *9*, 1179–1183.
116. Zhou, Z.; Sayer, B. G.; Hughes, D. W.; Stark, R. E.; Epand, R. M. Studies of phospholipid Hydration by High-Resolution Magic-Angle Spinning Nuclear Magnetic Resonance. *Biophys. J.* **1999**, *76*, 387-399.
117. Yamamoto, E.; Akimoto, T.; Yasui, M.; Yasuoka, K. Origin of Subdiffusion of Water Molecules on Cell Membrane Surfaces. *Sci. Rep*. **2014**, *4*, 4720.
118. Gawrisch, K.; Gaede, H. C.; Mihailescu, M.; White, S. H. Hydration of POPC Bilayers Studied by 1H-PFG-MAS-NOESY and Neutron Diffraction. *J. Biophys. Lett.* **2007**, *36*, 281-291.
119. Cevc, G.; Marsh, D. *Phospholipid Bilayers. Physical Principles and Models*, Wiley, New York, **1987.**
120. Franklin, J. C.; Cafiso, D. S. Internal Electrostatic Potentials in Bilayers: Measuring and Controlling Dipole Potentials in Lipid Vesicles. *Biophys. J.* **1993**, *65*, 289-299.
121. Gabdoulline, R. R.; Zheng, C.; Vanderkooi, G. Molecular Origin of the Internal Dipole Potential in Lipid Bilayers: Role of Electrostatic Potential of Water. *Chem. Phys. Lipids* **1996**, *84*,139–146.
122. Cladera, J.; O'Shea, P. Intramembrane Molecular Dipoles Affect the Membrane Insertion and Folding of a Model Amphiphilic Peptide. *Biophys. J.* **1998**, *74*, 2434-2442.
123. Voglino, L.; McIntosh,T. J.; Simon, S. A. Modulation of the Binding of Signal Peptides to Lipid Bilayers by Dipoles Near the Hydrocarbon-Water Interface. *Biochemistry* **1998**, *37*, 12241–12252.
124. Bakhshiev, N. G. *Spectroscopy of Intermolecular Interactions*, Nauka, Leningrad, **1972**.
125. Lippert, E. L. *Laser-spectroscopic studies of reorientation and other relaxation processes in solution*: J. B. Birks (Ed.), Organic Molecular Photophysics, vol. 2, Wiley, New York, **1975**.
126. Klymchenko, A. S.; Mely, Y.; Demchenko, A. P.; Duportail, G. Simultaneous Probing of Hydration and Polarity of Lipid Bilayers with 3-Hydroxyflavone Fluorescent Dyes. *Biochim. Biophys. Acta* **2004**, *1665*, 6-19.
127. Pratt, L. R.; Pohorille, A. Hydrophobic Effects and Modeling of Biophysical Aqueous Solution Interfaces. *Chem. Rev***.** **2002**, *102*, 2671-2692.
128. Zaccai, G.; Blasie, J. K.; Schoenborn, B. P. Neutron Diffraction Studies on the Location of Water in Lecithin Bilayer Model Membranes. *Proc. Natl. Acad. Sci. U.S.A.* **1975**, 72, 376-380.
129. Hubner, W.; Blume, H. A. Interactions at the Lipid-Water Interface. *Chem. Phys. Lipids* **1998**, *96*, 99-123.
130. Lakowicz, J. R. *Principles of Fluorescence Spectroscopy*, Plenum Press, Springer, New York, **1983.**
131. Perochon, E.; Lopez, A.; Tocanne, J. F. Polarity of Lipid Bilayers. A Fluorescence Investigation. *Biochemistry* **1992**, *31*, 7672-7682.
132. Kurad, D.; Jeschke, G. Marsh, D. Lipid Membrane Polarity Profiles by High-Field EPR. *Biophys. J*. **2003**, *85*, 1025-1033.
133. Chattopadhyay, A.; Mukherjee, S. Red Edge Excitation Shift of a Deeply Embedded Membrane Probe: Implications in Water Penetration in the Bilayer. *J. Phys. Chem. B* **1999,** *103,* 8180-8185.
134. Parasassi, T.; Krasnowska, E. K.; Bagatolli, L.; Gratton, E. Laurdan and Prodan as Polarity-Sensitive Fluorescent Membrane Probes. *J. Fluoresc.* **1998** *8,* 365-373.
135. Koehorst, R. B. M.; Vergeldt, R. B. F. J.; Hemminga, M. A. Lipid Bilayer Topology of the Transmembrane α-Helix of M13 Major Coat Protein and Bilayer Polarity Profile by Site-Directed Fluorescence Spectroscopy. *Biophys. J*. **2004**, *87*, 1445-1455.

136. Carney, J.; East, J. M.; Lee, A. G. Penetration of Lipid Chains into Transmembrane Surfaces of Membrane Proteins: Studies with MscL. *Biophys. J.* **2007**, *92*, 3556-3563.
137. Pandit, S. A.; Bostick, D.; Berkowitz, M. L. An Algorithm to Describe Molecular Scale Rugged Surfaces and Its Application to the Study of a Water/Lipid Bilayer Interface. *J. Chem. Phys.* **2003**, *119*, 2199-2205.
138. Jedlovszky, P.; Mezei, M. Orientational Order of the Water Molecules Across a Fully Hydrated DMPC Bilayer: A Monte Carlo Simulation Study. *J. Phys. Chem. B* **2001**, *105*, 3614–3623.
139. Egberts, E.; Berendsen, H. J. C. Molecular Dynamics Simulation of a Smectic Liquid Crystal with Atomic Detail. *J. Chem. Phys.* **1988**, *89*, 3718-3732.
140. Leneveu, D. M.; Rand, R. P.; Parsegian, V. A. Measurement of Forces Between Lecithin Bilayers. *Nature* **1976**, *259*, 601-603.
141. Essmann, U.; Perera, L.; Berkowitz, M. L. The Origin of the Hydration Interaction of Lipid Bilayers from MD Simulation of Dipalmitoylphosphatidylcholine Membranes in Gel and Liquid Crystalline Phases. *Langmuir* **1995**, *11*, 4519-4531.
142. Fukuma, T.; Higgins, M.; Jarvis, S. Direct Imaging of Individual Intrinsic Hydration Layers on Lipid Bilayers at Ångstrom Resolution. *Biophys. J.* **2007**, *92*, 3603-3609.
143. Pasenkiewicz-Gierula, M.; Takaoka, Y.; Miyagawa, H.; Kitamura, K.; Kusumi, A. Charge Pairing of Headgroups in Phosphatidylcholine Membranes: A Molecular Dynamics Simulation Study. *Biophys. J.* **1999**, *76*, 1228-1240.
144. Debnath, A.; Mukherjee, B.; Ayappa, K. G.; Maiti, P. K.; Lin, S. *T.* Entropy and dynamics of water in hydration layers of a bilayer. *J. Chem. Phys.* **2010**, *133*, 174704.
145. Bhide, S. Y.; Berkowitz, M. L. The Behavior of Reorientational Correlation Functions of Water at the Water-Lipid Bilayer Interface. *J. Chem. Phys.* **2006**, *125*, 94713.
146. Laage, D.; Hynes, J. T. On the Molecular Mechanism of Water Reorientation. *J. Phys. Chem. B* **2008**, *112*, 14230-14242.
147. Zhang, Z.; Berkowitz, M. L. Orientational Dynamics of Water in Phospholipid Bilayers with Different Hydration Levels. *J. Phys. Chem. B* ***2009***, *113*, 7676-7680.
148. Kyrychenko, A.; Tobias, D. J.; Ladokhin, A. S. Validation of Depth-Dependent Fluorescence Quenching in Membranes by Molecular Dynamics Simulation of Tryptophan Octyl Ester in POPC Bilayer. *J. Phys. Chem. B,* **2013**, *117*, 4770-4778.

Chapter 10

Precise Quantification of Probe-Location Dependent Polarity and Hydration at Lipid/Water Interfaces

In the preceding chapter, I have introduced the field of lipid research, particularly about different lipid phases and their role in biology, different probes that were used for studies of static and dynamic properties of lipid bilayers, and so on. The discussion on earlier reported studies has been made in the previous chapter pertaining toward understanding the polarity and hydration at lipid/water interfaces. This chapter will discuss some very new results on the depth-dependent interfacial polarity estimation at lipid/water interfaces in bilayers of fluid- and gel-phases simultaneously. For precise estimation of local polarity and hydration, a homologous series of newly synthesized fluorescent probe molecules of linearly varying lipophilicity (log*P*) based on 4-aminophthalimide (4AP) are used. The discussion on both experiment and MD simulation results has been made to understand how the same probes partition at different lipid/water interfaces of fluid- and gel-phases, and how they report on the local polarity and hydration at these interfaces at room temperature.

10.1. Introduction

Environment polarity and hydration plays significant role in the electrostatics of lipid/water interfaces, understanding of which is of utmost importance as they govern various essential phenomenon like charge transfer,[1] molecular interaction,[2] signal transduction,[3] protein insertion,[4] drug[5] and ion[6] transport across and within the lipid membrane. Polarity profiles and hydration across lipid/water interfaces vary drastically due to differential partitioning of water molecules around the hydrophobic and hydrophilic parts of lipid membranes.[7,8] Thus, the presence of small molecules adsorbed at various positions across and within these lipid interfaces would sense different local environment as well as different solute-lipid and solute-water interactions. Hence, would expectedly experience different solvation properties which are dependent on positions across the interfaces. For example see Figure 10.1. Therefore, precise understanding of hydration, polarity and interaction of solute at the interfaces of lipid bilayer is vital to explore their importance in membrane biology[9] as well as to develop effective drug-detoxification and drug-delivery systems.[10-13]

Ample studies have been done using NMR,[14-16] ESR,[7,8,17,18] X-ray,[19,20] fluorescence,[21-31] SPG[32-34,53,54] and molecular dynamics simulation[34-45] to explore hydration, local solvation and interaction of solute at lipid/water interfaces. Nonetheless, most of these studies are

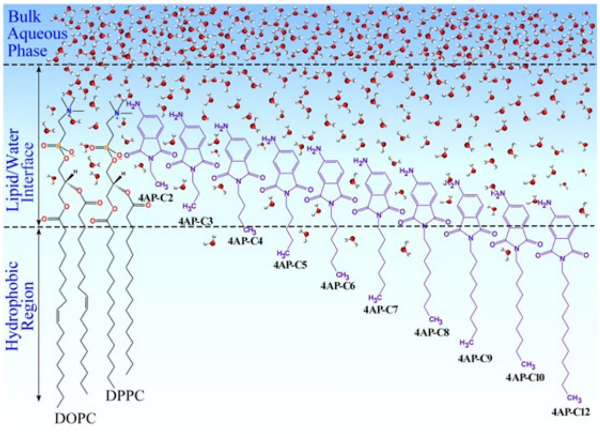

Figure 10.1: Schematic representation of lipid/water interface with probable position of 4AP-C*n* ($n = 2 - 10$, 12) probes. The probes are expected to reside at varying depths depending on different lipophilicities (log*P*) across the lipid/water interfaces.

concerned with fluid (liquid crystalline) phase of lipid and water interfaces. Understanding the solvation properties in gel-phase of lipid/water interface is not much explored regardless of their biological significance in membranes of eye-lens and outer epidermis.[46,47] This may be due to the fact that various fluorescent and ESR probes used to study gel form of lipid bilayers are either found to perturb lipid packing and/or get excluded from lipid-bilayer (gel phase), making the studies of gel-phase bilayers more difficult.[14,15,48-50] However, many questions are yet to be answered —(1) How does hydration and polarity profiles vary at the interfaces of fluid- and gel-phase lipid bilayer? (2) How the interaction of solute of varying lipophilicities differs at these interfaces? (3) How the local polarities experienced by probes vary at the interfaces and why?

This chapter addresses all the above questions by presenting a new homologous series of fluorescent 4-aminopthalimide based probes (4AP-C*n; n* = 2-10, 12) with varying lipophilicities (i.e., octanol/water partition coefficient – logP). These 4AP-C*n* probes scan different region of ($L_{\beta'}$)[51] DPPC (1,2-dipalmitoyl-sn-glycerol-3-phosphocholine) bilayer in its gel-phase at room temperature which shows a unique stepwise polarity-profile. However, the probes sense only subtle but continuous change in the local polarity at lipid/water interface of (L_{α})[51] DOPC (1,2-dioleoyl-sn-glycero-3-phosphocholine) bilayer in fluid-phase. Polarity (E_T^N) sensed by 4AP-C*n* probes in fluid- and gel-phase of lipid bilayers are quantified by steady state fluorescence spectroscopy. Fluorescence quenching experiments show that the solutes, depending upon their log*P* value, adsorb in different depths at these interfaces which correlate to the polarity profiles seen at these interfaces. Long MD simulations on few solute-lipid systems complement experimental findings and unfold intricate details about the hydration, relative position and angle distribution of the 4AP-C*n* at the lipid/water interfaces of fluid- and gel-phase of the lipid bilayers. Simulation results indicate that apart from the relative probe's position, their orientations also play critical role in defining the local solvation by changing the access of water molecules to these probes at the two lipid/water interfaces.

10.2. Experimental and Simulation Methods

10.2.1. Materials

DPPC, DOPC, 1-palmitoyl-2-(6,7-dibromostearoyl) phosphatidylcholine (6,7-Br_2PC) and 1-palmitoyl-2-(9,10-dibromostearoyl) phosphatidylcholine (9,10-Br_2PC) were used as received from Avanti Polar Lipids Inc. 4-Aminopthalimide (4AP) was from TCI chemicals, which was then recrystallized using mixture of ethanol and water prior to its use for synthesising 4AP-C*n* derivatives. Alkyl-bromide with different chain lengths from 2 to 10 and 12 carbons were purchased from TCI chemicals. Dry K_2CO_3 was taken from Fischer Scientific. Synthesis was performed using solvent of AR or HPLC grades and spectroscopic grade. Thioacetamide of AR grade was from Spectrochem.

10.2.2. Synthesis of 4AP-C*n* Probes

Synthesis of 4-Aminopthalimide probes was performed by attaching alkyl chain (single strand) of varying length (C2 to C10 and C12) to the fluorescent 4AP-moiety using a single step reaction (Scheme 1, a revised scheme of earlier work).[59] One equivalent of 4AP was blended thoroughly in dry acetonitrile in presence of anhydrous K_2CO_3 (1 equivalent) at reflux temperature. This was followed by drop wise addition of alkyl-bromide (0.9 equivalents) to the reaction mixture at periodic intervals. Finally, the reaction mixture was refluxed for 24h at a temperature of 65-75 ˚C. The final product was obtained after solvent removal and further purification by column chromatography and subsequent recrystallization.

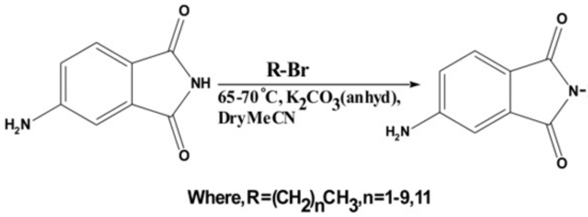

Scheme 1

10.2.3. Preparation of Lipid Vesicles

Freeze-thaw and sonification methods were used to prepare small unilamellar vesicles (SUVs) of DOPC and DPPC. Main stock of phospholipids were prepared by dissolving known amount of DOPC or DPPC in a chloroform/methanol mixture in ratio of 1:1 (v/v) in 10 ml glass tube, whereas, stock solutions for 4AP-C*n* were prepared in methanol. Required amount of stock solution of either DOPC or DPPC was mixed with 4AP-C*n* in a glass tube of 5 ml using a ratio of 1:35 for dye/lipid (or 1:40 for 4AP-C2 in DOPC). At this ratio all the 4AP-C*n* probes were expected to be bound at the lipid interface, which was confirmed by the titration of 4AP-C*n* with varying lipid amount (Figure 10.2). Further, gently warming the samples removes the solvent, and finally the residual organic solvent

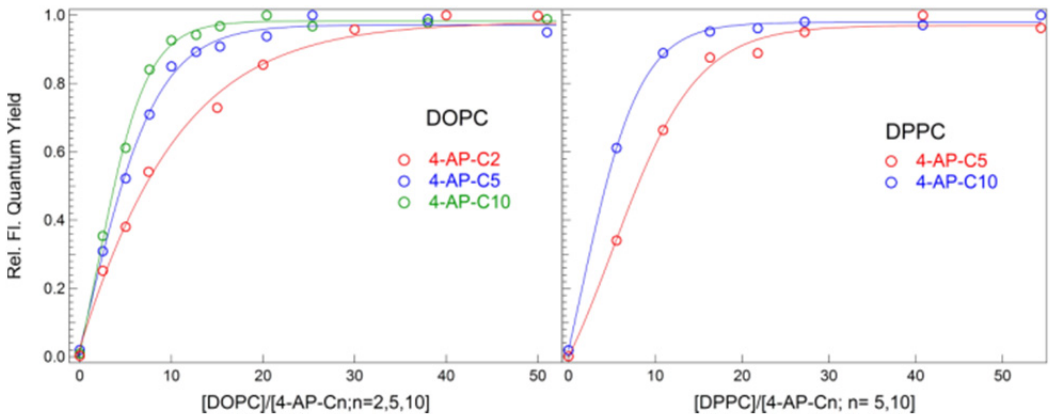

Figure 10.2: Binding kinetics of few 4AP-C*n* (*n* = 2, 5 and 10) probes with DOPC (left) and DPPC (right) vesicles.

was removed with the help of suction-pump for around 2 h, which yielded a thin film of lipid at the bottom of glass tube. HPLC-grade water (Merck) was added to rehydrate the dried films of lipid and subjected to vortex mixing for complete dispersion. The sample in the tube was rapidly cooled by dipping the glass tube into a mixture of calcium carbide and ice. Soon after (5 minutes), the frozen solution was sonicated for ~10 minutes at 60 ˚C using ultrasonic bath sonicator. This process was repeated for a number of times (50-100) until the mixture became visually clear. SUVs size and formation were confirmed by TEM images, which show size ranging from 50 to 150 nm (Figure 10.3).

Samples for measuring the absolute location of probes using parallax method were prepared by adding bromine-labelled lipids (6,7-Br_2PC or 9,10-Br_2PC) to the stock solution of DOPC before evaporation of organic solvents. The final concentration of the bromine labelled lipids was maintained at 15 mol% of the total DOPC lipids. Similar procedure was used to prepare vesicles with 4AP-C*n* probes and quencher lipids.

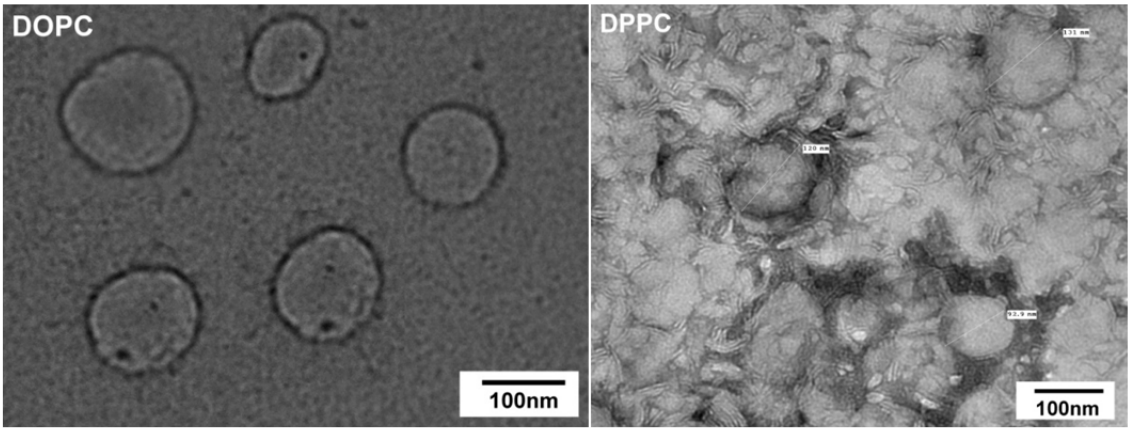

Figure 10.3: TEM images confirm the formation of DOPC and DPPC small unilamellar vesicles (SUVs) of size ~100 nm.

10.2.4. Estimation of the Octanol/water Partition Coefficient

Octanol/water partition coefficients (log*P*) of 4AP-C*n* probes were measured experimentally as well as calculated through software. Shake-flask method[60] was used to prepare samples for log*P* measurement: 4AP-C*n* probes (known concentration) were dissolved in octanol and 1 ml of this solution was layered on an appropriate volume (1-100 ml) of aqueous phase. The octanol/water volume ratios were kept such that after adding the aqueous phase, the final probe's (4AP-C*n*) concentration reaches 5-95% of the initial concentration. The mixtures were stirred at 25 ˚C for 1-2 days. To separate the phase, the mixture was kept in vibration isolation for 2-3 days. Concentration of the 4AP-C*n* probes were measured in each phase using extinction coefficient of 4AP-C*n* in water and octanol as 3382 M^{-1} cm^{-1} and 7835.4 M^{-1} cm^{-1} at 378 nm, respectively. Log*P* of 4AP-C*n* was calculated as,[58]

$$logP = log\ \frac{[Solute]_{octanol}}{[Solute]_{water}} \qquad (10.1)$$

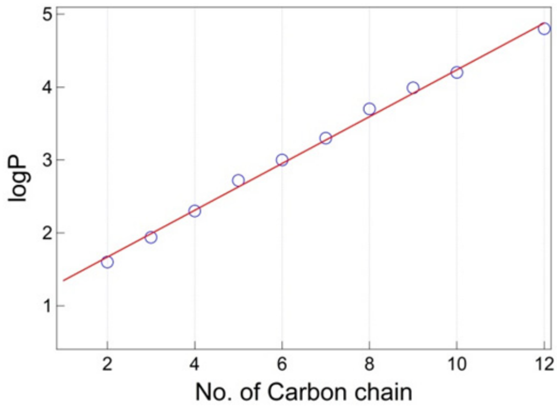

Figure 10.4: Plot of octanol/water partition coefficient (log*P*) of 4AP-C*n* probes with number of carbon atoms in the alkyl-chain obtained from shake-flask method. Line through pints show linear fit to data.

The obtained log*P* values show linear dependence on the number of carbon atoms in the chains of 4AP-C*n*. The calculated data were fitted to a straight line to get the experimental log*P* values as shown in Figure 10.4. log*P* of 4AP-C*n* obtained from different software show linear dependency on number of carbon atom (Table 10.1).

Table 10.1: Experimental and calculated (from software) partition coefficients (log*P*) of 4AP-C*n* probes.

4AP-C*n* Probes	**Octanol/Water Partition Coefficient (log*P*)**				
	Experiment	**Simulation (using various software)**			
		miLog*P*	**ACD**	**ALOPS**	**Clog*P***
4AP-C2	1.67	0.93	0.81	0.15	0.72
4AP-C3	1.99	1.45	1.34	0.50	1.18
4AP-C4	2.31	2.02	1.87	0.91	1.63
4AP-C5	2.63	2.52	2.55	1.50	2.09
4AP-C6	2.96	3.03	2.93	2.10	2.54
4AP-C7	3.27	3.53	3.46	2.72	2.99
4AP-C8	3.59	4.04	3.99	3.41	3.45
4AP-C9	3.92	4.54	4.52	3.95	3.90
4AP-C10	4.24	5.05	5.06	4.47	4.36
4AP-C12	4.88	6.06	5.60	5.44	5.27

10.2.5. Starting Structures for MD Simulation

Coordinates for 4AP-C*n* molecules were obtained through ChemDraw and were energy optimized at HF/6-31G* level using Gaussian 09.[61] Excited state atomic charges for these probe molecules were derived using two state RESP (restricted electrostatic potential)[62] methodology on the optimized 4AP-C*n* structure at CIS/6-31G* level. General amber force field (GAFF)[63] has been employed to generate the force field topologies and parameters for 4AP-C*n* using antechamber module of Amber-12.[64] ACPYPE[65] script was used to convert the format of obtained force field parameters for 4AP-C*n* molecules into GROMACS format for further simulation.

Pre-equilibrated (400-500 ns) DOPC and DPPC bilayers were obtained from an earlier study.[66] These bilayers are formed by 64 lipids in each leaflet, making a system of 128 lipid molecules with 5120 and 3480 TIP3P[67] water molecules in DOPC and DPPC bilayers, respectively. The 4AP-C*n* molecules were introduced near the lipid/water interface of DOPC and DPPC bilayers with the carbon chains of the probes placed towards bilayers tail. Slipids (Stockholms lipid)[68] for lipids and GAFF for 4AP-C*n* were used to carry out MD simulation in GROMACS v5.0.5[69] using CPU codes for equilibrating the system, and GPU codes for running the production simulation.

10.2.6. Molecular Dynamics Simulation Protocol

DOPC and DPPC bilayers with probes incorporated in them were relaxed through energy minimization process carried out using steepest decent algorithm. Lipid bilayers and 4AP-C*n* probes were position restrained with a force constant of 1000 kJ mol^{-1} nm^{-2} so as to remove any bad contacts which can result into unstable dynamics. This was followed by minimization of the entire system with reduced restraint of 500 kJ mol^{-1} nm^{-2} on the 4AP-C*n* probes. Final minimization was carried out without any restraint for proper optimization of the system. CPU codes of GROMACS were used to perform all the minimization steps.

10.2.6.1. Equilibration

Equilibration of these bilayers along with 4AP-C*n* probes were carried out on the minimized structures. Dealing with such heterogeneous system of the lipid-bilayer with incorporated 4AP-C*n* and TIP3P water molecules, requires long equilibration in NVT and NPT ensemble for proper equilibration of the entire system. The lipid bilayers were heated in NVT ensemble, restraining the position of lipid bilayer and 4AP-C*n* with a force constant of 1000 kJ mol^{-1} nm^{-2} for 100 ps. To maintain the fluid (liquid-crystalline - L_α) phase of DOPC bilayer, the system was kept at a production temperature of 303 K much above its transition temperature to gel phase, whereas $L_{\beta'}$ (tilted) gel-phase of DPPC bilayer was maintained at a temperature of 293 K. The system was heated using Berendsen thermostat[70] temperature coupling. 4AP-C*n* probes and lipid bilayers were separately coupled to the heat bath through velocity rescale Berendsen thermostat. The entire system was then equilibrated in NVT ensemble for 100 ps with decreased positional restraint of 500 kJ mol^{-1} nm^{-2} on 4AP-C*n* probes and lipid bilayers. Further, 100 ps of restraint free equilibration was carried out in the same ensemble. After the system acquires a stable production temperature, it was then equilibrated with respect to pressure. The system was equilibrated in NPT ensemble for 1 ns restraining the position of lipid-bilayer and 4AP-C*n* probes with a force constant of 1000 kJ mol^{-1} nm^{-2}, followed by equilibration of 1 ns with reduced restraint of 500 kJ mol^{-1} nm^{-2} on bilayer and 4AP-C*n* in the same ensemble. Finally, a restraint free equilibration was performed for 1 ns in NPT ensemble. Equilibration was carried out using Nose-Hoover thermostat[71,72] as it gives proper kinetic ensemble and maintains proper fluctuation to reproduce natural dynamics. Semi-isotropic pressure coupling was used for lipid bilayers and LINCS algorithm[73] to restraint bonds. CPU codes of GROMACS were utilized to perform equilibration of lipid bilayers.

10.2.6.2. Production Simulation

After the system has been equilibrated with respect to temperature and pressure, 2 ns of simulation in NPT ensemble has been performed using CPU codes prior to the final 300 ns production run on each system in GPU (Nvidia Tesla K20 card). Lipid bilayers (DOPC and DPPC) without any probes were minimized and equilibrated using the same steps as mentioned above in CPU prior to 100 ns of production run of each in GPU. Time step of 2 fs has been used for integration of molecular dynamics. Particle mesh Ewald[74,75] was used to treat the long range electrostatic interaction with a real space cut off of 10 Å. Constant atmospheric pressure (1 bar) was maintained using Parrinello-Rahman barostat[76] with an isothermal compressibility of 4.5 x 10^{-5} bar^{-1} and a coupling constant of 10 ps. MD simulation trajectories were saved at every 5 ps. Trajectories were analysed using analysis modules of GROMACS v5.0.5. Igor-Pro software and Chimera[77] were used for analysis and visualization. Simulations were carried out on eight lipid-probe systems.

10.3. Results and Discussions

10.3.1. Fluorescence Spectra of 4AP-C*n*

Steady state fluorescence spectra were measured by exciting the samples at 375 nm. The fluorescence spectra of 4AP-C*n* at the lipid/water interface of DPPC (gel phase) and DOPC (fluid-phase) vesicles, are plotted in Figure 10.5. 4AP-C*n* molecules at the two interfaces show drastically different spectral features. At DPPC/water interface, they show a peculiar spectral feature with stepwise fluorescence shifts. Spectral (and peak) shifts toward higher wavenumber are shown in Figure 10.5A (and Table 10.2 below). The variation follows a sequence: (4AP-C3 ≈ -C4) < (4AP-C5 ≈ -C6) < (4AP-C7 ≈ -C8) < (4AP-C9 ≈ -C10) and a

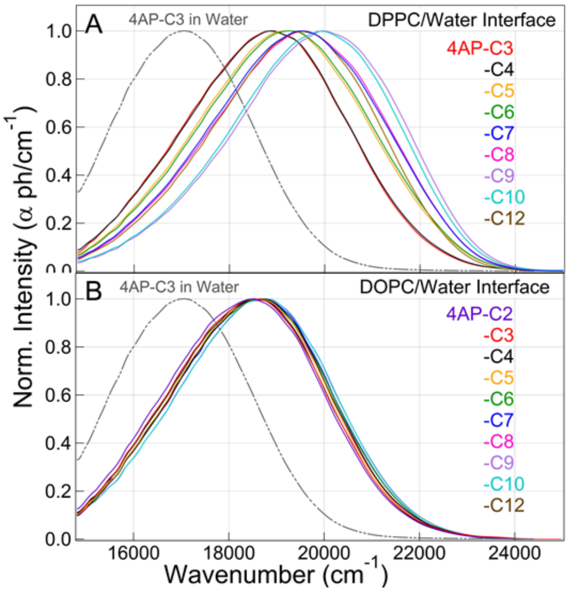

Figure 10.5: Corrected fluorescence spectra of 4AP-C*n* adsorbed at gel-phase DPPC/water interface (A) and fluid-phase DOPC/water interface (B), along with the (control) spectrum of 4AP-C3 in water. Spectra show stepwise shift at DPPC/water interface, while subtle but continuous shift at DOPC/water interface.

reverse trend for 4AP-C12. (Note here that, reliable data for 4AP-C2 in DPPC vesicles was not obtained because 4AP-C2 remained unbound to DPPC bilayer at similar concentration). 4AP-C3 and –C9 show a large difference in their Stokes shift of ~1130 cm^{-1}. Interestingly, probes show similar spectral shape and full width at half maxima (fwhm) of ~4100 cm^{-1} except for 4AP-C7 and –C8, showing a larger fwhm of ~4300 cm^{-1}. This suggests that probes sense similar heterogeneity in the local environment at DPPC/water interface except for a small deviation in case of 4AP-C7 and –C8 probes. On the other hand, the probes show only a subtle, but continuous monotonic shift of spectra (and peak) towards higher wavenumber from 4AP-C2 to 4AP-C9 at DOPC/water interface, whereas, 4AP-C12 shows a reverse trend (Figure 10.5B). 4AP-C3 and –C9 (or-C10) shows a small (~320 cm^{-1}) difference in their spectral shift. It can be seen that all the probes at DOPC/water interface show similar spectral shape and fwhm of ~4050 cm^{-1}, suggesting that probes experience a similar heterogeneity in the local environment. The overall similarity of spectral shape and fwhm of all the probes at both the lipid/water interfaces possibly suggests that only the changes in local solvation (dielectric constant) around the probes at the lipid/water interfaces leads to the spectral shifts, because the theory of solvation indicates that the spectral shape and width should remain same with the fluorescence shift.[78]

10.3.2. Quantification of Polarity

Considering the overall effect of hydrogen bond and dipolar interactions of solute with the molecules in its surrounding,[55-57] the solvatochromic shift of 4AP-C*n* probes at the lipid/water interface based on E_N^T polarity scale is quantified in Figure 10.6. Although, E_N^T scale was basically developed to quantify the polarity of bulk solvents,[55] but has been successfully employed to quantify the polarity of air/water interfaces.[52] Spectral (peak) shifts of 4AP-C*n* in water and 14 different alcohols of varying E_N^T values ranging from 1 to 0.24 were monitored in order to create a E_N^T scale (Figure 10.6A); using this scale the unknown E_N^T values at lipid/water interfaces were obtained. 4AP-C*n* probes at the

DPPC/water interface show a substantial E_N^T change from 0.53 to 0.18 (Figure 10.6A), whereas, a small change from 0.64 to 0.54 was seen at DOPC/water interface for the same probe molecules. One should note here that the emission maxima of the solvatochromic probes are generally obtained in a series of polar and non-polar (protic and aprotic) solvents in order to create the E_N^T scale. However, in the present case, only water and several alcohols that show large variation in the E_N^T values were used to create the scale (Figure 10.6B). This is because the 4AP-C*n* probes consist of polar 4AP- moiety linked to hydrophobic chain of different length, which would presumably partition the polar 4AP (fluorophore part) near the water rich zwitterionic head group region of the lipid bilayer and the hydrophobic carbon chain toward the tail region (non-polar part) of the lipid bilayer. This situation would create a local environment around 4AP-moiety in such a way that should resemble more to the less polar solvents like alcohols, rather than the nonpolar solvents like heptane or hexane. In fact, the 4AP-C*n* spectra in vesicles show smooth feature similar to that seen in less polar alcohols, rather than the vibronic features resembling those in pure nonpolar solvents (Figure 10.6B).

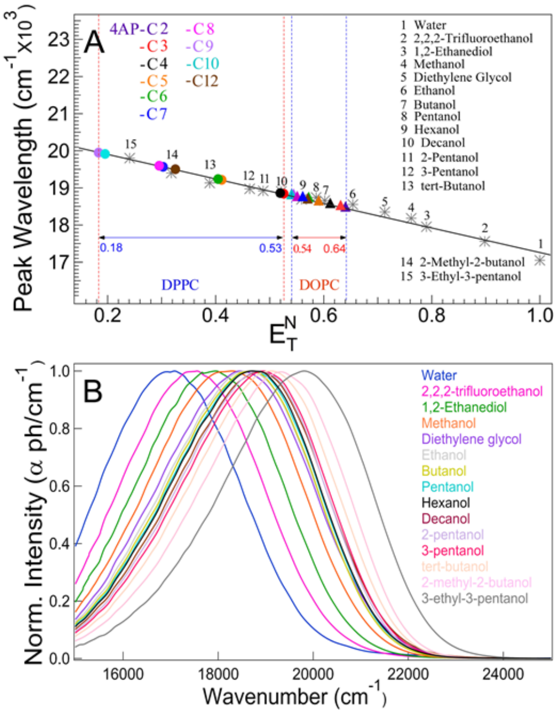

Figure 10.6: (A) Estimation of unknown polarity (E_T^N) at lipid/water interfaces: Plot includes fluorescence peak frequencies of 4AP-C3 in 15 different solvents of different E_T^N values (star). Line through points is best linear fit. Filled circles and triangles represent the E_T^N sensed by 4AP-C*n* in DPPC/water and DOPC/water interfaces, respectively, as obtained from respective fluorescence peak positions. (B) Normalized and corrected fluorescence spectra of 4AP-C3 in 15 different solvents from which the E_T^N-scale is generated. See the color code for solvents in panel.

10.3.3. Polarity Variation with log*P*

Variation of E_N^T values with solute lipophilicity (log*P*) for different 4AP-C*n* probes at DPPC/water and DOPC/water interfaces, respectively are plotted in Figure 10.7 which unfolds log*P* dependent polarity change at the two interfaces. At DPPC/water interface, the probes show stepwise decrease in the E_N^T values with increasing log*P* till 4AP-C10, with a reverse trend for 4AP-C12 (Figure 10.7A). It has been shown in Figure 10.7A that two (consecutive) solute with log*P* variation within ~0.32 display similar E_N^T value. This feature (possibly) indicates that depths of two (consecutive) 4AP-C*n* probes nearly remain same at

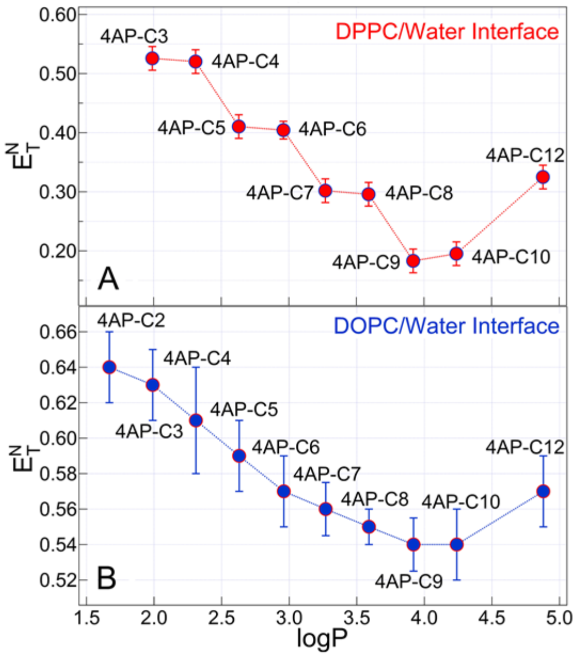

Figure 10.7: Plots of polarity (E_T^N) variation with probe-lipophilicity (log*P*) at gel-phase DPPC/water interface (A) and fluid-phase DOPC/water (B) interfaces, showing stepwise and continuous changes, respectively. Error bars (±SD) are obtained from repeated measurements.

this lipid/water interface. However, at DOPC/water interface, the probe show subtle, but continuous decrease of polarity with increasing log*P*, and 4AP-C12 shows an opposite trend (Figure 10.7B). This may suggest that probes experience only a subtle but continuous change in the depths at DOPC/water interface. In fact, fluorescence quenching and simulation studies have confirmed these possibilities to be correct as discussed below.

10.3.4. Depth Variation of 4AP-C*n* at the Interfaces

The relative fluorescence quenching of 4AP-C*n* probes at DPPC/water and DOPC/water interfaces were monitored using thioacetamide as a quencher to confirm the relative depth variation of 4AP-C*n* across the lipid/water interface. Thioacetamide resides near the water rich lipid surface and is unable to penetrate into the hydrophobic core of the lipid bilayer. Thus, it is used frequently to determine the accessibility of the fluorescent probes bound to macromolecules towards the aqueous phase.[79] Quenching experiments were performed here by monitoring the fluorescence intensity of 4AP-C*n* probes in lipid vesicles by adding required amount of thioacetamide stock solution (2.1M), prepared in water, to the lipid samples. Emission was measured at the peak maxima of the spectra. Depth dependent Stern-Volmer plot for fluorescence quenching of 4AP-C*n* probes in DPPC and DOPC vesicles are shown in Figure 10.8. These plots confirm that the fluorescence of the 4AP-C*n* probes is quenched in a stepwise manner at DPPC/water interface as (4AP-C3 ≈ -C4) > (4AP-C5 ≈ -C6) > (4AP-C7 ≈ -C8 ≈ -C12) > (4AP-C9 ≈ -C10). However, the relative quenching of the probes show continuous change at DOPC/water interface, with reverse trend for 4AP-C12. These results suggest that as the probes reside deeper inside the lipid bilayer, they sense a less polar environment at the interface; however, the two interfaces show considerable differences in the depth-dependent polarity profiles.

10.3.5. Absolute Positions of 4AP-C*n* from Parallax Method

Parallax method has been employed to determine the absolute positions of 4AP-C*n* probes at the lipid/water interface in DOPC vesicles using bromine labelled lipids (6,7-Br_2PC and 9,10-Br_2PC) as quencher[80,81]. The quenching data for DOPC vesicle system is shown in Figure 10.9. Fluorescence data were analysed in pairs to determine the probe's distances Z_{cB} from the center of bilayer according to[80,81]

$$Z_{cB} = \left[\frac{\left(\frac{-1}{\pi C}\right) ln\left(\frac{F_1}{F_2}\right) - L_{21}^2}{2L_{21}}\right] + Z_{c1} \qquad (10.2)$$

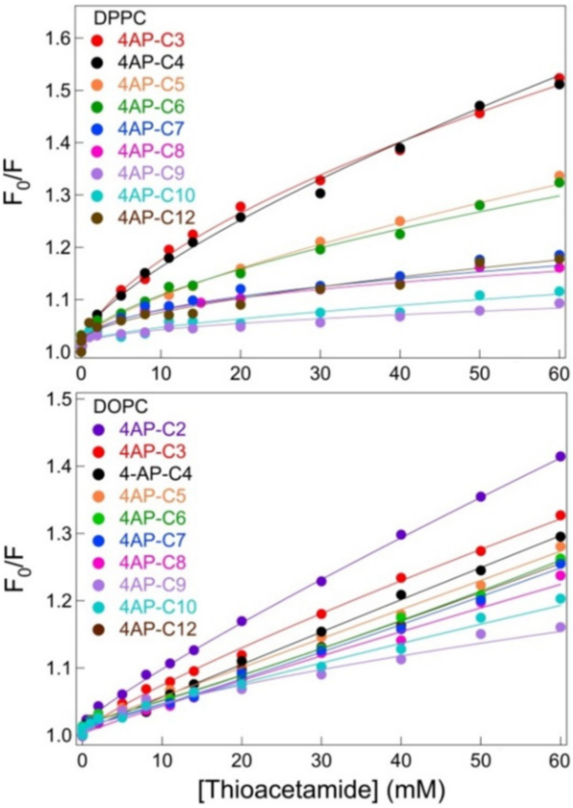

Figure 10.8: Stern-Volmer plots for fluorescence quenching of 4AP-C*n* probes at different concentrations of thioacetamide in DPPC (top panel) and DOPC (bottom panel) vesicles. Here, F_0 and F are the fluorescence intensity in absence and presence of quencher, respectively. The lines through points are guide to eye.

where C is the concentration of quencher-lipid per unit area, F_1 and F_2 are the fluorescence intensity of the probe in the presence of shallow quencher (6,7-Br_2PC) and deeper quencher (9,10-Br_2PC), respectively. L_{21} is the depth difference between the deep and shallow quenchers (2.5 Å), and Z_{c1} is the distance of the shallow quencher from the centre of the bilayer (10.8 Å for 6,7-Br_2PC). Value of C was determined by dividing the mole fraction of the quencher-lipid (in the total DOPC lipid) by the surface area per lipid (70 Å^2 in case of DOPC).[80,81] Only a subtle decrease in the distance calculated from the centre of lipid bilayer with increasing chain length of the probes is observed, but with a reverse trend for 4AP-C12 (Figure 10.9 and Table 10.2). The maximum change in depths between the probes 4AP-C2 and –C9 has been found to be ~4.9 Å. However, the 4AP-C*n* probes at the lipid/water interface can have large variation in the position, which eventually can induce small change in the average polarity (total E_N^T change of ~0.1). Similar parallax experiments were tried to measure depths of probe in DPPC vesicles, but due to structural changes in rigid DPPC vesicles upon incorporation of bromo-PCs the fluorescence spectra of 4AP-C*n* were found to get shifted and distorted. Nevertheless, the quenching data by thioacetamide in DPPC vesicles clearly shows

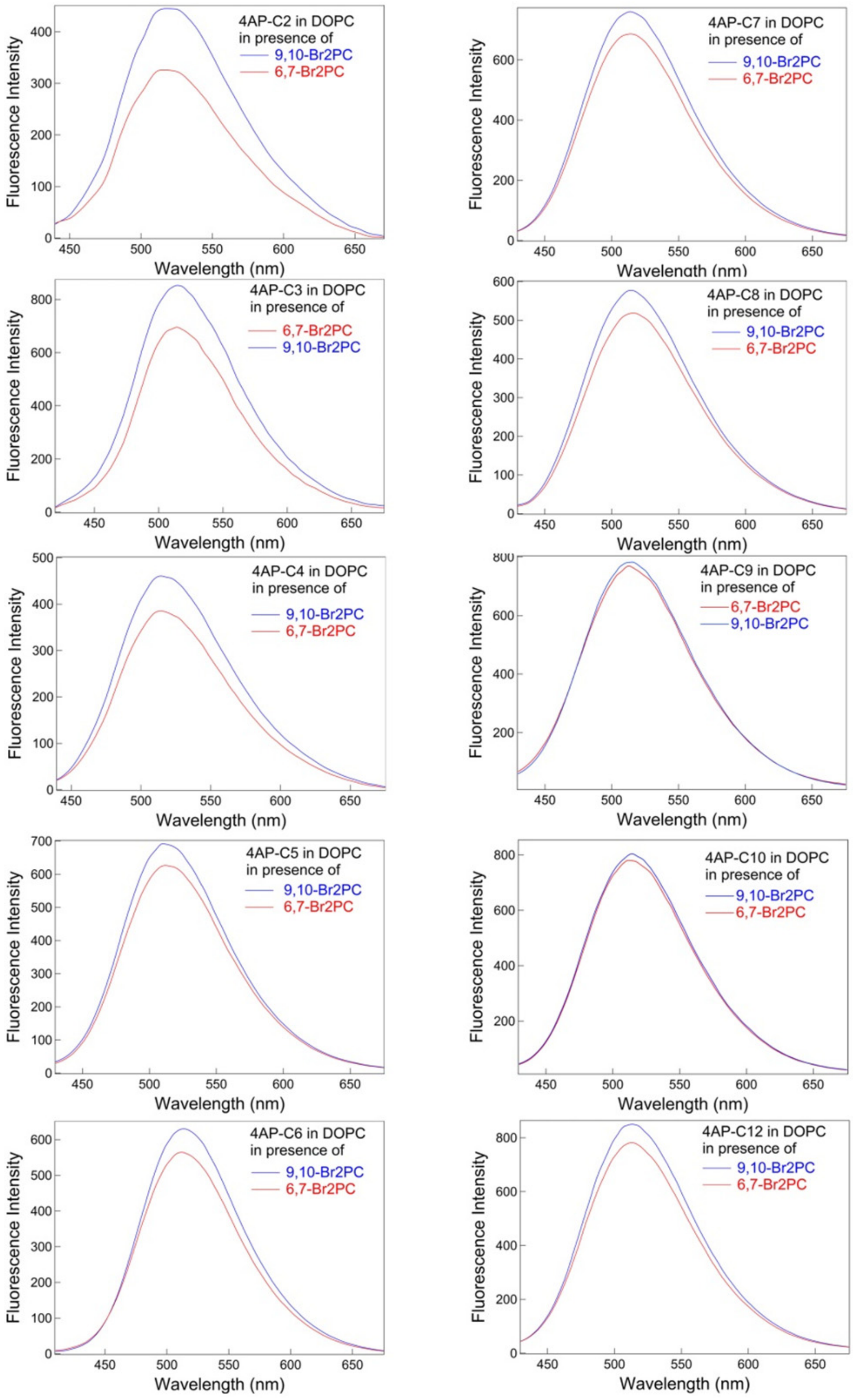

Figure 10.9: Relative fluorescence spectra of 4AP-C*n* (*n* = 2 to 10, 12) in DOPC vesicles in presence of shallow (6,7-Br_2PC) and deep (9,10-Br_2PC) quenchers. Quenching of fluorescence by the shallow quencher is higher in all cases. See plots for legends.

Table 10.2: Parameters for 4AP-C*n* probes at gel- and fluid-phase lipid/water interfaces obtained from experiment and simulation.

4AP-C*n* probes	**Experiment**						**Simulation**					
	log*P*[a]	Fluorescence maxima (cm^{-1})		Polarity[b] (E_T^N)		Position[c] (Å)	Position[d] (Å)		Angle[d] (degree)		Water number[d] (within 10 Å)	
		DPPC	DOPC	DPPC	DOPC	DOPC	DPPC	DOPC	DPPC	DOPC	DPPC	DOPC
4AP-C2	1.67	---	18467	---	0.64	14.9	---	---	---	---	---	---
4AP-C3	1.99	18832	18484	0.53	0.63	13.1	19.5	14.3	60	68	242	216
4AP-C4	2.31	18850	18553	0.52	0.61	12.4	---	---	---	---	---	---
4AP-C5	2.63	19212	18622	0.41	0.59	11.6	---	---	---	---	---	---
4AP-C6	2.96	19232	18692	0.40	0.57	11.8	---	13.8	---	54	---	204
4AP-C7	3.27	19569	18727	0.30	0.56	11.1	13.9	---	34	---	108	---
4AP-C8	3.59	19589	18744	0.30	0.55	11.0	---	---	---	---	---	---
4AP-C9	3.92	19960	18797	0.18	0.54	10.0	13.0	13.2	58	52	102	184
4AP-C10	4.24	19920	18798	0.20	0.54	10.3	---	---	---	---	---	---
4AP-C12	4.88	19493	18692	0.32	0.57	11.3	14.0	13.5	24	58	118	196

[a]Obtained from shake-flask method; [b]Error bars are provided in Figures 2D and 2E; [c]Calculated from parallax analysis of fluorescence quenching – error ±0.5 Å (from repeated measurements); [d]Obtained from peak-maxima of distributions in Figure 10.11C.

that the 4AP-C*n* probes are located at different positions across the DPPC/water interface, which is in agreement with the stepwise polarity sensed by the probes at this interface. In fact, the location, angle and hydration of few probes at DPPC/water and DOPC/water interfaces obtained from MD simulation provide further explanation (see below).

Although, data on continuous depth-dependent polarity and water gradients are available in the fluid-phase[7,8] and lipidic cubic phase[27] of lipid bilayer, the unique stepwise polarity sensed at the gel-phase lipid interface by the fluorescent probes has not been reported earlier. Marsh, in fluid phase of lipid bilayer found a continuous trapezoid shaped polarity as well as hydration profiles by using ESR of nitroxide probe which remains bound to lipid molecules at 12 different carbon position.[7,8] Freed *et al.*, in case of pure gel-phase ($L_{\beta'}$) lipid bilayer, recently found that the spin-lipids actually get excluded from the lipid bilayers thus forcing the lipid carbon chain to bend significantly.[17] Moreover, in ESR measurement,[18] spin-lipids produce strong background signals due to aggregation. It should also be noted that spin lipids cannot scan polarity profile of lipid/water interfacial region; rather it only gives the polarity profile of alkyl-chain region of the fluid-phase lipid bilayers. On the other hand, Zhong *et al.* observed that tryptophan moiety attached to alkyl chain of different lengths in lipidic cubic phase shows a systematic fluorescence shift, suggesting variation in the hydrophobicity of their local environment at the lipidic interface.[27] Chattopadhyay *et al.* reported red edge excitation shift (REES) of NBD fluorescence to show that the lipid head region (using NBD-PE) and interior of the lipid bilayer (using NBD cholesterol) experience different local solvation in both fluid- and gel-phases.[28] Moreover, Laura and co-workers in their recent study have argued that REES of NBD is insensitive to the hydration and mobility of lipid membranes.[82] Klymechenko *et al.* have used fluorescence of 3-hydroxyflavone derivative (F2N8 and F4N1) attached at different depths across the lipid-bilayer to measure hydration and polarity.[29] They found that polarity and hydration of the lipid bilayer decreases simultaneously with increasing lipid order. However, due to scarcity of suitable probe, a systematic study of polarity profiling and solute interactions at lipid/water interfaces, especially in pure gel-phase was challenging. Present results on 4AP-C*n* probes indicate that this set of probes is better suited for such kind of studies.

10.3.6. Molecular Dynamics Simulation of 4AP-C*n*/lipid Systems

MD simulations have proved to be an efficient method for determining the clear picture of biomolecules at molecular level. Results obtained from MD simulation compliments experimental findings with the detailed molecular interpretations which would have been difficult to obtain from only experiments. A total of eight lipid-probe complexes were simulated for a duration of 300 ns each in fluid-phase DOPC and gel-phase DPPC bilayers, which includes four probes of different chain length (4AP-C3, -C6, -C9 and -C12) in DOPC and four probes (4AP-C3, -C7, -C9 and -C12) in DPPC bilayers (total simulation run of 2.4 μs). Position and angle distributions of these probes in both fluid- and gel-phase of bilayers have been calculated in order to explore the importance of hydration in understanding the local dielectric environment at the interface of lipid bilayers. Figure 10.10 shows snapshot of the MD trajectories representing the most likely position of 4AP-C*n* probes in lipid bilayers and the corresponding plots shows position fluctuation of the centre-of-mass of the 4AP-moiety in 4AP-C*n* molecules at the lipid/water interfaces of gel-phase DPPC and fluid-phase DOPC bilayers. Position fluctuations were found to be smaller at the interface of gel-phase DPPC bilayer, thus showing a distinct difference in the average position values of the probes. On an average 4AP-C3 is found to stay near the carbonyl groups of bilayers, while the other probes are located much below the carbonyl region. More so, probes have large fluctuation in their positions at the fluid-phase DOPC/water interface over the entire 300 ns, showing that their average positions are near the carbonyl groups of the lipids in one leaflet of the bilayer.

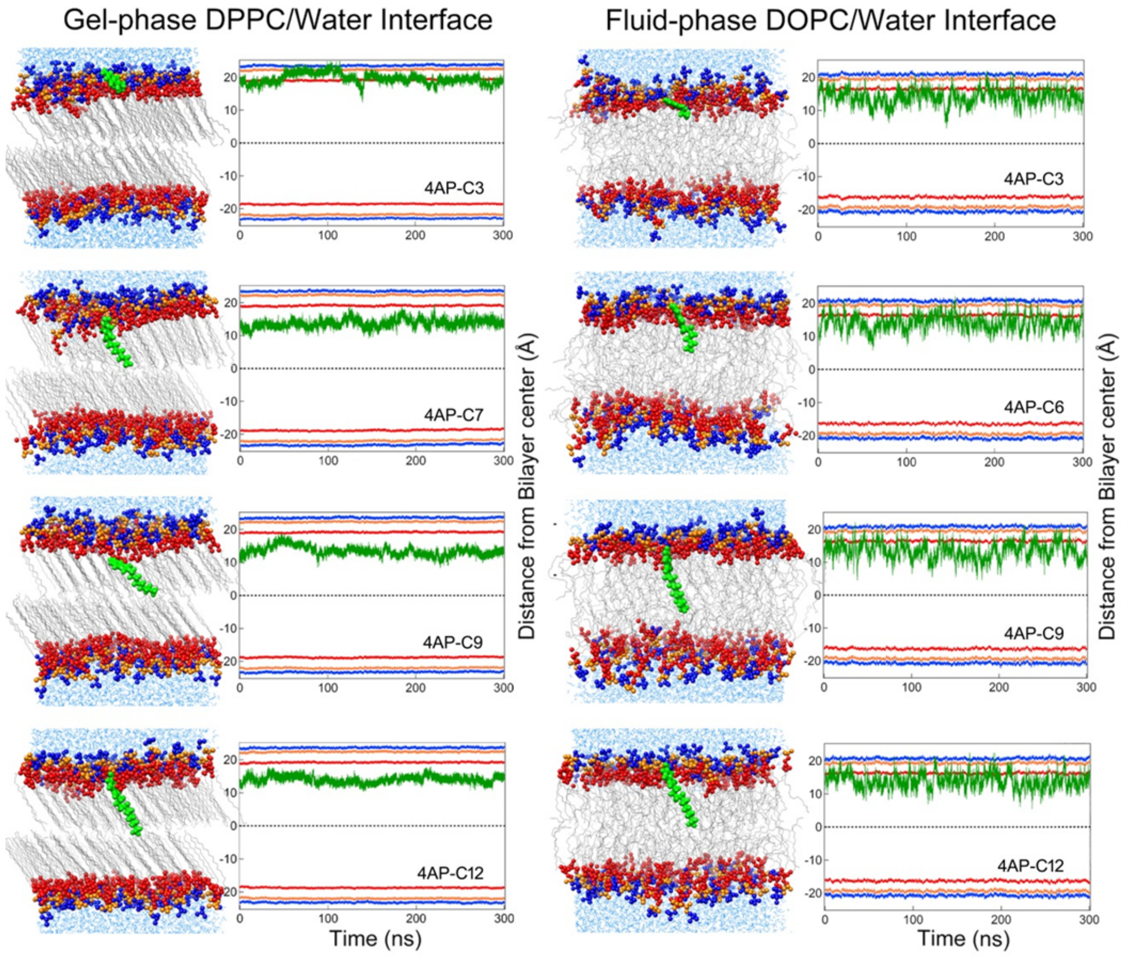

Figure 10.10: Static picture of MD simulation showing most likely positions of 4AP-C*n* probes at lipid/water interface of gel-phase DPPC and fluid-phase DOPC bilayers. Fluctuations of positions of probes throughout 300 ns of simulation are also plotted. Color code: light blue – water molecules; Blue – choline-groups, orange – phosphate-groups, red – glycerol along with carbonyl-groups, gray – hydrocarbon-tails of lipids; green – 4AP-C*n* probes.

10.3.7. Position Distribution of Probe

Position distributions of 4AP-C*n* probes in DOPC and DPPC bilayers were determined by monitoring the z-axis positions fluctuations of the centre-of-mass of the 4AP-moiety in the probes. Z-axis position of choline groups, phosphate and glycerol along with the carbonyl group of each leaflets were taken as reference position (see Figure 10.10). The position distributions of 4AP-moiety of each probe in DOPC and DPPC bilayers were compared with reference to the centre of lipid bilayers (Figure 10.11A and Table 10.2). Positions of the probes obtained from MD simulation can be correlated with the polarity profile scanned by them at the lipid/water interface of both the bilayers. Position distributions of probes in case of rigid gel-phase DPPC bilayer show a systematic drift towards deeper region (Figure 10.11A). This systematic change in position of probes shows similar trend as that of local polarity, i.e. probes residing at shallow region senses higher E_N^T value as compared to

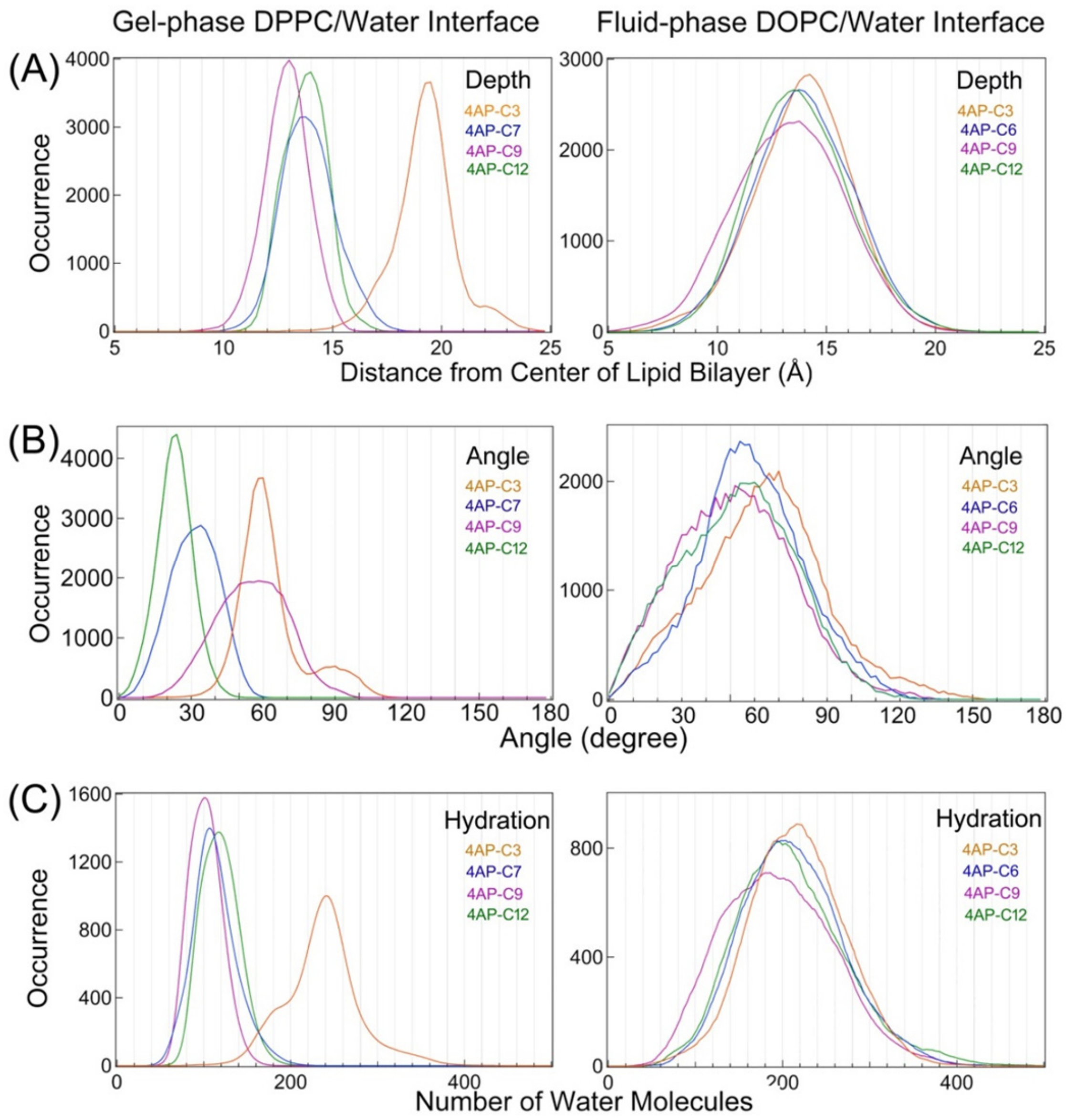

Figure 10.11: Plots showing distributions of (A) probe position, (B) angle and (C) hydration at DPPC/water interface in its gel-phase (shown in left panels) and DOPC/water interface in its fluid-phase (shown in right panel), obtained from simulated trajectories.

deeply located probes (see Figures 10.7A and 10.11A). Peak positions of 4AP-C3 and 4AP-C9 show a difference of ~6.5 Å, which shows a maximum change from 0.53 to 0.18 in E_N^T values (Table 10.2). It was difficult to obtain this depth information from parallax experiments in DPPC vesicles as most of the quenchers were excluded and/or perturb the gel-phase of DPPC/water interface. More importantly, it was found that 4AP-C7 and –C12 show similar distribution of their z-axis positions over the 300 ns simulation, indicating that these probes can sense nearly identical local dielectric environment at the lipid/water interface, similar as observed in experimental findings (Table 10.2 and Figures 10.7A and 10.11A).

However, position distributions of probes at labile DOPC/water interface have been found to be much broader, showing only a subtle change among themselves (Figure 10.11A). The most likely position of 4AP-C3 and –C9 at the labile interface of DOPC shows a difference of ~1.1 Å, compared to difference of ~3.1 Å obtained from parallax experiment. This difference in simulation and experimental results can be due to the large error introduced in the final results of fluorescence quenching through parallax method (± 0.5 Å in this case). Moreover, it could also be possible that within broad range of position fluctuations, a subset of probes come near the quenchers and get quenched by bromine-quenchers the most, as compared to the distant ones, which ultimately results in the deviation seen between experimental and simulation results. It is important to note that, 4AP-C6 and –C12 shows similar position distributions which can be related to the polarity sensed at DOPC/water interface by these two probes. This may result from the fact that alkyl chain of 4AP-C12 interacts with the lipid chains of opposite leaflets, which in due course is pushed back towards water –resulting into higher E_N^T value sensed by 4AP-C12 in comparison to –C9 (or –C10). Earlier studies using fluorescent probes such as NBD-C*n* at lipid/water interface of fluid-phase POPC bilayer prompts similar depth variation (~2 Å) between NBD-C2 and NBD-C8. However, insertion of NBD-probes into lipid-bilayers did not show any appreciable change in the quantum yield and fluorescence spectra. In fact, it has been indicated by a recent study that the fluorescence of NBD-probes is insensitive to the hydration and mobility of lipid-membranes. The present study, however, has indicated that fluorescence of 4AP-C*n* probes is highly sensitive and responsive to subtle change in the local environment at the lipid/water interfaces of both fluid- and gel-phase, which can ultimately scan and account for the position dependent polarity at the interfaces of these bilayers.

10.3.8. Angle Distribution of Probe

Inclination angle of the probes (4AP-moiety) relative to the bilayer normal was calculated by determining the angle formed between the vector connecting N2 and C2 atoms of fluorescent 4AP-moiety and normal to lipid bilayer (see Figure 10.12). Angle distributions and corresponding peak positions are given in Figure 10.11B and Table 10.2, respectively. At DPPC/water interface, the distributions of the relative angles of

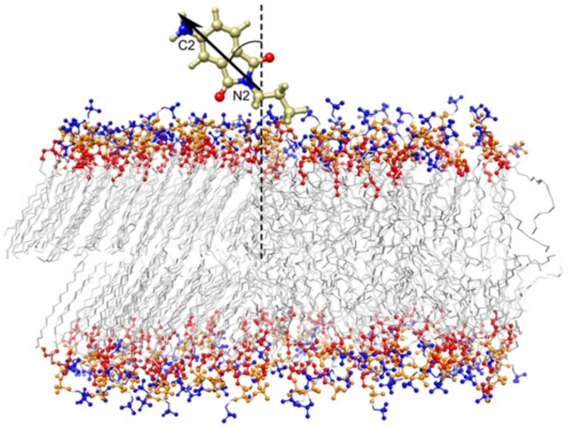

Figure 10.12: Cartoon showing the angle of 4AP-moiety (defined as the angle formed by vector connecting N2 and C2 of 4AP-moiety and normal to lipid bilayer) used for determining the angle-distributions of probes at the DOPC/water and DPPC/water interfaces from simulation trajectories.

the 4AP-C*n* probes show interesting characteristics: a broader angle distribution has been found in case of 4AP-C3 and –C9 showing nearly identical values of most probable angle. A second peak at ~90˚ with fewer occurrences is also seen for 4AP-C3 (see Figure 10.11b). The angle distributions of other probes sharpen systematically and drift toward smaller angles of ~34˚ for 4AP-C7 and ~24˚ for –C12. However, the angle distributions are significantly broadened at the labile interface of DOPC bilayer which shows a small, but systematic shift in the most probable angle from higher to smaller values for 4AP-C3 to –C9, with a reverse trend for 4AP-C12. Significance of probe-orientation in defining the local dielectric environment was found after its comparison with the distribution of water around the probes as discussed below.

10.3.9. Hydration of Probes at the Interfaces

Distribution of number of water molecules that stay within a region of 10 Å from 4AP-moiety has been calculated over 300 ns trajectory of each simulation. This region of 10 Å was chosen because earlier studies on DNA have shown that the dipolar/charged molecules that comes within ~9-15 Å of the probe-site govern the electrostatic solvation response of the probe.[83,84] Although, at DPPC/water interface, it has been found that the probable position of 4AP-C7 and –C12 are very similar, yet they show different relative hydration. 4AP-C7 has access to smaller number of water molecules (~108) than that around 4AP-C12 (~118) (Figure 10.11C). This difference in the relative hydration can arise due to the inclination angle of 4AP-C7 (~34˚) which is more tilted towards lipid bilayer as compared to the inclination angle of 4AP-moiety of –C12 (~24˚). This results into larger number of water molecules around 4AP-moiety of C12, thus making the local environment slightly polar (E_N^T = 0.33) as compared to –C7 (E_N^T = 0.30). Further interesting properties were observed for 4AP-C3, where the effect of dual peak in the angle distribution is reflected in the (nearly) mirror-imaged distribution of water molecules at lipid/water interface of DPPC, i.e., a subset of 4AP-moiety of C3 probes with larger angle (more inclined towards bilayer) has access to less number of water molecules as compared to less inclined (smaller angle) probes (see Figures 10.11B and 10.11C). These results validate the fact that exposure of probes toward water molecules is also controlled by their orientation. Similarly, the 4AP-C9 probes that are deeply located with larger inclination angle towards bilayer (*ca* 58˚) have less access to water molecules, resulting into less polar surrounding compared to others as seen in experimental results (see Figures 10.11B and 10.11C). The above findings indicate that apart from probes position, its orientation also governs the local solvation by changing the probe's access to the water molecules at the interface. In fact, a substantial effect of probe orientation on the local solvation at liquid/liquid and air/water interfaces have been anticipated by earlier experimental and simulation studies,[85] although similar effect at lipid/water interface has not been reported. This result, thus confirms the effect of probe's orientation at lipid/water interface. The effect of probe orientation at labile DOPC/water interface seems to be small or could not be determined accurately due to large fluctuations of angle, position and hydration of the probes, leading to broader distributions – all of which following the same trend. Nevertheless, at the interface of DOPC, the relative depth of the probe along with the orientation would apparently affect the local dielectric environment sensed by the 4AP-C*n* probes.

10.3.10. Perturbation of Bilayer by Incorporation of Probes

Area per lipid and deuterium order parameter of carbon chains of DOPC and DPPC in presence and absence of probes were calculated from the simulated trajectories to check the amount of perturbation induced by the incorporation of these fluorescent 4AP-C*n* probes.

10.3.10.1. Area per Lipid

Inter- and intra-molecular interactions affect the area per lipid of DOPC and DPPC bilayers, thus sensitivity of area per lipid to such interactions indicates whether the phase of lipid bilayer at a given temperature is maintained or not. Area per lipid is defined as the average area occupied by individual phospholipid, which can be calculated by dividing the size of the box in X and Y direction (Box-*X* × Box-*Y*) by the total number of lipids present in each leaflet. Area per lipid calculated from MD simulation for DOPC and DPPC bilayers in absence and presence of probes are given in Table 10.3. The calculated values of area per lipid from simulated trajectories for both DOPC and DPPC bilayers in absence and presence of fluorescent probes were found to be very similar and in well agreement with the previous reported experimental values.[86,87] This shows that the penetration of 4AP-C*n* probes into the fluid-phase DOPC and gel-phase DPPC bilayers is insignificant.

Table10.3: Area per lipid for different lipid-probe systems calculated from simulated trajectories and obtained from earlier experiments.

Lipid Bilayers	**Area per lipid (Å^2)**	
	Simulation[a]	**Experiment**
DPPC (only)	48.8 ± 0.5	47.2 ± 0.5[b]
DPPC with 4AP-C3	49.1 ± 0.4	--
DPPC with 4AP-C7	49.2 ± 0.4	--
DPPC with 4AP-C9	49.1 ± 0.4	--
DPPC with 4AP-C12	48.9 ± 0.4	--
DOPC (only)	66.4 ± 1.2	67.4 ± 0.1[c]
DOPC with 4AP-C3	66.3 ± 1.3	--
DOPC with 4AP-C6	66.0 ± 1.2	--
DOPC with 4AP-C9	66.1 ± 1.2	--
DOPC with 4AP-C12	66.5 ± 1.2	--

10.3.10.2. Order Parameter of Lipid Chain

Carbon-deuterium order parameters, S_{CD}, measures the order of per atom of carbon tail of lipid bilayer.[88,89] These order parameters are sensitive to the chain orientation and is expressed as,

$$S_{CD} = \frac{1}{2} < 3\cos^2\theta - 1 > \qquad (10.3)$$

where, θ is the angle formed between the vector joining i^{th} carbon to its hydrogen atom (as in simulation) or to deuterium atom (in experiments) and the bilayer normal. Time and ensemble average is represented by '< >'. Analysis module, g_order of GROMACS was used to compute the order parameter of lipid chains. To determine the perturbation induced by the penetration of the probes into lipid bilayers, ordering of the methylene carbons of *sn*-1 and *sn*-2 lipid tails of DOPC and DPPC bilayers with and without the probes were calculated and compared in Figure 10.13. From the order parameter of lipid chain of DOPC bilayers, it was found that the perturbation induced by the penetration of probes in fluid-phase bilayer is almost negligible and the *sn*-1 and *sn*-2 carbon chains retain initial configuration, whereas the orientation of lipid chain in gel-phase DPPC bilayer shows a change of ~3-7%. However, taking into account the rigidness of DPPC bilayer in its gel-phase, such small effect of probe's incorporation on lipid-chain is not surprising. This effect on DPPC bilayer is even smaller than that reported for perturbation on lipid-chains

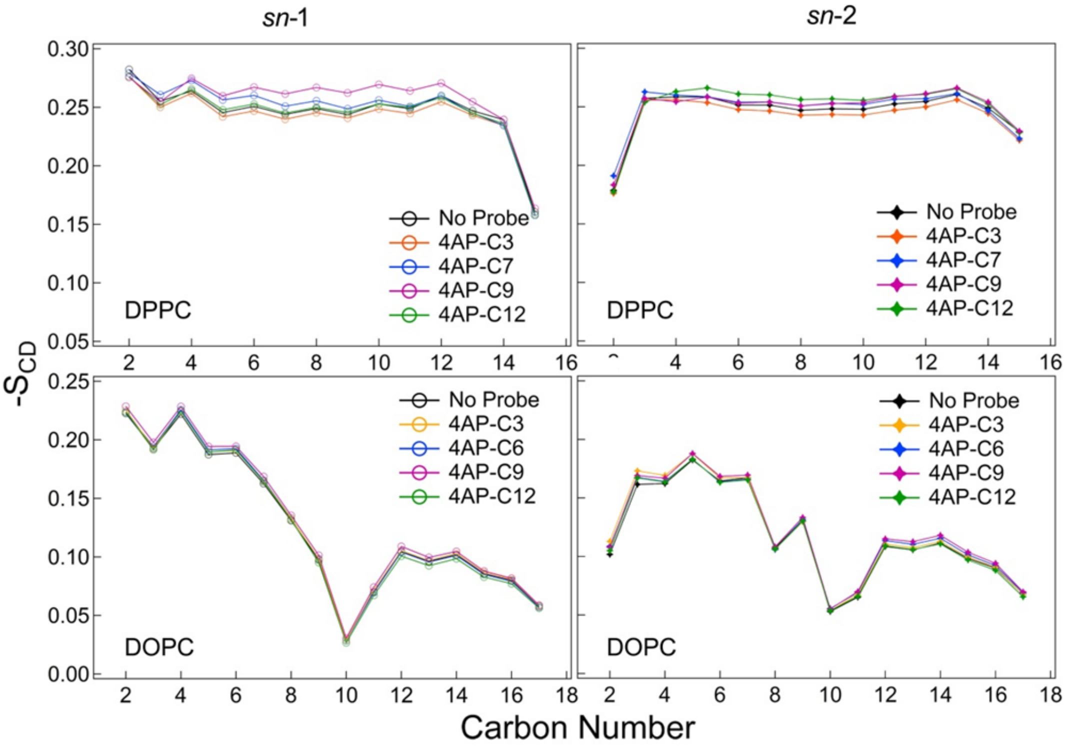

Figure 10.13: Comparison of deuterium order parameters of methylene carbons connected to *sn*-1 (panels in left) and *sn*-2 (panels in right) tail of DPPC and DOPC bilayer (of one leaflet) in presence and absence of 4AP-C*n* probes obtained from simulated trajectories.

after incorporation of probes such as DiI and NBD in even fluid-phase bilayers. These results suggest that the lipid bilayer in its gel-phase is barely perturbed by the introduction of 4AP-C*n* probes, whereas the perturbation of the fluid-phase of lipid bilayer is almost negligible. All the above results indicate that the 4AP-C*n* probes are much better suited than any other ESR or fluorescent probes to explore the (static) solvation properties and physiochemical characteristics of lipid membranes.

10.4. Conclusion

This chapter showed solvation properties at various positions of lipid/water interfaces as scanned by synthesized 4AP-C*n* fluorescent probes in fluid- and gel-phase lipid bilayers. Such measurements could have been difficult using ESR and other fluorescent probes. This study clearly stated that fluorescent 4AP-C*n* probes are much more suitable for exploring position-dependent solvation properties at lipid/water interfaces. It is believed that various other significant interfaces can also be explored using these probes. This study showed that hydration characteristics at the lipid/water interface of gel-phase bilayers are much more complex than the solvation properties of fluid-phase bilayers. These complex properties are manifested in the hydration and polarity at the two interfaces sensed by the homologues series of 4AP-C*n* probes. Comparison of experimental and simulation results showed that probe's orientation along with its position plays significant role in governing the local dielectric environment by modulating water access to the probe molecules at interface of lipid and water. 4AP-C*n* senses a stepwise polarity at the lipid/water interface of gel-phase DPPC bilayer which may actually have much broader importance. This stepwise behaviour may suggest the presence of four distinct regions where the entrapment and penetration of solute of varying hydrophobicity is controlled by solvation free energy. This may, in turn, have different effects on the fundamental biochemical reactions taking place at the fluid-phase lipid bilayers compared to the gel-phase bilayers, because the rate of chemical reactions is controlled by local solvation. Nevertheless, further experimental and long MD simulation studies are required to explicate the intricate picture of position-dependent hydration and polarity, along with its significance in the chemical reactions occurring at the lipid/water interfaces of various membranes.

The current study indeed showed that 4AP-C*n* can actually serve as excellent set of fluorescent molecules for study of various static and dynamic properties of lipid/water interfaces, including solvation dynamics, FRET and other photophysical processes with unprecedented details. This is because, these probes have the capability to adsorb at different depths across the lipid/water interface based on their relative lipophilicity – leading to a situation where properties of lipid bilayers and their water interfaces can be depicted by these probes at sub-nanometer length scale which is generally difficult to comprehend with existing fluorescence techniques. Hence, use of a set of these 4AP-C*n* probes would help to unfold the changes of local properties of regions that are only few angstroms apart. Thus, it is believed that 4AP-C*n* probes will serve several important purposes toward understanding the static and dynamic properties of lipid interfaces at unprecedented level in future as well.

References

1 Martin, D. R.; Lebard, D. N.; Matyushov, D. V. Coulomb Soup of Bioenergetics: Electron Transfer in a Bacterial Bc 1 Complex. *J. Phys. Chem. Lett.* **2013**, *4*, 3602-3606.

2 Fu, R.; Gordon, E. D.; Hibbard, D. J.; Cotten, M. High Resolution Heteronuclear Correlation NMR Spectroscopy of an Antimicrobial Peptide in Aligned Lipid Bilayers: Peptide-Water Interactions at the Water-Bilayer Interface. *J. Am. Chem. Soc.* **2009**, *131*, 10830-10831.

3 Miller, A. S.; Falke, J. J. Side Chains at the Membrane-Water Interface Modulate the Signaling State of a Transmembrane Receptor. *Biochemistry*, **2004**, *43*, 1763-1770.

4 Kuang, G.; Liang, L.; Brown, C.; Wang, Q.; Bulone, V.; Tu. Y. Insight into the Adsorption Profiles of the Saprolegnia Monoica Chitin Synthase MIT Domain on POPA and POPC Membranes by Molecular Dynamics Simulation Studies. *Phys. Chem. Chem. Phys.* **2016**, *18*, 5281-5290.

5 Xiang, T. X.; Anderson, B. D. Liposomal Drug Transport: A Molecular Perspective from Molecular Dynamics Simulations in Lipid Bilayers. *Adv. Drug Deliver Rev.* **2006**, *58*, 1357–1378.

6 Wang, S.; Larson, R. G. Water Channel Formation and Ion Transport in Linear and Branched Lipid Bilayers. *Phys. Chem. Chem. Phys.* **2014**, *16*, 7251-7262.

7 Marsh, D. Polarity and Permeation Profiles in Lipid Membranes. *Proc. Natl. Acad. Sci. USA* **2001**, *98*, 7777-7782.

8 Marsh, D. Membrane Water-Penetration Profiles from Spin Labels. *Eur. Biophys. J.* **2002**, *31*, 559-562.

9 Disalvo, E. A. *Membrane Hydration: Role of Water in Structure and Function of Biological Membranes*. Springer, Switzerland, **2015**.

10 Cipolla, D.; Shekunov, B.; Blanchard, J.; Hickey, A. Lipid-Based Carriers for Pulmonary Products: Preclinical Development and Case Studies in Humans. *Adv. Drug Deliver Rev.* **2014**, *75*, 53–80.

11 Maruyama, K. Intracellular Targeting Delivery of Liposomal Drugs to Solid Tumors Based on EPR Effects. *Adv. Drug Deliver Rev.* **2011**, *63*, 161-169.

12 Forster, V.; Signorell, R. D.; Roveri, M.; Leroux, J. C. Liposome-Supported Peritoneal Dialysis for Detoxification of Drugs and Endogenous Metabolites. *Sci. Transl. Med*. **2014**, 6, 258.

13 Damitz, R.; Chauhan, A. Parenteral Emulsions and Liposomes to Treat Drug Overdose. *Adv. Drug Deliver Rev.* **2015**, *90*, 12-23.

14 Dvinskikh, S. V.; Castro, V.; Sandstrom, D. Probing Segmental Order in Lipid Bilayers at Variable Hydration Levels by Amplitude- and Phase-Modulated Cross-Polarization NMR. *Phys. Chem. Chem. Phys.* **2005**, *7*, 3255-3257.

15 Gawrisch, K.; Ruston, D.; Zimmerberg, J.; Parsegian, V. A.; Rand, R. P.; Fuller, N. Membrane Dipole Potentials, Hydration Forces, and the Ordering of Water at Membrane Surfaces. *Biophys. J.* **1992**, *61*, 1213-1223.

16 Volke, F.; Eisenblatter, S.; Klose, G. Hydration Force Parameters of Phosphatidylcholine Lipid Bilayers as Determined from 2H-NMR Studies of Deuterated Water. *Biophys. J.* **1994**, *67*, 1882–1887.

17 Dzikovski, B.; Tipikin, D.; Freed, J. Conformational Distributions and Hydrogen Bonding in Gel and Frozen Lipid Bilayers: A High Frequency Spin-Label ESR Study. *J. Phys. Chem. B* **2012**, *116*, 6694-6706.

18 Earle, K. A.; Moscicki, J. K.; Ge, M.; Budil, D. E.; Freed, J. H. 250-GHz Electron Spin Resonance Studies of Polarity Gradients along the Aliphatic Chains in Phospholipid Membranes. *Biophys. J.* **1994**, *66*, 1213-1221.

19 Nagle, J. F.; Tristram-Nagle, S. Structure of Lipid Bilayers. *Biochim. Biophys. Acta*. **2000**, *1469*, 159-195.

20 Tristram-Nagle, S.; Petrache, H. I.; Nagle, J. F. Structure and Interactions of Fully Hydrated Dioleoylphosphatidylcholine Bilayers. *Biophys J.* **1998**, *75*, 917-925.

21 Haldar, S.; Chaudhuri, A.; Chattopadhyay, A. Organization and Dynamics of Membrane Probes and Proteins Utilizing the Red Edge Excitation Shift. *J. Phys. Chem. B* **2011**, *115*, 5693-5706.

22 Chattopadhyay, A. Chemistry and Biology of N-(7-nitrobenz-2-oxa-1,3-diazol-4-yl)-Labeled Lipids: Fluorescent Probes of Biological and Model Membranes. *Chem. Phys. Lipids.* **1990**, *53*, 1-15.

23 Mojumdar, S. S.; Ghosh, S.; Mondal, T.; Bhattacharyya, K. Solvation Dynamics under a Microscope: Single Giant Lipid Vesicle. *Langmuir* **2012**, *28*, 10230-10237.

24 Filipe, H. A. L.; Bowman, D.; Palmeira, T.; Cardoso, R. M. S.; Loura, L. M. S.; Moreno, M. J. Interaction of NBD-Labelled Fatty Amines with Liquid-Ordered Membranes: A Combined Molecular Dynamics Simulation and Fluorescence Spectroscopy Study. *Phys. Chem. Chem. Phys.* **2015**, *17*, 27534-27547.

25 Cardoso, R. M. S.; Filipe, H. A. L.; Gomes, F.; Moreira, N. D.; Vaz, W. L. C.; Moreno, M. J. Chain Length Effect on the Binding of Amphiphiles to Serum Albumin and to POPC Bilayers. *J. Phys. Chem. B* **2010**, *114*, 16337-13646.

26 Cardoso, R. M. S.; Martins, P. A. T.; Gomes, F.; Doktorovova, S.; Vaz, W. L. C.; Moreno, M. J. Chain-Length Dependence of Insertion, Desorption, and Translocation of a Homologous Series of 7-Nitrobenz-2-oxa-1,3-diazol-4-yl-Labeled Aliphatic Amines in Membranes. *J. Phys. Chem. B* **2011**, *115*, 10098-10108.

27 Kim, J.; Lu, W.; Qiu, W.; Wang, L.; Caffrey, M.; Zhong, D. Ultrafast Hydration Dynamics in the Lipidic Cubic Phase: Discrete Water Structures in Nanochannels. *J. Phys. Chem B* **2006**, *110*, 21994-2000.

28 Chattopadhyay, A.; Mukherjee, S. Red Edge Excitation Shift of a Deeply Embedded Membrane Probe: Implications in Water Penetration in the Bilayer. *J. Phys. Chem. B* **1999**, *103*, 8180-8185.

29 Klymchenko, A. S.; Mely, Y.; Demchenko, A. P.; Duportail, G. Simultaneous Probing of Hydration and Polarity of Lipid Bilayers with 3-Hydroxyflavone Fluorescent Dyes. *Biochim. Biophys. Acta* **2004**, *1665*, 6-19.

30 Choudhury, S. D.; Kumbhakar, M.; Nath, S.; Pal, H. Photoinduced Biomolecular Electron Transfer Kinetics in Small Unilamellar Vesicles. *J. Chem. Phys*. **2007**, *127*, 194901.

31 Jurkiewicz, P.; Cwiklik, L.; Jungwirth, P.; Hof, M. Lipid Hydration and Mobility: An Interplay between Fluorescence Solvent Relaxation Experiments and Molecular Dynamics Simulations. *Biochimie* ***2012***, *94*, 26-32.

32 Mondal, J. A.; Nihonyanagi, S.; Yamaguchi, S.; Tahara, T. Three Distinct Water Structures at a Zwitterionic Lipid/Water Interface Revealed by Heterodyne-Detected Vibrational Sum Frequency Generation. *J. Am. Chem. Soc*. **2012**, *134*, 7842-7850.

33 Mondal, J. A.; Nihonyanagi, S.; Yamaguchi, S.; Tahara, T. Structure and Orientation of Water at Charged Lipid Monolayer/Water Interfaces Probed by Heterodyne-Detected Vibrational Sum Frequency Generation Spectroscopy. *J. Am. Chem. Soc*. **2010**, *132*, 10656-10657.

34 Chen, X.; Hua, W.; Huang, Z.; Allen, H. C. Interfacial Water Structure Associated with Phospholipid Membranes Studied by Phase-Sensitive Vibrational Sum Frequency Generation Spectroscopy. *J. Am. Chem. Soc*. **2010**, *132*, 11336-11342.

35 Qiao, B.; de la Cruz, M. O. Driving Force for Water Permeation across Lipid Membranes. *J. Phys. Chem. Lett*. **2013**, *4*, 3233-3237.

36 Re, S.; Nishima, W.; Tahara, T.; Sugita, Y. Mosaic of Water Orientation Structures at a Neutral Zwitterionic Lipid/Water Interface Revealed by Molecular Dynamics Simulations. *J. Phys. Chem. Lett*. **2014**, *5*, 4343-4348.

37 Zhou, F.; Schulten, K. Molecular Dynamics Study of a Membrane-Water Interface. *J. Phys. Chem*. **1995**, *99*, 2194-2207.

38 Marrink, S. J.; Berendsen, H. J. C. Permeation Process of Small Molecules across Lipid Membranes Studied by Molecular Dynamics Simulations. *J. Phys. Chem.* **1996**, *100*, 16729-16738.

39 Filipe, H. A. L.; Moreno, M. J.; Loura, L. M. S. Interaction of 7-Nitrobenz-2-oxa-1,3-diazol-4-yl-labeled Fatty Amines with 1-Palmitoyl, 2-Oleoyl-sn-glycero-3-phosphocholine Bilayers: A Molecular Dynamics Study. *J. Phys. Chem*. B **2011**, *115*, 10109-10119.

40 Nitschke, W. K.; Vequi-Suplicy, C.; Coutinho, K.; Stassen, H. Molecular Dynamics Investigations of PRODAN in a DLPC Bilayer. *J. Phys. Chem. B* **2012**, *116*, 2713-2721.

41 Song, K. C.; Livanec, P. W.; Klauda, J. B.; Kuczera, K.; Dunn, R. C.; Im, W. Orientation of Fluorescent Lipid Analogue BODIPY-PC to Probe Lipid Membrane Properties: Insights from Molecular Dynamics Simulations. *J. Phys. Chem. B* **2011**, *115*, 6157-6165.

42 Parisio, G.; Marini, A.; Biancardi, A.; Ferrarini, A.; Mennucci, B. Polarity-Sensitive Fluorescent Probes in Lipid Bilayers: Bridging Spectroscopic Behavior and Microenvironment Properties. *J. Phys. Chem. B* **2011**, *115*, 9980-9989.

43 Murugan, N. A.; Apostolov, R.; Rinkevicius, Z.; Kongsted, J.; Lindahl, E.; Agren, H. Association Dynamics and Linear and Nonlinear Optical Properties of an N-acetylaladanamide Probe in a POPC Membrane. *J. Am. Chem. Soc.* **2013**, *135*, 13590-13597.

44 Barucha-Kraszewska, J.; Kraszewski, S.; Ramseyer, C. Will C-laurdan Dethrone Laurdan in Fluorescent Solvent Relaxation Techniques for Lipid Membrane Studies? *Langmuir* **2013**, *29*, 1174-1182.

45 Ackerman, D. G.; Heberle, F. A.; Feigenson, G. W. Limited Perturbation of a DPPC Bilayer by Fluorescent Lipid Probes: A Molecular Dynamics Study. *J. Phys. Chem. B* **2013**, *117*, 4844-4852.

46 Pilgram, G. S. K.; Meulen, J. V. R.; Gooris, G. S.; Koerten, H. K.; Bouwstra, J. A. The Influence of two Azones and Sebaceous Lipids on the Lateral Organization of Lipids Isolated from Human Stratum Corneum. *Biochim. Biophys. Acta* **2001**, *1511*, 244-254.

47 Raguz, M.; Mainali, L.; O'Brien, W. J.; Subczynski, W. K. Lipid Domains in Intact Fiber-Cell Plasma Membranes Isolated from Cortical and Nuclear Regions of Human Eye Lenses of Donors from Different Age Groups. *Exp. Eye Res*. **2015**, *132*, 78-90.

48 Chattopadhyay, A.; London, E. Parallax Method for Direct Measurement of Membrane Penetration Depth Utilizing Fluorescence Quenching by Spin-Labeled Phospholipids. *Biochemistry* **1987**, *26*, 39-45.

49 Krishnan, K. S.; Balaram, P. Perturbation of Lipid Structures by Fluorescent Probes. *FEBBS Lett*. **1975**, *60*, 419-422.

50 Ashcroft, R. G.; Thulborn, K. R.; Smith, J. R.; Coster, H. G. L.; Sawer, W. H. Perturbations to Lipid Bilayers by Spectroscopic Probes as Determined by Dielectric Measurements. *Biochim. Biophys. Acta* **1980**, *602*, 299-308.

51 Kranenburg, M.; Smit, B. Phase Behaviour of Model Lipid Bilayers. *J. Phys. Chem. B* **2005,** *109*, 6553-6563.

52 Sen, S.; Yamaguchi, S.; Tahara, T. Different Molecules Experience Different Polarities at the Air/Water Interface. *Angew. Chem. Int. Ed.* **2009**, *48*, 6439-644.

53 Steel, W. H.; Walker, R. A. Measuring Dipolar Width across Lipid-Lipid Interfaces with Molecular Rulers. *Nature* **2003**, *424*, 296-299.

54 Wang, H.; Borguet, E.; Eisenthal, K. B. Generalised Interface Polarity Scale Based on Second Harmonic Spectroscopy. *J. Phys. Chem. B* **1998**, *102*, 4927-4932.

55 Reichardt, C. Solvatochromic Dyes as Solvent Polarity Indicators. *Chem. Rev.* **1994**, *94*, 2319-2358.

56 Paul, A.; Samanta, A. Solute Rotation and Solvation Dynamics in an Alcohol-Functionalized Room Temperature Ionic Liquid. *J. Phys. Chem. B* **2007**, *111*, 4724-4731.

57 Ingram, J. A.; Moog, R. S.; Ito, N.; Biswas, R.; Maroncelli, M. Solute Rotation and Solvation Dynamics in Room-Temperature Ionic Liquids. *J. Phys. Chem. B* **2003**, *107*, 5926-5932.

58 Lipinski, C. A.; Lombardo, F.; Dominy, B. W.; Feeney, P. J. Experimental and Computational Approaches to Estimate Solubility and Permeability in Drug Discovery and Development Settings. *Adv. Drug Deliv. Rev.* **1997**, *23*, 3-25.

59 Saroja, G.; Samanta, A. Hydrophobicity-Induced Aggregation of N-alkyl-4-aminophthalimides in Aqueous Media Probed by Solvatochromic Fluorescence. *J. Chem. Soc. Faraday Trans.* **1998**, *94*, 3141-3145.

60 Sangster, J. Octanol-Water Partition Coefficients of Simple Organic Compounds. *J. Phys. Chem. Ref. Data.* **1989**, *18*, 1111-1227.

61 Frisch, M. J. et al. *Gaussian 09*, Revision A.02; Gaussian, Inc. Wallingford, CT, **2009**.

62 Cornell, W. D.; Cieplak, P.; Bayly, C. I.; Kollman, P. A. Application of RESP Charges to Calculate Conformational Energies, Hydrogen Bond Energies, and Free Energies of Solvation. *J. Am. Chem. Soc.* **1993**, *115*, 9620-9631.

63 Wang, J.; Wolf, R. M.; Caldwell, J. W.; Kollman, P. A.; Case, D. A. Development and Testing of a General Amber Force. *J. Comput. Chem.* **2004**, *34*, 1157-1174.

64 D. A. Case et al. *AMBER 12*, University of California: San Francisco, **2012**.

65 Sousa da Silva, A.; Vranken, W. ACPYPE- AnteChamber Python Parser InterfacE. *BMC Res. Notes* **2012**, *5*, 367.

66 http://www.fos.su.se/~sasha/SLipids/Downloads.html.

67 Jorgensen, W. L.; Chandrasekhar, J.; Madura, J. D.; Impey, R. W.; Klein, M. L. Comparison of Simple Potential Functions for Simulating Liquid Water. *J. Chem. Phys.* **1983**, *79*, 926-935.

68 Jambeck, J. P. M.; Lyubartsev, A. P. Comparison of Simple Potential Functions for Simulation Liquid Water. *J. Chem. Theory Comput*. **2012**, *8*, 2938-2948.

69 Spoel, D. V. D.; Lindahl, E.; Hess, B.; Groenhof, G.; Mark, A. E.; Berendsen, H. J. C. GROMACS: Fast, Flexible, Free. *J. Comput. Chem.* **2005**, *26*, 1701-1718.

70 Berendsen, H. J. C.; Postma, J. P. M.; Vangunsteren, W. F.; Dinola, A.; Haak, J. R. Molecular Dynamics with Coupling to an External Bath. *J. Chem. Phys.* **1984**, *81*, 3684-3690.

71 Hoover, W. G. Canonical Dynamics: Equilibrium Phase-Space Distributions. *Phys. Rev. A* **1985**, *31*, 1695-1697.

72 Nose, S. A Unified Formulation of the Constant Temperature Molecular Dynamics Methods. *J. Chem. Phys.* **1984**, *81*, 511-519.

73 Hess, B.; Bekker, H.; Berendsen, H. J. C.; Fraaije, J. G. E. M. LINCS: A Linear Constraint Solver for Molecular Simulations**.** *J. Comput. Chem.* **1997**, *18*, 1463-1472.

74 Darden, T.; York, D.; Pedersen, L. Particle Mesh Ewald: A Nlog(N) Method for Ewald Sums in Large Systems. *J. Chem. Phys.* **1993**, *98*, 10089-10092.

75 Essmann, U.; Perera, L.; Berkowitz, M. L.; Darden, T.; Lee, H.; Pedersen, L. G. A Smooth Particle Mesh Ewald Method. *J. Chem. Phys.* **1995**, *103*, 8577-8593.

76 Parrinello, M.; Rahman, A. Polymorphic Transitions in Single Crystals: A New Molecular Dynamics Method. *J. Appl. Phys.* **1981**, *52*, 7182-7190.

77 Pettersen, E. F.; Goddard, T. D.; Huang, C. C.; Couch, G. S.; Greenblatt, D. M.; Meng, E. C.; Ferrin, T. E. UCSF Chimera- A Visualization System for Exploratory Research and Analysis. *J. Comput. Chem.* **2004**, *25*, 1605-1612.

78 Mukamel, S. *Principle of Nonlinear Optical Spectroscopy*, Oxford university press, New York, **1995**.

79 Goldberg, J. M.; Speight, L. C.; Fegley, M. W.; Petersson, E. J. Minimalist Probes for Studying Protein Dynamics: Thioamide Quenching of Selectively Excitable Fluorescent Amino Acids. *J. Am. Chem. Soc.* **2012**, 134, 6088-6091.

80 Abrams, F. S.; Chattopadhyay, A.; London, E. Determination of the Location of Fluorescent Probes Attached to Fatty Acids using Parallax Analysis of Fluorescence Quenching: Effect of Carboxyl Ionization State and Environment on Depth. *Biochemistry* **1992**, *31*, 5322-5327.

81 Abrams, F. S.; London, E. Extension of Parallax Analysis of Membrane Penetration Depth to the Polar Region of Model Membranes: Use of Fluorescent Quenching by a Spin-Label Attached to the Phospholipid Polar Head Group. *Biochemistry* **1993**, *32*, 10826-10831.

82 Amaro, M.; Filipe, H. A.; Prates, J. P. R.; Hof, M.; Loura, L. M. Fluorescence of Nitrobenzoxadiazole (NBD)-Labeled Lipids in Model Membranes is Connected not to Lipid Mobility but to Probe Location. *Phys. Chem. Chem. Phys.* **2016**, *18*, 7042-7054.

83 Pal, N.; Shweta, H.; Singh, M. K.; Verma, S. D.; Sen, S. Power Law Solvation Dynamics in G-Quadruplex DNA: Role of Hydration Dynamics on Ligand Solvation Inside DNA. *J. Phys. Chem. Lett.* **2015**, *6*, 1754-1760.

84 Sen, S.; Andreatta, D.; Ponomarev, S. Y.; Beveridge, D. L.; Berg, M. A. Dynamics of Water and Ions Near DNA: Comparison of Simulation to Time Resolved Stokes-Shift Experiments. *J. Am. Chem. Soc.* **2009**, *131*, 1724-1735.

85 Benjamin, I. Static and Dynamic Spectroscopy at Liquid Interfaces. *Chem. Rev*. **2006**, *106*, 1212-1233.

86 Tristam-Nagle, S.; Zhang, R.; Suter, R. M.; Worthinton, C. R.; Sun, W. J.; Nagle, J. F. Measurement of Chain Tilt Angle in Fully Hydrated Bilayers of Gel Phase Lecithins. *Biophys. J.* **1993**, *64*, 1097-1109.

87 Kucerka, N.; Nagle, J. F.; Sachs, J. N.; Feller, S. E.; Pencer, J.; Jackson, A.; Katsaras, J. Lipid Bilayer Structure Determined by the Simultaneous Analysis of Neutron and X-Ray Scattering Data. *Biophys. J.* **2008**, *95*, 2356-2367.

88 Seelig, J.; Waespe-Sarcevic, N. Molecular Order in Cis and Trans Unsaturated Phospholipid Bilayers. *Biochemistry* **1978**, *17*, 3310-3315.

89 Lafleur, M.; Bloom, M.; Eikenberry, E. F.; Gruner, S. M.; Han, Y.; Cullis, P. R. Correlation Between Lipid Plane Curvature and Lipid Chain Order. *Biophys. J.* **1996**, *70*, 2747-2757.

Volume 18 | Number 35 | 21 September 2016 | Pages 24137–24758

PCCP

Physical Chemistry Chemical Physics

www.rsc.org/pccp

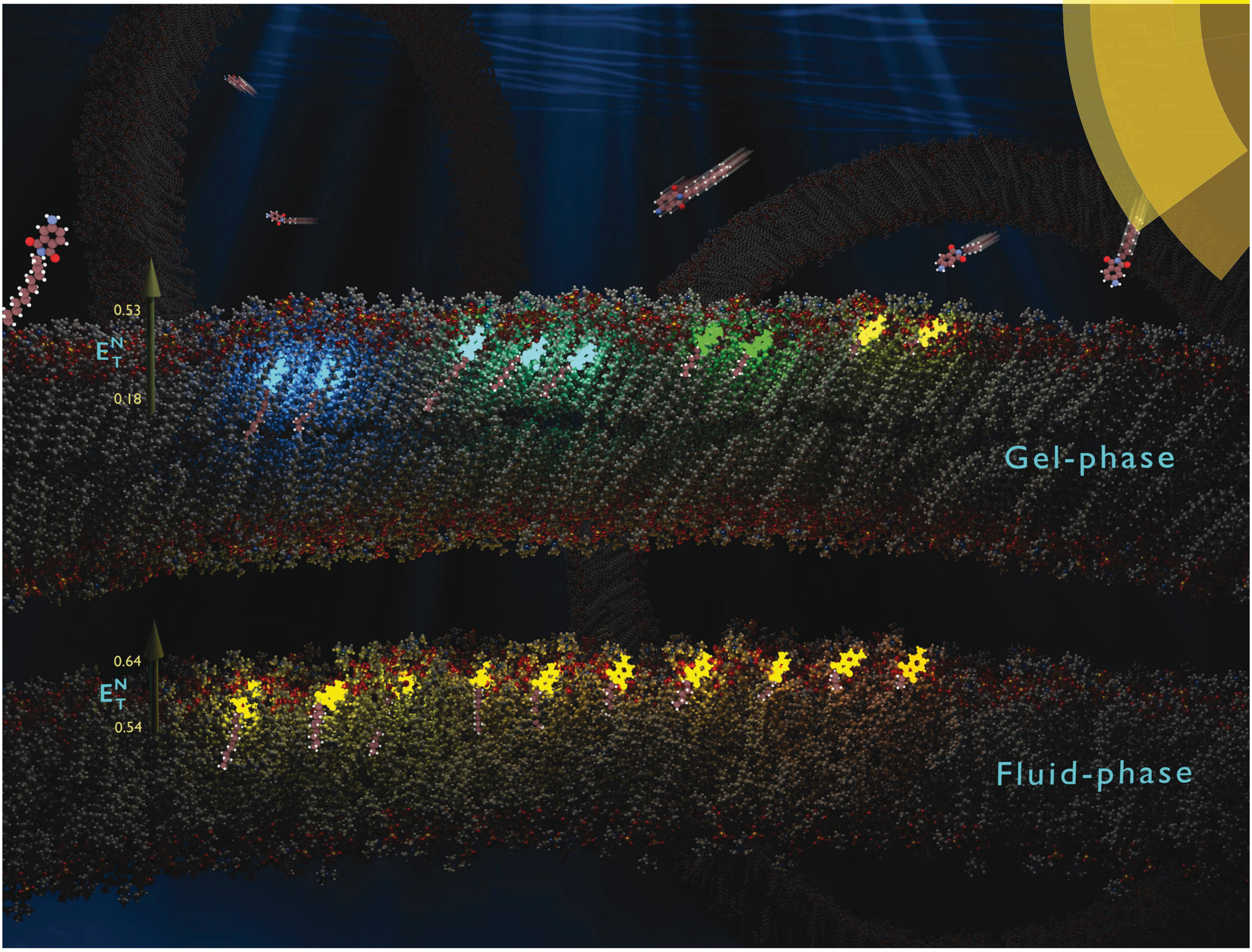

ISSN 1463-9076

ROYAL SOCIETY OF CHEMISTRY

PAPER

Sobhan Sen *et al.*

New insight into probe-location dependent polarity and hydration at lipid/water interfaces: comparison between gel- and fluid-phases of lipid bilayers

175 YEARS

M. K. Singh, H. Shweta, S. Sen *Methods Appl. Fluoresc.* **2016**, *4*, 034009

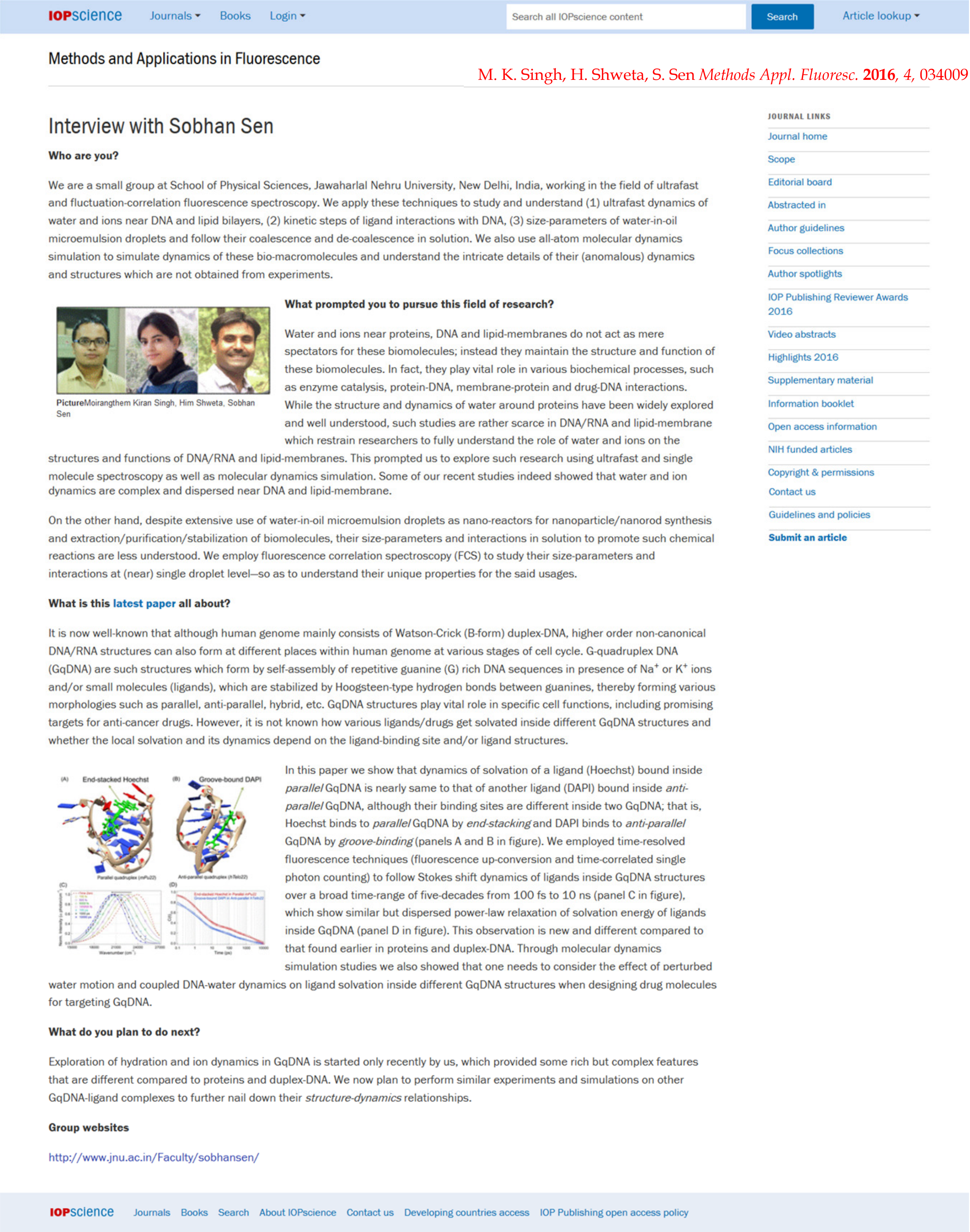

IOPscience Journals Books Login Search all IOPscience content Search Article lookup

Methods and Applications in Fluorescence

Interview with Sobhan Sen

Who are you?

We are a small group at School of Physical Sciences, Jawaharlal Nehru University, New Delhi, India, working in the field of ultrafast and fluctuation-correlation fluorescence spectroscopy. We apply these techniques to study and understand (1) ultrafast dynamics of water and ions near DNA and lipid bilayers, (2) kinetic steps of ligand interactions with DNA, (3) size-parameters of water-in-oil microemulsion droplets and follow their coalescence and de-coalescence in solution. We also use all-atom molecular dynamics simulation to simulate dynamics of these bio-macromolecules and understand the intricate details of their (anomalous) dynamics and structures which are not obtained from experiments.

PictureMoirangthem Kiran Singh, Him Shweta, Sobhan Sen

What prompted you to pursue this field of research?

Water and ions near proteins, DNA and lipid-membranes do not act as mere spectators for these biomolecules; instead they maintain the structure and function of these biomolecules. In fact, they play vital role in various biochemical processes, such as enzyme catalysis, protein-DNA, membrane-protein and drug-DNA interactions. While the structure and dynamics of water around proteins have been widely explored and well understood, such studies are rather scarce in DNA/RNA and lipid-membrane which restrain researchers to fully understand the role of water and ions on the structures and functions of DNA/RNA and lipid-membranes. This prompted us to explore such research using ultrafast and single molecule spectroscopy as well as molecular dynamics simulation. Some of our recent studies indeed showed that water and ion dynamics are complex and dispersed near DNA and lipid-membrane.

On the other hand, despite extensive use of water-in-oil microemulsion droplets as nano-reactors for nanoparticle/nanorod synthesis and extraction/purification/stabilization of biomolecules, their size-parameters and interactions in solution to promote such chemical reactions are less understood. We employ fluorescence correlation spectroscopy (FCS) to study their size-parameters and interactions at (near) single droplet level—so as to understand their unique properties for the said usages.

What is this latest paper all about?

It is now well-known that although human genome mainly consists of Watson-Crick (B-form) duplex-DNA, higher order non-canonical DNA/RNA structures can also form at different places within human genome at various stages of cell cycle. G-quadruplex DNA (GqDNA) are such structures which form by self-assembly of repetitive guanine (G) rich DNA sequences in presence of Na^+ or K^+ ions and/or small molecules (ligands), which are stabilized by Hoogsteen-type hydrogen bonds between guanines, thereby forming various morphologies such as parallel, anti-parallel, hybrid, etc. GqDNA structures play vital role in specific cell functions, including promising targets for anti-cancer drugs. However, it is not known how various ligands/drugs get solvated inside different GqDNA structures and whether the local solvation and its dynamics depend on the ligand-binding site and/or ligand structures.

(A) End-stacked Hoechst (B) Groove-bound DAPI

Parallel quadruplex (mPu22) Anti-parallel quadruplex (hTelo22)

(C) (D)

In this paper we show that dynamics of solvation of a ligand (Hoechst) bound inside *parallel* GqDNA is nearly same to that of another ligand (DAPI) bound inside *anti-parallel* GqDNA, although their binding sites are different inside two GqDNA; that is, Hoechst binds to *parallel* GqDNA by *end-stacking* and DAPI binds to *anti-parallel* GqDNA by *groove-binding* (panels A and B in figure). We employed time-resolved fluorescence techniques (fluorescence up-conversion and time-correlated single photon counting) to follow Stokes shift dynamics of ligands inside GqDNA structures over a broad time-range of five-decades from 100 fs to 10 ns (panel C in figure), which show similar but dispersed power-law relaxation of solvation energy of ligands inside GqDNA (panel D in figure). This observation is new and different compared to that found earlier in proteins and duplex-DNA. Through molecular dynamics simulation studies we also showed that one needs to consider the effect of perturbed water motion and coupled DNA-water dynamics on ligand solvation inside different GqDNA structures when designing drug molecules for targeting GqDNA.

What do you plan to do next?

Exploration of hydration and ion dynamics in GqDNA is started only recently by us, which provided some rich but complex features that are different compared to proteins and duplex-DNA. We now plan to perform similar experiments and simulations on other GqDNA-ligand complexes to further nail down their *structure-dynamics* relationships.

Group websites

http://www.jnu.ac.in/Faculty/sobhansen/

JOURNAL LINKS
- Journal home
- Scope
- Editorial board
- Abstracted in
- Author guidelines
- Focus collections
- Author spotlights
- IOP Publishing Reviewer Awards 2016
- Video abstracts
- Highlights 2016
- Supplementary material
- Information booklet
- Open access information
- NIH funded articles
- Copyright & permissions
- Contact us
- Guidelines and policies
- **Submit an article**

IOPscience Journals Books Search About IOPscience Contact us Developing countries access IOP Publishing open access policy